PHYSI

VOLUME 88

THE PHYSICAL REVIEW

A [illegible] *and theoretical physics established by E. L. Nichols in 1893*

Published by the American [illegible] for the

AMERICAN PHYSICAL [illegible]

Officers

President

J. H. Van Vleck
Harvard University
Cambridge, Massachusetts

Vice-President

Enrico Fermi
Institute for Nuclear [illegible]
University of Chicago
Chicago 37, Illinois

Secretary

K. K. Darrow
Bell Telephone Laboratories
Office
Columbia University
New York 27, New York

Treasurer

G. B. Pegram
Columbia University
New York 27, New York

Local Secretary for the Pacific Coast

J. Kaplan
University of California at Los Angeles
Los Angeles, California

Managing Editor

S. A. Goudsmit
Brookhaven National Laboratory
Upton, Long Island
New York

BOARD OF EDITORS

Editor

S. A. Goudsmit

Associate Editors

Harvey Brooks	M. Goldhaber	W. R. [illegible]
E. F. Caswell	R. Hofstadter	F. G. Houtermans
C. L. Critchfield	A. W. Lawson	W. E. Parker
S. Devons	A. Pais	Conyers Herring
T. H. Johnson	B. Serber	H. W. Lewis
Hans Bethe	C. H. Townes	Associate Secretary

Manuscripts for publication should be submitted to S. A. Goudsmit, Brookhaven National Laboratory, Upton, Long Island, New York. The authors' institutions are requested to pay a publication charge of $10 per page which, if honored, entitles them to 100 free reprints; additional ones will be sent at cost price.

Proof and all correspondence concerning papers in the process of publication should be addressed to the Publication Manager, American Institute of Physics, 57 East 55 Street, New York 22, New York.

Subscription Price

United States and Canada $10.00
Elsewhere $10.00

Bank Numbers[1]

Yearly bound number rate when complete year is available:
Prior to 1940: $25.00
Thereafter: $33.00

Single copies: $3.00 each, prior to July, 1929;
$1.50 each, July, 1929–December, 1941;
$3.00 each, January, 1942–December, 1945;
$1.50 each, thereafter.

General Index: 1913–1926: $4.00.

Subscriptions, renewals, and orders for back numbers should be addressed to the American Institute of Physics, 57 East 55 Street, New York 22, New York.

Changes of address in the case of members of the American Physical Society should be addressed to the Treasurer; in the case of other subscribers to the American Institute of Physics.

[1] For Society Journal of Physics Department, Cornell University, Ithaca, New York.

The Physical Review is published semi-monthly on 16 and 30 Lemon Street, Lancaster, Pennsylvania.

Entered as second-class matter August 6, 1947, at the Post Office at Lancaster, Pennsylvania, under the Act of March 3, 1879.

Acceptance for mailing at special rate of postage provided for in Section 34.40, P. L. & R. of 1948, authorized January 10, 1950.

THE
PHYSICAL REVIEW

A journal of experimental and theoretical physics established by E. L. Nichols in 1893

SECOND SERIES, VOL. 88, NO. 5 DECEMBER 1, 1952

Magnetic Analysis of the $Al^{27}(d,p)Al^{28}$ Reaction*

H. A. ENGE,† W. W. BUECHNER, AND A. SPERDUTO
Laboratory for Nuclear Science and Engineering, Massachusetts Institute of Technology, Cambridge, Massachusetts
(Received August 4, 1952)

Thin aluminum targets have been bombarded with 1.8-, 2.0-, and 2.1-Mev deuterons. Protons emerging at 90 degrees with respect to the deuteron beam have been analyzed in a magnetic spectrograph. Fifty proton groups have been assigned to the $Al^{27}(d,p)Al^{28}$ reaction, corresponding to the ground state and forty-nine excited states in Al^{28} between 0 and 6.35 Mev. Most of the levels form clusters, and spacings as low as 13 kev have been observed.

I. INTRODUCTION

SINCE the $Al^{27}(d,p)Al^{28}$ reaction was first observed in 1934 by Lawrence and Livingston,[1] it has been studied by a number of workers[2–11] in order to determine the positions of the energy levels in Al^{28} and the angular distribution of the protons in the various groups. A total number of fifteen proton groups assigned to Al^{28} levels has been reported.

Around 8-Mev excitation energy, the Al^{28} level structure has been investigated by Henkel and Barschall[12] by measurements of the neutron cross section in Al^{27}. The level density they find seems to be unusually high when comparison is made with neighboring nuclei at the same or higher excitation energies. It may therefore seem reasonable to expect a comparatively high level density at lower excitation energies in Al^{28} as well.

In this paper are reported the results of measurements on the $Al^{27}(d,p)Al^{28}$ reaction made with a 180-degree magnetic spectrograph. The Q value of the ground state and the existence of a 31-kev level have been previously reported.[13,14] This low-lying level has recently also been observed by Smith and Anderson,[15] who have found a 31.4-kev gamma-ray from aluminum targets bombarded with deuterons. Forty-eight more proton groups have now been assigned to energy levels in Al^{28} up to an excitation energy of 6.35 Mev. This large number of levels could not have been observed by previous workers for reasons of resolution.

The gamma-rays from the $Al^{27}(n,\gamma)Al^{28}$ reaction have been studied by Kinsey *et al.*,[16] using a pair spectrometer. Twenty-nine of the gamma-energies observed, taken in conjunction with the results of the present work, may be assigned to transitions from the capture state to an excited state or from an excited state to the ground state.

II. EXPERIMENTAL ARRANGEMENT

The apparatus and experimental techniques were essentially the same as those that have been described in previous papers.[17,13] Deuterons accelerated in the

* This work has been supported by the joint program of the ONR and AEC. Part of it was reported at the meeting of the American Physical Society in Washington, D. C., April 26, 1951, Phys. Rev. **83**, 212 (1951).
† On leave from the University of Bergen, Bergen, Norway.
[1] E. O. Lawrence and M. S. Livingston, Phys. Rev. **45**, 220 (1934).
[2] E. McMillan and E. O. Lawrence, Phys. Rev. **47**, 343 (1935).
[3] Schulz, Davidson, and Ott, Phys. Rev. **58**, 1043 (1940).
[4] H. R. Allan and C. A. Clavier, Nature **158**, 832 (1946).
[5] H. R. Allan and C. R. Wilkinson, Proc. Roy. Soc. (London) **194A**, 131 (1948).
[6] Pollard, Sailor, and Wyly, Phys. Rev. **75**, 725 (1949).
[7] Y. A. Nemilov and B. L. Funshtein, Dokl. Akad. Nauk, SSSR, **66**, 369 (1949).
[8] W. D. Whitehead and N. P. Heydenburg, Phys. Rev. **79**, 99 (1950).
[9] J. R. Holt and C. T. Young, Proc. Roy. Soc. (London) **A63**, 833 (1950).
[10] H. E. Gove, Phys. Rev. **81**, 364 (1951).
[11] K. K. Keller, Phys. Rev. **84**, 884 (1951).
[12] R. L. Henkel and H. H. Barschall, Phys. Rev. **80**, 145 (1950).
[13] Enge, Buechner, Sperduto, and Van Patter, Phys. Rev. **83**, 31 (1951).
[14] Enge, Van Patter, Buechner, and Sperduto, Phys. Rev. **81**, 317 (1951).
[15] R. D. Smith and R. A. Anderson, Nature **168**, 429 (1951).
[16] Kinsey, Bartholomew, and Walker, Phys. Rev. **83**, 519 (1951).
[17] Buechner, Strait, Stergiopoulos, and Sperduto, Phys. Rev. **74**, 1569 (1948).

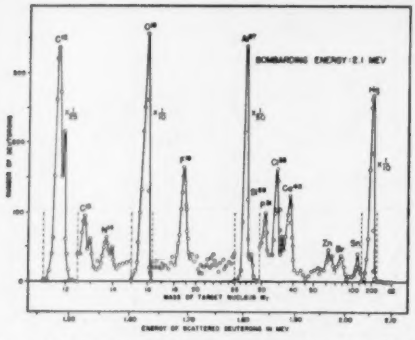

FIG. 1. Mass spectrum of aluminum-on-Formvar target obtained by observing elastically scattered deuterons.

field of an electrostatic generator were focused and deflected 90 degrees through a magnetic analyzer. After passing through a defining slit, the horizontal beam hit the target which was placed between the annular-shaped pole pieces of the magnetic spectrograph. Charged particles leaving the target at 90 degrees with respect to the incident beam were analyzed in the 180-degree, single-focusing spectrograph. Eastman Kodak NTA nuclear-track plates were used for recording the charged particles. Discrimination between protons, deuterons, and alpha-particles was made on the basis of differences in track lengths. Only results from the (d,p) and (d,d) reactions are presented in this paper, the $Al^{27}(d,\alpha)Mg^{25}$ reaction being reported elsewhere.[19] The tracks were counted under a microscope in strips of 0.23 or 0.50 millimeter in width, and the number of tracks in each strip was plotted *versus* strip distance from the target or *versus* $H\rho$.

Because of the complexity of the Al^{28} spectrum, it was necessary to improve the resolution of the apparatus for the present work. This was accomplished partly by reducing the width of the exposed strip of the target to 0.3 mm and partly by reducing the solid angle of the charged-particle bundle admitted through the spectrograph.

Experience has shown that the surface contamination collected on a target during exposures is of uneven thickness so that it affects the energy spread, or width, of the observed peaks of charged particles as well as their position in the $H\rho$ diagram. To minimize this effect, a liquid-air trap was mounted in the vacuum line between the 90-degree analyzer and the spectrograph. This trap collected most of the bothersome vapors that presumably originated in rubber gaskets and stopcock grease.

The excitation current for the spectrograph magnet was stabilized to about 1 part in 15,000 and the current for the 90-degree analyzer, to about 1 part in 5000.

The resolution obtained was $(H\rho)/\Delta(H\rho)\approx 1500$ at the upper end of the observed proton spectrum (390 kilogauss-centimeters) and 250 at the lower end (150 kilogauss-centimeters).

As in previous experiments in this laboratory, polonium alpha-particles were used to calibrate the fluxmeter of the annular magnet. For this purpose, the target was replaced by a silver wire coated with polonium. The value of $H\rho$ for polonium alpha-particles used as an absolute standard was 3.3159×10^3 gauss-centimeters (absolute emu), accurate to 1 part in 5000.

The incident energy of the deuterons was calculated from the observed energy of deuterons elastically scattered from the C^{12} nuclei in a thin Formvar target.

The aluminum targets employed in these experiments were prepared by evaporating aluminum onto Formvar films supported by nickel-wire frames. The 2- to 5-kev thick aluminum targets were found capable of withstanding a 1-microampere beam indefinitely, whereas a Formvar backing alone would break when exposed to more than 0.1 microampere.

III. MASS ANALYSIS OF THE TARGET

In addition to aluminum, the targets with backing and surface contamination contained several other elements, which all had to be considered as possible contributors to the yield of protons from (d,p) reactions. For the correct assignment of the different peaks observed, it was therefore highly desirable to know what elements were present and their relative abundance. In the present case, a quantitative analysis of the target material was most easily performed by aid of the energy spectrum of deuterons elastically scattered from the target.

Figure 1 shows the number of deuteron tracks as a function of the energy of the scattered deuterons. These

TABLE I. Mass analysis of aluminum target on Formvar backing.

Element	Element number Z	Significant isotope M	No. tracks in peak divided by Z^3	Origin
C	6	12, 13	620	Backing and vacuum system
N	7	14	1.9	Vacuum system
O	8	16	103	Backing, Al_2O_3, vacuum system
F	9	19	3.5	Vacuum system?
Al	13	27	100	Evaporated material
Si	14	28	7.2	Vacuum system
P	15	31	0.53	Backing and/or vacuum system
Cl	17	35, 37	0.97	Backing and/or vacuum system
Ca	20	40	0.43	Backing and/or vacuum system
Zn	30	66	0.09	Evaporator
Br	35	81	0.08	Vacuum system
Sn	50	120	0.02	?
Hg	80	202	0.47	Vacuum system

[18] Buechner, Strait, Sperduto, and Malm, Phys. Rev. **76**, 1543 (1949).

[19] Endt, Enge, Haffner, and Buechner, Phys. Rev. **87**, 27 (1952).

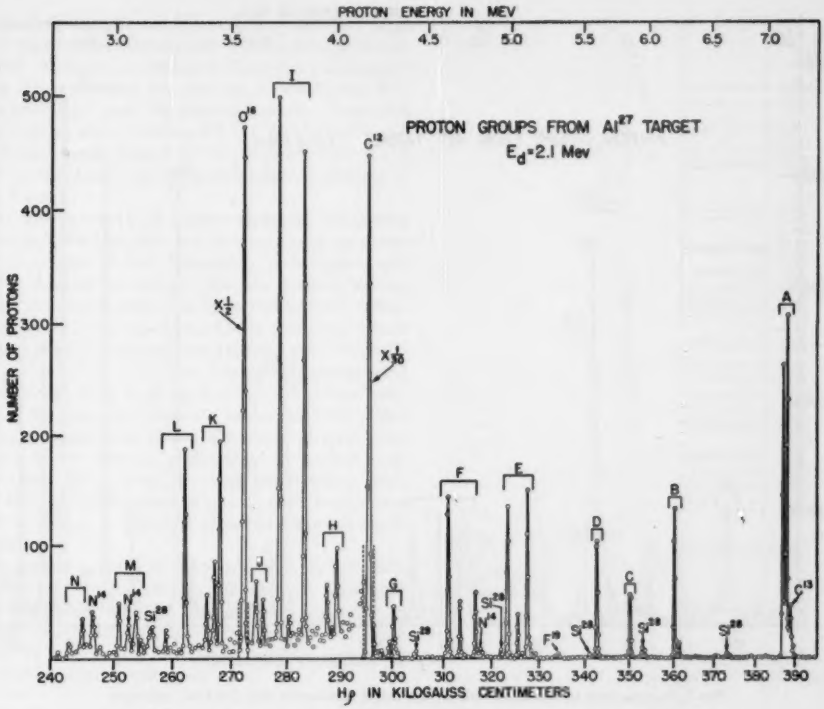

FIG. 2. Protons from an aluminum-on-Formvar target bombarded with 2.1-Mev deuterons.

deuterons were recorded simultaneously with the protons from the (d,p) reactions that took place in the same target. The bombarding energy was 2.1 Mev.

The observed output energy E_{out} is related to the mass of the target nucleus M_T through the equation

$$E_{out}=\frac{M_T-M_D}{M_T+M_D}E_{in}, \tag{1}$$

where M_D is the mass of the deuteron and E_{in} is the bombarding energy. The equation holds for scattering through 90 degrees, the relativistic correction being negligible for the present purpose.

The different peaks of deuterons shown in Fig. 1 have been assigned to different target nuclei according to Eq. (1). Both the energy and mass scales refer to the point of one-third maximum on the right side of a peak.[20] For the elements in the upper region where the resolution is poor, the mass of the heaviest isotope of appreciable abundance has been entered into Eq. (1). Peaks resulting from elements in the backing are displaced slightly to the left of their proper position in the diagram because of the energy loss of the deuterons which penetrated the aluminum layer twice. Peaks resulting from elements distributed through, or on both sides of, the target are broader than the others for the same reason (e.g., N^{14}).

No deuteron peaks were observed above the background in the energy region 0.92 to 1.45 Mev, corresponding to mass numbers 6 through 11. A detectable peak of inelastically scattered deuterons corresponding to the 0.837-Mev level[21] in Al^{27} thus also failed to appear.

Table I gives a list of elements which, according to Fig. 1, have been present in the target. An estimate of relative abundance of the various elements has been obtained by assuming Rutherford scattering. Therefore, the number of tracks in each peak has been divided by the square of the appropriate element number. The resulting figures are given, relative to that for aluminum, in column 4. In column 5, the different elements

[20] The energy scale in Fig. 1 is logarithmic. The mass scale therefore follows the equation $x_\infty - x = k\tanh^{-1}(M_D/M_T)$ and is nearly linear in M_D/M_T as long as this quantity is small.

[21] D. M. Van Patter and W. W. Buechner, Phys. Rev. 87, 54 (1952).

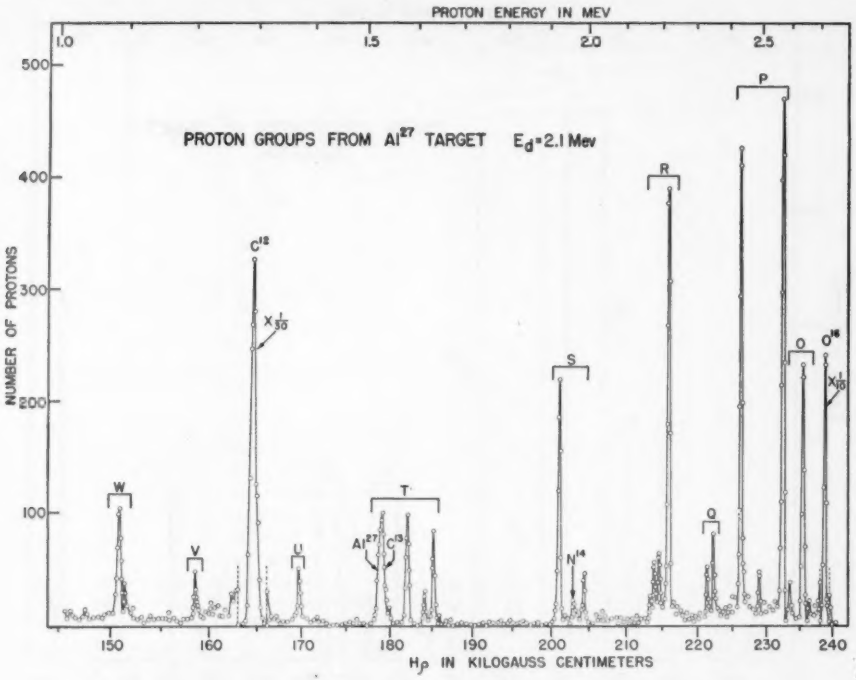

FIG. 3. Protons from an aluminum-on-Formvar target bombarded with 2.1-Mev deuterons.

have been tentatively assigned to backing, evaporated material, or surface contamination resulting from gaskets in the vacuum system. A further investigation as to the origin of the different contaminants is outside the scope of this paper.

IV. ASSIGNMENT OF THE PROTON PEAKS

Figures 2 and 3 give $H\rho$ diagrams of protons from an aluminum target bombarded with 2.1-Mev deuterons. Each exposure on one nuclear track plate covered about 5 percent in $H\rho(\Delta\rho/\rho=0.05)$, so that the whole region of $H\rho$ shown in Figs. 2 and 3 is made up of data from twenty-three exposures at different values of the field strength. The proton peaks that have been assigned to the $Al^{27}(d,p)Al^{28}$ reaction are designated in the figures by capital letters. In many cases, each letter refers to several closely spaced groups. This rather arbitrary division of the groups was chosen for convenience in reference, since, as the work progressed and the performance of the apparatus improved, additional weak peaks were found close to the previously discovered intense groups.

Several surveys were made at 1.5-, 1.8-, 2.0-, and 2.1-Mev bombarding energies.[22] The experimental improvements mentioned above were made while these surveys were in progress. All the proton peaks assigned to the $Al^{27}(d,p)Al^{28}$ reaction appeared in each of the three most recent surveys.

The double structure of the group labeled W in Fig. 3 was observed only in the last survey at maximum resolution. A slight possibility exists that the effect might be due to a double exposure; that is, the magnet current might have been out of control without this having been observed. Further work is required to clear up this point, and group W has been treated as corresponding to one level in the following. There are also some indications of weak structure between the three peaks in group E and between the two peaks in group B. These details will be further investigated with a new magnetic spectrograph which is now under construction.

The mass analysis of the target showed that a number of elements other than aluminum had to be considered as possible contributors to the yield of protons. It should be remembered, however, that at the

[22] The first survey, at 1.5 Mev, was made by K. Huang, B. Sc. thesis, Massachusetts Institute of Technology (May, 1950), unpublished. Because a fairly thick target was used, only fifteen levels in Al^{28} were reported.

bombarding energies used the cross sections for (d,p) reactions decrease very rapidly with increasing atomic number. Moreover, according to Table I, the abundance of the higher elements was very low. In addition to Al^{27}, the nuclei that could be expected to give detectable contributions were therefore C^{12}, C^{13}, N^{14}, O^{16}, F^{19}, and Si^{28}. Proton peaks caused by all of these target nuclei were actually found, and they are labeled accordingly in Figs. 2 and 3.

The sorting out of the peaks was greatly facilitated by the fact that parallel work on other target materials was in progress at this Laboratory. Comparison was made with work on nitrogen, fluorine, sodium, silicon, and phosphorus targets. The strong peaks from carbon and oxygen always appeared and are well known from previous work.[18,23] One of the peaks from the $C^{13}(d,p)C^{14}$ reaction coincided at 2.1-Mev bombarding energy with an aluminum peak in group T, Fig. 3. At other bombarding energies, two separate peaks appeared. Deuterium, nitrogen, and silicon also seem to have been present in all targets, presumably as surface contamination. At the position where the strongest peak from F^{19} could be expected to appear, a few tracks were found as shown in Fig. 2 at $H\rho = 334$ kilogauss-centimeters.

The proton peaks from (d,p) reactions on Si^{29}, Si^{30}, and P^{31} were not detected in the work on aluminum targets. Protons from the $D^2(d,p)T^3$ reaction have at 2.1-Mev bombarding energy approximately the same energy as those from O^{18}. These protons appear at $H\rho = 272$ kilogauss-centimeters.

TABLE II. $Al^{27}(d,p)Al^{28}$ Q values and energy levels in Al^{28}.

Group	Rel int	Q value Mev	Excitation energy Mev	Group	Rel int	Q value Mev	Excitation energy Mev
A_1	100	5.494	0	L_2	5.4	1.379	4.115
A_2	69	5.463	0.031	M_1	19	1.256	4.238
B_2	4.6	4.520	0.974	M_2	13	1.187	4.307
B_1	38	4.479	1.015	N_1	11	1.037	4.457
C	16	4.127	1.367	N_2	11	0.982	4.512
D	35	3.869	1.625	O_1	130	0.808	4.686
E_1	45	3.357	2.137	O_2	17	0.760	4.734
E_2	13	3.296	2.198	P_1	222	0.735	4.759
E_3	40	3.226	2.268	P_2	14	0.657	4.837
F_2	19	3.010	2.484	P_3	170	0.596	4.898
F_3	16	2.916	2.578	Q_1	30	0.506	4.988
F_1	49	2.842	2.652	Q_2	16	0.487	5.007
G_1	18	2.514	2.980	R_1	180	0.366	5.128
G_2	4.6	2.488	3.006	R_2	31	0.338	5.156
H_1	32	2.203	3.291	R_3	26	0.325	5.169
H_2	15	2.152	3.342	R_4	11	0.312	5.182
I_2	121	2.036	3.458	S_2	19	0.122	5.372
I_3	12	1.962	3.532	S_1	92	0.059	5.435
I_1	158	1.907	3.587	T_2	42	−0.241	5.735
J_2	11	1.829	3.665	T_4	13	−0.261	5.755
J_1	15	1.799	3.695	T_1	56	−0.298	5.792
K_1	71	1.621	3.873	T_3	35	−0.361	5.855
K_2	32	1.594	3.900	U	19	−0.517	6.011
K_3	18	1.562	3.932	V	44	−0.696	6.190
L_1	58	1.463	4.031	W	84	−0.813	6.307

[23] Sperduto, Holland, Van Patter, and Buechner, Phys. Rev. **80**, 769 (1950).

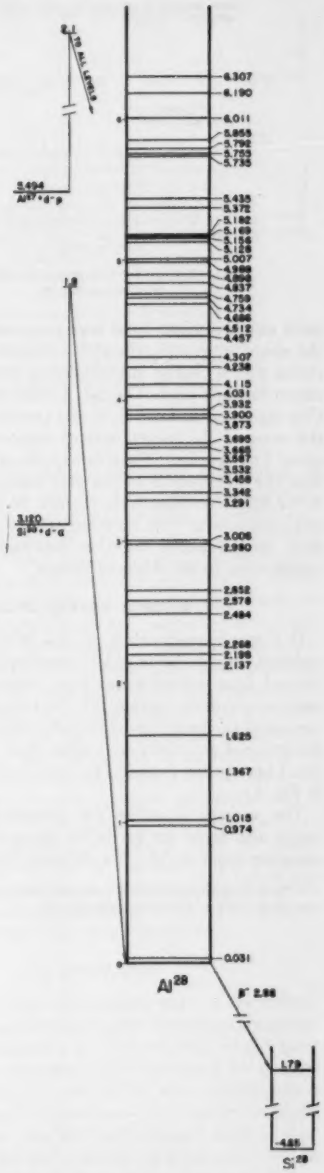

FIG. 4. Energy-level diagram for Al^{28}.

Through the comparison with work on other targets, all proton peaks resulting from contamination nuclei with mass number $A < 35$ were sorted out. Partly in order to rule out the possibility that nuclei of greater

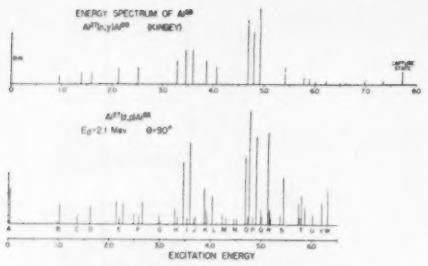

FIG. 5. Energy-level diagrams for Al^{28} with relative intensities.

mass number might have been responsible for any of the observed groups, the shift of proton energy associated with a change in bombarding energy was determined for each peak. Through a relationship similar to that expressed in Eq. (1), it was possible to determine the mass of the target nucleus responsible to within about 5 mass units.[24] These measurements also indicated that the assignments of the fifty proton peaks to the $Al^{27}(d,p)Al^{28}$ reaction were correct. It is felt that the comparison with work on other targets and the energy-shift measurements together provided unambiguous assignments to the observed groups.

V. ENERGY LEVELS IN Al^{28}

Q values corresponding to the fifty proton peaks assigned to the $Al^{27}(d,p)Al^{28}$ reaction have been calculated from experimental data obtained at two or more bombarding energies. Of the individual Q values, averages have been formed for each peak. The maximum deviation of any individual result from these averages was 4 kev for any peak in Fig. 2 and 2 kev for any peak in Fig. 3.

The average Q values are presented in Table II, which also gives the excitation energies of the corresponding levels in Al^{28}. The different levels are marked with the group letter and a subscript denoting a grading according to relative intensity as found under the present experimental conditions.

The probable errors associated with the Q values and excitation energies in Table II have not been evaluated for each level. As regards the Q values, the error for that of the ground state has previously been given as ± 10 kev ($Q = 5.494 \pm 0.010$ Mev[13]). The general trend is a decrease in error for decreasing Q values. The probable errors associated with the excitation energies increase from ± 7 kev for group B to ± 12 kev for the highest levels. Differences between excitation energies for levels in the same group are quite accurately known because the corresponding proton peaks as a rule appeared on the same nuclear-track plate. The directly measured differences have been conserved in the list of excitation energies in Table II. The close spacings between the levels R_2 and R_3 and between R_3 and R_4 have been most accurately measured, as 13.5 ± 1.0 kev and 12.5 ± 1.0 kev, respectively. The excitation energy of the first excited state has previously been given as 31.2 ± 2.0 kev.[13]

The relative intensities given in Table II apply to the number of protons emerging at 90 degrees with respect to the deuteron beam at a bombarding energy of 2.1 Mev.

A conventional energy-level diagram for Al^{28} is presented in Fig. 4. In Fig. 5, lower part, the diagram has a different orientation, and the relative intensities as given in Table II are represented by the height of the lines. The diagram in the upper part of Fig. 5 has been constructed from the (n,γ) results of Kinsey *et al.*[16] It is interesting to note that the maxima and minima in relative intensities have the same locations in the two diagrams.[25]

We are indebted to our colleagues in the High Voltage Laboratory who have collaborated in various stages of this work. We wish to thank all who have assisted in connection with the reading of photographic plates, especially Mrs. Cecilia Bryant, Mr. W. A. Tripp, and Miss Jane Pann.

[24] These measurements were performed with special care in the case of the 31-kev level (see reference 13).

[25] In Fig. 5, upper left, instead of (x 4), read (x 1/4).

Magnetic Lens Spectrometer Measurements of the Radiations from Light Nuclear Reactions*

R. G. THOMAS† AND T. LAURITSEN
California Institute of Technology, Pasadena, California
(Received July 28, 1952)

The radiations from a number of light nuclear reactions are studied with a magnetic lens spectrometer. The γ-ray energies and intensities are determined from the photoelectric and Compton conversion processes; a new method for intensity measurements is developed in which "thick" Compton converters are used. The complicating effects of Doppler shift and broadening on energy determinations are discussed. The following transition energies, obtained from thick targets at bombarding energies from one to two Mev, are reported: $C^{13}(d,n)N^{14}$: 725±4 (assignment uncertain), 1638±8, 2310±12, 3381±13, 5052±25, and 5690±50 kev; $C^{13}(d,p)C^{14}$: 6110±30 kev; $C^{13}(d,p)C^{13}$: 3082±7 kev; $N^{14}(p,\alpha)C^{11}$: 4443±20 kev; $B^{10}(p,\alpha)Be^{7}$: 428.5±1.8 kev; $Li^{6}(d,n)Be^{7}$: 428.9±2 kev; $Li^{6}(d,p)Li^{7}$: 477.4±2 kev; $O^{16}(d,p)O^{17}$: 870.5±2 kev. The internally formed positron distribution from the 3.08-Mev transition in C^{13} is found to be in agreement with the theoretical distribution for an electric dipole transition; the internally formed positron distributions from $C^{13}+d$ and $Be^{9}+d$ are also observed but because of the uncertainty of the background, it is not possible to make unambiguous multipole assignments. The observed internal conversion line spectrum from the 870-kev transition of O^{17} indicates that the transition is electric quadrupole or a mixture of this and magnetic dipole. Semi-empirical formulas are given in the appendix for the most probable and effective energy losses of fast electrons traversing light materials.

I. INTRODUCTION

THE study of gamma-ray transitions in nuclear reactions is an important complement to the identification of energy levels by particle group observations. Not only is it sometimes possible to obtain from gamma-ray measurements more accurate values for the level energies than can be obtained by particle measurement techniques, but often, by observation of cascade transitions, one can derive important information about the character of the levels involved. With quantitative determinations of the relative probabilities of various transitions, one might hope to construct detailed decay schemes which may then be of assistance in establishing spins, parities, and possibly other quantities of fundamental significance pertaining to the levels involved.

The measurement of even relative intensities of gamma-rays poses rather formidable problems. Particularly when the spectrum is complex and extends over a large range of energies, recourse to a variety of techniques may be required. A major part of the present investigation has been devoted to the question of the precise determination of γ-ray intensities from the secondary electron spectra, as observed in a magnetic lens spectrometer. It appears to be possible, using the present techniques, to obtain both relative and absolute γ-ray intensities to an accuracy of five to ten percent, in not-too-unfavorable cases.

Further information about the levels involved in γ-ray transitions can be obtained from the multipole order of the radiation, as determined from the coefficients of internal conversion and internal pair formation. The latter process, which is essentially independent of the nuclear charge and for which the coefficient increases with decreasing multipole order, is particularly useful in the light nuclei, for γ-ray energies above ~ 2 Mev. For the higher energy γ-rays, the conversion electrons and positrons are quite easily detectable, and a comparison of their spectrum with that of the secondary electrons produced by the γ-rays in a suitable converter yields the conversion coefficient directly, without knowledge of either the absolute intensity of the radiation or the solid angle of the spectrometer.

When a "prompt" gamma-ray produced in a nuclear reaction is observed in the direction of the bombarding beam, its energy may be subject to a Doppler shift, depending upon whether the radiation occurs before or after the emitting nucleus comes to rest in the target material. If the nuclei emitting the γ-radiation are traveling in various directions, the line may be broadened. The determination of whether or not Doppler effects occur may enable an estimate of the lifetime of the radiating nucleus, permitting again some inference as to the character of the states involved.

II. APPARATUS

The magnetic lens spectrometer used in the present investigation has been described in a previous communication.[1] Targets located at the focal point of the spectrometer were bombarded by deuterons or protons ranging in energy from 0.9 to 1.6 Mev, entering along the axis. Electrons and positrons produced in the target or in converters attached to the target were focused on an annular slit and counted by means of a Geiger counter with a 2–3 mg/cm² mica window. A helical baffle permitted observation of electrons and positrons

* This work was assisted by the joint program of the ONR and AEC.
† Now at Los Alamos Scientific Laboratory, Los Alamos, New Mexico.

[1] Hornyak, Lauritsen, and Rasmussen, Phys. Rev. 76, 731 (1949).

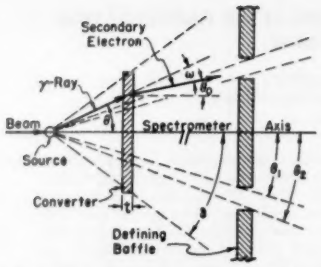

FIG. 1. The spectrometer source-converter-baffle geometry, illustrating a typical gamma-ray conversion process.

separately. Energy calibrations were generally based on the Th I and X lines, at 1754 and 9988 gauss cm, respectively.[2] The instrumental resolution curve was approximately Gaussian, with a width at half-maximum of 2.0 percent, and the effective solid angle, including transmission factor, was about two percent of a sphere.

III. DETERMINATION OF γ-RAY YIELDS AND CONVERSION COEFFICIENTS

The determination of the absolute number of gamma-rays produced in the target depends upon observation of the spectrum of the secondary electrons from a suitable converter. In general one may use the photoelectrons, Compton electrons, or pairs, depending upon the energy range of interest and upon the complexity of the primary spectrum. In each case the interpretation of the results requires consideration of the character of the converter and of the geometry of the instrument.

The source-converter geometry applicable to the present work is schematically illustrated in Fig. 1. The converter is a circular disk centered on the spectrometer axis and perpendicular to it. The axial distance of the converter from the source is ordinarily less than 3 mm and its diameter is 12 mm or less; it subtends an angle 2δ. The limiting acceptance angles of the spectrometer, $\theta_1=13°$ and $\theta_2=27°$, are determined by a circular baffle 16 cm from the source. If the source is produced in a nuclear reaction, the path of the incident beam is coincident with the spectrometer axis, and axial symmetry is maintained throughout. In the conversion process illustrated, θ is the angle between the direction of the gamma-quantum and the axis, ω is the angle between the directions of the gamma-quantum and the ejected electron, and θ_0 is the angle between the direction of the secondary electron and the axis. The dihedral angle between the planes defined by the quantum-electron paths and the quantum-axis directions will be referred to as ψ.

The following quantities are involved in the determination of the converter efficiencies: $\sigma(E)dE$, the total atomic conversion cross section for production of a secondary electron with an energy between E and $E+dE$; $S(\cos\omega)d(\cos\omega)d\psi$, the probability that the secondary electron is ejected into the solid angle $d(\cos\omega)d\psi$; and Y, the yield for a particular radiation from the source, integrated over the sphere. The angular distribution of the primary radiation is assumed to be isotropic so that the differential yield per unit solid angle is $Y/4\pi$ in any direction.

With a flat converter as shown in Fig. 1, the total number of gamma-rays traveling in the solid angle $2\pi d(\cos\theta)$ which eject electrons from a thickness dt into the solid angle $d(\cos\omega)d\psi$ and with energies between E and $E+dE$ is given by

$$(Y/4\pi)2\pi d(\cos\theta)\sigma(E)dENdt\sec\theta\, S(\cos\omega)d(\cos\omega)d\psi \quad (1)$$

$$\text{if } \theta<\delta, \text{ and is zero if } \theta>\delta,$$

where N is the number of atoms per unit volume. (The attenuation of the gamma-radiation has been ignored.) Using the relation $\cos\theta_0=\cos\theta\cos\omega+\sin\theta\sin\omega\cos\psi$, it is possible to integrate (1) over all values of the angles θ and ω, obtaining a result in the form[3]

$$(Y/4\pi)d\Omega_0\sigma(E)dENdt\langle\sec\theta(\theta_0)\rangle, \quad (2a)$$

where

$$\langle\sec\theta(\theta_0)\rangle=\int_{4\pi}S(\cos\omega)\langle\sec\theta(\omega,\theta_0)\rangle d(2\pi\cos\omega) \quad (2b)$$

for the yield of secondary electrons traveling in the solid angle $d\Omega_0=2\pi d(\cos\theta_0)$ and with energies between E and $E+dE$. The kernel $\langle\sec\theta(\theta_0)\rangle$ is interpreted as the average value of $\sec\theta$ for secondary electrons ejected at an angle θ_0 with the axis, and $\langle\sec\theta(\omega,\theta_0)\rangle$ as the average value of $\sec\theta$ for those electrons ejected in the (two) directions characterized by the angles ω and θ_0. The form of the latter kernel depends upon the limits of integration; here we are concerned with the case where $\theta_0+\omega<\delta$ for which

$$\langle\sec\theta(\omega,\theta_0)\rangle=(\cos^2\theta_0-\sin^2\omega)^{-1}. \quad (3)$$

Compton Conversion

The treatment of the energy distribution of the ejected Compton electrons is readily carried out in terms of the quantities $x\equiv(E_\gamma-E_e)/E_\gamma$ and $K\equiv E_\gamma/m_0c^2$, where E_γ is the energy of the incident quantum and E_e is the kinetic energy of the ejected electron. The most energetic secondary electron corresponds to a value $x_{\min}=(1+2K)^{-1}$. The Klein-Nishina cross section for the production of a secondary electron with an energy between x and $x+dx$ can be written as

$$\sigma(x)dx=\pi Zr_0^2K^{-1}f(x)dx, \quad (4)$$

where

$$f(x)=(Kx)^{-2}+x^{-1}(1-2K^{-2}-2K^{-1})+x+K^{-2}+2K^{-1}, \quad (4a)$$

[2] G. Lindstrom, Phys. Rev. **83**, 465 (1951); W. Brown, Phys. Rev. **83**, 271 (1951).

[3] Rasmussen, Hornyak, Lauritsen, and Lauritsen, Phys. Rev. **77**, 617 (1950).

$r_0=e^2/m_0c^2$, and Z is the atomic charge. The angle ω_0 between the initial path of the secondary electron and the incident quantum is given by

$$\sin^2\omega_0=[x(1+2K)-1]/[K^2(1-x)+2K], \quad (5)$$

the angular distribution function of Eq. (1) being the delta-function[4]

$$S(\cos\omega)=(2\pi)^{-1}\delta(\cos\omega-\cos\omega_0). \quad (6)$$

By integrating over the emergence angle θ_0 between the limits θ_1 and θ_2 set by the baffles, we obtain from (2), after substituting (4) and (3),

$$(Y/4\pi)\pi ZNdt\, r_0^2 f(x)K^{-1}dx\, q\langle\sec\theta\rangle\Omega_0, \quad (7)$$

where

$$\langle\sec\theta\rangle\Omega_0=2\pi\log\left\{\frac{\cos\theta_1+(\cos^2\theta_1-\sin^2\omega_0)^{\frac{1}{2}}}{\cos\theta_2+(\cos^2\theta_2-\sin^2\omega_0)^{\frac{1}{2}}}\right\}, \quad (7a)$$

for the number of secondary electrons emerging in the solid angle Ω_0 with energies corresponding to the interval between x and $x+dx$, $q(\leqslant 1)$ being a factor introduced to take into account the spectrometer transmission and counter efficiency. Since the angle ω_0 is small in the interesting high energy portion of the Compton spectrum and since the angles θ_1 and θ_2 are also small, it is evidently permissible to make the approximation[5]

$$q\langle\sec\theta\rangle\Omega_0=\Omega/\langle\cos\theta_0\rangle, \quad (7b)$$

where Ω is an effective solid angle which includes the q factor. If the spectrometer field setting is measured in units of gauss-cm $(B\rho)$,

$$dx=-3.00\times10^{-4}\beta d(B\rho)/E_\gamma, \quad (8)$$

E_γ being measured in Mev and $\beta=v/c$, where v is the velocity of the ejected electron.

For a "thin" converter, that is, a converter in which the electron energy loss is small compared to the energy spread represented by the spectrometer resolution function, expression (7) may, after convolution with the resolution function and the energy-loss distribution [Appendix, Eq. (22)], be matched to the observed spectrum. Adjustment of the parameters K and Y for best fit gives the gamma-ray energy and the yield in terms of the spectrometer constants.[3]

The energy distribution of secondary electrons emerging from a thick Compton converter is obtained by introducing an effective stopping force μ_e, by which the differential electron path length in the direction of the spectrometer acceptance solid angle, $dl/\langle\cos\theta_0\rangle$, is to be multiplied in order to obtain the energy loss in the converter:

$$-dE_e=E_\gamma dx=\mu_e dl/\langle\cos\theta_0\rangle. \quad (9)$$

Substituting (9) into (7) for dl and integrating from $x_{\min}$ to x, we obtain

$$\tfrac{1}{4}Y\Omega ZNr_0^2m_0c^2\mu_e^{-1}F(x)dx, \quad (10)$$

where

$$F(x)=2K^{-1}-\tfrac{1}{2}(1+2K)^{-2}+(1+2K)xK^{-2}+\tfrac{1}{2}x^2 -K^{-2}x^{-1}+(1-2K^{-2}-2K^{-1})\ln x(1+2K) \quad (10a)$$

for the number of electrons emerging from the converter into the spectrometer solid angle Ω in the energy range from x to $x+dx$. The determination of μ_e, which requires rather detailed considerations of the energy loss and scattering mechanisms in the converter, is discussed in the Appendix.

After convolution with the spectrometer resolution function, the distribution given by expression (10) may be compared with the observed spectrum from a thick converter to determine the gamma-ray energy and intensity. Except in the immediate neighborhood of the end point, it is permissible to ignore the curvature of $F(x)$ in the convolution with a symmetric resolution function, and one obtains for the number of counts recorded at the spectrometer field setting $B\rho$:

$$C(B\rho)=\tfrac{1}{4}Y\Omega ZNr_0^2m_0c^2\mu_e^{-1}F(x)\epsilon p B\rho dx/d(B\rho). \quad (11)$$

The factor $\epsilon pB\rho$ is the area under the resolution function,

$$\int_0^\infty R(B'\rho-B\rho)d(B'\rho)=\epsilon pB\rho, \quad (12)$$

where R is normalized to unity at the maximum. The quantity p represents the fractional resolution, and ϵ is a shape factor. For a Gaussian, if p is taken as the full width at half-maximum, $\epsilon=1.064$.

The comparison of expression (11) with the experimental data must be restricted to a rather limited energy range, in view of the assumption that μ_e is constant. For energies above 1 Mev, in aluminum and beryllium converters, however, μ_e varies by only a few percent over the upper 5 percent of the electron spectrum and quite good fits are possible. As a check on the method, we have determined the relative intensity of the two cascade gamma-rays of Na^{24} at 1.37 and 2.76 Mev, obtaining for the ratio, 1.03 ± 0.07. Using a calibrated Co^{60} source to determine the effective solid angle Ω, we obtained agreement within 10 percent of the published[6] value of the absolute yield of 6–7 Mev gamma-rays from $F^{19}(p,\alpha)O^{16*}$ (correcting for the known anisotropy).

Photoelectric Conversion in Thin Foils

It has not been possible to account for the observed thin-converter photoelectric line shapes in a quantita-

[4] A small redistribution in angle due to multiple scattering of electrons in the converter is considered in the Appendix.

[5] To the extent that approximation (7b) applies, the γ-rays whose yield is measured are those emitted in the direction of the spectrometer acceptance cone. Thus if the γ-radiation is not isotropic, the yield obtained is to be regarded as 4π times the differential yield in this direction.

[6] Chao, Tollestrup, Fowler, and Lauritsen, Phys. Rev. 79, 108 (1950).

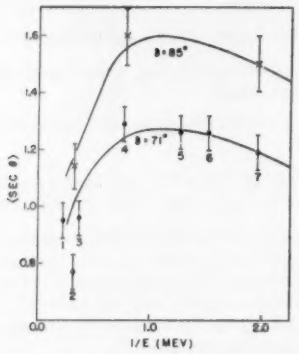

FIG. 2. Measured photoconversion geometrical efficiency factor $\langle\sec\theta\rangle$ plotted as a function of the reciprocal of the γ-ray energy in Mev. The sources used were: 1. $Be^9(p,\alpha)Li^6$, 2. $C^{13}(d,p)C^{13}$, 3. Na^{24}, 4. Co^{60}, 5. Cs^{134}, 6. Cs^{137}, 7. Na^{22}.

tive manner, the difficulty being the lack of precise knowledge concerning the angular distribution in the conversion process and the effects of elastic and inelastic scattering in the high atomic number materials required for this process. Therefore, the total area under the K-conversion line spectrum is used as a measure of the gamma-ray yield. We obtain from (2a) and (12)

$$(Y/4\pi)\Omega\sigma_K Nt\langle\sec\theta\rangle\epsilon p=\int C(B\rho)d\,\ln B\rho, \qquad (13)$$

for the relation between the yield and the area beneath the curve of counts divided by $B\rho$ for a converter of thickness t. The quantity $\langle\sec\theta\rangle$ now represents expression (2b) averaged over the solid angle Ω_0, and Ω includes the transmission factor q.

The total K-shell photoelectric cross section σ_K has been calculated by Hulme *et al.*,[7] for certain values of E_γ and Z. By means of a Z extrapolation of their results, one may obtain this cross section for thorium, the material used here for photoelectric converters, for values of E_γ equal to 1.13 and 0.354 Mev. Using Hall's asymptotic formula[8] it is possible to obtain a value of $\sigma_K{}^{\mathrm{Th}}\cdot E_\gamma$ for $E_\gamma=\infty$. A quadratic expression adjusted to these three values is

$$\sigma_K{}^{\mathrm{Th}}\cdot E_\gamma=0.371(1+0.418E_\gamma{}^{-1}+0.660E_\gamma{}^{-2})\times10^{-28}\ \mathrm{cm}^2, \qquad (14)$$

which is valid if $E_\gamma\geqslant0.3$ Mev. According to the considerations of Hulme *et al.*, such a formula should not be in error by more than about 5 percent, and it is in good agreement with Gray's formula,[9] extrapolated from lead, in the range 0.3 to 1.13 Mev.

[7] Hulme, McDougall, Buckingham, and Fowler, Proc. Roy. Soc. (London) **A149** (1935).
[8] H. Hall, Phys. Rev. **84**, 167 (1951).
[9] L. H. Gray, Proc. Cambridge Phil. Soc. **27**, 103 (1931).

Unfortunately the quantity $S(\cos\omega)$ required for the determination of $\langle\sec\theta\rangle$ is only known through Sauter's equation, which is valid in the limit $Z=0$. Therefore it was necessary to determine $\langle\sec\theta\rangle$ of (13) experimentally, using sources of various energies whose strengths could be obtained in other ways, such as by means of a calibrated Geiger counter or by measurement of the Compton conversion electrons with the spectrometer. Some experiments were performed using radioactive sources such as Na^{22}, Cs^{137}, Co^{60}, Na^{24}, and gamma-radiation from nuclear reactions in order to determine the dependence of $\langle\sec\theta\rangle$ on the converter angle δ, the converter thickness, and E_γ. The details of these measurements will not be given here, but some of the qualitative features of the results are worth mentioning. As regards the dependence on δ, it was observed that for $E_\gamma=1.28$ Mev and a foil thickness of 22 mg/cm^2 (small compared to the scattering length) the geometrical factor could be represented as

$$\langle\sec\theta\rangle=4.2\sin^2(\delta/2), \quad \text{when} \quad 0\leqslant\delta\leqslant85°, \qquad (15)$$

the dependence on δ being even more critical in the case of annihilation radiation. The importance of controlling the angle δ in intensity measurements is thus apparent. Again for $E_\gamma=1.28$ Mev, $\langle\sec\theta\rangle$ was observed actually to increase with increasing foil thickness, roughly according to $\langle\sec\theta\rangle=1.6(1+0.010t)$ for t between 5 and 40 mg/cm^2, when $\delta=85°$. This critical dependence on t for large δ is presumably to be attributed to "scattering in" of electrons originally ejected at large angles to the spectrometer axis. Because of the geometry of the converter and the preference for forward ejection of the electron at high quantum energies, there will be an excess of electrons at large angles, and multiple scattering will increase the number accepted by the spectrometer at the expense of this excess. On the other hand, with a smaller converter angle of $\delta=71°$, $\langle\sec\theta\rangle$ was found to be independent of t, being equal to 1.3 for $t<50$ mg/cm^2. Also with this converter angle, $\langle\sec\theta\rangle$ was measured as a function of E_γ and found to be rather insensitive to energy; the results are shown in Fig. 2 together with several determinations of $\langle\sec\theta\rangle$ with $\delta=85°$. According to the theory, in the limit as $E_\gamma\to\infty$, the photoelectrons are ejected in the direction of the incident quantum and scattering is negligible, so that the geometrical factor becomes equal to the secant of the mean spectrometer acceptance angle, which was 1.06 in these experiments. There is some indication of this tendency in the results presented in Fig. 2.

Those experiments described in Sec. V which involve intensity determinations by means of photoelectric conversion were performed prior to the above-described investigation of the dependence of $\langle\sec\theta\rangle$ on the various factors. It was the practice to use a converter angle δ of about 85° in order to obtain maximum sensitivity, but as we have shown, the factor is rather critical to the exact value of δ and to the converter thickness;

consequently these photoelectric intensity determinations may be in error by 25 percent or more.

It was thought that the complications due to the uncertain angular distribution in the conversion process and the redistribution due to multiple scattering might be avoided by substituting for the flat converter a hemispherical one, centered at the source position. This did not turn out to be the case. The efficiency of such converters were observed to be less than 80 percent, indicating that a significant number of photoelectrons are ejected backwards with respect to the direction of the incident quantum. Furthermore, the line shapes were broad and the efficiency sensitive to the thickness, dropping rapidly with increasing thickness, presumably due to the fact that the electrons have to traverse greater distances in the foil before emerging.

Internal Conversion

As in the case of external photoelectric conversion, a convenient measure of the intensity of an internal conversion process is the total area under the line spectrum. The expression relating this area to the product of the internal conversion coefficient Γ and the yield Y of the associated γ-radiation is obtained from (13) by replacing the external conversion coefficient $\sigma_K N l(\sec\theta)$ with the internal conversion coefficient:

$$(Y/4\pi)\Omega\Gamma\epsilon\rho=\int C(B\rho)d(\ln B\rho). \qquad (16)$$

Thus, if the gamma-ray yield can be measured by means of an external conversion process, Γ can be computed from (16), and multipolarities deduced by comparing Γ with the accurate theoretical values.[10]

Two complications arise in the application of (16) to the determination of Γ from the radiations from nuclear reactions. The first is that the angular distributions of the conversion electrons $\Gamma(\theta)$ and the associated γ-radiation $Y(\theta)$ may not be the same. That is, even ignoring the angular redistributions due to the external conversion process and to scattering, it may not be true that

$$\Gamma(\theta)/Y(\theta)=\int_{4\pi}\Gamma(\theta)d\Omega\Big/\int_{4\pi}Y(\theta)d\Omega, \qquad (17)$$

which is implied by the combined use of (16) and (11), or (13) for the determination of Γ. It remains in each case to examine the extent of the validity of (17) by computing these angular distributions from the assumed spin-parity assignments of all the states involved and their occupation probabilities in the various angular momentum states along the beam-spectrometer axis. From the expressions for the internal conversion and gamma-ray angular distribution functions as obtained by Rose, Biedenharn, and Arfken,[11] it is possible to state that (17) is valid for electric multipole radiation if $E_\gamma \gg m_0c^2$, and for magnetic multipole radiation in the field of low-Z nuclei provided that $E_\gamma \gtrsim m_0c^2$; (17) is, of course, always valid if the radiations are isotropic.

The second complication lies in the determination of the average K-shell occupation probability during the time that the excited nuclei are radiating. These nuclei have initial velocities of the order of $e^2/\hbar$, so that the cross sections for capture and loss of orbital electrons are of the order of the Bohr area. Capture-and-loss equilibrium is established, then, in condensed materials, in about 10^{-16} sec, which is shorter than most gamma-ray lifetimes. From a study of existing experimental and theoretical information on capture and loss ratios as a function of velocity, we conclude that the K-shell occupation probabilities will usually be close to unity even before the nuclei are decelerated.

Internal Pair Formation

In the approximation of representing the positron and electron wave functions by plane waves, formulas have been obtained by Rose[12] for the differential internal pair formation coefficient $\Gamma(w)dw$, for the production of a positron (or electron) of energy w for various electric and magnetic multipoles. End point corrections for $E1$ (electric dipole) and $E2$ (electric quadrupole), obtained by representing the slow particle by means of spherical waves, have been given by Rose and Uhlenbeck.[13] Except near the end point, we can neglect the effect of the spectrometer resolution function on the shape of the distribution, and obtain for the relation between $\Gamma(w)$ and the observed number of counts, $C(B\rho)$, as a function of $B\rho$:

$$(Y/4\pi)\Omega\Gamma(w)\epsilon\rho dw/d(B\rho)=C(B\rho)/B\rho, \qquad (18)$$

with

$$dw/d(B\rho)=5.86\beta\times10^{-4};$$

w is the total electron energy, in units m_0c^2; β is the velocity, in units of c.

When dealing with nuclear reactions where the radiations may not be isotropic, an assumption equivalent to (17) is also involved in the use of (18). It is not possible at present to estimate the validity of this assumption since the internal pair angular distribution functions have not been determined. If the transition energy is very large, however, the angular distribution of the positrons (and electrons) and the associated gamma-radiation will be the same.

From a theoretical point of view, the processes of internal conversion and internal pair formation are similar; in one case an orbital electron is ejected from the surroundings of the nucleus, and in the other case a negative-energy electron in the surroundings of the nucleus is raised to a positive-energy state, the resulting vacancy in the negative energy states being the positron. Therefore, we may expect the same order of magnitude of error to arise from the use of plane waves

[10] Rose, Goertzel, Spinrad, Harr, and Strong, Phys. Rev. **83**, 79 (1951).
[11] Rose, Biedenharn, and Arfken, Phys. Rev. **83**, 5 (1952).
[12] M. E. Rose, Phys. Rev. **76**, 678 (1949); **78**, 184 (1950).
[13] M. E. Rose and G. Uhlenbeck, Phys. Rev. **48**, 211 (1935).

in the internal pair formation process as does in the same approximation in the internal conversion process. When the internal conversion coefficients calculated by Dancoff and Morrison,[14] using relativistic plane waves and neglecting the binding of the orbital electrons, are compared with the calculations using exact Coulomb wave functions made by Rose and his collaborators,[10] considerable deviations are noted, of the order of 10 percent for Z as low as ten and at moderate energies. Thus we may expect similar deviations for the differential pair coefficient $\Gamma(w)$, although as noted by Rose and Uhlenbeck,[13] these deviations tend to cancel at each end point in the determination of the total pair formation coefficient. Unfortunately, in the present experiments it is possible to measure only the high energy portion of the positron distributions and consequently uncertainties of the order of 10 percent must be expected.‡

IV. DOPPLER EFFECTS

The Doppler shift due to the center-of-mass motion and the Doppler broadening due to the angular distribution of the radiating nuclei produced in a disintegration reaction can affect the spectrometer energy determinations by as much as one part in two hundred, which is usually more than the inherent uncertainty in the energy determination from other causes. From studies of such effects, it is sometimes possible to obtain information regarding the lifetimes of the excited nuclei involved, as was done by Elliott and Bell[15] and by Rasmussen, Lauritsen, and Lauritsen[16] in the case of the first excited state of Li^7. The existence or absence of a Doppler shift and broadening depends on whether the nuclei radiate before or after they are significantly decelerated in the target material. A measure of the time required for this deceleration is the ratio of their range to initial velocity; this ratio will be referred to as the stopping time, $T_0 \equiv R/v_0$.

With the geometry shown in Fig. 1, the center-of-mass motion will increase the energy of those quanta which produce secondary electrons in the direction of the spectrometer acceptance cone on the average by the Doppler shift,

$$\delta_s = (v_c/c)E_\gamma\langle\cos\theta\rangle,$$

where v_c is the velocity of the center of mass, E_γ is the quantum energy in the center-of-mass system, and the quantity $\langle\cos\theta\rangle$ will be approximately equal to $\langle\sec\theta\rangle^{-1}$ in the case of photoconversion or to the cosine of the spectrometer (mean) acceptance angle in the case of Compton conversion.

The full extent of the Doppler energy spread due to the angular distribution of the radiating nuclei in the center-of-mass system is given by

$$2\delta_b = 2(v_r/c)E_\gamma,$$

where v_r is their velocity in the center-of-mass system. If the angular distribution in the center-of-mass system is asymmetric about the plane perpendicular to the spectrometer axis, a shift in the observed photoconversion peak may occur. An energy determination by the Compton method, which is primarily based on the high energy edge of the spectrum, will be affected by this broadening even if the angular distribution is symmetric.

In order to determine the extent of the Doppler corrections, it is necessary to know the lifetime τ and the range-velocity relation of the radiating nuclei. For the low initial velocities which occur in the reactions to be studied, cloud-chamber measurements are available[17] on the range-velocity relations (reduced to standard air) of Li^7, C^{12}, N^{14}, O^{16}, Ne^{20}, and some heavier ions. The interpolation between these data, which is required to obtain the values for other light nuclei, can be accomplished with reasonable accuracy by means of the empirical expression,

$$R_{\text{air}}(\text{cm}) \sim 3\times10^{-10} M_1 Z_1^{-0.5} v - R_0,$$

for $v \gtrsim 1\times10^8$ and $Z_1 \lesssim 20$, where M_1 and Z_1 are the mass- and charge-numbers of the ion and v its velocity in cm/sec. For velocities $\sim 0.01c$ this expression appears to fit the experimental data with an accuracy of about 35 percent, which is adequate for the present purpose. The quantity R_0, which is rather small ($\sim\frac{1}{2}$ mm), and the restriction on v have to do with nuclear collision effects which are of negligible importance here.[18] Since there is no experimental information on the stopping powers relative to air of the stopping materials for these nuclei, we assume them to be the same as the stopping powers for protons or alpha-particles of the same velocity. The recent data of Warshaw[19] and others indicate that in the low velocity region the Bragg Z^1 dependence is probably adequate for interpolation.

Since the range is a nearly linear function of the

[14] S. M. Dancoff and P. Morrison, Phys. Rev. **55**, 122 (1939).

‡ *Note added in proof:* Dr. Rose has kindly pointed out to us that the error introduced by use of the Born approximation may be expected to be much less in the case of internal pair formation than in the internal conversion process, since no bound state is involved in the former.

[15] L. G. Elliott and R. E. Bell, Phys. Rev. **76**, 168 (1949); **74**, 1869 (1948).

[16] Rasmussen, Lauritsen, and Lauritsen, Phys. Rev. **75**, 199 (1949).

[17] C. W. Gilbert, Proc. Cambridge Phil. Soc. **44**, 447 (1948); J. K. Bøggild, Kgl. Danske Videnskab. Selskab, Mat.-fys. Medd. **23**, No. 4 (1945); N. Feather, Proc. Roy. Soc. (London) **141**, 194 (1933); G. A. Wrenshall, Phys. Rev. **57**, 1095 (1940); P. Blackett and D. Lees, Proc. Roy. Soc. (London) **A134**, 658 (1932); W. W. Eaton, Phys. Rev. **48**, 921 (1935); J. T. McCarthy, Phys. Rev. **53**, 30 (1938); R. L. Anthony, Phys. Rev. **50**, 726 (1936); W. Hansen and G. A. Wrenshall, Phys. Rev. **57**, 750 (1940).

[18] The linear dependence upon v reflects the predominant influence of capture and loss on the stopping phenomenon. Theoretical arguments for heavy ions in heavy substances suggest a Z_1^{-1} dependence and, for stopping materials other than air, a stopping power proportional to $Z_2^{\frac{1}{2}}$. See N. Bohr, Kgl. Danske. Videnskab. Selskab, Mat.-fys. Medd XVIII, 8 (1948) and Phys. Rev. **57**, 275 (1941).

[19] S. D. Warshaw, Phys. Rev. **76**, 1759 (1951).

velocity at low velocities, the time consumed in reducing the velocity of the nucleus from v_0 to v is approximately

$$t = T_0 \ln(v_0/v).$$

Thus, T_0 is actually the time required to reduce the velocity to $1/e$ of its initial value. The distribution of Doppler shifts due to the center-of-mass motion is immediately given in terms of the lifetime by

$$P(\delta)d\delta = \xi x^{\xi-1}dx,$$

where $\xi = T_0/\tau$ and $x = v/v_0 = \delta/\delta_0$, δ and δ_0 being the Doppler shifts in the direction of motion corresponding to velocities v and v_0, respectively. If $\xi = 1$, the distribution of Doppler shifts is rectangular.

Unless the lifetime τ is known, it is not possible to state whether the Doppler shift correction should be applied. However, if an energy level is known with sufficient precision from particle-group measurements, it may be possible by comparison with the γ-ray measurement to determine whether or not the Doppler shift exists and thereby to obtain a limit on the radiative lifetime. This can be done in two of the reactions studied in Sec. V.

It is also necessary to consider the possible effects on energy determinations of the Doppler broadening. In some reactions the particle group angular distributions are known so that the correction can be applied. If no angular-distribution data are available, it seems reasonable to regard $\pm\delta_b/2$ as a measure of the additional uncertainty in the energy determination due to possible asymmetry. The Li^{7*} radiation from Be^9+d is an extreme example of a peak shift which may be due to such an asymmetry.[16] In this reaction the Doppler broadening was so pronounced that the asymmetry was readily detected. More often the Doppler broadening will be less than the combined spectrometer and converter energy-loss width so that it may escape detection.

In the 717-kev B^{10*} radiation from Be^9+d, the absence of Doppler effects has been established by using a thin converter and high spectrometer resolution. Hornyak *et al.*[1] observed the secondary electrons from a 7-mg/cm² thorium converter, for which the energy loss distribution is expected to be about $0.008B\rho$, the spectrometer resolution width (at half-maximum) being $0.015B\rho$; the combination of these two widths is $0.017B\rho$. If the B^{10*} nuclei radiate before being significantly decelerated, there will be a Doppler broadening contribution of $0.013B\rho$ and, consequently, an over-all line width of about $0.021B\rho$. The observed line width (at half-maximum), however, is $0.017B\rho$, indicating no Doppler broadening. It may be concluded either that the lifetime of this state or of the higher states producing cascades to this state is greater than the stopping time of about 3×10^{-13} sec. Therefore, the energy determination which is uncorrected for Doppler shift, 716.6±1.0 kev, is preferred to the corrected value, 713±1.5 kev. This conclusion is also arrived at by Craig *et al.*[20] who obtain 719±1.6 kev by measurement of the energy of the protons inelastically scattered by B^{10}.

[20] Craig, Donahue, and Jones, Phys. Rev. **87**, 206 (1952).

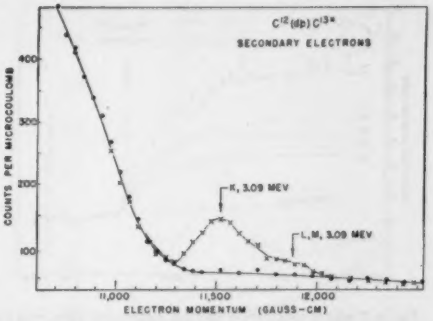

FIG. 3. Secondary photoelectric and Compton electron spectra from $C^{12}(d,p)C^{13*}$ at 1.46-Mev bombarding energy. Closed circles: 350-mg/cm² Al converter; crosses: same plus 22-mg/cm² Th. The target was graphite, 200 mg/cm² thick.

V. RADIATIONS FROM LIGHT NUCLEAR REACTIONS

A. $C^{12}+d$

The bombardment of C^{12} with deuterons of about 1.5 Mev energy leads to the following reactions:

$C^{12}(d,n)N^{13}$	$Q_0 = -0.280$
$C^{12}(d,p)C^{13}$	$Q_0 = 2.723.$

Aside from the annihilation radiation from the decay of N^{13}, only one γ-ray, from the 3.1-Mev state of C^{13}, is produced. This circumstance makes this reaction particularly appropriate for a study of the internal pair conversion coefficient. The pairs in question were first observed by Dougherty *et al.*,[21] who reported the conversion coefficient to be of the order of 10^{-3} pair per gamma-quantum. By utilizing the methods of intensity measurement described above, we have been able to obtain a more precise value for this coefficient, and thus to determine the multipole order of the transition. At the same time we have found it convenient to redetermine the γ-ray energy.

The energy of the γ-radiation was obtained from photoconversion in 15- and 22-mg/cm² foils of thorium, in which the photopeak shifts are 4 and 6 kev, respectively,[1] the spectrometer being calibrated by means of the nearby internal conversion X line of ThD. Both determinations gave 3094±6 kev. By averaging this value with previous determinations from this laboratory, we obtain 3097±5 kev, uncorrected for the Doppler shift, or 3082±7 kev corrected for the Doppler shift. The angular distribution of the short-range protons from this reaction has not been reported, so that it is not possible to make a correction for a possible asymmetry in the Doppler broadening; therefore we consider the corrected determination to be uncertain by an additional amount $\delta_b/2 = 5$ kev. Our resolution

[21] Dougherty, Hornyak, Lauritsen, and Rasmussen, Phys. Rev. **74**, 712 (1948).

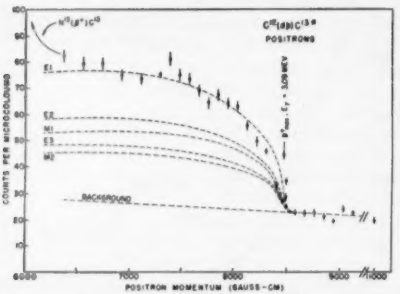

FIG. 4. Positron spectrum of internal conversion pairs from the 3.09-Mev gamma-ray of $C^{13}(d,p)C^{13*}$ at $E_d=1.46$ Mev. Target: 17-mg/cm² graphite. The dashed curves are theoretical distributions for various multipoles, normalized by the yield measurement of Fig. 3.

was not sufficient to detect this small broadening in the line spectrum should it exist. The photoconversion spectrum from the 22-mg/cm² foil is shown in Fig. 3, as is also the Compton electron spectrum from a thick aluminum converter. The absolute yield of the radiation obtained from the latter measurement, using Eq. (11), was 13.2×10^{-6} γ-quanta per deuteron at 1.46-Mev bombarding energy. An independent determination, using a 27.2-mg/cm², "thin" aluminum converter and Eq. (7) gave 13.3×10^{-6} γ-quanta per deuteron. Both measurements were made with graphite targets sufficiently thick to stop the deuterons.

The positron spectrum from a 17-mg/cm² graphite target, bombarded by 1.46-Mev deuterons, is shown in Fig. 4. The expected contribution of externally formed pairs from the target and support is of the order of one or two percent of the observed effect. Also indicated in the figure, by the dashed curves, are the theoretical distributions for several multipole orders, normalized in accordance with the measured γ-ray yield and added to the background. This background, determined from the beam-off counting rate in the spectrometer, increases slightly with decreasing positron momentum because of the presence of positrons from gaseous N^{13}. The positron spectrum was also observed through a 1.7-gram/cm² aluminum absorber; a gradual increase in the counting rate starting from about 8475 gauss-cm could be quantitatively ascribed to external pair formation in the "thick" converter, indicating that there were no extraneous sources of positrons from external pair formation in the baffles, spectrometer walls, etc., and that the background as shown in Fig. 4 is correct to ±2 counts at the lowest field setting.

Discussion

In comparing the theoretical and experimental distributions shown in Fig. 4, the uncertainty in the absolute γ-ray yield and possible error in the theoretical curves due to the use of plane wave functions, are estimated to be less than 10 percent, in addition to the background uncertainty of about 5 percent. Therefore, the observed distribution is consistent with only an $E1$ assignment. There is independent experimental and theoretical support[22] for such an assignment, based on the analysis of other data on the mirror levels of C^{13} and N^{13}. If the radiating state has a spin of $\frac{1}{2}$ as expected, both positron and γ-ray angular distributions must be isotropic so that assumption (17) is valid.

The most accurate values for the C^{13*} level position are 3083 ± 5 kev from the measurement[23] of the alpha-particle groups from $N^{15}(d,\alpha)C^{13}$ and 3086 ± 6 kev from the measurement of the proton groups from $C^{12}(d,p)C^{13}$; an average of these values is 3084 ± 4 kev. This average

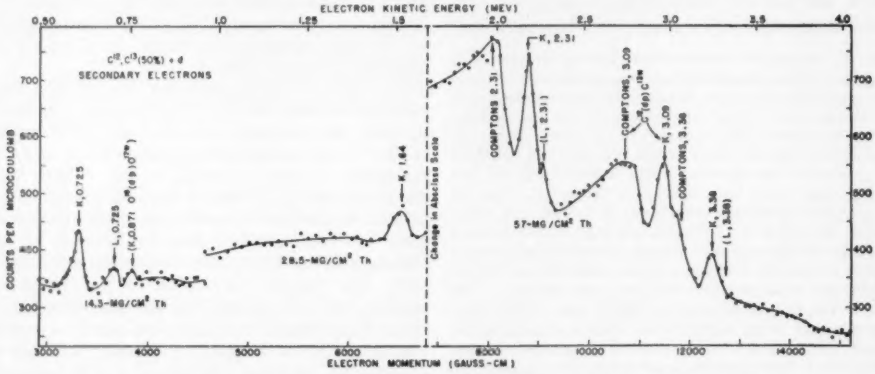

FIG. 5. Secondary photoelectric and Compton electron spectrum from an enriched C^{13} (50 percent) target bombarded by 1.58-Mev deuterons.

[22] R. G. Thomas (to be published).
[23] R. Malm and W. W. Buechner, Phys. Rev. **81**, 519 (1951) and D. M. Van Patter (private communication).

agrees with our Doppler corrected value but not with the uncorrected value, indicating that the lifetime of C^{13*} is less than 3×10^{-13} sec, its stopping time in the target material. This observation is consistent with the fact that the corresponding level in N^{13} at 2.37 Mev has a resonance radiative width of 0.63 ev, corresponding to a radiative lifetime of 10^{-15} sec.

B. $C^{13}+d$

The following reactions occur when C^{13} is bombarded with deuterons:

$C^{13}(d,n)N^{14}$	$Q_0=5312$ kev
$C^{13}(d,p)C^{14}$	$Q_0=5940$ kev
$C^{13}(d,\alpha)B^{11}$	$Q_0=5164$ kev
$C^{13}(d,\gamma)C^{12}$	$Q_0=1310$ kev.

In the first three reactions a deuteron energy of 1.5 Mev is sufficient to produce known excited levels of the residual nuclei. For a general survey of the γ-radiation a $C^{12}-C^{13}$ target was made by consolidating soot, enriched to 50 percent in C^{13}, to a thickness of about 30 mg/cm² in a 45-mg/cm² copper cup. To the back of the cup were attached photoconverters of thorium or Compton converters of beryllium or aluminum. Secondary electrons ranging from 0.4 to 4 Mev were observed from thorium foils of thickness 14.3, 28.5, and 57 mg/cm², the thicknesses having been selected so that the energy loss of the secondary electrons in passing through the converter would be comparable to the spectrometer resolution width, yielding optimum sensitivity without significant loss in resolution. The spectra observed at a bombarding energy of 1.58 Mev, are shown in Fig. 5 and the γ-ray energies determined therefrom are listed in Column 1 of Table I. The maximum possible Doppler shifts are given in Column 2. With the exception of the 3.1-Mev γ-ray from C^{13*} (see $C^{12}+d$), it is not known whether or not the nuclei radiate while in motion, so that it is likewise not known whether or not to include the Doppler correction. The uncertainties given in Column 1 for the uncorrected energies are based on the uncertainties in peak locations, and the peak-shift corrections, the additional uncertainties due to the possibilities of Doppler shift, complete or partial, being ignored. The yields obtained from (13), assuming the angular distributions to be isotropic, are listed in Column 3; these yields may be in error by 25 percent or more since a rather large converter angle, $\delta\sim85°$, was used. The relative excitation functions for deuterons ranging from 1.0 to 1.6 Mev are given in Fig. 6.

TABLE I. Energies and thick-target yields of C^{13}, C^{13} (50 percent) $+d$ γ-rays, determined from photoelectric conversion in thorium, at 1.58-Mev bombarding energy. The yields are uncorrected for isotopic abundance, and it is assumed that the angular distributions are isotropic. The energies are not corrected for the possible Doppler shifts δ_c which are given in Column 2; these shifts, if they apply, should be subtracted from the energies given in Column 1. Energies are given in kev.

Energy	δ_c	Yield $(\gamma/d)\times10^6$	Radiating nucleus
725±4	3	1.6	?
1638±8	6	1.5	N^{14}
2310±12	10	5.3	N^{14}
3092±15	15	5.5	C^{13}
3377±15	15	1.8	N^{14}

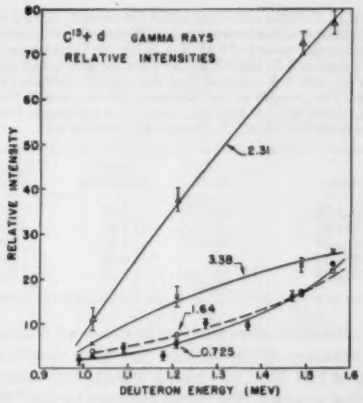

FIG. 6. Excitation functions for thick-target yields of the 0.725, 1.64, 2.31, and 3.38-Mev γ-rays from $C^{13}+d$. The general trend of the individual curves is believed to be correct within the probable errors indicated (shown only for a few typical points) but the relative scales may be subject to a considerably larger systematic error.

Compton conversion is a more sensitive process for detecting γ-radiation above about 3 Mev. Figure 7 shows the Compton spectrum obtained at a deuteron energy of 1.42 Mev from a 94-mg/cm² beryllium converter. The energies obtained by fitting "thick" converter distributions of the form given by Eqs. (10) and (11) to the front edges are given in Column 1 of Table II, and the maximum possible Doppler shifts due to the

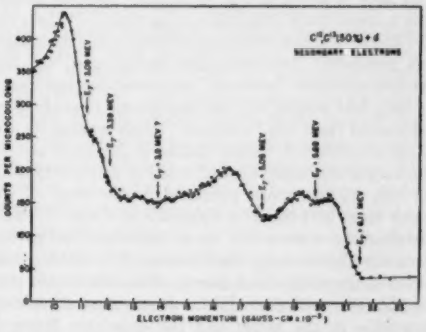

FIG. 7. Compton conversion spectrum from a $C^{13}+C^{13}$ (50 percent) target bombarded by 1.42-Mev deuterons. Converter: 94-mg/cm² Be.

TABLE II. Energies and yields of C^{12} (50 percent), $C^{13}+d$ γ-rays determined from Compton conversion. The energies were measured at a bombarding energy of 1.42 Mev, while the thick target yields were obtained at 1.21 Mev. The yields are uncorrected for isotopic abundance, and it is assumed that the angular distributions are isotropic. The energies are not corrected for the possible Doppler shifts δ_k; these shifts, if they apply, are to be subtracted from the energies given in Column 1. Energies are given in kev.

Energy	δ_k	Yield $(\gamma/d)\times10^5$	Radiating nucleus
3086±20	15	3.81	C^{13}
3390±20	15	1.85	N^{14}
5052±25	26	1.56	N^{14}
5690±50	29	0.69	N^{14}
6110±30	30	2.30	C^{14}

center-of-mass motion are given in Column 2. The yields were obtained from another run at a bombarding energy of 1.21 Mev, in which a 350-mg/cm² aluminum converter was used; the values obtained by the "thick" converter method of analysis are given in Column 3. The uncertainty in these yields is estimated to be about 15 percent, except for the 3.1-Mev line which is less certain because of the sloping background, and the 5.69-Mev line which is less certain because of its low intensity. These energies and yields appear to be in satisfactory agreement with the recent determinations of Baggett and Bame,[24] who used a magnetic pair spectrometer and 1.65-Mev deuterons.

An additional uncertainty in the Compton and photoconversion energy determinations is the possibility of Doppler broadening effects. However, in the (d,n) and (d,p) reactions the broadening will in any case be rather small, the quantity $\delta_k/2$ ranging from about 4 kev for the low energy radiations to about 10 kev for the high energy radiations.

In order to permit the observation of internally-formed positrons, a flake of C^{13} enriched soot, about 30 mg/cm² thick, was mounted in a light frame fabricated from 3.5-mg/cm² aluminum foil. The spectrum obtained from this target at a bombarding energy of 1.21 Mev is shown in Fig. 8. In this experiment there was a continuous production of gaseous N^{13} from the $C^{12}(d,n)N^{13}$ reaction, which gave rise to a field insensitive but somewhat time-dependent background. On this account alternate "beam-off" count readings were taken at each field setting and the background thus obtained subtracted from the "beam-on" count reading for the same time interval. Shown dashed in the figure are the theoretical internally formed positron distributions for $E1$ and $E2$ multipoles predicted on the basis of the γ-ray intensities listed in Column 3 of Table II, these distributions were added to an assumed background from the higher energy distributions. The distributions for all other multipoles follow in close order below that for $E2$. The total contribution from external positron formation in the target and the aluminum frame is about 5 percent of the $E1$ theoretical distribution in each case; no correction was made for this contribution. The positron spectrum was not studied below 5500 gauss-cm because of the intense β^+ activity from N^{13}.

[24] L. M. Baggett and S. J. Bame, Phys. Rev. **84**, 154 (1951).

Discussion

In the last columns of Tables I and II we have listed the probable sources of the radiation. The 6110-kev γ-ray is assigned to C^{14} because there was a small but definite yield observed with a deuteron energy of 650 kev, which is below the threshold for such a level in either B^{11} or N^{14}. This assignment has been confirmed by Sperduto *et al.*,[25] who find a level at 6096±9 kev in C^{14} from magnetic analysis of the protons; this value agrees with our determination, with or without the Doppler correction due to the center-of-mass motion. They observed no other proton groups which might correspond to levels in C^{14} from 5.2 to 6.1 Mev with an intensity of greater than 20 percent of that of the group associated with the 6.1-Mev level. This observation may exclude a level at 5.24 Mev in C^{14} reported by Humphreys and Watson[26] from range measurements; it may also exclude a level reported at 5.59±0.04 Mev by Curling and Newton,[27] also from range measurements. The 5.69-Mev γ-ray which was formerly thought to be associated with this level can easily be accommodated in the N^{14} level scheme.

Aside from the 3.1-Mev γ-ray from $C^{12}(d,p)C^{13*}$, the 6.1-Mev γ-ray from C^{14}, and the 725-kev γ-ray which is unassigned, all of the radiations listed in Tables I and II are believed to be from transitions in N^{14}. Three cascades are possible within the uncertainty of the measurements: (1) 1638+3381=5019, (2) 3381+2310 =5691, and (3) 1638+2310=3948, the last being considered since a weak γ-ray of about 3.9-Mev energy

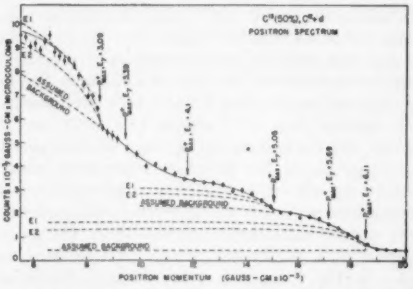

FIG. 8. Internally-formed positron spectrum from C^{13}, C^{12} (50 percent)$+d$. $E_d=1.21$ Mev; target, 30-mg/cm². Dashed curves labeled $E1$ and $E2$, are theoretical distributions for internal pair conversion, normalized according to the yields indicated in Table II.

[25] Sperduto, Holland, Van Patter, and Buechner, Phys. Rev. **80**, 769 (1950); Strait, Van Patter, Buechner, and Sperduto, Phys. Rev. **81**, 747 (1951); and Van Patter (private communication).

[26] R. F. Humphreys and W. W. Watson, Phys. Rev. **60**, 542 (1941).

[27] C. D. Curling and J. O. Newton, Nature **165**, 609 (1950).

cannot be excluded and since such a level is indicated by observed particle groups. From magnetic spectrometer analysis of α-particles from the bombardment of O^{16} with 6.8-Mev deuterons, Ashmore and Raffle[28] find levels in N^{14} at 5.70, 5.01, and 3.95-Mev, all uncertain by 0.08 Mev. From inelastic scattering of protons, Heydenburg, Phillips, and Cowie[29] report levels at 2.35 and 3.95 Mev, while Arthur *et al.*[30] report a possible additional level at 3.80 Mev. Mandeville and Swann[31] have observed the neutron groups from $C^{13}+d$ at 1.43-Mev bombarding energy: they find levels in N^{14} at 2.19, 3.47, 3.87, and 4.90 Mev, with probable errors of 0.07 Mev. Benenson,[32] who used a bombarding energy of 3.9 Mev, has reported neutron groups corresponding to levels at 2.23, 3.85, 4.80, 4.97, 5.5 (uncertain), 5.78 Mev, and several others at higher energies. A level scheme for N^{14} incorporating these data is exhibited in Fig. 9 together with the most plausible assignment of the γ-transitions. Cascade (1) has been eliminated because of lack of definite evidence for a 3.4-Mev state and because it seems unlikely that it can occur together with (2) and (3). The existence of cascades (2) and (3) requires that $Y(3.38)+Y(1.64) \leqslant Y(2.31)$: from Table I we find $Y(3.38)+Y(1.64)=3.3$ and $Y(2.31)=5.3\times10^{-6}\gamma/d$, so that the inequality is satisfied. Li and Whaling[33] have observed alpha-particles from $C^{13}+d$ which they attributed to the reaction $C^{13}(d,\alpha)B^{11*}$ leaving B^{11} in an excited state at 2107 ± 17 kev; such a level has also been observed in other reactions. A rough estimate indicates that the corresponding γ-ray would have only about one-tenth of the intensity of the neighboring 2.3-Mev line. The present data do not permit a definite statement of its presence or absence.

We have been unable to make an assignment for the 725-kev γ-ray. The possibility that it is a level at $6.11+0.73=6.84$ Mev in C^{14}, say of spin 0^- for which one-quantum radiation to the ground state would be forbidden, is excluded by the indication in Fig. 6 that its threshold lies below a deuteron bombarding energy of $(15/13)(6.84-5.94)=1.04$ Mev. It would appear not improbable that the 725-kev radiation is a part of a cascade transition involving some of the levels observed in the neutron spectrum which do not otherwise appear in the present work.[34]

In view of the evidence supporting the assumption that nuclear forces are charge-independent, it is of interest to look in N^{14} for the level corresponding to the 6.1-Mev level of C^{14}. On the basis of the beta-decay of

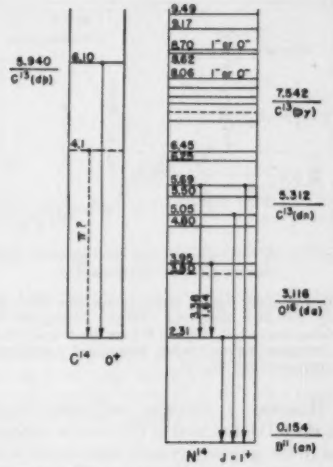

FIG. 9. The energy levels of C^{14} and N^{14} and the gamma-rays from $C^{13}+d$.

O^{14} and consideration of the Coulomb energies, Sherr, Muether, and White[35] conclude that the 2.31-Mev level of N^{14} is the analog of the ground state of C^{14}. Neglecting for the moment the contribution to level displacements from the differences of the boundary conditions on the nuclear surfaces, the mirror level in N^{14} is expected to appear at an excitation energy of $6.110+2.310=8.420$ Mev, which would correspond to a $C^{13}+p$ resonance at a proton bombarding energy 0.94 Mev. The nearest reported level is a narrow resonance at 1.16 Mev.[36] However, the well-known 554-kev resonance has a rather large reduced width which could give rise to an appreciable level displacement, as is observed in the case of the first excited states[22] of the mirror nuclei, N^{13} and C^{13}. If the variation of the level shift is taken into account, an s-wave assignment for the protons forming this state is the only one which yields a non-negative value for the reduced width, which is then 0.48 in units of $\hbar^2/2Ma$ for a channel radius $a=4.32\times10^{-13}$ cm. An s-wave assignment has also been made by Devons and Hine[37] on the basis of the isotropy of the capture γ-radiation. Using this reduced width in the one-channel, one-level approximation, the position of the mirror level in C^{14} is predicted to be 6.05 Mev. The small discrepancy of 60 kev may be due to the possible differences of the internal Coulomb energies of the various levels involved or to the approximation. Since the 554-kev resonance in $C^{13}+p$ is due to s-wave protons, it can have either spin 1 or 0 and odd

[28] A. Ashmore and J. F. Raffle, Proc. Phys. Soc. (London) **A64**, 754 (1951).
[29] Heydenburg, Phillips, and Cowie, Phys. Rev. **85**, 742A (1952).
[30] Arthur, Allen, Bender, Hausman, McDole, Diana, Rhodes, and Bajon, Phys. Rev. **87**, 237 (1952).
[31] C. E. Mandeville and C. P. Swann, Phys. Rev. **79**, 787 (1950).
[32] R. E. Benenson, Phys. Rev. **87**, 207 (1952) and private communication.
[33] C. W. Li and W. Whaling, Phys. Rev. **82**, 122 (1951) and private communication.
[34] H. T. Richards (private communication).
[35] Sherr, Muether, and White, Phys. Rev. **75**, 282 (1949).
[36] J. D. Seagrave, Phys. Rev. **85**, 197 (1952).
[37] S. Devons and M. G. N. Hine, Proc. Roy. Soc. (London) **A199** 56 (1949).

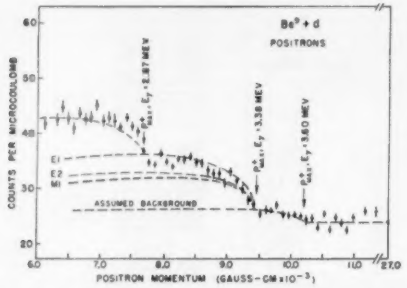

FIG. 10. Internally formed positron spectrum from Be^9 bombarded by 1.19-Mev deuterons. Target: 15-mg/cm² Be. The dashed curves marked $E1$, $E2$, and $M1$ are theoretical distributions for the corresponding multipoles, normalized according to the yields determined from Fig. 11.

parity. However, a zero-spin assignment cannot be given to the 6.11-Mev level of C^{14} because one-quantum emission to the spin-zero ground state would be strictly forbidden, contrary to observation. Therefore, on the basis of this reasoning, these two mirror levels would have a 1^- assignment, and the radiation from the C^{14} level would be $E1$. The internally formed positron distribution from this level as shown in Fig. 8 is in closest agreement with this assignment, but other assignments, such as $E2$ and $M1$, cannot be excluded because of the uncertainty in the γ-ray intensity and in our estimate of the background.

There are indications in Fig. 8 of internally formed positrons from the 5.69- and 5.05-Mev transitions, as well as the 3.1-Mev transition of C^{13} from $C^{12}+d$; the low intensity and uncertainty of the background and γ-ray intensity again preclude the determination of multipolarities for these transitions. There is a marked rise in the positron intensity which is associated with a transition energy of about 4.1 Mev. It is not entirely clear how this rise is to be accounted for, since only a very weak, if any, γ-radiation was observed at this energy. There is the possibility of a nuclear pair emitting state in C^{14} similar to the one in O^{16}; the observed slow rise of the distribution is characteristic of nuclear pairs as distinct from the abrupt rise which characterizes the more common internal or external pairs (see Fig. 1 of reference 3). Although no level has been reported in C^{14} below 5.2 Mev from particle-group measurements, it does not appear that any experiment has been performed which would have revealed a group associated with such a level; in the work of Humphreys and Watson[26] as well as that of Bennett *et al.*[28] such a group would have been obscured by the intense proton group from $C^{12}(d,p)C^{13}$, and Sperduto *et al.*[25] did not search for levels below 5.2 Mev.

[28] Bennett, Bonner, Richards, and Watt, Phys. Rev. **59**, 904 (1941).

C. Be^9+d

The γ-radiation from the bombardment of Be^9 by 1 to 1.5-Mev deuterons has been observed by Rasmussen *et al.*[30] Three of the high energy transitions at 2.87, 3.38, and 3.60 Mev arising from levels in B^{10}, Be^{10}, and B^{10}, respectively, are sufficiently intense to permit the detection of the internally formed positrons. The reactions involved are

$$Be^9(d,n)B^{10} \qquad Q_0=4.360$$
$$Be^9(d,p)Be^{10} \qquad Q_0=4.585.$$

The positron spectrum from the bombardment of a 15-mg/cm² Be target by 1.19-Mev deuterons is shown in Fig. 10, and the thick-converter Compton spectra from 350 mg/cm² of Al for the 3.60- and 3.38-Mev γ-rays are shown in Fig. 11. The dashed curves in the figure are calculated from Eq. (11). Table III lists the intensities determined from this calculation together with the values obtained by Rasmussen at the same bombarding energy using the thin converter method. We did not measure the intensity of the 2.87-Mev γ-ray since the background from the two higher-energy lines was rather intense for the thick converter method. In Fig. 10 we have indicated the calculated distributions for internally-formed positrons from the 3.38-Mev transition for $E1$, $E2$, and $M1$ multipoles, with a normalization based on the gamma-ray yield obtained from Fig. 11. The theoretical distributions for higher multipoles lie in close sequence below $M1$. Since the normalization does not depend upon the absolute value of Ω, it is somewhat more accurate than the yield. Unfortunately the uncertainty in the background in Fig. 10 is such that we cannot say definitely whether the transition is $E1$ or $E2$; $M1$ seems, however, less likely, and higher multipoles would appear to be excluded.

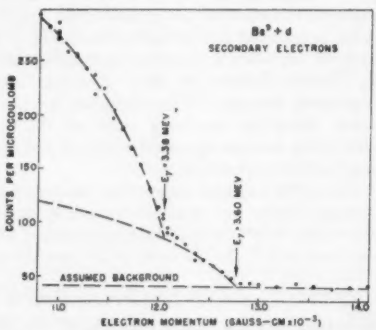

FIG. 11. Thick-converter Compton electron spectrum from Be^9+d. $E_d=1.19$ Mev: converter, 350-mg/cm² Al. Dashed curves are theoretical fits, using Eq. (11).

[30] Rasmussen, Hornyak, and Lauritsen, Phys. Rev. **76**, 581 (1949); and V. K. Rasmussen, Ph.D. thesis, California Institute of Technology (1950) (unpublished).

Discussion

The multipole order of the 3.38-Mev transition in Be^{10} is of particular interest since it bears on the determination of the spin and parity of the first excited state of Be^{10}. If the transition is $E1$, the 3.38-Mev state has total angular momentum 1 and odd parity, assuming the ground state to be 0, (even): $E2$ radiation implies $J2$, (even). Indications from the angular distributions of the protons[40] are that both states have even parity, which is consistent with $E2$ but not with $E1$. Cohen *et al.*[41] find that the angular correlation of short-range protons and γ-rays is consistent with $J=2$ for the excited state.

D. $N^{15}+p$

Bombardment of N^{15} with protons leads to production of the ground state and first excited state of C^{12} through the reaction

$$N^{15}(p,\alpha)C^{12} \qquad Q_0=4.961 \text{ Mev}.$$

The target in the present experiment consisted of a disk of titanium, nitrided on one surface with nitrogen enriched to 32 percent in N^{15}; the TiN layer was thick enough to constitute a thick target for the incident proton beam and the disk was a thick converter for the secondary Compton electrons. The Compton spectrum from the bombardment with 1.63-Mev protons is shown in Fig. 12. By fitting this spectrum and a similar one taken at $E_p=1.20$ Mev with a thick-converter Compton distribution, appropriately convoluted with the spectrometer resolution curve, we find the γ-ray energy to be 4463 ± 20 kev, uncorrected for Doppler effects. If the radiation is emitted before the C^{12*} nuclei are significantly decelerated, a Doppler correction of 14 kev due to the center-of-mass motion is to be subtracted. In addition, the front edge of the observed Compton distribution will be modified by the Doppler broadening ($\delta_b/2=20$ kev), requiring a further correction of 6 kev. The corrected energy of the first excited state of C^{12} is then 4443 ± 20 kev. The thick-target yields computed from the Compton spectra were $6.3\times10^{-5}\gamma/p$ at $E_p=1.20$ Mev and $8.7\times10^{-5}\gamma/p$ at $E_p=1.63$ Mev, assuming the angular distribution of the radiation to be isotropic. Analysis of the elastically scattered proton groups from the target[42] gave the composition near the surface as 1 nitrogen atom per 1.45 titanium atoms; taking the stopping power of Ti to be 2.1 times that of nitrogen, the above yields would be 13 times larger in pure N^{15}.

TABLE III. Be^9+d thick target γ-ray yields for $E_d=1.19$ Mev.

Reaction	Energy	Yield[a]	Yield[b]
$Be^9(d,n)B^{10}$	2.87	2.4 ± 0.6	...
$Be^9(d,p)Be^{10}$	3.38	2.1 ± 0.5	2.5 ± 0.3
$Be^9(d,n)B^{10}$	3.60	0.9 ± 0.2	0.96 ± 0.15

[a] Rasmussen (see reference 39) thin converter. [b] This work, thick converter. Yields are in units of 10^{-6} γ/d. The radiations are assumed to be isotropic.

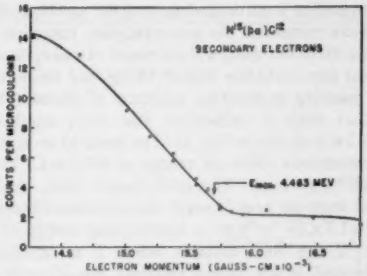

FIG. 12. Thick-converter Compton electron spectrum from $N^{15}(p,\alpha)C^{12}$. $E_p=1.63$ Mev; converter, ~300-mg/cm² Ti.

Discussion

Measurements have been made in this laboratory by Schardt[42] of the Q of the low energy alpha-particle group from $N^{15}+p$ and by Li and Whaling[43] of the Q of the ground-state group. The values obtained were 529 ± 8 and 4961 ± 6 kev, respectively, giving 4432 ± 10 kev for the energy of the C^{12} level. The level energy can also be obtained by using the Q of the reaction $N^{14}(d,\alpha)C^{12*}$ as measured by Malm and Buechner[23] together with other accurately known Q's: thus

$$Q[N^{14}(d,p)N^{15}]+Q[N^{15}(p,\alpha)C^{12}]-Q[N^{14}(d,\alpha)C^{12*}]$$
$$=(8608\pm9)+(4960\pm4)-(9137\pm6)$$
$$=(4431\pm12) \text{ kev}.$$

These particle group values are in agreement with our Doppler corrected value but not with the uncorrected value, suggesting that the C^{12*} lifetime is shorter than the stopping time of about 3×10^{-13} sec. There is some evidence that the first excited state of C^{12} has a spin of two with even parity[44]; since the ground state is spinless and presumably of even parity, the transition should be $E2$. For such a transition the lifetime estimates of Bethe[45] and Goldhaber-Sunyar[46] are $\sim10^{-15}$ and $\sim10^{-14}$ sec, respectively, both of which are consistent with the evidence for the Doppler correction.

E. $B^{10}+p$

The bombardment of B^{10} with protons was first shown by Brown *et al.*[47] to yield an α-particle group

[40] F. A. El Bedewi, Proc. Phys. Soc. (London) **A65**, 64 (1952); C. F. Black, Phys. Rev. **87**, 205 (1952).
[41] Cohen, Shafroth, Class, and Hanna, Phys. Rev. **87**, 206 (1952).
[42] Schardt, Fowler, and Lauritsen, Phys. Rev. **86**, 527 (1952).
[43] Li, Whaling, Fowler, and Lauritsen, Phys. Rev. **83**, 512 (1951).
[44] R. Haefner, Revs. Modern Phys. **23**, 228 (1951); A. Kraus and A. P. French (unpublished).
[45] H. A. Bethe, Phys. Rev. **55**, 436 (1939).
[46] M. Goldhaber and A. W. Sunyar, Phys. Rev. **83**, 1073 (1951).
[47] Brown, Snyder, Fowler, and Lauritsen, Phys. Rev. **82**, 159 (1951).

corresponding to an excited state of Be^7 at 434.4±4 kev. We have measured the accompanying radiation with the spectrometer using a thick target of amorphous B^{10}, pressed into a shallow cup of 14-mg/cm² thorium foil. The resulting momentum spectrum of photoelectrons, together with a calibration line from annihilation radiation is shown in Fig. 13. The mean of several such determinations yields an energy of 429.8±1.5 kev for the $(B^{10}+p)$ γ-ray. The thick target yield, as determined from the area beneath the conversion spectrum, is $Y=1.7\times10^{-6}\gamma/p$ at a bombarding energy of 1.41 Mev. If the Be^{7*} radiates before it is significantly decelerated in the target material, the Doppler shift due to the center-of-mass motion will be 1.3 kev and the transition energy 428.5±1.8 kev. According to the measurement of Elliott and Bell,[15] the lifetime of the mirror level of Li^{7*} is 0.75×10^{-13} sec; since only a slightly longer lifetime is to be expected for Be^{7*} and since the stopping time is about 5×10^{-13} sec, the Doppler correction is required.

Discussion

In an earlier communication[48] the gamma-radiation from $B^{10}+p$ was ascribed to the reaction $B^{10}(p,p')B^{10*}$ and was considered to establish that a line of energy 413 kev observed in the reaction $Be^9(d,n)B^{10*}$ represented the transition from the lowest excited state of B^{10}. Reference to the dashed curve of Fig. 13, where the K-conversion spectrum from this line is directly compared with the $(B^{10}+p)$ K-line, reveals that the two energies differ by 17 kev and that hence the earlier assignment was incorrect.

The measurements of the excitation energies of Be^{7*} have been reviewed in the paper by Brown *et al.* Subsequent accurate determinations, from $Li^7(p,n)Be^{7*}$ reaction are 431±5 kev[49] and 434±1 kev[50] and from $B^{10}(p,\alpha)Be^{7*}$, 430±3 kev.[20] Our determination appears to be slightly low, especially with the required Doppler correction. An extreme asymmetry in the Doppler broadening ($\delta_b=6$ kev) could account for the discrepancy but this seems unlikely for a (p,α) reaction. There appear to be no angular distribution measurements of the α-particles from this reaction, although it is noted that the yield of α-particles at 140° is nearly the same as the yield of γ-radiation at 90°,[47] the latter distribution being presumably isotropic, since Be^{7*} very likely has a spin of ½.

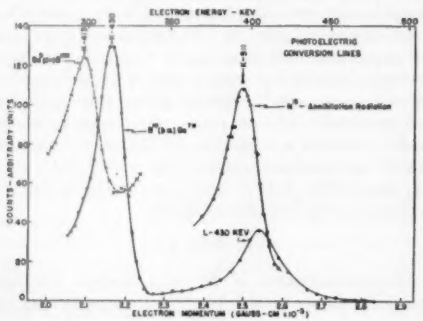

FIG. 13. Photoelectric conversion lines from $Be^9(d,n)B^{10}$, $B^{10}(p,\alpha)Be^7$ and annihilation radiation. Converter, 14-mg/cm² Th.

[48] Rasmussen, Hornyak, and Lauritsen, Phys. Rev. **76**, 581 (1949).

[49] C. H. Johnson and H. H. Barschall, Phys. Rev. **81**, 317 (1951).

[50] H. B. Willard and W. M. Preston, Phys. Rev. **81**, 480 (1951) (only the statistical and reading error is quoted).

F. Li^6+d

In the hope of obtaining a precise value for the displacement of the first excited states of the mirror nuclei, Be^7 and Li^7, we investigated the γ-ray spectrum from the bombardment by 1.5-Mev deuterons of a thick target of LiCl, the Li being enriched[51] to 96 percent in Li^6. Figure 14 displays the two prominent K-conversion lines observed with an 8.1-mg/cm² thorium converter. From calibrations using annihilation radiation as well as the thorium I line, the energies are found to be 430.0±1.5 kev for $Li^6(d,n)Be^{7*}$ and 478.5±1.5 kev for $Li^6(d,p)Li^{7*}$, uncorrected for possible Doppler effects. The latter determination agrees with previous spectrometer measurements in this laboratory from other reactions.

A striking feature of these mirror reactions is the near-equality of the intensities of the two radiations; correction of the peak heights for the difference of the photoconversion cross section shows that the radiations are of equal intensity to within 10 percent. The absolute yields were determined from a thick target of $(Li^6)_2SO_4$ bombarded with 1.49-Mev deuterons and was found to be $1.0\times10^{-6}\gamma/d$ for each line. Interpolating between available stopping-power data, the absolute yields for pure Li^6 would be about 14 times greater.

Referring again to Fig. 14, it appears that an upper limit of about 5 percent can be placed on the relative intensity of any other line below 420 kev, down to 100 kev, since the photoconversion efficiency is increasing so rapidly with decreasing γ-ray energy that even below the K-binding energy of 110 kev, the L conversion lines would give a sensitive indication of any gamma-radiation. In the region above the 479-kev line up to 1 Mev, an upper limit of about 25 percent can be set. The background in this region is partly due to Li^8 electrons from residual Li^7 in the target and partly from the strong 871-kev line of $O^{16}+d$, ascribed to oxygen present in the water of crystallization. The identification of this line was checked with a $(Li^6)_2SO_4$ target where it is about five times as strong as the lithium lines. From 1 to 6 Mev no γ-radiation was found but, because the Li^8 spectrum was quite intense in this region, we could not have detected any γ-radiation whose yield is less than $10^{-6}\gamma/d$.

[51] We are indebted to the Isotopes Division, AEC for the loan of this material.

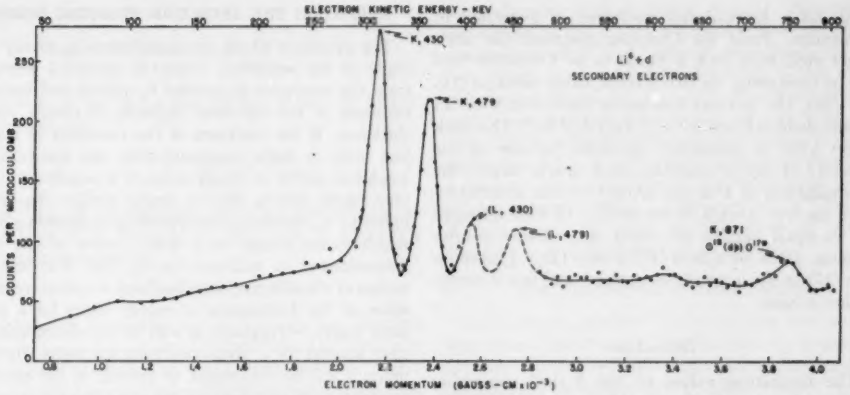

FIG. 14. Photoelectric conversion lines from $Li^6(d,p)Li^7$ and $Li^6(d,n)Be^7$. $E_d = 1.49$ Mev; converter, 8.1-mg/cm² Th.

Discussion

As in the case of the $B^{10}(p,\alpha)Be^{7*}$ γ-ray, Doppler corrections are required: the corrections to be subtracted for the center-of-mass motion are 2.6 kev for Be^{7*} and 2.9 kev for Li^{7*}. Whaling and Bonner[32] have measured the angular distribution of the short range protons from Li^6+d for bombarding energies below 1.4 Mev and observe considerable asymmetry. By using their angular distribution at 1.4 Mev to determine the Doppler broadening distribution ($\delta_b = 7$ kev) and convoluting this distribution with the spectrometer resolution curve, we find an effective "red" shift of 1.8 kev. The angular distribution of the short-range neutrons from the mirror reaction have not been reported but assuming it to be the same as that of the protons, we obtain for Be^{7*} ($\delta_b = 6$ kev) an effective "red" shift of 1.5 kev. The broadening shifts thus partially cancel the shifts due to center-of-mass motion, and the corrected transition energies are 428.9 and 477.4 kev, with a possible error of ±2 kev in each case, considering the uncertainty in the Doppler corrections. The Be^{7*} energy agrees with our value from the $B^{10}+p$ reaction so that the same comments in this connection given in the discussion of that reaction also apply here. A mean of the Li^{7*} energy determinations from particle group measurements and radiation determinations from other laboratories (involving no Doppler effects) is 478.5±0.5 kev; our value, though low, is in agreement within the combined stated errors. The level displacement, which is less subject to errors in the Doppler corrections and photopeak shifts, is 48.5 kev with an uncertainty of about ±1.0 kev.

G. $O^{16}+d$

An intense, low energy γ-radiation is observed in the deuteron bombardment of O^{16} from the reaction

$$O^{16}(d,p)O^{17}, \qquad Q_0 = 1.918.$$

The energy of this radiation was obtained from the photoconversion spectrum from 8.1-mg/cm² thorium observed when $(Li^6)_2SO_4$ was bombarded with 1.5-Mev deuterons. By calibrating the spectrometer with the thorium *I* line as well as with the photoconversion line of annihilation radiation in the same thorium foil, we obtained an energy of 870.5±2.0 kev, uncorrected for the Doppler shift, or 867.0±2.5 when corrected for the motion of the center-of-mass as well as the asymmetry of the angular distribution of the short-range protons[32] ($\delta_b/2 = 2$ kev).

Because of the high intensity of this transition, it was possible to detect the internal conversion electrons. Figure 15 shows the "no-converter" spectrum in the vicinity of the internal conversion line from the bombardment of an 8-mg/cm² SiO_2 target with 1.35-Mev deuterons; also shown is the thick converter Compton spectrum from 140-mg/cm² Al under otherwise identical experimental conditions. The arrow above the "no-converter line" indicates the position predicted for the peak on the basis of the spectrometer calibration; the observed line has the proper position, shifted slightly due to energy loss within the target, and the proper

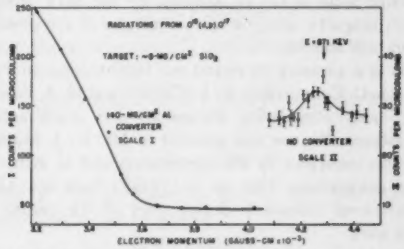

FIG. 15. Thick-converter Compton electron spectrum and internal conversion line from $O^{18}(d,p)O^{17}$. $E_d = 1.35$ Mev.

[32] W. Whaling and T. W. Bonner, Phys. Rev. **79**, 258 (1950).

[32] N. P. Heydenburg and D. R. Inglis, Phys. Rev. **73**, 230 (1948).

width for a spectrometer resolution of 2 percent in momentum. From the Compton spectrum the thick target yield from SiO_2 is found to be $Y \approx 6\times10^{-6}\gamma/d$ and by comparing the two spectra, using relations (11) and (16), the internal conversion coefficient from all atomic shells is found to be $(7.1\pm2.6)\times10^{-6}$. The thick target yield is somewhat uncertain because of the difficulty of charge collection on a quartz target; the determination of Γ is not subject to this uncertainty since the two spectra shown in Fig. 15 were obtained for an equal number of counts on a Geiger counter monitor. Since the spin of O^{17*} is very likely $\frac{1}{2}$, assumption (17) in the internal conversion coefficient determination is valid.

Discussion

The theoretical values of the K-shell conversion coefficient as given by Rose *et al.*[10] are (in units of 10^{-6}): $E1=3.71$, $E2=9.15$, $E3=21.2$, $M1=4.87$, $M2=11.90$, $M3=27.2$. In view of the large experimental uncertainty, we need not be concerned with the contribution from the L-shell or with screening corrections. The observed coefficient is consistent with pure $E2$ or a mixture of $E2$ and $M1$. On the basis of angular distribution measurements, the 0.87-Mev level of O^{17} is assigned a spin of $\frac{1}{2}$ (even),[54] and on the basis of spin, magnetic moment, and angular distribution measurements, the ground state is assigned a spin of 5/2 (even).[54,55] Therefore, there is little doubt that the radiation between these two levels should be predominently $E2$, as observed.

If the radiation is indeed $E2$, its lifetime can be estimated as $\sim10^{-11}$ sec from the formula given by Goldhaber and Sunyar[46] or 2×10^{-12} sec from Bethe's formula.[45] These times are longer than the stopping time of about 3×10^{-13} sec so we can be rather certain that the effective K-shell occupation probability for internal conversion is nearly unity. Moreover, the Doppler shift correction should not be included in the energy determination. Our uncorrected energy determination of 870.5 ± 2.0 kev is not, however, in agreement with the most recent value of 880 ± 5 kev for the first excited state of O^{17} as obtained by the MIT group[22] from magnetic analysis of the energies of the protons from this reaction.

It is a pleasure to record our indebtedness to Professors C. C. Lauritsen, R. F. Christy, and W. A. Fowler for many stimulating discussions and much active assistance. We are also grateful to Mr. R. J. Mackin for his assistance in the experiments and in many of the calculations. One of us (RGT) held an AEC predoctoral fellowship during part of the period of this work.

[54] Burge, Burrows, Gibson, and Rotblat, Proc. Roy. Soc. (London) **210**, 534 (1951).
[55] F. Alder and F. C. Yu, Phys. Rev. **81**, 1067 (1951).

APPENDIX: THE EFFECTIVE STOPPING FORCE

The extent to which the distribution in energy and angle of the secondary Compton electrons emerging from the converter is affected by elastic and inelastic collisions in the converter depends, of course, on its thickness. If the thickness of the converter in energy loss units is large compared with the spectrometer resolution width in energy units, it is possible to combine these effects into a single energy dependent quantity μ_e, referred to as the effective stopping force, which enters simply as a direct factor in the yield determination as indicated by Eq. (10). The determination of the effective stopping force involves consideration of the distribution of energy losses for a given path length (straggling) as well as the distribution of path lengths for a given converter thickness; furthermore, it will be convenient to include in the effective stopping force the effect on the yield determination of the angular redistribution of the secondary electrons due to the elastic collisions in the converter. These effects will be regarded as independent of one another and then combined in the final result; this procedure, though approximate, is sufficiently accurate for the present applications.

The most important consideration concerns the distribution of energy losses for electrons which have traveled a certain path length in the material; this distribution for fast electrons has been calculated approximately by Landau[56] and more recently in greater detail by Schultz,[57] and Blunck and Leisegang.[58] The characteristic feature of the distribution is the most-probable energy loss, and except for a minor correction, it is completely specified in terms of this quantity. Thus, the detailed consideration of the properties of the stopping material, such as the distribution of atomic oscillators, can be confined to the determination of the most probable loss.

The Most Probable Energy Loss

The most probable energy loss for electrons of velocity v traveling a path length l in a condensed medium is given by[59]

$$\Delta E_{mp}=\mu_{mp}l=Bl\left[\log\frac{2Blm_0v^2\gamma^2}{I(\gamma)^2}-(1-F_p)\beta^2+0.37\right], \tag{19}$$

where $B=2\pi NZe^4/m_0c^2\beta^2$, $\beta=v/c$, $\gamma=(1-\beta^2)^{-1}$, and N is the number of atoms of atomic number Z per unit volume. The quantity $I(\gamma)$ is the average excitation

[56] L. Landau, J. Phys. (U.S.S.R.) **8**, 201 (1944).
[57] W. Schultz, Z. Physik **129**, 530 (1951).
[58] O. Blunck and S. Leisegang, Z. Physik **128**, 500 (1950).
[59] This equation is derived from expressions given by N. Bohr, Kgl. Danske Videnskab. Selskab, Mat.-fys. Medd. XVIII, No. 8 (1948), with polarization effects included in accordance with a prescription by A. Bohr, Kgl. Danske Videnskab. Selskab, Mat.-fys. Medd. XXIV, No. 19 (1948), and using the limiting energy loss, Ble^{β^2} as given by Landau (see reference 56).

potential, defined by

$$\log I(\gamma)=F_p\log(\gamma\hbar\omega_p)+\sum_{\omega_i<\gamma\omega_p} f_i\log I_i,$$

where I_i is the excitation energy of the ith atomic transition and

$$F_p=\sum_{\omega_i<\gamma\omega_p} f_i$$

is the sum of the fractional oscillator strengths for all oscillators with frequencies less than γ times the polarization frequency,

$$\omega_p=(4\pi NZe^2F_p/m_0)^{\frac{1}{2}}.$$

In principle, the evaluation of (19) requires complete knowledge of the frequency distribution of the quantum mechanical oscillators of the stopping material, which can be obtained approximately from x-ray absorption data. Christy[60] has found that, within the accuracy of the somewhat limited experimental data, a reasonably good fit for platinum is given by

$$F(\omega)=\sum_{\omega_i<\omega} f_i=\frac{\omega}{\omega_0+\omega}, \tag{20}$$

the parameter ω_0 being adjusted to obtain the measured value $I(1)$. With the distribution represented by (20), it follows from a straightforward calculation that

$$I(\gamma)=\hbar\omega_0+\gamma\hbar\omega_p=\gamma\hbar\omega_pF_p^{-1},$$
$$F_p=[(1+\xi\gamma^2)^{\frac{1}{2}}-1][(1+\xi\gamma^2)^{\frac{1}{2}}+1]^{-1},$$

and

$$\mu_{mp}=B[\log(lF_p/a_0)-(1-F_p)\beta^2+0.37], \tag{21}$$

where

$$\xi\equiv 16\pi NZe^2/m_0\omega_0^3, \quad a_0\equiv\hbar^2/m_0e^2.$$

Of course the details of the absorption spectrum are not reproduced by (20), but it was observed that the deviations of (21) from the determination for aluminum using the x-ray data[61] were less than 1 percent for all $\gamma\geq 1$. A mean of the recent determinations[62] of $I(1)$ for aluminum is 155 ev, which yields a value of $\hbar\omega_0=148$ ev for the parameter in (20) and a value of $\xi=0.195$. The values of μ_{mp} given by (21) with this value of ξ are in good agreement with the recent measurements of Chen and Warshaw.[63]

Since the effects of scattering in a thick aluminum Compton converter become important for electrons whose energies are less than about 1 Mev, it is sometimes desirable to use a lighter material such as beryllium. Although no x-ray absorption data is available for Be, the theoretical expression, corrected in the usual manner for inner and outer screening, should provide an accurate description of the actual K-shell absorption for such a simple element. Moreover, a knowledge of the L-shell absorption spectrum is unnecessary in view of A. Bohr's[59] observation that the two valence electrons will be effectively bound by the polarization forces for all $\gamma\geq 1$. The most probable energy loss was evaluated in this way and compared with (21) in which $\xi=0.95$ as obtained from the measured value $I(1)=64$ ev[64]; the differences were less than 2 percent for all $\gamma\geq 1$. The energy losses given by (21) are in agreement with the measurements by Chen and Warshaw[63] of the most probable loss of 620-kev electrons in Be foils of various thicknesses.

The Distribution of Energy Losses

According to Landau[65] the probability that an electron whose initial energy is E suffers an energy loss between Δ and $\Delta+d\Delta$ after traveling a distance l in a material can be written as $W(l,\Delta)d\Delta$, where

$$W(l,\Delta)=\phi(\lambda)/lB,$$

$\phi(\lambda)$ being a universal function which is derived and plotted in his paper and whose argument is

$$\lambda=(\Delta/lB)+\lambda'; \quad -\lambda'=(\mu_{mp}/B)+0.05.$$

For the moment the effects of elastic scattering are neglected so that the path length l is equal to the component distance z along the spectrometer axis (for simplicity, we assume here that $\cos\theta_0=1$). If the number of electrons originating in the conversion process between z and $z+dz$ with initial energies between E and $E+dE$ is $Q(E)dEdz$, then the number of these electrons suffering losses between Δ and $\Delta+d\Delta$ in traveling to the converter surface is given by

$$Q(E)dEdzW(z,\Delta)d\Delta,$$

and the total number generated in a material of thickness t with these initial energies and energy losses is

$$Q(E)dEd\Delta B^{-1}\int_0^t\phi(\lambda)dz/z. \tag{22}$$

If the slowly varying logarithmic dependence of μ_{mp} on $l(=z)$ is neglected, then

$$dz/z=-d\lambda/(\lambda-\lambda'),$$

and the distribution (22) may then be written

$$-Q(E)dE\mu_{mp}^{-1}d\Delta(\lambda'+0.05)\int_{\lambda(t)}^{\infty}\phi(\lambda)d\lambda/(\lambda-\lambda'),$$

where

$$\lambda(t)=(\Delta/Bt)+\lambda'.$$

For a "thick" converter $t\to\infty$, and the emerging distribution can be written

$$Q(E)dEd\Delta G(\lambda')\mu_{mp}^{-1},$$

[60] R. F. Christy (unpublished).
[61] D. H. Tomboulian and E. M. Pell, Phys. Rev. **83**, 1196 (1951).
[62] E. L. Hubbard and K. R. MacKenzie, Phys. Rev. **85**, 107 (1952).
[63] J. J. L. Chen and S. D. Warshaw, Phys. Rev. **84**, 355 (1951).
[64] C. B. Madsen and P. Venkateswarlu, Phys. Rev. **74**, 648 (1948).

where

$$G(\lambda')=-(\lambda'+0.05)\int_{\lambda'}^{\infty}\phi(\lambda)d\lambda/(\lambda-\lambda').$$

The number of electrons emerging with energies between E_0 and E_0+dE_0, where $E_0=E-\Delta$, is therefore

$$\int_{E_0}^{E_{\max}} Q(E)dEdE_0\mu_e^{-1}, \tag{23}$$

where

$$\mu_e=\mu_{\mathrm{mp}}/G(\lambda') \tag{23a}$$

is the effective stopping force. By numerical integration, using the curve and asymptotic expression given by Landau for $\phi(\lambda)$, we find that

$$G(\lambda')=0.765-0.0058\lambda'$$

when $9<-\lambda'<17$, which is the range of λ' occurring in our applications. Thus the effective energy loss $\mu_e l$ is greater than the most probable energy loss but considerably less than the average energy loss. For the analysis of Compton thick converter spectra, μ_e should be evaluated for a thickness corresponding to the middle of the range of energies where the curve of Eq. (11) is fitted. The approximation of neglecting the variation of the logarithmic terms in μ_{mp} leads to an incorrect treatment of the electrons arising from very shallow and very deep laminae in the converter; however, the greater bulk of the electrons is accurately treated and the proper normalization is maintained for all laminae. For very small energy loss, of the order of a few times the atomic excitation energies, Landau's derivation no longer applies, and the somewhat better approximation of Blunck and Leisegang[65] should be used. Under the conditions of the present experiments, for $E_\gamma>1$ Mev in Al or >0.5 Mev in Be, the correction to $G(\lambda')$ is less than one percent.

A derivation of an effective stopping force which is similar to the one given above but uses the experimental results of White and Millington for $W(l,\Delta)$ has been given by Ellis and Aston.[65]

Corrections for Multiple Scattering

As a consequence of multiple scattering in the converter, an electron originating at a distance z within the converter will have traveled a path length $l\geq z$ on emergence. Since the energy loss is proportional to l rather than z, there will thus be fewer electrons emerging with an energy E_0 when multiple scattering is taken into account. In the small angle approximation, the distribution function giving the probability that an electron has a path length l after traveling a component distance z along a given direction has been obtained by Yang.[66] According to him (Case I, which corresponds approximately to the present situation) the average path length is given by

$$\langle l\rangle=z[1+(z/\Lambda)],$$

where Λ is the scattering length.[67] If we neglect straggling of energy losses by considering all losses to be given by the effective value $\mu_e l$ and in addition, if we neglect the distribution in path lengths by considering all path lengths to be given by $\langle l\rangle$, then to first order in z/Λ expression (23) is to be multiplied by

$$1-(2\Delta/\Lambda\mu_e). \tag{24}$$

A detailed derivation using Yang's distribution function for the path lengths also gives this result to first order in z/Λ.

Since a flat converter is used, the angular distribution of the most energetic Compton electrons will not be isotropic but will be very nearly $(\cos\theta_0)^{-1}$ for not-too-large angles, and the number of electrons emerging from the converter in the forward direction of the spectrometer acceptance solid angle ($\cos\theta_{1,2}\approx 1$) will therefore be increased as a result of angular redistribution in the multiple scattering. The redistribution process can be treated in the same manner as the angular redistribution in the conversion process. By carrying out a computation which is similar to (2b) but with $S(\cos\omega)$ as the multiple scattering law, given in the Gaussian small angle approximation by

$$S(\omega,z)=(\Lambda/4\pi z)\exp(-\omega^2\Lambda/4z),$$

we obtain to first order in z/Λ a factor

$$1+(2\Delta/\Lambda\mu_e), \tag{25}$$

by which (23) is to be multiplied to include this effect.

Thus, to first order, the multiple scattering effects leading to (24) and (25) compensate, and the effective stopping force can be taken directly from (23a). Because the factors (24) and (25) are approximate, the compensation cannot be expected to occur in general and it is therefore desirable to minimize both by using a light material as converter. For a 3-percent energy loss in aluminum, the correction term, $2\Delta/\Lambda\mu_e\approx 0.17\gamma^{-1}$ which may be quite significant for low energy electrons. In beryllium the term is only $0.052\gamma^{-1}$ and may be ignored for energies greater than 1 Mev.

[65] C. D. Ellis and G. H. Aston, Proc. Roy. Soc. (London) **129**, 180 (1930).

[66] C. N. Yang, Phys. Rev. **84**, 599 (1951).

[67] W. T. Scott, Phys. Rev. **76**, 212 (1949).

Discharge Mechanism in Argon Counters

LAURA COLLI AND UGO FACCHINI
Laboratori C.I.S.E., Milan, Italy
(Received June 30, 1952)

The multiplication curves and the pulse shapes have been studied in a counter filled with pure argon and argon plus carbon dioxide mixtures at pressures ranging from 150 to 1000 mm Hg.

The pulse shapes in argon in the high proportional zone and up to voltages corresponding to the corona threshold are explained by assuming a production in the Townsend avalanche of photons hard enough to extract electrons from the cathode. These photoelectrons are found to be produced during a time Tf_0 of the order of a few μsec when at 150 mm Hg pressure, and during a smaller time when at higher pressures. The analysis of the features of the excited levels of argon suggests the four lower excited levels to be responsible for the photoelectric effect. These photons are produced in collisions leading to destruction of these levels, and are not resonance photons. The Tf_0 values deduced from our measurements are in accordance with those obtained by extrapolating the Molnar values for the first metastable levels at the pressures used. This photoelectric process has been found to be the main one responsible for sustaining corona discharge, which starts at multiplication values of about 200.

If carbon dioxide concentrations varying from 10^{-4} to 5×10^{-3} are added to argon, one obtains an increase of Ns, the threshold multiplication, which is linear *versus* the carbon dioxide percentage. This fact is readily explained by assuming the quenching of argon excited levels by collisions of the second kind on carbon dioxide molecules. From the experimental results one may deduce a value of the quenching cross section which is about 600×10^{-16} cm^2 in a first approximation.

Further studies concern the space charge effect at the photoelectric process divergence threshold, which allows the formation of a very narrow Geiger zone at carbon dioxide concentrations over 5×10^{-4}.

No processes other than the photoelectric one have been found to be efficient in counters filled with argon plus carbon dioxide mixtures up to a concentration of 5×10^{-3}.

At higher percentages the photoelectric process is considerably reduced; there has been found to be effective in the discharge build-up a process by which electrons are released in the gas body. The counter behaves as a regular fast counter.

The effect of mercury vapor in the discharge in pure argon is also described; it is accounted for by the well-known Penning process of mercury ionization by collision on excited argon atoms. This process causes the discharge to start at extremely low multiplication values.

I. INTRODUCTION

THE aim of this work is to inquire into the elementary processes acting in Geiger counters and the building up of pulses in the Geiger zone, in counters filled with very pure argon or argon mixed with carbon dioxide, at concentrations ranging from 10^{-4} to 10^{-1}. Many researches have been carried out up to now to build a theory to account for the behavior and properties of counters.[1,2] These researches have high-lighted some fundamental points on this subject. However, the mechanisms acting in discharge building up are still uncertain, particularly as far as simple gas counters are concerned.

Evidently, a theory explaining the behavior of a counter requires a knowledge of the various processes responsible for the production of electrons, taking into account the gas mixtures and the cathode of the counter used. Researches on these processes in gas discharges have been extensively carried out by many authors; a review on this subject is given by Penning and Druyvesteyn and by Loeb.[3,4] These studies evidence the strong dependence on purity, pressure, and temperature of gas discharge mechanisms. Therefore, it may be said that the results of these measurements are valid only if strictly referred to the particular conditions of work.

[1] S. C. Curran and J. D. Craggs, *Counting Tubes* (Butterworths Scientific Publications, London, 1949).
[2] D. H. Wilkinson, *Ionization Chambers and Counters* (Cambridge University Press, Cambridge, 1950).
[3] M. J. Druyvesteyn and F. M. Penning, Revs. Modern Phys. **12**, 87 (1940).
[4] L. Loeb, *Fundamental Processes of Electrical Discharge in Gases* (John Wiley and Sons, Inc., New York, 1939).

II. METHOD OF MEASUREMENT

The experimental method in the present work makes use of the observation of pulses obtained from ionizing particles, in a regular cylindrical counter. Depending on the applied voltage, the counter acts first as an ionization chamber and later as a proportional counter. At a defined voltage value, the counter gets in the corona discharge zone; under suitable conditions, this zone is preceded by a Geiger zone.

Part of our measurements consists of taking the curves which give N, the multiplication factor, as a function of the voltage V; N represents the number of electrons generated on the counter wire in the Townsend avalanche, per primary electron. The primary ionization is obtained by α-particles from a polonium source placed in the counter, or by single fast electrons generated in the counter wall by a γ-ray source outside the counter (in the following called γ-pulses). The multiplication curves are taken by means of α-particles up to N values of about 50. At higher N values, since α-particles cause a distortion in the multiplication factor due to the high charge involved in the avalanche, γ-pulses are used which, under our conditions, give an undistorted multiplication.

Another part of the measurements consists of the study of the shape of pulses in the various zones of voltage of the counter, with different time constants in the amplification chain, in order to obtain pulses variously differentiated. From these observations of the shapes, it is possible to get the discharge development as a function of time, from which one can obtain

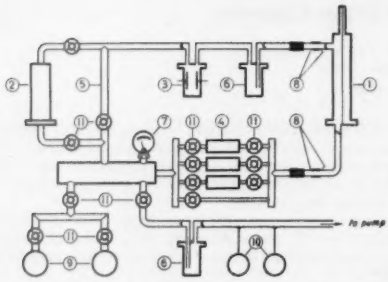

FIG. 1. Experimental apparatus: 1. counter; 2. purification furnace; 3. ionization chamber; 4. reservoirs; 5. heated tube; 6. traps; 7. manometer; 8. Kovar-glass seals; 9. argon and carbon dioxide tanks; 10. vacuum gauges; 11. stopcocks.

information on the nature of processes involved in the discharge and can measure some quantities related to these processes.

III. EXPERIMENTAL EQUIPMENT

The measurements have been taken with different equipment consisting of one or more counters mounted on a manifold suitable for evacuating and filling them with the proper gas mixtures. The apparatus to which most of our data refer is shown in Fig. 1. This consists of a counter inserted in a metal circuit, where the gas will circulate by heating, which provides a fast purification of the argon and a fast mixing of argon plus carbon dioxide mixtures. The counter is of brass; its diameter is 60 mm; the useful length of the tungsten wire is 200 mm and the wire diameter 0.2 mm. The counter can be heated up to 200°C for degassing purposes. The counter tube was degassed at 600°C for a few hours before mounting.

The outstanding elements of the circuit are as follows: (1) The circulation furnace filled with calcium magnesium alloy, with 10 percent magnesium, which provides the argon purification.[5] (2) The ionization chamber which is employed for the measurement of the electron drift-velocity in the gas. This measurement will control the argon purity at 99.99 percent accuracy for molecular impurities.[5] (3) The heated tube, which allows gas circulation even excluding the furnace.

The tight washers and the stopcocks are wholly metallic; in the apparatus there is neither grease nor mercury vapors.

This apparatus in connected to a diffusion vacuum pump, which works with silicone oil. The vacuum is measured by a Penning gauge. The whole apparatus is evacuated for many days at 10^{-5} mm Hg, degassing the counter and the furnace.

The argon employed is from different sources and of initial purity ranging from 98 to 99.9 percent. In every case, the results obtained can be reproduced. The purity of the carbon dioxide was 97 percent.

The counter wire is connected, through a conventional amplification chain, to a cathode-ray tube, Dumont 248 type, the sweep of which is triggered by a

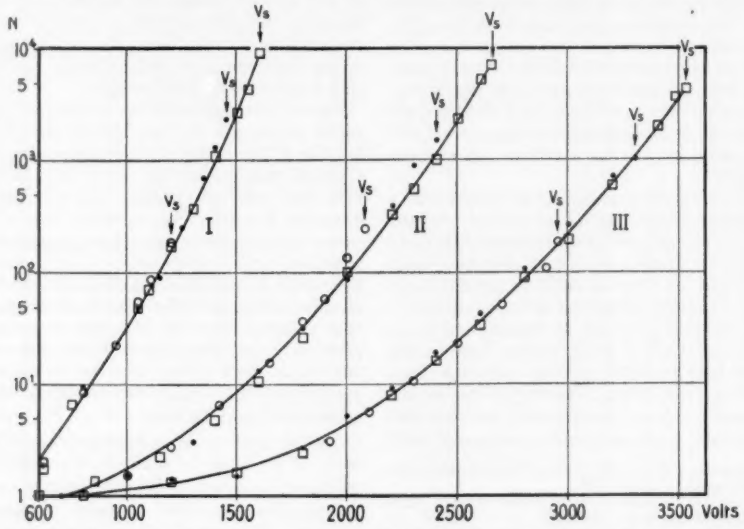

FIG. 2. Multiplication curves for argon and argon+carbon dioxide mixtures. (I) $p=150$ mm Hg; (II) $p=500$ mm Hg; (III) $p=1000$ mm Hg. ○—argon; ●—argon plus 3×10^{-4} carbon dioxide; □—argon plus 17×10^{-4} carbon dioxide.

[5] L. Colli and U. Facchini, Rev. Sci. Instr. **23**, 39 (1952).

synchroscope. The rise time of the circuit is 0.6 μsec. In a number of cases it has been found advisable to use a chain with a faster rise time.

The measurements of pulse amplitudes are taken through an input time constant RC much higher than the pulse rise time ($RC = 200$ μsec): In this case a pulse shaping delay line is inserted between the preamplifier and the amplifier, which line suppresses the pulse after a time varying from 1.2 to 6 μsec; thus, only the first

FIG. 3. α-particle pulse in the low proportional zone. Markers = 10 μsec; $RC = 1$ μsec.

rise of the pulse is recorded, corresponding to the collection of the avalanche electrons, and an eventual component due to a delayed production of electrons is left out. This cut is important in the measurement of the multiplication factor in the highest proportional zone, where these processes of delayed production are considerable.

The pulse shape as a function of time is observed by the synchroscope, using an input time constant varying from 1 to 200 μsec which gives different pulse differentiation. The pulse shape can be observed in a time duration varying from some μsec to about 30 msec using different oscillograph sweep durations.

IV. MEASUREMENT FOR ARGON

The multiplication curves N *versus* V, in argon for pressures ranging from 150 to 1000 mm Hg, are shown in Fig. 2. During the time of measurement the argon circulates in the purification furnace at 400°C (Fig. 1). Under these conditions the measurements are reproducible; no variation has been obtained by placing liquid air round the trap and leaving it there for some hours. The counter is at room temperature.

The α- and γ-pulses observed through the synchroscope are of the usual shape, up to multiplication values of about 50 (Fig. 3). Starting from these multiplication values, each α- or γ-pulse is followed by a convergent succession of pulses separated by a time T_0 (Figs. 4 and 5); the ratio of this succession increases as N increases. The time T_0 between the pulses of the succession is ~10 μsec, at all the pressures studied. These pulses are clearly observed with an RC of 1 μsec, much smaller than their separation.

Observing the pulse succession we can see that the rise time of successive pulses gets longer as the sequence number of the pulse in succession increases (Fig. 5); consequently, the sharpness of the separation between pulses decreases towards the end of the succession. This effect becomes more prominent as the pressure diminishes. At a pressure of 150 mm Hg the second pulse only is detectable, followed by a continuous slope (Figs. 6 and 7).

At a multiplication value of about 200 (Fig. 2), after a few volts of unstable zone the corona discharge starts in the counter. The α-pulse shapes at the beginning of the corona are shown in Figs. 4–7. It should be noted that the successions of pulses are always convergent, as is the case also for γ-pulses.

V. DISCUSSION OF THE RESULTS FOR ARGON

The results obtained for argon, and particularly the pulse shapes at high multiplication, can be accounted for by the processes governing the production and the decay of excited atoms in the Townsend avalanche.

(a) The Photopulses

As is well known, in the proportional zone an electron released in the counter may ionize the argon atoms by collision when it approaches the wire, where the electric field is sufficiently strong, and cause the Townsend avalanche. An electron generated in the counter will thus build up a pulse containing N electrons, the amplitude of which is proportional to N, the multiplication factor.

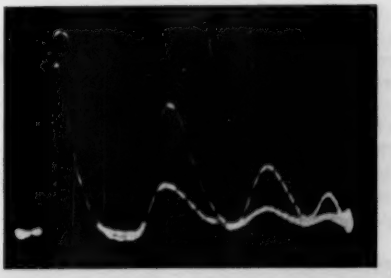

FIG. 4. α-particle pulses in argon at the corona threshold. Pressure = 1000 mm Hg; $N = 210$; markers = 1 μsec; $RC = 1$ μsec.

Let us consider now the excited atoms produced in the avalanche; let us call α the ratio between the number of excited atoms and the number of electrons produced by collision in the avalanche. The number of excited atoms produced per initial electron in the gas is $N\alpha$. It can be assumed that the excited levels have a lifetime $T/0$, and that in the decay processes they generate some photons hard enough to extract electrons from the cathode by photoelectric effect (photoelectric

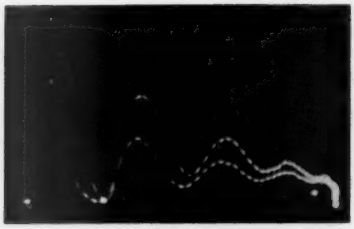

FIG. 5. α-particle pulses in argon at the corona threshold. Pressure = 500 mm Hg; $N = 250$; lengthening of rise time is detectable in the last photopulses; markers = 1 μsec; $RC = 1$ μsec.

threshold of brass 4–5 ev). Let us call β the mean number of "hard" photons emitted per excited atom, G the probability of a photon reaching the cathode without destruction, K the useful solid angle, and γ the mean number of electrons extracted from the cathode and reaching the wire per each photon.

In a time interval of the order of T_{f0}, the $N\alpha\beta$ photons produce $N\alpha\beta GK\gamma$ photoelectrons from the cathode. These photoelectrons reach the wire after a time T_{e0} (transit time in the counter) and multiply by N, giving rise to a second pulse of amplitude proportional to $(N\alpha\beta GK\gamma)\cdot N$ at a time interval about $T_{e0}+T_{f0}$ from the first. This process will repeat, so that a succession of pulses is obtained, the ratio $(N\alpha\beta GK\gamma)$ of which increases as the voltage increases; here we have disregarded the N variation due to the positive charge accumulated on the wire.

At the voltage value where

$$N\alpha\beta GK\gamma = 1, \tag{1}$$

there is the divergence threshold of the process in this approximation. The value of N which satisfies Eq. (1), the threshold multiplication factor, will be called N_S and the corresponding voltage V_S.

The pulse succession described in Sec. IV, the behavior as a function of voltage, and the starting of corona discharge can be explained by this process. The single photopulses of the succession can be observed properly separated only if the time T_{f0} is much lower than T_{e0}. If T_{f0} is not negligible compared to T_{e0}, the pulse rise times are obviously lengthened; therefore, their separation is worse.

The photographs of pulse successions show that pulse rise times get longer for the last pulses of the succession; this lengthening becomes more important as pressure decreases until, at lowest pressures, the photopulses are no more separated. These facts appear to indicate that the time T_{f0} increases as pressure decreases. A cause of lengthening of the rise times in the next pulses might be due to an action of the developing time of the electronic avalanche and also to a geometrical diffusion of the pulses along the counter. We may assume these effects to be negligible, since in $A+CO_2$ mixtures (see Sec. VII) several tens of well separate photopulses and no considerable lengthening of the rise times can be observed. Under these conditions, geometrical or avalanche actions will occur in a way similar to that which occurs in pure argon, without causing any considerable effect. Some information on

FIG. 7. α-particle pulse in argon at the corona threshold. Pressure = 150 mm Hg; $N = 180$; sweep time = 100 μsec; $RC = 10$ μsec.

the T_{f0} value can be obtained by measuring T_0, the distance between the maxima of the two first pulses, and calculating T_{f0} from the relation $T_{f0}+T_{e0}\simeq T_0$.

T_{e0} is calculated with sufficiently high accuracy by the drift-velocity values w^- of electrons *versus* E/p.[5] These drift-velocity values have been controlled in the same apparatus by the chamber shown in Fig. 1. Nielsen's values for w^- have been employed for E/p higher than 1.5 volt cm^{-1} mm Hg^{-1}.[6]

Values for T_0, T_{e0}, and $T_0-T_{e0}\simeq T_{f0}$ are shown in Table I. These values are to be looked on only as orders of magnitude of the lifetime of excited levels in the gas; in the case of high pressures the values obtained are actually only upper limits. The assumption of a decay time T_{f0}, of the order of magnitude shown in the table, accounts for the pulse shape and gives a simple explanation of the results obtained for the argon plus carbon dioxide mixtures, as will be seen later.

FIG. 6. α-particle pulse in argon at the corona threshold. Pressure = 150 mm Hg; $N = 180$; markers = 1 μsec; $RC = 1$ μsec.

[6] R. A. Nielsen, Phys. Rev. **50**, 950 (1936).

(b) The Decay of the Excited Levels

We now analyze more particularly the decay phenomena of excited levels in the avalanche, in order to make clear the meaning of the time T_{f0} and to discuss its order of magnitude.

In view of this, let us consider the level spectrum of argon as shown in Table II.[7,8] Among the four lower excited levels, the $^3P_1$ and $^1P_1$ are radiant resonance levels, the $^3P_2$ and $^3P_0$ are metastable levels. All these levels have a certain lifetime in the gas, as will be shown below.[9] Among the upper levels, only a few may decay directly to the fundamental level, sending out photons of 14–15 ev; most of these levels will decay, through successive steps or directly, to one of the four lower levels, releasing photons of energy less than 4 ev at all times. The lifetime for these transitions is generally of the order of 10^{-7}–10^{-9} sec, much smaller than the lifetime of the four lower levels.

It should be pointed out that the photons created in these transitions are too soft to produce photoelectric extraction from the cathode; therefore, no further mention of them will be made. Under these conditions, it appears that in any initial distribution of the excitation, after a time corresponding to a few radiant transitions, resonance and metastable levels only are present in the gas.

The $^3P_1$ and $^1P_1$ levels will decay at the fundamental state giving out resonance photons of 11.62 and 11.82 ev. The resonance photons, as is well known, will undergo a diffusion process through which they are captured and re-emitted many times by the nonexcited atoms in the gas. Holstein[10] developed a theory of this process; he calculates that the imprisonment factor $1/g$ (number of captures and re-emissions for a photon, before reaching the containing walls) for a cylinder a few centimeters in diameter is of the order of a few hundreds. According to this theory, the imprisonment duration in our case may be of about 10^{-4}–10^{-5} sec. Holstein deduces also that the imprisonment factor $1/g$ is independent of pressure in a pressure range where the shape of the emission line is determined by the pressure broadening. Experimental measurements giving a value for $1/g$ in argon are not available.

TABLE I. Values of the decay time T_{f0} in argon.

Pressure (mm Hg)	V_S volts	T_0 (μsec)	T_{e0} (μsec)	$T_{f0}=T_0-T_{e0}$ (μsec)	$(T_{f0})_M$ (μsec)
150	1200	10.8±1	6.3±1	4.5±2	4.1
300	1640	10.7±1	7.1±1	3.6±2	1.1
500	2070	10.2±1	7.7±1	<2.5	0.4
1000	3000	10.5±1	8.8±1	<1.7	0.1

[7] W. de Groot and F. M. Penning, *Handbuch der Physik* (J. Springer, Berlin, 1933), 23/1.
[8] C. E. Moore, *Atomic Energy Levels*, National Bureau of Standards Circular No. 4467 (1949).
[9] A. C. G. Mitchell and M. W. Zemansky, *Resonance Radiations and Excited Atoms* (MacMillan Company, New York, 1934).
[10] T. Holstein, Phys. Rev. **72**, 1212 (1947); **83**, 1159 (1951).

TABLE II. Excited levels of argon atom.

Term	Excitation energy ev	Remarks
$^1S_0$	0	Fundamental state
$^3P_2$	11.545	Metastable level
$^3P_1$	11.620	Resonance level
$^3P_0$	11.720	Metastable level
$^1P_1$	11.825	Resonance level
$^{1,3}S$, P, D	12.7–13.3	
$^{1,3}P$	14.0–14.9	
$^{1,3}P$, D, F	14.1–14.3	
	15.68 15.86	Ionization

Metastable levels have very long lifetimes of their own; the process causing their decay is collision with nonexcited atoms of the gas. The lifetime of the $^3P_2$ metastable level in argon has been recently investigated by Molnar[11,12] and Phelps,[13] at pressures from 1 to 10 mm Hg. From these measurements the metastable lifetime was found to be of the order of some msec, and the probability of destruction of metastables in the gas was found to be proportional to the square of the pressure.

According to these authors, the metastable destruction can be accounted for by some collision between metastable and unexcited atoms, leading to the formation of unstable excited molecules which will rapidly decay. There is good reason to assume that hard photons are produced by this process; these photons, being nonresonance ones, will reach the cathode without capture by gas atoms.

Many other phenomena of the gas discharge were interpreted through processes of this kind;[14] however, evidence of their existence is available at present only in the mercury[15] and helium[16] cases.

A suitable theory of the decay of metastable and resonance levels has not been developed up to now, and the experimental data are rather insufficient; furthermore, the decay is complicated by collision processes which, owing to the small energy difference among the first excited levels of argon, of the order of the thermal energy, may lead to transitions between them.

However, the following remarks can be made: At high pressures, the decay of all the first levels can be considered as a whole, taking into account the transitions by collisions. Two possibilities exist: (1) The levels decay through the emission of resonance photons reaching the cathode, with a probability per second almost independent of pressure, represented by g/τ^*, where τ^* is the radiant lifetime of resonance levels. (2) They decay through the process described by Molnar, the probability of which increases with the

[11] J. P. Molnar, Phys. Rev. **83**, 933, 940 (1951).
[12] J. P. Molnar, private communication.
[13] A. V. Phelps, Phys. Rev. **82**, 567 (1951).
[14] E. W. Pike, Phys. Rev. **53**, 921 (1938).
[15] A. Q. McCoubrey, Phys. Rev. **84**, 107 (1952).
[16] R. Meyerott, Phys. Rev. **70**, 670 (1946).

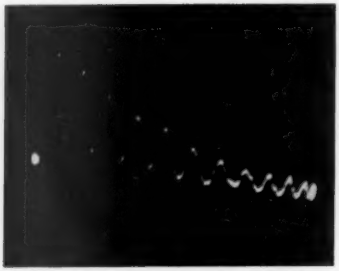

FIG. 8. β-pulse in argon plus 5×10^{-4} carbon dioxide near the Geiger threshold. Pressure = 500 mm Hg; markers = 1 μsec; $RC = 1$ μsec.

square of pressure. This process is likely to become more and more important at higher pressure, finally controlling completely the decay of all levels. As a result, the resonance photons practically do not reach the cathode and the photoelectric effect is caused by the photons originated in the collisions of the type described by Molnar. From the description given above β and γ should be referred to these photons and G is thought to be 1. Following these considerations we extrapolated Molnar's results, obtaining the values $(T_0)_M$ listed in Table I. These values are of the same order of those obtained by our measurements. Consequently our results give further evidence of the existence of a process causing fast destruction of the afore-mentioned levels in the argon at high pressure.

The decay processes will be further discussed in a subsequent paper.[17]

(c) The Corona Threshold

We now consider the pulse shapes at the corona threshold. If the corona discharge is sustained by the photoelectric process only, the corona threshold is reached when N, the multiplication factor, satisfies Eq. (1); $N\alpha\beta K\gamma$ represents the ratio of the pulse succession which, in this case, should have all the terms constant. When observed with a RC of 1 μsec the shape of the pulse succession from γ-pulses at the corona threshold is always convergent.

The small RC values used may produce a decrease in the ratio of the succession because of the fact that the pulse rise times will increase towards the end of the succession. Roughly considering this electronic distortion, the ratio of the succession at the corona threshold may be evaluated as no less than 0.7–0.9.

Under these conditions, a contribution to the corona discharge from some other processes cannot be completely disregarded. Such processes might be made undetectable in the pulse shape by the experimental conditions of the observation. It can be said, however, that processes other than the photoelectric effect do not contribute in a large measure to the corona discharge considerably at our gas pressures and with our brass cathode.[18]

[17] To be published in *Nuovo Cimento*.

VI. ARGON PLUS CARBON DIOXIDE MIXTURES—PHOTON QUENCHING

Argon plus carbon dioxide mixtures have been studied in the apparatus described under III, at pressure ranging from 150 to 1000 mm Hg. The results obtained with concentrations lower than 5×10^{-3} are reported here.

(a) Experimental Results

Multiplication curves and pulse shapes have been observed for different voltages and for different mixture concentrations. Figure 2 shows a number of these multiplication curves. The curves corresponding to the same pressure have a common part where they are coincident within the experimental accuracy, of the order of 20 percent.

The pulse shapes show that at high multiplication values, each ionizing particle gives rise to a pulse succession of the same kind as described for pure argon (Figs. 8 and 9). The ratio of the pulse succession increases with the multiplication factor as usual until the divergence is reached. In these mixtures a value for this ratio of 1 or over 1 has been observed without a stable corona discharge in the counter.

A detailed discussion of the behavior of the counter at the divergence threshold will be given in Sec. VII.

We are now interested in the study of N_S, the multiplication factor at the divergence threshold (by divergence threshold is meant the voltage value V_S where the ratio of the pulse succession is 1). N_S values obtained *versus* the carbon dioxide percentage X at various pressures are shown in Fig. 10. N_S is shown to increase almost linearly with X, and the slope of the straight lines $N_S(X)$ is found to be steeper for low values of pressure.

(b) Discussion

From the fact that in the proportional zone the same N value corresponds to the same voltage for different carbon dioxide concentrations, we can deduce that the structure of the Townsend avalanche does not depend on small carbon dioxide concentrations. As a consequence, the number α of excited atoms produced in

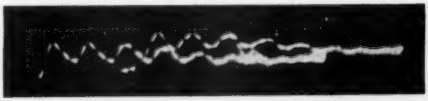

FIG. 9. β-pulses in argon plus 17×10^{-4} carbon dioxide around the Geiger threshold. Pressure = 150 mm Hg; markers = 1 μsec; $RC = 1$ μsec.

[18] We note that recently E. J. Lauer (J. Appl. Phys. **23**, 300 1952) has brought in view the presence of a process of ion cathode extraction in argon, using degassed nickel cathodes.

the avalanche per electron may be assumed to be independent of X.

The pulse successions observed in all mixtures hereto discussed may be interpreted as being caused by the photoelectric effect; the ratio of the succession is given by $N\alpha\beta\gamma KG(1-P)$, which will increase with the voltage. P stands for the probability of destruction of excited atoms of argon through collisions with carbon dioxide molecules, without sending out photons efficient in photoelectric extraction.

The threshold value N_S is determined by

$$N_S=1/[\alpha\beta\gamma KG(1-P)]. \quad (2)$$

The quantities involved generally depend on pressure and carbon dioxide concentration.

It is not definitely known if γ, photoelectric yield of the cathode, depends on X. We consider γ to be roughly independent of X; α, β, and K have to be considered constant. The strong variation of N_S as a function of X may therefore be attributed either to the reduction of G, the probability of the photons reaching the cathode, or to an increase of P. We shall now analyze these two cases. G could be reduced by absorption of photons by carbon dioxide. It may readily be seen that this process should produce an exponential dependence of N_S on the total amount of carbon dioxide contained in the counter. The experimental results disagree with this conclusion, the dependence of N_S on X being linear and the dependence of N_S on total pressure going in the opposite direction to that expected. This, as a consequence, will exclude photon absorption as the main process controlling the N_S reduction. We can say that $G=1$ even for the mixtures discussed here.

Let us now consider the P variation. In this case the collisions of the second kind between excited argon atoms and carbon dioxide molecules have to be taken into account.[9] The excitation energy of the atom is generally transferred to the molecules concerned, which may dissociate or be excited or ionized. In the case under consideration, the most probable reaction is as follows[19]:

$$CO_2+A^*\rightarrow CO^*+O+A+5.5 \text{ ev}.$$

The carbon monoxide molecule is left excited with 6 ev. The reaction energy is thus 11.5 ev, very close to the energy of the excited metastable and resonance levels of argon. This fact increases the probability of the process in question because of resonance.[20]

TABLE III. Values of $\bar{\sigma}T_{f0}$ and of $\bar{\sigma}$ deduced from the curves of Fig. 10.

Pressure (mm Hg)	$n_A\bar{V}\bar{\sigma}T_{f0}$	$n_A\bar{V}$ cm^{-2} sec^{-1}	$\bar{\sigma}T_{f0}$ cm^2 sec	$\bar{\sigma}$ cm^2
150	33,820	0.18×10^{26}	187.8×10^{-21}	458×10^{-16}
500	14,507	0.61×10^{26}	23.8×10^{-21}	595×10^{-16}
1000	7720	1.22×10^{26}	6.33×10^{-21}	633×10^{-16}

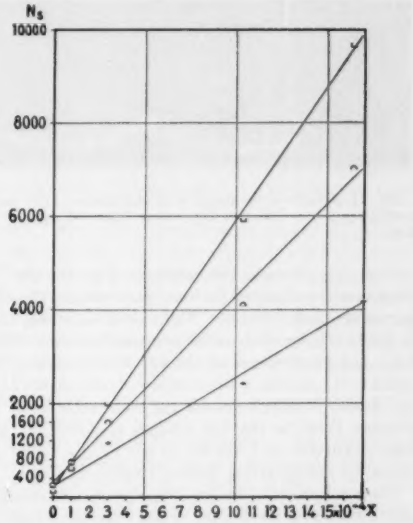

FIG. 10. Values of N_S *versus* CO_2 concentration X. The half-squares are for a pressure of 150 mm Hg; the half-circles are for a pressure of 500 mm Hg; and the bars are for a pressure of 1000 mm Hg.

In a first approximation, let us consider the excited atoms existing in an excited level only, and let N^* be their number in the counter. Under this hypothesis, the equation representing the decay of such atoms is

$$dN^*=-(N^*/T_{f0})dt-N^*n_AX\bar{\sigma}\bar{V}dt, \quad (3)$$

where T_{f0} in the lifetime of the level in pure argon. $-N^*/T_{f0}$ represents the exponential decay accounting for the destruction in argon. $-N^*n_AX\bar{\sigma}\bar{V}$ represents the destruction of excited levels by collisions on carbon dioxide molecules. n_AX is the number of carbon dioxide molecule per cm^3, n_A the number of argon atoms per cm^3, $\bar{\sigma}$ the mean cross section for the quenching process in carbon dioxide, and $\bar{V}$ the mean velocity of atoms.

The fraction of excited atoms destroyed in argon with production of the useful photons is given by

$$1-P=1/[1+n_A\bar{V}\bar{\sigma}T_{f0}X]. \quad (4)$$

From Eqs. (2) and (4) and assuming $G=1$, we have

$$N_S=(1+n_A\bar{V}\bar{\sigma}T_{f0}X)/(\alpha\beta\gamma K). \quad (5)$$

In this approximation the formula (5) indicates N_S to be a linear function of X. This formula is satisfactorily verified by the experimental results, considering the errors of the measurements.

[19] H. J. Henning, Ann. Physik **13**, 529 (1932).

[20] N. F. Mott and H. S. Massey, *The Theory of Atomic Collision* (Oxford University Press, London, 1949), Chapter XII.

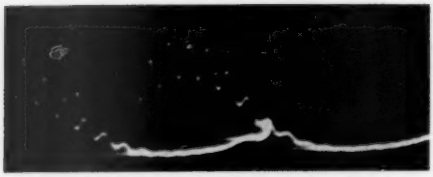

FIG. 11. β-pulses in the Geiger zone. Argon plus $\sim 10^{-3}$ carbon dioxide; pressure = 760 mm Hg; sweep time = 50 μsec; $RC = 1$ μsec.

From Eq. (5) and the results in Fig. 10, the $T_{f_0}\bar{\sigma}$ values can be obtained for various pressures, the other parameters being known. The values obtained, listed in Table III, decrease as the pressure increases, following a law proportional to the square of pressure. This result is in accordance with the law of destruction found by Molnar in pure argon for the metastable level. The $\bar{\sigma}$-values listed in the last column of Table III have been calculated with the aid of the $(T_{f_0})_M$ values, obtained by extrapolating Molnar's values (Table I).

Some information on the behavior of the resonance and metastable levels due to the different values for the quenching cross section and to the transition probabilities between them, may be obtained by studying the quenching curves to closer approximation, particularly the lower part where most of the excited atoms are destroyed. The poor accuracy of our measurements and the lack of information now available on these processes do not allow us to improve our own results. Therefore, the exact meaning of $\bar{\sigma}$ shown in Table III is uncertain too.

(c) Argon Purity

From Fig. 10, the N_S values appear to be influenced by carbon dioxide concentrations of the order of 10^{-4}. From this we can deduce that the argon used for mixtures contains less than 10^{-4} carbon dioxide or other impurities having the same quenching effect.

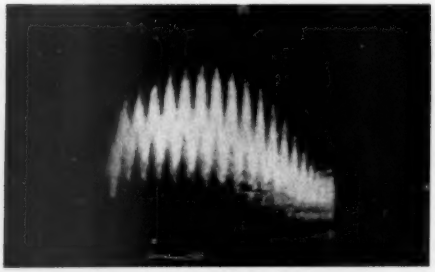

FIG. 12. Several superposed β-pulses in the Geiger zone. Argon plus 1.7 10^{-3} carbon dioxide; pressure = 1000 mm Hg; distance between photopulses = 4.4 μsec; $RC = 1$ μsec.

VII. ARGON PLUS CARBON DIOXIDE MIXTURES—GEIGER ZONE FORMATION

(a) Experimental Results

We consider here the pulse shapes observed in the case of argon plus carbon dioxide mixtures with carbon dioxide concentrations less than 5×10^{-3}, and particularly the pulse shapes at the divergence threshold of the photoelectric process.

(1) *Pulse Shapes*

As stated in Sec. VI, the α- or γ-pulses at high multiplication values consist of photoelectric pulse successions, whose ratio increases with the voltage. Examining the pulses obtained at pressure of 150, 500, 1000 mm Hg and with mixtures containing various carbon dioxide concentrations, the following results are obtained:

(1) The time distance T between the successive pulses of the succession decreases as the carbon dioxide percentage increases. The values of T obtained under the said conditions are shown in Table IV.

TABLE IV. Values of the total time T, between photopulses, in argon and argon + carbon dioxide mixtures.

Pressure (mm Hg)	CO_2 concentration	T (μsec)
1000	0	10.5
1000	10^{-4}	8.9
1000	3×10^{-4}	8.1
1000	9×10^{-4}	6.3
1000	17×10^{-4}	4.4
500	0	10.2
500	10^{-4}	8.3
500	3×10^{-4}	7
500	9×10^{-4}	6
500	17×10^{-4}	4.1

(2) The sharpness of the pulse separation will improve as the carbon dioxide percentage is increased. At 5×10^{-4} carbon dioxide concentrations and 500–1000 mm Hg pressure, some hundred pulses are clearly observable in a γ-pulse succession. Under these conditions, no lengthening of pulse rise times is observed. At 150 mm Hg pressure, the photopulses are well separated only at carbon dioxide concentrations higher than 10^{-3} (Fig. 9).

(2) *Divergence Corona Threshold; Mixtures with Carbon Dioxide Concentrations less than 5×10^{-4}*

In these mixtures, as the multiplication value N_S corresponding to the divergence threshold is reached, the unstable corona discharge will start abruptly. The γ-pulses at this corona threshold consist of a very long pulse succession, containing even some hundred pulses. The succession will first go on with ratio a little lower than 1 and later with ratio about 1. Each γ-pulse may be considered as a corona burst, statistically quenched. This unstable corona zone lasts for only a few volts, after which the corona discharge is stable.

(3) Geiger Zone Formation: Mixtures with Carbon Dioxide Concentrations Ranging from 5×10^{-4} to 5×10^{-3}

With these concentrations, the multiplication factor N may reach values above N_S without the corona discharge getting started in a zone of voltage of very small amplitude, a few tens of volts. In this zone a particle gives rise to a pulse of the kind shown in Fig. 11. The pulse succession will go on first with divergent terms, afterwards with convergent terms until it is exhausted. The structure of these pulse groups does not depend on the primary ionization (Fig. 12). For this reason this photopulse group may be called a Geiger pulse group, and the divergence threshold V_S corresponds to the Geiger zone threshold.

The Geiger zone is followed by the unstable corona zone, lasting a few volts, where the pulse groups are statistically quenched. Figure 13 represents the corona bursts where the photoelectric pulse structure is revealed by an RC of 1 μsec. The amplitude of single photopulses oscillates periodically.

At the end of this zone the coron discharge gets stable with oscillating amplitude.

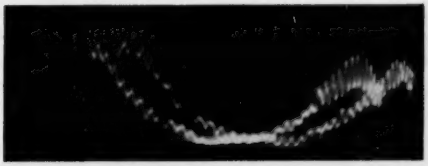

FIG. 13. Detailed bursts in unstable corona zone. Argon plus $\sim10^{-3}$ carbon dioxide; pressure = 760 mm Hg; sweep time = 100 μsec; RC = 1 μsec.

A behavior of this kind has been observed in many other counters 2 to 15 cm in diameter, at pressure ranging from 200 to 1500 mm Hg and filling mixtures of argon plus 0.1 percent carbon dioxide.[21] Complete corona bursts for these counters are shown in Figs. 14 and 15, which are taken with a high time constant.

(a) Discussion

(1) Time Distance between Photopulses

As discussed in Sec. V, the time distance T between the photoelectric pulses is the sum of the two times T_f and T_e; T_f is the decay time of the excited levels in the mixture and T_e the transit time of photoelectrons through the counter. From the considerations given in Sec. VII, it can be deduced that T_f is strongly reduced due to the effect of quenching of argon excited levels by carbon dioxide;[22] T_e is also reduced because of the carbon dioxide effect of increasing the electron drift-velocity.[23] The carbon dioxide percentage of 0.1 percent increases the drift-velocity in argon by a factor of two.[5]

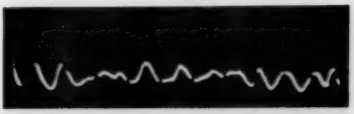

FIG. 14. Burst at the end of unstable corona zone. Argon plus $\sim10^{-3}$ carbon dioxide; counter diameter = 20 mm; pressure = 760 mm Hg; markers = 100 μsec; RC = 10 μsec; The photoelectric pulse groups appear like single pulses, due to the high RC value.

By the strong quenching effect shown in the curves of Fig. 10, T_f is found to be reduced more considerably than T_e. This agrees with the fact that the sharpness of the separation between the photopulse gets better as the carbon dioxide percentage increases.

(2) Space Charge Effect

The pulse shapes at the beginning of the corona discharge at various mixture concentrations and the Geiger zone formation are readily explained by considering the effect of the space charge accumulated on the wire. In the pulse succession, the delayed photoelectrons reaching the wire are affected in their multiplication process by the space charge formed in the preceding avalanches. Because of that, the multiplication factor N of the successive avalanches will be reduced.

The calculation of pulse build-up taking into account all the successions and the spreading of the pulse along the wire has not been attempted because of its difficulty; nevertheless, it is easily shown that the reduction of the multiplication factor is higher as the process of avalanche regeneration is faster and as the positive ion density is higher. This density is directly proportional to the multiplication factor, at the threshold N_S. Since the T values decrease and the N_S values increase as the carbon dioxide concentration increases, there is good reason to believe that the reduction effect on the succession ratio due to space charge is stronger at higher concentrations. Particularly, at concentrations higher than 5×10^{-4} ($T<7$ μsec, $N_S>2000$) this effect prevents the corona discharge from beginning at N_S

FIG. 15. Bursts in unstable corona zone. Argon plus $\sim10^{-3}$ carbon dioxide; counter diameter = 130 mm; pressure = 760 mm Hg; sweep time = 30 msec; RC = 200 μsec.

[21] Colli, Facchini, and Gatti, Phys. Rev. **80**, 92 (1950); **84**, 606 (1951).

[22] T_f is related to N_S and T_0 by the formula $T_f=(T_0/N_S)\cdot(1/\alpha\beta\gamma K)$.

[23] B. Rossi and H. Staub, *Ionization Chambers and Counters* (McGraw-Hill Book Company, Inc., New York, 1949).

FIG. 16. Geiger pulse in the middle Geiger zone. Argon plus 10^{-3} carbon dioxide; pressure = 500 mm Hg; markers = 1 μsec; $RC = 1$ μsec. The discharge spreading is due to both the photoelectric effect and a production of electrons in the gas.

and produces self-quenching of pulses, even though they have an initial ratio higher than 1.

The pulse shape shown in Figs. 11 and 12 may be explained as follows. Initially, the multiplication factor N is higher than N_S and consequently the succession proceeds at increasing terms. The positive space charge accumulated on the wire by the first pulses reduces the electric field so that N is brought below N_S; this occurs at the maximum photopulse of the succession. After this, N is kept below N_S until the whole succession is exhausted. By means of this mechanism, the discharge is spread along the whole counter wire.

The Geiger zone formation is clearly due to the space charge effect, which conclusion is in agreement with many authors.[1,24] From our observations, however, this occurs only at carbon dioxide concentrations higher than 5×10^{-4}.

The shapes of the corona bursts shown in Figs. 13, 14, and 15 are explained by the formation and the migration of positive ions, causing the field on the wire to oscillate about the threshold value. Evidently, N has the value N_S at the maxima and minima of the succession. Under these conditions, the space charge is no more able to quench the pulse succession.

(3) *Geiger Zone—Slow Counters*

As said above, the Geiger zones are very small and therefore cannot be used as counting zones. It may be noted, however, that they are observed with small time constant values (from 1 to 200 μsec) and without an external quenching circuit. Obviously, by using higher RC values or a quenching circuit, better Geiger zones could be obtained.

The behavior of these counters is of the same kind as that of the so-called slow counters.

(4) *Other Processes*

The sharpness of the photopulse separation and their time correlation up to several milliseconds indicate that other processes play a role negligible in comparison with the photoelectric process on the cathode, which process entirely explains the Geiger and corona zones. Particularly, a production of electrons in the gas is not important at the pressures and concentrations studied.

The electron extraction from the cathode by ion impact was not found to be efficient in our counters. This process should produce electrons after a time interval from the first avalanche corresponding to the ion transit time in the counter, which ranges from 2 to 8 msec, approximately, in the various conditions. Further, in the argon plus carbon dioxide mixtures, at concentrations between 5×10^{-4} and 5×10^{-3} where the Geiger zone is present, we have the following evidence against the ion-cathode process:

(1) The end of the Geiger zone is determined by the photoelectric process itself.

(2) In the corona bursts the single photopulses are clearly observable and correlated up to times corresponding to the ion transit time. A prominent electron production is not detectable here.

(3) The maxima of the corona bursts occur at a time smaller than the ion transit time.

(4) In the Geiger zone self-quenching separated pulses are observed. The total charge contained in a Geiger pulse is $\sim10^8$ electron charges. From this it can be deduced that the ion-cathode process yield is less than 10^{-8}.

VIII. ARGON PLUS CARBON DIOXIDE MIXTURES—FAST COUNTERS

In the case of mixtures with carbon dioxide percentage higher than 0.5 percent only a few observations have been made.

At pressures of 500 and 1000 mm Hg and 1 percent carbon dioxide percentage the photoelectric process will act at high multiplication values. The time interval between photopulses is about 2 μsec and the N_S value is about 20,000–40,000; here we have the beginning of the Geiger zone, which lasts a few hundred volts. In the first part of the Geiger zone the pulse shape is like Fig. 12 and its amplitude increases with voltage. Fur-

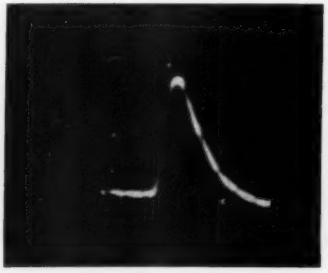

FIG. 17. Several superposed fast pulses at the end of the Geiger zone. Argon plus 10^{-3} carbon dioxide; pressure = 500 mm Hg; markers = 1 μsec; $RC = 1$ μsec. The discharge will spread solely by the process producing electrons in the gas body.

[24] C. G. Montgomery and D. D. Montgomery, Phys. Rev. **57**, 1034 (1940).

thermore, as the voltage increases the sharpness of the separation between photopulses gets worse until the Geiger pulse looks like Figs. 16 and 17. At 150 mm Hg pressure, the Geiger zone begins at an N_S value of about 80,000 and the Geiger pulses already at the threshold look less discontinuous as in Fig. 16.

With 10 percent carbon dioxide percentage, at the Geiger threshold, the pulses immediately take the continuous shapes shown in Fig. 17 at all pressures used, and there are no photoelectric pulses. Because of this, the threshold multiplication factor is difficult to measure.

The Geiger zone and the pulse shapes described above are of the kind obtained in the case of argon plus organic vapor mixtures.

The continuous shapes and the short durations of the observed Geiger pulses suggests a process of secondary electron production in the gas which is in accordance with the present knowledge on the discharge spreading mechanism in fast counters.[25] The high speed of the process both at the cathode and in the gas makes the quenching effect of the space charge very efficient and allows the formation of longer Geiger zones.

At the Geiger zone end, there are multiple pulses as in the argon plus alcohol counters. The corona discharge is started by these multiple pulses. The nature of these pulses has been investigated by many authors. However, the processes responsible of their formation are not known definitely at present.[26]

IX. ARGON PLUS MERCURY VAPOR MIXTURES

This section deals with the results obtained in argon contaminated with mercury vapor at 1.2×10^{-3} mm Hg pressure, corresponding to room temperature. This study has been carried out in an apparatus similar to that described under Sec. III.

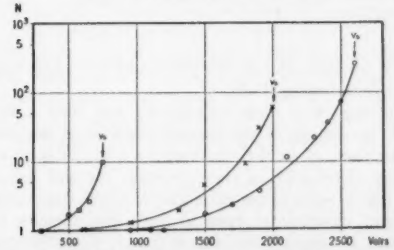

FIG. 18. Multiplication curves for argon plus mercury mixtures. Mercury at 20°C vapor pressure; □—pressure = 200 mm Hg; ×—pressure = 600 mm Hg; ○—pressure = 900 mm Hg.

FIG. 19. α-particle pulses in argon plus mercury vapor at the corona threshold. Pressure = 1000 mm Hg; markers = 1 μsec; RC = 1 μsec. The slow decay is due to production of electrons in the gas.

The multiplication curves for three pressures are shown in Fig. 18. At the V_S values the corona discharge will abruptly start. The corresponding N_S values are much smaller than for pure argon without mercury vapor.

At low pressures (200–500 mm Hg) no photopulse is detectable in the pulse shapes at the corona threshold, when observed by a 1 μsec time constant. The pulse shape at 1000 mm Hg pressure is shown in Fig. 19. Here the bump superposed on the continuous slope is due to the photoelectric effect on the cathode. The continuous slope drops more slowly than the time constant of the electronic circuit.

The results may be easily explained by the discussion of Secs. V and VI, after taking into account the Penning effect[7]; this effect is the ionization of mercury atoms by collision on the argon excited atoms. The ionization energy of mercury, 10.4 ev, is lower than the excitation energy of the first four argon levels. During their lifetime in the gas, the excited atoms may ionize by collision the mercury atoms; the free electrons created by this process will start the discharge again.

Our results in argon plus mercury vapor show that at low pressure this process of discharge restarting is more important than the photoelectric one; on the contrary, the contribution of the Penning effect is of the same order of the photoelectric effect at 1000 mm Hg pressure.

The pulse shapes at the corona threshold shown in Fig. 19 are in accord with this description of the mechanism controlling the corona discharge, due to the fact that the continuous slope of the pulses indicates a process of electron production in the gas.

Argon plus 0.1 percent carbon dioxide plus mercury vapor mixtures have also been studied. In this case the counter behaves as if filled with argon plus 0.1 percent carbon dioxide only. We observe that in these mixtures the quenching effect of carbon dioxide will reduce the lifetime of excited levels in the gas and consequently will reduce the collision probability on mercury atoms until the mercury ionization becomes negligible.

[25] Processes of this kind may be caused by the argon atoms excited in the upper levels (~15 ev), which may produce electrons by means of a reaction, for instance,

$$A^*+A\rightarrow(A_2)^*\rightarrow A_2^++e^-,$$

recently studied by Molnar and Hornbeck [J. A. Hornbeck, Phys. Rev. **84**, 615 (1951); J. A. Hornbeck and J. P. Molnar, Phys. Rev. **84**, 621 (1951)], or by means of ionizing collisions on atoms or molecules of a suitable gas. Under these conditions, the discharge spreading may be favored by the diffusion of the excited atoms in a small zone surrounding the wire, due to the imprisonment effect suffered by the resonance photons emitted by the highly excited atoms.

[26] D. Willard and C. G. Montgomery, Rev. Sci. Instr. **21**, 52 (1950).

X. CONCLUSION

In those mixtures where the photoelectric effect is the main process acting in the discharge build-up, the contribution to the pulse formation caused by the Townsend avalanche can be separated from the contribution caused by secondary processes. Consequently, it is possible to study the secondary process of electron production and measure its efficiency.

From our results the photoelectric process on the cathode is found to be responsible for the formation of the Geiger and corona zones in mixtures of argon plus carbon dioxide at concentrations less than 5×10^{-3} at any pressure used.

The same accuracy cannot be used in the study of mixtures where a process of electron production in the gas body will operate, as in the case of argon plus carbon dioxide, at percentage higher than 5×10^{-3}. However, these processes are very interesting due to their fast spreading.

Furthermore, the photons acting in the photoelectric effect on the cathode are found to be emitted by the first excited levels of argon. These photons are produced in collisions leading to destruction of these levels, and are not resonance photons. The values obtained for the lifetimes of these levels are roughly in accordance with the extrapolation of Molnar's values at the pressure used. More direct measurement of these lifetimes at pressures ranging from 10 to 1000 mm should be very interesting in order to investigate this effect further.

We wish to take this opportunity to thank Professor G. Bolla and Professor B. Ferretti for assistance received during this work, Dr. F. M. Penning for his interest and valuable discussions, Dr. Molnar and Dr. Hornbeck for notifying us of their results, and Dr. E. Gatti for helpful discussions. We finally wish to thank Professor L. Loeb for his interesting critique and for the useful suggestions offered to us.

PHYSICAL REVIEW VOLUME 88, NUMBER 5 DECEMBER 1, 1952

Range Distribution of Sea-Level Mesons at Low Geomagnetic Latitudes*

L. DEL ROSARIO AND J. DÁVILA-APONTE
Physics Department, University of Puerto Rico, Rio Piedras, Puerto Rico
(Received July 31, 1952)

Seven points of the meson differential spectrum at sea level have been obtained at a geomagnetic latitude of 29°N. The method used was that of delayed coincidences and anticoincidences, and the range interval covered has been from about 10 to 320 g/cm² of air equivalent. In this interval our spectrum curve is found to be nearly flat; that is, it does not show a clear maximum around 200 g/cm² air equivalent, as indicated by several authors working at geomagnetic latitudes around 45°N.

I. INTRODUCTION

THE range and the momentum distribution of sea-level ordinary mesons (μ-mesons) have been investigated in the past years by several authors[1] working at geomagnetic latitudes around 45°N. Various techniques have been employed for this purpose: coincidence, anticoincidence, delayed coincidence, and magnetic deflection methods.

Although it is quite well known that only a very small percentage of the charged particles at sea level are protons, as yet little information is available on the energy distribution of these protons. For this reason, and also in order to get rid of the electronic component, without uncertainty, even at very low energies the method of delayed coincidences (which yields the complete separation of the mesons at rest taking advantage of their instability) appears to be the most suitable to investigate the low energy end of the meson spectrum. This technique has also the advantage of being much simpler and less expensive than the one based on the use of a Wilson chamber in a magnetic field. It cannot be profitably used, however, for an accurate determination of the absolute number of the observed mesons, since it is in general difficult to evaluate the efficiency of the apparatus for the detection of the electrons resulting from the decay of the stopped mesons.

To overcome this point, delayed coincidences and anticoincidences have been recorded simultaneously in

* This investigation was sponsored jointly by the ONR and by a grant-in-aid from the Research Corporation.

[1] M. H. Shamos and M. G. Levy, Phys. Rev. **73**, 1396 (1948); A. Rogozinski and M. Lesage, Compt. rend. **227**, 1027 (1948); B. G. Owen and J. G. Wilson, Proc. Phys. Soc. (London) **62**, 600 (1949); E. W. Kellerman and K. Westerman, Proc. Phys. Soc. (London) **A62**, 356 (1949); W. L. Kraushaar, Phys. Rev. **76**, 1045 (1949); M. Sands, Phys. Rev. **77**, 180 (1950); M. Conversi, Phys. Rev. **79**, 749 (1950); L. Germain, Phys. Rev. **80**, 616 (1950); Glaser, Hamermesh, and Safonov, Phys. Rev. **80**, 625 (1950); Caro, Parry, and Rathgeber, Nature **165**, 688 (1950); M. G. Mylroi and J. G. Wilson, Proc. Phys. Soc. (London) **A64**, 404 (1951); B. G. Owen and J. G. Wilson, Proc. Phys. Soc. (London) **A64**, 417 (1951); J. L. Zar, Phys. Rev. **83**, 761 (1951); C. M. York, Phys. Rev. **85**, 998 (1952). For work previous to 1948, see B. Rossi, Revs. Modern Phys. **20**, 537 (1948); articles by G. Puppi and N. Dallaporta and by George in *Progress in Cosmic Ray Physics* (North-Holland Publishing Company, Amsterdam, 1952). An investigation on the spectrum of high range mesons has been recently published by Brini, Rimondi, and Filosofo, Nuovo cimento **9**, 505 (1952).

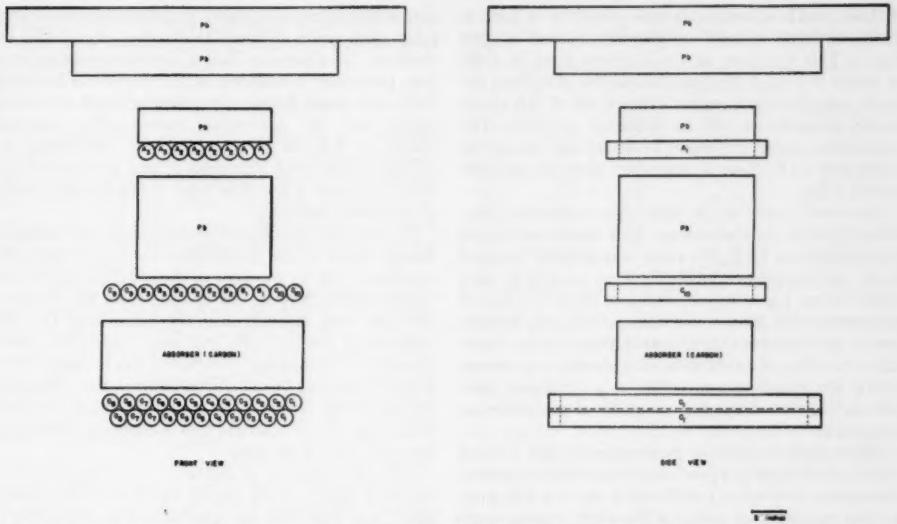

FIG. 1. Diagram of apparatus. The mesons actually recorded were those which, after crossing the counter telescope, were stopped in the graphite absorber and decayed between about 1.2 and 7 μsec into electrons discharging counters *C*.

recent experiments.[2] In this way the efficiency of the apparatus for the detection of the decay electrons can be directly derived from measurements taken under suitable conditions.

In the present experiment we have employed this method, though not much attention has been devoted to obtain a fully efficient anticoincidence system, since we were interested more in the spectrum shape than in the absolute numbers of mesons. Besides, apart from minor changes (see next section) we have employed the same apparatus designed and used by Conversi,[2] for which an accurate determination of the efficiency for the detection of the decay electrons was made in Chicago.

Actually the method used in the experiment reported in this paper yields the number of μ-mesons stopped in a given thickness of material (graphite) after crossing a certain variable amount of dense material, under the assumption that local production of π-mesons can be neglected. At the present stage of our knowledge, this assumption is certainly very reasonable at low altitudes, and, in particular, in the case of our experiment.

We thought that it might be of some interest to measure accurately a few points of the low range end of the meson spectrum at Río Piedras, Puerto Rico, in view of (a) the fact that the agreement among the results so far obtained by the various workers is not always very satisfactory, and (b) the possibility of comparing the shape of the meson spectrum at the relatively low geomagnetic latitude of our station (29°N) with that obtained in Chicago using essentially the same apparatus.

The range interval covered in our measurements was from about 10 to 320 g/cm² of air equivalent. The corresponding intervals in energy and momentum, as deduced from the conventional relationships[3] presumably valid for μ-mesons (rest energy = 110 Mev), are from 45 to 620 Mev and from 110 to 720 Mev/c, respectively.

II. EXPERIMENTAL PROCEDURE

As stated above, the apparatus used in the present experiment was essentially the same one employed in the experiments reported in reference 2. There is only a slight difference in the geometry, because we have preferred to use mostly 1-inch-diameter counters, as shown in the cross-sectional views of the disposition of the counters and absorbers reported to scale in Fig. 1.

All counters were of the all-metal type, had a 0.08-cm thick wall, and were filled with the usual argon-alcohol mixture. Counters with the same symbol and subscript were connected directly in parallel. The counters of group *C* were connected to a mixer circuit in order to mix their pulses and have each of them uncoupled with respect to all the others.

The following double coincidences were formed and then mixed together: $(A_1,\ B_1+B_2)$, (A_2, B_2), and (A_3, B_2+B_3). Thus, apart from random events, each

[2] M. Conversi, Phys. Rev. **79**, 749 (1950).

[3] G. C. Wick, Nuovo cimento **1**, 302 (1943); D. J. X. Montgomery, *Cosmic Ray Physics* (Princeton University Press, Princeton, 1949).

of these double coincidences was caused by a particle whose direction crossed in general counters C (see Fig. 1). This was done, as it will be seen later, in order to reduce to a small fraction the number of random delayed coincidences. In what follows, all of the above double coincidences will be indicated as (AB). The coincidence circuit employed to obtain any of the coincidences (AB) had a resolving time of approximately 2μsec.

Counters C were at the same time in delayed coincidence and in anticoincidence with respect to any of the coincidences (AB). An event was actually recorded as an anticoincidence $(AB-C)$ if no counter C fired within about 1 μsec before, to 8 μsec after, the time of occurrence of a double coincidence (AB). If, instead, one of the counters C fired within about 1.2 to 7 μsec after the time of occurrence of a double coincidence (AB), the event was recorded as a "delayed" coincidence" in one of the four channels of the electronic equipment.

More precisely, each of these channels had a "time width" θ of about 2.8 μsec, while the "time distance" between each of them and the next one was 0.96 μsec. In this manner, four points of the decay curve, corresponding to the mesons stopped in the graphite absorber after crossing the material placed above counters B, could be obtained simultaneously.

The pulse forming circuit triggered by counters C had a recovery time of 12 μsec. Consequently, random delayed coincidences could occur only when a single discharge of one of the counters C followed after a short time the instant of arrival of a particle producing a coincidence (AB) *but failing to discharge counters* C. If the counting rate of the latter events is indicated by $n_{(AB-C)}$ and n_C is the counting rate of counters C, the number of spurious delayed coincidences recorded per unit time in each channel is given by

$$N_r = n_{(AB-C)} n_C \theta. \qquad (1)$$

This is found to be very small under the conditions of our measurements (see below). For further details about the pulse recording circuits and for the final calculation of the numbers of mesons stopped in the absorber the reader should consult Conversi's paper.[2]

To obtain the various points of the range distribution of the meson component, measurements have been taken with seven different thicknesses of material in, or above, the apparatus. Part of the measurements have been performed in a shelter on the roof of our building, with only about $\frac{1}{2}$ inch of wood and $\frac{1}{4}$ inch of roofing board over the apparatus, corresponding approximately to 3 g/cm² of air equivalent. Alternately 0-, 2-, and 4-inch thick absorbers of lead were placed between counters A and B in order to obtain three points of the meson spectrum.

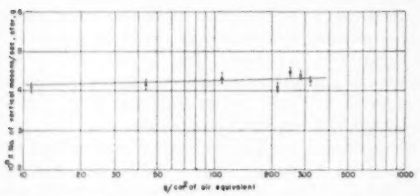

FIG. 2. The differential range spectrum of sea-level mesons at Rio Piedras, Puerto Rico—geomagnetic latitude 29°N. The absolute number of mesons per sec sterad g is represented as a function of their range expressed in g/cm² of air equivalent.

For the other four points, corresponding to the higher energy region of the distribution curve, the apparatus was placed on the top floor of the building, quite close to the ceiling. A large box holding sand was prepared over the roof, directly over the apparatus. The box measured 9 feet by 9 feet and had a depth of 1 meter of sand. The apparatus underneath was covered with a 6-inch thickness of lead, placed between the ceiling and the top of the frame. With this arrangement the total solid angle of the counters was completely covered by the sand and by the lead.

The total amount of material (1 m of sand plus 6 inches of lead), which, during this part of the experiment, was kept over the apparatus, was equivalent to about 200 g/cm² of air. The additional four points of the meson spectrum were obtained in these conditions by putting alternately 0-, 2-, 4-, and 6-inch thicknesses of Pb absorbers between counters A and B.

The thicknesses of air equivalent, corresponding to the seven points of the distribution curve investigated in the present experiment, have been obtained using Wick's calculations.[3] One must also add 8 g/cm² of air equivalent (corresponding to the half-thickness of the graphite absorber) in order to obtain the average amount of air equivalent crossed by an incoming vertical meson before stopping and being observed. Thus, the thicknesses for such mesons are found to be 11, 44, 110, 215, 250, 285, and 320 g/cm² of air equivalent. These figures are not given with a greater accuracy because our results show that the intensity of the observed mesons is nearly constant in the range interval investigated (see Fig. 2).

As stated in Sec. I above, we were more interested in the shape of the meson distribution curve than in the knowledge of the absolute numbers of mesons. For this reason the anticoincidence counters employed in the present experiment did not include the D counters used in the measurements taken with the same apparatus in Chicago.[4] The lack of a full efficiency of the anticoincidence system does not allow us to properly utilize the $(AB-C)$ counting rates, in order to get the absolute numbers of mesons through a sufficiently accurate determination of the efficiency of the apparatus for the recording of the decay electrons. The anticoincidence counting rate $n_{(AB-C)}$ has been measured during the experiment merely to introduce the correction for the

[4] See reference 2, Fig. 1.

spurious events, N_r, which becomes appreciable when no lead, or a small amount of lead, is placed between counters A and B.

III. RESULTS AND DISCUSSION

The seven points of the differential range spectrum of the sea-level mesons have been obtained through 1685 hours of effective observation. Each of these points was actually found by adding the results of a few (three or four) series of measurements performed in identical conditions, each partial series corresponding to a period of around 70 hours.

The results of the partial series were compared among themselves and their internal consistency was always found to be satisfactory. The recording of the delayed coincidences in four distinct channels allowed us to make, for each series of measurements, an evaluation of the meson lifetime τ. The values thus obtained for τ were found always to be in agreement with the best determination of this constant.[5]

It must be mentioned, however, that in part of our experiment only the delayed coincidences recorded in the last three channels have been considered, since unfortunately during these measurements the first channel of the electronic equipment did not work properly. In some of the partial series of measurements, therefore, not a very high accuracy was obtained in the determination of the number of stopped mesons and of their lifetime.

During the entire period of the performance of the experiment, checks were frequently made of the counting rate of the various groups of counters. In particular, the counting rate of the C group, which was necessary for the determination of the number N_r of random delayed coincidences, was recorded at the end of each individual measurement, namely, about four times per day. Frequent checks were also made of the pulse shape of the coincidence pulses and of other important points of the registering set, by means of a syncroscope.

The results of our measurements are summarized in Table I. In the first column of this table is reported the amount of material placed above the apparatus, plus that located between counters A and B, plus the half-thickness of the absorber, the total amount of material being expressed in g/cm² of air equivalent. As stated above, this represents the average range of the observed mesons (see Sec. II). The second column of the table contains the total time interval during which the corresponding data were obtained. The total number of spurious delayed coincidences occurring, within the time width of the channels, in the time interval specified in the second column, is reported in the third column.

For the sake of simplicity we are not reporting the numbers of counts recorded in each channel, but only the numbers of "extrapolated delayed coincidences,"

[5] N. Nereson and B. Rossi, Phys. Rev. **64**, 199 (1943). Also, see reference 2, and W. E. Bell and E. P. Hincks, Phys. Rev. **84**, 1243 (1951).

TABLE I. Results of measurements on the differential range distribution of sea-level mesons at a geomagnetic latitude of 29°N.

g/cm² of air equiv	Hours	Spurious counts N_r	Coinc./hr from mesons decaying within 0–2.8 μsec (N_0)	$10^3 \times$number of mesons per sec, g sterad
11	212	27	5.1±0.16	4.07±0.13
44	210	9	5.2±0.16	4.15±0.13
110	210	8	5.4±0.16	4.31±0.13
215	263	11	5.1±0.14	4.08±0.11
250	264	8	5.6±0.14	4.48±0.11
285	263	9	5.5±0.14	4.40±0.11
320	263	7	5.3±0.14	4.25±0.11

corrected for the spurious counts N_r. These numbers, which we have indicated as N_0 and reported in counts per hour, appear in the fourth column of the table. They have been obtained by fitting through the points corresponding to the counting rates recorded in the channels, the "most probable" decay curves of 2.2 μsec lifetime. They represent, therefore, the most probable numbers of mesons stopped in the absorber and decaying between 0 and θ ($\theta=2.8$ μsec) into electrons which discharge at least one of counters C.

The statistical accuracy of the numbers N_0 indicated in the table is based on the standard deviations of the numbers of counts recorded in the four channels. The errors relative to the N_0's do not include the error in the determination of the minimum delay for which a delayed coincidence can occur. This minimum delay, as stated in Sec. II, was found to be nearly 1.2 μsec and its error is supposed to be smaller than the statistical errors of the N_0's. Similarly, the statistical uncertainty of the random delayed coincidences, N_r, has not been taken into consideration because it is very small and cannot appreciably affect the precision of our results. In the evaluation of the N_0 errors, allowance has been made, of course, for the fact that the channels are partially overlapping.

Also, in the determination of the extrapolated delayed coincidences and of their errors, we have closely followed the method described in reference 2, where the reader can find further information.

If p represents the average value of the probability that the decay electron of a meson stopped in the absorber discharges one of the C counters, then the total number of mesons stopped per unit time in the graphite absorber is given by

$$M=N/p[1-\exp(-\theta/\tau)]. \qquad (2)$$

If, according to the determination of the constant p made in Chicago,[2] we assume $p=0.28$, we find that $M\approx 5N_0$. At 110 g/cm² of air equivalent this yields, according to the results of Table I, about 27.5 mesons per hour stopped in the 10-cm thick graphite absorber. In the same conditions 37 mesons per hour had been found in Chicago.[2] This corresponds to a ratio of about 1.35 between the intensities of mesons having ranges in the neighborhood of 100 g/cm² at the latitudes of

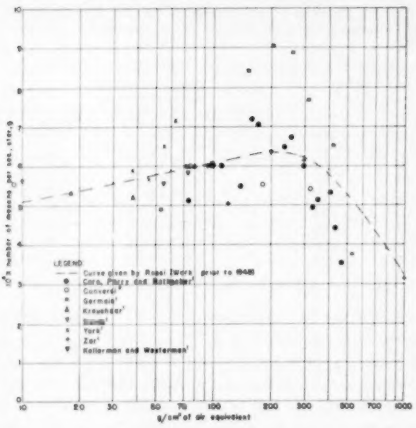

FIG. 3. A plot of most of the results obtained after 1948 on the differential meson spectrum. The dashed line represents the spectrum given by Rossi (see reference 6).

Chicago (46°N) and of Río Piedras (29°N). This ratio is smaller, but only slightly, than the ratio found for the same mesons and between the same latitudes at 30,000 feet above sea level.[6] Nevertheless, no great significance may be given to this comparison, on account of the relatively large statistical errors and also because the geometry of the apparatus was not exactly the same at the two stations where the observation have been made.

Again, following Conversi's paper, the absolute numbers of mesons (per sec steradian g) have been obtained by multiplying the results contained in the fourth column of Table I by 5 and then by the factor $16.\times10^{-7}$. These absolute numbers are reported in the fifth column of the table. They have been used in the graphical representation of our results, which have been plotted in Fig. 2. This figure gives, in a semilogarithmic plot, the differential range spectrum of the mesons observed at Río Piedras.

For the purpose of comparison we have reported in Fig. 3 the results obtained by a number of authors in works performed after 1948, at geomagnetic latitudes around 45°. Where necessary, conversion has been made from momentum into range of air equivalent by means of the nomograms reported in appendix E of Montgomery's book.[5] All the results have been normalized so as to give approximately the same number of mesons around a range of 100 g/cm² of air. This number has been chosen as equal to 6×10^{-6} meson per sec steradian gram, a figure which is supported by the results of various experiments.[7] The results previous to 1948 have not been included in the figure because they were already analyzed by Rossi,[7] who gave the spectrum which we have also represented, by a dotted line, in the same figure. In the plot we have not shown the results obtained by Owen and Wilson and by others, because they refer to momentum higher than 1 Bev/c and are out of the range interval in which we are interested in relation with the present experiment.

Figure 3 shows that most of the recent results seem to be in agreement, within their statistical errors (not shown in the figure) with the general shape of the spectrum given by Rossi. This is actually true with the exception of Germain's work whose final data, however, were obtained by introducing very large corrections, which for greater ranges increased considerably the intensity of the recorded events. The results reported in Fig. 3 indicate the presence of a broad maximum around 200 g/cm² of air equivalent, and show that the spectrum decreases, but slowly, for lower ranges.

The spectrum obtained by us, instead, does not show any maximum in the range interval explored. The number of mesons seems, in fact, to be constant, within the statistical errors which are rather small, between about 10 and 320 g/cm² of air (Fig. 2).

A possible shift of the maximum of the spectrum towards greater ranges may be qualitatively accounted for in terms of a latitude effect. In fact, the average energy of the meson spectrum should increase with decreasing latitudes since the magnetic field of the earth is more effective for the primaries of lower energies. However, this fact should also cause a depletion in the low energy end of the spectrum at low latitudes, whereas it seems from the comparison of Figs. 2 and 3 that the differential spectrum obtained at 29°N geomagnetic latitude is even flatter than that deduced by measurements performed at high latitudes.

Further data should be collected, nevertheless, before drawing any definite conclusion from this slight difference. As a matter of fact, there is enough agreement between our results and those obtained at high latitudes with similar techniques (Kraushaar, Sands, and Conversi) to make us think that the cause of this apparent difference lies rather in the diversity of the methods employed than in an actual change of the meson spectrum with latitude.

We are indebted to Professor M. Conversi for suggesting and directing the research in its beginning during his short sojourn in Puerto Rico. We wish also to express our sincere appreciation to Professor S. K. Allison, Director of the Institute for Nuclear Studies of the University of Chicago, who made possible the loan of the main apparatus previously used by Dr. Conversi in Chicago.

[6] See Fig. 2 of reference 2. Professor Conversi has pointed out to us that the errors represented in this figure include also the error relative to the determination of the constant p. By this data the latitude ratio at 30,000 feet between 28.5°N and 40°N geomagnetic latitude is found to be 1.45±0.1.

[7] B. Rossi, reference 1.

Remarks on Some Questions of Neutron Optics

OTTO HALPERN
University of Southern California, Los Angeles, California
(Received June 16, 1952)

Several derivations of the expression for the index of refraction of neutrons are discussed and difficulties recently raised are cleared up. The theory is extended to cover cases involving absorption (through capture or incoherent scattering). Formulas for the scattering due to disorder in crystals are used for the determination of scattering amplitudes of isotopes in agreement with direct experiments. It is shown how the polarization of neutrons scattered under small angles can be used to obtain information about the structure of mixed crystals. The problem of primary and secondary neutron extinction is also discussed in the light of a recent publication.

I. ON THE INDEX OF REFRACTION OF NEUTRONS IN MAGNETIC MATERIALS

AN expression for the index of refraction of neutrons including the case of magnetic refraction and of rotation of the plane of polarization was first given in the form[1]

$$n_{\pm}-1=\frac{N\lambda^2}{2\pi}(a_n\pm a_m)=\frac{N\lambda^2}{2\pi}a_n\pm\frac{4\pi\mu I}{2E}. \qquad (1)$$

In (1) N denotes the number of scattering centers per unit volume, λ the neutron wavelength, a_n the coherent scattering amplitude of the nucleus, μ the magnetic moment of the neutron, E its kinetic energy, and I the density of magnetization of the ferromagnet traversed; a_m stands for the suitably defined (see reference 8) amplitude of magnetic scattering in the forward direction. The formula was later[2] applied to devise a method for the production of polarized neutron beams by total reflection; an experimental approach of this kind was shown to allow a direct measurement of the neutron spin (as distinguished from the neutron's magnetic moment) and a study of the interaction function of the neutron's magnetic moment with the magnetic moment of the atom. It was also pointed out that, in general, $4\pi I$ would have to be replaced by B, the magnetic induction, to take into account the influence of a possibly present over-all magnetic field and its dependence on the shape of the magnetized body.

Equation (1) has been confirmed by a large series of experiments. While the well-known investigations by Fermi[3] and his collaborators on total reflection of neutrons dealt mostly with the nonmagnetic case, several papers by Hughes[4] and his associates took up the problem as formulated for the presence of a magnetic field and verified (1) in several cases. By studying polarization effects produced by double refraction, as suggested by the author,[2] Hughes and his collaborators could also obtain, as predicted, information concerning the interaction function.

The derivation of (1) for the general case followed the well-known classical procedure used in optics. This mode of approach was the more justified, since $n-1$ is very small compared to 1, so that no questions of differentiation between the real and exciting field need to be discussed. The wave propagated in the medium was the sum of the incident wave and all scattered wavelets coming from points reached before the point of observation. This procedure could be carried out following the well-known approach of Fresnel. After carrying through the integration, it was found in agreement with optics that the scattering amplitude of the elementary scatterer in the forward direction determined essentially the index of refraction.

Lately, criticism[5] has been raised against our derivation of (1). It was claimed to be in error because a detailed calculation of the magnetic scattering amplitude in the forward direction gave for it the value 0. The conclusion was drawn that the classical method breaks down for long-range forces like magnetic interactions. A modified derivation,[6] on the other hand, led to our results for the index of refraction and also confirmed our predictions,[2] experimentally verified by Hughes, concerning angular effects and the interaction function. No attempt was made to explain the surprising agreement of a supposedly wrong derivation with the "new" theory or the experiments.

This criticism has been taken up in some recent papers by Lax,[7] who obtained our results with an operational method but failed to give any reason for the apparent validity of a wrong proof.

The theoretical importance of this question as well as the various experimental confirmations of our theory may justify perhaps a few remarks intended to clear up these apparent contradictions. Summarizing in advance the results of the reasoning to be presented, we want to state that the criticisms raised are without any basis, that our derivation and the results obtained are correct and are, in fact, identical with the differently worded derivation given by Lax.[7] The origin of this

[1] Halpern, Hamermesh, and Johnson, Phys. Rev. **59**, 981 (1941).
[2] O. Halpern, Phys. Rev. **75**, 343 (1949); **76**, 1130 (1949).
[3] See, e.g., E. Fermi and L. Marshall, Phys. Rev. **71**, 666 (1947).
[4] See, e.g., D. J. Hughes and M. T. Burgy, Phys. Rev. **81**, 498 (1951).
[5] H. Eckstein, Phys. Rev. **78**, 731 (1950).
[6] H. Eckstein, Phys. Rev. **76**, 1328 (1949).
[7] M. Lax, Phys. Rev. **80**, 299 (1950); Revs. Modern Phys. **23**, 287 (1951).

untenable criticism is to be found, in our opinion, in a formalistic misunderstanding[5] of a very simple physical situation.

That the magnetic scattering amplitude for $\vartheta=0$ vanishes as especially proven in reference 5 is correct, but was known to us and is contained in formula (4.05) of an early investigation[8] in which the form of the interaction function has been studied carefully. Formula (4.05) of reference 8 shows that the magnetic scattering amplitude for all values of $\vartheta>0$ is a continuous function of the angles but has a (completely immaterial) discontinuity for $\vartheta=0$ at which it vanishes. This (completely immaterial) discontinuity has its origin in the fact that the vector potential of the neutron's magnetic field was for simplicity's sake permitted to have a singularity of the form $1/r^2$. Forming a matrix element with this vector potential, an ambiguity arises for $\vartheta=0$, since the infinite result of integration over the radius vector is canceled by the factor 0 coming from the integration over the angles.

This discontinuity at $\vartheta=0$ is called by us completely immaterial, since there does not exist a physical statement in which the wave function (or its square) has to be known at *one* point. In all cases of physical interest, one is concerned with integrals over domains (however small). We considered well known, and therefore failed to call attention to, the results of elementary calculus that show no integral is changed by changing the value of the integrand by a finite amount at one point (or, for that matter, at a suitably infinite number of points). Therefore, the expression for the magnetic scattering amplitude was made continuous at the point $\vartheta=0$. (4.06 of reference 8.)

It is, of course, this scattering amplitude made continuous which enters rigorously into the expressions for the index of refraction. As shown in detail in reference 1 and as mentioned in this introduction, the index of refraction arises through an integration over all elementary wavelets contributing to the eigenfunction at a specified point. Integrating over these wavelets and using partial integration, the value of the integrand is, of course, determined by the scattering amplitude made continuous and not by the, in principle, completely arbitrary value of the eigenfunction at $\vartheta=0$.

The procedure by Lax[7] follows in operational language exactly our classical procedure of summing the elementary wavelets contributed by all scatterers. It is not surprising that he arrives at our results. There is, of course, no need to discuss anomalous conditions arising from long-range magnetic forces, since there are no anomalies to be explained and since the classical method applies without any deviations.

II. THE INFLUENCE OF ABSORPTION PROCESSES ON TOTAL REFLECTION

As known from optics, the presence of an index of absorption affects the refractive processes, particularly the phenomenon of total reflection. Although in the case of neutrons the index of absorption is, as a rule, not only very small by itself but also small compared to $n-1$, it will turn out that absorptive processes have still a very characteristic effect.[9] Precision determinations of the coherent scattering amplitude made with the aid of measurements of the critical angle will be seen to depend in a noticeable amount on the presence of an absorption cross section.

Absorptive processes are, for the present purpose, not only produced by pure capture but equally by any incoherent scattering process that may occur. The incoherently scattered beam constitutes, as far as refractive processes are concerned, simply a loss to the original beam; for the formal treatment, capture cross section and incoherent cross section enter quite symmetrically.[9]

To account for such general absorption processes in the Schrödinger equation, we write it in the form

$$\Delta\psi+k^2\psi+i\gamma k\psi=0. \tag{2}$$

The expression γ stands for the sum

$$\gamma=N_c\sigma_c+N_i\sigma_i. \tag{3}$$

In (3), we have denoted by σ_c and σ_i the cross section of capture or incoherent scattering and by N_i and N_c the number of particles per unit volume possessing these cross sections. Since it is always true that $\gamma\ll k$, the solution

$$\psi=e^{-ikz}e^{-\frac{1}{2}\gamma z} \tag{4}$$

of (2) gives for the density of the neutrons the expression $\sim e^{-\gamma z}$. We see that the exponential damping has the right coefficient which justifies the addition of the imaginary part of the Schrödinger equation.

If we now study the reflection of a neutron wave incident under the glancing angle $\varphi\ll 1$ on a medium with the index of refraction n and the damping term γ, we find from the boundary condition at $x=0$ the following relations:

$$k_x'^2+k_y'^2=k^2(n^2+i\gamma/k)=k^2(1-2\delta+i\gamma/k), \tag{5}$$

$$1-n=\delta\ll 1, \tag{6}$$

$$k_y'=k_y=k\cos\varphi=k(1-\varphi^2/2), \tag{7}$$

$$k_x'^2\cong k_x^2-k_y^2(2\delta-i\gamma/k)\cong k^2(\varphi^2-2\delta+i\gamma/k)$$

$$\cong(k_x^2/\varphi^2)(\varphi^2-2\delta+i\gamma/k), \tag{8}$$

$$r=\left|\frac{k_x'-k_x}{k_x'+k_x}\right|^2\cong\left|\frac{\varphi-(\varphi^2-2\delta+i\gamma/k)^{\frac{1}{2}}}{\varphi+(\varphi^2-2\delta+i\gamma/k)^{\frac{1}{2}}}\right|^2, \tag{9}$$

where r = coefficient of reflection.

In the absence of absorption, the reflection coefficient for values of $\varphi=\varphi_0(1+p)$, where

$$\varphi_0^2=2\delta,$$

[8] O. Halpern and M. H. Johnson, Phys. Rev. **55**, 898 (1939).

[9] O. Halpern and C. B. Shaw, Phys. Rev. **78**, 88 (1950).

can be shown to be given by

$$r=1-(32p)^{\frac{1}{2}}, \quad (p\ll 1). \tag{10}$$

It is well worth remembering that according to (10) the reflection coefficient differs from unity by about 10 percent if p is as small as 3×10^{-4}.

In the presence of absorption, the reflection coefficient at the angle

$$\varphi^2=2\delta$$

(which would correspond to the critical angle in the absence of absorption) amounts to

$$r_0=1-(2\gamma/k\delta)^{\frac{1}{2}}. \tag{11}$$

Here we have assumed that

$$\gamma/k\delta\ll 1.$$

(11) is always valid except perhaps in the neighborhood of absorptive resonances as they may occur, for example, in Cd and Mn.

If we choose for illustrative purposes the values 10^{-2} and 10^{-3} for the ratio $2\gamma/k\delta$, we find that r_0 becomes, respectively 0.9 and 0.97.

Equation (9) shows that the angle $\varphi=\varphi_0(1-g)$,

$$\gamma/8k\delta\ll g\ll 1,$$

has to be used to obtain a reflection coefficient of about

$$r=1-(\gamma/k\delta)[1/(2g)^{\frac{1}{2}}]. \tag{12}$$

If the ratio $\gamma/k\delta=10^{-2}$ then one obtains for $g=1/30$ the value $r\sim0.96$.

The case of H and its components deserves special mention. Here the large incoherent scattering cross section $\sigma i\sim80$b makes the ratio exceptionally favorable for the discovery of the influence of "absorption" processes on total reflection.

III. SCATTERING DUE TO DISORDER IN CRYSTALS

It has been shown[1] that an otherwise ideal crystal composed of two randomly distributed constituents which have respectively the scattering amplitude, a_1 and a_2, has a cross section of disorder scattering of the amount

$$\sigma=4\pi c_1c_2(a_1-a_2)^2. \tag{13}$$

Here c_1 and c_2 denote the percentages of the two constituents. This formula has, among other things, been applied to the study of the scattering amplitudes of two isotopes constituting a single crystal.[1]

Lately,[10] this method has been used to determine the scattering amplitudes of mixed crystals, in particular NiMn. After determining the coherent scattering amplitude of the element Ni, a rather large disorder cross section was found for the mixed crystal, which fact constituted convincing proof that the scattering amplitudes of the elements Ni and Mn have opposite sign.

The authors,[10] in evaluating their data, have not paid attention to some additional information contained in them which does not seem to be without interest. They observed a disorder scattering cross section for pure Ni of the magnitude of $\sim$4b. Keeping in mind that the percentages of the two dominant Ni isotopes are $\sim$70 percent and 30 percent, one obtains for the coherent scattering cross section of Ni^{58} and Ni^{60}, respectively, the values

$$\sigma_{58}=25\text{b}; \quad \sigma_{60}=1\text{b}.$$

This result is somewhat surprising, since the two isotopes appear to have probably the largest and smallest coherent scattering cross sections known so far. Still, our result seems to be confirmed by measurements[11] on Ni in which one or the other of the isotopes was enriched, which led to the result of 27b and 1b, respectively.[12]

The study of the neutron polarization effect upon disorder scattering may in some cases lead to a deeper knowledge of the composition of a mixed crystal.

Consider the behavior of a mixed crystal or polycrystal, one component of which shall be, e.g., Fe. The mixed crystal shall be magnetized close to saturation. Denote the nuclear coherent scattering amplitude of Fe by a_1, its magnetic scattering amplitude, which, of course, depends on the direction of the spin of the incident neutron, by a_m, and the coherent scattering amplitude of the second component by a_2. To obtain insight into the effect which this admixture will have upon polarization phenomena we proceed as follows.

Imagine all atoms of the second component replaced by Fe atoms; also add at the places occupied by the atoms of the second component anti-Fe atoms, that means Fe atoms with inverted sign of the nuclear and magnetic scattering amplitude. We then have first a complete crystal (polycrystal) containing saturated Fe and, in addition to it, at random places an equal number of coincident atoms 2 and anti-Fe atoms. Their scattering amplitude will, therefore, be

$$\bar{a}=a_2-a_1-a_m. \tag{14}$$

Since they are distributed randomly, they will scatter isotropically as far as the nuclei are concerned and with the form factor of a_m as far as the magnetic scattering is concerned. They will add to the polarization effect of the Fe crystal (polycrystal) provided that $a_2<a_1$ since then the relative sign of nuclear and magnetic scattering is the same as it is in Fe and will diminish it if $a_2>a_1$.

[10] P. J. Bendt and I. W. Ruderman, Phys. Rev. **77**, 575 (1950).

[11] Koehler, Wollan, and Shull, Phys. Rev. **79**, 395 (1950).

[12] When the author described his result for Ni during a lecture course at Brookhaven National Laboratory in the summer of 1950, Professor M. Goldhaber pointed out that the values theoretically obtained were confirmed by some recent Oak Ridge measurements (reference 11). We want to thank Professor Goldhaber for calling our attention to these results.

The result just now obtained was essentially based on a random distribution of the atoms 2. But the method just discussed permits us, without too great difficulties, to discover experimentally a possible case in which the atoms 2 are not randomly distributed among the Fe atoms but form microcrystalline aggregates among themselves; these in turn may be randomly located among the Fe atoms.

The case just mentioned falls into a category discussed to some extent in Paragraphs VI and VII of an earlier investigation.[13] We proceed again by filling all spaces occupied by atoms 2 simultaneously with Fe and anti-Fe atoms, thus obtaining a complete iron crystal (polycrystal) and in addition randomly distributed microcrystals, the elements of which have again the scattering amplitude $\bar{a}$. We learn now from reference 13 that these randomly distributed microcrystals will essentially scatter into an angle of the order of magnitude $\lambda/dZ^{1/3}$, where d is the lattice distance; their integral cross section is proportional to $\bar{a}^2Z^{4/3}$, where Z denotes the total number of atoms contained in a microcrystal. If now the transmitted beam is analyzed with the aid of a counter subtending different angles, one can separate the small angle contribution arising from the presence of the microcrystals and, in particular, measure, without extreme difficulty, the influence of magnetization. Any polarization effect can be expected to be rather large because the form factor of the magnetic scattering amplitude will be close to 1; it is well known that at the angle at which the first Debye-Scherrer rings occur in Fe, the magnetic form factor is smaller than $\frac{1}{2}$. Experiments of this kind would permit direct study of possible agglomerations of the second component in ferromagnetic mixed crystals.

IV. NEUTRON EXTINCTION PHENOMENA

In a recent note, R. J. Weiss[14] discusses extinction effects in the transmission of neutrons through polycrystalline material; absence of extinction shows itself in the proportionality of the effective cross section with the cross section of the isolated nucleus. He arrives at the conclusion that the treatment of this question which for neutrons was first given in reference 1 (and later extended to the case of polyatomic lattices by Fermi, Sturm, and Sachs[15]) is insufficient in both papers; he claims that only his investigation shows how information concerning grain sizes and the length of the constitutive microcrystals (mosaic blocks) can be obtained. The position taken by Weiss[14] is not acceptable to us.

What follows is largely a paraphrased version of p. 984, the right column of p. 987, and the left column of p. 989 of reference 1. The discussion there given has apparently not been appreciated, to judge especially by the last paragraph of reference 14.

One talks about primary extinction if the cross section of a microcrystal (mosaic block) calculated by Born approximation is comparable with its geometric cross section. Similarly we say that secondary extinction is present if the cross section of the grain compares with its area.

If one assumes that the microcrystals (due to disorder within the grain) scatter incoherently so that their intensities add, then the grain cross section obviously reaches its maximum if the microcrystals, though disordered, are still so well aligned that the incident radiation can strike all of them approximately under the Bragg angle. For the estimate of the maximum cross section of the grain we had explicitly[1] introduced this assumption.

Denoting by N_i the number of scatterers along one linear dimension of the microcrystal, by N_k the same number for the grain, by a the nuclear scattering amplitude, and by d the length of the unit cell, we found [see Eqs. (2.9) to (2.12) of reference 1] the following conditions for the absence of primary and secondary extinction, respectively:

$$N_i a/d < 1; \tag{14a}$$

$$N_i N_k a^2/d^2 \ll 1. \tag{14b}$$

We showed numerically that for a typical case of Fe primary and secondary extinction are small; we also pointed out that for larger sizes of the constituents extinction may well be present and actually seems to have been observed, for example, with Cu.

After some deliberations which we were not quite able to follow, Weiss[14] also accepts our assumption that primary extinction is generally absent; his condition agrees with our (14a) after allowance is made for the new meaning of N in his Eqs. (6), (7) which now denote the number of scatterers per unit volume. Similarly his condition for the absence of secondary extinction $\sigma T \ll 1$ is equivalent with (14b). This is not surprising since we both are dealing with conventional x-ray theory applied to neutron diffraction. The lengthy and comprehensive formulas quoted by Weiss from the monograph of Zachariasen reduce, of course, for the limiting cases discussed, to the simple expressions underlying our treatment.

Weiss[1] points out that particularly near the cut-off wavelength strong diffraction occurs over a wide angular range in the neighborhood of the Bragg angle. He therefore concludes (rightly) that this case is most favorable for secondary extinction since it is then likely that the microcrystals are better aligned than this angular spread around the Bragg angle; to have overlooked this fact is his principal accusation against the earlier treatments.[1,15] But he has missed the point that for the purpose of making our condition for the absence of secondary extinction most stringent we have

[13] O. Halpern and E. Gerjuoy, Phys. Rev. **76**, 1117 (1949).
[14] R. J. Weiss, Phys. Rev. **86**, 271 (1952).
[15] Fermi, Sturm, and Sachs, Phys. Rev. **71**, 589 (1947).

just assumed[1] such a behavior of the microcrystals within a grain to occur, even far away from cutoff. Very clearly his condition for the absence of secondary extinction in the most unfavorable case is no more restrictive than ours.

But there exists a physical difference between x-ray and neutron diffraction in the case of a ferromagnet which leads to the well-known transmission effects due to polarization. We have laid[1] great emphasis on the fact that marked extinction would show itself in a radical reduction of these transmission effects. Obviously if the cross section of the grain is no longer proportional to the cross section of the elementary scatterer, then a slight change of the latter, produced by magnetization, will not affect the total transmission very much. A study of the transmission effects therefore permits insight into extinction effects even if sharp spectral resolution is not feasible.

In this connection an extinction problem deserves to be mentioned which is not treated in any exposition based on conventional x-ray theory. For wavelengths very near the cutoff it may occur that the angular width of the beam is larger than the deviation of the Bragg angle from $\pi/2$. This is contrary to the assumption underlying all x-ray theories; these x-ray treatments are realistic since one can see by a closer study that the case mentioned before can be established experimentally only with great difficulty. Still, it constitutes at least a mathematical problem which perhaps at some future time will find its experimental counterpart.

The author appreciates the cordial hospitality extended to him by the Brookhaven National Laboratory.

PHYSICAL REVIEW VOLUME 88, NUMBER 5 DECEMBER 1, 1952

Angular Correlations in the Reaction $F^{19}(p,\alpha\gamma)O^{16}$

J. SEED AND A. P. FRENCH
Cavendish Laboratory, Cambridge, England
(Received June 19, 1952)

The angular correlations between alpha-particles and gamma-rays in transitions between states of Ne^{20} and the low excited states of O^{16} have been studied at the 669-, 874-, and 935-kev resonances for proton capture in fluorine. The alpha-particle groups were separated magnetically from each other and from scattered protons. The results lead to definite assignments of spin and parity to the nuclear states involved, and show that the first four excited levels of O^{16} are consistent with a simple alpha-particle model for this nucleus. Where interference between states occurs in the reaction, the phase differences are in accord with the predictions of modern dispersion theory.

I. INTRODUCTION

THE level structure of O^{16} has been the subject of many experimental and theoretical studies, and particular interest has been directed at those states which can be reached by the $F^{19}(p,\alpha)$ reaction. (See, for example, the review article by Hornyak *et al.*[1]) The resonance levels in Ne^{20} formed in this reaction decay predominantly by alpha-particle emission; besides the transition to the ground state of O^{16}, four distinct alpha-particle groups have been observed, associated with transitions to the first four excited states of O^{16}. Much of the interest in these levels in O^{16} lies in the attempt to identify them with the low states of excitation of a bound system of four alpha-particles (Wheeler[2] and Dennison[3]). It is known that the first excited state of O^{16} (6.05 Mev) has spin zero and even parity [denoted by $(0,+)$] (Devons and Lindsey[4]) and that the second excited state (6.13 Mev) has the designation $(3,-)$ (Barnes *et al.*[5]). These do in fact correspond (though in reversed order) to the first two excited states predicted by Wheeler and Dennison for a tetrahedral arrangement of alpha-particles, and the experiments described in this paper were carried out with the aim of extending the comparison to higher levels.

The levels in Ne^{20} formed by resonance capture of protons in fluorine seem to be of two kinds, namely, (a) those that can decay by emission of long-range alpha-particles to the ground state of O^{16}; (b) those that emit short-range alpha-particles followed by gamma-rays. (From all levels of type (a) one also observes transitions to the well-known pair emitting state of O^{16} at 6.05 Mev.) It is usual to ascribe the absence of long-range alpha-particle emission for type (b) to a strict selection rule arising from the need to conserve total angular momentum (J) and parity (P) in the transitions; this is achieved by supposing that the Ne^{20} levels concerned have odd J with even P, or even J with odd P. A full discussion is given by Chao.[6] The present work was confined to levels of this type, and consisted of a study of angular correlations between the various alpha-particle groups and their associated gamma-rays.

[1] Hornyak, Lauritsen, Morrison, and Fowler, Revs. Modern Phys. **22**, 291 (1950).
[2] J. A. Wheeler, Phys. Rev. **52**, 1083 (1937).
[3] D. M. Dennison, Phys. Rev. **57**, 454 (1940).
[4] S. Devons and G. R. Lindsey, Nature **164**, 539 (1949).
[5] Barnes, French, and Devons, Nature **166**, 145 (1950).
[6] C. Y. Chao, Phys. Rev. **80**, 1035 (1950).

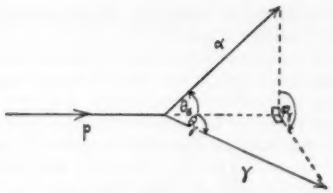

FIG. 1. The three-stage process.

II. PLAN OF THE EXPERIMENTS

The reaction with which we are concerned is essentially a three-stage process, with two well-defined intermediate states:

$$p+F^{19}\rightarrow Ne^{20*},\quad Ne^{20*}\rightarrow O^{16*}+\alpha,\quad O^{16*}\rightarrow O^{16}+\gamma.$$

It is thus possible to observe three types of angular correlation, which we can denote by (p,α), (p,γ), and (α,γ), respectively. In the usual experimental arrangement with a fluorine target and a collimated beam of protons the first two types correspond to straightforward angular distribution measurements. The third type must involve coincidence measurements in order to define a unique direction for the emitted alpha-particles. The three angular distribution functions are clearly related, since they are determined by the spins and parities of the nuclear states and by the orbital angular momenta of the captured and emitted particles, and it may be necessary to study all three types of correlation in order to obtain an unambiguous analysis of the process.

The proton capture resonances suitable for a complete study of this sort are those at 340-, 669-, 874-, and 935-kev proton energy, if we restrict attention to energies below 1 Mev (the highest energy available to us). These resonances are fairly narrow and have sufficiently large cross sections; the branching of the competing alpha-particle emissions to the gamma-emitting states of O^{16} (denoted in the usual way by α_1, α_2, and α_3 in ascending order of excitation) changes markedly from one resonance to another. At the lowest resonance (340 kev) nearly all the transitions are to the α_1 level of O^{16} at 6.13 Mev. Studies at 340 kev of the (α_1,γ) correlation (Arnold[7] and Barnes *et al.*[8]) and of the polarization of the gamma-rays (French and Newton[8]) have shown that the gamma-rays are electric octupole, and also that the compound state in Ne^{20} is $(1,+)$ and is formed by s protons. The observed isotropy of both alpha-particles (Van Allen and Smith[9]) and gamma-rays (Devons and Hine[10]) with respect to the protons supports these conclusions.

We have used the definite assignment $(3,-)$ for the 6.1-Mev level in O^{16} to find spin values for the higher resonances in Ne^{20} by observing their (α_1,γ) correlations. Measurements of the (α_2,γ) and (α_3,γ) correlations at these resonances have then enabled us to find the spins of the 6.9- and 7.1-Mev levels in O^{16}, with supporting evidence from the corresponding (p,α) and (p,γ) angular distributions.

III. THEORY OF THE METHOD

(a) Statement of the Problems

Before describing the experiments we shall give a brief outline of the theory of a three-stage process as it applies to the present problem. Let the incident proton define a z axis, and let the compound state in Ne^{20} be denoted by C_r. Suppose that C_r breaks up with the emission of an alpha-particle at an angle θ_α to the proton beam, leaving an excited state of O^{16} denoted by C_s. Emission of a gamma-ray from C_s then takes place at an angle θ_γ to the proton beam and in a plane at an angle φ_γ to the plane defined by the proton and alpha-particle directions. This is illustrated in Fig. 1. The differential cross section for emission of an alpha-particle into a solid angle $d\Omega_\alpha$ at θ_α and a gamma-ray into $d\Omega_\gamma$ at $(\theta_\gamma,\varphi_\gamma)$ when the proton bombarding energy is E is then given by

$$d\sigma(E,\theta_\alpha,\theta_\gamma,\varphi_\gamma)$$
$$=\pi\lambda^2\left|\sum_{r,s}\frac{\langle A|H_1|C_r\rangle\langle C_r|H_2|C_s\rangle\langle C_s|H_3|B\rangle}{E-E_r+\frac{1}{2}i\Gamma_r}\right|^2 d\Omega_\alpha d\Omega_\gamma,$$

where the numerator inside the modulus is a product of three matrix elements representing the formation and break-up of C_r and C_s. These matrix elements can then be resolved into an unknown factor depending on the specifically nuclear properties of the process and a transformation coefficient which describes the combination of angular momenta and is precisely known (Condon and Shortley[11]).

In the $F^{19}(p,\alpha\gamma)$ reactions it is reasonable to assume that only one excited state of Ne^{20} and one excited state of O^{16} are involved for a given type of transition, but a summation must be made over (a) the spin states of the participating nuclei and (b) the various possible orbital momenta of the incoming protons and the outgoing alpha-particles. Since the final state in O^{16} has zero spin, only one type of multipole transition is possible for the gamma-radiation from a state of given spin and parity in the excited O^{16}. To take the analysis further it is convenient to discuss the three types of angular correlation separately.

(b) (p,α) Correlations

In this case we are not concerned with the direction of emission of the gamma-ray, and the function de-

[7] W. R. Arnold, Phys. Rev. **79**, 170 (1950); **80**, 34 (1950).
[8] A. P. French and J. O. Newton, Phys. Rev. **85**, 1041 (1952).
[9] J. A. Van Allen and P. Smith, Phys. Rev. **59**, 501 (1941).
[10] S. Devons and M. G. N. Hine, Proc. Roy. Soc. (London) **A199**, 56 (1949).
[11] E. U. Condon and G. H. Shortley, *The Theory of Atomic Spectra* (Cambridge University Press, Cambridge, 1935 and 1951).

scribing the angular distribution of alpha-particles relative to protons becomes

$$W(\theta_\alpha)=\sum_{j,j_z}\sum_{J_{zz}}|\sum_{l}(2l+1)^{\frac{1}{2}}f_r(l)\langle j,j_z;l,0|J_r,J_{rz}\rangle \times\sum_{l'}f_z(l')\langle J_r,J_{rz}|J_z,J_{zz};l',m'\rangle Y_{l'}^{m'}(\theta_\alpha,0)|^2$$

$$=\sum_{j,j_z}\sum_{J_{zz}}|\sum_{l}(2l+1)^{\frac{1}{2}}f_r(l)\langle j,j_z;l,0|J_r,J_{rz}\rangle|^2 \times|\sum_{l'}f_z(l')\langle J_r,J_{rz}|J_z,J_{zz};l',m'\rangle Y_{l'}^{m'}(\theta_\alpha,0)|^2.$$

Here j is the resultant spin (0 or 1) of the F^{19} nucleus and a proton, and J_r, J_z are the total angular momenta of the excited Ne^{20} and O^{16}, respectively. $f_r(l)$ and $f_z(l')$ are complex factors describing the probability amplitudes associated with the different orbital momenta. $Y_{l'}^{m'}$ is a spherical harmonic. (It should be noted that the Ne^{20} levels with which we are concerned can arise only from the spin state $j=1$.)

In the present reaction it is sufficient to consider the two lowest possible values of l and l'. (For the latter only one value is in fact allowed for some transitions by the conservation rules for total angular momentum and parity.)

(c) (p,γ) Correlations

In this case we must integrate the differential cross section over all directions of the outgoing alpha-particle. Since the alpha-particle wave is described by a superposition of spherical harmonics, which are orthogonal, the integration eliminates interference between the different l', and the angular distribution of gamma-rays becomes

$$W(\theta_\gamma)=\sum_{j,j_z}\sum_{l',m'}|\sum_{l}(2l+1)^{\frac{1}{2}}f_r(l)\langle j,j_z;l,0|J_r,J_{rz}\rangle \times f_z(l')\langle J_r,J_{rz}|J_z,J_{zz};l',m'\rangle \mathbf{E}_{J_z}^{J_{zz}}(\theta_\gamma,\varphi_\gamma)|^2$$

$$=\sum_{j,j_z}\sum_{l',m'}|\sum_{l}(2l+1)^{\frac{1}{2}}f_r(l)\langle j,j_z;l,0|J_r,J_{rz}\rangle|^2 \times|f_z(l')\langle J_r,J_{rz}|J_z,J_{zz};l',m'\rangle|^2 \times|\mathbf{E}_{J_z}^{J_{zz}}(\theta_\gamma,\varphi_\gamma)|^2.$$

$\mathbf{E}_{J_z}^{J_{zz}}$ is the matrix element for the radiative transition to the ground state of O^{16}. All other quantities have the same meaning as before.

(d) (α,γ) Correlations

Since we are now interested in the angular distribution of the gamma-rays relative to the alpha-particles, it is convenient to use the alpha-particle direction to define a new axis of z. Let us call it z'. The problem can then be stated as follows: We quantize the system C_r along an axis which is the direction of an incident proton. We then wish to quantize it again along the direction z' before going through those transformations that correspond to the break-up processes. A compound state characterized by given values of J and J_z with respect to the original z axis is then described as a *coherent* superposition of states of the same J but with all possible values of $J_{z'}$ between $+J$ and $-J$, and the probability amplitude associated with a given $J_{z'}$ is given by a transformation coefficient $C_{J_z,J_{z'}}$. In our experiments z' is at right angles to z, so that $C_{J_z,J_{z'}}$ can be written as the amplitude associated with J_x in a scheme in which J_z is diagonal. Once one has set up the matrix of J_z (e.g., Schiff[12]) the C's can be very easily found; they are solutions to equations of the type

$$\langle J_z|J_z-1\rangle C_{J_z,J_z-1}+\langle J_z|J_z+1\rangle C_{J_z,J_z+1}=J_z C_{J_z,J_z}.$$

The angular correlation function is then given by

$$W_{\alpha,\gamma}(\theta)=\sum_{j,j_z}|\sum_{l}(2l+1)^{\frac{1}{2}}f_r(l)\langle j,j_z;l,0|J_r,J_{rz}\rangle \times\sum_{J_{rz'},l'}C_{J_{rz},J_{rz'}}(2l'+1)^{\frac{1}{2}}f_z(l') \times\langle J_r,J_{rz'}|J_z,J_{zz'};l',0\rangle\mathbf{E}_{J_z}^{J_{zz'}}(\theta,\varphi)|^2.$$

Here θ represents the angle between alpha-particle and gamma-ray, and φ, the angle between the p-α plane and the α-γ plane. An equivalent treatment is to transform to the z' axis before considering formation of the compound Ne^{20}. (We are grateful to Mr. G. A. Jones for suggesting this method.) In this case an incident proton wave described by $P_l(\cos\theta)$ can be expressed as a coherent superposition of the $(2l+1)$ spherical harmonics $Y_l^{m'}(\theta',\varphi')$, where angles θ are measured relative to z and (θ',φ') relative to z'. The transformation coefficients are the spherical harmonics $Y_l^{m'}(\theta_\alpha,0)$ (see, for example, Smythe[13]). By this method the (α,γ) correlation in a plane perpendicular to the proton beam is given by

$$W_{\alpha,\gamma}(\theta)=\sum_{j,j_z}|\sum_{l,m'}f_r(l)Y_l^{m'}(\pi/2,0) \times\langle j,j_z;l,m'|J_r,J_{rz'}\rangle\sum_{l'}(2l'+1)^{\frac{1}{2}}f_z(l') \times\langle J_r,J_{rz'}|J_z,J_{zz'};l',0\rangle\mathbf{E}_{J_z}^{J_{zz'}}(\theta,\varphi)|^2.$$

(e) Tabulation of the Formulas

In Table I we have set out the explicit formulas for (p,α), (p,γ), and (α,γ) correlations for those quantum states of Ne^{20} and O^{16} that are of possible relevance to our experiments. Where two angular momenta of protons or alpha-particles contribute to the reaction, we put

$$f_r(l+2)/f_r(l)=Ae^{i\alpha},\quad f_z(l'+2)/f_z(l')=Be^{i\beta}.$$

Thus, α and β represent the phase differences between

[12] L. I. Schiff, *Quantum Mechanics* (McGraw-Hill Book Company, Inc., New York, 1949), p. 143.
[13] W. R. Smythe, *Static and Dynamic Electricity* (McGraw-Hill Book Company, Inc., New York, 1949), p. 151.

TABLE I. Theoretical angular correlation patterns. [Note: In transitions from (2,—) levels of Ne^{20} the (α,γ) pattern depends on the angle φ (Sec. III(d)) since $l \neq 0$. The formulas given are obtained for $\varphi = 90°$.]

^{20}Ne \ ^{16}O		$(1,-)$	$(1,+)$	$(2,-)$
		$l' = 1$	$l' = 0,2$	$l' = 1,3$
$(1,+)$ $l = 0,2$	(p,α)	$1 + \frac{1}{\sqrt{21}} A \cos\alpha (-1 + 3x) + \frac{1}{8} A^2 (41 - 39x)$	$1 + B^2 + \sqrt{3} A \cos\alpha (\sqrt{3} B \cos\beta - \frac{1}{2} B^2)(-1 + 3x) + \frac{1}{20} A^2 [14 - 13\sqrt{3} B \cos\beta (-1 + 3x) + \frac{1}{2} B^2 (5 + 13x)]$	$1 + B^2 + \frac{1}{2\sqrt{21}} A \cos\alpha (1 + 2\sqrt{3} B \cos\beta + 4B^2)(1 - 3x) + \frac{1}{200} A^2 [(37 + 39x) + 78\sqrt{3} B \cos\beta (1 - 3x) + 4B^2 (32 + 39x)]$
	(p,γ)	$1 + \frac{1}{2\sqrt{21}} A \cos\alpha (1 - 3x) + \frac{1}{16} A^2 (43 + 39x)$	$1 + B^2 + \frac{1}{2\sqrt{3}} A \cos\alpha (1 + \frac{1}{10} B^2)(-1 + 3x) + \frac{1}{40} A^2 [(41 - 39x) + \frac{1}{10} B^2 (293 - 39x)]$	$1 + B^2 + \frac{1}{2\sqrt{21}} A \cos\alpha (1 + \frac{1}{2} B^2)(1 - 3x) + \frac{1}{80} A^2 [(43 + 37x) + \frac{1}{2} B^2 (61 + 13x)]$
	(α,γ)	$1 + x$	$1 + \frac{1}{\sqrt{3}} B \cos\beta (-1 + 3x) + \frac{1}{4} B^2 (5 - 3x)$	$1 + x + 2\sqrt{\frac{3}{7}} B \cos\beta (1 - 9x + 10x^2) + \frac{1}{2} B^2 (1 + 6x - 5x^2)$
$(2,-)$ $l = 1,3$	(p,α)	$l' = 2$	$l' = 1,3$	$l' = 0,2,(4)$
		$1 + x + 2\sqrt{\frac{3}{7}} A \cos\alpha (1 - 9x + 10x^2) + \frac{1}{4} A^2 (1 + 6x - 5x^2)$	$(1 + \frac{3}{14} x) + \frac{3}{14}\sqrt{\frac{6}{7}} B \cos\beta (1 - 3x) + \frac{11}{28} B^2 (1 + 2x) + \frac{6}{7}\sqrt{\frac{3}{7}} A \cos\alpha [\frac{1}{2}(1 - 3x) + 2\sqrt{\frac{2}{3}} B \cos\beta (2 - 21x + 35x^2) + B^2 (-1 + 18x - 35x^2)] + \frac{3}{7} A^2 [\frac{1}{2}(1 + 2x) + \frac{1}{28} B \cos\beta (-(+18x - 35x^2) + \frac{1}{14} B^2 (33 + 66x + 35x^2)]$	$1 + \sqrt{\frac{3}{10}} B \cos\beta (1 - 3x) + \frac{1}{28} B^2 (31 - 9x) + \sqrt{\frac{6}{7}} A \cos\alpha [\sqrt{\frac{3}{10}} B \cos\beta (-1 + 3x) + \frac{1}{28} B^2 (-1 + 9x - 10x^2)] + A^2 [\frac{1}{2} + 4\sqrt{\frac{3}{70}} B \cos\beta (1 - 3x) + \frac{1}{196} B^2 (37 - 18x + 15x^2)]$
	(p,γ)	$1 + \frac{7}{11} x + \frac{3}{11}\sqrt{\frac{3}{7}} A \cos\alpha (1 - 3x) + \frac{8}{33} A^2 (4 + 3x)$	$(1 - \frac{24}{77} x) + \frac{4}{11} B^2 (7 - x) + \frac{4}{11}\sqrt{\frac{3}{7}} A \cos\alpha (1 + \frac{1}{7} B^2)(-1 + 3x) + \frac{2}{77} A^2 [(12 - x) + \frac{1}{21} B^2 (37 - 6x)]$	$(1 + x) + \frac{1}{42} B^2 (59 - 9x) + 2\sqrt{\frac{3}{7}} A \cos\alpha [(1 - 9x + 10x^2) + \frac{1}{14} B^2 (3 - 33x + 40x^2)] + \frac{1}{7} A^2 [(1 + 6x - 5x^2) + \frac{1}{7} B^2 (7 + 3x - 5x^2)]$
	(α,γ)	x	$1 - \frac{4}{13} x + \frac{6}{13}\sqrt{\frac{3}{7}} B \cos\beta (1 + 2x) + \frac{12}{13} B^2 (1 - \frac{1}{4} x)$	$1 + \sqrt{\frac{3}{70}} B \cos\beta (2 - 3x) + \frac{5}{14} B^2 (4 + 13x - 16x^2)$

^{20}Ne \ ^{16}O		$(2,+)$	$(3,-)$	$(3,+)$
		$l' = 2$	$l' = 3$	$l' = 2,4$
$(1,+)$ $l = 0,2$	(p,α)	$1 + \frac{1}{21} A \cos\alpha (-1 + 3x) + \frac{1}{28} A^2 (41 - 39x)$	$1 + \frac{1}{28} A \cos\alpha (-1 + 3x) + \frac{1}{20} A^2 (41 - 39x)$	$1 + B^2 + \frac{1}{7}\sqrt{7} A \cos\alpha (1 - 6\sqrt{3} B \cos\beta + \frac{6}{7} B^2)(1 - 3x) + \frac{1}{140} A^2 [(85 + 39x) + 78\sqrt{7} B \cos\beta (1 - 3x) + \frac{1}{2} B^2 (15x + 195x^2)]$
	(p,γ)	$1 + \frac{1}{2\sqrt{21}} A \cos\alpha (-1 + 3x) + \frac{1}{80} A^2 (23 - 13x)$	$1 + \frac{1}{4\sqrt{21}} A \cos\alpha (-1 + 3x) + \frac{1}{160} A^2 (151 - 117x)$	$1 + B^2 + \frac{3}{4\sqrt{21}} A \cos\alpha (1 + \frac{4}{11} B^2)(1 - 3x) + \frac{1}{220} A^2 [(101 + 117x) + \frac{12}{7} B^2 (33 + 13x)]$
	(α,γ)	$1 - 3x + 4x^2$	$1 + 111x - 305x^2 + 225x^3$	$1 + \frac{2}{3} x + x^2 + \frac{1}{10}\sqrt{3} B \cos\beta (-11 + 245x - 725x^2 + 525x^3) + \frac{2}{45} B^2 (17 - 65x + 255x^2 - 175x^3)$
$(2,-)$ $l = 1,3$	(p,α)	$l' = 1,3$	$l' = 2,4$	$l' = 1,3,(5)$
		$(1 - \frac{3}{7} x) + \frac{3}{7} B \cos\beta (1 - 3x) + \frac{3}{7} B^2 (3 + x) + \frac{2}{7}\sqrt{\frac{3}{7}} A \cos\alpha [(-1 + 3x) + 2B \cos\beta (-3 + 24x - 25x^2) + \frac{1}{2} B^2 (7 - 66x + 75x^2)] + \frac{1}{28} A^2 [(7 - 6x) + \frac{1}{2} B \cos\beta (9 - 42x + 25x^2) + \frac{1}{8} B^2 (29 + 78x - 75x^2)]$	$(1 - \frac{1}{3} x) + \frac{1}{3}\sqrt{\frac{3}{7}} B \cos\beta (1 - 3x) + \frac{1}{14} B^2 (9 + x) + \frac{1}{2\sqrt{21}} A \cos\alpha [(-1 + 6x + 15x^2) + 4\sqrt{\frac{3}{7}} B \cos\beta (-3 + 24x - 25x^2) + 2B^2 (4 - 39x + 45x^2)] + \frac{1}{14} A^2 [73 - 42x - 15x^2) + 4\sqrt{\frac{3}{7}} B \cos\beta (9 - 42x + 25x^2) + 2B^2 (23 + 42x - 45x^2)]$	$(1 + \frac{1}{3} x) + \frac{2}{35} B \cos\beta (1 - 3x) + \frac{1}{14} B^2 (71 - 33x) + \frac{2}{7}\sqrt{\frac{3}{7}} A \cos\alpha [(1 - 3x) + \sqrt{\frac{3}{7}} B \cos\beta (-3 + 6x + 25x^2) + \frac{2}{7} B^2 (-8 + 69x - 75x^2)] + \frac{1}{28} A^2 [(26 + 12x) + \frac{1}{2}\sqrt{\frac{3}{7}} B \cos\beta (39 - 102x - 35x^2) + \frac{1}{28} B^2 (79 - 198x + 75x^2)]$
	(p,γ)	$(1 + \frac{4}{7} x) + \frac{4}{49} B^2 (8 - 3x) + \frac{6}{7}\sqrt{\frac{3}{7}} A \cos\alpha [(-3 + 33x - 40x^2) + \frac{4}{7} B^2 (-1 + 6x - 5x^2)] + \frac{1}{28} A^2 [(3 - 3x + 5x^2) + \frac{1}{14} B^2 (33 - 18x + 5x^2)]$	$(1 + \frac{3}{14} x) + \frac{6}{49} B^2 (19 - 9x) + \frac{3}{14}\sqrt{\frac{3}{7}} A \cos\alpha [(3 - 24x + 25x^2) + \frac{2}{7} B^2 (-3 + 3x + 10x^2)] + \frac{1}{14} A^2 [(71 + 42x - 25x^2) + \frac{2}{7} B^2 (87 - 42x - 5x^2)]$	$(1 + \frac{2}{7} x) + \frac{1}{14} B^2 (91 - 33x) + \frac{1}{2\sqrt{21}} A \cos\alpha [(3 + 6x - 25x^2) + \frac{1}{2} B^2 (-9 + 57x - 50x^2)] + \frac{1}{84} A^2 [(81 + 102x + 25x^2) + B^2 (141 - 78x + 25x^2)]$
	(α,γ)	$1 - \frac{2}{7} x + \frac{2}{7} B \cos\beta (4x - 5x^2) + \frac{1}{7} B^2 (5 - 18x + 15x^2)$	$1 + \frac{2}{13} x - \frac{2}{13} x^2 + \frac{1}{7}\sqrt{\frac{3}{7}} B \cos\beta (10 - 151x + 440x^2 - 315x^3) + \frac{1}{28} B^2 (4 + 109x - 286x^2 + 189x^3)$	$1 + 7x + \frac{1}{7}\sqrt{\frac{3}{7}} B \cos\beta (13 + 44x - 75x^2) + \frac{2}{49} B^2 (197 - 1206x + 3525x^2 - 2500x^3)$

interfering states of the system, A and B their relative amplitudes. One simplification has been made in setting up the table, namely, the restriction of l (but not l') to its lowest value only in the formulas for (α,γ) correlations. This has some justification (see Sec. VI below). All angular distributions are expressed for brevity in powers of $x=\cos^2\theta$; the absence of odd powers of $\cos\theta$ comes from our initial assumption that there is no interference between different states in Ne^{20} and O^{16}.

(f) Evaluation of Phase Shifts

According to the modern dispersion theory (Wigner and Eisenbud[14]) the intrinsic widths of nuclear levels are real, so that the phase shifts α and β (apart from an uncertainty of π) are due entirely to the Coulomb and angular momentum barriers. In our problem there is no relative phase shift associated with the resonance denominator $(E-E_r+\frac{1}{2}i\Gamma_r)$ since it remains the same for all orbital momenta, only one nuclear level in Ne^{20} or O^{16} being involved.

The phase shift associated with an orbital momentum l in a Coulomb field is given (e.g., Bloch *et al.*[15]) by

$$\delta_l=-\tan^{-1}(F_l/G_l)-\eta\log(2kR)+\sigma_l-\tfrac{1}{2}l\pi,$$

where the quantities have their usual significance, *viz.*, F_l, G_l are the regular and irregular solutions of the Coulomb wave equation; $\eta=(Z_1Z_2e^2/\hbar v)$; $k=\mu v/\hbar$, μ being the reduced mass of the system; R=nuclear radius; and $\sigma_l=\arg\Gamma(l+1+i\eta)$.

In the present reaction the proton and alpha-particle energies are well below the respective barrier heights, so that $F_l\ll G_l$, and the phase difference between two waves of orbital momenta l, $l+2$ becomes

$$\delta_{l,\,l+2}=\sigma_{l+2}-\sigma_l-\pi$$

$$=\tan^{-1}\frac{\eta}{l+2}+\tan^{-1}\frac{\eta}{l+1}-\pi.$$

The numerical values of $\cos\alpha$ and $\cos\beta$ are therefore determined by the energies and orbital momenta of the protons and alpha-particles, and do not depend on a choice of nuclear radius. Thus, the only parameters at our disposal in fitting an observed correlation are the magnitudes of A and B and the signs of $\cos\alpha$ and $\cos\beta$.

IV. EXPERIMENTAL METHOD

(a) Angular Correlations

(1) *Detectors*

At the 340-kev resonance, the α_1-particles have a longer range than the scattered protons, so that measurements on the (α_1,γ) and (p,α_1) correlations can be made with a proportional counter or ionization chamber with a thin window to exclude the protons. For the higher resonances, all three alpha-particle groups have shorter ranges than the scattered protons, and some form of energy analysis becomes necessary. The most convenient method, also allowing complete separation of the alpha-particle groups from each other, is to use a magnetic spectrometer.

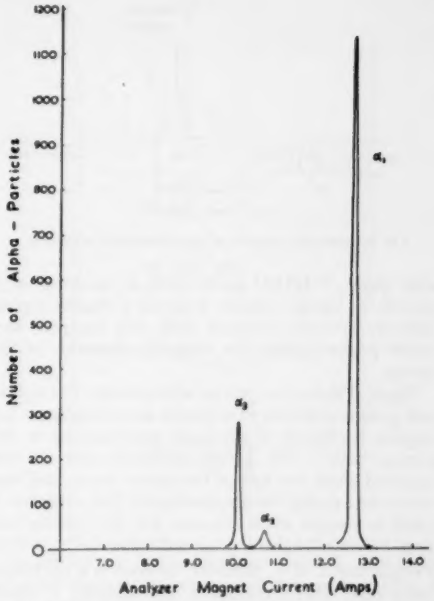

FIG. 2. Alpha-particle spectrum at 935-kev proton energy.

In the early stages of the work an analyzer with 60° inflection focusing was used. It had a resolution of 4 percent in energy and a solid angle of 1/5000 of a sphere. In the (α,γ) angular correlation measurements alpha-particles emitted at 90° to the incident proton beam were observed; the detector was a thin zinc sulfide screen with photomultiplier. In conjunction with this, a liquid scintillation counter was used to detect the gamma-rays. The phosphor was a 2 percent solution of terphenyl in toluene which subtended a solid angle of 1/25 of a sphere at the target, and had a counting efficiency of 10 percent for 7-Mev gamma-rays. With this arrangement it was possible to study angular correlations for the more intense alpha-particle groups.

A substantial improvement in the experiments was effected later when a 180° double focusing magnetic analyzer for the alpha-particles and a sodium iodide scintillation counter for the gamma-rays became available. The magnet was designed by Dr. J. M. Freeman and is of the type described by Snyder *et al.*[16] It has a

[14] E. P. Wigner and L. Eisenbud, Phys. Rev. **72**, 29 (1947).
[15] Bloch, Hull, Broyles, Bouricius, Freeman, and Breit, Revs. Modern Phys. **23**, 147 (1951).
[16] Snyder, Rubin, Fowler, and Lauritsen, Rev. Sci. Instr. **21**, 852 (1950).

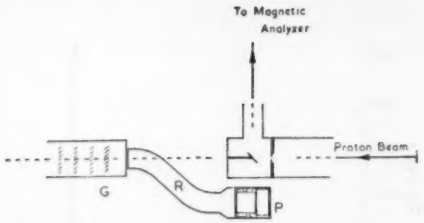

FIG. 3. Schematic diagram of experimental arrangement.

solid angle of 1/1500 sphere with a resolution of 4 percent in energy. Figure 2 shows a typical alpha-particle spectrum obtained with this analyzer and serves to demonstrate the complete separation of the groups.

Figure 3 shows the general arrangement. The alpha- and gamma-detectors were placed so as to measure the angular correlation in the plane perpendicular to the proton beam. The gamma-photomultiplier G was mounted along the axis of the proton beam, and was not moved during the measurements. The phosphor P could be rotated about this axis and the scintillations were conveyed to the photomultiplier by a curved Perspex rod R of 1″ diameter enclosed in a light-tight brass case. This construction was adopted to avoid changes of gain of the photomultiplier which would result from moving it in the stray magnetic field. The angular aperture of the gamma-phosphor was about 35°; this was obtained in the later arrangement with a $1\frac{1}{2}$ in.$\times 1\frac{1}{2}$ in. mosaic of sodium iodide crystals placed $2\frac{1}{4}$ in. from the target. The large angle of the gamma-detector, together with an intrinsic detection efficiency of 35 percent, helped to compensate for the small solid angle of the alpha-particle detector.

Although the main use of the improved apparatus was to study the weaker reactions, the work on the more intense reactions was repeated for the sake of completeness, and all angular correlations illustrated in this paper were obtained with the new system.

(2) *Coincidence Circuits*

The outputs of the alpha- and gamma-photomultipliers were amplified and fed into a coincidence circuit of conventional design having a resolving time of 0.3 μsec. The amplified pulses from the gamma-detector were delayed by about 0.15 μsec before being put into coincidence, in order to compensate for the time of flight of the alpha-particles in the spectrometer. As the fraction of random coincidences in the total coincidence count was appreciable, the random coincidence counting rate was continuously monitored: The alpha-particle pulses were delayed by 2 μsec and put into coincidence with the gamma-ray pulses in a second and identical coincidence unit. (This method is described by Littauer.[17])

(3) *Experimental Procedure*

In all the experiments the target was a thin CaF_2 layer (5 kev for 500-kev protons) evaporated on a copper foil 0.004 inch thick. The proton beam current was continuously monitored and was maintained at about 1 to 2 μA so as to secure a real to random coincidence ratio of at least unity. Besides the real and random coincidence rates, the individual alpha- and gamma-counts were measured. After a desired alpha-particle group had been selected with the magnetic analyzer, alpha-gamma coincidences were measured for 15-minute periods at a series of angles between 90° and 180°. An average of six measurements was made for each angle, and observations were made at 15° intervals in most of the correlations.

The alpha-particle counting rate with the later arrangement varied from about 100 per minute (α_2 at 935 kev) to 3000 per minute (α_1 at all resonances). The corresponding real coincidence rate was between 1 and 50 per minute. It is perhaps of some interest to note that in the most favorable cases a correlation could be established to a few percent in $1\frac{1}{2}$ hours. At the other extreme the (α_2,γ) correlation at 935 kev took 25 hours, the α_2 group having an intensity of only 3 percent of the main group (see Fig. 2).

(b) Angular Distributions

Measurements were made at the 874-kev resonance on the angular distributions of the alpha-particle groups. This work was done with the 60° magnetic analyzer at three angles only (90°, 120°, 135°). The arrangement was far from ideal, but the results were of value in establishing the level schemes.

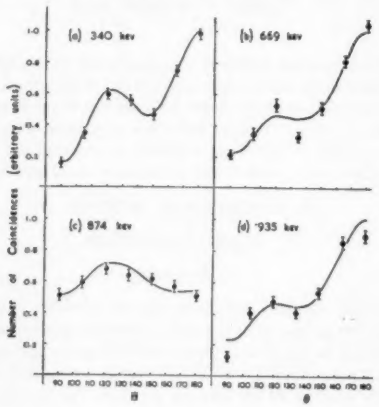

FIG. 4. (α_1,γ) correlations.

[17] R. M. Littauer, Rev. Sci. Instr. 21, 750 (1950).

V. RESULTS

(a) (α_1,γ) Correlations

Figure 4 shows our results for the (α_1,γ) correlations at the 669-, 874-, and 935-kev proton resonances in Ne^{20}. The 340-kev curve, from Barnes *et al.*,[5] is inserted for comparison. The full curves in (a), (b), and (d) represent the modification by the finite geometry of the apparatus of a pure octupole pattern:

$$I(\theta)=1+111\cos^2\theta-305\cos^4\theta+225\cos^6\theta.$$

It can be seen that in each case the curve is a good fit to the experimental points. Following the analysis given by Barnes *et al.*,[5] we can infer with certainty that the Ne^{20} resonance levels at 669- and 935-kev proton energy have spin 1 and even parity. This was suspected previously (Chao[6]) because of the isotropy of the gamma-rays relative to the protons at these resonances (Devons and Hine,[10] Day *et al.*[18]). More recent work by Sanders[19] on the angular distributions of the gamma-rays has shown that they are separately isotropic at 935 kev, so that it is probable that this level is formed mainly by s protons.

From curve (c) of Fig. 4 it is apparent that the 874 kev level is not (1,+). Possible alternatives are (2,−) and (3,+), and the latter is unlikely since the (α_1,γ) correlation due to it would be very strongly anisotropic. Assuming that the level is (2,−) and is formed by p protons, the theoretical correlation in a plane at an angle φ to the proton beam is given by

$$\begin{aligned}I(\theta,\varphi)\sim&(25+46\cos^2\theta-55\cos^4\theta)\\&+\cos^2\varphi(1-131\cos^2\theta+355\cos^4\theta-225\cos^6\theta)\\&+(\sqrt{10})B\cos\beta[(10-151\cos^2\theta+440\cos^4\theta-315\cos^6\theta)\\&+\cos^2\varphi(-1+131\cos^2\theta-355\cos^4\theta+225\cos^6\theta)]\\&+(5/2)B^2[(4+109\cos^2\theta-286\cos^4\theta+189\cos^6\theta)\\&+\cos^2\varphi(1-131\cos^2\theta+355\cos^4\theta-225\cos^6\theta)].\end{aligned}$$

B and β give the relative amplitude and phase of alpha-particles having $l'=4$ and 2, respectively. The full curve in the figure is calculated for $A=0$, $B=0.54$, $\cos\beta=-0.245$, and is corrected for the spread in θ and φ due to the finite geometry of the apparatus, the average value of φ being $\pi/2$. The size of $\cos\beta$ is obtained theoretically [Sec. III(f)], and its sign and the value of B are chosen to give the best fit to the experimental points.

We consider that these assignments for the Ne^{20} levels [(1,+) at 669 kev, (2,−) at 874 kev, (1,+) at 935 kev)] are almost certainly correct, and we shall now use them in discussing the transitions to the third and fourth excited levels in O^{16}.

(b) (α_2,γ) Correlations

Figure 5 shows the (α_2,γ) correlations obtained at the 874- and 935-kev resonances in Ne^{20}. (The correlation at 669 kev could not be attempted because of its very low intensity.) The broken curve of Fig. 5(b) is the expected pattern (allowing for finite geometry) for a pure quadrupole correlation given by

$$I(\theta)=1-3\cos^2\theta+4\cos^4\theta.$$

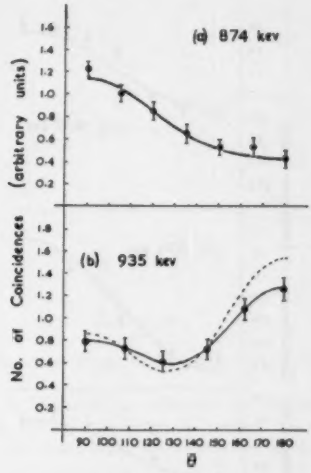

FIG. 5. (α_2,γ) correlations.

Despite the rather poor statistics, one can see that the curve is a reasonable fit to the experimental points. This pattern can only arise if the α_2 particle is emitted with 2 units of orbital momentum and is followed by an electric quadrupole gamma-ray. The α_2 level in O^{16} would therefore be (2,+).

Strong supporting evidence for this assignment is provided by the (α_2,γ) correlation at 874 kev [Fig. 5(a)]. If our level assignments are correct, Table I indicates that the pattern will be dominated by a term,

$$I(\theta,\pi/2)=1-\tfrac{3}{4}\cos^2\theta,$$

due to p-wave alpha-particles, and that the presence of f-wave alpha-particles will reduce the anisotropy. The full curve of Fig. 5(a) is obtained by putting $A=0$, $B=0.35$, $\cos\beta=-0.244$, and correcting for the finite geometry as for the (α_1,γ) correlations. The phase angle β is again obtained from the Coulomb wave functions. Further support for these values comes from the (p,α_2) angular distribution at 874 kev [see Sec. V(d) below].

(c) (α_3,γ) Correlations

Figure 6 shows the (α_3,γ) correlations at 669, 874, and 935 kev. The curves at 669 and 935 kev can be well fitted by the formula

$$I(\theta)=1+\cos^2\theta.$$

This suggests that the α_3 level is (1,−), although the

[18] Day, Chao, Fowler, and Perry, Phys. Rev. **80**, 131 (1950).
[19] J. E. Sanders, Phil. Mag. **43**, 630 (1952).

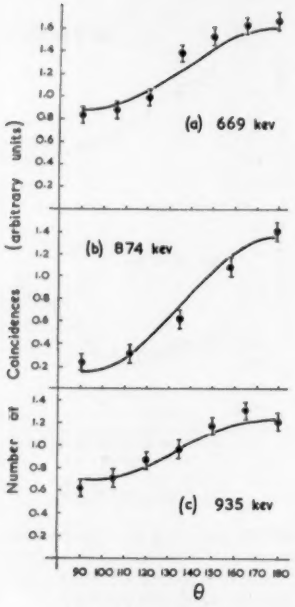

FIG. 6. (α_3,γ) correlations.

pattern could also be obtained with a $(2,-)$ level in O^{16} if B were small (see Table I). The (α_3,γ) correlation observed at 874 kev, however, confirms the former assignment, for which the theoretical pattern is

$$I(\theta,\varphi)=\cos^2\theta\sin^2\varphi+\cos^2\varphi.$$

A satisfactory fit to the 874-kev correlation could not be obtained by assuming the α_3 level to be $(2,-)$, even with an arbitrary choice of α and β and the introduction of terms due to alpha-particles having $l'=4$.*

All three curves of Fig. 6 are obtained by correcting the theoretical curves for the finite geometry of the apparatus, assuming $A=0$.

(d) (p,α) Angular Distributions

The alpha-particle angular distributions at the 874-kev resonance are given in Fig. 7. The full curves are those calculated assuming that the 874-kev level in Ne^{20} is $(2,-)$ and that the α_1, α_2, and α_3 levels in O^{16} are $(3,-)$, $(2,+)$, and $(1,-)$, respectively, with the values of B and $\cos\beta$ deduced from the (α,γ) correlations. The (p,α_3) curve has special interest because the shape of the distribution is very sensitive to the value of A. Taking $|\cos\alpha|=0.439$ as given by the Coulomb functions, we find the value of A to be 0.1 ± 0.1. This is our justification for setting $A=0$ throughout our calculations. It would clearly be desirable to measure these angular distributions in more detail.

(e) (p,γ) Angular Distributions

Sanders[19] has used a deuterium chamber to separate the 6.1-Mev gamma-rays (γ_1) from the mixture $(\gamma_2+\gamma_3)$ and has measured the angular distributions of these two groups at 874 and 935 kev. As we have mentioned previously, the 935-kev γ-rays appear to be separately isotropic. At 874 kev, Sanders found the (p,γ_1) distribution to be again isotropic within 5 percent, and using our values of A, B, and $\cos\beta$, the expected angular distribution is

$$I_1(\theta)=1+0.04\cos^2\theta,$$

which agrees well with his results.

To compute the theoretical angular distribution for $(\gamma_2+\gamma_3)$ at 874 kev, we have taken the relevant parameters from our fitting of the (α,γ) correlations, and have assumed that the over-all intensities of γ_2 and γ_3 are in the ratio 3:1. This approximate figure is obtained from our measurements of alpha-particle yield, taking account of the angular distributions, and the computed $(\gamma_2+\gamma_3)$ curve is

$$I_{2+3}(\theta)=1+0.36\cos^2\theta,$$

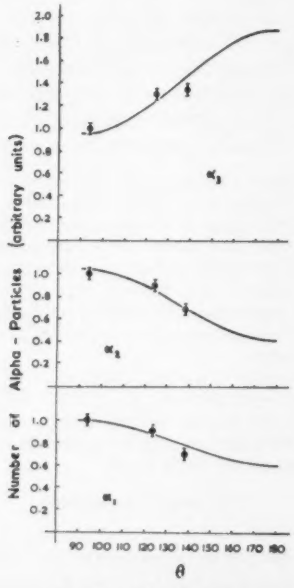

FIG. 7. (p,α) distributions.

* (*Note added in proof:* We have since measured the (α_3,γ) correlation in the plane $\varphi=0$ at 874 kev. The result was isotropic within ±10 percent, thus supporting the $(1,-)$ assignment.)

whereas Sanders found

$$I_{2+2}(\theta)=1+0.32\cos^2\theta,$$

which agrees within the errors of the observations.

VI. DISCUSSION

The results described above have suggested a complete level scheme for the reactions $F^{19}(p,\alpha\gamma)$. It is illustrated in Fig. 8. The theoretical analysis has been given very briefly so as not to obscure the main arguments, and it may seem at first sight that several other level schemes could fit the experiments. When the detailed comparison with Table I is carried out, however, one finds that the choice of levels is very limited.

The identification of the states taking part in a given transition has been made in the first instance from the (α,γ) angular correlation pattern. One can see from Table I that when a mixture of two orbital momenta for the alpha-particles is possible the shape of the pattern may be strongly modified. Despite this complication, any one correlation measurement usually gives the parity of a given level in O^{16} without any ambiguity, and limits the choice of angular momentum (J) to two or, at most, three values. The combined evidence from our total of nine angular correlation measurements then leads to a unique value of J for each level in O^{16}. The experiments are not accurate enough to establish the precise values of the amplitude and phase factors (A,α) and (B,β), but at 874 kev, where we have evidence for the (p,α) and (p,γ) correlations as well as the (α,γ), the same set of values of B, together with the theoretical phase shifts, will fit all three measurements for a given level in O^{16}.

We have mentioned earlier (Sec. III) that we have not considered more than one orbital momentum for the incoming protons in obtaining the theoretical expressions of Table I for (α,γ) correlations. This is on the whole justifiable for a correlation observed in a plane at right angles to the proton beam, as the essential features of the pattern are not affected by a contribution from higher l values. (We have checked this in individual cases.) No such simplification can be made for correlations observed in a plane containing the proton beam direction, nor, of course, for the angular distributions of alpha-particles and gamma-rays relative to the protons. One drawback of our simplified scheme is that the quantities (B,β) must now serve to describe the mixing both of incoming proton waves and of outgoing alpha-particle waves. Their physical significance is thus slight unless the reaction is dominated by the lowest possible orbital momentum for the protons, which does seem to be the case in the present reaction.

Certain features of the results may be specially noted. So far as one can tell, there is no difference in properties of the 669- and 935-kev resonance levels in Ne^{20}. Both the (α_1,γ) and the (α_2,γ) correlations are identical within the accuracy of the measurements. The occurrence of radiative capture at 669-kev proton energy and not at 340 or 935 kev (Devons and Hereward[20]) is therefore rather surprising, if indeed the capture gamma-ray comes from the same state as the alpha-particles. A careful study by J. E. Sanders (private communication) has failed to reveal any difference between the excitation functions for the two processes.

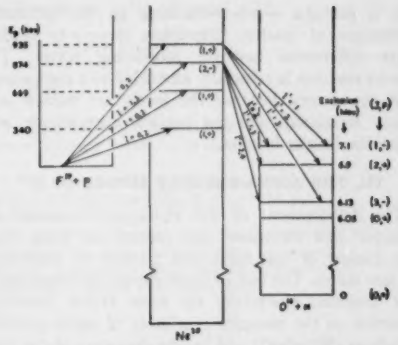

FIG. 8. Level scheme for the reaction $F^{19}(p,\alpha\gamma)O^{16}$.

The difficulty of drawing reliable conclusions from considerations of potential barrier penetrability is well known. In the present reaction it is interesting to compare the observed branching ratio between the alpha-particles with what one would expect for the orbital momenta involved. To make the comparison we have computed the penetrabilities by simple barrier theory (WKB method as presented by Bethe[21]) for the orbital momenta suggested by our analysis, and have normalized them so that the sum of all three alpha-particle intensities at a given resonance is unity. The experimental branching ratios are taken from the results of Freeman,[22] corrected for angular distribution according to Fig. 7 of the present paper and normalized in the same way. The results are given in Table II. It may be seen that there is a rough correspondence between theory and experiment except for the α_3 group at 874 kev and the α_2 group at 669 and 935 kev. These last modes of decay seem to be strongly discouraged.

TABLE II. Branching of competing alpha-particle emissions. The upper figure of each pair is the computed branching ratio.

	α_1	α_2	α_3
669 kev	0.68	0.13	0.19
	0.82	0.003	0.17
874 kev	0.82	0.17	0.01
	0.74	0.19	0.07
935 kev	0.49	0.18	0.33
	0.75	0.03	0.22

[20] S. Devons and H. G. Hereward, Nature **162**, 331 (1948).
[21] H. A. Bethe, Revs. Modern Phys. **9**, 177 (1937).
[22] J. M. Freeman, Phil. Mag. **41**, 1225 (1950).

It is perhaps worth remarking on the successful application of modern dispersion theory to predict phase differences between interfering states. The present reaction is especially amenable to a comparison with the theory because the levels are narrow and clearly separated, and the particle energies are well below the barrier heights.

VII. THE ALPHA-PARTICLE MODEL OF O^{16}

The development of the alpha-particle model by Wheeler[2] and Dennison[3] was carried out when little was known of the spins and parities of individual nuclear states. The link between theory and experiment was provided essentially by some rather indefinite evidence on the resonant scattering of alpha-particles in helium (Wheeler[22]) and by the discovery of the pair-emitting state of O^{16} (Fowler and Lauritsen[24]). This, together with a knowledge of the binding energy of one alpha-particle in the nuclei C^{12} and O^{16} in their ground states, made it possible to advance plausible values for the rotational and vibrational energies of an alpha-particle system. The symmetry of the system then imposed limitations on the quantum numbers of the excited states, and tentative level schemes could be set up.

The picture of O^{16} as a regular tetrahedron implies that it has characteristic frequencies for pulsation, twisting, and flattening; these are usually denoted by ω_1, ω_2, and ω_3, respectively, and are in the ratio of approximately $2:1:\sqrt{2}$. The lowest nonrotational state allowed by the symmetry is a pulsating mode with energy $\hbar\omega_1$, zero total angular momentum, and even parity. It thus reproduces the properties of the pair state very well. On the other hand, one would expect the lowest rotational state, with no vibration, to lie at a lower energy than the pair level at 6.05 Mev. Symmetry requires that it should have the designation $(3,-)$, and a conventional figure ($\sim 4\times 10^{-13}$ cm) for the nuclear radius, on which the energy alone depends, would place such a level at about 2 Mev.

Since there is almost certainly no excited state of nonzero spin below 6.05-Mev excitation in O^{16}, it seems reasonable to identify the 6.13-Mev level with this pure rotational state, and to make use of this identification to deduce an effective moment of inertia for the oxygen nucleus. The corresponding nuclear radius is 2.5×10^{-13} cm. This is less than the accepted value by about the range of nuclear forces, and might perhaps represent the mean distance of nuclear particles from the center of the nucleus.

If we take the first two states in O^{16} as defining the parameters for the higher rotational-vibrational levels, we find that the next three levels would be a doublet $(2,+;\ 2,-)$ and a singlet $(1,-)$ in ascending order. The splitting of the doublet is due to an inversion mechanism, and its size cannot be accurately predicted, although according to Dennison[3] it should be small. It is satisfactory that the $(2,+)$ and $(1,-)$ levels do occur in the predicted order, but the absence of the $(2,-)$ level remains an anomaly.

The treatment given by Dennison[3] does not assume that ω_1 is exactly twice ω_2. One might therefore use the following relations to establish the energies of the various modes in O^{16}:

$$\begin{aligned}&\text{Pair state:} && \hbar\omega_1 = 6.05 \text{ Mev},\\ &(3,-)\text{ state:} && 6\hbar^2/I = 6.13 \text{ Mev},\\ &(1,-)\text{ state:} && (17\hbar^2/8I)+\hbar\omega_3 = 7.11 \text{ Mev}.\end{aligned}$$

With these assumptions it is possible to estimate the approximate level density for higher excitations of an alpha-particle structure. In the region 12- to 13.5-Mev excitation the predicted level spacing in O^{16} agrees fairly well with that found by Schardt *et al.*[25] in a study of the $N^{15}(p,\alpha\gamma)$, $N^{15}(p,\alpha)$, and $N^{15}(p,\gamma)$ reactions. Other regions of excitation have not been studied in sufficient detail to make an extensive comparison possible.

VIII. CONCLUDING REMARKS

This study of the $F^{19}(p,\alpha\gamma)$ reaction seems to bear out the usefulness of the alpha-particle model as a description of the low states of O^{16}. It is certainly rather difficult to describe all first four states in terms of the shell model.

Although it is unlikely that the alpha-particle model will remain valid above the first few excited states, it would be interesting to carry the comparison of theory with experiment to higher levels in this nucleus, particularly those in the region between 8 and 12 Mev, which has not yet been thoroughly studied. One might also hope to obtain fuller information about the level structure of Be^8 and C^{12}, and to find whether these related systems can be incorporated within the same theoretical framework.

One of us (J.S.) is indebted to the Department of Scientific and Industrial Research for the tenure of a research grant over the period in which this work was performed.

[22] J. A. Wheeler, Phys. Rev. **59**, 16 (1941).
[24] W. A. Fowler and C. C. Lauritsen, Phys. Rev. **56**, 840 (1939).
[25] Schardt, Fowler, and Lauritsen, Phys. Rev. **86**, 527 (1952).

The Interactions of High Energy Nucleons with Nuclei. II*

G. BERNARDINI,† E. T. BOOTH, AND S. J. LINDENBAUM‡
Columbia University, New York, New York
(Received August 1, 1952)

Part I of this paper presented an analysis of the experimentally observed interactions of 300–400 Mev protons and neutrons with the nuclei of *G*-5 emulsion. General evidence for the nucleonic cascade mechanism of interaction was deduced from these results.

Goldberger had previously calculated the interaction of high energy nucleons (~90 Mev) with heavy nuclei on the basis of an internal nucleonic cascade generated in a Fermi nucleon gas. However, the experimental test of these calculations by Hadley and York was indecisive.

Calculations basically similar to the Goldberger type were performed for these interactions, employing the Monte Carlo method to treat the rather complicated cascades involved. The theoretical and experimental results are compared in detail and found to be essentially in agreement within error limits. Hence it is concluded that the nucleonic cascade mechanism can satisfactorily explain these interactions.

I. INTRODUCTION

PART I[1] of this paper presented the phenomenological analysis of the nuclear interactions produced in nuclear β-sensitive emulsions by high energy nucleons, i.e., by protons and neutrons of energy 300–400 Mev. Since it was demonstrated that at least 80 percent of the observed interactions were due to collisions of an incident nucleon with the nuclei of the heavy component of the emulsion (AgBr), the observed events should exhibit the general features of the interactions of 300–400 Mev protons and neutrons with the nucleus $A \approx 100$.

The light element interactions could be approximately subtracted from the results by applying the data of Blau and Oliver[2] obtained using stratified emulsions. However, the differences in light and heavy element events are not sufficiently great that the small percentage of light element events included in the data changes the results appreciably within the statistical and other error limits.

For reasons given in the introduction of Part I,[1] it was felt that these experiments could provide a sensitive test of the nucleon-nucleus collision model previously proposed by Goldberger.[3] This paper will report the results of Goldberger-type Monte Carlo calculations for these interactions and compare them with the experiments.

II. THE NUCLEON-NUCLEUS INTERACTION MODEL

The heavy nucleus was represented by the usual Fermi statistical gas theory. In this approximation one considers the ground state of the nucleus as composed of ideal zero temperature noninteracting fermion gases of neutrons and protons bound in a uniform potential well:

$$-|V| \text{ for } r \leq \text{nuclear radius},$$
$$0 \text{ for } r > \text{nuclear radius}.$$

The resulting Fermi-momentum distribution depends upon the effective density of nucleon matter and the temperature.

The simple cubical well solution for the momentum distribution was considered sufficient for these crude calculations and was employed. It can be represented by a sphere of radius equal to the maximum Fermi momentum:

$$P_{\max} = (3h^3/8\pi)^{\frac{1}{3}}(\rho)^{\frac{1}{3}}, \quad (1)$$

where ρ is the effective nucleon density, i.e., number of nucleons per unit volume. The probability that the Fermi momentum of a nucleon will lie in any volume element of the sphere is proportional to the volume. The nuclear radius was calculated from the relationship

$$R = 1.4A^{\frac{1}{3}} \times 10^{-13} \text{ cm}. \quad (2)$$

Since the numbers of neutrons and protons in the nucleus $A = 100$ are approximately equal (5:4) and $P_{\max}$ depends only on $\rho^{\frac{1}{3}}$, the value for the average $P_{\max} = 22$ Mev was employed for all nucleons. The average binding energy $-|\alpha|$ per nucleon was assumed to be -9 Mev. Hence the average potential well depth is

$$V = P_{\max} + |\alpha| = 31 \text{ Mev}. \quad (3)$$

The Coulomb barrier for protons was calculated to be about 8 Mev.

The collisions of the incident high energy nucelon ($E \gtrsim 50$–100 Mev) with the nucleus were treated according to the Serber[4] point of view. Since the DeBroglie wavelength $\lambda \ll$ nuclear radius, the concept of a definite classical trajectory relative to the nucleus was employed. Because the effective ranges of high energy nucleon-nucleon scattering forces are small in comparison with the mean free path in nuclear matter, it was assumed that the general features of the inter-

* Jointly sponsored by the ONR and AEC.
† Now at the University of Illinois, Urbana, Illinois.
‡ Now at the Brookhaven National Laboratory, Upton, New York.
[1] Bernardini, Booth, and Lindenbaum, Phys. Rev. **85**, 826 (1952).
[2] M. Blau and A. R. Oliver, Phys. Rev. **87**, 182 (1952).
[3] M. L. Goldberger, Phys. Rev. **74**, 1268 (1948).
[4] R. Serber, Phys. Rev. **72**, 1114 (1947).

action are determined by a series of single nucleon-nucleon scattering collisions. Precisely in this approximation the process is represented as a cascade of free nucleon-nucleon scatterings. The influence of the other nucleons is felt only through the potential barrier, the initial Fermi-momentum distribution, and the Pauli exclusion principle which forbids collisions corresponding to final states already filled by other nucleons. Furthermore, the scattering collisions inside nuclear matter are described by asymptotically measured free nucleon-nucleon scattering cross sections.

The Fermi gas nucleus is assumed to remain in the ground state during the development of the internal nucleonic cascade. This is equivalent to stating that the many-body wave functions describing the nucleus are not appreciably affected by the binding forces during the cascade collision time. The cascade proper is considered to continue until either the moving nucleons reach the edge of the nucleus with energy greater than the nuclear (plus Coulomb) barrier and escape, or as a result of a collision the cascade nucleons are degraded in energy below the barrier and are then considered thermally captured. The cascade stage then ends, and the excited nucleus is considered to enter the thermal evaporation stage which will be described by the Weisskopf theory.[5]

This treatment of the problem would clearly become more and more justified as the density of nuclear matter were progressively decreased by an expansion of the nuclear volume. However, as long as the incident nucleon in a collision is characterized by a λ (DeBroglie wavelength) much less than the nuclear diameter, and a mean free path in nuclear matter long compared to the effective scattering ranges, this treatment could perhaps be expected to predict at the very least the gross statistical features of a large number of interactions. This is likely even though each individual calculation was appreciably in error, since the quantum-mechanical departures from this simple semiclassical cascade (which probably corresponds to the mean behavior) would tend to average out when one groups together a large number of interactions. Chew and Wick[6] have considered the errors involved in these assumptions in their treatment of the impulse approximation and have concluded that, at least for nucleons of energy greater than 50 Mev, multinucleon scattering corrections are not too large. Hence, at least for the faster nucleons, these assumptions may appear reasonable. For those below 50 Mev they certainly become less valid; however, one can hope that the important characteristics of these collisions will still correspond, in general, to the single nucleon-nucleon collision.

In any case the treatment of so complicated an interaction by a simple and crude model cannot possibly be justified analytically, and one will have to decide its usefulness in the last analysis simply by comparing predictions with experiment.

III. THE GOLDBERGER MODEL CALCULATIONS

A. The Goldberger Work

Goldberger developed the Serber ideas on high energy nucleon-nucleus interactions into a detailed model for calculating these interactions on the basis of the generation of a semiclassical internal nucleonic cascade in a Fermi gas nucleus.

To treat complex cascades of this type and retain all the natural statistical fluctuations he employed the Monte Carlo method.[7] His original evaluations were performed for the interactions of 90-Mev neutrons with a Pb nucleus. An experimental check of Goldberger's calculations by Hadley and York[8] was interpreted to be at best only in partial qualitative agreement.

For reasons previously given (see the Introduction of Part I), it was decided that the interaction of 300–400 Mev protons and neutrons, with the Ag-Br nuclei ($A \approx 100$) of β-sensitive emulsion would provide a sensitive test of the model at these higher energies, where it would be expected to be intrinsically more reliable. Some general evidence for the internal nucleonic cascade was deduced from the experimental results described in Part I.[1] In this paper detailed calculations of the Goldberger type for these interactions will be described and the results compared with the experimental data.

B. The Monte Carlo Method

The Monte Carlo Method[7] is a generally valid procedure for treating an ordered sequence of processes $(A, B, C \cdots)$ each of which is characterized by its own statistical distribution. One divides each statistical distribution into equally probable intervals, and then starting with a random choice for A chooses in sequence at random equally probable events for B, then for C, etc., until one finally arrives at the end state. It is obvious that for sufficiently fine intervals what one does is to merely naturally reproduce the process, and hence the inherent statistical fluctuations in the final state distribution curves should be the same for N Monte Carlo calculations as one obtains for results based on N experimentally observed events. Of course, this assumes that the statistical distribution curves put into the calculations are correct and completely describe what happens. The manner of application of the method to the present problem will be made clear by a description of the procedure.

[5] V. Weisskopf, Phys. Rev. **52**, 295 (1937).
[6] G. Chew and G. C. Wick, Phys. Rev. **85**, 636 (1952).
[7] S. Ulam and J. VonNeumann, Bull. Am. Math. Soc. **53**, 1120 (1947).
[8] J. Hadley and H. York, Phys. Rev. **80**, 345 (1950).

C. The Mean Free Path in Nuclear Matter

The cross section for $p-p$ scattering has been experimentally investigated from 18 Mev to 340 Mev.[9–11] It was found to be essentially isotropic in the c.m. system at all energies, to be essentially constant in magnitude from 340–120 Mev, to increase more slowly than a 1/energy law between 120 and 31 Mev, and to follow a 1/energy law from 31 Mev to 18 Mev. The circled points of Fig. 1 represents the experimental points, and the solid curve down through them represents the variation with energy assumed for these calculations.

The $n-p$ cross section has been investigated from 40–270 Mev.[12–14] It was found to be anisotropic in the center-of-mass system, and characterized by a rather flat valley around 90° with symmetrical sharp peaks in the forward and backward directions. The effect of these peaks is sharply reduced inside nuclear matter by the Pauli exclusion principle, which discourages small momentum transfer collisions. Hence it was felt that a simplification could be introduced by replacing the $n-p$ cross section by an equivalent isotropic cross section chosen so as to yield the same average energy transfer as the actual anisotropic cross section. It was found in all cases that the equivalent isotropic cross section differed only slightly in magnitude from the average height of the valley in the region of the $n-p$ scattering curve around 90°. This demonstrates that the energy transfer characteristics are mostly determined by this region and are not much affected by the forward and backward peaks.

The total cross section of the equivalent isotropic curve was reduced by at most 30 percent from the original. The actual reduction after taking into account the Pauli exclusion principle would be much smaller. The equivalent isotropic $n-p$ cross section as a function of energy is given by the dashed curve in Fig. 1. The circled points were fitted by a smooth curve of the form $1/E^{\alpha}$, where $0 \leq \alpha \leq 1$. The extrapolation of the $p-p$ curve to higher energies ($\sim$400 Mev) is fairly reliable since the curve is constant over the large region 120–340 Mev, and it is unlikely that it would change suddenly. The $n-p$ extrapolation is not so reliable, but it is a reasonable guess.

The mean of the $p-p$ and $n-p$ curves is represented by the dash-dot curve of Fig. 1. At the higher energies the mean is quite close to the individual cross sections, but at the lower energies the separation of the $n-p$ and $p-p$ curves becomes appreciable. It is generally assumed that nuclear forces are charge independent; therefore, one should expect that $\sigma_{n-n} \approx \sigma_{p-p}$. Inelastic

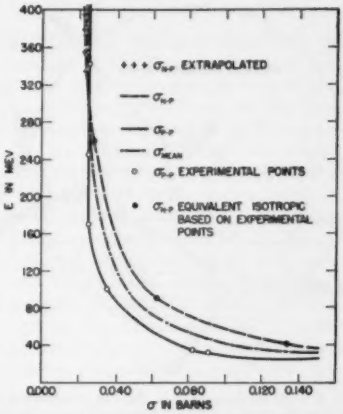

FIG. 1. The nucleon-nucleon scattering cross sections as a function of energy.

cross section measurements with high energy neutrons[14,15] generally agree with this assumption. Furthermore, the similarity of the neutron stars to the proton stars, as reported in Part I, is further evidence for this assumption.

The calculations are greatly simplified if one treats a nucleonic cascade of nucleons without regard to their charge identity. Since the shape of the differential cross sections is considered the same (i.e., isotropic), the number of neutrons and protons is roughly equal, and the mean total cross-section curve does not differ too drastically from the individual curves, one can approximately replace the neutrons and protons by a single type of nucleon whose cross section is equal to the mean cross section and whose density is equal to the mean nucleon density. This approximation will be expected to give reasonable results for the characteristics of all nucleons, that is, neutrons and protons taken together, but will lead to uncertainties in the ratio of protons to neutrons. This point will be considered later, and it will be shown that it is probable that the emitted nucleons are roughly half neutrons and half protons.

The mean cross section given in Fig. 1 as a function of the moving nucleon energy must of course be averaged over the Fermi sphere. The probability W_i of a collision with a nucleon in a volume element of the Fermi sphere dV_i is

$$W_i = \text{const}\sigma(P_{ri})P_{ri}dV_i, \tag{4}$$

where P_{ri} is the momentum of the incident nucleon relative to the target nucleon.

With the exception of the low energy region the mean cross section varies in a manner not too different from

[9] Chamberlain, Segrè, and Wiegand, Phys. Rev. **81**, 661 (1951)
[10] B. Cork, Phys. Rev. **80**, 321 (1950).
[11] W. Birge, Phys. Rev. **80**, 490 (1950).
[12] Hadley, Kelly, Leith, Segrè, Wiegand, and York, Phys. Rev. **75**, 351 (1950).
[13] Kelly, Leith, Segrè, and Wiegand, Phys. Rev. **79**, 96 (1950).
[14] Cook, McMillan, Peterson, and Sewell, Phys. Rev. **75**, 7 (1950).
[15] Fox, Leith, Wouters, and MacKenzie, Phys. Rev. **80**, 23 (1950).

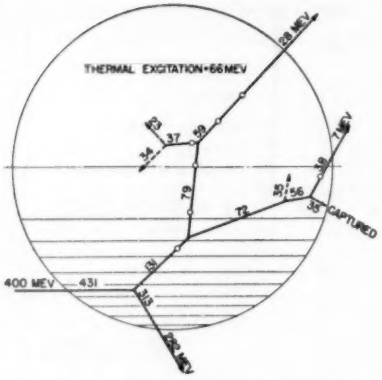

FIG. 2. A work diagram used in the two-dimensional calculations, illustrating the actual development of an interaction. The circle represents the cross section of a nucleus of mass number 100. Its radius is taken to be $R=1.40A^{\frac{1}{3}}\times10^{-13}$ cm.

a const$/P_{r_i}$ law. Hence,

$$\sigma(P_{r_i})P_{r_i}dV_i=\text{const}dV_i=W_i, \tag{5}$$

and, therefore, the average cross section over the Fermi sphere is the same as the mean cross section for the incident energy. In the low energy region the mean cross section varies like a 1/energy law, and it can be easily shown that in this case also the average cross section over the Fermi sphere is the same as the mean cross section for the incident energy. Hence, the mean free path is a function of energy,

$$\lambda(E)=1/\rho\bar{\sigma}(E), \tag{6}$$

where E is the energy of the moving nucleon inside the nucleus, ρ is the density of the nucleons, and $\bar{\sigma}(E)$ is the mean cross section as a function of energy given in Fig. 1.

The path length distribution inside the nucleus is obviously given by the following distribution law:

$$q=e^{-x/\lambda(E)}, \tag{7}$$

where q is the probability of a collision not having occurred in a distance x inside the nucleus. The distribution of path lengths is taken into account by dividing q into 1000 equally probable intervals and picking one at random. To each interval, of course, there corresponds a particular value of $x/\lambda(E)$ given by Eq. (6). Evaluating $\lambda(E)$ from Eq. (6) yields the particular path length.

D. The Two-Dimensional Geometry

One is concerned here with the interaction of a parallel beam of high energy nucleons with a spherical nucleus of uniform density. The momentum distribution of the nucleons inside the nucleus is spherically symmetric and characterized by a Fermi sphere. The experimentally determined nucleon-nucleon scattering cross sections all possess polar symmetry around the line of mutual approach in the center-of-mass system. Therefore, it is obvious that there must be a polar symmetry around the incident beam direction for all final distribution curves. This polar symmetry around the incident beam direction suggests that the problem might be considerably simplified by an appropriate two-dimensional treatment. This is necessary, as a three-dimensional treatment would be prohibitively lengthy. Let us replace the three-dimensional spherical nucleus with a two-dimensional great circle, of which a diameter is chosen to be along the incident beam direction. A three-dimensional factor which we must incorporate in our two-dimensional treatment is that segments of this circle formed by a series of chords parallel to the beam direction must be weighted proportionately according to the ring area they present normal to the incident beam. The division of half the circle of nuclear radius into ten such weighted segments is shown in Fig. 2. Only half a circle was used for convenience since the final distributions are symmetrical around the beam direction. By considering equal numbers of incoming nucleons incident upon each of the ten segments, one weights the initial geometry according to the true three-dimensional case.

The three-dimensional Fermi sphere was transformed into a two-dimensional circle of the same radius, such that the two-dimensional polar angle corresponds to the original three-dimensional polar angle relative to the incident nucleon direction. However, the two-dimensional polar angle now has positive and negative values in order to take into account the fact that the resultant vector momentum can be directed toward the center of the two-dimensional nucleus or away from it. The resultant two-dimensional area elements are weighted according to the three-dimensional volume elements corresponding to their rotation about the incident beam direction.

The division of the three-dimensional Fermi sphere into 1000 equal volume elements is given in terms of this correspondingly weighted two-dimensional repre-

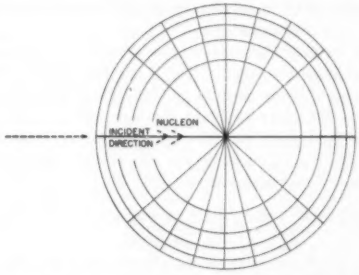

FIG. 3. The Fermi momentum sphere. The Fermi sphere used in the calculations contained 1000 volume intervals; the above sphere contains only 80 for illustrative purposes.

sentation in Fig. 3. When a collision takes place, the relative probability for the target nucleon to lie in the volume element dV_i of the Fermi momentum sphere is seen from Eq. (5) to be proportional to dV, for all but the low energy region. Therefore, equal volume elements represent equal collision probabilities, and hence the appropriate choice of a collision partner for the moving nucleon is a random choice of one of the equal 1000 volume elements represented by Fig. 3. The low energy region would require a different weighting of the Fermi sphere; but this only affects the tail end of the nucleonic cascade, and it is felt that the results will not be affected much by the use of the same Fermi sphere weighting throughout.

This procedure insures that the kinetics of the scatterings such as energy transfer and relative angle between the two nucleons involved in a collision will be preserved in these two-dimensional calculations.

E. The Scattering Calculation

From the directions and momenta of the incident nucleon and the target nucleon, one calculates the kinetic relations in the center-of-mass system before the collision. All differential cross sections are assumed to be isotropic; hence, the appropriate division of the scattering angle θ into equal probability intervals is according to equal cosine θ intervals.

The choice of a scattering angle interval at random then enables one to calculate completely the angles and energies of the scattered nucleons. Relativistic calculations were used for an incident energy >150 Mev. Nonrelativistic calculations were used for energies below 150 Mev. If the final energy of either scattered nucleon was less than 22 Mev (top of the Fermi sphere), the collision was forbidden by the Pauli exclusion principle and was assumed not to have taken place. The use of the mean free path for free nucleons, the subsequent calculation of the scattering collisions, and then finally the application of the Pauli principle is merely a matter of calculatory convenience. It can be shown that the appropriate reduction of the scattering cross section to only those parts which lead to allowed collisions yields the same results as the above procedure.

F. The Barrier

In Sec. II it was shown that the average nuclear well depth is 30.6 Mev and the Coulomb barrier is 8 Mev for protons. Since we are treating average nucleons in this calculation, the average Coulomb barrier is about 4 Mev. Therefore, the total average nuclear barrier is about 35 Mev. Hence, it is assumed that if, after any collision, a nucleon has an energy of less than 35 Mev, it is thermally captured. A nucleon which reaches the edge of the nucleus must for consistency lose a kinetic energy equal to the well depth (31 Mev) upon escaping. Reflection and refraction by the barrier are neglected.

G. The Working Procedure

Figures 2 and 4 are replicas of actual work diagrams. Equal numbers of 400-Mev nucleons were considered incident upon each of the ten ring area weighted segments shown in the figures. Upon entering the nucleus the 400-Mev nucleons gained the 31-Mev nuclear potential. The mean free path for 431-Mev nucleons was calculated according to Eq. (6), Sec. II-C. A random number table was used for all random choices. A three-place random number was chosen to select one of the 1000 equally probable intervals for $x/\lambda(E)$, given by Eq. (7). Having already calculated $\lambda(E)$, x was obtained, and the incoming nucleon trajectory was extended a distance x beyond its entrance point. If x fell outside the nucleus, this was considered to represent the phenomenon of nuclear transparency. If x fell inside, a collision was assumed to attempt to take place at x.

A second random number was chosen to select one of 1000 equally probable Fermi momentum intervals (shown in Fig. 3). The Fermi momentum and direction together with the incoming nucleon momentum and direction were used to calculate relativistically the kinetic characteristics in the center-of-mass system before the collision. A third random number was chosen to select a scattering angle interval. The scattering angle was introduced, and the calculation was completed relativistically to yield the final angles and energies of the scattered nucleons. These were plotted on the diagram as shown in Figs. 2 and 4. If the final energies of either nucleon fell below 22 Mev (the top of the Fermi sphere), the collision was assumed not to have occurred and the incident nucleon was given a

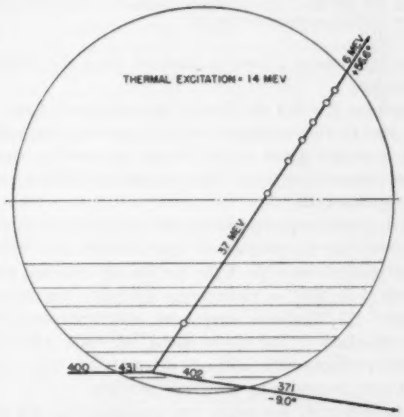

FIG. 4. Another work diagram used in the two-dimensional calculations, illustrating the actual development of an interaction. The circle represents the cross section of a nucleus of mass number 100. Its radius is taken to be $R=1.40A^{\frac{1}{3}}\times10^{-13}$ cm.

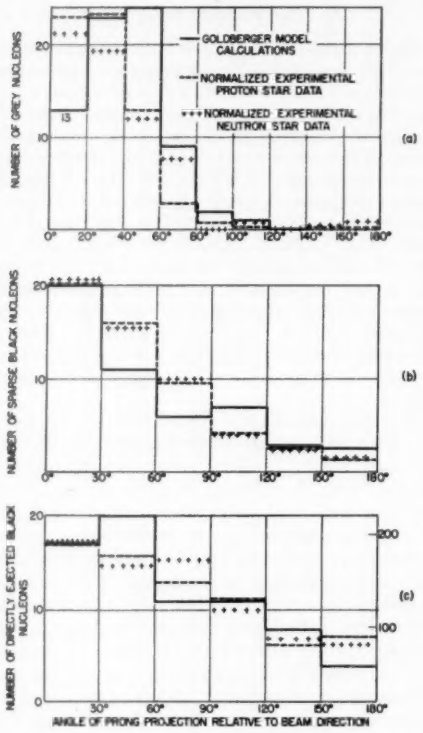

FIG. 5. A comparison of the calculated and experimental: (a) gray (>100 Mev) nucleon angular distribution; (b) sparse black (30–100 Mev) nucleon angular distribution; (c) black (≤30 Mev) nucleon angular distribution.

new path length (chosen at random) along the original direction.

In Figs. 2 and 4 the first collision occurred. Each of the two moving nucleons resulting from the first collision was then given a path length (at random) along their plotted directions. The appropriate $\lambda(E)$ for each energy was used.

The previous procedure for the incident nucleon was followed for all products of the cascade until either they reached the edge of the nucleus and escaped with a loss of 31 Mev, or their energy fell below the nuclear barrier (35 Mev) and they were considered captured (as illustrated). The circles along the trajectories indicate positions were collisions attempted to take place but were forbidden by the Pauli principle.

As previously discussed, due to symmetry, only the magnitude of the angles of the emergent prongs relative to the incident beam direction has significance. The sign is meaningless.

H. The Thermal Excitation

One can write the conservation of energy equation for these interactions as

$$400=\sum_{n=1}^{N} E_n+|\alpha|(N-1)+U, \tag{8}$$

where N is the number of emergent nucleons, $|\alpha|$ is the nucleon binding energy, and U is the thermal excitation. The 400 on the left side represents the incident energy. The term $\sum E_n$ on the right side represents the sum of the kinetic energies of the N emergent nucleons, and $|\alpha|(N-1$ represents the binding energy of the emerging nucleons. The -1 is due to the fact that the incoming nucleon is not bound. Hence, it is clear that U must represent the thermal excitation. Solving for U, one has

$$U=400-\sum_{n=1}^{N} E_n-|\alpha|(N-1). \tag{9}$$

The thermal excitation so defined represents the sum of two effects. These are the direct contribution of thermally captured nucleons, and the excitation energy represented by the holes left in the Fermi distribution by the directly ejected target nucleons. These two effects are roughly comparable in magnitude.

I. Interpretation of Results

The two-dimensional treatment used in the calculations suggests that probably a reasonable comparison of the calculated angular distributions and the experimental projected angular distributions can be made. Of course, the two angles do not correspond in any exact manner, but they both have similar two-dimensional characteristics and it is reasonable to expect that the important features of the distributions would be common to both.

The calculations performed give the numbers of neutrons and protons emitted lumped together as a total number of nucleons. The estimation of the ratio of emitted protons to neutrons is a rather difficult one to make. This ratio depends in a complex way upon the charge of the incident nucleon, the relative values of $p-p$, $n-n$, and $n-p$ scattering cross sections, the relative numbers of neutrons and protons, and the number of collisions inside the nucleus. The average ratio of protons to neutrons is about 5:4 and could be roughly considered equal to 1. The assumption of charge independence of nuclear forces is made, and therefore $\sigma_{n-n}\approx\sigma_{p-p}$. Figure 1 shows that over the high energy regions $\sigma_{n-p}\approx\sigma_{p-p}$. Hence, $\sigma_{n-p}\approx\sigma_{p-p}\approx\sigma_{n-n}$.

One would expect the ratio of fast protons to neutrons to be statistically weighted in favor of the incoming charge after the first collision. A very rough estimate of this factor would be about 3:1, since only half of the $n-p$ cross section (the exchange half) yields fast neutrons, while most of the $p-p$ cross section and

the nonexchange half of the $n-p$ yield fast protons. After a few collisions (estimated 2–3), the ratio would begin to approach 1, since this statistical factor is very rapidly reduced by the inherent symmetry of our assumed cross sections. Furthermore, the excess number of neutrons and the faster rise of the $n-p$ cross section with decreasing energy than the $p-p$ would also tend to reduce this ratio.

Since the average number of nucleon-nucleon collisions found per interaction in the calculations is about 4.5, it is reasonable to assume that approximately equal numbers of protons and neutrons are ejected in these interactions.

The similarity of the neutron and proton induced interactions reported in Part I provides direct experimental evidence for the validity of this assumption.

IV. COMPARISON OF GOLDBERGER CALCULATIONS WITH EXPERIMENTAL RESULTS

A. Introduction and Terminology

The results described in this chapter are based on 90 incident 400-Mev nucleons, of which 60 resulted in inelastic events and 30 went through the nucleus without interacting. Within statistics this division agrees with the expected calculated reduction of the geometric cross section by about 35 percent due to nuclear transparency.

In order to compare the results with the experimental proton and neutron star data, the same terminology was used in classifying the emitted nucleons as gray, sparse black, or black corresponding to kinetic energy greater than 100 Mev, between 100 and 30 Mev, and less than 30 Mev, respectively. To correspond to the experimental terminology, "prong" is used as a synonym for "emitted nucleon."

B. Angular Distributions

The comparison is made directly with projected experimental angles as discussed under "Interpretation of Results" in Sec. III. Figure 5(a) is a comparison of the calculated gray prong angular distribution with the experimental proton and neutron star gray prong angular distribution. Figure 5(b) is a comparison of the calculated sparse black prong angular distribution with the experimental proton star sparse black prong angular distribution. The agreement in both cases is reasonable within statistical limits. However, there seems to be a tendency for the experimental gray curve to be somewhat lower, and the experimental sparse black curve to be somewhat higher, in the forward half plane. This could represent a real experimental technique effect due to the erroneous inclusion of some border gray prongs in the sparse black region.

Figure 5(c) presents the directly ejected black prong angular distribution. An exact comparison with the experimental results was not possible in this case, since the evaporation and light element star components are included in the experimental curve. However, if one normalizes the experimental curve to the same total number [this was done in Fig. 5(c)], one can see a general agreement in the shapes of the curves. The additional isotropic component in the experimental curve is what one would expect as due to the evaporation and light element star components.

C. Mean Prong Numbers

The experimental results for neutron and proton induced interactions have already been compared in Part I[1] and shown to be in reasonable agreement within the energy differences involved and the added difficulties in detecting small neutron events. Since the proton interactions are the ones on which the actual calculations were based and are also the most complete, the comparison will be made with their results.

Table I, line (a), lists the mean numbers per interaction of directly ejected sparse black and gray nucleons. In Sec. III of Part I, it was concluded that a reasonable assumption for the fraction of emitted nucleons which are protons is $\frac{1}{2}$. Using this factor, line (b) of Table I is an estimate of the mean number of directly ejected sparse black and gray protons per event. Line (c) is the experimentally determined mean number per proton star.

The agreement is reasonable for the statistical limits given. However, there seems to be a systematic tendency for calculated values to be slightly higher than experimental values. This is what one expects due to the loss of zero prong stars in the area scanning which are rich in fast prongs. A correction for this could have been applied and would have led to an even closer agreement. However, this was not considered worth while, since one is already within statistical and other error limits.

This systematic experimental underestimation of fast prongs will of course operate in all comparisons.

The black prongs require special considerations, as one must add the estimated evaporation contribution to the mean number of directly ejected protons. Furthermore, the conclusions reached about the black prongs will be expected to be less reliable than those pertaining to the faster nucleons, for several reasons. First, the general validity of the model becomes questionable at these low energies, since the range of free scattering forces becomes larger than the nucleon radius, and hence, the effects of multiple interactions

TABLE I. Comparison of experimental and calculated mean numbers of gray and sparse black protons.

Line	Sparse black	Grey
(a) Mean No. of directly ejected nucleons	0.83±0.16	1.2 ±0.22
(b) Estimated mean No. of protons	0.42±0.1	0.6 ±0.12
(c) Experimental mean No. of protons	0.35±0.04	0.42±0.04

TABLE II. Comparison of experimental and calculated mean numbers of black prongs.

Line (a)	Mean No. of directly ejected black nucleons	1.15±0.22
Line (b)	Estimated mean No. of directly ejected protons	0.58±0.12
Line (c)	Estimated mean No. of evaporation prongs	1.5 ±0.2
Line (d)	Estimated Mean No. of visible black prongs	2.1 ±0.4
Line (e)	Experimental mean corrected value	2.5 ±0.2

with more than one nucleon can be important. Reflection and refraction effects at the nuclear surface, which are neglected, can also be important and change the results appreciably. It is also doubtful whether a moving nucleon of kinetic energy close to the well depth can be considered as interacting with a free particle gas of nucleons in the potential well. Furthermore, in treating the evaporation contribution to the black prongs, one is confronted with the lack of knowledge of the relation between nuclear temperature and entropy, and must rely on empirical results for the relation between excitation and number of evaporation prongs. These are not too reliable, due to inherent mixing of knock-ons and evaporation prongs; and also the effects of the Coulomb barrier at low excitations cannot be estimated well due to lack of knowledge of the temperature. In addition, it is very doubtful that temperature equilibrium can even be established in an evaporating Fermi nucleus, due to the relatively weak coupling for the statistical sharing of energy.

Nevertheless, it can be hoped that these difficulties will not be too serious, and it is worth while to attempt to take the calculations seriously even for the black prongs and see what results one gets. As we shall see shortly, even the black-prong-predicted results seem to agree with the experimental determinations.

The mean number of directly ejected black nucleons is given in line (a) of Table II. The estimated mean number of black protons is given in line (b). The calculated average thermal excitation for all interactions is 50 Mev. To estimate the number of black prongs corresponding to this average excitation, we shall use the value of 35-Mev excitation per black prong experimentally determined by Bernardini *et al.*[16] from similar cosmic-ray stars. Undoubtedly there were appreciable numbers of knock-ons in the spectrum used. Also, we are extrapolating to lower excitation energies perhaps without justification. However, it is the best estimate that can be made at the present time. A thermal excitation of 50 Mev would then be expected to yield a mean evaporation contribution of 1.5 black prongs per interaction. One should also include a statistical error due to the limited number of interactions. This expected evaporation mean prong number is given in line (c) of Table II. The sum of lines (b) and (c) is given in line (d) and is the theoretical prediction for the mean observed prong number. The experimental mean value is given in line (e), and is in reasonable agreement.

From Table II, lines (b) and (d), one can can calculate the percentage of visible black prongs which are knock-ons. The result is that 28 percent±7 percent of the visible black prongs are expected to be knock-ons. In Part I,[1] the experimental result was that at least 25 percent of the black prongs are knock-ons. Hence, the results seem to agree. However, the experimental value was determined by assuming that the isotropic component of the black prong distribution curve was entirely due to evaporation and did not contain any isotropic knock-on component. An inspection of Fig. 5(c) reveals that there is an isotropic component in the knock-ons. The value of this isotropic component is difficult to estimate because the statistics are very limited; and secondly, the shape of the directly ejected black prong distribution curve cannot be considered too reliable, since refraction effects, etc., at the edge of the nucleus could change the distribution considerably.

Considering the ordinate in the extreme backward direction of Fig. 5(c) as the average knock-on isotropic ordinate, the predicted percentage of forwardly projected knock-ons is about 20±5 percent, and is still in reasonable agreement with the experimental estimate.

D. Distribution of Interactions with Gray or Sparse Black Protons

The distribution of stars as a function of the number of fast (gray or sparse black) prongs provides a sensitive test of the nucleonic cascade mechanism. It has already been demonstrated from their angular distributions (see Part I[1]) that they are definitely knock-ons, and hence their frequency distribution should be expected to reflect the nature of the type of internal nucleon cascade involved (i.e., single nucleon-nucleon scatterings or scatterings involving several nucleons).

The angular distributions, and mean prongs number have already been found to agree with the single nu-

TABLE III(a). Comparison of experimental and calculated distribution of gray proton interactions. (b) Comparison of experimental and calculated distribution of fast proton interactions.

(a)

No. of gray protons	% of interactions calculated	% of interactions experimental result
0	46±11	57 ±4
1	48±11	40 ±4
2	7±4	2.5±1

(b)

No. of fast protons	% of interactions calculated	% of interactions experimental result
0	30±7	35 ±3
1	48±8	54 ±4
2	21±7	9 ±2
3	3±1.5	1.7±0.7

[16] Bernardini, Cortini, and Manfredini, Phys. Rev. **79**, 952 (1950).

cleon-nucleon scattering hypothesis. Tables III(a) and (b) list the experimentally determined percentages of events with various numbers of outgoing gray protons, and fast (gray plus sparse black) protons. As previously discussed, the appropriate assumption for estimating the numbers of emitted protons is that of equally probable proton or neutron emission. Using this relation, the estimated distributions of gray proton events and fast (gray plus sparse black) proton events are also given in Tables III(a) and (b) and are in reasonable agreement with the experimental results.

E. The Energy Spectrum

The energy spectrum of the directly ejected nucleons is given in Fig. 6(a). The mean number of gray, sparse black, and black nucleons has been shown to be in agreement with the experimental results in Sec. C. The characteristics of *G*-5 plates allowed only an energy determination for the gray prongs which was reported in Part I.[1] The experimentally determined gray prong spectrum is compared to the calculated one in Fig. 6(b) and is in reasonable agreement. It should be noted that the large peak of the knock-on nucleon spectrum, which occurs in the black prong region (0–30 Mev), is suspiciously similar in appearance to the type

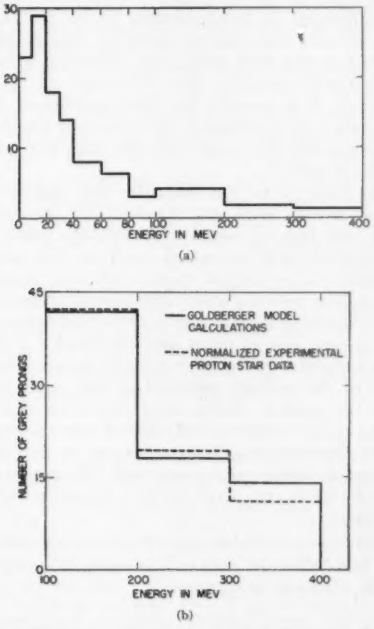

FIG. 6(a). The energy spectrum of the knock-on nucleons directly ejected. (b) A comparison of the calculated and experimental gray (>100 Mev) nucleon spectrum.

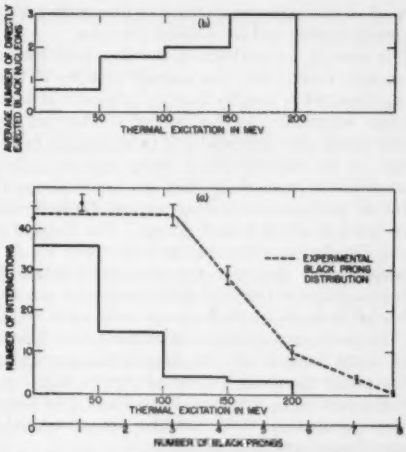
AVERAGE NUMBER OF DIRECTLY EJECTED BLACK NUCLEONS
(b)
50 100 150 200
THERMAL EXCITATION IN MEV
NUMBER OF INTERACTIONS
(a)
EXPERIMENTAL BLACK PRONG DISTRIBUTION
50 100 150 200
THERMAL EXCITATION IN MEV
0 1 2 3 4 5 6 7 8
NUMBER OF BLACK PRONGS

FIG. 7(a). The distribution of interactions as a function of thermal excitation and the experimental black prong distribution curve are given. The relationship of 35 Mev per black prong (as explained in text) was used to convert thermal excitation to number of black prongs. (b) The average number of directly ejected black nucleons as a function of thermal excitation.

of spectrum interpreted in cosmic-ray stars by Le Couteur[17] and others as an evaporation spectrum.

The percentage of the black prongs which are caclulated to be knock-ons is about 30 percent. Therefore, it is clear that the knock-on black prongs are approximately comparable in number and are probably similar in energy characteristics to the evaporation prongs.

It is possible in our interactions to separate most of the knock-ons from the evaporation prongs by the difference in angular distribution. However, an inspection of Fig. 5(c) shows that the knock-on black prong angular distribution is approaching isotropicity except for the extreme backward direction. When one selects large stars, such as Le Couteur,[17] who treated 7–14 prong stars, it is expected, on this model at least, that the black prong angular curve will become practically isotropic. This is so because large stars mean large nucleonic cascades, in which the preference for the incoming direction is lost by many collisions. For instance, in the present calculations the largest events corresponded to 16 nuclear collisions. In the case of large stars there is probably no experimental way of separating the knock-ons from the evaporation protons.

F. The Thermal Excitation Distribution

Figure 7(a) represents the distribution of events *versus* thermal excitation in Mev. One should notice that the average thermal excitation of 50 Mev is only a small fraction of the incident 400 Mev. The maximum excitation was found to be only about 200 Mev. This is

[17] K. J. Le Couteur, Proc. Phys. Soc. (London) **A63**, 259 (1950).

a result of the high transparency of the nucleus to the incoming nucleon and its collision products.

One expects, on the basis of the Weisskopf thermodynamical model, that the average number of black prongs emitted is roughly linearly proportional to the thermal excitation (see LeCouteur[17]). Therefore, one would expect the horizontal axis to be roughly proportional to the emitted black prong number. (Using Bernardini's[16] value of 35 Mev per black prong, the cutoff of the thermal excitation curve at 200 Mev would correspond to about 6 black prongs.) The shape of the prong distribution curve due to evaporation would be expected to be similar to the thermal excitation distribution curve of Fig. 7(a) if the horizontal axis were relabeled in terms of black prongs, with each 35 Mev of excitation corresponding to an additional black prong. This would disagree with the shape of the experimental black prong distribution [also plotted in Fig. 7(a)], which is seen to be flatter in the region of 1 to 4 black prongs (corresponds to 35–160 Mev excitation) and to decrease more gradually thereafter.

Consider Fig. 7(b) plotted above the thermal excitation distribution. Figure 7(b) represents the average number of directly ejected black nucleons as a function of thermal excitation. On the average, half of these will be protons, and this increasing number of directly ejected protons as a function of thermal excitation (or equivalently mean prong number) is just what is needed to flatten the black prong distribution curve in the region of 1–4 prongs and to extend its tail appropriately. In particular, the stars corresponding to 200-Mev excitation have an expected mean prong number of about 6. The average number of ejected protons is 1.5 in this region. Therefore, the effective cutoff (neglecting fluctuations) would be expected at about 7.5 black prongs, which is reasonable compared with the experimental results. The addition of these two effects (evaporation plus knock-on), together with a reasonable allowance for the fluctuations, seems to present a mechanism which in a very crude way would reproduce the essential features of the black-prong distribution curve.

V. CONCLUSIONS

A detailed comparison of all the experimentally measured characteristics of the interactions of 300–400 Mev protons and neutrons and the Goldberger model calculations has been made. The results were all in reasonable agreement within the error limits, and hence it appears safe to assume at the very least that the internal nucleonic cascade mechanism is useful as a calculatory tool for high energy interactions ~400 Mev.

Furthermore, the very nature of the results very strongly implies the necessity of this mechanism for their explanation. Consider the gray (>100 Mev) and sparse black (30–100 Mev) protons. It has already been experimentally demonstrated by their angular distributions that they are definitely almost exclusively knock-ons. Hence, the only question that remains is whether the cascade in which they originated essentially consists of single nucleon-nucleon scatterings or some sort of multiple nucleon scatterings.

Our results are that the angular distributions, mean numbers, energy spectrum, and the frequency of interactions as a function of the numbers of these fast knock-ons are all in agreement with the single nucleon-nucleon cascade hypothesis. Since these calculated cascades are rather large (average number of collisions $=4.5$, maximum number $=16$) one should definitely expect any multiple nucleon type of internal cascade to have entirely different characteristics. Furthermore, (see arguments given in Part I[1] under Discussion) the abundance of black knock-on prongs (at least 25–40 percent), the steady transfer of energy from the fast nucleons to the black nucleons as star size increases, and the similarity of the properties of proton and neutron induced interactions all strongly imply the nucleonic cascade mechanism.

In order to determine whether the model breaks down at lower energies (~100 Mev) as perhaps implied by the Hadley and York[8] results, a similar investigation is being carried out for the interactions of 150-Mev protons with the emulsion nuclei. Preliminary results have indicated that it is quite reliable even at these lower energies. At higher energies (in the Bev range) it is obvious that inelastic processes such as meson production and their subsequent interaction with the nucleus will drastically alter this simple mechanism. However, it is possible that the inclusion of these processes in the calculations (provided they are known and are sufficiently simple) will still make this type of approach useful.

One should point out that since their discovery in cosmic ray by Blau and Wambacher,[18] the nuclear stars have been submitted to a very large number of experimental and theoretical analyses. The general tendency was to consider them mostly as an evaporation process following a very high internal excitation of the evaporating nucleus. This tendency was emphasized by the early type of plates used like Ilford C-2 which were insensitive to the more energetic prongs. The results of the analysis presented in this paper imply that the residual nuclear excitation responsible for evaporation is quite low and that the essential process which determines the characteristics of the stars is the internal nucleonic cascade generated. The evaporation contribution is only more or less a by-product of the cascades.

The authors are indebted to Mr. Leon Landovitz and Mr. Jack Leitner for their excellent work in performing the Monte Carlo computations.

[18] M. Blau and H. Wambacher, Sitzber. Akad. Wiss. Wien, Math.-naturw. Kl. Abt. IIa, **146**, 259, 469, 623 (1937).

Pressures, Densities, and Temperatures in the Upper Atmosphere

THE ROCKET PANEL*
Harvard College Observatory, Cambridge, Massachusetts
(Received July 1, 1952)

Averaged and internally consistent values of atmospheric pressure, density, and temperature from the ground to an altitude of 219 km have been determined and compiled by the United States groups active in upper-atmospheric research by rockets. Additional relevant data by similar groups engaged in research on meteors and on the anomalous propagation of sound are also included, particularly in a brief discussion of variations with time and with place of these three atmospheric parameters.

I. INTRODUCTION

SINCE the first V-2 rocket was fired on April 16, 1946 by the U. S. Army Ordnance at the White Sands Proving Gound at Las Cruces, New Mexico, a number of research groups have contributed an enormous amount of work to the determination of pressures, densities, and temperatures in the upper atmosphere. Firings of 68 V-2 rockets, 63 Aerobee rockets, and 7 Viking rockets have in most cases carried complicated and short-lived instrumentation for such measurements.

The present paper presents a brief summary of the data so obtained, combines these data into an average smoothed representation of pressure, density, and temperature as a function of altitude to 220 km, and briefly discusses variations in these quantities as a function of geographical position and time on the basis largely of nonrocket methods of measurement.

These current results represent the efforts of a large number of investigators, no one of whom should be credited individually for the group effort. Hence, this paper is presented by the Upper Atmosphere Rocket Research Panel whose members and their colleagues have done the research. Almost all of the funds for the various investigations have been provided by the United States Department of Defense.

The Rocket Panel hopes that the averaged results here presented will not be considered as a "standard atmosphere" but simply as a representation of the combined results to January, 1952. So many problems remain unsolved, or partially solved, that the rocket investigations of the upper atmosphere must be continued for some time if we are to master scientifically this domain such a few miles distant.

II. THE BASIC DATA

Since the physical measurements lead to determinations of ambient pressure p, ram pressure (leading to density ρ), Mach number M, and the velocity of sound v_s, at various altitudes and times, the observational data are most readily combined in terms of derived "temperatures" based upon an assumed constant mean molecular weight μ of 28.966 g/mole for the atmosphere. These temperatures will be indicated by T_{29}. A short study of the perfect-gas laws discloses that pressure, density, Mach number, and the velocity of sound can all be interrelated theoretically and numerically without inclusion of μ. Hence, μ cannot be determined from measures of these quantities, while the temperature T can be evaluated from them only with μ as an assumed direct proportionality factor.

Table I contains the rocket derived temperatures T_{29} in degrees Kelvin from the various groups, at steps of 5 or 10 km in sea-level altitude h, the adopted weights (in parentheses) of these determinations, the weighted mean values of T_{29}, and the finally adopted values of T_{29} after smoothing. The sources and methods of observation and the system of weights will be described in the following paragraphs.

TABLE I. Observed and adopted temperatures (°K, μ=28.966).

Height h km	NRL[a]	SCEL[b]	UMAF[c]	UMSC[d]	Weighted mean	Adopted
30	232(12)	235(9)	230(6)	227(5)	231.7(32)	231.7
35	249(12)	249(9)	238(6)	234(5)	244.6(32)	244.5
40	264(12)	260(9)	271(6)	253(5)	262.5(32)	262.5
45	273(12)	264(9)	272(6)	278(5)	271.1(32)	271.3
50	280(12)	260(9)	268(6)		270.7(27)	270.8
55	278(12)	252(9)	258(5)		265.2(26)	265.8
60	262(12)	243(9)	238(5)		250.8(26)	252.8
65	248(12)	238(9)	209(5)		237.0(26)	235.0
70	228(12)	218(9)	189(5)		217.0(26)	218.0
75	208(12)	227(9)	185(5)		210.2(26)	209.1
80	200(8)	213(5)			205.0(13)	205.0
85	205				205	208.9
90	216				216	217.0
95	229				229	227.5
100	240				240	240.0
110	270				270	270.0
120	330				330	330.0
130	390				390	390.0
140	450				450	447.0
150	500				500	503.0
160	560				560	560.0
219	*				900[e]	900.9[e]

[a] NRL = Naval Research Laboratory, R. Havens, R. Koll, and H. Lagow.
[b] SCEL = Signal Corps Electronic Laboratory, U. S. Army, M. Ference.
[c] UMAF = H. S. Sicinski, N. W. Spencer, and W. G. Dow, University of Michigan, Air Force.
[d] UMSC = University of Michigan, Signal Corps.
[e] See text for basis.

* The Upper Atmosphere Rocket Research Panel. The membership of this unofficial research group in January, 1952 consisted of the following: Chairman: Dr. J. A. Van Allen, State University of Iowa; Secretary: Mr. G. Megerian, General Electric Company; Dr. L. A. Delsasso, Ballistics Research Laboratory; Professor W. G. Dow, University of Michigan; Dr. M. Ference, Jr., Signal Corps Engineering Laboratory; Dr. C. F. Green, General Electric Company; Dr. H. E. Newell, Jr., Naval Research Laboratory; Dr. M. D. O'Day, A. F. Cambridge Research Center; Dr. W. H. Pickering, California Institute of Technology; and Dr. F. L. Whipple, Harvard College Observatory.

TABLE II. Adopted atmospheric data.

Height (sea level) km	Temp. (μ=28.966) °K	Pressure $\log_{10}$ dyn/cm²	Density $\log_{10}$ g/cm³
1.216	291.0	5.945	−2.977
2	282.0	5.905	−3.003
4	272.6	5.799	−3.095
6	260.0	5.688	−3.185
8	245.0	5.571	−3.276
10	230.8	5.446	−3.375
12	219.5	5.315	−3.484
14	211.6	5.178	−3.606
16	208.0	5.037	−3.739
18	209.0	4.895	−3.883
20	212.8	4.755	−4.030
22	216.7	4.618	−4.176
24	220.9	4.484	−4.318
26	225.1	4.352	−4.458
28	228.5	4.222	−4.594
30	231.7	4.095	−4.728
32	235.7	3.969	−4.861
34	241.2	3.846	−4.994
36	248.1	3.726	−5.126
38	255.6	3.610	−5.256
40	262.5	3.497	−5.380
42	267.6	3.386	−5.499
44	270.5	3.278	−5.612
46	271.7	3.170	−5.722
48	271.6	3.062	−5.829
50	270.8	2.955	−5.936
52	269.7	2.847	−6.042
54	267.6	2.738	−6.147
56	263.7	2.629	−6.250
58	258.6	2.517	−6.353
60	252.8	2.404	−6.457
62	246.5	2.287	−6.563
64	239.0	2.167	−6.669
66	231.0	2.044	−6.778
68	223.2	1.916	−6.891
70	218.0	1.784	−7.012
72	213.6	1.650	−7.138
74	210.5	1.513	−7.268
76	207.9	1.375	−7.401
78	205.8	1.235	−7.536
80	205.0	1.094	−7.676
82	205.8	0.953	−7.818
84	207.7	0.814	−7.962
86	210.3	0.675	−8.105
88	213.5	0.539	−8.248
90	217.0	0.405	−8.389
92	220.7	0.274	−8.528
94	225.0	0.144	−8.666
96	230.0	0.018	−8.802
98	235.0	−0.106	−8.935
100	240.0	−0.227	−9.065
102	245.0	−0.345	−9.192
104	250.0	−0.461	−9.317
106	255.0	−0.575	−9.440
108	261.0	−0.686	−9.561
110	270.0	−0.794	−9.684
115	300.0	−1.045	−9.981
120	330.0	−1.273	−10.249
125	360.0	−1.480	−10.495
130	390.0	−1.670	−10.720
135	419.0	−1.845	−10.927
140	447.0	−2.009	−11.119
145	475.0	−2.163	−11.299
150	503.0	−2.308	−11.468
155	531.0	−2.445	−11.629
160	560.0	−2.574	−11.781
170	618.7	−2.813	−12.062
180	676.9	−3.030	−12.318
190	734.9	−3.228	−12.552
200	792.5	−3.411	−12.768
210	849.8	−3.580	−12.968
220	906.6	−3.738	−13.154

The NRL (Naval Research Laboratory) data in Table I by Havens, Koll, and Lagow[1] were obtained from pressure measures at the surface of the rocket at a carefully selected point such that the surface and ambient pressures are known to be equal when yaw is absent. Results from six firings were used by the Rocket Panel to derive temperatures by measuring the slopes at various heights on a mean curve of $\log_{10}p$ *versus* h. The temperatures so derived were appreciably greater than those previously derived by Havens, Koll, and Lagow. Additional measures by these investigators of the ram pressure at the nose of the rocket in four firings transform into density measures at various heights, up to h=156 km on March 7, 1947, and 219 km on August 7, 1951. The NRL temperatures in Table I are based entirely on these density determinations for $h>122$ km. In the range from 61 to 73 km the densities derived from the ambient pressure measures are somewhat smaller than those derived from the ram pressure. In the region around h=80 to 90 km, the adopted temperatures, which depend mostly upon NRL data, have been increased appreciably to allow for the systematic larger values given by the ram pressure (density) measures and to insure that the NRL data are reasonably well fitted at greater heights.

The SCEL (Signal Corps Electronic Laboratory, U. S. Army) temperatures of Table I were provided by Ference.[2] They were obtained from determinations of the vertical velocity of sound measured by the differential time lags in sounds received at the ground from grenades exploded at various heights near Aerobee rockets. Results from five firings are represented, and the height intervals over which the velocities have been averaged range from 5 to 12 km. All firings were made at night, in contrast to the daylight firings of NRL. It is believed that the possible systematic errors, including the effects of averaging in height, are small, of the order of only 4°K (except for the measures at h=75 and 80 km).

The UMAF data of Table I were provided by Sicinsky,[3] Spencer, and Dow of the University of Michigan, under a contract with the U. S. Air Force. Two Aerobee firings are represented. Measures of the surface pressure on the conical nose of the rocket were made directly at the tip and a short distance from the tip. Application of the Taylor-Maccoll theory for conical projectiles, as tabulated by Z. Kopal, led to a determination of the Mach number and hence to the ambient air temperature. In cases of large yaw angle the corrections to the theory are troublesome.

The UMSC data of Table I were provided by a second University of Michigan group under a contract

[1] Havens, Koll, and Lagow, J. Geophys. Res. **57**, 59 (1952).
[2] M. Ference, J. Meteorol. (to be published).
[3] H. S. Sicinsky, Sci. Rept. No. 4, Engineering Research Institute, University of Michigan (January, 1952) (unpublished).

with the U. S. Army Signal Corps.[4] In one V-2 firing an array of probes near the nose of the rocket measured the angle of the shock wave and hence the Mach number.

It will be seen that four (or five) essentially independent methods were used in the determinations of upper atmospheric temperature recorded in Table I. In determining the relative weights of the various determinations, a weight of 4 was given to each method and roughly 1 to each firing represented. The true or absolute weight decreases more rapidly with height than the relative weight tabulated because most methods become less precise at lower atmospheric pressures.

Below a height of 30 km the values of T_{29} in Table II were adopted from the radiosonde balloon measures made from the White Sands Proving Ground by Detachment 19-14*L* of the U. S. 19th Weather Squadron, and by the U. S. Army Signal Corps. Near the ground the tabulated values of T are consistent with the mean yearly ground pressures but are not mean temperatures.

The smoothing of the adopted values of T_{29} *versus* h (Table I and Table II) was carried out in an arbitrary manner so as to make functions of T_{29}, $\log_{10}p$, and $\log_{10}\rho$ numerically integrable to an accuracy of about three significant figures for steps of 2 km in h. Certain of the "standard atmospheres" suffer from discontinuities in dT/dh that render them useless in some problems,

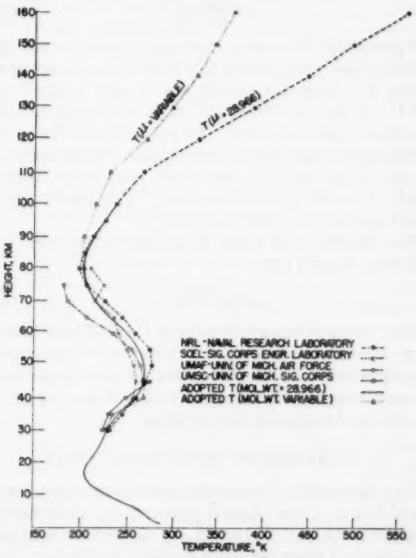
HEIGHT, KM
TEMPERATURE, °K
T(μ = VARIABLE)
T(μ = 28.966)
NRL - NAVAL RESEARCH LABORATORY
SCEL - SIG. CORPS ENGR. LABORATORY
UMAF - UNIV. OF MICH. AIR FORCE
UMSC - UNIV. OF MICH. SIG. CORPS
ADOPTED T (MOL. WT. = 28.966)
ADOPTED T (MOL. WT. VARIABLE)

FIG. 1. Basic temperature data.

[4] Bartman, Liu, and Schaefer, *An Aerodynamic Method of Measuring the Ambient Temperature of Air at High Altitudes*, Engineering Research Institute, University of Michigan (July, 1950) (unpublished); and unpublished progress reports.

TABLE III. Atmospheric data.

Height sea level km	Adopted mol. wt. g/mol	Temp. (μ varies) °K	Scale height km	Accel. gravity cm/sec²	Mean free path cm
1.216	28.97	291.0	8.53	979.2	8.6×10^{-6}
5	28.97	276.8	7.83	978.0	1.2×10^{-5}
10	28.97	230.8	6.78	976.5	2.1×10^{-5}
15	28.97	209.1	6.16	974.9	4.2×10^{-5}
20	28.97	212.8	6.28	973.4	9.7×10^{-5}
25	28.97	223.0	6.59	971.9	2.2×10^{-4}
30	28.97	231.7	6.85	970.4	4.8×10^{-4}
35	28.97	244.5	7.24	968.9	1.0×10^{-3}
40	28.97	262.5	7.79	967.3	2.2×10^{-3}
45	28.97	271.3	8.06	965.8	4.2×10^{-3}
50	28.97	270.8	8.06	964.3	7.8×10^{-3}
55	28.97	265.8	7.93	962.8	1.4×10^{-2}
60	28.97	252.8	7.55	961.3	2.6×10^{-2}
65	28.97	235.0	7.03	959.8	4.8×10^{-2}
70	28.97	218.0	6.53	958.4	9.3×10^{-2}
75	28.97	209.1	6.27	956.9	2.0×10^{-1}
80	28.97	205.0	6.16	955.4	4.3×10^{-1}
85	28.23	203.6	6.29	953.9	9.5×10^{-1}
90	27.52	206.2	6.54	952.4	2.1×10^{0}
95	26.86	210.9	6.87	951.0	4.5×10^{0}
100	26.22	217.3	7.26	949.5	9.5×10^{0}
110	25.03	233.3	8.19	946.6	3.8×10^{1}
120	23.95	272.8	10.04	943.6	1.3×10^{2}
130	22.50	302.9	11.90	940.7	3.7×10^{2}
140	21.21	327.3	13.68	937.9	8.7×10^{2}
150	20.06	348.4	15.44	935.0	1.8×10^{3}
160	19.34	368.0	17.24	932.1	3.6×10^{3}
170	18.10	386.7	19.11	929.3	6.1×10^{3}
180	17.26	403.4	20.97	926.4	1.0×10^{4}
190	16.50	418.5	22.84	923.6	1.8×10^{4}
200	15.79	432.1	24.70	920.8	3.0×10^{4}
210	15.15	444.4	26.57	918.0	5.1×10^{4}
220	14.55	455.5	28.43	915.2	8.7×10^{4}

without annoying modifications. The third difference in a 2-km tabulation of T_{29} exceeds 1° only three times above $h=30$ km. Table II is rougher than this below 30 km, but the known atmosphere is largely to blame.

The measured and adopted temperatures of Tables I and II are plotted *versus* height in Fig. 1. No correction has been applied to the temperatures for the decrease in mean molecular weight above 80 km that probably arises from the dissociation of O_2. Nor has a correction for seasonal effects been applied. The differences among the various observed curves are believed to represent largely the differences dependent upon method and instrumentation rather than upon variation in the atmosphere, although the latter factor may be appreciable. Figure 1 indicates that a significant degree of uncertainty still remains in the observed mean dependence of temperature upon height.

The dotted curve above 80 km in Fig. 1 includes an arbitrary correction for a uniform dissociation rate from zero to completion for O_2 between 80 and 120 km and for N_2 between 120 and 220 km.

III. THE CALCULATIONS

Table II, which presents values of T_{29}(°K), $\log_{10}p$ (dynes cm^{-2}), and $\log_{10}\rho$ (g cm^{-3}) at intervals of 2 km to 110 km, 5 km to 160 km, and 10 km to 220 km, is given with much more than the observational accuracy

in order to expedite numerical integration involving the fundamental data. Above 160 km the temperatures and pressures become increasingly uncertain. They are based on the NRL observation of $\rho = 1.0 \times 10^{-13}$ g cm^{-3} at 219 km during the firing of August 7, 1951. It is impossible to reconcile this value of ρ at 219 km with $\rho = 1.5 \times 10^{-13}$ g cm^{-3} at 156 km by means of a constant temperature gradient between the two heights. Thus, the adopted value of $\log_{10}\rho$ at 219 km is too small by about 0.14. The variations from 160 km to 220 km are based upon a constant gradient in scale height. It must be emphasized that the results are highly uncertain in this region.

Table III presents arbitrarily assumed mean molecular weights, derived temperatures based upon the adopted T_{29} combined with these molecular weights, scale heights, accelerations of gravity, and mean free paths, all as functions of sea-level heights at intervals of 5 and 10 km. This table is intended as a ready reference table for these auxiliary atmospheric quantities.

At any height the adopted temperature of Tables I and II can be reduced to a gas temperature corresponding to any adopted value of mean molecular weight μ by the linear correction factor $\mu/28.966$. Changes in the mean molecular weight of the atmosphere to an altitude of about 70 km have been observed to be negligible, although a slight effect is definitely observed near the 70-km level. L. M. Jones and E. A. Wenzel of the University of Michigan, under an Army Signal Corps contract, have succeeded in sending up and recovering three steel sampling bottles which were filled at altitudes from 64 to 72 km. These air samples have been analyzed by Chackett, Paneth, Reasbeck, and Wiborg.[8] They find that the He/N_2 ratio is increased by about a factor of two at these altitudes and find a correspondingly small increase in the Ne/N_2 ratio and a decrease in the A/N_2 ratio. Hence, in view of the high uncertainty concerning diffusive separation in the higher atmosphere and no precise knowledge concerning the dissociation, the mean molecular weights in Table III were obtained on the assumption that the dissociation of O_2 begins at 80 km and proceeds uniformly to completion at 120 km. It is further assumed that the N_2 dissociation begins at 120 km and proceeds uniformly to completion at 220 km altitude. At these greater altitudes and higher, the mean molecular weight of the atmosphere is almost completely unknown. Undoubtedly, diffusion effects, as well as dissociation effects, are important. For example, the assumption of the pure He atmosphere would reduce the adopted temperature by a factor 0.138 to give the actual gas kinetic temperature.

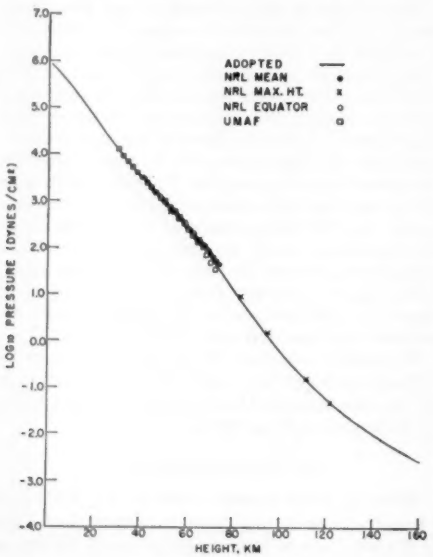

FIG. 2. Pressure vs height.

The pressures p in Tables II and III are based upon the adopted temperature T_{29} and are obtained by numerical integration (at 2-km intervals) of the equation

$$d \ln p/dh = -1/H, \tag{1}$$

where the scale height H (see Table III) is given by

$$H = RT/g\mu. \tag{2}$$

Numerically the mean molecular weight μ equals 28.966 g/mole; the gravity g is based upon the inverse square law from the earth's center with g equal to 979.15 cm/sec^2 (see Table III) at White Sands, 1.2165 km above mean sea level; the gas constant R equals 8.31436×10^7 ergs deg^{-1} mole^{-1}; the temperature T equals 273.16° at 0°C; the mean pressure at White Sands p equals 1.3332 dyne cm^{-2}. The observations were made at lat. 33°N, long. 106°W.

The densities ρ of Table II are calculated from T_{29} and p by Boyle's law,

$$\rho = \mu p/RT. \tag{3}$$

The values of mean free path in Table III are based upon a mean free path of 7.37×10^{-6} cm in standard atmospheric conditions. The mean free path is assumed to vary inversely as the number of particles per cm^3; all effects of ionization are neglected.

IV. COMPARISONS WITH OBSERVATION

The adopted and measured temperatures are compared in Fig. 1, the adopted pressures and those measured by NRL and UMAF in Fig. 2, and the adopted densities and those measured by NRL in Fig. 3.

The systematic trends shown by the various temperatures measures in Fig. 1 appear largely to stem from

[8] Chackett, Paneth, Reasbeck, and Wiborg, Nature **168**, 358 (1951).

methodological differences. This is particularly true of the NRL *versus* the SCEL data, where several firings are involved in each mean curve. Quite possibly part of the effect arises from the fact that the NRL data were obtained in daylight hours, the SCEL data at night. *A priori*, one might expect somewhat higher temperatures during the daylight hours, although there is no clear evidence to support this expectation.

On the other hand, the SCEL observers found marked differences in temperatures from two firings separated only a few hours on the same night (December, 1950). Hence, the differences between the two sets of data obtained by the two groups from the University of Michigan may be appreciably affected by the peculiar atmospheric characteristics at the times of the few firings involved. However, when such differences are measured in pressure instead of temperature (for example, see Fig. 2, NRL *versus* UMAF), quite small systematic effects such as 0.1 to 0.2 in $\log_{10}p$ can produce marked changes in the derived temperatures.

The measures in density are only slightly more sensitive to atmospheric conditions than those in pressure. The NRL density measures shown in Fig. 3 show a conspicuous systematic deviation from the adopted curve between 60 and 80 km. This deviation must depend, to a considerable degree, upon the method of measurement, although the deviation is smaller when derived internally from all of the NRL data.

Generally, we must conclude that large variations in conditions of the upper atmosphere take place within short intervals of time but that real systematic effects depend upon the instrumentation and method of measurement used.

V. VARIATIONS IN THE UPPER ATMOSPHERE

The investigators agree that the mean conditions in the atmosphere above about 40 km very poorly represent the conditions at any given moment. The temperature maximum near 50 km (Fig. 1) is probably not a smoothly rounded curve at any instant but is much more peaked. Probably the momentary maximum is not only much sharper and rises to a much higher temperature, but the altitude of the maximum may vary over 10 km or more. Furthermore, the maximum may possibly be double or multiple. Appropriately similar remarks probably apply to the temperature minimum near 80 km. Indeed it is quite likely that above about 40 km the true curve of temperature *versus* height is very irregular at any given moment.

Systematic diurnal changes in temperature, pressure, or density in the upper atmosphere have not yet been firmly established, nor have correlations with solar phenomena, aurorae, terrestrial magnetism, or ionospheric activity.

Seasonal effects are not evident in the rocket material. On the other hand, the Harvard photographic meteor

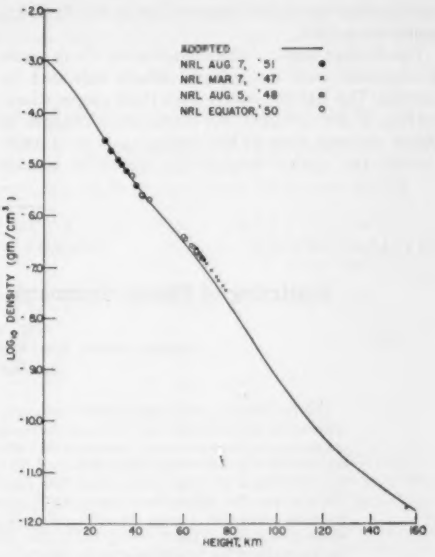

FIG. 3. Density *vs* height.

data[6] indicate higher densities in summer months than in winter months, the effect being more marked over Massachusetts than over New Mexico. The meteoric seasonal effect correlates directly with ground temperatures, has a maximum total amplitude of the order of 0.3 in $\log_{10}\rho$ near 60–70 km, and decreases markedly by 90 km.

An NRL rocket fired at the equator on May 11, 1950, indicates no systematic deviations in pressure and density from the mean of the 8 fired in New Mexico (see Fig. 2 for the comparison in $\log_{10}p$). On the other hand, the meteoric data tentatively indicate higher densities, of the order of 0.15 in $\log_{10}\rho$, over Massachusetts than over New Mexico, in the height range 70–90 km.

Acoustical propagation studies by Crary[7] for the U. S. Air Force Cambridge Research Laboratories have been made in the Canal Zone, Bermuda, and Alaska during the summer and in Alaska during the winter. The velocities of sound and wind were studied in the altitude range 30–60 km. Regarding temperatures Crary concludes: (a) temperatures are generally less in that altitude region than those given by previous observers who have assumed winds to be negligible; (b) the height of the maximum temperature layer is greatest in the Alaskan winter; (c) summer results in Bermuda are not in general accord with the other tests; and (d) no diurnal

[6] Under contracts with the U. S. Naval Bureau of Ordnance and ONR. See Whipple, Jacchia, and Kopal, *The Atmospheres of the Earth and Planets* (University of Chicago Press, Chicago, 1949), pp. 149–158; and F. L. Whipple, Bull. Am. Met. Soc. **33**, 13 (1952).

[7] A. P. Crary, J. Meteorol. **7**, 233 (1950).

variations of winds and temperatures in the 30–60 km region are evident.

The Alaskan seasonal effect observed by Crary agrees in character with the seasonal effects indicated by meteors. The latitude effects from these propagational studies, if not reversed by temperature changes at higher altitudes than 60 km, appear to confirm qualitatively the meteor results with regard to latitude dependence. It is clear, however, that more data are required to establish definitively the dependences of temperature, pressure, and density in the upper atmosphere with season and with latitude. Possibly some of the observed variations are really more influenced by geographical position with respect to continental masses and atmospheric circulation patterns than with respect to latitude.

PHYSICAL REVIEW VOLUME 88, NUMBER 5 DECEMBER 1, 1952

Scattering of Charge Symmetric Pseudoscalar Mesons by Nucleons

W. W. WADA
Electricity Division, Naval Research Laboratory, Washington, D. C.
(Received June 2, 1952)

The Pauli theory of extended source interacting with the neutral pseudoscalar field with pseudovector coupling has been extended to the case of the charge symmetric pseudoscalar field, and has been applied to the problem of the scattering of mesons by the nucleons. The results of our calculation show that the scattering cross sections are strongly dependent upon the energy of the incoming mesons, that the cross section for the scattering of π^+ by protons is larger than that for π^- by factor 2.25 at all kinetic energies up to about 150 Mev, and that within the scattering of π^- by protons the cross section for the scattering involving charge exchange interaction is larger than that with ordinary interaction by a factor which varies from 2.1 to 1.5 as one goes from zero kinetic energy to 150 Mev. When the coupling constant $(f_\mu)^2$ is taken to be about 0.3, the maximum of the theoretical cross section curve coincides with the experimental maximum if one assigns 1.25μ (μ = the reciprocal Compton wavelength of the meson) for the spin and isotopic spin inertia of the nucleon. The scattering cross-section curves for π^+ and π^- approximately agree with the experimental curves if one assigns a value 1.58 for $|G(K)|$, which appears in the original theory of Pauli.

I. INTRODUCTION

THE experimental investigation of the scattering of π^- and π^+ mesons by hydrogen[1] revealed the following three important facts:

a. The total scattering cross sections for both mesons are strongly dependent upon the energy of the mesons. For π^- the total scattering cross section rises rapidly from 20×10^{-27} cm^2 at 60 Mev to a plateau of 60×10^{-27} cm^2, which begins at about 150 Mev kinetic energy.

b. The total scattering cross section of π^+ is approximately three times as large as that of π^- in the range of energies of the experiment.

c. Within the scattering of π^- the total scattering cross section involving charge exchange interaction is approximately twice as large as that arising from ordinary (no charge exchange) interaction.

The quantum theoretical investigations to account for these experimental facts have already been given by Brueckner[2] and Wentzel[3] in their respective papers. These authors have proceeded along the line of strong coupling theory, which provides the possibility of isobaric states of the spin and the isotopic spin of nucleon leading to large scattering cross sections due to the resonance. It was pointed out by Brueckner that the isobaric state characterized by the isotopic spin $\frac{3}{2}$ of the proton would make the resonance scattering of π^+ approximately three times as large as that of π^- in hydrogen, when both ordinary and charge exchange interactions are simultaneously considered for the latter. This point was amply confirmed by the experiment.

When the interaction between the meson and the nucleon is strong, the existence of a dense meson cloud in the close vicinity of the nucleon makes the quantum theoretical investigation very difficult, and no rigorous methods have yet been developed to deal with this problem. Under such circumstances it was thought to be of some interest to restrict ourselves to the classical approximations and investigate the possibility of accounting for experimental facts along the line of the classical theory developed by Pauli.[4] This approach has already been employed by Brueckner and Case in their paper on the production of neutral photomesons.[5]

II. CHARGE SYMMETRIC PSEUDOSCALAR FIELD

We shall employ in our calculation of meson scattering the charge symmetric pseudoscalar field with pseudovector coupling. Then, the procedure is only a slight

[1] Nagle, Anderson, Fermi, Long, and Martin, Phys. Rev. **86**, 603 (1952); **85**, 934, 935, 936 (1952).
[2] K. A. Brueckner, Phys. Rev. **86**, 106 (1952).
[3] G. Wentzel, Phys. Rev. **86**, 437 (1952).
[4] W. Pauli, *Meson Theory of Nuclear Forces* (Insterscience Publishers, Inc., New York, 1946).
[5] K. A. Brueckner and K. M. Case, Phys. Rev. **83**, 1141 (1951).

generalization of the Chapters II and III of Pauli's book,[4] in which the neutral field alone is considered.

In the theory of extended source the total Hamiltonian of the meson field interacting with a nucleon may be written

$$H=\frac{1}{2}\int\{\tau_\alpha^2+(\nabla\varphi_\alpha)^2+\mu^2\varphi_\alpha^2\}d^3x + (4\pi)^{\frac{1}{2}}f\int u(\mathbf{x})(\boldsymbol{\sigma}\cdot\nabla)\tau_\alpha\varphi_\alpha(\mathbf{x})d^3x. \quad (1)$$

$U(x)$ is a real function representing the spatial extension of the nucleon, which must satisfy the condition that the spatial integral is unity, the value that it would have if the nucleon were considered a point particle. μ and f are reciprocal Compton wavelength and the coupling constant of the meson, respectively. We use units $\hbar=c=1$. $\boldsymbol{\sigma}$ and $\boldsymbol{\tau}$ are the spin and the isotopic spin vectors of the nucleon, considered in our classical theory as unit vectors in coordinate and charge space, respectively. α runs from 1 to 3, corresponding to the charged and neutral states of the meson.

Following Pauli's methods closely[6] we obtain from Eq. (1)

$$H=\frac{1}{2}\int d^3k\{G(\mathbf{k})\mathfrak{p}_\alpha(\mathbf{k})\mathfrak{p}_\alpha(-\mathbf{k}) + (k_0^2/G(\mathbf{k}))\mathfrak{q}_\alpha(\mathbf{k})\mathfrak{q}_\alpha(-\mathbf{k})\} + if(\pi\sqrt{2})^{-1}\int d^3k(\boldsymbol{\sigma}\cdot\mathbf{k})\tau_\alpha\mathfrak{q}_\alpha(\mathbf{k}), \quad (2)$$

where $k_0^2=k^2+\mu^2$ and $G(\mathbf{k})=V(\mathbf{k})V(-\mathbf{k})$. $V(\mathbf{k})$ is the Fourier transform of $U(x)$ in Eq. (1). From this Hamiltonian we obtain the following equation of motion of the meson field in momentum space:

$$d^2\mathfrak{q}_\alpha(\mathbf{k})/dt^2+k_0^2\mathfrak{q}_\alpha(\mathbf{k})=if(\pi\sqrt{2})^{-1}G(\mathbf{k})(\boldsymbol{\sigma}\cdot\mathbf{k})\tau_\alpha. \quad (3)$$

Assuming $\boldsymbol{\sigma}$ and $\boldsymbol{\tau}$ obey the classical Poisson bracket equations (l, m, n cyclic),

$$[\sigma_l,\sigma_m]=-2\sigma_n, \quad [\tau_l,\tau_m]=-2\tau_n,$$

we obtain the following equations of motion for $\boldsymbol{\sigma}$ and $\boldsymbol{\tau}$ vectors:

$$d\boldsymbol{\sigma}/dt=[H,\boldsymbol{\sigma}]=-i\sqrt{2}f\pi^{-1}\left[\boldsymbol{\sigma}\times\int d^3k\mathbf{k}\mathfrak{q}_\alpha(\mathbf{k})\tau_\alpha\right],$$
$$d\boldsymbol{\sigma}/dt=[H,\boldsymbol{\tau}]=-i\sqrt{2}f\pi^{-1}\left[\boldsymbol{\tau}\times\int d^3k\mathbf{q}(\mathbf{k})(\boldsymbol{\sigma}\cdot\mathbf{k})\right]. \quad (4)$$

Expanding $\boldsymbol{\sigma}$, $\boldsymbol{\tau}$, and $\mathfrak{q}_\alpha(\mathbf{k})$ into Fourier series individually, we have

$$\boldsymbol{\sigma}=\sum_\nu\boldsymbol{\sigma}_\nu e^{-i\nu t}, \quad \boldsymbol{\tau}=\sum_{\nu'}\boldsymbol{\tau}_{\nu'}e^{-i\nu' t}, \quad \mathfrak{q}_\alpha(\mathbf{k})=\sum_{\nu''}\mathfrak{q}_{\alpha,\nu''}(\mathbf{k})e^{-i\nu'' t}, \quad (5)$$

where frequencies ν, ν', and ν'' take on values O, ω, 2ω, $\cdots$. Substituting Eq. (5) into Eq. (3), one obtains

$$\mathfrak{q}_{\alpha,\nu''}(\mathbf{k})=if(\pi\sqrt{2})^{-1}G(\mathbf{k})(k_0^2-\nu''^2)(\boldsymbol{\sigma}_\nu\cdot\mathbf{k})\tau_{\alpha,\nu'}, \quad (6)$$

where $\nu''=\nu+\nu'$. Rewriting Eq. (4) in the form

$$d\boldsymbol{\sigma}/dt=[\boldsymbol{\sigma}\times\mathbf{F}_\sigma] \quad d\boldsymbol{\tau}/dt=[\boldsymbol{\tau}\times\mathbf{F}_\tau] \quad (7)$$

and following Pauli's procedure closely, one obtains

$$\mathbf{F}_\sigma=\tfrac{2}{3}f^2\sum_{\nu',\nu''}\epsilon^{-i(\nu'+\nu'')t}(\boldsymbol{\tau}_{\nu''}\cdot\boldsymbol{\tau}_{\nu'})\boldsymbol{\sigma}_\nu[N-a^{-1}(\mu^2-\omega^2) + \epsilon(\mu^2-\omega^2)^{\frac{1}{2}}],$$
$$\mathbf{F}_\tau=\tfrac{2}{3}f^2\sum_{\nu,\nu''}\epsilon^{-i(\nu+\nu'')t}(\boldsymbol{\sigma}_\nu\cdot\boldsymbol{\sigma}_\nu)\boldsymbol{\tau}_{\nu'}[N-a^{-1}(\mu^2-\omega^2) + \epsilon(\mu^2-\omega^2)^{\frac{1}{2}}], \quad (8)$$

where

$$\epsilon=\begin{cases}+1 & \text{for } \nu''^2<\mu^2\\ +1 & \text{for } \nu''^2>\mu^2,\ \nu''>0\\ -1 & \text{for } \nu''^2>\mu^2,\ \nu''<0.\end{cases}$$

N and a^{-1} are new mechanical constants introduced by Pauli, of which the first plays no role in the dynamics of the meson field, while the second is identified as the spin and isotopic spin inertia of the nucleon.

In the Fourier expansions, Eqs. (5), we take at present only terms with O and $\pm\omega$ frequencies, and disregard terms with higher harmonics. Since the higher harmonics contribute higher order effects in the scattering of a meson by a nucleon, we assume that their contributions are small compared with those arising from the zero and the fundamental frequency ω. Then, keeping in mind $\nu''=\nu+\nu'$, one obtains from Eq. (8)

$$\mathbf{F}_\sigma=\tfrac{2}{3}f^2[\boldsymbol{\sigma}_\omega e^{-i\omega t}A_++\boldsymbol{\sigma}_{-\omega}e^{i\omega t}A_-],$$
$$\mathbf{F}_\tau=\tfrac{2}{3}f^2[\boldsymbol{\tau}_\omega e^{-i\omega t}A_++\boldsymbol{\tau}_{-\omega}e^{i\omega t}A_-], \quad (9)$$

where $A_\pm=\omega^2a^{-1}-\mu^3\pm i(\omega^2-\mu^2)^{\frac{1}{2}}$. For scattering processes the condition $\omega^2>\mu^2$ is required.

III. CALCULATION OF THE SCATTERING OF MESONS BY NUCLEONS

The incident meson field may be written

$$\varphi_\alpha{}^I(\mathbf{x})=\chi p_{I\alpha}\exp[iK(\mathbf{n}_I\cdot\mathbf{x})-i\omega t]+\text{c.c.},$$

where $\mathbf{n}_I$ is a unit vector in the direction of the incoming field, χ the amplitude, and $\mathbf{p}_I$ a unit vector in charge space representing the charge state of the incoming meson. Here, $K^2=\omega^2-\mu^2$, where ω is the energy of the incoming meson. Introducing the Fourier transform of $\varphi_\alpha{}^I$ into $\mathbf{F}_\sigma$ and $\mathbf{F}_\tau$ [see Eq. (4) and Eq. (7)], we obtain for the incoming field

$$\mathbf{F}_\sigma{}^I=-if4\pi^{\frac{1}{2}}V(K)\mathbf{n}_I(\boldsymbol{\tau}_0\cdot\mathbf{p}_I)(\chi e^{-i\omega t}-\text{c.c.}),$$
$$\mathbf{F}_\tau{}^I=-if4\pi^{\frac{1}{2}}V(K)\mathbf{p}_I(\boldsymbol{\sigma}_0\cdot\mathbf{n}_I)(\chi e^{-i\omega t}-\text{c.c.}). \quad (10)$$

We now introduce Eqs. (5), (9), and (10) into Eq. (7) and retain terms linear in χ, $\sigma_{\pm\omega}$, and $\tau_{\pm\omega}$ only under

[6] We follow Pauli's notation (see reference 4), except that we use $\mathfrak{p}_\alpha$ and $\mathfrak{q}_\alpha$ in place of his $\tilde{p}_\alpha$ and $\tilde{q}_\alpha$.

the assumption that the motions of $\boldsymbol{\sigma}$ and $\boldsymbol{\tau}$ caused by the incoming field are small in comparison to their stationary values. We then obtain

$$\frac{d}{dt}(\boldsymbol{\sigma}_\omega e^{-i\omega t})+\frac{d}{dt}(\boldsymbol{\sigma}_{-\omega}e^{i\omega t})+\frac{d}{dt}(\boldsymbol{\sigma}_0)\cong[\boldsymbol{\sigma}_0\times\mathbf{F}_\pi{}^I]$$
$$+\tfrac{2}{3}f^2A_+e^{-i\omega t}[\boldsymbol{\sigma}_0\times\boldsymbol{\sigma}_\omega]+\tfrac{2}{3}f^2A_-e^{i\omega t}[\boldsymbol{\sigma}_0\times\boldsymbol{\sigma}_{-\omega}].$$

Proceeding similarly for the analogous equation for $\boldsymbol{\tau}$, we obtain

$$\begin{aligned}\boldsymbol{\sigma}_\omega&=4\pi^{\frac{1}{2}}fV(K)K\omega^{-1}\chi(\boldsymbol{\tau}_0\cdot\mathbf{p}_I)[\boldsymbol{\sigma}_0\times\mathbf{n}_I]\\&\quad+i\tfrac{2}{3}f^2A_+\omega^{-1}[\boldsymbol{\sigma}_0\times\boldsymbol{\sigma}_\omega],\\ \boldsymbol{\tau}_\omega&=4\pi^{\frac{1}{2}}fV(K)K\omega^{-1}\chi(\boldsymbol{\sigma}_0\cdot\mathbf{n}_I)[\boldsymbol{\tau}_0\times\mathbf{p}_I]\\&\quad+i\tfrac{2}{3}f^2A_+\omega^{-1}[\boldsymbol{\tau}_0\times\boldsymbol{\tau}_\omega].\end{aligned}\tag{11}$$

By solving these equations for $\boldsymbol{\sigma}_\omega$ and $\boldsymbol{\tau}_\omega$ one obtains

$$\begin{aligned}\boldsymbol{\sigma}_\omega&=\beta(1-R^2)^{-1}\{[\boldsymbol{\sigma}_0\times\mathbf{n}_I]+iR[\boldsymbol{\sigma}_0\times(\boldsymbol{\sigma}_0\times\mathbf{n}_I)],\\ \boldsymbol{\tau}_\omega&=\beta'(1-R^2)^{-1}\{[\boldsymbol{\tau}_0\times\mathbf{p}_I]+iR[\boldsymbol{\tau}_0\times(\boldsymbol{\tau}_0\times\mathbf{p}_I)],\end{aligned}\tag{12}$$

where

$$\beta=4\pi^{\frac{1}{2}}fV(K)K\omega^{-1}\chi(\boldsymbol{\tau}_0\cdot\mathbf{p}_I),$$
$$\beta'=4\pi^{\frac{1}{2}}fV(K)K\omega^{-1}\chi(\boldsymbol{\sigma}_0\cdot\mathbf{n}_I),$$
$$R=\tfrac{2}{3}f^2A_+\omega^{-1}.$$

The scattered field can be obtained by following the procedure described in the Appendix in Pauli's book:

$$\varphi_\alpha{}^a(\mathbf{x})=i(2\sqrt{\pi})^{-1}fV(K)K\frac{e^{iKr}}{r}\sum_{\nu,\nu'}\tau_{\alpha,\nu'}(\boldsymbol{\sigma}_s\cdot\mathbf{n}_s)+\text{c.c.}$$

The complex amplitude of the field with the positive frequency ω scattered into the directions of $\mathbf{n}_s$ and $\mathbf{p}_s$ in the coordinate and charge space, respectively, is then given by

$$(\chi_s\cdot\mathbf{p}_s)=i(2\sqrt{\pi})^{-1}fV(K)K\{(\boldsymbol{\tau}_0\cdot\mathbf{p}_s)(\boldsymbol{\sigma}_\omega\cdot\mathbf{n}_s)+(\boldsymbol{\tau}_\omega\cdot\mathbf{p}_s)(\boldsymbol{\sigma}_0\cdot\mathbf{n}_s)\}.\tag{13}$$

Introducing Eqs. (12) into (13), we obtain finally

$$\begin{aligned}(\chi_s\cdot\mathbf{p}_s)&=D\chi[(\boldsymbol{\tau}_0\cdot\mathbf{p}_s)(\boldsymbol{\tau}_0\cdot\mathbf{p}_I)\{([\boldsymbol{\sigma}_0\times\mathbf{n}_I]\cdot\mathbf{n}_s)\\&\quad+i(\xi+i\zeta)([\boldsymbol{\sigma}_0\times[\boldsymbol{\sigma}_0\times\mathbf{n}_I]]\cdot\mathbf{n}_s)\}\\&\quad+(\boldsymbol{\sigma}_0\cdot\mathbf{n}_s)(\boldsymbol{\sigma}_0\cdot\mathbf{n}_I)\{([\boldsymbol{\tau}_0\times\mathbf{p}_I]\cdot\mathbf{p}_s)\\&\quad+i(\xi+i\zeta)([\boldsymbol{\tau}_0\times[\boldsymbol{\tau}_0\times\mathbf{p}_I]]\cdot\mathbf{p}_s)\}],\end{aligned}\tag{14}$$

where

$$\xi=\tfrac{3}{2}(f\mu)^2\{(a\mu)^{-1}\omega^2\mu^{-2}-1\}\mu\omega^{-1},$$
$$\zeta=\tfrac{3}{2}(f\mu)^2(\omega^2\mu^{-2}-1)^{\frac{1}{2}}\mu\omega^{-1},$$
$$D=2if^2K^2\omega^{-1}[V(K)]^2[1-(\xi+i\zeta)^2]^{-1}.$$

The square of the absolute value of Eq. (14) corresponds to the intensity of the scattered field along the unit vectors $\mathbf{n}_s$ and $\mathbf{p}_s$ due to a particular set of orientations of the vectors $\boldsymbol{\sigma}_0$ and $\boldsymbol{\tau}_0$ in the coordinate and charge space, respectively.

IV. SCATTERING CROSS SECTIONS

If the kinetic energy of the incoming meson is not too large, so that for each incoming meson only one meson is created in the scattering, there exists the following ten different reactions between the mesons and the nucleons:

$$\begin{aligned}&(1)\ \pi^++p\rightarrow p+\pi^+\\&(2)\ \pi^++n\rightarrow n+\pi^+\\&(3)\ \pi^++n\rightarrow p+\pi^0\\&(4)\ \pi^-+n\rightarrow n+\pi^-\\&(5)\ \pi^-+p\rightarrow p+\pi^-\\&(6)\ \pi^-+p\rightarrow n+\pi^0\\&(7)\ \pi^0+n\rightarrow n+\pi^0\\&(8)\ \pi^0+n\rightarrow p+\pi^-\\&(9)\ \pi^0+p\rightarrow p+\pi^0\\&(10)\ \pi^0+p\rightarrow n+\pi^+.\end{aligned}\tag{15}$$

Of these the reactions (1) and (4) are unique in the sense that they have no alternative, whereas each of the remainder is accompanied by an alternative reaction. It is considered that for the reactions (1) and (4) the charge vector $\boldsymbol{\tau}$ of the nucleon does not play any role at all, and hence the scattering cross section for these can be considered to be the same as the one orginally given by Pauli for the neutral pseudoscalar meson. For these reactions we must in our theory first put $\mathbf{p}_I=\mathbf{p}_s$ in Eq. (14), since the charge states of the incoming and out-going particle are the same. Moreover, since $\boldsymbol{\tau}$ plays no role, we must consider it fixed along $\mathbf{p}_I$ or $\mathbf{p}_s$. Thus, we obtain from (14)

$$(\chi_s\cdot\mathbf{p}_s)=D\chi[([\boldsymbol{\sigma}_0\times\mathbf{n}_I]\cdot\mathbf{n}_s)+i(\xi+i\zeta)([\boldsymbol{\sigma}_0\times[\boldsymbol{\sigma}_0\times\mathbf{n}_I]]\cdot\mathbf{n}_s)].\tag{16}$$

This agrees with the corresponding expression given by Pauli (see p. 29 of his book). The differential scattering cross section is obtained by averaging $|(\chi_s\cdot\mathbf{p}_s)|^2/|\chi|^2$ over all directions of $\boldsymbol{\sigma}_0$:

$$dQ_a=|D|^2[\tfrac{4}{3}\sin^2\theta+(\xi^2+\zeta^2)(1+7\cos^2\theta)/15]d\Omega.\tag{17}$$

Here θ is the angle between $\mathbf{n}_s$ and $\mathbf{n}_I$ and $d\Omega$ the differential solid angle. The total scattering cross section is obtained by integrating Eq. (17) over all directions of $\mathbf{n}_s$ in the coordinate space:

$$Q_a=(8\pi/9)|D|^2(1+\xi^2+\zeta^2),\tag{18}$$

where one obtains from Eq. (14)

$$|D|^2=4f^4K^4\omega^{-2}|G(K)|^2[(1-\xi^2-\zeta^2)^2+4\zeta^2]^{-1}.\tag{19}$$

Q_a given by Eq. (18) agrees with that by Pauli.

For the rest of the reactions in Eqs. (15) in which ordinary as well as charge exchange interactions are involved, the square of the absolute value of Eq. (14)

must be properly averaged over all directions of τ_0 and σ_0 vectors. We then obtain

$$|(\chi_s\cdot \mathbf{p}_s)|^2=|D|^2|\chi|^2[\{(1+2\cos^2\delta)/15\}\times\{\tfrac{1}{3}\sin^2\theta+(\xi^2+\zeta^2)(1+7\cos^2\theta)/15\}+\{(1+2\cos^2\theta)/15\}\{\tfrac{1}{3}\sin^2\delta+(\xi^2+\zeta^2)\times(1+7\cos^2\delta)/15\}+(2/225)(\xi^2+\zeta^2)\times(1-3\cos^2\delta)(1-3\cos^2\theta)], \quad (20)$$

where θ and δ are the angles between $\mathbf{n}_I$ and $\mathbf{n}_s$ and $\mathbf{p}_I$ and $\mathbf{p}_s$, respectively. Let us first consider the reactions (2), (5), (7), and (9) of Eqs. (15) which involve no charge exchange. The vector amplitude of the scattered waves along the charge vector $\mathbf{p}_s$ of the field will be given by $(\chi_s\cdot \mathbf{p}_s)\mathbf{p}_s$, and its projection along the vector $\mathbf{p}_I$ is then given by $(\chi_s\cdot \mathbf{p}_s)(\mathbf{p}_s\cdot \mathbf{p}_I)$. In order to obtain the intensity of the scattered meson waves along the vector $\mathbf{p}_I$ we now average $|(\chi_s\cdot \mathbf{p}_s)|^2(\mathbf{p}_s\cdot \mathbf{p}_I)^2$ over all directions of $\mathbf{p}_s$. The result obtained must further be multiplied by two, because the charge state of the incoming meson designated by the negative of the vector $\mathbf{p}_I$ is the same as that by $\mathbf{p}_I$ itself. For reactions involving no charge exchange we thus obtain from Eq. (20) the following expression for the differential scattering cross section:

$$dQ_b=2\langle|(\chi_s\cdot \mathbf{p}_s)|^2(\mathbf{p}_I\cdot \mathbf{p}_s)^2\rangle_{Av}/|\chi|^2d\Omega=(2/225)|D|^2[\{(13-7\cos^2\theta)/3\}+(\xi^2+\zeta^2)\{(29+153\cos^2\theta)/15\}]d\Omega. \quad (21)$$

The corresponding total scattering cross section turns out to be

$$Q_b=(8\pi/9)|D|^2[(32/225)+(\xi^2+\zeta^2)(48/225)]. \quad (22)$$

Let us now consider the reactions (3), (6), (8), and (10) in Eq. (15) which involve charge exchange. The projection of the vector amplitude $(\chi_s\cdot \mathbf{p}_s)\mathbf{p}_s$ on the plane perpendicular to the vector $\mathbf{p}_I$ will be given by $(\chi_s\cdot \mathbf{p}_s)[\mathbf{p}_s\times \mathbf{p}_I]$. The average of the square of the absolute value of this over all the directions of $\mathbf{p}_s$, multiplied by two, is the intensity of the scattered field. Then the differential scattering cross section is found to be

$$dQ_e=2\langle|(\chi_s\cdot \mathbf{p}_s)|^2|[\mathbf{p}_s\times \mathbf{p}_I]|^2\rangle_{Av}/|\chi|^2d\Omega=(2/225)|D|^2[\tfrac{2}{3}(11+\cos^2\theta)+(\xi^2+\zeta^2)\{(46+122\cos^2\theta)/15\}]d\Omega. \quad (23)$$

The corresponding total scattering cross section becomes

$$Q_e=(8\pi/9)|D|^2[(68/225)+(\xi^2+\zeta^2)(52/225)]. \quad (24)$$

When the ordinary interaction and the charge exchange interaction are not distinguished from one another [reactions (2) and (3); (5) and (6); (7) and (8); and (9) and (10)], the resultant differential scattering cross section for each one of these sets would be

$$dQ=dQ_b+dQ_e=(2/45)|D|^2[\tfrac{1}{3}(7-\cos^2\theta)+(\xi^2+\zeta^2)(1+\tfrac{1}{3}\cos^2\theta)]. \quad (25)$$

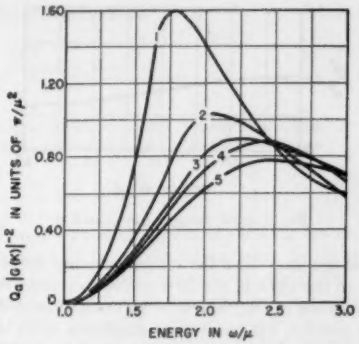

FIG. 1. $Q_a|G(K)|^{-2}$ in units of $\pi\mu^{-2}$ *versus* energy.

The last term in Eq. (20) proportional to $(1-3\cos^2\delta)(1-3\cos^2\theta)$ vanishes in Eq. (25), although it stays in the individual differential cross sections Eqs. (21) and (23). The sum of Q_b and Q_e becomes

$$Q=(8\pi/9)|D|^2(1+\xi^2+\zeta^2)(4/9). \quad (26)$$

V. DISCUSSION

According to the experimental results[1] on the scattering of π^+ and π^- by protons the total scattering cross section of π^+ is larger than that of π^- for the range of energy of the incoming mesons from about 50 Mev to 150 Mev. From Eqs. (18) and (26) we find that the ratio of the scattering cross section of π^+ to that of π^- to be 2.25 at all kinetic energies of the incoming mesons up to about 150 Mev ($\omega\cong 2\mu$). This ratio does not appear to be in disagreement with the experimental ratio in this energy range. However, beyond this range of energy the effects of higher harmonics mentioned at the end of Sec. II are expected to begin to show up, causing deviations from our results. Although the effects of the higher harmonics have not yet been investigated, the experimental observation that at 180 Mev the ratio of the scattering cross section for π^+ over that for π^- is somewhat larger than the ratio at lower energies may perhaps be ascribable to these effects.

From Eq. (18) and Eq. (19) one obtains

$$Q_a=(32/9)(f\mu)^4\mu^2\omega^{-2}(\omega^2\mu^{-2}-1)^2(1+\xi^2+\zeta^2)\times[(1-\xi^2-\zeta^2)^2+4\zeta^2]^{-1}(\pi\mu^{-2})|G(K)|^2. \quad (27)$$

Here, $\pi\mu^{-2}$ is the geometrical area of the nuclear force range, and is equal to 62×10^{-27} cm^2 for π-mesons. Figure 1 shows the curves of $Q_a|G(K)|^{-2}$ in units of $\pi\mu^{-2}$ at various energies of the incoming mesons for different values of the spin inertia a^{-1}; namely, the curve (1) for $a\mu=0.40$, (2) for 0.60, (3) for 0.80, (4) for 1.0, and (5) for 2.0. For the coupling constant we take for convenience the value $(f\mu)^2=0.318$, or $(f\mu)^4=0.100$. Assuming that the factor $|G(K)|$ does not vary appreciably within the range of energy considered, it appears that there is a

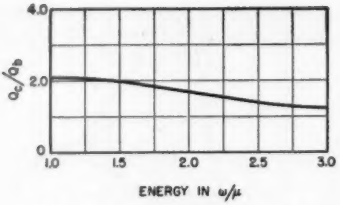

FIG. 2. Q_c/Q *versus* energy ($a\mu=0.8$).

general tendency that the maximum point lowers and shifts to the right in the direction of increasing energy as the values of the parameter $a\mu$ are increased. If one takes $a\mu=0.8$, the theoretical maximum point of the scattering cross-section curve occurs at about 160 Mev ($\omega/\mu=2.17$), which is also the approximate experimental maximum. Hence, we may tentatively take $a\mu=0.8$ or $a^{-1}=1.25\mu$ as the spin and isotopic spin inertia of the nucleon.

The experimental observations also indicate that in the case of the scattering of π^- by protons the total cross section involving the charge exchange interaction is about twice as large as the one involving no charge exchange interaction. From Eqs. (22) and (24) we obtain for this ratio

$$Q_c/Q_b=[17+13(\xi^2+\zeta^2)]/[8+12(\xi^2+\zeta^2)].$$

Figure 2 shows the variation of Q_c/Q_b with the energy of the incoming mesons. Since $(\xi^2+\zeta^2)$ increases with the energy moderately fast, it appears that the two cross sections tend to equalize when the energy of the mesons is sufficiently high.

The parameter $|G(K)|$ is now determined from the experimental observation that the maximum value of the total scattering cross section for π^- equals the geometrical area of the nuclear force range, namely, $\pi\mu^{-2}=62\times10^{-27}$ cm^2. It turns out from Eqs. (19) and (26) that the maximum of the calculated cross section can be made equal to the above experimental value if one takes $|G(K)|=1.58$, which value may be theoretically not unreasonable. It is easily seen that $|G(K)|=1$, if the nucleon were considered a point particle. In the theory of extended source all that is required is that $|G(K)|\approx1$. Figure 3 gives the curves of the total scattering cross section of π^+ and π^- by protons obtained from Eqs. (18) and (26), respectively, with $|G(K)|=1.58$.

In this manner it appears that the classical theory of meson dynamics involving the Pauli theory of extended source for the nucleon is capable of approximately accounting for the principal experimental facts in the scattering of π^+ and π^- by the protons mentioned in Sec. I.

Another experimental fact[7] that the scattering cross sections of π^+ and π^- for deuterium at about 60 Mev are approximately equal to each other may approximately be discussed from Eqs. (15), (18), and (26); namely, the cross sections for $\pi^++p\rightarrow p+\pi^+$ and $\pi^-+n\rightarrow n+\pi^-$ are given by Q_a, those for $\pi^++n\rightarrow n+\pi^+$ and $\pi^-+p\rightarrow p+\pi^-$ by Q_b, and those for $\pi^++n\rightarrow p+\pi^0$ and $\pi^-+p\rightarrow n+\pi^0$ by Q_c.

As to the resonance in the scattering discussed by Brueckner[2] and Wentzel,[3] we may give its analog in our classical theory in the following manner. Fixing our attention on the denominator of Eq. (27); namely, $\omega^2[(1-\xi^2-\zeta^2)^2+4\zeta^2]$, it is seen that ζ can be regarded as expressing the effects of radiation reaction of the meson field. This is due to the fact that it reduces to ω^2, the radiation reaction term for a Maxwell field, when μ is allowed to vanish (see Bhabha[8]). In the absence of this term the scattering cross section Q_a of Eq. (27) becomes infinite when $\xi=1$, or at the energy of the meson ω given by the equation [see Eq. (14)]

$$\tfrac{2}{3}(f\mu)^2\{(a\mu)^{-1}\omega\mu^{-1}-1\}\mu\omega^{-1}=1.$$

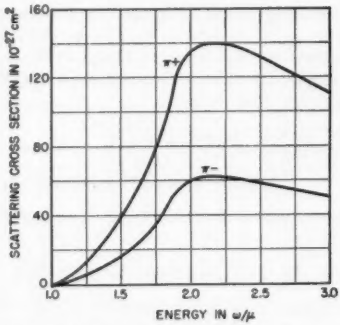

FIG. 3. Scattering for cross-section curves for π^+ and π^- for $a\mu=0.8$, $(f\mu)^2=0.10$ and $|G(K)|=1.58$.

The effect of the radiation reaction term ζ is to make the value of the scattering cross section finite even at this energy. This may be considered roughly as the resonance in our classical theory.

The classical treatment of the interaction of the meson field with nucleons disregards the momentum properties of individual field quanta. However, like the case of the classical electrodynamics, the classical meson dynamics is expected to give approximately correct results for range of energies in which momenta of individual mesons are small compared with the mass of the nucleon.[8] This certainly covers the range of energies up to a few hundred millon electron volts with which we are primarily concerned. Thus, within this range of energies the classical theory is also expected to be applicable to the process of photomesonic production.[8]

The author wishes to thank Professor K. A. Brueckner for valuable discussions.

[7] Isaacs, Sachs, and Steinberger, Phys. Rev. **65**, 803 (1952).

[8] H. J. Bhabha, Proc. Roy. Soc. (London) **A172**, 384 (1939).

Field Emission from Photoconductors

L. Apker and E. Taft
General Electric Research Laboratory, Schenectady, New York
(Received August 15, 1952)

Field emission current was drawn from sharp needles of the photoconductors CdS and CdSe. It increased greatly when light that excited photoconductivity was incident on the emitting area. Possible mechanisms are mentioned.

FIELD emission from metals has been rather thoroughly studied. Mueller's[1] electron projection microscope, for example, has afforded a particularly elegant approach to the problem. In contrast, little is known about field emission from semiconductors, although one would expect several new effects to appear. This note reports briefly on one of these—an unusual phenomenon that occurs when field emission is drawn from a photoconductor like CdS.

In our experiments, single-crystal needles of CdS (or CdSe) were mounted in a Mueller-type electron projection tube. They were sharpened by electron bombardment from a surrounding W wire loop. The CdS points reached temperatures above 500°C, as judged by the shift in the fundamental optical absorption edge. The lower parts of the needles were cooler. Sharpening apparently occurred by preferential evaporation.

Smooth points were very rarely obtained. Projection patterns characteristic of lattice symmetry were therefore extremely difficult to observe. Nevertheless, the emission had an interesting characteristic not found for metals or other substances of high conductivity: it was extremely sensitive to radiation that excited photoconductivity in the CdS.

In a particular case, 12 kv could be applied to the transparent anode[2] in the dark without producing a field emission of more than 10^{-8} ampere. When a small spot of light (from a 2-watt Western Union zirconium arc) was focused on the tip of the CdS needle, however, more than 10^{-6} ampere could be drawn at 6 kv. Internal reflections and scattering of light over large distances in the crystal were prevented by introducing a filter that passed only wavelengths below 500 mμ, well within the fundamental absorption band of CdS. It was then apparent that the effect occurred only when the emitting area was irradiated. With light incident from one side, the illuminated half of the point emitted preferentially.

In one case, two points emitted current. One was on the side of the needle near the middle; the other was at the tip. Currents over 10^{-6} ampere could be drawn from either point alone by irradiating it with the blue light for which CdS is opaque. As judged by projection patterns, the potential distribution along the needle changed radically when the light spot was shifted. In tubes with phosphor coatings, images could be observed at very low current levels, and there was evidence that the potential distribution around the needle tip changed under illumination.

Several factors may be involved in these effects. One of them is simply the spreading resistance associated with the emission of field currents through a needle tip only a micron or thereabouts in diameter. This resistance R is of order $k\rho/d$, where ρ is the resistivity, d is the tip diameter, and k is a geometrical constant of order 10. In the dark, ρ for CdS may be $>10^7$ ohm cm. With $d\sim10^{-4}$ cm, R may be $>10^{12}$ ohms. Thus, even when the field current in the dark is less than 10^{-8} ampere, several thousand volts may be lost in the needle resistance instead of appearing in the vacuum. When the needle is illuminated, the CdS resistance decreases, the voltage appears in the vacuum, and the field emission accordingly goes up.

Another important influence has been pointed out to us by M. H. Hebb. The equipotential surfaces in the vacuum at the end of the needle have a smaller curvature than the surface of the needle tip itself because of the current flow through the high resistance of the needle material. Hebb's calculations show that these departures become very important when the voltage drop in the spreading resistance is an appreciable fraction of the applied voltage. Thus, the field at the needle tip is smaller than one would calculate for a metal from the tip radius and from the voltage in the vacuum between the end of the tip and the anode. This deficiency in field, which is superposed on that due to simple voltage loss in the needle, decreases when the needle resistance is reduced by illumination. The field emission accordingly increases. These considerations are attractive because they do not involve such large electric fields in the volume of the CdS as does a simple voltage drop in the spreading resistance.

Several of our observations were consistent with these general pictures. First, as mentioned above, illumination was correlated with changes in potential distribution around the emitting points. Second, when the light was switched off, the increase in applied voltage required to maintain constant current became larger

[1] E. W. Mueller, Z. Physik **106**, 132 (1937).
[2] No phosphor coating was used here. The light produced would have returned to the CdS, of course, unless an opaque backing were used. Resultant feedback would have destroyed the significance of the results. A slight effect of this kind may even have been present without phosphor, since the transparent coated glass anode fluoresced faintly.

as the current level increased. Third, quenching phenomena were evident and were characteristic of CdS photoconduction.[3] Finally, atomic hydrogen destroyed the effects, presumably because the surface conductivity was increased by reduction of the CdS.

One expects other phenomena that are absent in metals to play a role in this kind of emission. Barrier layers are present. It is conceivable that a Zener type of breakdown may occur in a p-type semiconductor when emission is drawn from it. Further evaluation of these possibilities can perhaps best await theoretical treatment of field emission under these unusual conditions.

We are indebted to Malcolm H. Hebb and John K. Bragg for many interesting discussions

[3] E. Taft and M. H. Hebb, J. Opt. Soc. Am. 42, 249 (1952).

PHYSICAL REVIEW VOLUME 88, NUMBER 5 DECEMBER 1, 1952

Nuclear Mass Determinations from Disintegration Energies: Oxygen to Sulfur

C. W. Li
Kellogg Radiation Laboratory, California Institute of Technology, Pasadena, California
(Received July 30, 1952)

Values of the atomic masses from O^{18} to S^{33} have been derived from the Q-values of nuclear reactions with a procedure of statistical adjustment. Tables are given of the most probable Q-values and the atomic masses. In combination with a previous calculation, they give a set of consistent mass values from n^1 to S^{33}, based on nuclear disintegration energies.

In a previous calculation[1] the atomic masses from n^1 to F^{20} relative to $O^{16}=16.000\,000$ have been derived from the Q-values of nuclear reactions. Following a similar procedure, the atomic masses from $A=17$ to 33 are derived in the present work from recently available Q-value measurements.

Table I lists the Q-values used in deriving the masses. In most of these measurements, electrostatic or magnetic analysis has been used to determine the energy of the incident particles and emitted particles: electrons, heavy particles, or pairs or converted electrons produced by gamma-rays. In some cases, reaction thresholds or radiative capture transition energies of thermal neutrons have been involved. Except in a few reactions, there is yet only one accurate measurement for each reaction. Fortunately, enough cross checks have been established to provide a test on the internal consistency of the data. In this calculation 46 reactions have been used to determine the masses of 29 nuclei. The extensive magnetic analysis work by W. W. Buechner's group at the Massachusetts Institute of Technology accounts for almost half of the reactions listed in Table I. Three connections between the heretofore very loosely linked Ne and F isotopes have been furnished by recent measurements: $F^{20}(\beta^-)Ne^{20}$, $Ne^{20}(d,\alpha)F^{18}$, and $Ne^{21}(d,\alpha)F^{19}$. The second one is a range measurement in photographic emulsion. However, in view of its accuracy and its consistency with other data, it has been included, in contrast to the practice in I. This is the only range measurement which is used in these calculations. Another difference from I is that measurements with reported errors up to 40 kev have been included, instead of the earlier limit of 30 kev. The error of the heavier of the resultant masses turns out to be of the order of 40 kev.

Figure 1 illustrates graphically the interconnections between the nuclei which are of interest in this discussion. The solid lines represent reactions forming nuclear cycles. As in I, these cycles are useful in that (1) they give values of certain fundamental mass differences (or zero); (2) these fundamental mass differences can serve as tests of internal consistency of the nuclear data; and (3) they can be used to make regional least-squares adjustment of the experimental Q-values and thereby to obtain the values of masses which are numerically consistent and, presumably, have some improved precision. The improvement in precision is a possible result of the adjustment of overdetermined but statistically consistent data.

Table II exhibits the simplest set of independent nuclear cycles in the region of interest in the present discussion. It can be seen that, while the general precision is somewhat inferior to that of reactions in I, the present data are statistically consistent and the values of fundamental mass differences computed from them are consistent with those derived from I, namely, $n-H^1=0.7823\pm0.001$ Mev, $n+H^1-H^2=2.225\pm0.002$ Mev, and $2H^2-He^4=23.834\pm0.007$ Mev. An exception is the fourth cycle in Group 4 of Table II. This cycle gives a value for $2H^2-He^4$ which is inconsistent with the other values for $2H^2-He^4$, the discrepancy being many times the average error of the other cycles. Therefore we have omitted this cycle in the adjustment of the Q-values. In order to calculate the masses of Ne^{22} and Ne^{29} we have adopted the (d,p) reaction Q-values without adjustment and have omitted the beta-

[1] Li, Whaling, Fowler, and Lauritsen, Phys. Rev. 83, 512 (1951) (referred to as I).

TABLE I. Nuclear reaction energies used in evaluating masses.

Reaction	Experimental Q-value (Mev)	Weighted mean of experimental Q (Mev)	Adjusted value of Q (Mev)	Reference*
*$Li^7(l,\alpha)He^4$	9.79 ±0.03		(unadjustable)	De 52
$O^{16}(d,n)F^{17}$	−1.631 ±0.003		−1.631 ±0.003	Bo 51
$O^{18}(p,n)F^{18}$†	−2.453 ±0.004		−2.453 ±0.004	Ri 50ρ
$O^{18}(p,\alpha)N^{15}$	3.96 ±0.04		3.969 ±0.023	Se 51
$F^{17}(\beta^+)O^{17}$	2.742 ±0.03		2.767 ±0.006	Pe 50
$F^{18}(\beta^+)O^{18}$†	1.657 ±0.015	1.667 ±0.008	1.671 ±0.004	Bl 49a
	1.671 ±0.009			Ru 51
$F^{19}(n,\gamma)F^{20}$	6.63 ±0.03		6.600 ±0.007	Ki 51
$F^{19}(p,n)Ne^{19}$	−4.039 ±0.005		−4.038 ±0.005	Wi 52
$F^{19}(d,p)F^{20}$†	4.373 ±0.007		4.375 ±0.007	St 51
$F^{20}(\beta^-)Ne^{20}$	7.038 ±0.018		7.052 ±0.012	Al 52
$Ne^{19}(\beta^+)F^{19}$	3.202 ±0.03		3.256 ±0.005	Sc 52
$Ne^{20}(d,p)Ne^{21}$	4.529 ±0.007		4.530 ±0.006	Va 52
$Ne^{20}(d,\alpha)F^{18}$	2.78 ±0.02		2.781 ±0.018	Mi 51
$Ne^{21}(d,p)Ne^{22}$	8.137 ±0.011		(unadjustable)	Mi 52
$Ne^{21}(d,\alpha)F^{19}$	6.432 ±0.010		6.434 ±0.009	Mi 52
$Ne^{22}(d,p)Ne^{23}$	2.964 ±0.007		(unadjustable)	Va 52
$Na^{21}(\beta^+)Ne^{21}$	3.522 ±0.03		(unadjustable)	Sc 52
$Na^{23}(\beta^+)Ne^{23}$	2.841 ±0.006		(unadjustable)	Al 49, Ma 50
$Na^{23}(p,n)Mg^{23}$	−4.877 ±0.010		(unadjustable)	Wi 52a
$Na^{23}(p,\alpha)Ne^{20}$	2.372 ±0.008		2.372 ±0.007	Va 52
$Na^{23}(d,p)Na^{24}$	4.731 ±0.009	4.727 ±0.006	4.730 ±0.006	St 51
	4.723 ±0.008			Mi 52
$Na^{23}(d,\alpha)Ne^{21}$	6.902 ±0.010		6.902 ±0.007	St 51
$Na^{24}(\beta^-)Mg^{24}$	5.526 ±0.008[b]		5.531 ±0.007	Si 46, Wo 50
$Mg^{24}(d,p)Mg^{25}$	5.097 ±0.007		5.099 ±0.006	Va 52
$Mg^{24}(d,p)Mg^{25}$	8.880 ±0.012		(unadjustable)	Va 52
$Mg^{25}(d,\alpha)Na^{23}$	7.019 ±0.013		7.031 ±0.010	Va 52
$Mg^{26}(d,p)Mg^{27}$	4.207 ±0.006		(unadjustable)	Va 52
$Al^{27}(n,\gamma)Al^{28}$	7.724 ±0.010		7.722 ±0.007	Ki 51
$Al^{27}(p,\alpha)Mg^{24}$	1.585 ±0.015	1.593 ±0.006	1.594 ±0.005	Fr 50
	1.595 ±0.007			Va 52
$Al^{27}(d,p)Al^{28}$	5.494 ±0.010		5.497 ±0.007	En 51
$Al^{27}(d,\alpha)Mg^{25}$	6.694 ±0.010		6.693 ±0.007	En 51
$Al^{28}(\beta^-)Si^{28}$	4.647 ±0.014		4.650 ±0.011	Mo 52a
$Si^{28}(n,\gamma)Si^{29}$	8.51 ±0.04		8.472 ±0.008	Ki 51
$Si^{28}(d,p)Si^{29}$	6.246 ±0.008		6.247 ±0.007	St 51
$Si^{29}(d,p)Si^{30}$	8.388 ±0.013		8.386 ±0.010	Va 52
$Si^{29}(d,\alpha)Al^{27}$	5.994 ±0.011		5.997 ±0.010	Va 52
$Si^{30}(d,p)Si^{31}$	4.364 ±0.007		4.367 ±0.007	Va 52
$Si^{30}(d,\alpha)Al^{28}$	3.120 ±0.010		3.108 ±0.009	St 51
$Si^{31}(\beta^-)P^{31}$	1.486 ±0.012	1.476 ±0.007	1.480 ±0.007	Wa 52, Mo 52
	1.471 ±0.008			
$P^{31}(n,\gamma)P^{32}$	7.94 ±0.03		7.930 ±0.008	Ki 52
$P^{31}(d,p)P^{32}$	5.704 ±0.008		5.705 ±0.008	Va 52
$P^{31}(p,\alpha)Si^{28}$	1.909 ±0.010		1.911 ±0.008	Va 52
$P^{31}(d,\alpha)Si^{29}$	8.158 ±0.011		8.158 ±0.008	Va 52
$P^{32}(\beta^-)S^{32}$	1.712 ±0.008	1.707 ±0.004	(unadjustable)	Si 46, La 49, Ag 50, Wa 50, Je 52
	1.689 ±0.01			
	1.718 ±0.01			
	1.708 ±0.008			
	1.704 ±0.008			Je 52
$P^{33}(\beta^-)S^{33}$	0.26 ±0.02	0.265 ±0.014	(unadjustable)	Je 52
	0.27 ±0.02			Sh 51
$S^{32}(n,\gamma)S^{33}$	8.64 ±0.02		8.645 ±0.010	Ki 52
$S^{33}(d,p)S^{34}$	6.422 ±0.011		6.420 ±0.010	St 51

* See text, p. 000.
† Occurred in *J*. The value has been changed here.
[b] Error assigned.

* References:

Ag 50 H. M. Agnew, Phys. Rev. **77**, 655 (1950).
Al 49 D. E. Alburger, Phys. Rev. **76**, 435 (1949).
Al 52 D. E. Alburger (to be published).
Bl 49a Blaser, Boehm, and Marmier, Phys. Rev. **75**, 1953 (1949).
Bo 51 T. W. Bonner and J. W. Butler, Phys. Rev. **83**, 1091 (1951).
De 52 Dewan, Pepper, Allen, and Almqvist, Phys. Rev. **86**, 416 (1952).
En 51 Enge, Buechner, Sperduto, and Van Patter, Phys. Rev. **83**, 31 (1951).
Fr 50 J. M. Freeman, Proc. Phys. Soc. (London) **A63**, 668 (1950).
Je 52 Jensen, Nichols, Clement, and Pohm, Phys. Rev. **85**, 112 (1952).
Ki 51 Kinsey, Bartholomew, and Walker, Phys. Rev. **83**, 519 (1951).
Ki 52 Kinsey, Bartholomew, and Walker, Phys. Rev. **85**, 1012 (1952).
La 49 L. M. Langer and H. C. Price, Jr., Phys. Rev. **76**, 641 (1949).
Ma 50 Macklin, Lidofsky, and Wu, Phys. Rev. **78**, 318 (1950).
Mi 51 R. Middleton and C. T. Tai, Proc. Phys. Soc. (London) **A64**, 801 (1951).
Mi 52 Mileikowsky and Whaling, Phys. Rev. (to be published).
Mo 52 H. T. Motz, Phys. Rev. **85**, 501 (1952).
Mo 52a H. T. Motz and D. E. Alburger, Phys. Rev. **86**, 165 (1952).
Pe 50 V. Perez-Mendez and P. Lindenfeld, Phys. Rev. **80**, 1097 (1950).
Ri 50ρ Richards, Smith, and Browne, Phys. Rev. **80**, 524 (1950).
Ru 51 L. Ruby and J. R. Richardson, Phys. Rev. **83**, 698 (1951).
Sc 52 G. Schrank and J. R. Richardson, Phys. Rev. **86**, 248 (1952).
Se 51 J. Seed, Phil. Mag. **42**, 566 (1951).
Sh 51 Sheline, Holtzman, and Fan, Phys. Rev. **83**, 919 (1951).
Si 46 K. Siegbahn, Phys. Rev. **70**, 127 (1946).
St 51 Strait, Van Patter, Buechner, and Sperduto, Phys. Rev. **81**, 747 (1951).
Va 52 Van Patter, Sperduto, Endt, Buechner, and Enge, Phys. Rev. **85** 142 (1952).
Wa 50 Warshaw, Chen, and Appleton, Phys. Rev. **80**, 288 (1950).
Wa 52 A. H. Wapstra, Phys. Rev. **86**, 562 (1952).

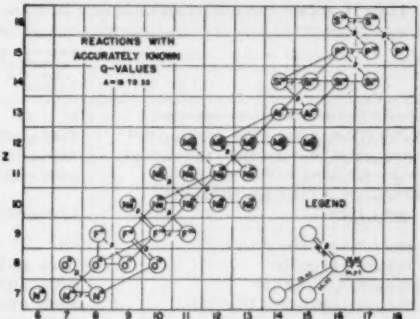

FIG. 1. The nuclear reactions with accurately known *Q*-values are represented on this chart by lines connecting target nucleus and residual nucleus. Solid lines: *Q*-values which form cycles, adjustable; dashed lines: unadjustable *Q*-values.

measurement, believing that the latter is more susceptible to error.

At first thought, it would seem that the next step should be to calculate the values of the fundamental mass differences from the present data alone or, better, from all data from S^{33} down to n^1. In view of the lower precision of the present data, the first alternative would not be so reliable and the second alternative, after considerably more work, would give essentially the same results as those given by I. Therefore, we have instead used the values of fundamental mass differences from I to adjust the present data.

The assumptions or approximations regarding the input data and the procedure of adjustment are exactly the same as those discussed in I. The adjusted values are listed in column 4 of Table I. Among the 37 adjustable reactions, there are two adjustments which are outside the respective reported errors. The adjustments are slightly on the positive side, i.e., there are more *Q*'s whose absolute values have been increased than *Q*'s whose absolute values have been decreased.

The adjusted *Q*-values and unadjustable ones (indicated by dashed lines in Fig. 1) were then combined with the fundamental mass differences and the adjusted data from I to yield the atomic masses listed in Table III. In all cases the *Q*-values were taken as the difference in atomic masses (not nuclear) on the two sides of a nuclear reaction equation. This is believed to be a very good approximation for reactions involving nuclei with $A \gtrsim 16$. The errors quoted are determined by a Gaussian compounding of the errors in the *Q*-values entering into the evaluation of each mass. Together with I, the present work gives a consistent set of masses from n^1 to S^{33}, based on nuclear data.[2]

[2] See also H. A. Wilson, Phys. Rev. **84**, 836 (1951).

Wi 52 Willard, Bair, Kington, Hahn, Snyder, and Green, Phys. Rev. **85**, 849 (1952).
Wi 52a Willard, Kington, and Bair, Phys. Rev. **86**, 259 (1952).
Wo 50 J. L. Wolfson, Phys. Rev. **78**, 176 (1950).

TABLE II. Nuclear cycles and fundamental mass differences.

Cycle	Mass difference from experimental Q (Mev)
Group 1. Nuclear cycles giving a sum of zero.	
$Na^{23}(d,\alpha)Ne^{21}$, $Ne^{20}(d,p)Ne^{21}$, $Na^{23}(p,\alpha)Ne^{20}$	0.001±0.015
$Al^{27}(d,\alpha)Mg^{25}$, $Mg^{24}(d,p)Mg^{25}$, $Al^{27}(p,\alpha)Mg^{24}$	0.004±0.014
$P^{31}(d,\alpha)Si^{29}$, $Si^{28}(d,p)Si^{29}$, $P^{31}(p,\alpha)Si^{28}$	0.003±0.017
$Si^{30}(d,\alpha)Al^{28}$, $Al^{27}(d,p)Al^{28}$, $Si^{29}(d,\alpha)Al^{27}$, $Si^{29}(d,p)Si^{30}$	0.020±0.022
Group 2. Nuclear cycles giving $n-H^1$.	
$O^{18}(p,n)F^{18}$, $F^{18}(\beta^+)O^{18}$	0.786 ±0.009
$F^{19}(p,n)Ne^{19}$, $Ne^{19}(\beta^+)F^{19}$	0.837 ±0.030
$O^{16}(d,p)O^{17}$, $O^{16}(d,n)F^{17}$, $F^{17}(\beta^+)O^{17}$	0.806 ±0.024
From I	*0.7823±0.001*
Group 3. Nuclear cycles giving $n+H^1-H^2$.	
$F^{19}(d,p)F^{20}$, $F^{19}(n,\gamma)F^{20}$	2.257±0.031
$Al^{27}(d,p)Al^{28}$, $Al^{27}(n,\gamma)Al^{28}$	2.230±0.014
$Si^{28}(d,p)Si^{29}$, $Si^{28}(n,\gamma)Si^{29}$	2.264±0.041
$P^{31}(d,p)P^{32}$, $P^{31}(n,\gamma)P^{32}$	2.236±0.031
$S^{32}(d,p)S^{33}$, $S^{32}(n,\gamma)S^{33}$	2.218±0.023
From I	*2.225±0.002*
Group 4. Nuclear cycles giving $2H^2-He^4$.	
$Ne^{20}(d,p)Ne^{21}$, $Ne^{21}(d,\alpha)F^{19}$, $F^{19}(d,p)F^{20}$, $F^{20}(\beta^-)Ne^{20}$, with $2H^1-H^2$ [a]	23.815±0.023
$Mg^{24}(d,p)Mg^{25}$, $Mg^{25}(d,\alpha)Na^{23}$, $Na^{23}(d,p)Na^{24}$, $Na^{24}(\beta^-)Mg^{24}$, with $2H^1-H^2$ [a]	23.812±0.018
$Si^{28}(d,p)Si^{29}$, $Si^{29}(d,\alpha)Al^{27}$, $Al^{27}(n,\gamma)Al^{28}$, $Al^{28}(\beta^-)Si^{28}$, with $n-H^1$ [a]	23.829±0.022
$Na^{23}(d,\alpha)Ne^{21}$, $Ne^{21}(d,p)Ne^{22}$, $Ne^{22}(d,p)Ne^{23}$, $Ne^{23}(\beta^-)Na^{23}$, with $2H^1-H^2$ [a]	23.656±0.025 [c]
$P^{31}(d,\alpha)Si^{29}$, $Si^{29}(d,p)Si^{30}$, $Si^{30}(d,p)Si^{31}$, $Si^{31}(\beta^-)P^{31}$, with $2H^1-H^2$ [a]	23.829±0.020
$F^{19}(p,\alpha)O^{16}$, [b] $O^{16}(d,\alpha)N^{14}$, [b] $N^{14}(d,p)N^{15}$, [b] $O^{18}(p,\alpha)N^{15}$, $O^{18}(p,n)F^{18}$, $Ne^{20}(d,\alpha)F^{18}$, $Ne^{20}(d,p)Ne^{21}$, $Ne^{21}(d,\alpha)F^{19}$, with $n+H^1-H^2$ [a]	23.841±0.048
From I	*23.834±0.007*

[a] $n-H^1=0.7823\pm0.001$ Mev, $n+H^1-H^2=2.225\pm0.002$ Mev, $2H^1-H^2=(n+H^1-H^2)-(n-H^1)=1.443\pm0.002$ Mev; from I.
[b] From I, adjusted values.
[c] This cycle has not been included in the adjustment. $Ne^{23}(\beta^-)Na^{23}=4.21\pm0.015$ Mev. H. Brown and V. Perez-Mendez, Phys. Rev. **78**, 812 (1950).

The masses F^{17} and F^{20} have been recalculated in the present work. Since the calculation of I, many new Q measurements pertinent to the masses from $A=1$ to 16 have been made, in different laboratories. No essential discrepancy has appeared except in the case of He^6, which was connected to Li^6 by an unadjustable beta-measurement. Using the new measurement $Li^7(t,\alpha)He^6=9.79\pm0.03$ Mev[a] and the adjusted data of I, the atomic mass of He^6 becomes 6.020 833 (±39), and the He^6-Li^6 mass difference becomes 3.549±0.032 Mev.

DISCUSSION: COMPARISON WITH MASS SPECTROMETRIC DETERMINATIONS

Table IV gives a comparison between the mass values from nuclear data and the recent mass spectrometric values by Nier[4] and by Ewald.[5] The nuclear data include both those in I and those in the present calculation. The differences between the mass spectrometric values and the corresponding nuclear values, Δ, are listed following the mass spectrometric values. Nier's values are consistently larger than the nuclear values. The disagreement is 3 to 2 times the sum of probable errors for the lighter nuclei. Nier's values for Ne^{20} and S^{32} agree with the nuclear values within the sum of probable errors. Ewald's values differ from nuclear values randomly. The agreement with the nuclear values is excellent for the lighter nuclei. His value for N^{15} [based on his 1946 measurement of the CH_3-N^{15} doublet[5,6]] is larger than the nuclear value by twice the sum of probable errors, and his value for Ne^{21} is smaller by two and one-half times the sum of probable errors. His values for P^{31} and S^{32} are both larger than the nuclear values, while his value for Si^{28} is close to

TABLE III. Table of atomic masses.

	A, mass number	$M-A$, mass defect (Mev)	M, atomic mass from nuclear data (amu) [a]
He†	6	19.399±0.036	6.020 833 (±39)
O	18	4.522±0.022	18.004 857 (±23)
F†	17	6.988±0.005	17.007 505 (±5)
F	18	6.193±0.021	18.006 651 (±22)
F†	20	5.913±0.016	20.006 350 (±17)
Ne	19	7.405±0.014	19.007 952 (±15)
Ne	20	−1.139±0.019	19.998 777 (±21)
Ne	21	0.469±0.021	21.000 504 (±22)
Ne	22	−1.529±0.023	21.998 358 (±25)
Ne	23	1.646±0.023	23.001 768 (±26)
Na	21	3.991±0.037	21.004 286 (±39)
Na	22	1.312±0.023	22.001 409 (±25)
Na	23	−2.742±0.023	22.997 055 (±25)
Na	24	−1.333±0.024	23.998 568 (±26)
Mg	23	1.353±0.024	23.001 453 (±26)
Mg	24	−6.864±0.024	23.992 628 (±26)
Mg	25	−5.824±0.025	24.993 745 (±27)
Mg	26	−8.565±0.027	25.990 802 (±29)
Mg	27	−8.633±0.028	26.992 876 (±30)
Al	27	−9.245±0.028	26.990 071 (±30)
Al	28	−8.603±0.030	27.990 760 (±32)
Si	28	−13.253±0.030	27.985 767 (±32)
Si	29	−13.362±0.032	28.985 650 (±34)
Si	30	−15.609±0.034	29.983 237 (±36)
Si	31	−13.837±0.036	30.985 140 (±39)
P	31	−15.317±0.036	30.983 550 (±39)
P	32	−14.883±0.038	31.984 016 (±41)
P	33	−16.606±0.042	32.982 166 (±44)
S	32	−16.590±0.039	31.982 183 (±42)
S	33	−16.871±0.041	32.981 881 (±44)

† Occurred in I. The value has been changed here.
[a] 1 amu = 931.152 Mev.

[a] See reference De 52 of Table I.

[4] A. O. Nier, Phys. Rev. **81**, 624 (1951).
[5] H. Ewald, Z. Naturforsch. **6a**, 293 (1951).
[6] H. Ewald, Z. Naturforsch. **1**, 136 (1946).

the nuclear value. This discrepancy has already been pointed out by Wapstra[7] with the $P^{31}-Si^{28}$ mass difference computed from nuclear data.

Direct comparison of the mass values between nuclear data and mass spectrometric data is superficial, because neither is the primary experimental data. Nuclear values are calculated from disintegration energies as already discussed, and mass spectrometric values are calculated from mass doublet measurements. In most precision mass spectrometric measurements a system of three easily accessible secondary standards, namely, H^1, H^2, and C^{12}, has been used, relating to the main standard $O^{16}=16.000\,000$. The three fundamental mass doublets $2H^1-H^2$, $3H^2-\frac{1}{2}C^{12}$, and $C^{12}H_4{}^1-O^{16}$, which form a closed ring, are usually used to obtain these secondary standards.[8] A fourth secondary standard is S^{32}, which can be linked to O^{16} directly by the doublet $(O^{16})_2-S^{32}$. Nier[4] has used, in addition, a closed ring containing H^1, C^{12}, S^{32}, and O^{16} to obtain these secondary standards, and thus provided an independent check on the values of these secondary standards. After the determination of these secondary standards, especially H^1, H^2, and C^{12}, they are then considered as established anchor points for computing mass values from other doublets.

Table V gives a comparison between the values of mass doublets as computed from nuclear data and those directly determined in recent mass spectroscopy. Among the fundamental doublets containing the secondary standards, $2H^1-H^2$ is in very good agreement. The doublet $2H^2-He^4$, also one of the fundamental mass differences used in evaluating masses from nuclear data, is essentially in agreement, though it should be further improved. The doublet $(O^{16})_2-S^{32}$ determines the mass of S^{32} directly. The old discrepancy[9–11] of 1 Mev in the mass of S^{32} is removed now, and all data come into agreement by the order of 100 kev. Not listed in Table V, the doublet $(O^{16})_2-S^{32}$ was measured by Aston[9] to be 17.7 ± 0.3 mMU, by Okuta and Ogata[10] to be 19.15 ± 0.11 mMU, and also the doublet $C^{12}(O^{16})_2-C^{13}S^{32}$ was measured by Okuta and Ogata to be 18.94 ± 0.23 mMU; the latter two averaged to 19.11 ± 0.07 mMU.[12] With the new "synchrometer" time-of-flight mass spectrometer, Smith[13] reported a measurement of the mass of S^{32}, representing a doublet value of 17.7 ± 1.0 mMU; later, Hays, Richards, and Goudsmit's measurement[14] represents a doublet value of 17 ± 1 mMU. The nuclear value is higher than all but one of the other measurements, though essentially in agreement with Nier's and several other values. The doublet containing Si^{28} is in good agreement. The doublet containing Al^{27}, heretofore used for the determination of the mass of Al^{27}, shows a large change.

No further analysis of either nuclear data or mass spectrometric data has been attempted here. New independent measurements on both nuclear reaction energies, especially many beta-decay energies, and mass spectrographic doublets would be very desirable. Though present technique does not yet permit the measurement of $n-H^1$ by the mass spectrometer, doublet measurements with radioactive nuclei, like He^3,[15] Be^7, and C^{14}, would be very interesting and of great theoretical importance. Also the fundamental mass difference $2H^2-H^1H^3$ should be measured directly

For convenience of reference, a portion of the table of atomic masses in *I* is reproduced here.

	A, mass number	$M-A$, mass defect (Mev)	M, atomic mass from nuclear data (amu)
n	1	8.3638 ± 0.0029	1.008 982 (±3)
H	1	7.5815 ± 0.0027	1.008 142 (±3)
H	2	13.7203 ± 0.006	2.014 735 (±6)
He	4	3.6066 ± 0.014	4.003 873 (±15)

TABLE IV. Comparison of masses from nuclear data and from mass spectrograph measurements.

		Nuclear data	Nier (1951)[a]	$\Delta\times10^6$	Ewald (1951)[b]	$\Delta\times10^6$
H	1	1.008 142 (±3)	1.008 165 (±4)	+23	1.008 141 (±2)	−1
H	2	2.014 735 (±6)	2.014 778 (±8)	+43	2.014 732 (±4)	−3
He	4	4.003 873 (±15)	4.003 944 (±19)	+71	4.003 860 (±12)	−13
C	12	12.003 804 (±17)	12.003 842 (±6)	+38	12.003 807 (±11)	+3
N	14	14.007 515 (±11)	14.007 564 (±7)	+49	14.007 525 (±15)	+10
N	15	15.004 863 (±12)			15.004 928 (±20)	+65
O	17	17.004 533 (±7)			17.004 507 (±15)	−26
O	18	18.004 857 (±23)			18.004 875 (±13)	+18
F	19	19.004 456 (±15)			19.004 414 (±17)	−42
Ne	20	19.998 777 (±21)	19.998 835 (±43)	+58	19.998 771 (±12)	−6
Ne	21	21.000 504 (±22)			21.000 393 (±22)	−111
Ne	22	21.998 358 (±25)			21.998 329 (±19)	−29
Si	28	27.985 767 (±32)			27.985 792 (±32)	+25
P	31	30.983 550 (±39)			30.983 622 (±23)	+72
S	32	31.982 183 (±42)	31.982 218 (±25)	+35	31.982 272 (±19)	+89

[a] See reference 4.
[b] See reference 5.

[7] A. H. Wapstra, Phys. Rev. **86**, 561 (1952).
[8] For example, J. Mattauch and S. W. Flügge, *Nuclear Physics Tables* (Interscience Publishers, Inc., New York, 1946), p. 9.
[9] G. H. Aston, Proc. Roy. Soc. (London) **A163**, 391 (1937).
[10] T. Okuta and K. Ogata, Phys. Rev. **60**, 690 (1941).
[11] L. Penfold, Phys. Rev. **80**, 116 (1950); H. T. Motz, Phys. Rev. **81**, 1060 (1951).
[12] This value has been used to give the S^{32} mass in most compilations in recent years.
[13] L. G. Smith, Phys. Rev. **81**, 295 (1951).
[14] Hays, Richards, and Goudsmit, Phys. Rev. **84**, 824 (1951).
[15] Planned by Professor K. T. Bainbridge (private communication).

TABLE V. Mass spectrographic doublets.

	Computed from nuclear data (mMU)[a]	Nier and Roberts[b]	Δ (mMU)	Ewald[c]	Δ (mMU)	Others	Δ (mMU)
$2H^1-H^2$	1.5494±0.0024	1.5519±0.0017	+0.0025	1.5503±0.0015	+0.0009		
$2H^2-He^4$	25.596±0.008	25.612±0.009	+0.016	25.604±0.009	+0.008		
$3H^2-\frac{1}{2}C^{12}$	42.302±0.016			42.292±0.012	−0.010		
$2[(H^2)_2O^{16}-\frac{1}{2}A^{40}]$ $-[(C^{12})_2(H^1)_4-A^{40}]$	14.958±0.033	15.057±0.050	+0.099				
$C^{12}(H^1)_4-O^{16}$	36.372±0.019	36.478±0.022	+0.106	36.371±0.012	−0.001	36.443±0.005[d]	+0.071
$(C^{12})_2(H^1)_4-C^{12}O^{16}$		36.443±0.022	+0.071			36.451±0.006[d]	+0.079
$\frac{1}{2}[(C^{12})_2(H^1)_8-C^{12}(O^{16})_2]$		36.484±0.020	+0.112				
$C^{12}(H^1)_2-N^{14}$	12.573±0.012	12.586±0.013	+0.013	12.564±0.010	−0.009	12.597±0.003[d]	+0.024
$(N^{14})_2-C^{12}O^{16}$	11.227±0.011	11.280±0.013	+0.053				
$(C^{12})_2(H^1)_8-(N^{14})_2O^{16}$	61.517±0.024	61.76±0.09	+0.24				
$C^{12}(H^1)_3-N^{15}$	23.367±0.011			23.302±0.015	−0.065	23.395±0.005[d]	+0.028
$(H^2)_2H^1O^{16}-(H^2)_2O^{17}$	3.610±0.005			3.634±0.015	+0.024		
$(H^2)_2O^{16}-(H^1)_2O^{18}$	8.329±0.026			8.312±0.012	−0.017		
$(H^2)_2O^{16}-F^{19}H^1$	16.872±0.011			16.909±0.015	+0.037		
$(H^2)_2O^{16}-Ne^{20}$	30.693±0.019	30.721±0.039	+0.028	30.688±0.010	−0.005		
$(H^1)_2O^{18}-Ne^{20}$	22.364±0.022			22.391±0.010	+0.027		
$(H^2)_2H^1O^{18}-Ne^{21}$	37.108±0.020			37.212±0.020	+0.104		
$(H^2)_2O^{18}-Ne^{22}$	45.847±0.024			45.867±0.015	+0.020		
$(C^{12})_2(H^1)_2-Al^{27}$	41.963±0.029					42.35±0.065[e]	+0.387
$C^{12}O^{16}-Si^{28}$	18.037±0.031			18.015±0.030	−0.022	18.06±0.08[f]	+0.02
$(C^{12})_2(H^1)_4-Si^{28}$	54.409±0.035					54.46±0.17[f]	+0.05
$C^{12}(H^1)_2-\frac{1}{2}Si^{29}$	36.612±0.019					36.795±0.075[f]	+0.18
$(O^{16})_2-P^{31}H^1$	8.308±0.039			8.249±0.030	−0.059		
$P^{31}H^1-S^{32}$ $P^{31}(H^1)_2-S^{32}(H^1)_2$	9.509±0.010			9.504±0.020	−0.005		
$(O^{16})_2-S^{32}$	17.818±0.042			17.716±0.020	−0.102	17.63±0.10[f]	−0.19
$C^{12}(O^{16})_2-C^{12}S^{32}$		17.782±0.025	−0.036				
$(C^{12})_4-S^{32}O^{16}$	33.034±0.045	33.182±0.007	+0.148				
$(C^{12})_6(H^1)_4-C^{12}(S^{32})_2$	87.223±0.092	87.326±0.058	+0.103				
$(H^2)_2O^{16}-\frac{1}{2}A^{40}$		41.967±0.018		41.953±0.012			
$Ne^{20}-\frac{1}{2}A^{40}$		11.280±0.018					

[a] 1 amu = 931.152 Mev, J. W. M. DuMond and E. R. Cohen, Phys. Rev. **82**, 555 (1951).
[b] A. O. Nier and T. R. Roberts, Phys. Rev. **81**, 507 (1951); A. O. Nier, Phys. Rev. **81**, 624 (1951); T. R. Roberts, Phys. Rev. **81**, 624 (1951).
[c] H. Ewald, Z. Naturforsch. **6a**, 293 (1951); **5a**, 1 (1950); and **1**, 136 (1946).
[d] K. Ogata and H. Matsuda, Phys. Rev. **83**, 180 (1951).
[e] J. Mattauch and H. Ewald [see S. W. Flügge and J. Mattauch, Physik. Z. **44**, 181 (1943)].
[f] H. E. Duckworth and R. S. Preston, Phys. Rev. **79**, 188, and 402 (1950); and **81**, 268 (1951).

by mass spectrometer, as well as additional measurements on $2H^2-He^4$, to check the accuracy of nuclear data.

It is interesting to compare the present mass values with those in two of the recently most used tables.[16,17] Both tables are based on earlier mass spectrographic data for the main mass scale and use nuclear disintegration energies in an auxilliary way. For most of the masses listed in Table III of the present discussion, Bethe's table quotes errors of the order of 200 to 900 kev, while Wapstra's table[17] quotes errors of the order of 100 to 400 kev. In parallel with recent improvement in mass spectrometric measurements, the present mass values have errors of order of 20 to 40 kev, as an indication of the late improvement of nuclear reaction energy measurements. It is of interest to note that, compared with the present mass values, the number of nuclei whose masses have been changed by more than their respective listed errors in each of the two above-mentioned tables is very close to half of the number of nuclei so compared, just as the definition of "probable error" stipulates.

The author wishes to thank Dr. C. Mileikowsky, Dr. W. Whaling, and Dr. D. E. Alburger of the Brookhaven Laboratory for important prepublication information, and Professor T. Lauritsen for interesting discussions. It is a pleasure to express his appreciation to Professors Charles C. Lauritsen and W. A. Fowler for the privilege of working with them. He is indebted to the California Institute of Technology for a Research Fellowship.

[16] H. A. Bethe, *Elementary Nuclear Theory* (John Wiley and Sons, Inc., New York, 1947), p. 123.
[17] L. Rosenfeld, *Nuclear Forces, II* (Interscience Publishers, Inc., New York, 1949), p. 497.

Color Centers in Alkali Halides at 5°K*

WILLIAM H. DUERIG† AND JORDAN J. MARKHAM
Applied Physics Laboratory, The Johns Hopkins University, Silver Spring, Maryland
(Received May 26, 1952)

This paper reports experimental data on the effect of x-raying NaCl, KCl, and KBr at 5°K (approximately liquid helium temperature). These crystals, grown by Harshaw, were exposed to x-rays (50 kv at 20 and 48 ma) at 5°K, and the absorption spectra were measured from 210 mμ to 1100 mμ. A large concentration of *F*-centers was produced after an exposure of 15 minutes. The *F*-center is narrower than those obtained in additively colored crystals at 20°K. This difference in width also occurs in crystals x-rayed at 78°K. The narrowing of the *F*-band does not seem to be due to the temperature difference, i.e., 5°K and 20°K. No bands were observed to the infrared with the exception of a small *F'*-band in NaCl and KBr. Bands which were not known previously were obtained to the ultraviolet. Some bands decrease on warming to 78°K while others grow.

INTRODUCTION

UNTIL recently color centers in alkali halide crystals were produced at high temperatures or by irradiating the crystals with x-rays or other high energy radiation at room temperature. By lowering the temperature at which the crystals are x-rayed, additional color centers appear, some of which are stable only at low temperatures. Considerable work has been done down to 78°K (liquid nitrogen temperature), and a number of absorption bands have been found. Pick[1] has studied the *F'*-bands which can be produced in additively colored KCl and KBr by irradiating with light in the *F*-band at low temperatures. Casler, Pringsheim, and Yuster[2] have produced additional bands by x-raying NaCl, KCl, and KBr at 78°K and at dry ice temperature. They have also shown that some of these bands are unstable when the temperature is raised. Dorendorf[3] has x-rayed KCl and KBr at several different temperatures ranging from −180°C to +75°C. He observed seven bands on the ultraviolet side of the *F*-band which are produced at various temperatures and have various ranges of temperature stability. Martienssen[4] has shown that KBr x-rayed at 20°K possesses a large α-band and an *F*-band. He has also reported the β-band in KBr which can easily be produced by x-raying KBr at 20°K. The properties of the α-band and β-band have been studied previously by Delbecq, Pringsheim, and Yuster[5] in KI.

In order to achieve a more complete understanding of color center formation at low temperature, it is desirable to extend these investigations to 5°K (liquid helium temperature).

This paper will report work on NaCl, KCl, and KBr x-rayed at 5°K. This is the measured temperature of the crystals within the low temperature cell. The work has been of a survey nature and many individual results remain to be fully explored. Since the work indicates important results, the authors deem it advisable to publish these data now, rather than to withold publication until such time as all the individual phenomena are fully explored. The experimental procedure will be described first, then results on the individual crystals will be given, and finally a summary will be made. No attempt will be made to give a theoretical interpretation of the results.

EXPERIMENTAL PROCEDURE

The experimental procedure consisted of four parts: obtaining the crystal, cooling it, x-raying it, and measuring its absorption spectrum. We shall now describe the parts in detail.

Some alkali halide crystals of unknown purity can be obtained from chemical companies. Pohl[6] has pointed out that for optical measurements crystals should have no more than 1 part per 10^5 or 10^6 of any one foreign element. A qualitative spectroscopic analysis of the impurities in several of the available alkali halides was made for us by Dr. S. Zerfoss of the Naval Research Laboratory and by Mr. B. F. Scribner of the National Bureau of Standards. The results are given in Table I. Unfortunately, the analysis gives information only about those elements listed. Thus, for example, we have no knowledge regarding the content of hydrogen which causes the *U*-band.[7] We would like to stress the fact that these figures are only qualitative and that further analysis is needed. Some estimates in the table may be changed upon improvement of the analytic technique. Table I indicates the following:

(1) The impurities in the samples tested are much higher than one would like for color-center work;

(2) Crystals from various chemical companies

* This research was supported by the Bureau of Ordnance, U. S. Navy.
† Part of a dissertation presented to the Faculty of the Graduate School of the University of Maryland as partial fulfillment for the degree of Doctor of Philosophy.
[1] H. Pick, Ann. Physik **31**, 365 (1938), **37**, 421 (1940).
[2] Casler, Pringsheim, and Yuster, J. Chem. Phys. **18**, 887, 1564 (1950).
[3] H. Dorendorf, Z. Physik **129**, 317 (1951).
[4] W. Martienssen, Z. Physik **131**, 488 (1952) and Naturwiss. **38**, 482 (1951).
[5] Delbecq, Pringsheim, and Yuster, J. Chem. Phys. **19**, 574 (1951).
[6] R. W. Pohl, Proc. Phys. Soc. (London) **49**, extra part 4 (1937).
[7] R. Hilsch and R. W. Pohl, Nachr. Akad. Wiss. Göttingen Math.-physik. Kl. **2**, 139 (1936–39).

TABLE I. Spectroscopic impurity analysis of several alkali halide crystals.*

Element	NaCl Har NRL	NaCl Har NRL	NaCl Har NBS	NaCl Har NBS	NaCl Opt NRL	KCl Har NRL	KCl Har NBS	KBr Har NRL	KBr Har. NBS	KBr Pil NRL	NaF Zer NBS
Ag	*T*	—	*T*	—	—	—	—	*T*	—	—	—
Al	*W*	*W*	*T*	*T*	*W*	*VW*	*T*	*W*	*T*	*W*	—?
As			—	—			—		—		—
Au			—	—			—		—		—
B			—	—			—		—		—
Ba			—	—			—		—		—
Be			—	—			—		—		—
Bi			—	—			—		—		—
Ca	—	—	*VW*	*VW*	*M*	*VW*	*VW*	—	*VW*	—	*W*
Cb			—	—			—		—		—
Cd			—	—			—		—		—
Ce	—	—	—	—	—	—	—	—	—	—	—
Co			—	—			—		—		—
Cr			—	—	*W*	*T*	—		—		—
Cs			—?	—?			—?		?		?
Cu	*VW*	—	—?	—?	*VW*	—	—?	*VW*	?	—	*T*
Fe	*VW*	*W*	*T*	*T*		*VW*	*T*	*T*	*T*	*T*	*T*
Ga			—	—			—		—		—
Ge			—	—			—		—		—
Hf			—	—			—		—		—
Hg			—	—			—		—		—
In			—	—			—		—		—
Ir			—	—			—		—		—
K	—	—	—	—	—	*VS*	*VS*	*VS*	*VS*	*VS*	*W*
Ka			—	—			—		—		—
Li	—	—	*T*	*T*?	*T*	—	—	—	*T*	—	*T*
Mg	—	—	*T*	*T*	*T*	—	*T*	—	*T*	—	*T*
Mn			—	—			—		—		—?
Mo			—	—			—		—		—
Na	*VS*	*VS*	*VS*	*VS*	*VS*	*VW*	*W*	*T*	*W*	*W*	*VS*
Ni			—	—	*T*	—	—		—		*T*
Os			—	—			—		—		—
P			—	—			—		—		—
Pb			—?	—?			—		—		—
Pd			—	—			—		—		—
Pt			—	—			—		—		—
Rb	—	—	—	—	—	—	*T*	—	*T*	—	—?
Rh			—	—			—		—		—
Ru			—	—			—		—		—
Sb			—	—			—		—		—
Sc			—	—			—		*T*		—
Si			*T*	*T*	*VW*		*T*		—		—?
Sn			—	—			—		—		—
Sr	—	—	—	—	—	—	—	—	—	—	—?
Ta			—	—			—		—		—
Te			—	—			—		—		—
Th			—	—			—		—		—
Ti			—	—			—		—		—
Tl			—	—			—		—		—
U			—	—			—		—		—
V			—	—			—		—		—
W			—	—			—		—		—
Y			—	—			—		—		—
Zn			—	—			—		—		—
Zr			—	—			—		—		—

* The terms or symbols used in the above table are as follows Har, Opt, Pil, and Zer, designate respectively, samples of the alkali halide obtained from the Harshaw Chemical Company, the Optovac Chemical Company, the Pilot Chemical Company, and Dr. Samuel Zerfoss of the Naval Research Laboratory, Washington, D. C.; NBS analysis made by the Spectrochemistry Section of the National Bureau of Standards, courtesy of Mr. B. Scribner; NRL analysis made by the Crystal Branch of the Naval Research Laboratory, courtesy of Dr. S. Zerfoss; *VS*—greater than 10 percent; *M*—0.1 to 1.0 percent; *W*—0.01 to 0.1 percent; *VW*—0.001 to 0.01 percent; *T*—0.0001 to 0.001 percent; —not detected.

generally have about the same order of magnitude of impurity content although variation in distribution occurs;

(3) There are considerable variations of the impurity content in samples of the same alkali halide obtained from any one company.

The justification for using these relatively impure crystals in the experiments is that they are the best obtainable at present. In order to produce purer crystals, two problems must be solved. First, exceptionally pure raw material must be obtained and second, the crystal must be grown from this material without introducing impurities. Impurity ions are rejected from the melt during the growth process,[8] but when a degree of purity of 1 part in 10^6 or better is required, injection of impurities from the crucible may occur unless exceptional care is taken to eliminate such contamination. In short, the acquisition of a highly pure crystal is in itself a major problem not fully solved as yet.[9]

The cell used in these experiments has been described elsewhere.[10]

The radiation sources were 50-kv Machlett C-524A molybdenum target x-ray tubes, one having maximum rating of 20 ma and the other 50 ma. The crystal was about 3 cm from the tube window, and the x-rays had to penetrate the beryllium window, 0.05 cm thick, of the cell.

The optical measurements were made on a Beckman Model Du Spectrophotometer adapted to be used with the cell. Before exposing the crystal to x-rays, a blank transmission run was made. The data will be reported in terms of k', which is defined as:

$$k' = \log_{10}(I_0/I),$$

where: I_0 = fraction of light transmitted before x-raying; I = fraction of light transmitted after x-raying. The quantity k' should be proportional to the absorption coefficient. Unfortunately, the depth of the color layer is unknown in these experiments and an absolute value of the absorption coefficient cannot be obtained. If the depth of coloration is assumed to remain constant during the x-raying, k' can be used to obtain the relative concentrations of color centers.[11] At present one can only obtain an order of magnitude of the number of color centers formed at low temperatures by assuming an average depth of coloration from measurements made with a travelling microscope on crystals irradiated at room temperature. Our measurements of this depth give values which are less than those of Dorendorf's.[3]

[8] R. McFee, J. Chem. Phys. **15**, 856 (1947).

[9] The workers at Göttingen assumed that they were dealing with crystals of high purity; the authors, however, do not know of any spectroscopic test of crystals grown in Germany. The purity of the material used to grow the crystals is given in some of the papers, but the impurities introduced in growing the crystals is not known. The Applied Physics Laboratory is presently trying to obtain crystals of higher purities.

[10] W. H. Duerig and I. L. Mador, Rev. Sci. Instr. **23**, 421 (1952).

[11] A. Smakula, Z. Physik **59**, 603 (1930).

TABLE II. Wavelengths of the maximum of various bands observed in NaCl.

Band name	U	V_3	V_2	260	330	V_1	F	F'	R_1	R_2	M
Wavelength, mμ	192[a]	210[b]	223[b]			345[b]	454[c]	510[d]	540[e]	595[e]	710[e]
Temperature	Room	Room	Room	5°K	5°K	80°K	20°K	140°K	90°K	90°K	90°K

[a] R. Hilsch and R. W. Pohl, Nachr. Akad. Wiss. Göttingen, Math.-physik. Kl. 322 (1933).
[b] See reference 2.
[c] See reference 13.
[d] See reference 11.
[e] See reference 14.

EXPERIMENTAL RESULTS

In order to gain an over-all view of the color centers in the alkali halides, a tabular summary will be given of the major known bands (Table II–IV). We shall include the new bands found in this paper. These tables are extensions of summaries given by Ivey.[12] The reference given with each band is not meant to exclude the fact that other workers have observed it, but is intended to be a leading reference. Except for the V_0-band, no letter will be assigned to the new bands reported in this paper. The results and effects observed will be given in detail after each table.

NaCl

Careful measurements have been made on the F-band, so that the peak and half-widths are well known. For NaCl at 20°K, Mollwo[13] presents the following data:

$$\lambda_v = 426\ \text{m}\mu, \quad \lambda_m = 454\ \text{m}\mu, \quad \lambda_r = 482\ \text{m}\mu.$$

λ_m is the wavelength at the peak of the F-band. λ_v is the wavelength on the ultraviolet side of λ_m where $k' = 0.5k'_{max}$ (i.e., at λ_m) and λ_r is the wavelength on the infrared side where $k' = 0.5k'_{max}$. Mollwo's values at 90°K agree with the measurements at 90°K of Molnar.[14] Flechsig[15] has measured at 90°K the F-band produced at room temperature by x-rays in natural and synthetic NaCl. All values of λ_v agree very well; however, Flechsig's value of λ_r(505 mμ) on synthetic crystals disagrees with the one given above.

Figure 1, curve 1, shows the absorption spectrum of a Harshaw NaCl crystal which has been exposed to x-rays (50 kv–48 ma) at 5°K for two hours. The spectrum which is found when the crystal is raised to 78°K after this exposure is also shown in this figure. The following conclusions seem justified:

(1) An F-band comparable in size with those produced at 78°K and higher temperatures appears with the following values:

$$\lambda_v = 426\ \text{m}\mu, \quad \lambda_m = 450\ \text{m}\mu, \quad \lambda_r = 471\ \text{m}\mu.$$

The values of λ_v and λ_m agree with previous measurements, but λ_r disagrees. The difference is too large to be ascribed to experimental error. Four other separate runs also using Harshaw crystals produced spectra substantiating Fig. 1. On three of these, the x-ray tube was run at 50 kv–20 ma and in the other at 50 kv–48 ma. The variation of the λ's between the runs is less than 1 mμ and the average value has been given above.

(2) In Fig. 2, k' is plotted against time of exposure to x-rays. Similar data taken on other runs support these data. This curve should be compared with Harten's[16] data on KCl at higher temperatures.

(3) In NaCl the F'-band is difficult to detect since the F-band overlaps it. In three runs at 20 ma, no indication of an F'-band appeared. The runs at 48 ma, however, indicate a rise on the infrared side of the F-band. This is interpreted as an F'-band which appears when the intensity of x-radiation is high.

(4) The M- and R-bands do not appear.

(5) A broad well-defined band forms at 330 mμ which is not the V_1-band. The V_1-band is produced by x-rays at 78°K and is much narrower (see item 8 below).

(6) A band has been measured at 260 mμ. A second weak band may form at 230 mμ although the data do not establish this band conclusively. This structure appears on large-scale plots of the data and not in Fig. 1.

(7) The data suggest the possibility of a band between the F-band and the 330 mμ-band. The band would correspond to the V_0-band which will be described in KCl.

(8) Heating to 78°K caused the 330 mμ-band to disappear and the narrower V_1-band to appear at 345 mμ. When measured immediately after warming to 78°K, the V_1 absorption maximum is greater than the absorption maximum of the 330 mμ-band. During this

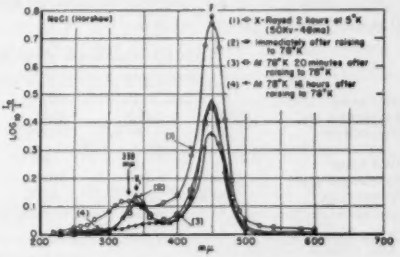

FIG. 1. Effect of x-raying NaCl at 5°K. The effect of warming to 78°K is also shown.

[12] H. F. Ivey, Phys. Rev. **72**, 341 (1947).
[13] The figure for the F-band was taken from a paper of E. Mollwo, Z. Physik **85**, 56 (1933). The authors have been unable to find just how the F-bands were produced. In the paper he used both natural and synthetic crystals. Most probably the centers were produced by additive coloration.
[14] J. P. Molnar, unpublished thesis, Massachusetts Institute of Technology (1940). We would like to thank Dr. Molnar for a copy of his thesis.
[15] W. Flechsig, Z. Physik **36**, 605 (1926).
[16] H. Harten, Z. Physik **126**, 619 (1949).

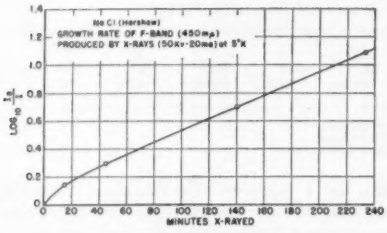

FIG. 2. Plot of the growth of the F-band against time at 5°K.

heating the number of F-centers is reduced to about 60 percent of its previous value at 5°K (curve 2 of Fig. 1).

(9) The effect described in (8) occurs immediately after warming to 78°K and is followed by a gradual bleaching of both the V_1- and F-bands until the V_1-band is gone (curves 3 and 4 of Fig. 1), and the number of F-centers is reduced to about 48 percent of the previous value at 5°K. No further changes occur after this. The percentage changes are estimated with the use of Smakula's formula.[17] The effects of the band width are included.

(10) Warming to 78°K causes a small change in the width of the F-band, i.e.,

$$\lambda_v = 427\ \text{m}\mu, \quad \lambda_m = 451\ \text{m}\mu, \quad \lambda_r = 473\ \text{m}\mu.$$

Crystals x-rayed at 78°K have within our ability to measure them the same values of λ_v and λ_r. Mollwo's values at 90°K are:

$$\lambda_v = 426\ \text{m}\mu, \quad \lambda_m = 455\ \text{m}\mu, \quad \lambda_r = 483\ \text{m}\mu,$$

which disagree with our own values. Molnar's measurements at 90°K on F-centers produced at higher temperatures agree with Mollwo's values. X-raying these same crystals at room temperature gives:

$$\lambda_v = 422\ \text{m}\mu, \quad \lambda_m = 465\ \text{m}\mu, \quad \lambda_r = 506\ \text{m}\mu,$$

which is in excellent agreement with Mollwo's data.

Assuming the color layer in NaCl to be uniform and 0.07 mm thick, and an oscillator strength of 0.7, the F-center density after 4 hours of x-raying at 50 kv and 20 ma is 1.6×10^{18} per cm³ at 5°K.

KCl

As can be observed in Table III the U-band and the V_2-band lie close together. Since we do not know the hydrogen content of the crystals, the V_2-band may be the same as the U-band.

Mollwo's[13] values for the F-band at 28°K are:

$$\lambda_v = 515\ \text{m}\mu, \quad \lambda_m = 540\ \text{m}\mu, \quad \lambda_r = 560\ \text{m}\mu.$$

The value of λ_m and λ_r shift to the infrared with rising temperature, but λ_v is apparently constant below 78°K.

The absorption spectrum of a Harshaw KCl crystal which was exposed to x-rays (50 kv–48 ma) at 5°K is shown in Fig. 3, curve 1. Curve 2 of this figure shows the effect of raising the crystal to 78°K, and curve 3 to room temperature. One other run was made with KCl at 5°K which substantiates the data. The following conclusions appear justified:

(1) An F-band comparable in growth rate with those produced at 78°K and higher temperatures appears with the following values:

$$\lambda_v = 518\ \text{m}\mu, \quad \lambda_m = 540\ \text{m}\mu, \quad \lambda_r = 557\ \text{m}\mu.$$

Unfortunately, only one run was made in which it was possible to obtain the half-width points.

(2) There are no indications of any band structure (F', R_1, R_2, and M) to the infrared side of the F-band.

(3) Two distinct V-bands are formed. The predominant band occurs at about 345 mμ. This band may correspond to the V_1-band which appears at 78°K. This rise, however, shifts with exposure from 355 mμ to 343 mμ. This suggests the possibility of a new band at about 340 mμ which forms at 5°K. Shortly we shall see that this is the case for KBr. The V_0-band appears here as it does at higher temperatures.[g] A very small band is indicated at about 255 mμ which is 20 mμ to the red side of the V_2-band. Our measurements did not extend far enough in the ultraviolet to measure V_3.

(4) On warming to 78°K, the 255 mμ-band apparently disappears and a band at 238 mμ appears, probably the V_3-band, with over twice the maximum absorption of the small 255 mμ-band it replaces. This same band (V_2) occurs when KCl is x-rayed initially at 78°K. Although the above values are only approximate, the authors believe that the difference between 255 mμ

TABLE III. Wavelength of the maximum of the various bands obtained in KCl.

Band name	V_3	V_3	U	V_2	V_4		V_7	V_6	
Wavelength mμ	<200[a]	212[a]	214[b]	230[c]	~254[a]	255	300[a]	334[a]	345
Temperature	90°K	90°K	Room	90°K	90°K	5°K	90°K	90°K	5°K
Band name	V_1	V_0	F	R_1	R_2	F'	M	N	
Wavelength mμ	356[a]	455[c]	540[d]	680[e]	730[e]	750[f]	820[e]	980[e]	
Temperature	90°K	5°K	28°K	Room	Room	170°K	Room	80°K	

[a] See reference 3.

[b] See reference a of Table II.

[c] The V_0-band appears when KCl is x-rayed. It is not in Pick's curves on additively colored KCl crystals at 38°K although there is a band at this wavelength in the curves of F. G. Kleinschrod, Ann. Physik **27**, 97 (1936).

[d] See reference 13.

[e] See reference 14.

[f] See reference 1.

[g] E. Burstein and J. J. Oberly, Phys. Rev. **76**, 1254 (1949).

at room temperature which may be the V_0-band. The value of V_0 was obtained from the present set of measurements.

[17] A. Smakula, Z. Physik **59**, 603 (1930).

and 238 mμ is real. The authors' belief that the V_2-band appears on warming is based on the assumption that a band does not shift to the violet on heating. The V_0- and F-bands are reduced on warming, the F-band to about 45 percent of its value at 5°K. The maximum of the V_0-band shifts about 15 mμ to the red. The structure at 345 mμ (see item 3) bleaches, leaving the V_1-band.

(5) The F-band attains the following values on raising to 78°K:

$$\lambda_v = 516 \text{ m}\mu, \quad \lambda_m = 540 \text{ m}\mu, \quad \lambda_r = 563 \text{ m}\mu.$$

We have x-rayed KCl at 78°K. The values agree with those just given. Casler, Pringsheim, and Yuster's[2] curves give values at 78°K (514 mμ and 563 mμ) in close agreement with our data. There is only a very small variation in the half-width from run to run.

The values of λ_r are considerably less than values obtained by creating the F-band by x-raying at room temperature or heating in the alkali vapor and then cooling to 78°K. Mollwo's values at 90°K are:

$$\lambda_v = 515 \text{ m}\mu, \quad \lambda_m = 548 \text{ m}\mu, \quad \lambda_r = 571 \text{ m}\mu.$$

Molnar's values are in agreement with these values.

The above data seem to indicate that the F-band has a different half-width at 78°K for both NaCl and KCl, depending on whether it was created at high or low temperatures.

(6) Warming to room temperature bleaches the V_0- and V_1-bands and greatly reduces the F-band.

If the colored layer is assumed to be 0.08 mm thick, and the oscillator strength 0.81, the F-center density is 10^{18} per cm^3 after fifteen minutes of x-raying with 50 kv at 20 ma at 5°K.

KBr

From Table IV, the similarity between the U- and the V_3-bands should again be noted. Mollwo[18] obtained three bands at 430 mμ, 270 mμ, and 230 mμ at room temperature by heating KBr in Br vapor. These bands appear to be the V_1-, V_2-, and V_3-bands although considerable work is necessary before this statement can be confirmed.

Mollwo's data taken at 28°K on the F-band for synthetic KBr are:

$$\lambda_v = 570 \text{ m}\mu, \quad \lambda_m = 602 \text{ m}\mu, \quad \lambda_r = 628 \text{ m}\mu.$$

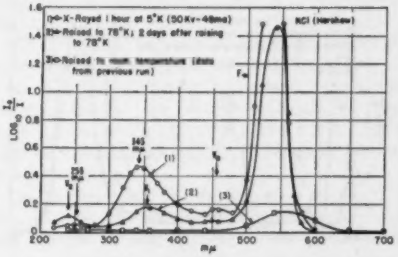

FIG. 3. Effect of x-raying KCl at 5°K. The effects of warming the crystal to 78°K and room temperatures are shown.

Further, λ_v does not change with temperature but λ_m and λ_r shift to the infrared with rising temperatures.

The absorption spectrum of a Harshaw KBr crystal x-rayed at 5°K is given in Fig. 4, curve 1. Curves 2 and 3 of this figure show the effects of raising the crystal to 78°K. The following conclusions appear justified:

(1) A large F-band appears at 5°K. Its growth rate at this temperature is comparable with that at 78°K. Our measurements on the F-band at 5°K give:

$$\lambda_v = 577 \text{ m}\mu, \quad \lambda_m = 601 \text{ m}\mu, \quad \lambda_r = 624 \text{ m}\mu.$$

These figures are an average of two runs. The band is narrower than Mollwo's value at 28°K. The difference between Mollwo's value of λ_v and the one given here seems to be due to the monochromator used. It does not seem to be due to the difference in temperature, since Mollwo's value of λ_v does not change between 28°K and 300°K.

(2) The R- or M-bands do not seem to appear. The F'-band does not appear for an exposure of 20 ma but seems to appear for an exposure of 28 ma for 50 kv x-rays.

(3) There are several bands to the ultraviolet of the F-band. At 230 mμ a band appears. It is well formed although it appears to the infrared side of another very large band (probably the α-band)[4] whose peak is beyond the Beckman range.

A band occurs at 380 mμ which does not correspond to any previously observed bands. We have x-rayed KBr at 78°K and produced a substantial V_1-band at 410 mμ. This band shifts less than 2 mμ on cooling to

TABLE IV. Wavelength of the maximum of various bands observed in KBr.

Band name	β	U'	α	U		V_3	V_2	U''	V_4		V_1
Wavelength, mμ	193[a]	200[b]	202[a]	224[a]	230	231[d]	265[d]	267[b]	275[d]	285	308[d]
Temperature	90°K	80°K	90°K	90°K	5°K	90°K	90°K	80°K	90°K	5°K	90°K
Band name	V_4		V_1	V_0	F	F'	R_1	R_2	M	N	
Wavelength, mμ	362[d]	380	410[d]	530	602[e]	700[f]	730[g]	790[g]	895[g]	1090[h]	
Temperature	90°K	5°K	90°K	5°K	28°K	170°K	90°K	90°K	90°K	Room	

[a] See reference 4.
[b] H. Thomas, Ann. Physik **38**, 600 (1940).
[c] See reference a of Table II.
[d] See reference 3.
[e] See reference 13.
[f] See reference 1.
[g] See reference 14.
[h] J. J. Oberly, Phys. Rev. **84**, 1257 (1951).

[18] E. Mollwo, Ann. Physik **29**, 394 (1937).

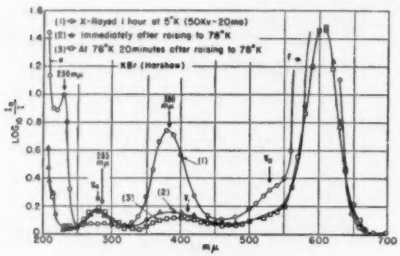

FIG. 4. Effect of x-raying KBr at 5°K. The effect of warming the crystal to 78°K is shown.

5°K and cannot be confused with the 380 mμ-band which forms at 5°K.

A slight rise at 530 mμ to the ultraviolet side of the F-band indicates a structure which may correspond to the V_0-band. This rise appears in additively colored crystals (see Martienssen, reference 4). At 285 mμ a weak band seems to form which is 10 mμ to the infrared of the V_4-band.

To summarize, two well-defined bands are resolved at 230 mμ and at 380 mμ, and one weak band at 285 mμ (V_4). Two other bands, one corresponding to V_0 and one beyond 210 mμ, are indicated to the ultraviolet of the F-band.

(4) On warming to 78°K, the V_0-, 380 mμ-, and F-bands decrease considerably. It cannot be determined whether the band to the ultraviolet of the 230 mμ-band (probably the α-band) changes. The 230 mμ-band bleaches out entirely. The 285 mμ-band seems to disappear and another band forms slightly to the ultraviolet. This new band is probably the V_4-band which by our measurements at 5°K and 78°K peaks at 277 mμ. The effect is much like that discussed above for KCl. The magnitude of the bands is small and this effect is difficult to measure accurately.

(5) A further phenomenon shown in Fig. 5 occurs at 78°K. The broad band at 380 mμ is not stable. Its ultraviolet side bleaches with time. This seems to indicate that the band is composed of two centers, one of which dissociates with time at 78°K. The remaining centers seem to be those associated with the V_1-band. As can be seen in Fig. 4, curves 2 and 3, the F-band continues to bleach with the decay of the 380 mμ-band at 78°K.

(6) The shape of the F-band when warmed to 78°K is close to what we have obtained when KBr is x-rayed initially at 78°K, the values being

$$\lambda_v = 576\ \text{m}\mu, \quad \lambda_m = 604\ \text{m}\mu, \quad \lambda_r = 632\ \text{m}\mu,$$

which again do not agree with Mollwo's values at 90°K, i.e.,

$$\lambda_v = 573\ \text{m}\mu, \quad \lambda_m = 609\ \text{m}\mu, \quad \lambda_r = 639\ \text{m}\mu.$$

Molnar's value does not agree with either set of figures.

(7) A very puzzling effect was observed at 5°K. After obtaining a spectrum, the sample was allowed to remain at that temperature for 4 hours and another spectrum obtained. Following the 4-hour measurement, it was again allowed to stay for another 4 hours and again measured. There was no difference between the spectra taken after the 4- and after the 8-hour period. There was a slight bleaching, however, of the bands to the ultraviolet side of the F-band between the first two measurements. The amount of bleaching to the ultraviolet side of the 380 mμ-band was very small and within the accuracy of our measurements. However, the effects on the F- and 380 mμ-bands seem measurable. It is to be stressed that only one set of measurements has been taken in KBr. However, many points were taken and the results look reliable. Obviously, more measurements are necessary.

If the depth of the color layer is assumed to be 0.06 mm, the number of F-centers produced at 5°K is 10^{18} per cm^3 after 15 minutes of x-raying at 50 kv and 20 ma.

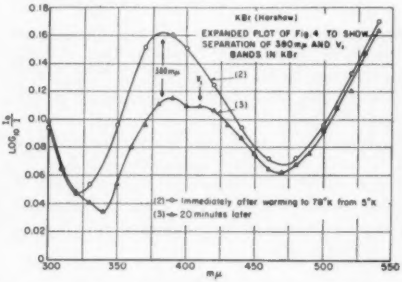

FIG. 5. The effect of time on the 380 mμ-band of KBr. Curve 2 shows the band immediately after warming to 78°K from 5°K. Curve 3 is 20 minutes later. Note the appearance of the V_1-band as the band at 380 mμ fades.

CONCLUSIONS AND DISCUSSION

Since most of the results are preliminary, no attempt to build a model will be made. Further, the impurity content of the crystals is relatively high. We shall attempt to summarize the results as far as possible and suggest lines along which further experiments could be carried out. It is to be stressed that the conclusions presented here are tentative, although the authors have tried as far as possible to report only those data which can be justified.

The general conclusions which apply to all the crystals are:

(1) The impurity content of the commercially available alkali halides is too high to consider the crystals fully suitable for optical work.

(2) The F-band forms easily by x-raying at 5°K. There appears to be a real difference between its shape when formed at low temperatures and when formed at high temperatures but measured at this low temperature.

(3) With the exception of possibly small F'-bands formed after high intensity x-raying in NaCl and KBr, no bands appear to the infrared of the F-band after x-raying at 5°K.

(4) New bands appear to the ultraviolet of the F-band after x-raying at 5°K. On warming to 78°K, these bands bleach, resulting in a reduction of the number of F-centers and the growth of certain of the V-bands normally produced by x-rays at higher temperatures.

The possible future experiments at 5°K are so large that it is difficult to list them. Some suggestions are:

(1) An attempt should be made to obtain very high purity material to use at these temperatures.

(2) Curves showing the rate of growth of the bands with time of x-ray exposure should be very valuable. It would be particularly interesting to see if the past history of the crystal affects the growth-rate curves and what influence the x-ray intensities have.

(3) The optical and photoelectrical properties of the ultraviolet bands should be studied in detail.

(4) It will undoubtedly be necessary for a general understanding of the ultraviolet bands to measure the properties of these crystals between 5°K and 78°K. This will close the gap between Dorendorf's results and those given here.

The authors would like to state their appreciation to Mrs. B. Grisamore for help in taking and computing the data; to Dr. I. Mador for his cooperation in these experiments; to Dr. S. Zerfoss of the Naval Research Laboratory and Mr. B. Scribner of the National Bureau of Standards for analyzing the purity of the crystals; and to Professor F. Seitz for a helpful discussion of the results.

PHYSICAL REVIEW VOLUME 88, NUMBER 5 DECEMBER 1, 1952

The Thermal Resistivity of Superconductors*

D. P. Detwiler† and Henry A. Fairbank
Sloane Physics Laboratory, Yale University New Haven, Connecticut

(Received August 14, 1952)

The thermal resistance of tin, indium, and an alloy of tin with 0.134 percent bismuth have been measured as a function of transverse magnetic field strength from zero to values greater than critical at temperatures below their respective superconducting transition temperatures. Measurements have been carried out on tin at several temperatures and with polycrystalline and single-crystal specimens. In all cases a distinct maximum is found in the intermediate state thermal resistance of the pure metals, while no such anomaly is observed in the alloy. The probable origin of this phenomenon is discussed.

I. INTRODUCTION

In general, at all temperatures below the zero-field superconducting transition temperature, two values are found for the thermal resistivity of a superconductor, one when the specimen is electrically superconducting, and a different one, usually higher, when superconductivity is destroyed by the application of a magnetic field greater than the critical field. This is in qualitative agreement with the assumption that when a metal is in the superconducting state a certain fraction of the conduction electrons are in their lowest energy state and not available for heat transport.

Until recently, very little information was available on the thermal resistivity of superconductors in the intermediate state since most of the measurements had been made on thin cylindrical specimens with the magnetic field applied parallel to the geometrical axis of the cylinder, in which case there is no intermediate state. With the applied magnetic field normal to the axis of the cylinder, it would be reasonable to predice on the basis of the laminar structure of the intermediatt state[1–3] that the intermediate state thermal resistance (for $\frac{1}{2} H_c < H < H_c$ where H_c is the critical magnetic field) would vary linearly with magnetic field between the values characteristic of the superconducting and normal states, respectively, in analogy to the behavior of the electrical resistance.

Mendelssohn and Pontius[4] in 1937 did, indeed, find this intermediate state behavior for a lead-bismuth alloy (10 percent Bi) at about 5°K. However, in 1950, Mendelssohn and Olsen[5,6] made further measurements on niobium and a Pb-Bi alloy (0.1 percent Bi) and found a distinct maximum in the intermediate state resistance. More recently, a similar phenomenon has been reported in pure lead below about 4°K by Webber

* Assisted by the ONR.

† AEC Pre-doctoral Fellow, 1950–1952; now at The Franklin Institute, Philadelphia, Pennsylvania. This material is part of a dissertation presented to the Faculty of the Graduate School of Yale University in partial fulfillment of the requirements for the Ph. D. degree.

[1] L. Landau, J. Phys. (U.S.S.R.) **7**, 99 (1943).
[2] E. R. Andrew, Proc. Roy. Soc. (London) **A194**, 98 (1948).
[3] C. G. Kuper, Phil. Mag. **42**, 961 (1951).
[4] K. Mendelssohn and R. B. Pontius, Phil Mag. **24**, 777 (1937).
[5] K. Mendelssohn and J. L. Olsen, Proc. Phys. Soc. (London) **A63**, 2 (1950).
[6] K. Mendelssohn and J. L. Olsen, Phys. Rev. **80**, 859 (1950).

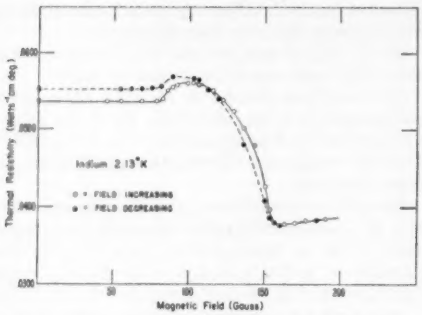

FIG. 1. The thermal resistivity of indium in a transverse magnetic field at 2.13°K.

and Spohr[7] and in tin and indium by the present authors.[8] In this paper we report in greater detail the results on tin and indium, as well as an alloy of tin and bismuth, and discuss the possible explanations of this anomalous behavior.

II. APPARATUS

The standard steady-state temperature gradient method was employed in the thermal resistance determinations. The specimen, a cylinder about 10 cm in length and 4 mm in diameter, was suspended from the top of a highly evacuated brass cavity. An electrical resistance heater, mounted on the lower end of the specimen, served as a heat source. The upper end of the specimen protruded through a sleeve in the top of the cavity into the surrounding helium bath which served as the heat sink. The thermometers used to determine the temperature gradient were two carbon composition resistors placed in thermal contact with the specimen at two points along its length. Rose alloy solder was used for all soldered connections to the specimen, its low melting point minimizing the danger of crystalline damage by overheating.

To permit evacuation of the specimen cavity, it was suspended in the helium bath by a stainless steel tube leading through the flask cap to vacuum gauges and an oil diffusion pump. A valve inserted between the pump and the gauges was closed when the cavity was immersed in helium to prevent back-diffusion of air through the pump. Baffles were placed in the pumping tube immediately above the specimen cavity to prevent room temperature radiation and "hot" gas molecules from impinging on the thermometers. To eliminate heat leakage to the specimen and thermometers by conduction down the electrical leads, these were led through the helium bath and into the specimen cavity via Stupakoff Kovar-glass insulators mounted in the bottom of the cavity. The calculated heat transfer from the specimen to the liquid helium bath through these leads (copper 0.003-inch diameter) was negligibly small compared to that through the specimen in every case.

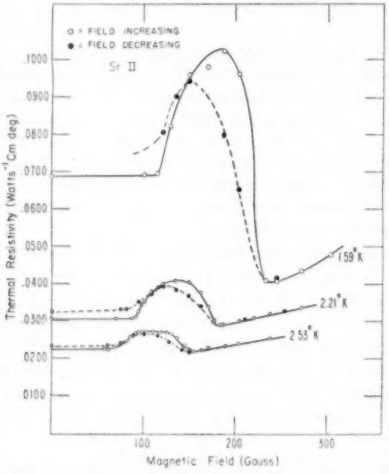

FIG. 2. The thermal resistivity of Sn II in a transverse magnetic field at various temperatures.

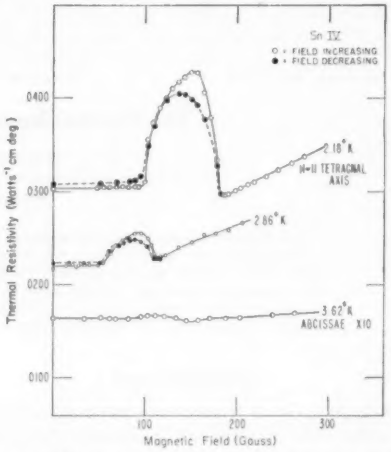

FIG. 3. The thermal resistivity of Sn IV in a transverse magnetic field at various temperatures. The angle between magnetic field and the tetragonal axis of the crystal was approximately 20°.

The thermometer resistances were measured with a bridge circuit, the power input to the resistors being maintained at less than 1 microwatt, and were calibrated against the vapor pressure of the helium bath using the vapor pressure tables of van Dijk and Shoen-

[7] R. T. Webber and D. A. Spohr, Phys. Rev. **84**, 384 (1951).
[8] D. P. Detwiler and H. A. Fairbank, Phys. Rev. **86**, 574 (1952).

berg.[9] Interpolation between the calibrating temperatures was made by fitting the data to an empirical formula of the form suggested by Clement and Quinnell[10] for carbon composition resistors.

III. SPECIMENS AND RESULTS

A. Indium

A rod 2.8 mm in diameter was cast from Johnson Matthey spectroscopically standardized indium, J. M. Lab. No. 3249. The resulting specimen was a single crystal with a number of small surface pits which owing to its softness was somewhat strained in mounting in the apparatus. Consequently, although a ratio of electrical resistance at 0°C to resistance at 4.2°K of 5500 was found, indicating a rather good chemical and physical purity, the thermal resistance values shown in Fig. 1 are no doubt somewhat higher than for a perfect specimen of identical chemical purity.

A definite maximum in the thermal resistance is nevertheless plainly evident in the intermediate state.

B. Tin

Two specimens were prepared from Johnson-Matthey tin, J. M. Lab. No. 2356, with a stated purity of 99.996 percent. The specimen designated Sn II was 4.1 mm in diameter and consisted of several large crystals. The ratio of its electrical resistance at 0°C to that at 4.2°K was 8000. Sn IV was a single crystal, 4.3 mm in diameter, with an electrical resistance ratio of 11,200. In this specimen the tetragonal axis of the crystal lay at an angle of about 70° from the geometric axis.

Figures 2 and 3 show that a strong maximum exists in the intermediate-state thermal resistivity of tin. Although much less pronounced at higher temperatures, the maximum is present at temperatures as little as 0.1°K below the superconducting transition temperature. Sn IV exhibited no dependence of intermediate-state thermal resistance upon orientation of the magnetic field relative to the crystallographic axes in increasing fields, although some dependence upon orientation was observed in the hysteresis and in the magneto-thermal-resistance in fields greater than critical.

The intermediate-state electrical resistance of Sn IV as a function of applied magnetic field is shown in Fig. 4. The close approximation to linearity is in excellent agreement with theoretical predictions[1,3] and magnetization measurements[11] assuming that the fraction of normal resistance attained is equal to the fraction of the specimen converted to the normal state.

C. Tin+0.134 Percent Bismuth

A polycrystalline specimen, prepared of Johnson-Matthey materials and having a diameter of 5.0 mm was also investigated. As shown in Fig. 5, this alloy has a much higher thermal resistance than pure tin. No evidence of a maximum in the intermediate state was found.

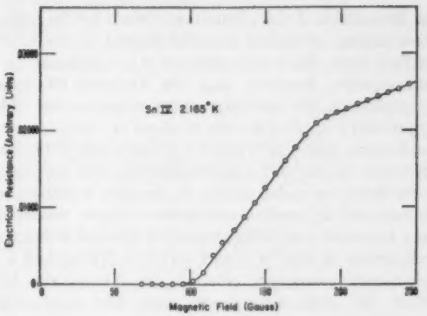

FIG. 4. The electrical resistivity of Sn IV as a function of transverse magnetic field at 2.165°K.

IV. DISCUSSION

Several hypotheses have been offered[7] to explain qualitatively the maximum observed in the intermediate-state thermal resistance. It is not yet possible to state unequivocally which, if any, of these suggestions is correct; however, two of them are open to serious criticism.

The first proposal, due to Mendelssohn and Olsen,[4] postulated a new mechanism of heat transport in the superconducting state in the form of a circulation current of normal and super-electrons, analogous to the heat transport in superfluid helium. The maximum in the intermediate-state resistance is then attributed to

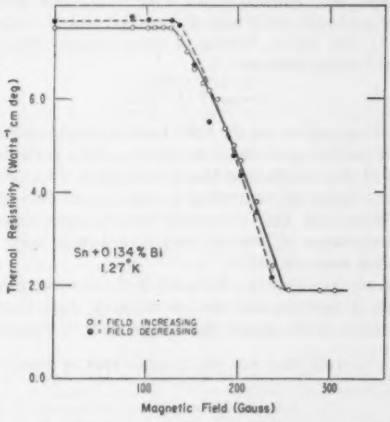

FIG. 5. The thermal resistivity of tin+0.134 percent bismuth in a transverse magnetic field at 1.59°K.

[9] H. van Dijk and D. Shoenberg, Nature **164**, 151 (1949).
[10] J. R. Clement and E. H. Quinnell, Rev. Sci. Instr. **23**, 213 (1952).
[11] M. Desirant and D. Shoenberg, Proc Roy. Soc. (London) **A194**, 63 (1948).

the destruction of this circulation current by the transverse lamina of normal material present in the intermediate state. Since the existance of a circulation current requires, however, that the Meissner effect be incomplete in the specimen under consideration, this hypothesis is applicable only to alloys or "hard" superconductors, and would predict no anomalous thermal resistance in the soft superconductors here reported.

Furthermore, a calculation of the heat transport to be expected by such a circulation current, assuming very favorable conditions, namely a residual resistance comparable to that of a pure metal, a driving emf for the normal component equal to the thermal emf between the pure metals composing the alloy, and the entire cross section of the specimen available for the normal current flow, leads to a figure several orders of magnitude smaller than the observed anomalies.

A second hypothesis[7] is based on Hulm's[12] suggestion that the heat transport by the lattice is important in the superconducting state. It is proposed that as the specimen enters the intermediate state the scattering of lattice waves by electrons increases rapidly, thus reducing the heat transport by the lattice, while the heat transport by the electrons increases initially more slowly, thus leading to a maximum in the total resistance. This implies that the intermediate state is distinguished from the normal and superconducting states by having a normal electron density differing from either of these states. While such is undoubtedly the case on the average throughout the specimen, it is not true for any particular region. According to the present understanding of the intermediate state in a long, thin cylinder,[1,3] the structure consists of laminae, alternately normal and superconducting, perpendicular to the specimen axis. A heat current flowing parallel to the specimen axis, then, may be considered to flow through a group of thermal resistances in series, these having alternately the resistance of a normal and of a superconducting region, leading to the conclusion that the total thermal resistance is

$$\omega = \alpha\omega_n + (1-\alpha)\omega_s, \qquad (1)$$

where ω_n and ω_s are the resistances in the normal and superconducting states, respectively, and α is the fraction of the specimen in the normal state. This clearly gives a linear dependence of ω upon α, and thus, also, according to the intermediate-state magnetization measurements of Desirant and Shoenberg,[11] upon the applied magnetic field.

If we are to accept this picture of the intermediate state, it appears that the anomalously high thermal resistance in the intermediate state must be associated with some new resistance mechanism not present in either the superconducting or the normal states. It seems reasonable to assume that the scattering of either electrons[7] or lattice waves[13] at the superconducting-normal region boundaries gives rise to this additional intermediate-state resistance. One would not expect this boundary scattering resistance to be significant in specimens where the phonon or electron mean free paths due to other scattering mechanisms are short compared to the distance between boundaries; hence it is not surprising that in our Sn-Bi alloy specimen the impurity scattering masks any such boundary scattering and the thermal resistance does, indeed, approximate Eq. (1).

The drastic reduction in the density of normal electrons in the superconducting state at temperatures appreciably below the transition temperature indicates that, since in this temperature region the conduction electrons are the chief scattering mechanism for phonons in a metal,[14] the heat transport by the lattice should be much greater in the superconducting than in the normal state. At sufficiently low temperatures, the thermal resistance in the superconducting state should then be similar to that of an insulating crystal. de Haas and Biermasz[15] have shown that insulating crystals may have in this temperature region thermal conductivities of several watts cm^{-1} deg^{-1}, so in superconducting metals it appears likely that a comparable lattice conductivity should be present in parallel with the residual electronic conductivity.

The measurements of de Haas and Biermasz indicate that a phonon mean free path of several millimeters is associated with such values of heat transport. Comparing this figure with the value of 0.1 mm found by Andrew[16] for the mean free path of an electron in tin at 4.2°K and the separation of about 0.1 mm of the normal-superconducting boundaries, it appears likely that the observed intermediate-state resistance maximum is due to scattering of phonons at the boundaries.

Clearly, however, it is premature to claim any explanation as final until more quantitative data is available. Further study of the dependence of the anomalous resistance upon specimen dimensions and impurity concentration would be particularly useful.

We are indebted to the other members of the Yale University low temperature group for assistance in acquiring this data, and particularly to Dr. G. B. Yntema, who generously loaned the apparatus used in the electrical resistance measurements.

[12] J. K. Hulm, Proc. Roy. Soc. (London) **A204**, 98 (1950).

[13] R. T. Webber and J. K. Hulm, private communication.

[14] R. E. B. Makinson, Proc. Cambridge Phil. Soc. **34**, 474 (1938).

[15] W. J. de Haas and Th. Biermasz, Physica **5**, 47, 320, 619 (1938).

[16] E. R. Andrew, Proc. Roy. Soc. (London) **A194**, 80 (1948).

Pseudoscalar Mesons with Applications to Meson-Nucleon Scattering and Photoproduction*

S. D. DRELL† AND E. M. HENLEY‡
Stanford University, Stanford, California
(Received August 22, 1952)

The scattering of π^+ and π^- mesons by protons and the production of π^+ mesons by gamma-rays incident on protons are studied with the quantized theory of pseudoscalar mesons with pseudoscalar coupling. The Dyson transformation is applied to the Hamiltonian to yield a new representation in which the velocity-independent aspects of the nucleon dynamics are more readily identified. A large "core" term appears in the meson-nucleon interaction in this representation and is incorporated into the zero-order Hamiltonian. The remaining interaction terms are treated perturbation-wise or according to the Heitler damping procedure. It is found that even after separating out the large core term, this method of approach fails to give agreement between theory and experiment. It does, however, improve on the results of the straight perturbation approximation and brings the theory in closer accord with the observations. It is suggested that a direct test of the role of the "core" term is possible in the process of double meson production by gamma-rays incident on protons.

I. INTRODUCTION

THERE are but a very few physical processes that are both measurable and sufficiently simple from the point of view of meson theory that one can avoid phenomenological methods, and, using only the Yukawa field equations, attempt to correlate the theory with the experimental data. It is important to study these processes and to attempt to uncover what, if any, aspects of the present field theory formalism can be used in establishing a quantitative check between theory and experiment. Perhaps characteristic discrepancies will be useful in pointing the way to appropriate modification of the theory.

In this paper we study the scattering of π^+ and π^- mesons by protons and the production of π^+ mesons by gamma-rays incident on protons. The quantized pseudoscalar meson and Dirac nucleon fields are assumed to interact by means of the nonderivative pseudoscalar coupling. Results obtained on the basis of a derivative pseudovector meson-nucleon interaction are compared. Perturbation calculations of the scattering and photoproduction cross sections assuming weak coupling between the meson and nucleons have already been given,[1] and they do not fit the experimental data. The aim of the present work is to narrow the gap between theory and experiment by going beyond the perturbation approximation rather than by adopting a phenomenological approach.

We apply the Dyson[2] transformation to the Hamiltonian for pseudoscalar mesons with pseudoscalar coupling. This yields a new representation in which the velocity-independent aspects of the nucleon dynamics are more readily identified.[3] The meson-nucleon interaction as described in the transformed Hamiltonian can be separated into one large term suggestive of a repulsive short-range core interaction between the mesons and nucleons plus other terms, one of which is the usual derivative coupling form. The large core term is incorporated into the zero-order Hamiltonian, and the remaining interaction terms are treated perturbation-wise or according to the Heitler damping procedure. It is found that even after separating out the large core term, a perturbation approach to the remaining portion of the meson-nucleon interaction fails to give agreement between theory and experiment.[4] With this method of approach it does prove possible, however, to improve on the straight perturbation approximation results in the pseudoscalar theory and to bring the theoretical results closer to the observations. We are encouraged to believe that the quantized field theory of charge-symmetric pseudoscalar mesons with pseudoscalar coupling to Dirac nucleons may prove fully adequate for quantitative analysis of elementary π-meson and single nucleon interactions when suitable methods for calculating in the intermediate coupling region are developed.

II. HAMILTONIAN

We treat the mesons as elements of a charge-symmetric pseudoscalar field. This choice is suggested by recent data and analyses of meson interactions with nucleons and deuterons.[5] We assume that the neutrons and protons (nucleons) represent the two charge states of a Dirac spinor field. The meson and nucleon fields are taken to interact by means of the nonderivative pseudoscalar coupling. Ward, Matthews, and Salam[6] have shown that this form of coupling has the advantage of yielding a theory that is renormalizable in the sense of Tomonaga, Schwinger, Feynman, and

* Assisted in part by the joint program of the ONR and AEC.
† Now at Physics Department, Massachusetts Institute of Technology, Cambridge, Massachusetts.
‡ Now at Physics Department, Columbia University, New York, New York.
[1] References to the literature will be given in the following.
[2] F. J. Dyson, Phys. Rev. **73**, 929 (1948).
[3] L. L. Foldy, Phys. Rev. **84**, 168 (1951) and private communication. Foldy has recently developed a somewhat different transformation to a representation with similar features to the one we discuss here. See also G. Wentzel [Phys. Rev. **86**, 802 (1952)] for a brief discussion of this transformation and its application.
[4] See conclusion in letter by G. Wentzel mentioned in reference 3.
[5] R. E. Marshak, Revs. Modern Phys. **23**, 137 (1951).
[6] P. T. Matthews and A. Salam, Revs. Modern Phys. **23**, 311 (1951).

Dyson. On the other hand, it is known that the derivative (pseudovector) coupling form gives a nonrenormalizable theory.

Including interactions with the electromagnetic field, the Hamiltonian is thus written as ($\hbar=c=1$):

$$H=H_0+H_f+H_e;$$

$$H_0=\tfrac{1}{2}\sum_{\alpha=1}^{3}\int(\pi_\alpha^2+|\nabla\phi_\alpha|^2+\mu^2\phi_\alpha^2)d\mathbf{r}$$
$$+\int\bar{\psi}(\gamma\cdot\nabla+M)\psi d\mathbf{r}+\frac{1}{2}\int(\mathfrak{E}^2+\mathfrak{H}^2)d\mathbf{r},$$

$$H_f=if\sum_{\alpha=1}^{3}\int\bar{\psi}\gamma_5\tau_\alpha\phi_\alpha\psi d\mathbf{r}, \tag{1}$$

$$H_e=-e\int[\mathbf{A}\cdot(\phi_2\nabla\phi_1-\phi_1\nabla\phi_2)-\Phi(\pi_2\phi_1-\pi_1\phi_2)]d\mathbf{r}$$
$$+e\int\bar{\psi}\tau_P(-i\gamma\cdot\mathbf{A}+\gamma_4\Phi)\psi d\mathbf{r}$$
$$+e^2/2\int A^2(\phi_1^2+\phi_2^2)d\mathbf{r}.$$

M and μ are the nucleon and meson masses, respectively; f and e represent the meson and electromagnetic (for positive charge) coupling constants; ψ and $\bar{\psi}=\psi^*\gamma_4$ are the quantized nucleon field amplitudes (ψ^* is the Hermitian conjugate of ψ); π_α and ϕ_α, with $\alpha=1, 2, 3$, are the conjugate momenta and amplitudes of the charge symmetric meson field; $\mathbf{A}$ and Φ are the vector and scalar potentials of the electromagnetic field, related to the field strengths by $\mathfrak{H}=\operatorname{curl}\mathbf{A}$, $\mathfrak{E}=-\operatorname{grad}\Phi-\partial\mathbf{A}/\partial t$; $\gamma=i\alpha\beta$, $\gamma_4=\beta$, $\gamma_5=\gamma_1\gamma_2\gamma_3\gamma_4$ are the usual Dirac spinors; τ_α, $\tau_P=(1+\tau_3)/2$ are, similarly, the two by two isotopic spin (charge) matrices. The nonvanishing commutation relations in the Schrödinger representation for the field amplitudes are

$$[\pi_\alpha(\mathbf{r}),\phi_\beta(\mathbf{r}')]=-i\delta_{\alpha\beta}\delta(\mathbf{r}-\mathbf{r}'),$$
$$[\mathfrak{E}_i(\mathbf{r}),\mathfrak{H}_{jk}(\mathbf{r}')]=i(\delta_{ij}\partial/\partial x_k-\delta_{ik}\partial/\partial x_j)\delta(\mathbf{r}-\mathbf{r}'), \tag{2}$$
$$[\psi_\mu^*(\mathbf{r}),\psi_\nu(\mathbf{r}')]_+=\delta_{\mu\nu}\delta(\mathbf{r}-\mathbf{r}'),$$

where μ and ν specify different spin and charge solutions of the Dirac equations.

The Schrödinger equation reads

$$i\partial\Omega/\partial t=H\Omega, \tag{3}$$

where Ω is the functional specifying the state of the fields. We proceed now by making a canonical transformation to a representation in which the velocity-independent aspects of the nucleon motion are more readily identified. By means of a time independent canonical transformation,

$$\Omega=\exp(-iS)\Psi, \tag{4}$$

Eq. (3) becomes

$$i\partial\Psi/\partial t=\exp(iS)H\exp(-iS)\Psi$$
$$=(H+i[S,H]+i^2/2![S,[S,H]]$$
$$+i^3/3![S,[S,[S,H]]]+\cdots)\Psi. \tag{5}$$

We choose S to be[7]

$$S=f/2M\int\bar{\psi}\gamma_4\gamma_5\tau\cdot\phi\psi d\mathbf{r}. \tag{6}$$

This is the canonical transformation suggested by Dyson[2] in demonstrating the equivalence of pseudoscalar and pseudovector coupling forms through the first order in f and used more recently by Lepore[8] in discussing higher order processes. The repeated commutators of Eq. (5) may be summed exactly with the above choice of S to give, with $\sigma_i=-\gamma_5\alpha_i(i=1, 2, 3)$,

$$H'=\exp(iS)H\exp(-iS)=H_0+H_e$$
$$+\frac{f}{2M}\int\psi^*[(\sigma_i\nabla_i\phi-\gamma_5\pi)\cdot\tau-e\sigma A_i(\tau\times\phi)_3]\psi d\mathbf{r}$$
$$+M\int\psi^*\gamma_4\left[\left(1+i\frac{f}{M}\gamma_5\tau\cdot\phi\right)\right.$$
$$\left.\times\exp[-i(f/M)\gamma_5\tau\cdot\phi]-1\right]\psi d\mathbf{r}$$
$$+\left(\frac{f}{2M}\right)^2\int\psi^*\gamma_5\left[\tfrac{1}{2}(\sigma_i\nabla_i\phi-\gamma_5\pi)\cdot\phi\times\tau\frac{\sin^2\chi}{\chi^2}\right.$$
$$+\frac{1}{2}\frac{\sin^2\chi}{\chi^2}(\sigma_i\nabla_i\phi-\gamma_5\pi)\cdot\phi\times\tau$$
$$\left.-e\sigma_i A_i(\phi\times(\tau\times\phi))_3\frac{\sin^2\chi}{\chi^2}\right]\psi d\mathbf{r}+\frac{2}{3}\left(\frac{f}{2M}\right)^3$$
$$\times\int\psi^*\left[\tfrac{1}{2}(\sigma_i\nabla_i\phi-\gamma_5\pi)\times\phi\cdot\phi\times\tau\frac{2\chi-\sin 2\chi}{4\chi^3/3}\right.$$
$$+\frac{1}{2}\frac{2\chi-\sin 2\chi}{4\chi^3/3}\phi\times\tau\cdot(\sigma_i\nabla_i\phi-\gamma_5\pi)\times\phi$$
$$\left.-e\sigma_i A_i\phi^2(\phi\times\tau)_3\frac{2\chi-\sin 2\chi}{4\chi^3/3}\right]\psi d\mathbf{r}$$
$$+\frac{1}{2}\left(\frac{f}{2M}\right)^2\int|\psi^*\gamma_5\tau\psi|^2 d\mathbf{r}-\frac{2}{3}\left(\frac{f}{2M}\right)^4$$
$$\times\int|\psi^*\gamma_5\tau\times\phi\psi|^2\frac{\chi^2-\sin^2\chi\cos^2\chi}{4\chi^4/3}d\mathbf{r}$$
$$+\frac{1}{2}\left(\frac{f}{2M}\right)^4\int|\psi^*\tau\times\phi\psi|^2\frac{\sin^4\chi}{\chi^4}d\mathbf{r}$$
$$+\frac{1}{2}\left(\frac{f}{2M}\right)^2\int(\psi^*\tau\psi\cdot\psi^*\gamma_5\tau\times\phi\psi$$
$$-\psi^*\gamma_5\tau\psi\cdot\psi^*\tau\times\phi\psi)\frac{\sin^2\chi\cos\chi}{\chi^2}d\mathbf{r}, \tag{7}$$

[7] In the following we apply vector notation in isotopic spin space and use component notation for ordinary space vectors.

[8] J. V. Lepore, Phys. Rev. 87, 209 (1952). The interaction representation is used in this work. We stay in the Schrödinger representation here, since we do not make a straight perturbation expansion.

where $\chi=(f/2M)\tau\cdot\phi$, and expansions of all factors which involve χ contain only χ^{2n}, with n an integer and $\chi^2=(f/2M)^2\phi^2$. The transformed Hamiltonian H' can be analyzed to show where perturbation calculations may be expected to be valid and for what processes the pseudoscalar and pseudovector coupling theories will yield different results. In Eq. (7) H_0 and H_s are the same expressions as in Eq. (1) for the uncoupled fields and their electromagnetic interactions. The third term, which we denote hereafter as H_{ps}, is the usual derivative coupling form of the meson-nucleon Hamiltonian and shows the equivalence of the two couplings in the pseudoscalar theory through terms of first order in the coupling constant. The coupling constant g normally used for the derivative interaction is related to the constant f used here by

$$g/\mu=f/2M. \tag{8}$$

An expansion of the fourth term in H', hereafter referred to as H_c, in powers of f, gives to leading order

$$(f^2/2M)\int\bar{\psi}\psi\phi^2d\mathbf{r}. \tag{9}$$

This expression is analogous to the quadratic term, $(e^2/2m)A^2$, in the vector potential that appears in a two-component reduction of the Dirac equation.[9] The importance of this term has been recognized and emphasized in the analysis of the nucleon-nucleon interaction problem.[8,10,11] Even in a perturbation expansion in powers of f it has been shown to give a large spin independent contribution to nuclear forces. The relative importance of this term may be understood by inspection of Eq. (7). The H_c term is proportional to the large nucleon mass M, whereas M appears in other terms there describing the meson-nucleon interaction only in the combination (f/M). Also the characteristic length associated with the meson field is $1/\mu$, and we may expect the other terms in H' to be reduced relative to H_c by various powers of the ratio $\mu/M\cong0.15$.

In the elastic scattering of very low energy mesons by nucleons, matrix elements of Eq. (9) are known to give the dominant contribution in a perturbation calculation. This explains much of the difference in scattering cross sections between the pseudoscalar and pseudovector coupling theories as calculated by Ashkin, Simon, and Marshak.[12] The contribution of the quadratic term, Eq. (9), is analogous to the Thomson scattering of light by charged particles in the low energy limit. Since nucleon recoil may be neglected at low energies, Eq. (9) may be written as

$$(f^2/2M)\int K(\mathbf{r}-\mathbf{r}_N)\phi^2d\mathbf{r}, \tag{10}$$

where $\int K(\mathbf{r}-\mathbf{r}_N)d\mathbf{r}=1$ represents a fixed nucleon "source" at $\mathbf{r}_N$. The form and sign of Eq. (10) suggest a short-range interaction of mesons with a repulsive nucleon core. Indeed, we note that Eq. (10), together with the mass term, $\frac{1}{2}\mu^2\int\phi^2d\mathbf{r}$ of the meson self-field can be interpreted as giving the meson an effective mass $\mu'=(\mu^2+f^2K(\mathbf{r}-\mathbf{r}_N)/M)^{\frac{1}{2}}$ inside the nucleon source. For a constant source of radius equal to a nucleon Compton wavelength $1/M$, this gives

$$\mu'=\mu(1+3(f^2/4\pi)(M/\mu)^2)^{\frac{1}{2}}. \tag{11}$$

An analogous result has been obtained by Schiff[13] in his nonlinear meson theory. The nonlinearity in the meson equations was observed there to give rise to a strong short-range repulsion between nuclear matter and small amplitude meson waves in the vicinity. In order to estimate the effect of the mass change due to the core, we may tentatively assign a value to $f^2/4\pi$ of the order of 7,[14] as suggested by perturbation calculations of the anomalous magnetic moment of the neutron[15] and of the nucleon-nucleon interaction.[16] The effective mass of the meson interacting with the nucleon source thus appears to be approximately 30μ. It increases for smaller source radii. For a large source radius, of the order of $5/2M$, as suggested by Lévy[11] and Jastrow,[17] the effective mass is still approximately 8μ. These surprisingly large results for μ' suggest two things: (a) It is exceedingly dangerous to attempt to draw any conclusions from meson theoretic calculations based on a perturbation expansion in powers of f, and (b) it is necessary to consider the terms of higher order in f in H_c.

The fifth and sixth terms in Eq. (7) (we denote the fifth term by H_s hereafter) are given in a form that exhibits both their relation to H_{ps} and their invariance under a gauge transformation of the electromagnetic potentials. This latter property is seen to follow directly from the usual gauge invariant prescription

$$\nabla\phi_1\rightarrow\nabla\phi_1-e\mathbf{A}\phi_2,$$
$$\nabla\phi_2\rightarrow\nabla\phi_2+e\mathbf{A}\phi_1,$$
$$\nabla\phi_3\rightarrow\nabla\phi_3,$$

with which the potentials are introduced into a Hamiltonian theory. The trigonometric factors that multiply

[9] L. I. Schiff, *Quantum Mechanics* (McGraw-Hill Book Company, Inc., New York, 1949), p. 317.
[10] R. P. Feynman, hectographed notes of lectures at California Institute of Technology on "High Energy Phenomena and Meson Theories," January (1951), unpublished.
[11] M. M. Lévy, Phys. Rev. **86**, 806 (1952).
[12] Ashkin, Simon, and Marshak, Prog. Theor. Phys. **5**, 634 (1950). See also M. Peshkin, Phys. Rev. **81**, 425 (1951).
[13] L. I. Schiff, Phys. Rev. **84**, 1 (1951); see also L. L. Foldy, reference 3.
[14] By Eq. (8) this corresponds to a $g^2/4\pi\sim0.04$.
[15] J. M. Luttinger, Helv. Phys. Acta **21**, 483 (1948); M. Slotnick and W. Heitler, Phys. Rev. **75**, 1645 (1949); K. M. Case, Phys. Rev. **76**, 1 (1949); S. D. Drell, Phys. Rev. **76**, 427 (1949); L. L. Foldy, Phys. Rev. **83**, 688 (1951); B. D. Fried, Phys. Rev. **86**, 434 (1952).
[16] K. M. Watson and J. V. Lepore, Phys. Rev. **76**, 1157 (1949).
[17] R. Jastrow, Phys. Rev. **81**, 636 (1951); **87**, 209 (1952).

these terms in Eq. (7) reduce to unity in the weak coupling limit, $\chi \ll 1$, but are much smaller than one for larger values of χ (or of the coupling constant f), decreasing at least as $1/\chi^2$ for χ larger than one. The fifth term H_τ contributes to the matrix elements of order f^2 in a perturbation calculation of meson-nucleon scattering. The seventh term in Eq. (7) has the form of a nucleon-nucleon direct interaction and will not operate in the processes with which this paper is concerned.[18] The remaining terms in the Hamiltonian, expressed in the form of Eq. (7), are quadratic in the bilinear form $(\bar{\psi}O\psi)$, where O is any operator, and involve only f^3 and higher powers of the coupling constant. If the meson-nucleon interaction is weak and the perturbation procedure of expanding in powers of f is valid, then these higher order terms may be expected to add only a minor contribution, relative to H_{pv} and H_c, to matrix elements for elementary processes such as meson-nucleon scattering and photoproduction of mesons. In this weak coupling limit all the trigonometric factors, such as $(\chi^2-\cos^2\chi \sin^2\chi)3/4\chi^4$, approach unity. If, on the other hand, we go to the strong coupling limit of large f, these trigonometric factors may be expected to be considerably reduced, the one exhibited above decreasing as $1/\chi^2$. However, since these terms are seen to be proportional to a high power of f, it is difficult to estimate their relative importance in the Hamiltonian when the weak coupling approximation breaks down. We have no methods at present that permit a complete study of them in the form in which they are displayed in Eq. (7).

From the Hamiltonian in the form of Eq. (7), one can see which basic processes will have identical or different matrix elements in a lowest order perturbation treatment of the pseudoscalar and derivative coupling forms. As mentioned above, the quadratic term [Eq. (9)] resulting from a reduction of the series H_c in Eq. (7) contributes to the matrix elements of order f^2 for the elastic scattering of mesons by nucleons only for a pseudoscalar coupling theory, as does H_τ. They are not present in the usual derivative coupling theory. For photoproduction of mesons by gamma-rays incident on protons, and two coupling forms are identical to order ef in the matrix elements.[19] In the calculation of the anomalous magnetic moments of nucleons the matrix elements of order ef^2 are identical for both coupling forms.[20] However, the matrix elements of this order for the electron-neutron interaction differ for the two types of coupling and converge only in the pseudoscalar coupling theory in virtue of the H_τ term in Eq. (7).[21]

We have seen that the leading order contribution [Eq. (9)] in the expansion of H_c is quite large. We are thus motivated to study the higher order terms. An attempt to estimate their contribution in the nonrelativistic limit is developed as follows. We separate H_c of Eq. (7) into terms proportional to even and odd powers of f. The even terms contain $\gamma_5^2=1$ and $\tau_z^2=1$ and thus may be written, as in Eq. (10), as an interaction of mesons with a classical nucleon source density in the limit of a nonrelativistic treatment of the nucleons. The odd terms (f^3 is the lowest order of the coupling constant that appears), on the other hand, are proportional to γ_5, which has matrix elements between positive energy nucleon states of order $|v_N| \ll 1$. Neglecting the odd terms in our approximation, we write

$$H_c \approx M \int K(\mathbf{r}-\mathbf{r}_N)\{\cos 2\chi + 2\chi \sin 2\chi - 1\} d\mathbf{r}. \quad (12)$$

The matrix element of Eq. (12) for meson scattering and pair creation or annihilation can be evaluated by the methods of Glauber.[22] We obtain, in the notation of Glauber,

$$\begin{aligned}\langle H_c\rangle_2 &= M \int K(\mathbf{r}-\mathbf{r}_N)\langle \cos 2\chi + 2\chi \sin 2\chi - 1\rangle_2 d\mathbf{r}, \\ &= M \int K(\mathbf{r}-\mathbf{r}_N)(f^2/2M^2)\langle \phi^2\rangle_2 \\ &\qquad \langle \cos 2\chi - 2\chi \sin 2\chi\rangle_0 d\mathbf{r}, \\ &= M \int K(\mathbf{r}-\mathbf{r}_N)(f^2/2M^2)\langle \phi^2\rangle_2 \\ &\quad \times [1-(f^2/M^2)\langle \phi^2\rangle_0] \exp[-(f^2/2M^2)\langle \phi^2\rangle_0] d\mathbf{r}. \quad (13)\end{aligned}$$

Since nucleon recoil has been neglected, we use a maximum meson momentum cutoff of $k_m \approx M$ in evaluating $\langle \phi^2\rangle_0$, obtaining $3M^2/8\pi^2$. This gives

$$\begin{aligned}\langle H_c\rangle_2 &= (f^2/2M) \int K(\mathbf{r}-\mathbf{r}_N)\langle \phi^2\rangle_2 d\mathbf{r} \\ &\quad \times [1-(3/2\pi)f^2/4\pi] \exp[-(3/4\pi)f^2/4\pi]. \quad (14)\end{aligned}$$

If we compare Eqs. (10) and (14), we see that the higher order terms are responsible for a reduction of roughly

$$[1-(3/2\pi)f^2/4\pi] \exp[-(3/4\pi)f^2/4\pi]. \quad (15)$$

This reduction factor is plotted in Fig. 1. It vanishes at $f^2/4\pi = 2.1$. For $f^2/4\pi = 7$ it is equal to -0.44; the minus sign indicates that the interaction is one of attraction, in contrast to the repulsive core result indicated by Eq. (10). For a maximum momentum cutoff of $k_m = 2M/5$, corresponding to a larger core radius,[11,17] the reduction factor is equal to $+0.38$.

[18] Such terms are discussed by R. K. Osborn, Phys. Rev. **86**, 370 (1952).

[19] B. Araki, Prog. Theor. Phys. **5**, 507 (1950); K. M. Case, Phys. Rev. **76**, 14 (1949).

[20] B. D. Fried, Ph.D. thesis, University of Chicago, Department of Physics, June (1952), unpublished.

[21] The terms H_τ and H_{pv} give individually diverging contributions to the matrix elements of order ef^2 describing the electron-neutron interaction. It is only their sum that converges in this order of a perturbation calculation to the pseudoscalar result. See also B. D. Fried, Phys. Rev. **88**, 1152 (1952), and reference 20.

[22] R. J. Glauber, Phys. Rev. **84**, 395 (1951).

If we treat H_c in Eq. (12) as a self-energy term and calculate its vacuum expectation value, we obtain by the same methods a reduction

$$[(3/4\pi)f^2/4\pi]^{-1}\{[1+(3/2\pi)f^2/4\pi]\times\exp[-(3/4\pi)f^2/4\pi]-1\}, \quad (16)$$

owing to the higher order terms. This factor is also plotted in Fig. 1 for comparison with Eq. (15).

In view of the fact that only the first-order scattering matrix element is evaluated in Eq. (14) and that the effect of nucleon recoil, neglected in this procedure, is simulated by a maximum momentum cutoff $k_m \approx M$, we can draw only qualitative suggestions from this calculation. Clearly, for values of $f^2/4\pi$ as large as those quoted above, the entire S matrix, must be studied and the renormalization techniques employed. However, it is immediately obvious that the power series expansion from which Eqs. (10) and (11) are derived is not to be trusted. Only for small effective values of χ can the trigonometric factors $\cos 2\chi + 2\chi \sin 2\chi - 1$ in Eq. (12) be approximated by $2\chi^2$. For larger values of χ, this factor oscillates with period 2π and increases in amplitude in proportion to χ. Also, unless the effective value of χ is much smaller than unity, a perturbation calculation is, at best, of questionable validity. We see from Eq. (15) that for scattering, it is necessary that $f^2/4\pi < 1.0$ for perturbation methods to be applicable.

We make here the basic assumption that will guide our treatment of H_c in the following sections of this paper. In studying the elastic scattering of mesons by nucleons and meson photoproduction in energy ranges which admit a nonrelativistic description of the nucleon source, we replace H_c of Eq. (7) by

$$\lambda(f^2/2M)\int \bar{\psi}\psi\phi^2 d\tau, \quad (17)$$

with λ a constant of magnitude less than one, whose value remains to be specified. For positive (negative) values of λ, Eq. (17) corresponds to a repulsive (attractive) short-range meson-nucleon interaction. The "constant" λ in general may have different values depending on the manner in which Eq. (17) operates in various processes. Thus, the two reduction factors in Eqs. (15) and (16), plotted in Fig. 1, apply when H_c is treated as a scattering and self-energy term, respectively. However, in applying the Hamiltonian in Eq. (7) to scattering and photoproduction in the following paragraphs, we shall be able to deduce only that the predictions of the pseudoscalar meson theory suggest qualitatively some features of the observed cross sections when $\lambda < 1$ is introduced into the core term H_c.

We take as a working Hamiltonian with which to discuss current accelerator experiments on meson scattering and photoproduction from nucleons,

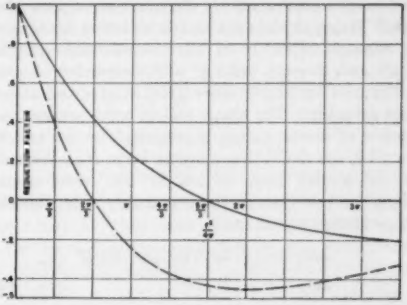

FIG. 1. Reduction in the core term due to higher order contributions plotted *vs* $f^2/4\pi$. The dashed curve represents the factor in Eq. (15) expressing the reduction for a scattering or pair process. The solid curve represents the factor in Eq. (16) for the reduction in the self-energy.

$$H = H_0 + H_c + f/2M \int \psi^*[\sigma_i \nabla_i \phi \cdot \tau - e\sigma_i A_i(\tau \times \phi)_3]\psi d\tau$$

$$+\lambda f^2/2M \int \bar{\psi}\psi\phi^2 d\tau + (f/2M)^2 \int \psi^* \pi \cdot \tau \times \phi \psi d\tau. \quad (18)$$

Terms proportional to the nucleon velocity are neglected since their contributions are small compared to the effects we are interested in studying.

III. ELASTIC SCATTERING

We consider in this section the elastic scattering of mesons by protons. The following three processes have been investigated at Columbia[23] and Chicago[24–27]

$$P+\pi^+ \rightarrow P+\pi^+ \quad \text{(a)},$$
$$P+\pi^- \rightarrow P+\pi^- \quad \text{(b)}, \quad (19)$$
$$P+\pi^- \rightarrow N+\pi^0 \quad \text{(c)}.$$

The observations on the angular and energy dependence of the cross sections for these processes are shown in references 26 and 27.

Theoretical interpretation of these curves has succeeded only when phenomenology has been used. Brueckner[28] has interpreted the results in terms of nucleon isobars, and the Chicago group in terms of scattering phase shifts.[27] Our aim here is to see to what extent a straight meson field theoretic approach succeeds in fitting the data.

Perturbation calculations fail to predict the observed behavior. A thorough relativistic treatment of this

[23] Isaacs, Sachs, and Steinberger, Phys. Rev. 85, 803 (1952).
[24] Anderson, Fermi, Long, Martin, and Nagle, Phys. Rev. 85, 934 (1952).
[25] Fermi, Anderson, Lundby, Nagle, and Yodh, Phys. Rev. 85, 935 (1952).
[26] Anderson, Fermi, Long, and Nagle, Phys. Rev. 85, 936 (1952).
[27] Anderson, Fermi, Nagle, and Yodh, Phys. Rev. 86, 793 (1952).
[28] K. Brueckner, Phys. Rev. 86, 106 (1952).

problem has been given by Ashkin, Simon, and Marshak.[19] They calculate the matrix elements for scattering through order f^4 in the pseudoscalar coupling theory and through order g^2 with derivative coupling (in this case the higher order terms diverge and are not renormalizable). The sharp rise in cross section as a function of meson energy is suggested by the calculation with the derivative coupling form H_{pv}. We write the differential cross section in the center-of-mass system for this case, in the low energy approximation that neglects nucleon recoil, as

$$d\sigma(\pi^+)=(g^2/4\pi)^2(4q^4/\mu^2\omega^2)d\Omega/\mu^2 \quad \text{(a)},$$
$$d\sigma(\pi^-)=d\sigma(\pi^+) \quad \text{(b)}, \quad (20)$$
$$d\sigma(\pi^0)=2\cos^2\theta d\sigma(\pi^+) \quad \text{(c)},$$

where $d\sigma(\pi^+)$, $d\sigma(\pi^-)$, and $d\sigma(\pi^0)$ are the differential cross sections for the three processes as given in Eq. (19). The coupling constant g for the derivative coupling theory is defined by Eq. (8), ω and q are the meson energy and momentum, and θ is the meson scattering angle in the collision center-of-mass system. The theoretical prediction of a spherically symmetric π^+ scattering cross section is in serious disagreement with the experimental results, as is the ratio of the elastic π^+ to elastic plus charge exchange π^- total cross sections. The experimental ratio is of the order of 2 at 137 Mev, whereas the above formulas predict a ratio of 3/5 for all energies.

The cross sections derived on the basis of a weak coupling pseudoscalar coupling theory differ from the results in Eq. (20), as mentioned earlier, in virtue of the pair term H_c of Eqs. (7) and (10) and the fifth term H_τ to order f^3 in Eq. (7). The results are

$$d\sigma(\pi^+)=(f^2/4\pi)^2[(1+\omega/2M)^2+q^4/4M^2\omega^2 - (q^2/M\omega)(1+\omega/2M)\cos\theta]d\Omega/M^2 \quad \text{(a)},$$
$$d\sigma(\pi^-)=(f^2/4\pi)^2[(1-\omega/2M)^2+q^4/4M^2\omega^2 + (q^2/M\omega)(1-\omega/2M)\cos\theta]d\Omega/M^2 \quad \text{(b)}, \quad (21)$$
$$d\sigma(\pi^0)=2(f^2/4\pi)^2[(\omega/2M)^2+(q^4/4M^2\omega^2)\cos^2\theta - (q^2/M\omega)(\omega/2M)\cos\theta]d\Omega/M^2 \quad \text{(c)}.$$

These formulas are calculated from Eq. (7) with neglect of nucleon recoil[20] or from Eq. (18) in the perturbation limit $\lambda\to 1$. The second term in the right-hand member of these expressions represents the contribution of H_{pv} and is seen to correspond to the cross-section result of Eq. (20) when relation (8) is inserted. The core term H_c contributes the factor unity in the first terms in the right members of $d\sigma(\pi^+)$ and $d\sigma(\pi^-)$ but does not operate in calculations of the charge exchange scattering to this order in f. The factor $\omega/2M$ in the first terms results from H_τ, the fifth term in Eq. (7). The third terms in the right members are cross terms that appear when the matrix elements are squared to give a cross section.

Again we see that these cross sections stand in disagreement with the experimental data. Whereas the experimental points indicate a sharp rise in cross section with energy and a strong $\cos^2\theta$ angular dependence for π^+ mesons with energies of the order of 100 Mev, the expressions (21a) and (21b) are essentially energy and angle independent in this energy range in virtue of the dominant contribution from the core term H_c. Also the ratio of the total cross sections $\sigma(\pi^+):\sigma(\pi^-):\sigma(\pi^0)\cong 1:1:\omega^2/2M^2$ is seen to differ considerably from observation.

It is clear from the above that the first step in an attempt to reconcile the pseudoscalar coupling theory with observation must reduce the core contribution relative to the p wave contribution of H_{pv}, as expressed in Eq. (20), so that the rapid rise of the experimental cross section with meson energy may be understood. As discussed in the previous section, we may expect such a reduction when higher order terms in f are considered, and we have lumped their effect into a constant λ given in Eq. (18). A perturbation calculation on the basis of this Hamiltonian gives scattering cross sections that differ from those given by Eq. (21) only in that the constant $\lambda<1$ replaces unity whenever the latter appears there, i.e., $(1\pm\omega/2M)\to(\lambda\pm\omega/2M)$. The charge exchange cross section $\sigma(\pi^0)$ is unchanged since H_c does not contribute to it. The energy variation indicated by these results for $\lambda\leq\mu/2M\sim 1/13$ suggests the sharp experimentally observed rise with energy, but it is still somewhat too gradual. Also, the predicted angular asymmetry is not in accord with the data. We reserve further discussion of this latter point till later. We note here, however, that it is possible to achieve a more accurate treatment of H_c and that it is reasonable to expect an improved calculation of H_c to increase the relative importance of the p wave contribution H_{pv}, thereby sharpening the predicted energy rise of the cross sections.

The argument for this develops as follows. Consider the wave equation for the meson amplitudes as obtained from the Hamiltonian [Eq. (18)] in the absence of electromagnetic fields. If we neglect for the moment all terms but those obtained from H_0+H_c, the wave equation is

$$[\Delta+k^2-\lambda(f^2/M)K(\mathbf{r})]\phi_{\mathbf{k}\alpha}=0, \quad (22)$$

for an eigenstate of energy $\omega=(k^2+\mu^2)^{\frac{1}{2}}$. The straight perturbation procedure given above for evaluating the scattering matrix elements corresponds to solving Eq. (22) by ordinary Born approximation. That is, the zero-order equation and solutions for the meson amplitudes are

$$(\Delta+k^2)\phi_{\mathbf{k}\alpha}{}^0=0, \quad (23)$$

$$\phi_{\mathbf{k}\alpha}{}^0=(2\omega L^3)^{-\frac{1}{2}}[a_{\mathbf{k}\alpha}\exp(i\mathbf{k}\cdot\mathbf{r})+\text{complex conj.}], \quad (24)$$

where L^3 is the normalization volume, and $a_{\mathbf{k}\alpha}(a_{\mathbf{k}\alpha}{}^*)$

[20] Recoil corrections to Eqs. (21a) and (21b) due to the core term are of the same order of magnitude as the ω^3/M^3 terms in the square brackets and must be included if the formulas are to be discussed with this order of accuracy.

is the meson annihilation (creation) operator. The third term in Eq. (22) is then treated as a small perturbation. However, the usual criterion for application of the Born approximation to scattering of a particle of mass μ by a potential of radius a and height V_0 requires[30]

$$|\mu V_0 a^2| \ll 1 \tag{25}$$

for $ka \ll 1$, where k is the particle momentum. The core term of Eq. (22) corresponds to a square potential of radius a and height $(\lambda f^2/2\mu M)(3/4\pi a^3)$, so that the criterion (25) becomes $|(3/2)\lambda f^2/4\pi| \ll 1$ for slow mesons with $ka \approx k/M \ll 1$, where a has been chosen the order of a nucleon Compton wavelength. We shall see below, however, that it will be necessary to take $\lambda f^2/4\pi > 1$ in order to approximate data on meson scattering and photoproduction. It, therefore, becomes desirable to abandon the Born approximation. We solve Eq. (22), instead, by the method of phase shifts as applied in ordinary single particle scattering by a fixed potential. Since we have $ka \ll 1$ for the processes under discussion, we can confine our attention to the s and p wave phase shifts. This method of calculation gives directly the amplitude of the scattered wave due to H_c. We also use solutions of Eq. (22) as the zero-order meson amplitudes in terms of which to calculate the scattering matrix elements of $H_{pv}+H_s$.

Since the matrix elements of H_{pv} are proportional to gradϕ inside the nucleon core, whereas those of H_s depend on the amplitude, the ratio of the p wave scattering of H_{pv} to the s wave scattering of H_s is increased over the value obtained when perturbation methods were applied to the core. In other words, the effect of treating the core in the zero-order wave equation is to cut down the amplitude of the meson field at the nucleon source and to thereby increase the ratio of p to s wave scattering.

In order to compare the solutions of Eq. (22) with the ones exhibited above for Eqs. (23)–(24), we expand the latter in radial and angular functions

$$\phi_{k\alpha}{}^0 = (2\omega L^3)^{-\frac{1}{2}}[a_{k\alpha}\textstyle\sum_l c_l j_l(kr) P_l(\cos\theta) + \text{complex conj.}],$$

where j_l is a spherical Bessel function and P_l is a Legendre polynomial of order l. The radial solutions of Eq. (22) inside and outside the core give in place of $c_l j_l(kr)$

$$\begin{aligned} l=0 \quad & r \lesssim a \cdots c_0 \operatorname{sech}\beta a \; i_0(\beta r), \\ & r > a \cdots c_0[j_0(kr) + ka(1-\tanh\beta a/\beta a) n_0(kr)], \\ l=1 \quad & r \lesssim a \cdots -c_1 ka \operatorname{csch}\beta a \; i_1(\beta r), \\ & r > a \cdots c_1[j_1(kr) + (ka)^3\{\tfrac{1}{3} - \coth\beta a/\beta a \\ & \qquad + 1/(\beta a)^2\} n_1(kr)], \end{aligned} \tag{26}$$

where

$$\beta a = \left[3\lambda\left(\frac{f^2}{4\pi}\right)\left(\frac{1}{Ma}\right) - k^2a^2\right]^{\frac{1}{2}} \approx \left[3\lambda\left(\frac{f^2}{4\pi}\right)\left(\frac{1}{Ma}\right)\right]^{\frac{1}{2}}$$

is approximately constant if $\lambda \gg (k^2/3M^2)(f^2/4\pi)^{-1}$ for $a \approx 1/M$; η_l is the spherical Neumann function, and i_l is the spherical Bessel function of imaginary argument defined so that $i_0(z) = \sinh z/z$ and $i_1(z) = \sinh z/z^2 - \cosh z/z$; $c_l = (2l+1)i^l$. Corrections to these solutions are of order $(ka)^2 \ll 1$. The s wave scattering amplitude due to the core alone is then given by [31]

$$-a(1-\tanh\beta a/\beta a) = k^{-1}\sin\delta_0. \tag{27}$$

Furthermore, we can use the solutions given in Eq. (26) rather than the plane waves [Eqs. (23)–(24)] in calculating the scattering matrix elements due to $H_{pv}+H_s$. An additional improvement is possible if we modify the perturbation method to include radiation damping in the manner first developed by Heitler.[32] Unfortunately, there exists no quantitative procedure (short of an exact solution) by which to gauge the accuracy of the Heitler approximation, which (approximation) takes into account only the "resistive" effect of higher order processes.[33] It will be seen, however, that as a result of invoking the Heitler damping theory, we are able to bring the calculated cross sections one step closer to the observed scattering data.

Goldberger[34] and others have already applied the Heitler damping procedure to the calculation of meson scattering by nucleons for the pseudovector theory in which only H_{pv} operates in the meson-nucleon interaction and H_0 describes the propagation of free mesons. The work we wish to present here is an extension of the methods given by Lippman and Schwinger[35] and by Goldberger to the case in which the zero-order Hamiltonian is taken as H_0 plus the core term H_c, and the interaction is given by $H_{pv}+H_s$. But first we present for discussion the differential cross sections calculated in the straight pseudovector coupling theory. With neglect of nucleon recoil, they are

$$\begin{aligned} d\sigma(\pi^+) &= 4(g^2/4\pi)^2 \frac{q^4}{\omega^2\mu^2}\left(\frac{1+4x^2\cos^2\theta}{(1+2x^2)^2+x^3}\right)\frac{d\Omega}{\mu^2}, \\ d\sigma(\pi^-) &= 4(g^2/4\pi)^2 \frac{q^4}{\omega^2\mu^2}\left(\frac{1}{1+9x^2}\right)\frac{d\Omega}{\mu^2}, \\ d\sigma(\pi^0) &= 8(g^2/4\pi)^2 \frac{q^4}{\omega^2\mu^2}\left(\frac{\cos^2\theta}{1+2x^2}\right)\frac{d\Omega}{\mu^2}, \end{aligned} \tag{28}$$

where $x = \frac{2}{3}(g^2/4\pi)(q^2/\omega\mu^2)$ corresponds to the x of

[30] L. I. Schiff, reference 13, p. 168.

[31] For $\beta a \gg 1$ this reduces to the strong coupling limit given by Wentzel, (see reference 3) and references to previous work given there. Recently the wave equation of the form Eq. (22) has been studied more thoroughly in connection with the nonlinear meson theory, as formulated by Schiff (reference 13), by D. R. Yennie (to be published) and by E. M. Henley, unpublished. The methods we use here are sufficiently precise for our purposes since the core in our equation is the heavy nucleon.

[32] W. Heitler, Proc. Cambridge Phil. Soc. **37**, 291 (1941).

[33] J. M. Blatt, Phys. Rev. **72**, 461 (1947).

[34] M. Goldberger, Phys. Rev. **84**, 929 (1951); E. Corinaldesi and G. Field, Phil. Mag. **41**, 364 (1950); Lepore, Ruderman, and Wolff, unpublished.

[35] B. Lippman and J. Schwinger, Phys. Rev. **79**, 469 (1950).

Goldberger, except for a factor 2 that results from using the charge-symmetric meson theory instead of the pure charged theory. In the limit $x\to 0$, Eqs. (28) are seen to reduce directly to the perturbation results presented in Eqs. (20). If we adjust the coupling constant to fit an experimental value of 120 mb for the total π^+ elastic cross section at a meson kinetic energy of 135 Mev in the lab system, we find $g^2/4\pi\approx 0.4$, corresponding by Eq. (8) to a pseudoscalar coupling constant of $f^2/4\pi \approx 70$. Several interesting features emerge in Eqs. (28). The variation of the total cross sections for π^+ and for π^- mesons as a function of meson energy indicates a sharp rise in the region 60 to 150 Mev, followed by a general flattening at higher energies in accord with the data on π^- scattering (elastic plus charge exchange). A choice of $g^2/4\pi>0.5$ or $g^2/4\pi<0.3$ shifts the energy plateau for the calculated cross section to too high or too low an energy value, respectively. However, if we were to adjust the angular distribution of $d\sigma(\pi^+)$ to fit the observed distribution, of roughly $1+3\cos^2\theta$ at an energy of 135 Mev, we would require $g^2/4\pi\approx 0.9$. For $g^2/4\pi=0.4$ the predicted distribution is $1+0.6\cos^2\theta$. The ratio of $\sigma(\pi^+):\sigma(\pi^-)+\sigma(\pi^0)$ is still less than unity, in disagreement with the data which indicate this ratio to be 1.4 at 60 Mev and 3 above 100 Mev, but is increased slightly to 0.72 from the perturbation result of 0.6. In accord with observation, $d\sigma(\pi^-)$ is isotropic.

Proceeding now to a discussion of the damping theory as applied to the pseudoscalar Hamiltonian we write first, in Goldberger's notation,[34] the scattering matrix for elastic scattering due to H_c:

$$R_{\mathbf{q}\mathbf{q}_0}{}^{(c)} = -(\Phi_{\mathbf{q}}, H_c\Psi_{\mathbf{q}_0}{}^{(c)+}), \tag{29}$$

where $\mathbf{q}_0$ and $\mathbf{q}$ denote, respectively, the momenta of the initial and scattered meson, and $\Psi_{\mathbf{q}_0}{}^{(c)+}$ is defined by the integral equation

$$\Psi_{\mathbf{q}_0}{}^{(c)+} = \Phi_{\mathbf{q}_0} + \Delta^{-1}H_c\Psi_{\mathbf{q}_0}{}^{(c)+}, \tag{30}$$

with $\Delta=\omega+i\epsilon-H_0$. This solution incorporates the boundary condition of an incident free wave, $(\Phi_{\mathbf{q}_0})$, plus an outgoing scattered wave due to the core term H_c. The R matrix defined as above is related to the scattering phase shift δ_0, given in Eq. (27), by

$$R_{\mathbf{q}\mathbf{q}_0}{}^{(c)} = (2\pi/\omega q L^3)\,\sin\delta_0\exp(i\delta_0). \tag{31}$$

The total R matrix for elastic scattering is

$$R_{\mathbf{q}\mathbf{q}_0} = -(\Phi_{\mathbf{q}}, \{H_c+H_{pv}+H_\pi\}\Psi_{\mathbf{q}_0}{}^{+}) \tag{32}$$

with H_c, H_{pv}, and H_π as in Eq. (18) and $\Psi_{\mathbf{q}_0}{}^{+}$ defined by

$$\Psi_{\mathbf{q}_0}{}^{+} = \Phi_{\mathbf{q}_0} + \Delta^{-1}(H_c+H_{pv}+H_\pi)\Psi_{\mathbf{q}_0}{}^{+}. \tag{33}$$

It is useful to define $\Psi_{\mathbf{q}_0}{}' = \Psi_{\mathbf{q}_0}{}^{+} - \Psi_{\mathbf{q}_0}{}^{(c)+}$. By Eqs. (30) and (33), it satisfies the relation

$$\Psi_{\mathbf{q}_0}{}' = \Delta^{-1}(H_{pv}+H_\pi)\Psi_{\mathbf{q}_0}{}^{(c)+} + \Delta^{-1}(H_c+H_{pv}+H_\pi)\Psi_{\mathbf{q}_0}{}'. \tag{34}$$

There are two elements in the prescription yielding the Heitler damping theory approximation to the solution of Eq. (34).

(1) Only the lowest order matrix elements which contribute to the scattering, as found by an iteration procedure, are to be kept (first order for H_π, second order for H_{pv}).

(2) The energy denominator

$$\Delta^{-1} = (\omega+i\epsilon-H_0)^{-1} = (\omega-H_0)^{-1}\mathbf{P} - i\pi\delta(\omega-H_0)$$

is replaced by its second term $-i\pi\delta(\omega-H_0)$, indicating that contributions from terms off the energy shell are neglected. Use of the above prescription and Eqs. (29), (32), and (34) allows us to express the R matrix of $H_{pv}+H_\pi$ as

$$R_{\mathbf{q}\mathbf{q}_0}{}' = R_{\mathbf{q}\mathbf{q}_0} - R_{\mathbf{q}\mathbf{q}_0}{}^{(c)} = -(\Phi_{\mathbf{q}}, \{H_\pi+H_{pv}\Delta^{-1}H_{pv}\}\Psi_{\mathbf{q}_0}{}^{(c)+}) + i\pi\textstyle\sum_{\mathbf{q}'}\delta(\omega-\omega_{\mathbf{q}'})B_{\mathbf{q}\mathbf{q}'}R_{\mathbf{q}'\mathbf{q}_0}{}', \tag{35}$$

where

$$B_{\mathbf{q}\mathbf{q}'} = -(\Phi_{\mathbf{q}}, \{H_c+H_\pi+H_{pv}\Delta^{-1}H_{pv}\}\Phi_{\mathbf{q}'}) \tag{36}$$

is the lowest order Born approximation scattering matrix. Equation (35) is the desired extension of the usual Heitler integral equation, expressed in terms of the known solutions $\Psi_{\mathbf{q}_0}{}^{(c)+}$. These are essentially the state functionals for meson field amplitudes given as solutions of Eq. (22). In the absence of H_c, which we treat by the previously discussed phase shift method, Eq. (35) reduces to Goldberger's result.

It is possible to solve Eq. (35) exactly with the trial form

$$R_{\mathbf{q}\mathbf{q}_0}{}' = -L^{-3}(s_0q^2 + s_1\mathbf{q}\cdot\mathbf{q}_0 + is_2\boldsymbol{\sigma}\cdot\mathbf{q}_0\times\mathbf{q}), \tag{37}$$

since all higher order terms in σ can be reduced to these. We consider specifically the scattering of π^+ mesons by protons. The Born approximation scattering matrix is just

$$B_{\mathbf{q}\mathbf{q}_0}(\pi^+) = -(f^2/2M\omega L^3)(\lambda+\omega/2M - \boldsymbol{\sigma}\cdot\mathbf{q}_0\boldsymbol{\sigma}\cdot\mathbf{q}/2\omega M), \tag{38}$$

corresponding to the cross section (21a) with $\lambda\to 1$. The first term on the right member of Eq. (35) differs from the Born approximation result because of the appearance of $\Psi_{\mathbf{q}_0}{}^{(c)+}$, defined by Eq. (30), in place of $\Phi_{\mathbf{q}_0}$. This means that in calculating the matrix elements of H_π and H_{pv} we insert the solutions written in Eq. (26) for the meson field amplitude that annihilates the incident meson state of momentum $\mathbf{q}_0$ in place of the usual plane wave, Eqs. (23)–(24). The effect of thus including the core H_c in the zero-order Hamiltonian is to reduce the s and p wave scattering matrix elements by the factors

$$r_s = 3(\beta a)^{-2}(1-\tanh\beta a/\beta a), \qquad r_p = 3\coth\beta a/\beta a(1-\tanh\beta a/\beta a), \tag{39}$$

respectively, relative to the Born approximation. These factors neglect terms $(ka)^2\ll 1$ and reduce to unity for $\beta a\to 0$. Introducing Eqs. (36)–(39) into Eq. (35), we

obtain after some algebra

$$s_0^+=(f/2M)^2(r_s/q^2)\times[1+(i/2\pi)(f/2M)^2q\omega(1+2M\lambda/\omega)]^{-1},$$
$$s_1^+=-(f/2M)^2(r_p/\omega^2)(1+2ix)/(1-ix+2x^2),$$
$$s_2^+=-(f/2M)^2(r_p/\omega^2)(1-ix+2x^2)^{-1}.$$

The complete R matrix is now known since, by Eqs. (27) and (31),

$$R_{qq_0}{}^{(+)}(\pi^+)=-(2\pi/\omega L^3)a(1-\tanh\beta a/\beta a),$$

to order $(ka)^2\ll 1$. The procedure is entirely similar in the cases of elastic and charge exchange scattering of π^- mesons by protons. Relating the R-matrix to the differential scattering cross sections by

$$d\sigma=(L^6\omega^2/4\pi^2)\langle|R|^2\rangle_{\Omega}d\Omega,$$

we obtain finally

$$d\sigma(\pi^+)=a^2\left(1-\frac{\tanh\beta a}{\beta a}\right)^2\left\{1+\frac{\omega}{2M\lambda}\frac{2+\omega/2M\lambda}{1+y_+^2}+\frac{\beta^3a^3\coth^2\beta a}{4\lambda^2}\frac{q^4}{\omega^2M^2}\frac{1+4x^2\cos^2\theta}{(1+2x^2)^2+x^2}-\frac{\beta a\coth\beta a}{\lambda}\frac{q^2}{\omega M}\frac{\cos\theta}{(1+2x^2)^2+x^2}\times\left[1+\frac{\omega}{2M\lambda}\frac{1-x(3+4x^2)y_+}{1+y_+^2}\right]\right\}d\Omega,$$

$$d\sigma(\pi^-)=a^2\left(1-\frac{\tanh\beta a}{\beta a}\right)^2\left\{1-\frac{\omega}{2M\lambda}\frac{2-\omega/2M\lambda}{1+y_-^2}+\frac{\beta^3a^3\coth^2\beta a}{4\lambda^2}\frac{q^4}{\omega^2M^2}\frac{1}{1+9x^2}+\frac{\beta a\coth\beta a}{\lambda}\frac{q^2}{\omega M}\times\frac{\cos\theta}{1+9x^2}\left[1-\frac{\omega}{2M\lambda}\frac{1+3xy_-}{1+y_-^2}\right]\right\}d\Omega,$$

$$d\sigma(\pi^0)=2a^2\left(1-\frac{\tanh\beta a}{\beta a}\right)^2\left\{\frac{(\omega/2M\lambda)^2}{1+2(f^2/4\pi)^2(q\omega/2M^2)^2}+\frac{\beta^3a^3\coth^2\beta a}{4\lambda^2}\frac{q^4}{\omega^2M^2}\frac{\cos^2\theta}{1+2x^2}-\frac{\beta a\coth\beta a}{\lambda}\frac{q^2}{\omega M}\times\frac{\cos\theta}{1+2x^2}\frac{\omega}{2M\lambda}\frac{1-2x(f^2/4\pi)(q\omega/2M^2)}{1+2(f^2/4\pi)^2(q\omega/2M^2)^2}\right\}d\Omega, \quad (40)$$

where $y_\pm$ represent

$$y_\pm=\frac{f^2}{4\pi}\lambda\frac{q}{M}\left(1\pm\frac{\omega}{2M\lambda}\right).$$

The total cross sections, integrated over angle, are

$$\sigma(\pi^+)=4\pi a^2\left(1-\frac{\tanh\beta a}{\beta a}\right)^2\left\{1+\frac{\omega}{2M\lambda}\frac{2+\omega/2M\lambda}{1+y_+^2}+\frac{\beta^3a^3\coth^2\beta a}{4\lambda^2}\frac{q^4}{\omega^2M^2}\frac{1+4x^2/3}{(1+2x^2)^2+x^2}\right\},$$

$$\sigma(\pi^-)=4\pi a^2\left(1-\frac{\tanh\beta a}{\beta a}\right)^2\left\{1-\frac{\omega}{2M\lambda}\frac{2-\omega/2M\lambda}{1+y_-^2}+\frac{\beta^3a^3\coth^2\beta a}{4\lambda^2}\frac{q^4}{\omega^2M^2}\frac{1}{1+9x^2}\right\},$$

$$\sigma(\pi^0)=8\pi a^2\left(1-\frac{\tanh\beta a}{\beta a}\right)^2\left\{\frac{(\omega/2M\lambda)^2}{1+2(f^2/4\pi)^2(q\omega/2M^2)^2}+\frac{1}{3}\frac{\beta^3a^3\coth^2\beta a}{4\lambda^2}\frac{q^4}{\omega^2M^2}\frac{1}{1+2x^2}\right\}. \quad (41)$$

We comment here that proton recoil has been neglected in these calculations. This means that terms reduced by ω/M relative to unity are omitted. They have been explicitly calculated and shown to be indeed small and not to materially affect the above results. The terms proportional to ω/M in the above formulas appear only in combination with the constant $1/\lambda>1$.

In analyzing the above formulas we make the following observations:

(1) The data indicate that p wave scattering (due to H_{pv}) dominates above $\sim$60 Mev and, therefore, in order to approximate the energy variation of the experimental cross sections, we must take $0.3\leqslant g^2/4\pi\leqslant 0.5$ as we did in the discussion below Eqs. (28); or by Eq. (8), $53\leqslant f^2/4\pi\leqslant 89$.

(2) If we restrict $g^2/4\pi$ to lie within the above-indicated limits, there remain two constants λ and a (or β) to adjust in order to bring these cross sections in as close agreement as possible with some of the data. If we take a to correspond to the nucleon Compton wavelength, $a=1/M$, we find that we must take $\lambda=\mu/2M=0.075$ to fit the magnitude of π^- elastic plus charge exchange scattering for mesons in the energy range of 135–215 Mev. The data and theoretical curve are presented in Fig. 2. The data of Anderson *et al.* and of Steinberger *et al.* are seen to fall somewhat below the theoretical curve for meson energies below 120 Mev. We may also take a larger source radius of $a=2/M$. Choosing $\lambda=\mu/M=0.15$ we fit the data for the higher energy π^- mesons, but the curve is again high below 120 Mev. This curve is also plotted in Fig. 2.

(3) The cross section for π^+ scattering given in Eq. (41) is smaller by a factor of roughly $\frac{1}{4}$ than $\sigma(\pi^-)+\sigma(\pi^0)$ with the above-indicated choice of parameters and thus is in disagreement with the observation. If we attempt to fit $\sigma(\pi^+)$ with the data, the π^- cross sections are then much too large.

(4) The data indicate a ratio of $\sigma(\pi^0):\sigma(\pi^-)=2:1$ for incident π^- mesons of energy above 100 Mev. The formulas in Eq. (41) yield a value for this ratio of approximately 1.2 at 132 Mev, increasing to 2 at 200 Mev with both of the above sets of parameters. The calculated ratio is perhaps on the low side of the experimental determination.

(5) The data on the angular distributions of the scattered π^+, π^-, and π^0 mesons are too crude to permit a detailed comparison with the above formulas. The experiments suggest, however, that at 135 Mev, the π^- elastic scattering is essentially isotropic, the charge exchange cross section varies largely as $\cos^2\theta$, and the π^+ cross section has the rough form of $1+3\cos^2\theta$ as predicted in a phenomenological analysis that assumes the scattering to take place predominantly in a spin $\frac{3}{2}$ state. We tabulate here the angular distributions predicted by Eqs. (40) with the above choices of parameters. For $g^2/4\pi=0.4$, $a=1/M$, and $\lambda=\mu/2M$, we obtain at a meson kinetic energy of 132 Mev:

$$d\sigma(\pi^-)\sim[1+0.35\cos\theta]d\Omega,$$
$$d\sigma(\pi^0)\sim[1+1.3\cos\theta+36\cos^2\theta]d\Omega,$$
$$d\sigma(\pi^+)\sim[1-0.20\cos\theta+0.49\cos^2\theta]d\Omega;$$

at the same energy, for $g^2/4\pi=0.4$, $a=2/M$, and $\lambda=\mu/M$ we obtain:

$$d\sigma(\pi^-)\sim[1-0.04\cos\theta]d\Omega,$$
$$d\sigma(\pi^0)\sim[1+1.3\cos\theta+36\cos^2\theta]d\Omega,$$
$$d\sigma(\pi^+)\sim[1-0.51\cos\theta+0.39\cos^2\theta]d\Omega.$$

The calculated distributions for π^- elastic and charge exchange scattering are in satisfactory agreement with present experimental data. However, the $\cos^2\theta$ contribution to π^+ scattering is too small by a factor ~ 6 relative to the data.

It would appear from the above discussions that it is possible to select a physically reasonable set of three parameters—the meson-nucleon coupling strength, the depth and the radius of a repulsive nucleon core potential for meson interactions—which permits reasonable agreement with experiment on the elastic and charge exchange scattering of π^- mesons. On the other hand, the calculated π^+ cross section is considerably too small in magnitude and too flat in angular distribution. It is encouraging to note, however, that by going somewhat beyond a straight weak coupling perturbation approximation, it has been possible to narrow the gap between theory and experiment. An analysis of the perturbation theory suggests that an improved, intermediate coupling calculation of the meson-nucleon interaction may be expected to increase the ratio of π^+ to π^- scattering by protons. For π^- scattering, the proton must absorb the incident π^- meson before emitting the scattered one, *viz.*,

$$\pi^-+p\rightarrow N\rightarrow\pi^{-\prime}+p'.$$

The energy denominator for this process in a second-order perturbation calculation is $E_p+\omega-E_N\sim\omega$. For π^+ scattering, the final meson is emitted first:

$$\pi^++p\rightarrow\pi^++\pi^{+\prime}+N\rightarrow\pi^{+\prime}+p',$$

and the energy denominator is $E_p-\omega-E_N\sim-\omega$. However, a bound state of one of the mesons about the neutron in the intermediate step would reduce the energy denominator and thereby increase the cross section.[36] Such a state would correspond to a nucleon isobar. This mechanism would also serve to increase the ratio $\sigma(\pi^0):\sigma(\pi^-)$ which we observed to be on the small side in the preceding discussion, since charge exchange scattering proceeds in either of the two ways,

$$\pi^-+p\rightarrow\underset{N}{\pi^-+\pi^{0\prime}+p'}\rightarrow\pi^{0\prime}+N'.$$

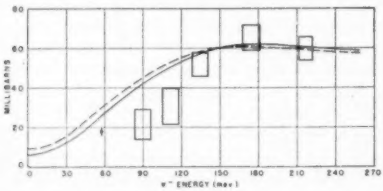

FIG. 2. Elastic plus charge exchange scattering of π^- mesons by protons as a function of π^- energy. The blocks represent the data obtained at Chicago and the low energy point was obtained at Columbia. The theoretical curves are deduced from Eq. (41) with $g^2/4\pi=0.4$. The solid curve is for $a=1/M$, $\lambda=\mu/2M$ and the dashed curve is for $a=2/M$, $\lambda=\mu/M$.

IV. PHOTOPRODUCTION

We next apply the Hamiltonian [Eq. (18)] to a brief discussion of the photoproduction of π^+ mesons by gamma-rays of several hundred Mev energy incident on protons. The zero-order Hamiltonian is taken to be

$$H_0+\lambda f^2/2M\int K(\mathbf{r}-\mathbf{r}_N)\phi^2 d\mathbf{r}, \qquad (42)$$

and $H_{p\phi}+H_e$ is treated as a small perturbation. This calculation differs from the previous work of Brueckner[37] and Araki[38] by the inclusion of the core term in the zero-order Hamiltonian in Eq. (42). The core term alters the relative amounts of s and p wave production and hence alters the angular distribution and excitation function for π^+ production.

A repulsive core with $\lambda>0$ suppresses the s wave relative to the p wave production, thereby increasing the angular variation of the differential cross section. It appears from the experimental and perturbation-

[36] An actual calculation has shown that the introduction of a phenomenological constant $\Gamma=\omega/\omega'>1$, with ω' the reduced energy denominator, in both $\pi^++p\rightarrow\pi^++\pi^{+\prime}+N\rightarrow\pi^{+\prime}+p'$ and $\pi^-+p\rightarrow\pi^-+\pi^{0\prime}+p'\rightarrow\pi^{0\prime}+N'$, makes agreement with experiment at 135 Mev possible in both magnitude and angular distribution.

[37] K. Brueckner, Phys. Rev. **79**, 641 (1950).

[38] G. Araki, Prog. Theor. Phys. **5**, 507 (1950).

weak-coupling curves given by Steinberger and Bishop[39] (Figs. 17 and 20 of this reference) that such an increase in the relative p wave contribution may be desirable. We shall see below that it is also possible to improve the agreement between the theoretical curve and the data on the excitation function for π^+ production by increasing the relative p wave contribution in the pseudoscalar theory. We remark here that suppression of the s wave in π^+ production operates so as to increase the theoretical ratio of π^0 and π^+ photoproduction cross sections, since π^0 production occurs predominantly in the p state.

Foldy[40] has given a nonrelativistic perturbation calculation of π^+ photoproduction. Plane wave solutions to the Klein-Gordon equation for the meson amplitudes [Eqs. (23)–(24)] are used in calculating the matrix elements for this process. For the differential cross section in the pseudoscalar theory Foldy obtains (both the pseudoscalar and pseudovector coupling terms yield the same result)

$$d\sigma_F = \frac{2e^2}{\mu^2}\frac{g^2}{4\pi}\frac{q}{k}\left(1-\frac{2q^2\mu^2}{\omega_{q-k}{}^4}\sin^2\theta\right)d\Omega_q, \qquad (43)$$

for incident photons of momentum k, and π^+ mesons of momentum $q=(k^2-\mu^2)^{\frac{1}{2}}$ and energy ω_{q-k} emerging at an angle θ with the incident photon direction. The meson-nucleon coupling constant in Eq. (43), $g^2/4\pi$, is for the derivative coupling form and corresponds to Foldy's[41] $\frac{1}{2}g^2$. If we calculate the π^+ photoproduction cross section with the zero-order Hamiltonian taken as Eq. (42), the meson amplitudes are taken as the solutions [Eq. (26)] of the modified wave equation (22), so that the s and p wave contributions are reduced, respectively, by r_s and r_p as given in Eq. (39). The resulting cross section is then

$$d\sigma = \frac{e^2}{2M^2}\frac{f^2}{4\pi}\left(\frac{3}{\beta a}[\coth\beta a - 1/\beta a]\right)^2\frac{q}{k}\left[\left(\frac{\tanh\beta a}{\beta a}\right)^2 - \frac{2q^2\mu^2 - 2(1-\tanh\beta a/\beta a)q^2\omega_{q-k}{}^2}{\omega_{q-k}{}^4}\sin^2\theta\right]d\Omega_q. \qquad (44)$$

In the limit $\beta a \to 0$ this reduces to Eq. (43), with the coupling constants f and g related by Eq. (8). There are two constants in Eq. (44), $g^2/4\pi$ and βa, to be adjusted to give the best fit with the data on the angular and energy variation of the cross section. In the discussion of the preceding paragraph on meson scattering we specified $g^2/4\pi=0.4$ and $\beta a=4$. This choice of parameters in Eq. (44) gives a photoproduction cross section with an energy variation appropriate for the data but too small in magnitude by roughly 35 percent, and with too sharp and too forward an angular distribution. If we keep $g^2/4\pi=0.4$, we find that $\beta a=2.3$ gives a cross section of magnitude in accord with the data. The energy distribution of photomesons at 90° in the laboratory and the angular distribution at a photon energy of 255 Mev as calculated from Eq. (44) are compared with the data in Figs. 3 and 4. The results of a straight perturbation calculation as calculated from Eq. (43) and normalized to the data by a choice of $g^2/4\pi=1/11$ are also presented for comparison. The fit between theory and experiment on the energy distribution of π^+ mesons is considerably improved over the straight perturbation result (corresponding to $\beta a=0$). The curve for the angular distribution of π^+ mesons predicts more scattering in the angular interval 60°–120° than indicated by the rather limited data. On the other hand, the straight perturbation result seems to indicate relatively too much s wave production and to predict too many mesons in the backward direction. It is tempting to suggest that one should choose a smaller value of βa in the neighborhood of 1.5 and thereby obtain a theoretical angular distribution median between the two curves drawn and thus in better accord with the data. If we do this, however, the energy distribution of mesons at 90° becomes more similar to the perturbation result and deviates from the shape of the excitation curve given by Steinberger and Bishop. When more quantitative data become available it will be possible to analyze more accurately the relative roles of s and p wave π^+ meson photoproduction.

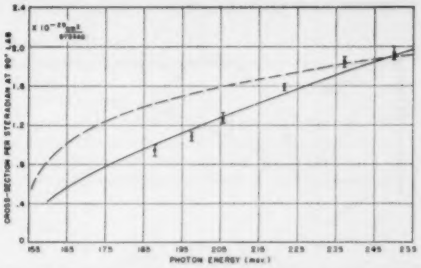

FIG. 3. The energy distribution of photomesons at 90° in the laboratory as a function of incident gamma-energy. The solid theoretical curve results from Eq. (44) with $g^2/4\pi=0.4$ and $\beta a=2.3$. The dashed curve is the perturbation result [Eq. (43)] fitted to the data with $g^2/4\pi=1/11$.

The fact that the value of βa used to fit the magnitude of the photoproduction cross section is smaller than for the π^- scattering cross section suggests that the amplitude of the nucleon-meson core, λ, is smaller in the photoproduction than in the scattering process, for a fixed radius. This result indicates that the higher order terms in Eq. (7) that are lumped into the constant λ in Eq. (18) operate somewhat differently in these two physical processes, and it is a further manifestation of

[39] J. Steinberger and A. S. Bishop, Phys. Rev. **86**, 171 (1952).
[40] L. L. Foldy, Phys. Rev. **76**, 372 (1949).
[41] The factor $\frac{1}{2}$ appears since we use the charge-symmetric meson theory in this work, whereas Foldy calculated with a charged meson theory.

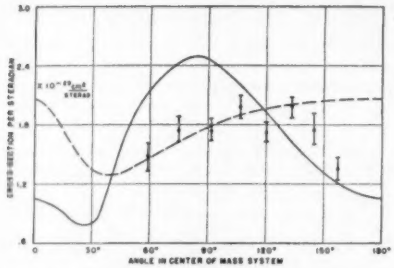

FIG. 4. The angular distribution of photomesons in the center-of-mass system for an incident gamma-energy of 255 Mev. The solid theoretical curve results from Eq. (44) with $g^2/4\pi=0.4$ and $\beta a=2.3$. The dashed curve is the perturbation result [Eq. (43)] fitted to the data with $g^2/4\pi=1/11$.

the failure of a perturbation approach to meson theoretic calculations.

V. CONCLUSION

In conclusion we summarize briefly the aims, methods, and deductions of this work. We have sought to harmonize the predictions of the pseudoscalar meson theory with the observations on meson scattering and photoproduction from protons. Cross sections previously derived for these processes with the assumption of weak meson-nucleon coupling disagree with the experimental data. On the other hand, Brueckner[28] and Watson[42] have achieved striking success by means of a phenomenological approach. In this paper we have adopted a field theoretic approach to the calculations and improved on the weak coupling perturbation approximation in two instances. First, we have used the Dyson transformation to a new representation for the pseudoscalar theory that permits a large meson-nucleon interaction term carrying the factor M—the core term H_c—to be treated with the zero-order Hamiltonian with methods that do not limit the meson-nucleon coupling strength to be small. In this representation we can also readily identify the velocity-independent features (σ, τ) of the nucleon dynamics. Secondly, we have improved on the perturbation results in the scattering calculations by applying the Heitler damping theory.

[42] K. Brueckner and K. M. Watson, Phys. Rev. 86, 923 (1952).

The formulas derived by this method come closer to fitting the observations than do the perturbation weak-coupling results but are far from satisfactory. It appears that more powerful techniques of calculation in the intermediate coupling region must be developed to provide an adequate basis for the study of the meson-nucleon interaction, even in a representation that permits separation of the large core term.[4]

In particular the higher order terms in the exact Hamiltonian, Eq. (7), remain to be studied. It is of interest to note here that the core term H_c and the constant λ which we incorporate with it in Eq. (17) may be checked directly in the very near future, when electron accelerators are operating in the 400-Mev region, by the process of double meson production by gamma-rays incident on protons. Thus, at 400 Mev, the cross section for production of π^- mesons in the reaction

$$\gamma+p\rightarrow\pi^++\pi^-+p'$$

is calculated to be[43] $\sigma\sim(g^2/4\pi)^2 10^{-27}$ cm^2 in a weak coupling perturbation calculation. The dominant contribution results from the core term H_c for which $\lambda=1$ in the weak coupling approximation. This cross section result is proportional to λ^2, and thus a direct measurement of the photoproduced π^- serves to limit the possible range of values. This is an important point for the pseudoscalar theory, since we have seen that small values of $\lambda\sim\mu/M$ to $\mu/2M$ are necessary in the interpretation of the scattering and single photoproduction data.

As discussed at the end of Secs. III and IV, the failure to match the π^+ meson scattering data and the difference in the vales of parameters introduced to fit the calculations on π^- scattering and on π^+ photoproduction indicate that an intermediate coupling approximation is necessary. We are encouraged by our results, however, to believe that charge-symmetric pseudoscalar meson theory with renormalizable pseudoscalar coupling may prove adequate for a quantitative analysis of the processes discussed.

We wish to thank Dr. J. V. Lepore and Mr. R. D. Lawson for valuable discussion.

[43] R. D. Lawson (to be published) has made a perturbation study of the double photomeson production processes in the pseudoscalar theory with both direct and derivative coupling.

Polarization Correlations of the Gamma-Rays of Cs^{134} and of Annihilation Radiation*†

BEROL L. ROBINSON‡ AND LEON MADANSKY
Department of Physics, The Johns Hopkins University, Baltimore, Maryland
(Received August 21, 1952)

The polarization correlation of the antiparallel cascade gamma-rays of Cs^{134} has been observed. The well-known cross-polarization property of the annihilation radiation has been utilized to determine the effective geometry of the polarimeters. The observed ratio of coincidences in perpendicular and parallel orientations is 0.91 ± 0.08. This ratio is not in disagreement with previous assignments of spin and parities to the excited states of the daughter nucleus, Ba^{134}.

I. INTRODUCTION

IN 1940, Hamilton presented theoretical predictions for the directional correlations of cascade gamma-rays[1] and showed that they depended upon the spins of the nuclear states involved and upon the multipolarity of the transitions. The pioneer experiments of Brady and Deutsch[2] showed extensive agreement with Hamilton's theory. This technique has now become a valuable tool for the nuclear spectroscopist. It then became worthwhile to inquire into what additional information might be deduced from this type of measurement. One of the authors (L.M.) suggested the possibility of polarization measurements, and Falkoff[3] calculated the polarization correlations for antiparallel cascade gamma-rays, demonstrating that changes in parity could be deduced from these correlations. Hamilton[4] quickly pointed out that it is much simpler to observe the polarization of only one gamma-ray and presented theoretical predictions for the polarization-direction correlations (i.e., the polarization of one gamma-ray as a function of the angle between the directions of propagation of the two gamma-rays). This theory was verified in detail by the experiments of Metzger and Deutsch,[5] and has been extended by MacDonald and Falkoff[6] and by others.[7]

The object of the work reported here was to study the polarization correlation effect, utilizing the polarization properties of the annihilation radiation to determine the polarization sensitivity of the polarimeters. In a solid such as aluminum, the dominant mode of positron annihilation occurs with the emission of two quanta. Wheeler,[8] Pryce and Ward,[9] and Snyder, Pasternack, and Hornbostel[10] have calculated the polarization correlation to be expected in the Compton scattering of annihilation radiation. The experiments[11] of Bleuler and Bradt, of Hanna, and of Wu and Shaknov are in agreement with the theory of Snyder *et al.*

The work reported here is to our knowledge the first polarization correlation observed, and the first use of Metzger-Deutsch[5] polarimeters for the observation of the annihilation radiation. Our method utilized the known polarization correlation of the annihilation radiation to determine the effective solid angle corrections which were necessary. Using these values, the polarization detection efficiency of the polarimeter was calculated for the gamma-rays of Cs^{134}, and an attempt was made to observe the polarization correlation in this isotope.

II. THE EXPERIMENTAL METHOD

The source was located at the center of a lead block (6 in.×6 in.×8 in.) in which tapered collimating holes were cut. This collimator was large enough to attenuate[12] by a factor 10^4 the direct radiation to the crystals which were intended as detectors of scattered radiation. Cylinders of clear crystalline stilbene (4.3 cm diam ×3.2 cm length) were used as Compton scatterers, and cubes of NaI(Tl) (3 cm on edge) were used to detect the scattered quanta. The NaI and stilbene crystals were $2\frac{1}{2}$ inches apart, center to center. (It would have been desirable to have scatterers whose height was greater than the diameter; and to have two additional NaI cubes in order to increase the rates fourfold. However these were not available.) The material in the crystal holders was kept to a minimum consistent with

* The work reported here constitutes part of a dissertation submitted by Berol L. Robinson in partial fulfilment of the requirements for the Ph.D. degree in the Faculty of Philosophy of The Johns Hopkins University.

† This work was supported in part by an AEC contract.

‡ AEC Predoctoral Fellow, 1950-1952; now at Department of Physics, University of Arkansas, Fayetteville, Arkansas.

[1] D. R. Hamilton, Phys. Rev. **58**, 122 (1940). In keeping with more recent practice we call all experiments of this type angular correlations, and distinguish between polarization (both detectors polarization sensitive), polarization-direction (one detector polarization sensitive), and directional (neither detector polarization sensitive) correlation.

[2] E. L. Brady and M. Deutsch, Phys. Rev. **78**, 558 (1950). This paper has references to earlier reports.

[3] D. L. Falkoff, Phys. Rev. **73**, 518 (1948).

[4] D. R. Hamilton, Phys. Rev. **74**, 782 (1948).

[5] Franz Metzger and Martin Deutsch, Phys. Rev. **78**, 551 (1950). This paper has references to earlier reports.

[6] J. E. MacDonald and D. L. Falkoff, Phys. Rev. **83**, 875 (1951); also thesis of J. E. MacDonald, University of Notre Dame (1952); also private communication from Dr. D. L. Falkoff.

[7] Stuart P. Lloyd (private communication); Irving Zinnes, Phys. Rev. **80**, 386 (1950).

[8] J. A. Wheeler, Ann. N. Y. Acad. Sci. **48**, 219 (1946).

[9] M. H. L. Pryce and T. C. Ward, Nature **160**, 435 (1947).

[10] Snyder, Pasternack, and Hornbostel, Phys. Rev. **73**, 440 (1948).

[11] E. Bleuler and H. L. Bradt, Phys. Rev. **73**, 1398 (1948); R. C. Hanna, Nature **162**, 332 (1948); C. S. Wu and I. Shaknov, Phys. Rev. **77**, 136 (1950).

[12] Charlotte M. Davisson and Robley D. Evans, Phys. Rev. **81**, 404 (1951).

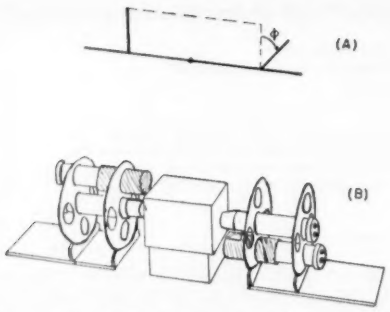

FIG. 1. Sketch of polarization apparatus. (A) ϕ is the angle between the planes of the polarimeters; (B) the sketch shows the antiparallel (A) configuration.

mechanical stability and oil tightness in the case of the NaI detectors. As the experiment progressed, it was found that $\frac{1}{4}$-inch lead shields around the NaI detectors with windows facing the scattering crystal seemed to reduce the amount of extraneous scattered radiation which reached these detectors.

RCA 5819 photomultiplier tubes were used throughout; they were operated at about minus 1000 volts supplied by a well-regulated power supply of a modified University of Pittsburgh design. Magnetic shields consisting of one thickness of 22 gauge galvanized iron were found to reduce the effect of stray magnetic fields on the gain of the phototubes.

Figure 1 is a sketch of the apparatus. Figure 2 shows a block diagram of the system. A coincidence between signals in the scattered quantum detectors causes a sweep to be triggered on the oscilloscope. The signals arising from the recoil Compton electrons in the scattering crystals are mixed in a standard subtraction circuit,[13] one signal being delayed and inverted with respect to the other. The mixer output is amplified and delayed still further and presented on the triggered sweep. The number of sweeps is continuously monitored. The cathode-ray tube display is photographed on a continuously moving 35-mm film, and upon development it may be read at leisure in a microfilm reader.

The oscilloscope was a Tektronix Model 517, equipped with a 5 XP 11 A metallized screen tube, and using 20 kilovolts post-deflection acceleration. The camera was built in the physics department shop and was equipped with a Wollensack $f/1.5$ lens and no shutter. The film was driven by a synchronous motor through a gear train which could be changed to provide different film rates. Fresh Eastman Linagraph Pan film was used, and it was developed to a slight chemical fog. In this manner it is possible to photograph single sweeps of the fastest sweep speed available on the model 517 oscilloscope, 10 mμsec/cm (millimicrosecond per centimeter).

[13] Samuel Seely, *Electron-tube Circuits* (McGraw-Hill Book Company, Inc., New York, 1950), p. 146.

Figure 3 is a print of some typical traces, at a sweep speed of 50 mμsec/cm.

The advantage of this method of coincidence analysis is that it enables one to resolve on the width of the oscilloscope trace and on the start of the pulse, rather than on the width of the pulse itself as is the case in most electronic coincidence circuits. The disadvantage is of course the tedium of reading the film.

III. EXPERIMENTAL DETERMINATION OF THE EFFECTIVE GEOMETRY

Using a Cu^{64} source of positrons, a calibration of the polarimeters was undertaken. This procedure was based on the well-known cross-polarization property of the annihilation radiation.

The source was a 0.010×0.50 inch disk of copper which had been irradiated in the pile at Oak Ridge. Fractions of it were placed in the collimator enclosed in sufficient aluminum to stop the positrons. As the source decayed more of the irradiated disk was added. The sweep rate was about 100 per minute, and successive fifteen minute runs were taken, alternately in the parallel and perpendicular orientations of the polarimeters. The film rate was 1 foot per minute. A total of 28 runs were taken, comprising about 40,000 sweeps on 400 feet of film.

Figure 4(A) shows a histogram of the delay distribution for a typical run. The unit along the abscissa is approximately 5 mμsec. The width of the peak may be attributed to (1) nonlinearity and nonreproducibility of the sweep; (2) poor definition of the start of the pulse (due to the finite band width of the deflection amplifiers); (3) inherent random delays in the detecting

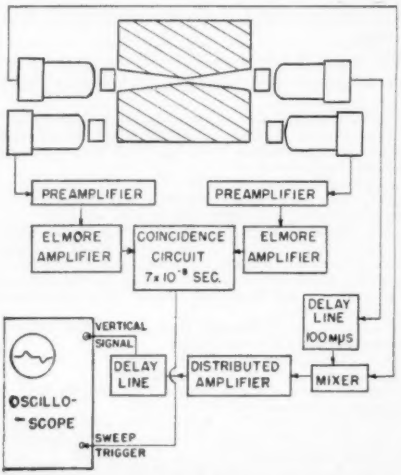

FIG. 2. Block diagram of the electronic system.

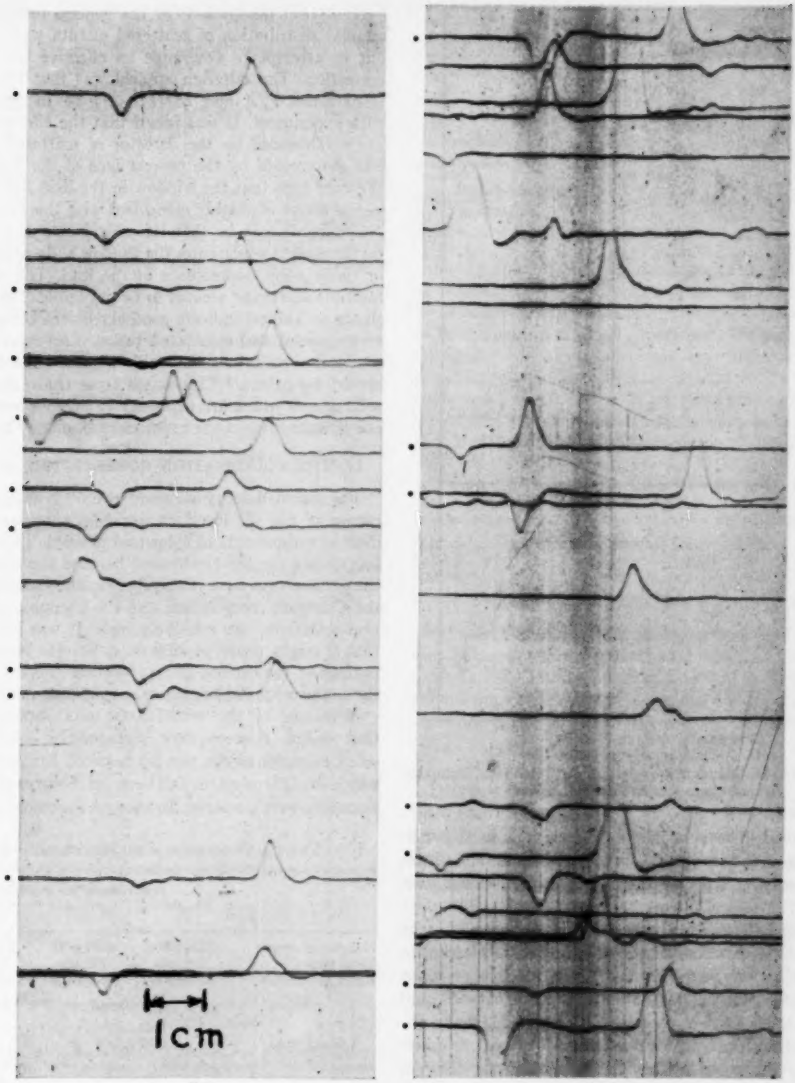

FIG. 3. Typical film records of oscilloscope traces, 50 mμsec/cm.

mechanism[14]; (4) errors made by the reader of the film record. The peak seemed to be sharp enough for our purposes and no attempt was made to determine the relative weights of these contributions; the effective resolving time is ~10 mμsec.

Figure 4(B) is a compound histogram of the wings of over half the runs. Its shape is attributable to the finite resolving time of the coincidence circuit which triggers

[14] R. F. Post, Nucleonics **10**, 56 (June, 1952); R. R. Law, Nucleonics **10**, 38 (March, 1952).

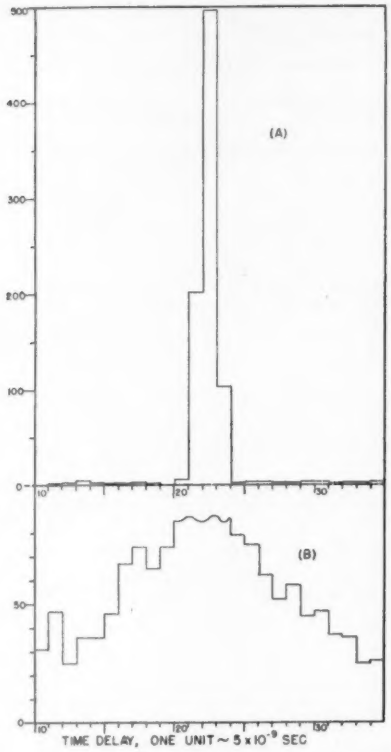

FIG. 4. (A) Histogram of a single run, Cu^{64}; (B) Total histogram of wings of delay distribution, Cu^{64}.

the sweep. The coincidences represented in this histogram are not genetically related but fall within the resolving time of the sweep trigger coincidence circuit.

Table I shows the number of events observed for the different orientations of the polarimeters. Referring to Fig. 1(A), we have designated the relative positions $\phi = 0°$, 90°, 180° as parallel (P), perpendicular (S), and antiparallel (A), respectively. The parallel and antiparallel positions are equivalent with respect to determining the polarization, but their rates are different because of the unique angular correlation of the annihilation radiation, and because the scattering crystal is quite large. The ratio P/A is sensitive to the amount of multiple scattering in the scattering crystal. The ratio $2S/(P+A)$ is the measure of the polarization sensitivity. The numbers in Table I have been corrected for the decay of the source. The errors shown are counting statistics only.

Numerical integrations of the general formula[15] for angular distribution of scattered quanta were carried out to attempt to determine an effective solid angle correction. The criterion applied was that the calculated ratios P/A and $2S/(P+A)$ be in agreement with experiment. It was found that the effective solid angle subtended by the detector of scattered quanta was determined by the nearest face of the NaI cube. We note here that the window in the lead shield mentioned above is roughly coincident with this face of the NaI cube. It may be that this shield acts as a "trap" for the quanta which enter the window and are scattered or cause x-ray fluorescence in the lead. The effect of multiple scattering seemed to be negligible. The results shown in Table I indicate good agreement between the experimental and calculated ratios. The experimental correlation ratio is considerably smaller than that observed by others.[11] This arises from the rather large solid angles which are necessary to achieve reasonable coincidence rates in the experiment discussed below.

IV. THE POLARIZATION CORRELATION IN Cs^{134}

The assumed decay scheme[16] of Cs^{134} is shown in the corner of Fig. 5. Previous work[2,5,17] suggests the indicated assignments of spins and parities. This isotope was chosen for the experiment because the energies of the gamma-rays were relatively low, and therefore both the Compton cross section and the Compton polarization sensitivity are relatively high. It was also hoped that it might prove possible to determine some of the parities of the excited states; however the statistics of the experiment did not allow such a determination.

A sample of the radioisotope was obtained from Oak Ridge. Sources were prepared by sandwiching small amounts of the powder between Lucite disks in which small depressions had been cut. Sources of various strengths were prepared. In view of the resolving times

TABLE I. Coincidences of annihilation radiation.

	Orientation of the polarimeter		
	Parallel (P)	Antiparallel (A)	Perpendicular (S)
Number of events	3724±80	4559±90	13,401±150
Total time	105 min	105 min	210 min
Rates per minute	35.5±0.8	43.4±0.9	63.8±0.6
Ratios	Experimental		Calculated
P/A	0.82±0.05		0.76
$2S/(P+A)$	1.62±0.03		1.60

[15] See, for instance, Enrico Fermi, *Nuclear Physics* (University of Chicago Press, Chicago, 1950), p. 42 (note that the formula given is for intensity, not number of quanta).

[16] *Nuclear Data*, National Bureau of Standards Circular 499 (1950). The simplicity of this decay scheme is not well established in view of recent work [F. H. Schmidt, Rev. Sci. Instr. **23**, 361 (1952); F. H. Schmidt and G. L. Keister, Phys. Rev. **86**, 632 (1952)].

[17] Waggoner, Moon, and Roberts, Phys. Rev. **80**, 420 (1950); C. L. Peacock and J. L. Braud, Phys. Rev. **83**, 484 (1951); B. L. Robinson and L. Madansky, Phys. Rev. **84**, 604 (1951).

attainable, it was found that about 1 millicurie was the optimum source strength. The sweeps averaged about 10 per minute, and a film rate of 7 feet per hour was used. About 100 hours of useful data were obtained. This comprised about 70,000 sweeps and about 14,000 events. Since one might expect drift in bias voltages and amplification during such a long period, it was decided to normalize the true events to the accidentals. The efficiencies for real and accidental events are affected in exactly the same manner by the suspected instabilities. The ratio of real to accidental events is therefore proportional to the correlation function. In this case it is an advantage to have a large accidental counting rate, but only because the accidentals are separable from the reals.

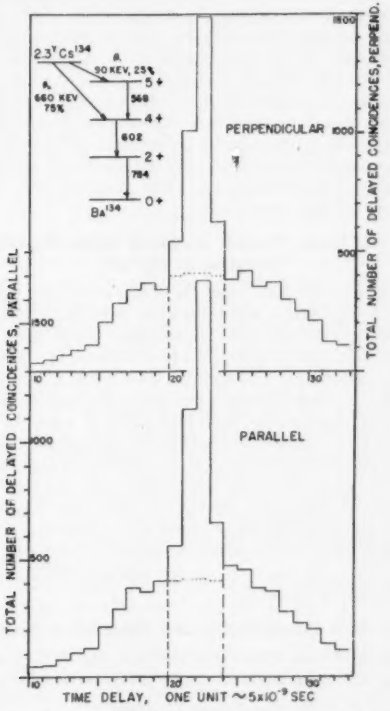

FIG. 5. Total histograms for Cs^{134}, parallel and perpendicular configurations; (inset) decay scheme of Cs^{134}.

TABLE II. Polarization correlation of Cs^{134} gamma-rays.

	Parallel	Perpendicular
Accidentals in the wings	4722±69	4418±66
True events (peak minus accidentals under peak)	2409±76	2063±72
$\frac{\text{True events}}{\text{Accidentals in wings}}$	0.51±0.02	0.47±0.02
Ratio $\frac{\text{Perpendicular}}{\text{Parallel}}$	0.91±0.08	

Figure 5 shows the total histograms for data taken at parallel and perpendicular orientations. These data are tabulated in Table II. Using the effective solid angle as determined in the Cu^{64} experiment, the polarization sensitivity of the polarimeters was determined by numerical integration of the scattering formula[15] for the energies 0.6 and 0.8 Mev. When these efficiencies were introduced into the polarization correlations of Falkoff and MacDonald[6] the results shown in Table III were obtained. In deducing these ratios, the spins and parities were taken as follows: ground state 0+; first state 2+; second state 4+; third state as shown in the table. The angular correlations of the cascades were also taken into account.[16,1]

TABLE III. Expected polarization correlations for finite geometry, Cs^{134}.

Spin and parity of third excited state	5+	5−	6+	6−
Expected ratio	0.96	0.91	0.90	0.96
Experimental ratio		0.91±0.08		

V. CONCLUSIONS

Previous work[17] has indicated that the spin of the third excited state is 5 and its parity is +. The work reported here is not in disagreement with these results. In conclusion we may remark that the polarization correlation effect has been observed; i.e., the coincidence rate is not isotropic. In order to distinguish between the various possibilities in the case of Cs^{134}, it would have been necessary to accumulate about ten times as much data as are represented in this paper. In view of the small counting rates, this would require a prohibitive amount of time.

[15] Biedenharn, Arfken, and Rose, Phys. Rev. 83, 586 (1951).

Spin Echo Measurements of Nuclear Spin Coupling in Molecules*

E. L. HAHN†‡ AND D. E. MAXWELL
Stanford University, Stanford, California
(Received August 4, 1952)

A new type of nuclear spin-spin coupling in molecules in liquids is investigated by means of the spin echo technique. A coupling interaction of the rotationally invariant form $h\mathbf{J}\mathbf{I}_1\cdot\mathbf{I}_2$ in the nuclear induction Hamiltonian predicts the detailed shape of the spin echo envelope. Echo modulation frequencies corresponding to the coupling J and the chemical shift between nonequivalent protons are measured in a variety of compounds. A generalized method for calculating the spin echo is presented for large chemical shift and weak coupling among an arbitrary number of spins. The damping of the echo modulation, due to spin relaxation and molecular effects which interrupt the J coupling, is accounted for by a phenomenological treatment of the quantum-mechanical expectation value of nuclear magnetization.

I. INTRODUCTION

ASIDE from the measurement of spins and gyromagnetic ratios by the method of nuclear resonance or nuclear induction,[1,2] there are many problems in molecular structure and the solid state which have been studied by this technique. This paper deals primarily with one of a group of higher order effects determined by the chemical environment of the nucleus. The nuclear configurations in crystals and the electronic configurations about nuclei in atoms, molecules, and in metals cause definite shifts in the nuclear resonance frequency. The resonance frequency of the nuclear moment is shifted from that value which it would have if the nucleus were isolated from neighboring nuclei, and; stripped of all extra-nuclear electrons. In some instances a single resonance line may be split into two or more lines by local magnetic fields in the lattice, or an electric field gradient may interact with any nuclear electric quadrupole moment and cause line splitting. In the case of single resonance shifts, actual experiment reveals the differences in absolute shifts between resonance frequencies of like nuclear species as they occur in different chemical environments. An outline of the known effects which produce resonance shifts is given below.

A. The Chemical Shift

A shift in the nuclear resonance, known as the chemical shift,[3,4] is due to the effects of diamagnetism and induced paramagnetism in a molecule. Because these two effects are linearly proportional to the applied magnetic field, it is impossible to distinguish them from one another. A local magnetic field at the position of the nucleus is caused by the Larmor precession of extra-nuclear electrons in an externally applied magnetic field. In first order, the effect due to a spherically symmetric electron distribution is given by the Lamb diamagnetic correction.[5] In second order, where electrons undergo attraction by two or more nuclei in molecules, it has been shown by Ramsey[6] that the induced paramagnetism (which in many cases is comparable to, or larger than, the diamagnetic correction) arises from a perturbation in which the ground state mixes with a paramagnetic excited state of the molecule. This causes the observed large chemical shift when the energy level of the paramagnetic state lies very close to that of the ground state.

B. Direct Nuclear Magnetic Dipole-Dipole Coupling in Crystals

Pake first showed[7] that the resonance of two proton nuclear moments, which are close neighbors, reveals a splitting into two lines. The magnetic dipole fields, due to parallel and antiparallel orientations of the protons, respectively add and subtract local fields at the positions of these protons throughout the lattice. These values superimpose upon the constant value of the externally applied field and cause the splitting. More complicated spin systems in crystals have been studied which show resonance line shapes determined by the direct dipole-dipole interaction.[8] No case has been confirmed in which the direct interaction prevails in liquids. This is to be expected since this direct coupling averages out due to rapid and random rotations of a molecule in a liquid.[1,9]

C. Shift Due to Conduction Electrons in Metals

Knight[10] has found that the paramagnetism due to conduction electrons in metals causes a net local mag-

* Supported in part by the ONR.
† National Research Council Post-doctoral Fellow during a portion of this research.
‡ Present address: Watson Computing Laboratory, Columbia University, New York 27, New York.
[1] Bloembergen, Purcell, and Pound, Phys. Rev. **73**, 679 (1948).
[2] F. Bloch. Phys. Rev. **70**, 460 (1946).
[3] W. G. Proctor and F. C. Yu, Phys. Rev. **77**, 717 (1950).
[4] W. C. Dickenson, Phys. Rev. **77**, 736 (1950).
[5] W. E. Lamb, Phys. Rev. **60**, 817 (1941).
[6] N. F. Ramsey, Phys. Rev. **78**, 699 (1950).
[7] G. E. Pake, J. Chem. Phys. **16**, 327 (1948).
[8] E. R. Andrew and R. Bersohn, J. Chem. Phys. **18**, 159 (1950).
[9] The interaction between two parallel dipoles is proportional to $1-3\cos^2\theta$, where θ is the angle between the internuclear axis and the direction of the dipoles. This quantity averages to zero over a sphere but its square does not. During discussions at the American Physical Society meeting in Washington, D. C., April, 1951, Purcell pointed out that for this reason the direct interaction, in second order, can exist in liquids with a magnitude inversely proportional to the applied magnetic field. As yet this small effect has not been observed.
[10] W. D. Knight, Phys. Rev. **76**, 1259 (1949).

netic field at the position of the nucleus. The magnitude of this shift is proportional to the value of the applied magnetic field.

D. Quadrupole Splitting in Crystals

Pound has demonstrated[11] for nuclei with spin $I>\frac{1}{2}$ that the gradient of the electric field at the nucleus in crystals splits the magnetic resonance into $2I$ lines. In liquids electric field gradients have zero average value, and only a broadening of a single resonance line can result because of the quadrupole interaction.

E. Indirect Nuclear Spin-Spin Coupling

A new type of splitting is observed in liquids which is independent of the applied magnetic field and the temperature. The bonding electrons between nuclear magnetic dipoles in a molecule serve as a medium which communicates a nuclear spin-spin magnetic interaction. The first case of such a field independent splitting was observed by the slow passage method in Sb^{121} contained in the SbF_6^- ion.[12] The effect was first attributed[12,13] to various local fields due to the possible F^{19} nuclear orientations (direct dipole coupling discussed in B above) which could split the Sb^{121} resonance into a number of lines. This requires the assumption that a hindrance of the random rotation of the SbF_6^- ion takes place in the liquid state so that the dipole fields due to the six F^{19} nuclei do not average out completely at the position of the Sb^{121} nucleus. The effect of such a splitting with use of spin echoes was later found in ethanol[14] and similar organic compounds. With the subsequent appearance of many cases of such splittings in liquids by the groups at Illinois[15–17] and at Stanford,[18,19] it became apparent that, although the direct nuclear dipole coupling mechanism might explain some general features of this splitting, the following difficulties arise: (a) it is difficult to account for rotational hindrance in a wide variety of molecules in liquids; and (b) the absence of splitting among chemically equivalent nuclear moments is not explained by this interaction.

Previously the authors have reported a measurement[18] of the spin echo envelope due to two coupled protons in dichloroacetaldehyde. An interaction of the form $J'\boldsymbol{\mu}_1\cdot\boldsymbol{\mu}_2$ was used in the Hamiltonian to predict the shape of the echo envelope in this molecule, and precise agreement was obtained with experiment. We may express $J'\boldsymbol{\mu}_1\cdot\boldsymbol{\mu}_2=\hbar J\mathbf{I}_1\cdot\mathbf{I}_2$, where $\mathbf{I}\equiv\mathbf{I}(I_x, I_y, I_z)$ is the spin operator and J is expressed in angular frequency. This form of the interaction is invariant to rotation, which predicts the fact that the coupling can be observed in molecules in liquids. A generalized form of this operator correctly accounts for the number, relative amplitudes, and relative splittings of absorption lines observed by the slow passage method[15] when coupling takes place between nonequivalent groups of nuclear dipoles in the same molecule. No splitting or echo modulation is predicted by such a coupling between equivalent spins, although the coupling still exists.

Several specific spin-electron-spin coupling mechanisms are possible in molecules. A majority of them give rise to the $\boldsymbol{\mu}_1\cdot\boldsymbol{\mu}_2$ form of interaction and may all play a role in accounting for observed values of J of the order of 1 cps or less. In order to account for larger values of J observed in many cases (of the order of kilocycles), Ramsey and Purcell[20] have shown that the $\boldsymbol{\mu}_1\cdot\boldsymbol{\mu}_2$ interaction is due mainly to one mechanism which can make J so large that probably all other mechanisms are of negligible influence in most of the observed cases. In the example of two indirectly coupled moments in the HD molecule, Ramsey and Purcell have shown that the bonding electrons, with spins normally antiparallel, are parallel in the triplet state for a small percentage of the time because of the perturbing influence of parallel orientations of the H and D nuclei. The hyperfine interaction of the electrons with the H and D nuclei then cause net local magnetic fields to appear at the positions of these nuclei. The energy expression $J'\boldsymbol{\mu}_1\cdot\boldsymbol{\mu}_2$ thus accounts for the fact that nucleus 1 sees a local field proportional to $J'\mu_2$ and conversely for nucleus 2, where J' accounts for the mechanism by which the bonding electrons communicate such a local field. In frequency units $(J/2\pi)$, each nucleus will see the same splitting, which Ramsey and Purcell have calculated to be approximately 70 cps for the HD molecule.

In this paper a transient analysis of the indirect spin-spin coupling effect (hereafter denoted by J coupling or splitting) is made of spin echo measurements.[14] The equivalent information in many respects is available from the analysis of steady-state resonance experiments, and yet the two methods serve to supplement each other. Many points which are discussed in this paper have been arrived at independently by the Gutowsky-Slichter group at Illinois.[17] In the course of our research we have learned, through exchange of information with the Illinois group, of the important results which they established from slow passage experiments.

The echo method possesses certain inherent advantages. For long relaxation times this method is able to resolve frequencies of the order of 1 cps, although an external field inhomogeneity over the spin sample produces a spread in Larmor frequencies much greater than this. Resolution is primarily limited because

[11] R. V. Pound, Phys. Rev. **79**, 685 (1950).
[12] W. G. Proctor and F. C. Yu, Phys. Rev. **81**, 20 (1951).
[13] E. R. Andrew, Phys. Rev. **82**, 443 (1951).
[14] E. L. Hahn, Phys. Rev. **80**, 580 (1950).
[15] H. S. Gutowsky and D. W. McCall, Phys. Rev. **82**, 748 (1951).
[16] Gutowsky, McCall. and Slichter, Phys. Rev. **84**, 589 (1951); McNeil, Slichter, and Gutowsky, Phys. Rev. **84**, 1245 (1951).
[17] Gutowsky, McCall, and Slichter, J. Chem. Phys. (to be published). We are grateful to them for an advance copy of this paper.
[18] E. L. Hahn and D. E. Maxwell, Phys. Rev. **84**, 1246 (1951).
[19] M. E. Packard and J. T. Arnold, Phys. Rev. **83**, 210 (1951); Arnold, Dharmatti, and Packard, J. Chem. Phys. **19**, 507 (1951).
[20] N. F. Ramsey and E. M. Purcell, Phys. Rev. **85**, 143 (1952).

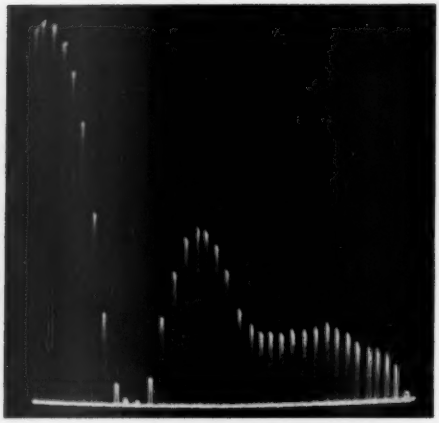

FIG. 1. Multiple photographic exposures of proton echo oscilloscope signals obtained in 2-bromo-5-chlorothiophene. The first rf pulse initiates the sweep. An exposure is made of the echo for each position of the second pulse (the pulses are not visible). As τ is increased, the maximum of the spin echo at the time 2τ traces out the modulation of the echo envelope. The time duration of the total sweep is 0.66 sec, and the Larmor frequency is 31 Mc.

thermal self-diffusion of molecules in liquids destroys the coherence of precession frequency as the nucleus migrates from one field value to another. This effect, however, is not as serious as that due to field inhomogeneity in slow passage experiments. In experiments where the effect of small splittings must be resolved, and where theory must be checked in detail, it is advantageous to study echo signals because they occur in the absence of a driving rf field. Accurate information can be obtained from the detailed shape of the echo envelope without having to consider the effect of a driving rf field on the measured decay of the echo signal.

II. THEORY AND EXPERIMENT OF THE TWO-PROTON COUPLING CASE

The majority of nuclear resonance effects observed in an ensemble of nuclear moments in a liquid are well described by the classical Bloch equations.[2] The longitudinal relaxation time T_1 and the transverse relaxation time T_2 can be measured as definite quantities providing that the nuclei are perturbed only by local fields which are completely random and isotropic. With the presence of J type coupling between nuclei within molecules in liquids, it is no longer possible to develop a general set of classical nuclear induction equations from the quantum-mechanical expectation values of the components of nuclear magnetization which are measured. Although the purely quantum-mechanical treatment which is to be presented shall at first not include the damping effect due to T_1 and T_2, a phenomenological treatment, which uses the quantum-mechanical result, will show that the over-all effect of these relaxation times is the same as in the Bloch equations; the coherence of the additional Larmor precession frequencies caused by the J splitting is also given by T_2 and is destroyed exponentially.

According to the echo method,[14] two short, intense pulses of radiofrequency power are applied to the spin ensemble at resonance and are separated by the time interval τ. The echo appears with a maximum amplitude at time 2τ after the application of the first pulse. At the onset of the first radiofrequency pulse the spin ensemble is at thermal equilibrium. For each setting of τ the maximum of the echo signal is measured and plotted as a function of increasing τ. The echo envelope thus obtained will normally decay monotonically with time in the absence of J splitting, and can yield an accurate measure of T_2 in those cases where molecular self-diffusion is not important. Consider now the simplest case of J splitting in which two resonant protons are close neighbors in a molecule, and in addition are chemically nonequivalent. This is denoted by assigning to proton 1 an absolute chemical shift of h_1 gauss, and to proton 2 the value h_2. The J splitting is not observed unless coupled nuclei are nonequivalent in the sense that (1) they have different chemical shifts, as in this particular case for identical nuclei, or (2) that they are not identical. The reason for this can be understood in the case of two-proton coupling where the J splitting appears in transitions between pure triplet states and states which are linear combinations of singlet and triplet terms. Normally transitions to the singlet state are forbidden unless the identity between the two protons is removed by a difference in chemical shift, With a chemical shift, as seen in Fig. 1, two frequencies then appear to modulate the decay of the spin echo envelope, which depend upon both J and $\delta=\gamma(h_1-h_2)$, where δ is the angular frequency which corresponds to the chemical shift and γ is the nuclear gyromagnetic ratio. The shape of this echo envelope can be described (as well as properties of J splitting observed in slow passage experiments) if the Hamiltonian,[18]

$$\mathcal{H}=-\gamma\hbar[\mathbf{I}_1\cdot(\mathbf{H}_0+\mathbf{h}_1)+\mathbf{I}_2\cdot(\mathbf{H}_0+\mathbf{h}_2)]-\hbar J\mathbf{I}_1\cdot\mathbf{I}_2, \quad (1)$$

is chosen to describe the two-proton coupled system in a constant magnetic field H_0. Both nuclei are subjected to the nuclear resonance imposed by the application of two radiofrequency pulses, where the rf frequency $\omega=\gamma H_0$. Each pulse at H_1 gauss maximum amplitude lasts for t_w seconds, where $t_w\ll\tau$, and $1/t_w$, $\gamma H_1(=\omega_1)$ $\gg\gamma\Delta H, \delta, J$; ΔH is the magnitude of the external field inhomogeneity over the sample. If only one of two coupled nuclei is subjected to resonance (e.g., between F^{19} and H) no echo envelope modulation will appear for either of such coupled nuclei, although the steady state resonance will still reveal the J splitting.

The zero order two-proton spin wave function, which applies both in the presence and absence of pulses, is

given by

$$\psi=\sum_{S=0}^{1}\sum_{m=-S}^{S}a_{S,m}(t)\phi_{S,m}\exp-iE_{S,m}t/\hbar, \quad (2)$$

where the total spin $S=1$ for the triplet state and $S=0$ for the singlet state. $\phi_{S,m}$ specifies the spin state function characterized by the magnetic quantum number m, and $E_{S,m}$ is the corresponding eigenvalue. The three triplet state probability amplitudes $a_{1,m}$ ($m=1,0,-1$) are time dependent during the application of H_1 and the singlet state amplitude $a_{0,0}$ remains constant. The Hamiltonian,

$$\mathcal{H}=-\gamma\hbar(\mathbf{I}_1+\mathbf{I}_2)\cdot(\mathbf{H}_0+\mathbf{H}_1), \quad (3)$$

describes the system during a pulse, and terms due to δ and J are omitted for $1/t_w\gg\delta$ and J. Upon substituting (2) and (3) into the time-dependent Schrödinger equation,

$$i\hbar\dot{\psi}=\mathcal{H}\psi, \quad (4)$$

and solving for $a_{1,m}(t)$, we obtain

$$a_{1,0}(t)=a_{1,0}(t_i)\cos(\omega_1 t)+(i/\sqrt{2})\times[a_{1,1}(t_i)+a_{1,-1}(t_i)]\sin(\omega_1 t), \quad (5a)$$

$$a_{1,\pm1}(t)=a_{1,\pm1}(t_i)\cos^2(\omega_1 t/2)-a_{1,\mp1}(t_i)\sin^2(\omega_1 t/2)+\frac{i}{\sqrt{2}}a_{1,0}(t_i)\sin(\omega_1 t). \quad (5b)$$

The pulse is turned on at $t=t_i$ and turned off at $t=t_i+t_w=t_i'$. These coefficients can also be obtained from a general method given by Bloch and Rabi,[21] which will be applied later in cases involving more than two spins. In the absence of H_1, during the relatively long time of free Larmor precession, it is necessary to correct the wave function given by (2) in order to include the perturbation effects of δ and J on the Larmor precession. The Hamiltonian given by (1) shall apply. The coefficients $a_{S,m}$ become constants determined by initial conditions due to pulses. By the Ritz variational method[22] the following normalized and corrected wave function is obtained:

$$\psi=a_{1,1}(t_i')[\exp(-iE_{1,1}t/\hbar)]\alpha_1\alpha_2+a_{1,-1}(t_i')[\exp(-iE_{1,-1}t/\hbar)]\beta_1\beta_2 \quad (6a)$$

$$+\frac{1}{\sqrt{2}}\left(\frac{a_{0,0}(t_i')-a_{1,0}(t_i')Q'}{Q-Q'}\right)[\alpha_1\beta_2(1+Q)+\alpha_2\beta_1(1-Q)]\exp(-iE_0t/\hbar) \quad (6b)$$

$$-\frac{1}{\sqrt{2}}\left(\frac{a_{0,0}(t_i')-a_{1,0}(t_i')Q}{Q-Q'}\right)[\alpha_1\beta_2(1+Q')+\alpha_2\beta_1(1-Q')]\exp(-iE_0't/\hbar), \quad (6c)$$

[21] F. Bloch and I. I. Rabi, Revs. Modern Phys. 17, 237 (1945).
[22] L. Pauling and E. B. Wilson, *Introduction to Quantum Mechanics* (McGraw-Hill Book Company, Inc., New York, 1935), p. 189.

where

$$Q=[J-(J^2+\delta^2)^{\frac{1}{2}}]/\delta,\quad Q'=[J+(J^2+\delta^2)^{\frac{1}{2}}]/\delta,$$

$$E_{1,1}=-\gamma\hbar(H_0+\tfrac{1}{2}h_1+\tfrac{1}{2}h_2)-\tfrac{1}{4}\hbar J,$$

$$E_{1,-1}=\gamma\hbar(H_0+\tfrac{1}{2}h_1+\tfrac{1}{2}h_2)-\tfrac{1}{4}\hbar J,$$

$$E_0=\hbar[\tfrac{1}{4}J-\tfrac{1}{2}(J^2+\delta^2)^{\frac{1}{2}}],$$

$$E_0'=\hbar[\tfrac{1}{4}J+\tfrac{1}{2}(J^2+\delta^2)^{\frac{1}{2}}],$$

and $\phi_{S,m}$ is a product function of component spin states of the system, with each state given by α for $I=\frac{1}{2}$ and β for $I=-\frac{1}{2}$. The constants $a_{1,m}(t_i)$ of Eqs. (5) and $a_{0,0}(t_i)$ are amplitudes of the above four stationary states at $t=t_i$. The coefficients of $\alpha_1\alpha_2$, $\beta_1\beta_2$, and $(\alpha_1\beta_2+\alpha_2\beta_1)\sqrt{2}$ are then equal to the constants $a_{1,m}(t_i)$ in Eqs. (5), where only the triplet states are involved. The factor of $(\alpha_1\beta_2-\alpha_2\beta_1)/\sqrt{2}$, the singlet state, remains unchanged, and is set equal to $a_{0,0}(t_1')$ in Eq. (6). The eigenvalues and the splittings which result in slow passage are shown by the Zeeman level diagram in Fig. 2. The top and bottom levels (terms in (6a)) are pure triplet states and each of the two closely spaced levels is a linear combination of singlet and triplet states (terms (6b) and (6c)). For $\delta\to0$, $Q=0$ and $Q_1=\infty$, and the mixed state with the energy eigenvalue E_0' now becomes a pure singlet state. The J splitting therefore disappears because transitions to and from the pure singlet state are forbidden. This supports the fact in the case of two equivalent nuclei that no J splitting is observed.[15] For $\delta\sim J$ the intensities of the transitions indicated are determined by the particular transition probabilities between the given states as well as by their statistical weights. In the order of increasing frequency the magnitudes of the absorption lines are in the ratio of

$$\frac{1}{1+Q'^2}:\frac{1}{1+Q^2}:\frac{1}{1+Q^2}:\frac{1}{1+Q'^2}.$$

In the limit $J\ll\delta$ then $Q=-1$, $Q'=+1$, all of the amplitudes are equal, and the J splittings conform to the rule given by Gutowsky.[15]

The expectation value of the precessing components

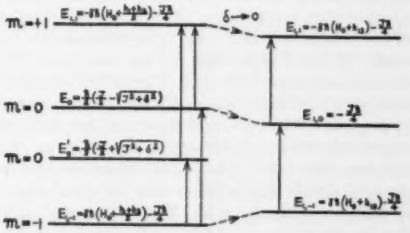

FIG. 2. Zeeman energy level diagram for a nonequivalent two-spin system ($I=\frac{1}{2}$ for each spin). For $\delta=0$ the magnitude of $h_{12}=h_1=h_2$ chosen is arbitrary.

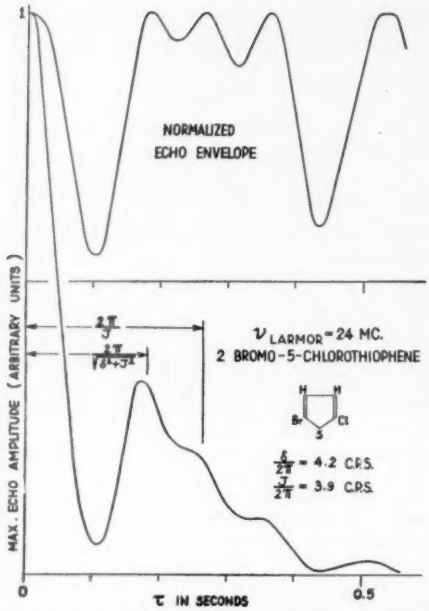

FIG. 3. Experimental echo envelope plots for protons in 2-bromo-5-chlorothiophene. The lower plot of the observed envelope is normalized to unity in the upper plot in order to correct for the damping due to spin relaxation and diffusion. The upper plot refers to the abscissa directly beneath it. Because of thermal diffusion, the damping for this particular measurement is greater than the damping shown for the same compound in Fig. 1. The magnetic field H_0 over the sample for the above measurement happened to be more inhomogeneous than the field over the sample when the plot in Fig. 1 was photographed.

of nuclear magnetization for $t \gg \tau + t_w$ will be given by

$$V = u + iv = (\psi^* | I_+ | \psi), \tag{7}$$

where the spin operator

$$I_\pm = I_x \pm iI_y = I_{x1} + I_{x2} \pm i(I_{y1} + I_{y2})$$

is averaged over ψ given by (6), and the integral is written in Dirac notation. u and v are the observed real and imaginary components of induction, respectively. For the condition that H_1 and t_w are the same for both pulses, the exact expression for the maximum of the spin echo amplitude, at $t = 2\tau$, is given in Appendix A. In the spin echo experiment only the absolute value of (7), given by $|V|$ at $t = 2\tau$, is observed. Only the terms independent of H_0 contribute to the echo at $t = 2\tau$, assuming that $\tau \gg 1/\gamma \Delta H$, and therefore the free induction signals which follow directly after pulses do not interfere with the echo. We have neglected any damping due to T_2 and thermal diffusion in arriving at this result. The observed spin echo envelope must therefore be normalized and plotted as a function of τ in order to compare with theory. This procedure is valid, as we shall point out, providing that both of the coupled nuclei have the same T_2 and that the presence of other neighboring nuclei with finite magnetic moments in the molecule do not effectively couple, in this case, with the two proton system. For example, the influence of the Cl^{35}, Cl^{37} moments on the J coupling between the protons in dichloroacetaldehyde ($CHCl_2CHO$) appears to be absent. This can be accounted for by the fact that the quantum states of the chlorine nuclei are short lived due to quadrupole broadening, and thus chlorine has a relaxation time which is small compared to T_2 of the protons and to $1/J$. This process is treated later in a special case (Part IV). Thus, any J coupling that exists between chlorine and hydrogen averages to zero as far as the experiment can detect.

For $\omega_1 t_w = \pi/2$ the observed and the normalized plots of the envelope due to protons in 2-bromo-5-chlorothiophene[22] are given in Fig. 3. In this case the theoretical expression for the envelope is given by

$$|V| = \frac{M_0 \delta^2}{2(\delta^2 + J^2)} \left| 1 + \frac{J^2}{2\delta^2} - 2 \sin^2(J\tau/2) \sin^2[\tau(J^2+\delta^2)^{\frac{1}{2}}/2] \right|, \tag{8}$$

which agrees with the normalized plot within experimental error. At a Larmor frequency $\omega/2\pi = 24$ Mc, $J/2\pi = 3.9$ cps and $\delta/2\pi = 4.2$ cps. At $\omega/2\pi = 32$ Mc, $\delta/2\pi = 5.6$ cps, and J remains unchanged. The parameter δ appears to be linearly proportional to H_0, and every case bears out this fact where δ can be resolved. For $\delta \sim J$ in this case, the xy components of J coupling cannot be neglected in comparison to the coupling in the z direction, and the magnetic quantum number m is not a constant of the motion. In most cases, however, it is observed that $J \ll \delta$, and we let $J\mathbf{I}_1 \cdot \mathbf{I}_2 \rightarrow J I_{1,z} I_{2,z}$. This is analogous to the approximation made in the Paschen-Back effect, where the large magnetic field in that case plays the role of δ. The observed plot has been reported[18] for the echo envelope of protons in dichloroacetaldehyde, giving $\delta/2\pi = 10\frac{1}{2}$ cps and $J/2\pi = 2.7$ cps at $\omega/2\pi = 32$ Mc. The plot agrees with the expression (8) for $J \ll \delta$.

One might suspect that the protons in dichloroacetaldehyde do not have just single chemical shifts h_1 and h_2, but several because of the possible structural isomers of $CHCl_2CHO$. However, we assume that the rapid transfer between these possible isomers causes an averaging into two definite chemical shifts, one for each proton. This will be shown to result when the lifetimes in each isomeric state (estimated from known chemical barriers which give rise to hindered rotation) are much shorter than $2\pi/\delta$.

[22] We wish to thank Professor H. S. Mosher of the Stanford Chemistry Department for a special synthesis of this compound.

III. *J* COUPLING AMONG THREE OR MORE SPINS

A generalized form of the J coupling Hamiltonian among n spins, given by

$$\mathcal{H}=-\sum_{j=1}^{n}[h\gamma_j\mathbf{I}_j\cdot(\mathbf{H}+\mathbf{h}_j)+\tfrac{1}{2}\sum_{\substack{i=1,\\ i\neq j}}^{n}hJ_{ij}\mathbf{I}_i\cdot\mathbf{I}_j], \quad (9)$$

shall be used to express the coupling, where $\mathbf{H}$ is an arbitrary external magnetic field and $\mathbf{h}_j$ is the chemical shift of the jth nucleus. Consider the coupling of two nonequivalent spin groups A and B, where K_A and K_B denote the coupling between equivalent spins in groups A and B, respectively. The Hamiltonian (9) can then be written as

$$\mathcal{H}=-\gamma h[\mathbf{S}_A\cdot(\mathbf{H}+\mathbf{h}_A)+\mathbf{S}_B\cdot(\mathbf{H}+\mathbf{h}_B)] -hJ\mathbf{S}_A\cdot\mathbf{S}_B-C(K_AS_A^2, K_BS_B^2, K_AI_A^2, K_BI_B^2), \quad (10)$$

where

$$\mathbf{S}_A=\sum_{k=1}^{n_A}\mathbf{I}_k, \quad \mathbf{S}_B=\sum_{l=1}^{n_B}\mathbf{I}_l,$$

$\gamma=\gamma_A=\gamma_B$, and I_A and I_B are the spin values of component nuclei in groups A and B, respectively. C is a function of terms, as indicated, which commutes with $\mathcal{H}$, and introduces the coefficients K_A and K_B as constants in the energy eigenvalues of this system. These coupling constants do not appear in the differences between these eigenvalues, and therefore are not observed in resonance splittings. Of course, if $\delta=0$ then J coupling disappears for the same reason, namely, that $\mathbf{S}_A\cdot\mathbf{S}_B\rightarrow S^2_{A+B}$, and a single resonance line results. In the spin echo experiment the interference effect which gives rise to the envelope modulation correspondingly vanishes.

A. Coupling Among Three Spins

The result for the exact calculation (δ and J arbitrary) in which two equivalent spins couple with a third spin ($I=\frac{1}{2}$ for each spin and $\gamma_A=\gamma_B$) is given in the Appendix B. In Fig. 4 the observed echo envelope due to three protons in $CHCl_2CH_2Cl$ is plotted, where $J/2\pi=6.0$ cps and $\delta/2\pi=48$ cps at $\omega/2\pi=24$ Mc. Figure 5 shows photographs of these echoes at 31 Mc. This case also applies to protons in $CHCl_2CHClCHCl_2$, where $J/2\pi=5.3$ cps and $\delta/2\pi=38$ cps at $\omega/2\pi=24$ Mc. The proton echo envelopes for both of these molecules is accurately described if terms involving only the ratio J/δ, taken to the first power, are retained in the exact expression given in Appendix B. The Zeeman energy level diagram is shown in Fig. 6. Schiff[24] describes the symmetry properties of the various spin functions which are linearly combined to give the particular states as indicated. For $\delta=0$ the states corresponding to the eigenvalues E_3 and E_5 can only have

[24] L. I. Schiff, *Quantum Mechanics* (McGraw-Hill Book Company, Inc., New York, 1949) p. 229.

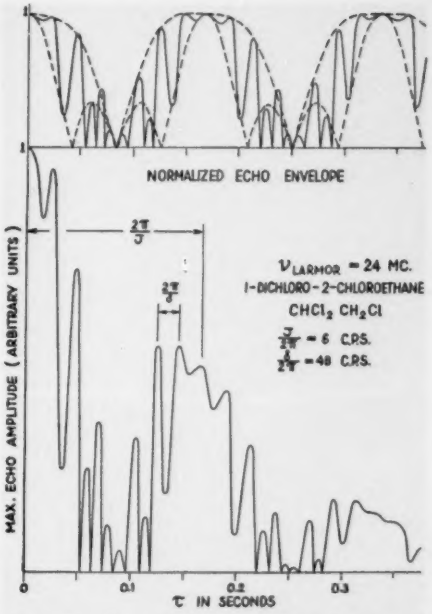

FIG. 4. Experimental echo envelope plots for protons in 1-dichloro-2-chloroethane. The meaning of the lower and upper solid line plots is the same as in Fig. 3. The dotted lines plotted from the theory trace out the envelope of the upper and lower limits of the echo envelope modulation plot. The periodic doubling of the modulation frequency appears because the echo experiment reveals only the absolute magnitude of the echo modulation. The region of modulation doubling (as indicated within the small dotted lobes which meet the abscissa) signifies in the theory that the sinusoidal plot changes sign for a few cycles; that is, with respect to a reference axis, the nuclear magnetization vector of the echo reverses direction by 180°.

transitions between themselves and cannot combine with any other state. All transitions then involve only a single energy difference, and a single resonance absorption line results. Under any circumstance, the coupling between the equivalent protons cannot be observed for reasons which have been discussed in the two proton case.

In the approximation that $J\ll\delta$, the relative intensities and the number of lines which result are in accordance with the following empirical rules found by Gutowsky[15] for nuclei with $I=\frac{1}{2}$. (*a*) The resonance of n_A equivalent spins in group A, with maximum total spin $S_A=n_A/2$, is split into $2S_B+1$ equidistant lines by an equivalent spin group with total maximum spin S_B, and conversely for the resonance of spin group B. (*b*) The relative intensities of the resonance lines of A are determined by the binomial coefficient $\binom{2S_B}{N_A-1}$, which determines the relative amplitude of the N_Ath

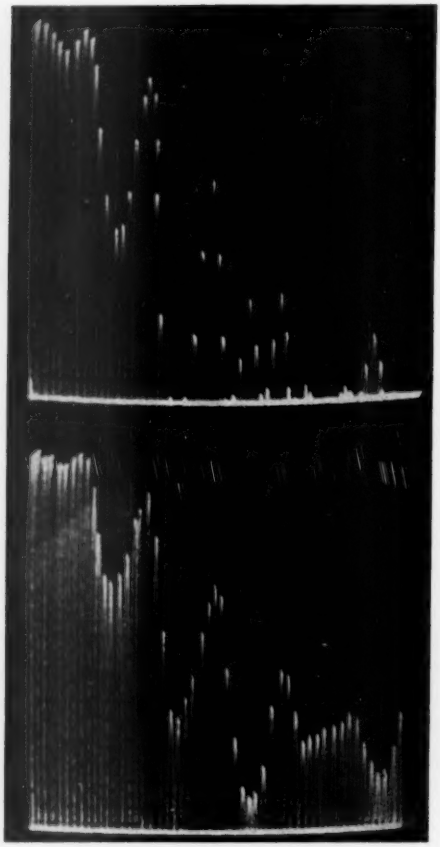

FIG. 5. The upper photograph shows the echo envelope due to protons in pure $CHCl_2CH_2Cl$ at a Larmor frequency of 31 Mc. Both photographs are obtained by the method indicated in Fig. 1. The time duration of the total sweep is 0.22 sec. The lower photograph shows, on the same time scale as the upper one, the echo envelope due to protons in a mixture of $CHCl_2CH_2Cl$ and chloroform ($CHCl_3$). The echo modulation frequency doubling effect, which is seen in the pure compound above, does not appear below because the echo component produced by the protons in $CHCl_3$ (which alone does not exhibit envelope modulation) serves as reference upon which the sinusoidal echo modulation due to $CHCl_2CH_2Cl$ may superimpose. Thus, the total echo vector never reverses direction (see caption of Fig. 4).

line ($N_A=1, \cdots, 2S_B+1$). (*c*) In addition, the ratio of the splitting, measured in gauss, between adjacent lines of group A to that in group B is given by $\mu_B I_A/\mu_A I_B$.[25] However, in cases where $\delta \sim J$ the above rules break down. In Fig. 6 more than $2(S_A+S_B+1)=5$ lines appear in this case.

[25] Although rule (*b*) holds only for $I=\frac{1}{2}$, rules (a) and (c) hold for arbitrary I, where $S=nI$ replaces $S=n/2$.

B. Generalization of the Coupling for $J \ll \delta$

In most of the observed cases it is found that $J \ll \delta$, and the Hamiltonian (10) in the absence of H_1 can be written as

$$\mathcal{H}=-\gamma\hbar[S_{z,A}(H_0+h_A)+S_{z,B}(H_0+h_B)]-\hbar J S_{z,A}S_{z,B}. \tag{11}$$

The average of the x and y components of J coupling over the period $2\pi/\delta$ is negligible compared to the coupling in the z direction. The rule given for the number and intensities of the lines may be understood, for example, if we consider that spin group A sees a local magnetic field given by $H_0(A)=H_0+h_A+JS_{z,B}/\gamma$ and conversely for group B. There are $2S_B+1$ possible values of $S_{z,B}$, where each of these values has the statistical weight given by the number of ways in which the component spins of a group may be oriented in order to provide a given S_z. For $I=\frac{1}{2}$ this statistical weight is given by the binomial coefficient presented previously, where $N_A-1=S_B+S_{z,B}$ and $S_{z,B}=S_B, S_B-1, \cdots, -S_B$.

With the above approximation in mind, consider a physical model of the echo modulation in which the local magnetic J field due to the z component of a macroscopic spin vector $\mathbf{M}_A$ is seen by $\mathbf{M}_B$ and vice versa (let M_A and M_B). If both of these vectors precess with precisely the same Larmor frequencies, which is to say that $\delta=0$, it becomes impossible by means of rf absorption to cause the z magnetic fields due to J, seen by both vectors, to differ. In the more precise terms of the quantum-mechanical calculation, a constant J term is added to all of the energy eigenvalues of the coupled system, and J does not appear in the differences between those eigenvalues of spin states involved in allowed transitions. However, if δ is finite, a vector model will show how the difference in Larmor precession frequencies makes it possible for $\mathbf{M}_A$ and $\mathbf{M}_B$ to interfere with each other due to J coupling. Let both of these vectors precess in the xy plane after the first pulse (let $\omega t_w=\pi/2$) and view the system from xy coordinates which precess at the Larmor frequency of $\mathbf{M}_A$. Since $M_{z,A}=M_{z,B}$ after the first pulse (which is true regardless of the value of $\omega_1 t_w$ under the conditions of the experiment), the only difference in Larmor precession frequency between these vectors during the time between t_w and τ is that due to the chemical shift. At the time a second rf pulse is turned on at $t=\tau$, then $M_{xy,A}$ and $M_{xy,B}$ are out of phase by $\delta\tau$ radians. After the second pulse rotates the $\mathbf{M}$ vectors 90 degrees in their respective cones,[14] the difference

$$M_{z,A}(\tau+t_w)-M_{z,B}(\tau+t_w)=M_A-M_B\cos\delta\tau.$$

Now, following the time $t=t_w+\tau$, the $\mathbf{M}$ vectors precess freely with a difference in Larmor frequency given by the chemical shift δ plus a difference in frequency due to the J coupling z field; the vectors $\mathbf{M}_A$ and $\mathbf{M}_B$ do not precess in equal fields due to J because $M_{z,A}\neq M_{z,B}$. According to our model, this frequency difference is

proportional to the difference in M_z between the two vectors after the second pulse. Consequently the echoes formed at $t=2\tau$ by each of the spin groups, represented by the vectors $\mathbf{M}_A$ and $\mathbf{M}_B$, will get out of phase with each other. The magnitude of the resultant formed by these component echoes will depend upon the difference $M_{z,A}(\tau+t_w)-M_{z,B}(\tau+t_w)$, which determines the extent to which $\mathbf{M}_A$ and $\mathbf{M}_B$ precess in different local fields after the second pulse. As τ is increased, the phase difference at $t=2\tau$ between $M_{xy,A}$ and $M_{xy,B}$ varies sinusoidally, the maximum echo amplitude therefore varies sinusoidally, and the echo envelope modulation will contain frequencies which depend upon J and δ. If $J=0$, on echo modulation cannot appear because the phase difference between $M_{xy,A}$ and $M_{xy,B}$ due to δ, which is accumulated before the second pulse, is exactly reversed or neutralized at the time the echo is formed. If $\delta=0$, no accumulated frequency difference may arise due to J coupling, although the coupling still exists, because $M_{z,A}$ is always equal to $M_{z,B}$. This model also explains why no echo modulation is observed for one equivalent spin group at resonance which is coupled to another spin group off resonance. It is obvious that both nonequivalent spin groups ($\mathbf{M}_A$ and $\mathbf{M}_B$) must be flipped by rf pulses in order that they may interfere with each other in a sinusoidal manner. It must be kept in mind that this macroscopic model does not give the correct quantitative expression given by Eq. (8), derived quantum-mechanically.

A generalized method for calculating the spin echo due to two nonequivalent groups which couple is now presented. The Hamiltonian (11) has the useful properties (1) that the magnitudes of the total spins $S=|S_{\max}|$, $|S_{\max}-1|$, $|S_{\max}-2|$, $\cdots$ of each group are constants of the motion, and (2) that the S_z operators are good quantum numbers in the approximation that $J\ll\delta$. For each group with a given S, providing that $\delta t_w\ll 1$, the probability amplitudes $a_{m,S}$ are transformed to $a_{m',S}$ (by an rf pulse) by the function

$$T_{S,m,m'}=[(S+m)!(S-m)!(S+m')!(S-m')!]^{\frac{1}{2}}$$
$$\times i^{2S-m-m'}\sin^{2S}(\omega_1 t_w/2)\sum_{\rho=0}^{\infty}(-1)^{\rho}$$
$$\times\frac{\cot^{m+m'+2\rho}(\omega_1 t_w/2)}{(m+m'+\rho)!(S-m'-\rho)!(S-m-\rho)!\rho!}, \quad (12)$$

given by Bloch and Rabi.[21] The terms in the sum over ρ are suppressed for any factorial of a negative integer which appears in the denominator, since the factorial is then infinite. For two rf pulses applied to the spin ensemble, which is initially at thermal equilibrium, the

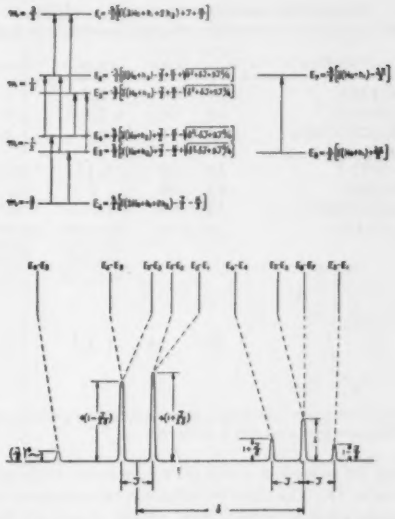

FIG. 6. Zeeman energy level diagram for a three spin system with $S_A=1$, $S_B=\frac{1}{2}$, $I_A=I_B=\frac{1}{2}$. The solid vertical lines indicate the number and arbitrary spacing of the resonance transitions which would be observed in the steady state for $J\sim\delta$. The dotted lines show how these lines relate to the resonance lines at the bottom for the condition that $J<\delta$.

spin wave function at $t=2\tau$ is given by

$$\psi(2\tau)=\sum_{\substack{S_A,S_B,m_A,m_B,\\ m_A',m_B',m_A'',m_B''}}\{\phi_{S_A,m_A''}\phi_{S_B,m_B''}T_{S_A,m_A',m_A''}$$
$$\times T_{S_B,m_B',m_B''}T_{S_A,m_A,m_A'}T_{S_B,m_B,m_B'}$$
$$\times a_{S_A,m_A(0)}a_{S_B,m_B(0)}\exp-i\tau[\gamma(H_0+h_A)$$
$$\times(m_A'+m_A'')+\gamma(H_0+h_A)(m_B'+m_B'')$$
$$+J(m_A'm_B'+m_A''m_B'')]\}, \quad (13)$$

where

$$\sum_{S_A,m_A}|a_{S_A,m_A(0)}|^2+\sum_{S_B,m_B}|a_{S_B,m_B(0)}|^2=1.$$

The eightfold sum indicates that each of the two spin groups A and B are separately summed over S and that the probability amplitudes for each group are transformed twice by two rf pulses. The component wave functions characterized by m are transformed as follows: for the first pulse, ending at $t=t_w$, $m\to m'$, and m' remains constant for $t_w\le t\le\tau$; after the second pulse ending at $t=\tau+t_w$, $m'\to m''$, and m'' is constant for $t\ge\tau+t_w$. The arrow indicates that the final state is built up from a superposition of initial m states. The pulse duration time t_w is neglected in the exponent since $t_w\ll\tau$, but appears in the T functions. The maximum of the echo at $t=2\tau$ is determined by calculating the expectation value of the I_+ operator with Eq. (13),

TABLE I. Echo modulation data at $\nu_{Larmor}=32$ Mc.

Compound	$J/2\pi$ in cps*	$\delta/2\pi$ in cps*	Figure	Appendix
$CHCl_2CHO$	2.7	104	2, 7	A
$CH_2ClCHCl_2$	6.0	64	4, 5, 6, 8	B
$CHCl_2CHClCHCl_2$	5.3	51	6, 8	B
CH_3OH (anhydrous, at $-78°C$)	5.0	79	9, 17	C-2
CH_3CHBr_2	6.3	108	9	C-2
$CH_3CH_2COOCCl_3$	7.1	94	11, 13	C-3
CH_3CH_2OH	7.5	80	compares approximately to 11, 13	compares approximately to C-3
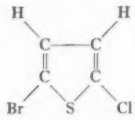	3.9	5.6	1, 2, 3	A

* Estimated error of all data is ±5 percent.

using the procedure which led to the expectation value given by (8). The observed echo can be considered as a superposition of echoes from groups A and B. Each group in turn is a superposition of echoes due to the invariant total spins S_A and S_B, respectively. Therefore

$$u+iv=\sum_{S_A}(\psi^*|I_{+,A}|\psi)+\sum_{S_B}(\psi^*|I_{+,B}|\psi), \qquad (14)$$

and the matrix elements of I_+, I_-, and I_z are given by

$$\begin{aligned}(m|I_+|m-1)&=[(S+m)(S-m+1)]^{\frac{1}{2}},\\ (m[I_-|m+1)&=[(S-m)(S+m+1)]^{\frac{1}{2}},\\ (m|I_z|m)&=m,\end{aligned} \qquad (15)$$

where ΔS_A, $\Delta S_B=0$; $|\Delta m_A|=1$, $\Delta m_B=0$; $|\Delta m_B|=1$, $\Delta m_A=0$. After the operation is performed in Eq. (14) it is necessary to collect common factors of the term $|a(0)_{S,m}|^2$ and relate them to M_0, the macroscopic equilibrium magnetization. This is done by using the following relations:

$$\begin{aligned}M_0=\sum_{S_A}\sum_{S_B}|(2S_B+1)\sum_{m_A}m_A|a_{S_A,m_A}(0)|^2\\ +(2S_A+1)\sum_{m_B}m_B|a_{S_B,m_B}(0)|^2],\\ (2S_{B,A}+1)\sum_{m_{A,B}}m_{A,B}|a_{S_{A,B},m_{A,B}}(0)|^2\\ =M_0F_{A,B}/\sum_{S_A}\sum_{S_B}F_{A,B},\end{aligned} \qquad (16)$$

where

$$F_{A,B}=(2S_{B,A}+1)(S_{A,B})(S_{A,B}+1)(2S_{A,B}+1).$$

The above treatment can apply to more than two spin groups which couple, and the number and type of rf pulses (characterized by t_w and H_1) may be arbitrary. Both of the spin groups A and B for most of our experiments are taken to be at the nuclear resonance condition during the application of pulses because of the condition $\omega_1\gg\gamma\Delta H, \delta, J$. We have treated several cases involving three spin groups (Appendix C-5, C-6) in which two are at resonance and the third group is not at resonance.[26] The group off resonance, such as F^{19}, usually has a gyromagnetic ratio sufficiently different from the nuclei at resonance, such as protons, so that $(\gamma_F-\gamma_H)H_0\gg\omega_1$. The modifications required of the above calculations are obvious in these cases and we shall not discuss them here. Experimental values of $J/2\pi$ and $\delta/2\pi$ are given in Table I for typical cases. The experimental echo plots for these cases are in agreement within experimental error with the theoretical plots. Particular references to formulas in the appendix and to figures are given in this table.

IV. DAMPING OF THE J COUPLING

For most of the cases which exhibit echo modulation it is found that the entire envelope decays with a lifetime determined by T_2 and thermal diffusion. The observed envelope is normalized to unity and agreement is obtained with the above theory, in which the J coupling is assumed to be undamped or uninterrupted. However, it is possible that the J coupling may be perturbed not only because of T_2, but also because of certain effects such as rotational hindrance (discussed in II with respect to $CHCl_2CHO$) and molecular dissociation. In all of these cases the phase coherence of the spin ensemble, which must be maintained in order to observe the J coupling, is destroyed to some extent because of the random interruption of the magnetic coupling between neighboring nuclei. The mechanisms

[26] We have discovered in the liquid compounds $CFClHCHCl_2$ and CF_2HCHCl_2 (which were reasonably pure) that fluorine echoes exhibit modulation and that there is a main splitting (~1 kc at $\omega/2\pi=30$ Mc) of the fluorine resonance into two lines which is proportional to H_0. This is unexpected because (1) equivalent nuclei alone cannot exhibit a field dependent splitting which is due to the chemical shift, and (2) there can be no echo modulation from equivalent nuclei at resonance unless they are coupled to a second group of nuclei which is also at resonance and is nonequivalent with respect to the first group. In the molecules above, anomalous signals are obtained from fluorine nuclei which are coupled to two neighboring protons which are not at the echo resonance and which are nonequivalent among themselves. However, fluorine echoes do not show a modulation (nor is there a field dependent splitting of the fluorine resonance) in similar molecules where equivalent fluorine nuclei are neighbors of protons which are equivalent among themselves. We suggest, therefore, that the anomalous fluorine signals are due to the J_{FH} coupling of fluorine with the nonequivalent protons, and that the anomaly will be particularly strong if $J_{HH}\sim\delta_{AB}$ for the protons. In this event the xy component of J_{HH} coupling (which derives from the term $[I_{x_1}I_{x_2}+i(I_{y_1}+I_{y_2})]J_{HH}$) is sufficiently strong to cause the protons to flip each other at a rate which may be comparable to the inverse of the lifetime of the fluorine echo envelope. Consequently the J_{FH} coupling between the protons and fluorine will be modulated by the change in proton spin orientation. In turn the local field at the fluorine nucleus (due to J_{FH} coupling) will be modulated at the rate at which the protons are flipping. This modulation, together with the magnitude of J_{FH}, determines the magnitude of the fluorine resonance splitting and echo modulation. The frequency of the echo modulation is not related to the fluorine resonance splitting, and, in fact, is field independent. We shall not attempt here to account for this characteristic of the echo modulation, but the above argument thus far does account for the fact that the fluorine resonance splitting should depend on the ratio δ_{HH}/J_{HH}, and therefore on the field H_0 (since $\delta_{HH}\propto H_0$).

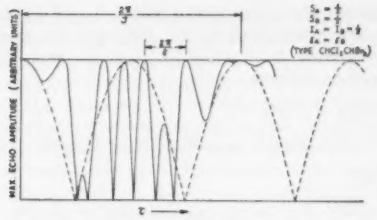

FIG. 7.

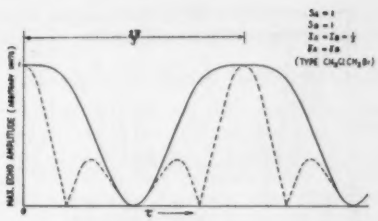

FIG. 10.

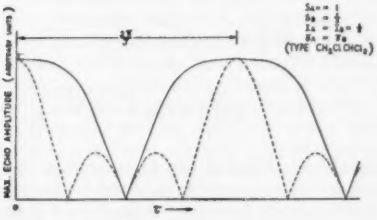

FIG. 8.

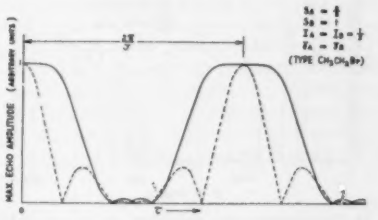

FIG. 11.

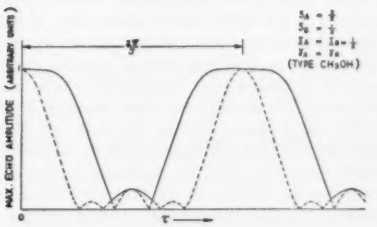

FIG. 9.

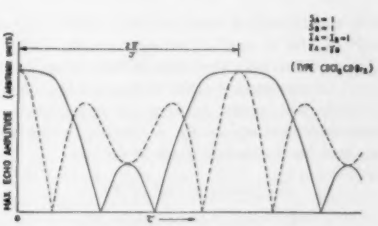

FIG. 12.

FIGS. 7–12. For the condition $J \ll \delta$, theoretical plots for various spin systems (obtained from formulas in the appendix) are shown which trace out the upper and lower limits of the echo envelope modulation. These traces are periodic with frequency $J/2\pi$. The echo envelope, modulated at a higher frequency $\delta/2\pi$, may be fitted and plotted within the solid and dotted lines, as shown in Figs. 4 and 7. Frequency doubling occurs within the first dotted lobes which meet the axis symmetrically in time, and the doubling reappears periodically.

by which this random process takes place shall be described (1) by letting δ and J take on different discrete values (m constant in the absence of H_1) in order to describe such effects as the transfer between rotational molecular isomers, and (2) by letting the quantum state m change to other allowed m states in a random manner (J and δ constant) in order to describe the effect of T_1 and T_2.

A. Damping by Fluctuations of J and δ

First let us treat the damping process of the case previously treated by the Hamiltonian (1) above. Assume for a given orientation of two coupled nuclear moments in a molecule that a certain J and δ can be assigned to the system. During the time the molecule exists in an alternate form the coupled nuclei are described by the parameters J' and δ'. By the method given in III the expectation value of I_+ after the first rf pulse is given by

$$V=\frac{iM_0}{4}\{\exp i[\gamma(H_0+h_1)+J/2]t + \exp i[\gamma(H_0+h_1)-J/2]t + \exp i[\gamma(H_0+h_2)+J/2]t + \exp i[\gamma(H_0+h_2)-J/2]t\}=\sum_{n=1}^{4} f_n, \quad (17)$$

where $I=\frac{1}{2}$, $J\ll\delta$; $h_1, h_2 \rightarrow h_1', h_2'$, and $J\rightarrow J'$ for the other structure. Each of the two states of the molecule will have a lifetime given by $(\lambda)^{-1}$ and $(\lambda')^{-1}$. The term f_n (where $n=1, \cdots 4$, in this case) represents the nth component of n terms, each characterized by frequency ω_n, which add to give the macroscopic transverse

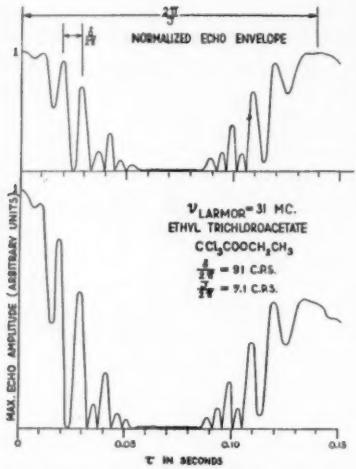

FIG. 13. Experimental echo modulation plot due to protons in ethyl trichloroacetate. See Fig. 3 for meaning of both plots.

nuclear magnetization after the first rf pulse. The interchange of the h and J parameters ($h_1, h_2 \rightleftarrows h_1', h_2'$; $J \rightleftarrows J'$) requires that the expectation value given by Eq. (17) be corrected in order to account for the damping which will result because of incoherence. The phenomenological equations of coupling which we use to account for the damping are as follows:

$$\begin{aligned} \dot{F}_n - i\omega_n F_n &= -\lambda F_n + \lambda' F_n', \\ \dot{F}_n' - i\omega_n' F_n' &= -\lambda' F_n' + \lambda F_n. \end{aligned} \tag{18}$$

The solutions for F_n are now the corrected values which include the damping and replace f_n in Eq. (17). For our particular case there are four pairs of equations of this type, one set for F_n and another set for F_n'. In order to obtain the echo at $t=2\tau$ it is again convenient to calculate $\mu+i\nu$ for $t \geq \tau+t_w$ with no damping. The result is

$$V = \frac{-i}{M_0} \sum_{k=1}^{4} [f_k(t) \sum_{n=1}^{4} f_n^*(\tau)(1-2\delta_{k,5-n})], \tag{19}$$

where $f_n^*(\tau)$ is the complex conjugate of $f_n(\tau)$, and $\delta_{k,5-n}$, the Kronecker delta, is zero for $k \neq 5-n$ and unity for $k=5-n$. Each product of $f_k(t)$ and the sum of four constant $f_n(\tau)$ terms is one of four such product terms, each characterized by frequency ω_k, which sum to give the solution for $V=u+iv$ after the second pulse. Now all of the f terms of Eq. (19) must be corrected for damping. The corrected solutions $F_n(\tau)$ of Eq. (18) replace $f_n(\tau)$ in the expression for V in Eq. (19). A new set of equations, analogous to the set given by Eq. (18), is then solved for the corrected F_k terms, and these terms replace the $f_k(t)$ terms in Eq. (19). Two sets of such equations, one for the prime and one for the unprime system, form two solutions V_1 and V_2 for the echo expression given by Eq. (19), and the observed echo is given by $V=V_1+V_2$. V is obtained for the following conditions:

$(\lambda, \lambda' \ll \delta, \delta', J, J')$

$$|V| = \tfrac{1}{2} M_0 |1 - 2\sin^2(\delta_a \tau/2)\sin^2(J_a \tau/2)|, \tag{20a}$$

where

$$\delta_a = (\lambda\delta' + \lambda'\delta)/(\lambda+\lambda') \text{ and } J_a = (\lambda J' + \lambda' J)/(\lambda+\lambda');$$

$(\lambda, \lambda' \ll \delta, \delta', J, J')$:

$$|V| = \frac{M_0}{2(\lambda+\lambda')} \left| \lambda' \left(1 - 2\sin^2\frac{\delta\tau}{2}\sin^2\frac{J\tau}{2}\right) + \lambda\left(1 - 2\sin^2\frac{\delta'\tau}{2}\sin^2\frac{J'\tau}{2}\right)\right|. \tag{20b}$$

The above calculation can be generalized to apply to any case, and appears to be useful for the analysis of observable rate processes which cause a change in the chemical environment of the nucleus.[27] We see from Eq. (20a) that a fast interchange between different values of J and h results in the observation of average values of these parameters, and justifies our assumption that J and h are averaged over all possible rotational isomers of the ethyl type compounds which we have investigated. No echoes have been observed in which case Eq. (20b) above applies. We shall not give the general solution for the damping of V, which can be obtained from Eq. (19). In Appendix D the random process for the above case of damping, which is described by the phenomenological equations of Eq. (18), is treated by a Fourier analysis and shown to lead to the same result which is obtained by the use of Eq. (18).

B. Effect of Relaxation Time on the Echo Envelope

The damping effect due to relaxation is treated by considering the random change of the quantum state m. Let us use a model in which two nuclei with $I=\frac{1}{2}$ have different relaxation times, and are coupled by J under the conditions which led to the result given by (8), except that we let $J \ll \delta$. Assume, as t increases after the first pulse, that the states described by m_A and m_B, which are initially established after the first pulse, may undergo the possible transformations indicated by the schemes (1) $m_A \rightleftarrows -m_A$, $\Delta m_B = 0$, (2) $m_B \rightleftarrows -m_B$, $\Delta m_A = 0$, and (3) $m_A \rightleftarrows -m_A$, $m_B \rightleftarrows -m_B$, $\Delta(m_A+m_B)=0$, where $m=\frac{1}{2}$. Each of these three schemes is specified by different relaxation times $(\lambda_1)^{-1}$, $(\lambda_2)^{-1}$, and $(\lambda_3)^{-1}$.

[27] J. T. Arnold and M. E. Packard, J. Chem. Phys. **19**, 1608 (1951), have found for protons in the OH and CH_3 groups in CH_3OH and C_2H_5OH that δ varies with temperature and concentration of several dissolved substances. This may be interpreted as a variation in λ and λ' for the associated and dissociated states of the OH group [U. Liddel and N. F. Ramsey, J. Chem. Phys. **19**, 1608 (1951)].

Schemes (1) and (2) represent the effect of T_1 and mutual spin-spin flipping between nuclei of different molecules. Scheme (3) represents the effect of mutual spin-spin flipping between the coupled spins in the same molecule, where the states m_A and m_B change simultaneously. Consider only the damping effect on the J coupling due to schemes (1) and (2), and assume that the effect due to (3) is negligibly small. The changes in the sign of m for these schemes are made in the wave function given by (13), and the expectation value of the I_+ operator is calculated for the initial unrelaxed state and each of the two states into which the system can relax. Component f terms from each of the expectation values are again coupled by equations of the form given in Eq. (18). Each f term is again characterized by a frequency as in the damping calculation discussed in Part IV. A term f can be correlated with the corresponding f' by noting that both of these terms will have a common initial condition factor which is established after the first rf pulse. The solution, including the damping of the echo envelope, is then obtained in the same manner by which the damping in the previous case was calculated (Eq. (20)). V is obtained for the following conditions:

$(1/T_2, 1/T_2' \gg J)$:

$$|V| = \tfrac{1}{4}M_0(e^{-\theta/T_2}+e^{-\theta/T_2'}), \tag{21a}$$

$(1/T_2, 1/T_2' \ll J)$:

$$|V| = \tfrac{1}{4}M_0 e^{-\frac{1}{2}\theta(1/T_2+1/T_2')}\left|(e^{-\theta/2T_2}+e^{-\theta/2T_2'})\cos^2(J\tau/2) + 2e^{-\frac{1}{2}\theta(1/T_2+1/T_2')}\cos\delta\tau\sin^2(J\tau/2)\right|$$

$$= \tfrac{1}{2}M_0 e^{-3\theta/2T_2}\left|1-2\sin^2(\delta\tau/2)\sin^2(J\tau/2)\right| \quad \text{for } T_2=T_2'; \tag{21b}$$

$(1/T_2 > J \gg 1/T_2')$:

$$|V| = \tfrac{1}{4}M_0\left|\exp(-J^2\theta T_2/4)+e^{-\theta/T_2}\cos^2(J\tau/2)\right|; \tag{21c}$$

where $1/2\lambda_1 = T_2$, $1/2\lambda_2 = T_2'$, $\theta = 2\tau$, and no restrictions are imposed on δ except that $J \ll \delta$. In Eq. (21a) the echo envelope is damped exponentially, and no modulation appears. The exponent $3\theta/2T_2$ in Eq. (21b) indicates that an additional relaxation mechanism is present. It arises from the fact that the flipping of one nucleus interrupts the local field due to J seen by the other nucleus. In the approximation that $J \ll \delta$ this effect reduces the coherence of precession of the system by contributing a relaxation time of $T_2/2$ to the exponent. For $J \sim \delta$ this relaxation time is a function of J and δ, and Eq. (21b) becomes a very complicated expression which will not be given here. The condition expressed by Eq. (21c) shows how the J coupling is severely damped by a very short relaxation time of one of two coupled nuclei. Although both nuclei in this model are at the resonance condition, the same damping effect applies for one of the nuclei off resonance. This justifies the assumption in cases such as $CHCl_2CHO$, that the coupling due to the chlorine nuclei is absent for small values of T_2 due to quadrupole broadening.

C. Damping of the Proton Coupling in CH_3OH

It is observed that the echo modulation due to coupled protons in pure CH_3OH (see Figs. 14–17) is damped when a very small percentage of water is added. Aside from the dissociation effect[27] in CH_3OH, a direct interchange of protons takes place between H_2O and CH_3OH molecules.[28] Ignore the contribution of the dissociation effect to the damping, and assume that the damping is due entirely to the random change of m, the spin state of the proton in the OH group of CH_3OH introduced by protons transferred from H_2O molecules. Let λ represent the reciproçal of the lifetime of a proton with a given m state in the OH group of CH_3OH. The echo signal from the small amount of H_2O may be neglected. The result for the echo envelope due to CH_3OH, including the damping, is given for these cases:

$(\lambda \gg J)$:

$$|V| = (M_0/28)\left|3+11e^{-4\lambda\tau}\cos^2(J\tau/2)\right|, \tag{22a}$$

$(\lambda \ll J)$:

$$|V| = (M_0/112)\left|e^{-2\lambda\tau}[(11/2)\cos J\tau+6\cos^2 J\tau + \tfrac{1}{2}\cos 3J\tau]+e^{-2\lambda\tau}[4(2+\cos J\tau) - 12\cos 2J\tau]\cos\delta\tau+44e^{-4\lambda\tau}\cos^2(J\tau/2)\right|, \tag{22b}$$

where no restrictions are imposed on δ except that $J \ll \delta$. It appears from Figs. 14–17 that dissociation as well as proton exchange is effective in damping the echo envelope. As the concentration of H_2O is increased, δ decreases, which is considered to be chiefly caused by the dissociation effect.[27] We shall omit a discussion of the damping calculations for CH_3OH in the case of dissociation, where δ and J fluctuate. The results are very similar to the form of Eqs. (20). On the basis of proton exchange we estimate $\lambda \sim 1$ sec^{-1} ($\lambda \ll J, \delta$) for a mixture of ~ 1 percent by weight of water at a temperature of -4°C.

V. ORIGIN OF THE J COUPLING

Ramsey and Purcell[20] have suggested that the J coupling derives mainly from a nuclear-electron-nuclear spin interaction. Gutowsky, McCall, and Slichter[17] have extended their treatment of the coupling in the HD molecule to the coupling between pairs of coupled spin groups in more complicated molecules, and thus account for their observed J values. We shall not treat this coupling mechanism in detail here, nor attempt to correlate measured J values with theoretical values,

[28] Many compounds with ionizable hydrogen, such as NH_4OH and CH_3COOH, exchange protons with CH_3OH and damp the echo envelope. For references and a general discussion of proton exchange, see N. V. Sidgwick, *Chemical Elements and their Compounds* (Clarendon Press, Oxford, 1950, Vol. 1, Chapter 1).

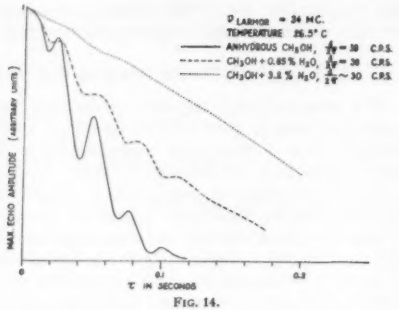
ν LARMOR = 24 MC.
TEMPERATURE 26.5° C
ANHYDROUS CH3OH, 1/2π = 38 C.P.S.
CH3OH + 0.85 % H2O, 1/2π = 38 C.P.S.
CH3OH + 3.2 % H2O, 1/2π ~ 30 C.P.S.
MAX. ECHO AMPLITUDE (ARBITRARY UNITS)
τ IN SECONDS

FIG. 14.

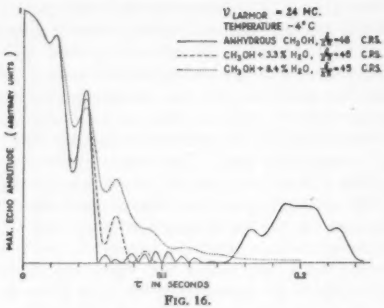
ν LARMOR = 24 MC.
TEMPERATURE −4° C
ANHYDROUS CH3OH, 1/2π = 46 C.P.S.
CH3OH + 3.3 % H2O, 1/2π = 46 C.P.S.
CH3OH + 8.4 % H2O, 1/2π = 45 C.P.S.
MAX. ECHO AMPLITUDE (ARBITRARY UNITS)
τ IN SECONDS

FIG. 16.

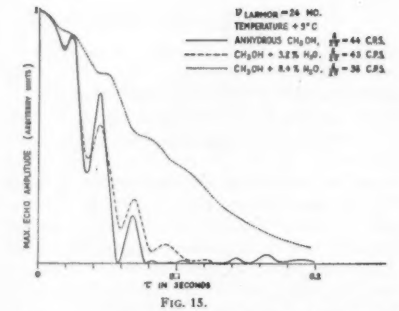
ν LARMOR = 24 MC.
TEMPERATURE + 5° C
ANHYDROUS CH3OH, 1/2π = 44 C.P.S.
CH3OH + 3.2 % H2O, 1/2π = 43 C.P.S.
CH3OH + 8.4 % H2O, 1/2π = 36 C.P.S.
MAX. ECHO AMPLITUDE (ARBITRARY UNITS)
τ IN SECONDS

FIG. 15.

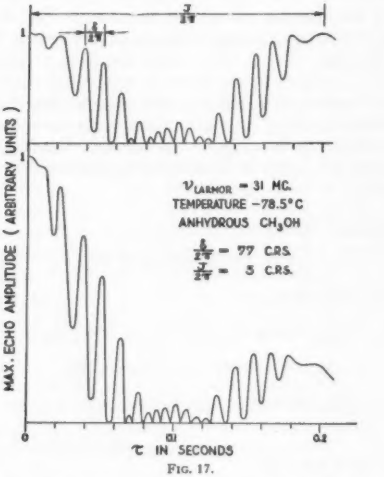

FIG. 17.

FIGS. 14–17. Proton echo envelope plots in methyl alcohol for various temperatures and concentrations of water (expressed in percentage by weight).

but refer the reader to the very adequate discussions of the above authors.

In addition to the spin coupling mechanism there are other mechanisms which give rise to the J coupling operator, but only account for magnitudes of J of the order of 1 cps or less. The Hamiltonian which describes the magnetic interaction of nuclei with orbital electrons, from which all the types of J coupling terms may be obtained, has been given elsewhere.[29] Ramsey and Purcell use this Hamiltonian and outline the origin and approximate magnitudes of the various coupling mechanisms. A paper by Ramsey[30] discusses and completes the formal analysis of these effects by a generalized treatment of the Hamiltonian which he used to explain the origin of the chemical shift.

The $\mathbf{I}_1 \cdot \mathbf{I}_2$ operator can be deduced by assuming that the wave packets representing two neighboring protons in a molecule overlap to a sufficient extent. However, this mechanism must be excluded because of mass considerations, especially since the J coupling is observed to involve nuclei much heavier than protons. We have considered a rotationally invariant form of magnetic interaction $\boldsymbol{\mu}_1 \cdot \boldsymbol{\mu}_2$, which can be obtained from the Hamiltonian which Ramsey used to explain the chemical shift.[6] For l nuclei interacting with k electrons this term is expressed as

$$\mathcal{E} = \frac{e^2}{2mc^2} \int \psi^*(\rho) \sum_k [\sum_l \gamma_l \mathbf{I}_l \times \mathbf{r}_{kl}/r_{kl}^3]^2 \psi(\rho) d\rho, \qquad (23)$$

where r_{kl} is the electron-nuclear distance and $\psi(\rho)$ is the total electron wave function. In the case of two coupled protons the interaction energy may be estimated from a mechanism analogous to that which leads

[29] A. Abragam and M. H. L. Pryce, Proc. Roy. Soc. (London) **A205**, 135 (1951).

[30] N. F. Ramsey, Phys. Rev. **87**, 1077 (1952). The authors are grateful to Professor Ramsey for an advance copy of this paper.

to the Lamb diamagnetic correction.[5] Consider the dipole field $H\sim\mu_1/r_{kl}^3$ (~ 10 gauss) for a proton nucleus, which causes a Larmor precession of the kth electron. The resulting current produces a field H' at the position of a neighboring nucleus. A crude estimate of H' may be obtained by multiplying H by the Lamb diamagnetic correction factor ($\sim 10^{-5}$) for the hydrogen atom, and a splitting of ~ 0.5 cps is obtained. This splitting compares to the approximate value Drell has calculated[21] for this interaction in the HD molecule, using Heitler-London electron wave functions in Eq. (23). The small size of this splitting is of the order of magnitude of the splitting due to electron orbital contributions[17] and to cross terms due to direct dipole coupling between the electron and the nucleus.[20]

VI. CONCLUDING REMARKS

Throughout this work we have studied shapes of echo envelopes under the rf pulse condition that $\omega_1 t_w=\pi/2$. Slight deviations from this condition will cause a marked deviation of the observed envelopes from the theoretical plots; the shape of the envelope depends critically on trigonometric terms which have quadratic and cubic dependence on the magnitude of H_1. The inhomogeneity of H_1 over the sample is minimized by placing the sample in the center of a transmitter coil of larger diameter (three or four times as large as the receiver coil) where H_1 is homogeneous. This is done most conveniently by fashioning the transmitter coil according to the Helmholtz condition, and crossing the transmitter and receiver at right angles according to the nuclear induction technique.[2]

Most of the compounds measured have involved relaxation times T_1 and T_2 of the order of several seconds, and in principle the parameters J and δ of the order of $1/T_2$ are resolvable. However, an inhomogeneous field H_0 over the sample aggravates the damping effect due to thermal diffusion,[16] which becomes greater than the damping due to T_2, and it is important to shim the magnetic field sufficiently in order to obtain a reasonable field homogeneity.

The authors are grateful to Professor F. Bloch for many discussions and valuable suggestions during the course of this research. They wish to acknowledge the highly informative discussions and helpful interchange of information with Professors H. S. Gutowsky and C. P. Slichter of the University of Illinois. They thank Dr. S. D. Drell for discussions concerning some of the calculations, and Dr. M. E. Packard and Mr. J. T. Arnold for slow passage measurements of some of the compounds they studied. One of the authors (E.L.H.) wishes to acknowledge and thank the National Research Council for postdoctoral fellowship support during the early part of this research.

[21] S. D. Drell, private communication.

APPENDIX

The echo at $t=2\tau$ is given for the following cases, where groups A and B are at resonance:

(A) $S_A=S_B=\frac{1}{2}$, $I_A=I_B=\frac{1}{2}$, $\gamma_A=\gamma_B$, $\delta\sim J$ (Type $CHCl_2CHO$):

$$|V|=\frac{M_0\delta^2\sin\varphi}{\delta^2+J^2}\left|\left(\sin^2\frac{\varphi}{2}\right)\left(\sin^2\left[\frac{\tau}{2}(J^2+\delta^2)^{\frac{1}{2}}\right]\right)\cos J\tau+\left(\frac{\sin^2\varphi}{4}\right)\left\{\frac{2J^2+\delta^2}{\delta^2}+\cos[\tau(J^2+\delta^2)^{\frac{1}{2}}]\right\}-(\cos\varphi)\left(\sin^2\frac{\varphi}{2}\right)\left(\frac{\cos J\tau}{2}\right)\left\{1+\frac{2J^2+\delta^2}{\delta^2}\times\cos[\tau(J^2+\delta^2)^{\frac{1}{2}}]\right\}+\frac{J(J^2+\delta^2)^{\frac{1}{2}}}{\delta^2}\times(\sin J\tau)\sin[\tau(J^2+\delta^2)^{\frac{1}{2}}]\right|,$$

where $\varphi=\omega_1 t_w$.

(B) $S_A=\frac{1}{2}$, $S_B=1$, $I_A=I_B=\frac{1}{2}$, $\gamma_A=\gamma_B$, $\delta\sim J$, $\omega_1 t_w=\pi/2$ (Type $CH_2ClCHCl_2$):

$$\begin{aligned}|V|=\tfrac{1}{32}M_0|&[\bar{z}x(\bar{w}-2w)-2y(\bar{w}^2-2x^2)]\times\exp[i\tau(\delta/2+3J/4)]+\text{c.c.}\\&+[\bar{z}x(y-2\bar{y})-2\bar{w}(y^2-2\bar{x}^2)]\times\exp[i\tau(\delta/2-3J/4)]+\text{c.c.}\\&+[wy-2\bar{x}\bar{z}]\exp[-i3J\tau/2]+\text{c.c.}\\&+(4/3)x^2(y^2+\bar{y}^2)+(10/3)xz(w-\bar{w})(y-\bar{y})\\&-3(|w|^2+|y|^2)-(8/3)|w|^2|y|^2\\&+(15/3)x^2z^2+(4/3)z^2(w^2+\bar{w}^2)-(4/3)|,\end{aligned}$$

where c.c. indicates the complex conjugate of the preceding expression, the bar over a symbol denotes the complex conjugate, and

$$w=\cos[\tfrac{1}{2}\tau(\delta^2+\delta J+9J^2/4)^{\frac{1}{2}}]+\frac{i(\delta/3+3J/2)}{(\delta^2+\delta J+9J^2/4)^{\frac{1}{2}}}\times\sin[\tfrac{1}{2}\tau(\delta^2+\delta J+9J^2/4)^{\frac{1}{2}}],$$

$$x=\frac{-2i\delta\sqrt{2}}{3(\delta^2+\delta J+9J^2/4)^{\frac{1}{2}}}\sin[\tfrac{1}{2}\tau(\delta^2+\delta J+9J^2/4)^{\frac{1}{2}}],$$

$$y=\cos[\tfrac{1}{2}\tau(\delta^2-\delta J+9J^2/4)^{\frac{1}{2}}]-\frac{i(\delta/3-3J/2)}{(\delta^2-\delta J+9J^2/4)^{\frac{1}{2}}}\times\sin[\tfrac{1}{2}\tau(\delta^2-\delta J+9J^2/4)^{\frac{1}{2}}],$$

$$z=\frac{2i\delta\sqrt{2}}{3(\delta^2-\delta J+9J^2/4)^{\frac{1}{2}}}\sin[\tfrac{1}{2}\tau(\delta^2-\delta J+9J^2/4)^{\frac{1}{2}}].$$

For $J\ll\delta$ in this case, V reduces to

$$|V|=(M_0/48)|11+12\cos J\tau+\cos 2J\tau+(8\cos\delta\tau)(\cos J\tau/2-\cos 3J\tau/2)|.$$

(C) The cases given below apply for $I_A=I_B=\frac{1}{2}$, $\gamma_A=\gamma_B$, $J\ll\delta$, $\omega_1 t_w=\pi/2$:

(1) $S_A=1$, $S_B=1$, (Type CH_2ClCH_2Br):

$$|V|=\tfrac{1}{16}M_0|3+4\cos J\tau+\cos 2J\tau+4(\cos\delta\tau)\sin^2 J\tau|.$$

(2) $S_A=\frac{3}{2}$, $S_B=\frac{1}{2}$, (Type CH_3OH):

$$|V|=(M_0/224)|50+\cos 3J\tau+6\cos 2J\tau+55\cos J\tau+(8\cos\delta\tau)(2+\cos J\tau-3\cos 2J\tau)|.$$

(3) $S_A=\frac{3}{2}$, $S_B=1$, (Type CH_3CH_2Br):

$$|V|=(M_0/272)|45+66\cos J\tau+23\cos 2J\tau+2\cos 3J\tau+(8\cos\delta\tau)\times(5\cos J\tau/2-2\cos 3J\tau/2-3\cos 5J\tau/2)|.$$

(4) $S_A=1$, $S_B=1$, *except that* $I_A=I_B=1$, (Type $CDCl_2CDO$):

$$|V|=(M_0/12)|1+4\cos J\tau+\cos 2J\tau+(4\cos\delta\tau)\sin^2 J\tau|.$$

The cases below apply for three spin-groups A, B, and C, where A and B are at resonance and C is off resonance ($I_A=I_B=I_C=\frac{1}{2}$, $\gamma_A=\gamma_B\neq\gamma_C$):

(5) $S_A=S_B=S_C=\frac{1}{2}$, (Type $CFHClCHCl_2$):

$$|V|=\tfrac{1}{2}M_0|\cos^2 J\tau/2+(\sin^2 J\tau/2)\times(\cos[(K-L)\tau/2])\cos\delta\tau|,$$

(6) $S_A=S_B=\frac{1}{2}$, $S_C=1$, (Type CF_2HCHCl_2):

$$|V|=\tfrac{1}{2}M_0|\cos^2 J\tau/2+(\sin^2 J\tau/2)\times(\cos^2[(K-L)\tau/2])\cos\delta\tau|,$$

where K and L denote the coupling of groups A and B with C.

(D) The solution of Eq. (20) is

$$F_n=\frac{iM_0\lambda'}{4(\lambda+\lambda')}e^{[i(\omega_n+\omega_n')-\lambda-\lambda']t/2}\times\left[1+\frac{\lambda+\lambda'+i\Delta\omega_n}{\alpha}\sinh\left(\frac{\alpha t}{2}\right)-e^{-\alpha t/2}\right],$$

where $\Delta\omega_n=\omega_n-\omega_n'$ and

$$\alpha=[(\lambda+\lambda')^2-\Delta\omega_n{}^2-2i(\lambda-\lambda')\Delta\omega_n]^{\frac{1}{2}}.$$

A similar solution exists for F_n'. F_n can be expanded and expressed in the form

$$F_n=\frac{iM_0\lambda'}{4(\lambda+\lambda')}\Bigg\{e^{(i\omega_n-\lambda)t}+\lambda\int_0^t e^{(i\omega_n-\lambda)t_1+(i\omega_n'-\lambda')(t-t_1)}dt_1+\lambda\lambda'\int_0^t\int_0^{t-t_1}e^{(i\omega_n-\lambda)(t-t_2)+(i\omega_n'-\lambda')t_2}dt_2dt_1$$
$$+\lambda^2\lambda'\int_0^t\int_0^{t-t_1}\int_0^{t-t_1-t_2}e^{(i\omega_n-\lambda)(t_1+t_2)+(i\omega_n'-\lambda')(t-t_1-t_2)}dt_3dt_2dt_1+\cdots$$
$$+\lambda^k\lambda'^k e^{(i\omega_n-\lambda)t}\int_0^t\int_0^{t-t_1}\cdots\int_0^{t-t_1-t_2-\cdots-t_{2k-1}}e^{(i\Delta\omega_n-\lambda+\lambda')(t_2+t_4+t_6+\cdots+t_{2k})}dt_{2k}dt_{2k-1}\cdots dt_1$$
$$+\lambda^{k+1}\lambda'^k e^{(i\omega_n'-\lambda')t}\int_0^t\int_0^{t-t_1}\cdots\int_0^{t-t_1-t_2-\cdots-t_{2k}}e^{(i\Delta\omega_n-\lambda+\lambda')(t_1+t_3+t_5+\cdots+t_{2k+1})}dt_{2k+1}dt_{2k}\cdots dt_1\Bigg\}$$

Each term of the expansion represents a mode of switching between two frequencies of precession ω and ω'. The first term of the expansion is determined by the probability $e^{-\lambda t}$ that the ensemble precesses at a frequency ω_n for a time t. The second term accounts for the probability $(e^{-\lambda t_1}\lambda dt_1)e^{-\lambda'(t-t_1)}$ that the ensemble precesses at frequency ω_n for a time between t_1 and t_1+dt_1, then switches to the frequency ω_n' and remains for a time $t-t_1$. The third term includes the probability that the ensemble returns to frequency ω_n and remains. Successive terms account for increasingly frequent jumps between frequencies ω_n and ω_n'. Each mode of interrupted precession is therefore weighted and the observed nuclear magnetization is a superposition of all modes. A similar argument applies to the expansion of F_n'.

Radiofrequency Spectra of Li^6F^{19} by the Molecular Beam Electric Resonance Method*†

J. C. Swartz‡ and J. W. Trischka
Department of Physics, Syracuse University, Syracuse, New York
(Received July 23, 1952)

The electric resonance method of molecular beam spectroscopy has been used to study the rotational Stark transitions $J, m_J \rightarrow J, m_J$ for Li^6F^{19}. A new type of homogeneous electric field of high resolution was used to observe the transitions. A mass spectrometer was used to separate the Li^6 (8 percent abundant) and Li^7 (92 percent abundant) positive ions coming from the hot wire detector. From observations of the $1, \pm1 \rightarrow 1, 0$ and $2, \pm2 \rightarrow 2, \pm1$ transitions for a variety of electric field strengths it was concluded that the principal nuclear molecular interaction was of the type specified by the operator $c\mathbf{I}\cdot\mathbf{J}$, where c is a constant, I is the spin of the F nucleus, and J is the rotational quantum number. The effects of the Li^6 quadrupole and $\mathbf{I}\cdot\mathbf{J}$ interactions were below the limits of observation. The constant c/h was found to be $+37.3\pm0.7$ kc/sec for both transitions. This value is approximately twice that calculated from molecular beam magnetic resonance experiments at strong fields. Using the electric resonance strong field data, calculations determined the constant μ^2A to be $(747.2\pm0.9)\times10^{-78}$ cgs units for the lowest vibrational state. This quantity for the next vibrational state was greater by (4.3 ± 0.1) percent. μ is the electric dipole moment, and A is the moment of inertia of the molecule.

I. INTRODUCTION

A COSINE–TYPE coupling between nuclear spin and molecular rotation in $^1\Sigma$ diatomic molecules has been observed[1,2] by the electric and magnetic resonance methods of molecular beam spectroscopy. Foley[3] and Wick[4] have given theoretical discussions of this interaction. The energy operator associated with the interaction may be written in the form $c\mathbf{I}\cdot\mathbf{J}$, where I is a nuclear spin, J is the rotational quantum number of the molecule, and c is a constant characteristic of the molecule and of the particular nucleus. It will prove convenient throughout this paper to refer to the cosine-type coupling as the $\mathbf{I}\cdot\mathbf{J}$ interaction.

Both the electric and the magnetic resonance methods yield spectra which exhibit structure due to the nuclear-molecular interactions; however, there is a fundamental difference in the nature of these spectra. In the electric resonance method spectra are obtained which belong to the molecules in a single rotational state. The magnitude of the $\mathbf{I}\cdot\mathbf{J}$ interaction energy is determined for that rotational state by the relative line positions within a spectrum. The magnetic resonance method, on the other hand, does not distinguish between the molecules in the different rotational states, and spectra are observed which represent a summation of the intensities contributed by all the rotational states. The analyses of these spectra require a calculation of a statistical average over the rotational states of the beam molecules. A measure of the $\mathbf{I}\cdot\mathbf{J}$ interaction is obtained from the width of the nuclear resonance line at strong fields.

Trischka[1] found that the fluorine $\mathbf{I}\cdot\mathbf{J}$ interaction energy in CsF in rotational state $J=1$ is approximately twice the value determined by Nierenberg and Ramsey[2] in a magnetic resonance experiment at strong fields. As an explanation Trischka[1] suggested that the $\mathbf{I}\cdot\mathbf{J}$ interaction constant c might be a function of J.

In the present work radiofrequency spectra of Li^6F^{19} were observed by the electric resonance method primarily to obtain additional information on the $\mathbf{I}\cdot\mathbf{J}$ interaction. Magnetic resonance data[2,5] indicated that in this molecule the $\mathbf{I}\cdot\mathbf{J}$ interaction of F is so much larger than the other nuclear-molecular interactions that the electric resonance spectra would exhibit fine structure which would be, for the most part, characteristic of an $\mathbf{I}\cdot\mathbf{J}$ interaction. Consequently, the molecule is particularly adapted to a study of this interaction. Moreover, the fact that the F interaction had already been measured by the magnetic resonance method stimulated a measurement by the electric resonance method in order to compare the results obtained by the two methods.

II. EXPERIMENTAL DETAILS

The electric resonance apparatus, shown schematically in Fig. 1, operates on the same general principles as the machine constructed by Hughes[6] and modified by Trischka.[1] The present apparatus was, for the most part, designed and constructed by Luce and Trischka.[7] New features, a C field of new design[8] and a mass spectrometer, will be discussed in detail here.

A. The C Field

In the course of the beam path from oven to detector, as shown in Fig. 1, the molecules pass through a homogeneous, static electric field, called the C field, in which transitions are induced between the Stark

* This research has been supported in part by the ONR.
† Submitted by John C. Swartz in partial fulfillment of the requirements for the degree of Doctor of Philosophy in the Graduate School of Syracuse University.
‡ Now with Distillation Products Industries, Rochester, New York.
[1] J. W. Trischka, Phys. Rev. **74**, 718 (1948).
[2] W. A. Nierenberg and N. Ramsey, Phys. Rev. **72**, 1075 (1947).
[3] H. M. Foley, Phys. Rev. **72**, 504 (1947).
[4] G. C. Wick, Phys. Rev. **73**, 51 (1948).
[5] P. Kusch, Phys. Rev. **75**, 887 (1949).
[6] H. K. Hughes, Phys. Rev. **72**, 614 (1947).
[7] R. G. Luce and J. W. Trischka (to be published).
[8] Trischka, Swartz, and Luce, Phys. Rev. **83**, 881 (1951).

levels of the molecules by a superposed, weak, oscillating field. In the present experiments a C field of novel design was used.[9] Two pieces of $\frac{1}{4}$-in. plate glass, coated on adjacent surfaces with an evaporated metal film and separated by three glass spacers, served as the parallel-plate electrodes. The plates were 10 cm long, in the beam direction, and 6 cm high. These plates, supported by a brass mount, were clamped together over the three spacers by adjustable, spring-brass clamps. To align the plates to optimum plane-parallelism light from a Na vapor lamp was transmitted through the field normal to the coated surfaces, and the clamping pressure over each spacer was adjusted while observing the Haidinger interference fringes. The physical arrangement and alignment procedure are thus basically the same as for a Fabry-Perot interferometer.

The metal films were nearly opaque (giving about one percent transmission of white light). The rf segment was formed by making a narrow scratch in one of the films so as to isolate electrically a rectangle eight cm long in the beam direction by three cm high at the top center of the film. The oscillating voltage was applied between this rectangle and the rest of the film. Both gold and aluminum films were used with success although some difficulty was experienced in maintaining a low resistance at each contact to the film. The contacts were made at the edges of the glass plates by silver-plated spring clips. If the contact resistance was at all comparable to the leakage resistance across the spacers, the films, of course, assumed a difference of potential below the potential applied across the contacts. This effect was observed by a displacement and drift in spectral line positions which resulted from the development of a poor contact. This difficulty could apparently be attributed to transient charging and discharging currents which removed the film in the immediate vicinity of the contact. No such difficulty was encountered when care was taken to include a damping resistance in series with the supply batteries when the supply voltage was changed abruptly by switching operations.

Measurements of the position of a spectral line with the field intensity first in one direction, then in the opposite direction, showed that the residual potential difference between the two plates of the C field in the absence of an applied voltage was less than 0.01 volt.

With $\frac{1}{4}$-inch spacers (measured spacing $=0.25696 \pm 0.00005$ inch) the measured inhomogeneity in the beam region was the order of ± 2 parts in 10,000. At 43.6 Mc/sec this degree of inhomogeneity was expected to contribute at most 18 kc/sec to the line breadth. In all spectra of value the output of the rf signal generator was reduced to such an extent that on further decrease the line width remained unchanged. Under this condition, for a completely homogeneous C field, the expected single line width as calculated from the molecular transit time was about 11 kc/sec.[9] This figure was obtained from a calculation using an oven temperature of 950°K and a length of the transition region of eight cm. The observed width of each line at 43.6 Mc/sec (see Fig. 3) was 18 kc/sec. Therefore, it is evident that the effect of the field inhomogeneity on line breadth was somewhat less than the calculations would indicate.

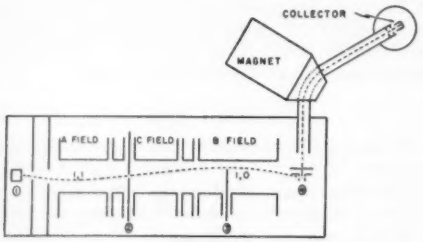

FIG. 1. Schematic diagram of electric resonance apparatus: (1) oven, (2) collimator slit, (3) knife edge for stopping molecules in high rotational states, (4) beam detector and ion gun.

B. The Mass Spectrometer

The molecular beam was detected by means of surface ionization on a hot, oxygenated W wire. The Li^6 ions thus formed were separated from the Li^7 ions by a 60° magnetic mass spectrometer of 12.5-cm radius (see Fig. 1). A $\frac{3}{8}$-inch square, brass tube, bent to conform to the ion trajectory, was soldered at one end to the main vacuum chamber and at the other end to a brass pillbox containing the exit slits and the collector. The electrometer tube of the dc amplifier was mounted in a container, at fore vacuum pressure, directly below the collector. Except for a few minor modifications the magnet was identical to that described by Nier.[10] Storage batteries were used to supply the magnet current.

Because of the limited space available for the magnet the initial ion path had to be normal to the direction of the molecular beam. An electron gun design by Thorp[11] was adapted to this purpose. Figure 2 shows a horizontal cross section of the ion gun. The filament (F) was recessed $\frac{1}{16}$ inch into a channel, 0.195 inch wide, between two side electrodes (A and B). These elements were kept at approximately the same positive potential.[12] The ions from the filament were focused by A and B and accelerated toward a 1-mm slit in a grounded plate C. A small slit in A allowed the molecular beam to strike the filament, while a similar slit in B provided an exit for that part of the beam not striking F and also permitted optical alignment of the filament with the other apparatus elements. The filament was heated with stabilized alternating current,

[9] H. C. Torrey, Phys. Rev. **59**, 293 (1941).
[10] A. O. Nier, Rev. Sci. Instr. **11**, 212 (1940).
[11] J. S. Thorp, J. Sci. Instr. **26**, 201 (1949).
[12] Improved mass spectrometer efficiencies were obtained with A and B biased, respectively, 18 and 26 volts above the filament.

and the accelerating voltage was supplied by an electronically stabilized supply with variable output from 300 v to 800 v. Under the best conditions of alignment of the ion gun, 60 percent of the Li^6 ions formed at the filament arrived at the collector of the mass spectrometer.

There were several factors which made imperative the use of a mass spectrometer in these experiments: (1) In order to observe spectra that were clearly due only to Li^6F it was necessary to measure the Li^6 ion current separately from the Li^7 ion current. (2) Because only 8 percent of the ion beam coming from the hot wire was due to Li^6, direct collection of all ions would have meant a large and fluctuating background current produced by the Li^7 ions. (3) Because the hot wire contained small amounts of impurity atoms which were ionized at the surface, direct collection of the ion beam would have meant a large, fluctuating background current from this source. When the impurity ion current (believed to be due mainly to K ions) was observed by direct collection from the wire, it was found to be of the order of 50 times the normal amplifier noise. With the mass spectrometer the fluctuations in ion current at the collector when the molecular beam was turned off were less than the amplifier noise.

C. Procedure

It was not possible with the available inhomogeneous fields to make a single state of LiF follow the sigmoid path necessary for reaching the detector. However, it was possible to observe the $J, m_J \rightarrow J, m_{J'}$ transitions $1, \pm1 \rightarrow 1, 0$ and $2, \pm2 \rightarrow 2, \pm1$ by causing those molecules in the $J=1$ or $J=2$ states (depending on the deflecting field strengths) which underwent transitions of the proper type in the C field to be refocused on the detector wire. For example, as indicated in Fig. 1, molecules in the $1, \pm1$ state in the A field which underwent transitions to the $1, 0$ state in the C field were redirected by the B field to strike the detector wire. Spectra were observed by noting each increase in the detected beam resulting from a given voltage and frequency combination on the C field.

At fields sufficiently large so that the positions of the fine structure lines relative to the hypothetical Stark line were not appreciably affected by small variations in the field, either of two techniques was employed to observe spectra. The oscillating frequency was held constant and the C field voltage varied point by point (yielding a spectrum such as that shown in Fig. 5), or the voltage was held constant and the frequency varied. For all other, lower, field strengths the voltage was fixed and the frequency varied.

The frequencies above 500 kc/sec were measured by a General Radio heterodyne wave meter No. 620A. The fixed frequency spectra were observed at harmonic frequencies of the calibrating crystal in the wave meter. Thus it was possible to make the random frequency

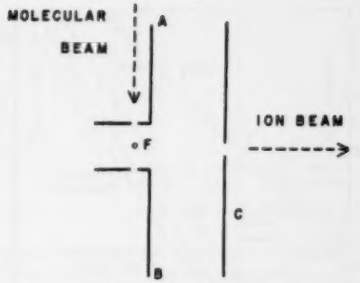

FIG. 2. Cross section of ion gun.

error for each observation point in these spectra less than 5 parts in 10^8. In all other spectra the random frequency error was determined by the least count of the wave-meter dial. This gave a random frequency error of 20 parts in 10^8. Below 500 kc/sec General Radio wave meter No. 616D was used. Both wave meters were calibrated against station WWV.

The C field potential was measured using a Leeds and Northrup voltbox, 746816, a Rubicon potentiometer, and an Eppley standard cell calibrated by the National Bureau of Standards. The random error in the voltage adjustments during the course of observation of each spectrum was the order of 25 parts in 10^6. Other errors contributed to the uncertainty in the absolute voltage measurements. The standard cell calibration was known within 0.01 percent, the potentiometer calibration within 0.01 percent, and the voltbox ratios were measured within 0.02 percent, giving a total possible error in absolute voltage of 4 parts in 10^4. In addition, it was found that at voltages near the limit of the voltbox (750 v) the increased temperature of the voltbox resistors introduced an error in recorded voltage of up to +2 parts in 10^4.

III. THEORY

The Hamiltonian containing the perturbations on the rotational energy of LiF in an electric field is

$$\begin{aligned}\mathcal{H} = {} & (h^2/2A)\mathbf{J}^2 - \boldsymbol{\mu}\cdot\mathbf{E} + c_1\mathbf{I}_1\cdot\mathbf{J} + c_2\mathbf{I}_2\cdot\mathbf{J} \\ & - (eqQ)_2 \frac{[3(\mathbf{I}_2\cdot\mathbf{J})^2 + (3/2)(\mathbf{I}_2\cdot\mathbf{J}) - \mathbf{I}_2^2\mathbf{J}^2]}{2I_2(2I_2-1)(2J-1)(2J+3)} + (g_1 g_2 \mu_N^2/r^3) \\ & \times \frac{[3(\mathbf{I}_1\cdot\mathbf{J})(\mathbf{I}_2\cdot\mathbf{J}) + 3(\mathbf{I}_2\cdot\mathbf{J})(\mathbf{I}_1\cdot\mathbf{J}) - 2(\mathbf{I}_1\cdot\mathbf{I}_2)J(J+1)]}{(2J+3)(2J-1)}. \end{aligned} \tag{1}$$

The first term is the rotational energy operator for a molecule with moment of inertia A about its center of mass. J is the rotational quantum number. The second term is the energy operator of an electric dipole moment $\boldsymbol{\mu}$ in an electric field $\mathbf{E}$. The third and fourth terms

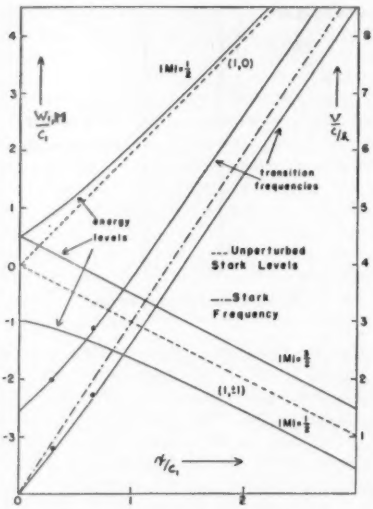

FIG. 3. Theoretical curves showing the variations of energy levels and transition frequencies with electric field, assuming the $\mathbf{I}\cdot\mathbf{J}$ interaction of F to be the only nuclear-molecular interaction. Circles indicate points calculated from experimental data. $J=1$, $I_1=\frac{1}{2}$, $c_1>0$.

represent the $\mathbf{I}\cdot\mathbf{J}$ interactions of the two nuclei. In accordance with the usual notation, subscript 1 refers to the nucleus with the strongest nuclear-molecular coupling, which in this case is the F nucleus, and therefore subscript 2 refers to the Li^6 nucleus. The fifth term is the energy operator associated with the Li^6 quadrupole interaction. eqQ is defined by Bardeen and Townes.[13] There is no corresponding term for the F nucleus, as this nucleus has a spin of $\frac{1}{2}$. The last term in the Hamiltonian is the nuclear spin-spin energy operator in which g_1 and g_2 are the nuclear gyromagnetic ratios, μ_N is the nuclear magneton, and r is the internuclear distance.

By making use of previous measurements the nuclear-molecular interaction constants in Li^6F^{19} can be estimated. Kusch[5] has measured the Li quadrupole interaction in Li^7F^{19}. His result is $|eqQ|_{Li^7}/h=408$ kc/sec. Schuster and Pake[14] have determined $|Q|_{Li^6}/|Q|_{Li^7}=0.023\pm0.002$ by a nuclear induction experiment. Since the electronic structure and internuclear distance are expected to be the same in Li^6F^{19} as in Li^7F^{19}, q should be the same for these two molecules. Therefore, combining the above figures, we obtain $|eqQ|_{Li^6}/h=|eqQ|_2/h=9$ kc/sec. For the purpose of comparing the effect of this interaction with that of other interactions in the molecule, calculations of the matrix elements of the quadrupole interaction operator show that $|eqQ|_2/10h=0.9$ kc/sec is representative of the quadrupole perturbation energies for small J.

Nierenberg and Ramsey[3] observed an F magnetic resonance spectrum of a molecular beam consisting primarily of Li^7F^{19}. The half-width of the resonance line was 0.50 Mc/sec. Assuming[15] a moment of inertia for this molecule of 27×10^{-40} g cm^2 and using their oven temperature of 1150°K, this width gives $|c_1|/h=18$ kc/sec. Here again the electronic structures of the isotopic molecules have been assumed to be identical.

From the molecular beam magnetic resonance spectrum of Li^7 obtained by Kusch[5] the magnitude of the $\mathbf{I}\cdot\mathbf{J}$ interaction constant of Li^7 can be estimated. On reducing this quantity by the ratio of the gyromagnetic ratios of the two Li isotopes the value $|c_2|/h=0.5$ kc/sec is obtained. Finally, assuming[15] $r=1.8$A, the spin-spin interaction energy is of the order of $g_1g_2\mu_N^2/2r^3h=1.5$ kc/sec.

It is apparent from the above information that the $\mathbf{I}\cdot\mathbf{J}$ interaction of F is by far the largest interaction. In fact, except for small corrections, our observed spectra can be explained by using solutions of the following Hamiltonian:

$$3\mathcal{C}=(\hbar^2/2A)\mathbf{J}^2-\boldsymbol{\mu}\cdot\mathbf{E}+c_1\mathbf{I}_1\cdot\mathbf{J}. \tag{2}$$

The eigenvalues of (2), assuming $\mu E/(\hbar^2/2A)$ and $c_1/(\hbar^2/2A)\ll J(J+1)$, are readily computed in an

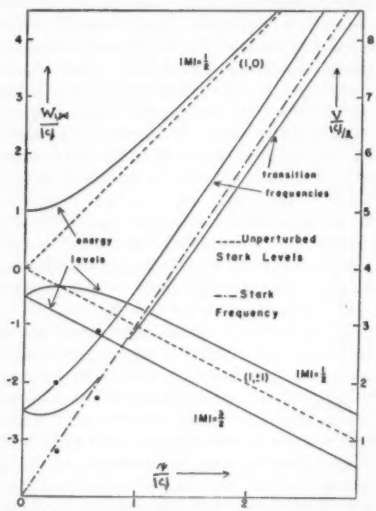

FIG. 4. Theoretical curves showing the variation of energy levels and transition frequencies with electric field, assuming the $\mathbf{I}\cdot\mathbf{J}$ interaction of F to be the only nuclear-molecular interaction. Circles indicate points calculated from experimental data. $J=1$, $I_1=\frac{1}{2}$, $c_1<0$.

[13] J. Bardeen and C. H. Townes, Phys. Rev. 73, 97 (1948).
[14] N. A. Schuster and G. E. Pake, Phys. Rev. 81, 157 (1951).
[15] This assumption will be discussed in a later section of this paper.

m_J, m_I representation for all field strengths from well-known matrix elements.[16,17] Since transitions observed in the apparatus are of the $\Delta J=0$ type, only the last two terms in (2) need concern us here. Denoting the eigenvalues for these terms by $W_{J,|M|}$, where $M=m_J+m_I$, we have

for $J=1$:

$$W_{1,3/2}=-x+c_1/2,$$
$$W_{1,1/2}=\tfrac{1}{2}\{x-c_1/2\pm[(3x+c_1/2)^2+2c_1^2]^{\frac{1}{2}}\}; \quad (3)$$

and for $J=2$:

$$W_{2,5/2}=-2y+c_1,$$
$$W_{2,3/2}=\tfrac{1}{2}\{-y-c_1/2\pm[(3y+3c_1/2)^2+4c_1^2]^{\frac{1}{2}}\}, \quad (4)$$
$$W_{2,1/2}=\tfrac{1}{2}\{3y-c_1/2\pm[(y+c_1/2)^2+6c_1^2]^{\frac{1}{2}}\},$$

in which $x=1/20(\mu^2E^2)/(h^2/2A)$ and

$$y=1/84(\mu^2E^2)/(h^2/2A).$$

Figure 3 contains plots of $W_{J,|M|}$ for $J=1$ and $c_1>0$ *vs* the field parameter x. Figure 4 shows these energies for the case in which $c_1<0$. As the field increases, the levels approach a constant separation from the unperturbed Stark level. For practical purposes we define the strong field region as the field region for which the level separations from the unperturbed Stark level are, within experimental error, field independent.

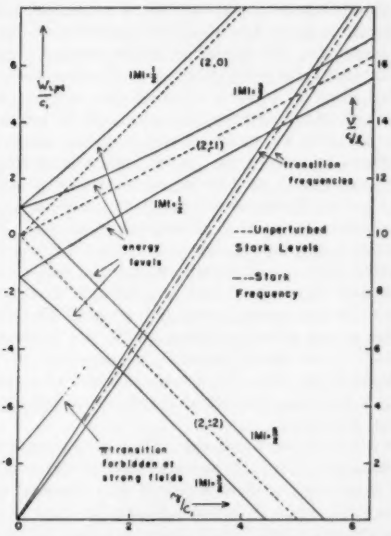

FIG. 5. Theoretical curves showing the variation of energy levels and transition frequencies with electric field, assuming the $\mathbf{I}\cdot\mathbf{J}$ interaction of F to be the only nuclear-molecular interaction. $J=2$, $I_1=\frac{1}{2}$, $c_1>0$.

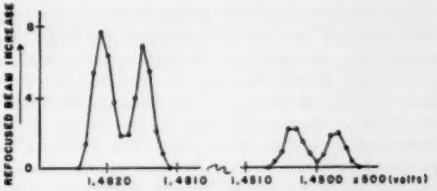

FIG. 6. 1, $\pm1\rightarrow1$, 0 spectrum at 43.600 Mc/sec.

The selection rules and criteria determining which allowed transitions may actually be observed in this apparatus have been discussed elsewhere.[18] The observable transitions for $J=1$ are plotted in Figs. 3 and 4 for the two possible signs of c_1. Two lines are expected which at high fields approach a constant separation. As the field is decreased to zero these two lines either separate further or merge, depending on the sign of c_1. Thus, weak field measurements provide a decisive means for determining the sign of the interaction constant.

The $J=2$ energy levels and observable transitions are shown in Fig. 5 for $c_1>0$. The behavior of the $J=2$ lines at weak field strengths is also characteristic of the sign of c_1. However, since the results to be presented show that the sign of c_1 is positive, the $J=2$, $c_1<0$ case is not shown.

The effects of the other interactions in (1) on the transition frequencies will be discussed in a later section.

IV. RESULTS

Data were taken on the 1, $\pm1\rightarrow1$, 0 transitions with x/c_1 in the range $0.035\leqslant x/c_1\leqslant 394$, and on the 2, $\pm2\rightarrow2$, ±1 transitions with y/c_1 in the range $0.15\leqslant y/c_1\leqslant 61$. Figure 6 shows an example of the spectrum obtained for the 1, $\pm1\rightarrow1$, 0 transition at the strongest fields used. Lines arising from molecules in two different vibrational states are present, the two lines for the ground vibrational state appearing at the higher voltages and the two weaker lines from the first excited vibrational state appearing at the lower voltages. Lines from higher vibrational states were too weak to be detected.

The circles in Figs. 3 and 4 represent points calculated from weak field data and the value of c_1/h determined from strong field measurements. A comparison of these points with the theoretical curves shows beyond doubt that the sign of c_1 is positive. At all values of field strength, the appearance of our spectra is consistent with the idea that an $\mathbf{I}\cdot\mathbf{J}$ interaction is the dominant interaction in Li^6F^{19}. However, in order to state that this interaction involves the F nucleus it is necessary to take into account the magnetic resonance data previously mentioned.[7,8,14]

[16] P. Debye, *Polar Molecules* (Dover Publications, New York, 1945), pp. 142 ff.

[17] E. U. Condon and G. H. Shortley, *Theory of Atomic Spectra* (Cambridge University Press, Cambridge, 1935), pp. 58, 59.

[18] V. Hughes and L. Grabner, Phys. Rev. 79, 829 (1950).

The solutions of (1) for strong fields and for zero field indicated that the Li quadrupole and $\mathbf{I}\cdot\mathbf{J}$ interactions and the spin-spin interaction could have a considerably greater effect on the weak field line positions than on the strong field line positions. Moreover, the effect of these interactions on the centers of the unresolved lines observed at weak fields could not be predicted precisely because the relative intensities of the transitions due to the different components of the oscillating field were not known. For these reasons the strong and intermediate field spectra rather than the weak field spectra were used to determine the magnitude of the $\mathbf{I}\cdot\mathbf{J}$ interaction of F for the two rotational states.

Table I summarizes the values of c_1/h, the $\mathbf{I}\cdot\mathbf{J}$ interaction constant for F, calculated from measurements made with large values of the field parameters x and y. The frequency of the unperturbed Stark line was determined with much greater accuracy than is indicated in the third column in the table. The measurements for $J=1$ were taken in the strong field region. For $J=2$ the fields in the range $61\geqslant y/c_1\geqslant 15$ were in the intermediate field region, and line separations differed as much as 10 percent from those to be expected if strong field conditions are assumed. However, accurate values of c_1/h were calculated with the use of (4), where y was computed from the value of μ^2A determined from strong field measurements; and the sign of c_1 was found by means of weak field measurements, as already mentioned.

Since the two lines used for computing the values of c_1/h in Table I were not completely resolved, as can be seen from Fig. 6, some correction to the observed line positions was necessary. Observed line positions were defined as the observed centers at half-maximum. By adding two lines possessing the theoretical line shape[9] and having the observed width and separation, a correction of $+0.5$ kc/sec was found for all measurements summarized in Table I except the $J=2$, 1.7 Mc/sec measurements, which required a correction of $+0.3$ kc/sec. The corrected values are given in the table. Since the theoretical line shape probably does not represent accurately the actual line shape, particularly for frequencies far from the resonant frequency, a systematic error of ± 0.3 kc/sec, representing the uncertainty in the above correction, was assumed for all the data in the table.

TABLE I. Experimental values of c_1/h.

Rotational state J	Vibrational state v	Frequency of Stark line Mc/sec	Number of measurements	c_1/h kc/sec	Random error kc/sec	Systematic error kc/sec
1	0	44	10	37.2	±1.8	±0.4
		7	10	37.16	±0.36	±0.4
		1.8	5	37.56	±0.45	±0.4
			Grand mean	37.3	±0.3	±0.4
2	0	⩾3.8[a]	7	37.56	±0.63	±0.4
		1.7	6	37.26	±0.27	±0.4
			Grand mean	37.3	±0.3	±0.4
1	1	44	4	35.5	±3.4	±0.4
2	1	1.7	1	37.3	±2.8	±0.4

[a] Measurements made at various frequencies in the range 3.8 to 6.8 Mc/sec.

The Li^6 quadrupole and $\mathbf{I}\cdot\mathbf{J}$ interactions and the spin-spin interaction at strong fields may produce a shift in each line position of no more than 0.05 kc/sec for both $J=1$ and $J=2$. This shift is in such a direction that the separation of the two lines of a spectrum may be greater or less than the values predicted by (3) and (4) by no more than 0.1 kc/sec, depending on whether $(eqQ)_2$ is positive or negative, respectively. Since the sign of $(eqQ)_2$ is not now known, an additional systematic error of ± 0.1 kc/sec was included, bringing the total systematic error to ± 0.4 kc/sec.

Each value of c_1/h given in Table I for a given Stark line frequency is a weighted mean of the individual measurements whose total number is given in the table. The stated random errors are the precision indices of the mean values. The weight assigned to each line measurement was determined from the random errors in frequency, voltage, and galvanometer deflection for each point on the line and from the density of data points defining the line shape. Since, for strong fields, c_1/h is given by the difference of the two line positions, twice the single line error was the probable error of each c_1/h value.

Table II compares the observed and calculated line positions at fields for which the unperturbed Stark frequency (the line frequency in the absence of any nuclear-molecular interactions) is of the same order as or less than c_1/h. Each observed line position was obtained from a single run. The calculated line positions were obtained by means of (3) and (4), using the constants obtained from strong field measurements. The value of c_1/h used in the calculations was $+37.3$ ± 0.7 kc/sec. Values of μ^2A are given for the first two vibrational states in a subsequent paragraph. The calculated line positions take into account the fact that at these fields the observed lines are the sum of two unresolved lines arising from two different vibrational states (the only states appreciably present). The effect of the second vibrational state on the line position is actually quite small, requiring a correction to the position of the line arising from the first vibrational state of less than 1 kc/sec at the strongest field represented in Table II.

It will be noted that in the column of calculated line positions in Table II $\mp$ appears before the error of the low frequency line of each pair of lines observed at a given field, while $\pm$ appears before the error of the high frequency line. This notation indicates that when the error in the low frequency line is negative the error in the high frequency line is positive. However, since the errors in the observed lines are random, the arrangement of the signs of the errors in the calculated line positions are of no significance when comparing observed and calculated values.

Additional quantities determined from the strong

field spectra were

$$(\mu^2A)_0=(747.2\pm0.9)\times10^{-76}\ \text{esu}^2\ \text{g cm}^4,$$

and

$$[(\mu^2A)_1-(\mu^2A)_0]/(\mu^2A)_0=0.043\pm0.001,$$

where $(\mu^2A)_v$ is the square of the electric dipole moment times the moment of inertia of Li^6F^{19} in the vibrational state with quantum number v.

It was not possible to obtain values of μ and A by the usual method[6] because the very large homogeneous field strengths required could neither be obtained nor accurately measured with our apparatus. The large field requirement is a consequence of the very small moment of inertia of LiF.

V. DISCUSSION

No accurate comparison of our value of c_1/h, $+37.3\pm0.7$ kc/sec can now be made with the value calculated from the magnetic resonance results of Nierenberg and Ramsey,[2] because the internuclear distance of LiF is unknown. However, it is not difficult to show that a considerable discrepancy must exist between the two values.

From data in reference 2, i.e., an oven temperature of 1150°K and a line width of 500 kc/sec, we find $c_1/h=32/r$ kc/sec, where r is the internuclear distance. If use is made of the semi-empirical formula of Schomaker and Stevenson[19] to calculate the internuclear distance, a value of 1.8A is found. This gives $c_1/h=18$ kc/sec, a value almost half as large as our electric resonance value. Some idea of the validity of the Schomaker and Stevenson formula can be obtained by comparing internuclear distances for the alkali halides computed from this formula with those already obtained experimentally. Such a comparison shows discrepancies which are at most of the order of 10 percent.

A more striking way to demonstrate the discrepancy between the electric and magnetic resonance results is to compute the value of the internuclear distance required to bring about agreement between the two values of c_1/h. This calculation gives $r=0.85$A, a value which is quite obviously too small.

Since it is clear that the electric resonance value of c_1/h is roughly twice as large as the magnetic resonance value, it is of some interest to examine other experiments for the purpose of comparing the $\mathbf{I}\cdot\mathbf{J}$ interaction constants. In the case of CsF the electric resonance value[1] of the F interaction constant is approximately twice as large as the magnetic resonance value.[2] For the Cl interaction constant in TlCl just the reverse situation apparently occurs; the magnetic resonance value[20] is larger than the electric resonance value.[21] However, the two values agree within experimental error, while the maximum disagreement makes the magnetic resonance value 50 percent larger than the electric resonance value. It should be mentioned that the magnetic resonance experiments in TlCl were done at zero field, while the experiments on LiF and CsF were done at strong magnetic fields.

From the preceding information it is not possible to make any general statements about the differences between electric and magnetic resonance determinations of $\mathbf{I}\cdot\mathbf{J}$ interaction constants. However, some explanation must be found for the large differences which exist for LiF and CsF. The plausibility of two possible explanations will be examined.

Since the lines observed by the magnetic resonance method are a composite of many lines arising from all the rotational and vibrational states in the molecular beam, while the lines observed by the electric resonance method are produced by only those molecules which are in a single rotational state and a single vibrational state, there may be a variation of the $\mathbf{I}\cdot\mathbf{J}$ interaction constant with rotation and vibration of the molecule.

We shall examine the last possibility first. An examination of Table I reveals that within the accuracy of our measurements the largest possible variation of the $\mathbf{I}\cdot\mathbf{J}$ interaction with vibrational state is about 10 percent per vibrational state. At the oven temperature used in the LiF experiments described in reference 2 only three vibrational states would be appreciably excited, so that the difference between the magnetic and electric resonance results cannot be ascribed to a vibrational effect.

A comparison of the values in Table I of the $\mathbf{I}\cdot\mathbf{J}$ interaction constants for $J=1$ and $J=2$, using the random errors only, indicates a possible decrease of the constant per rotational state of 0.6 kc/sec. The average value of J in the LiF beam described in reference 2 is about 25. Hence, the possibility of a variation of the

TABLE II. Comparison of line positions observed at weak fields with positions calculated on the assumption that only the $\mathbf{I}\cdot\mathbf{J}$ interaction of F was present.

Rotational state J	Unperturbed Stark frequency kc/sec	Observed line positions kc/sec	Calculated line positions kc/sec
1	71.6	64.0±3.0	60.8∓0.13
		107.0±3.0	105.2±0.8
	31.8	28.5±3.0	24.8∓0.1
		74.0±3.0	73.4±1.0
	17.9	...	13.1∓0.1
		64.6±1.2	64.3±1.0
	8.0	...	5.6∓0.1
		60.5±1.2	59.1±1.0
	3.9	...	2.7∓0.1
		58.5±1.2	57.4±1.0
2	68.2	66.2±1.2	63.9∓1.3
		144.5±1.2	145.4±1.6
	38.3	...	35.2∓1.8
		119.4±0.7	120.5±1.7
	17.0	...	15.2∓4.0
		103.2±0.7	104.4±1.7

[19] V. Schomaker and D. P. Stevenson, J. Am. Chem. Soc. **63**, 37 (1941).
[20] D. Bolef and H. Zeiger, Phys. Rev. **85**, 799 (1952).
[21] Carlson, Lee, and Fabricand, Phys. Rev. **85**, 784 (1952).

interaction constant with J is not excluded by our experiments as an explanation for the discrepancy between the electric and magnetic resonance results. Unfortunately, with the inhomogeneous fields available in our apparatus it was not possible to examine spectra for J greater than 2.

It will be noted that in Table II the calculated and observed line positions in all but two cases agree within experimental error. Thus, a single $\mathbf{I}\cdot\mathbf{J}$ interaction, the F interaction, explains the data rather well. However, there are indications that there may be systematic differences between the observed and calculated line positions; e.g., for $J=1$ the observed line positions are all higher than the calculated positions. If such systematic differences do in fact exist, they might be expected to be caused by the interactions involving the Li nucleus. In order to determine the effect of these interactions it would be necessary, in general, to solve sixth degree equations, a rather hopeless procedure with the present information about the Li interactions. Calculations at zero field, however, showed that shifts in line positions of several kc/sec might be produced by the Li interactions. Thus, though it is not possible with the present resolution of the apparatus to resolve the fine structure produced by the Li interactions, it might be possible nevertheless to get some information about these interactions from the line positions observed near zero field. Unfortunately, such a program is not feasible at present because of the lack of information about the relative amplitudes of the different spatial components of the radiofrequency voltage.

The authors are indebted to Dr. R. G. Luce for his help in the construction of the mass spectrometer used in these experiments. The help of Mr. R. Braunstein and Mr. D. T. F. Marple in the laboratory is gratefully acknowledged.

PHYSICAL REVIEW VOLUME 88, NUMBER 5 DECEMBER 1, 1952

The Resistivity of Lanthanum, Cerium, Praseodymium, and Neodymium at Low Temperatures*

N. R. JAMES,† S. LEGVOLD, AND F. H. SPEDDING
Institute for Atomic Research and Department of Physics, Iowa State College, Ames, Iowa
(Received August 15, 1952)

The electrical resistivity of lanthanum, cerium, praseodymium, and neodymium metals from room temperature to 2.2°K is presented. The h.c.p. modification of lanthanum is found to possess a higher resistivity than the f.c.c. The mean of the observed superconducting transition temperatures for lanthanum is 5.8°K. Anomalies in the resistivity of cerium which occur at liquid nitrogen temperatures and between 11 and 14° K are discussed in connection with the crystal structure. An anomaly in the resistivity of neodymium occurs at approximately 12°K.

I. INTRODUCTION

THE anomalous behavior of some of the rare earth metals has long been recognized and studied. It has appeared in numerous investigations of the mechanical, thermal, electrical, and magnetic properties of the metals and has led to disagreement among investigators which has been furthered by lack of reproducible data. Previous studies make obvious the fact that the purity, heat treatment, crystal structure, and state of strain of the samples all affect the results. Of these, there is no doubt that the crystal structure and purity bear the greatest significance. In this preliminary study an attempt has been made to ascertain how these factors affect the electrical resistivity.

II. EXPERIMENTAL METHOD

A Collins Helium Cryostat with the samples and thermometers mounted just above the bottom of the experimental chamber was used for the experiments. The length of time required to cool the apparatus averaged 7½ hours; heating occurred over an average period of 45 hours.

Temperatures between 300 and 15°K were determined by a four-lead standard platinum resistance thermometer, No. 718171, made by Leeds and Northrup Company and calibrated down to 10°K by the National Bureau of Standards. Below 15°K a four-lead constantan resistance thermometer was used. The thermometer winding consisted of No. 30 B. and S. cotton-covered wire, wound loosely, in order to be strain-free, and non-inductively on Bakelite micarta tubing. The constantan thermometer was calibrated between 25 and 10°K against the platinum thermometer, at 4.2 and at 2.2°K by immersion in liquid helium at atmospheric pressure and at the λ-point. Temperatures below 15°K

* Contribution No. 203 from the Institute for Atomic Research and Department of Physics, Iowa State College, Ames, Iowa. Work was performed in the Ames Laboratory of the AEC.

† Now at Chalk River, Ontario, Canada. The material reported here appears in the first author's thesis presented to the Graduate Faculty of the Iowa State College in partial fulfillment of the requirements for the Doctor of Philosophy degree.

TABLE I. Method of preparation and properties of specimens.

Sample	Method of preparation	Runs preceded[a] by annealing	Length of cooling period, hours	Iron content, parts per million	Density, g/cm³	Structure[b]
La I	Cast	No. 1, No. 3	3, 3	4200	6.08	After Run 4: two-thirds h.c.p., one-third f.c.c.
La II	Extruded	No annealing		85.5	5.98	After Run 2: one-half h.c.p., one-half f.c.c.
Ce I	Cast	No. 1	3	700	Not obtained	Not obtained
Ce II	Cast	No. 1	1	2835	6.66	After Run 2: predominantly f.c.c., small amount h.c.p. After Run 5: some increase in amount of h.c.p.
Ce III	Extruded	No. 1	Quenched in water at 25°C	291	6.68	Before Run 1: entirely f.c.c. After Run 3: small amount h.c.p.
Ce IV	Extruded	No. 1	24	291	6.68	Before Run 1: predominantly f.c.c., some h.c.p. After Run 3: considerable increase in amount of h.c.p.
Pr I	Cast	No. 1, No. 3	3, 1	315	6.59	After Run 3: three-fourths h.c.p., one-fourth f.c.c.
Nd I	Cast	No. 1, No. 3	3, 1	178	6.86	After Run 3: entirely h.c.p.

[a] Samples were annealed for 19 hours at 600°C.
[b] The relative amounts of the two crystal forms present in the samples was determined by x-rays on samples cut from the ends of the rods and then filed into the form of needles. As a consequence these results are only qualitative.

were then obtained from the resistance *versus* temperature curve. Throughout the range of calibration the curve was smooth; from 24 to 10°K it was linear with a sensitivity of 0.027 ohm per degree. The calibration, repeated several times during successive experiments, remained essentially constant below 15°K, the range in which the thermometer was used.

The resistance of the thermometers was read on a Rubicon Mueller temperature bridge. Thermometer readings were taken both before and after the measurements of the potential drop across any sample, and the mean temperature was taken to be that of the sample when its resistance was measured. Above 40°K temperatures were read to at least the nearest degree and below 40°K temperatures were read to the nearest one-tenth of a degree.

The metals used were prepared by a bomb reduction technique.[1] Rods for the experiments were either cast or extruded from the pure metal. The casting process consisted of heating the metal in a tantalum-lined funnel of magnesium oxide and allowing the metal to run into a 1-cm diameter magnesium oxide tube, the process being done in a vacuum. The extruded rods were 6.4 mm in diameter. All rods were turned on a lathe to approximately 3.6 mm in diameter and cut to 5 cm in length. They were generally stored in a helium atmosphere in soft glass tubes, although for a short time they were kept under mineral oil. Properties of the specimens are shown in Table I.

Spectrographic analyses showed that all specimens contained less than 1-percent magnesium, less than 0.025 percent calcium, and less than 0.01 percent other rare earths. These values represent the limits of detectability spectrographically. The iron content varied with the specimen. Samples for the x-ray analyses were cut from the rods and filed to the shape of needles approximately 0.2 mm in diameter.

The resistivity was determined by the standard method of comparing the potential drop across the sample to that across a standard resistance connected in series with it. Readings were taken with the current in the normal and in the reverse direction in order to eliminate effects due to the junctions and the mean values were used. Three 6-volt storage batteries, connected in parallel in order to insure a more uniform current, were used for the supply. A current of approxi-

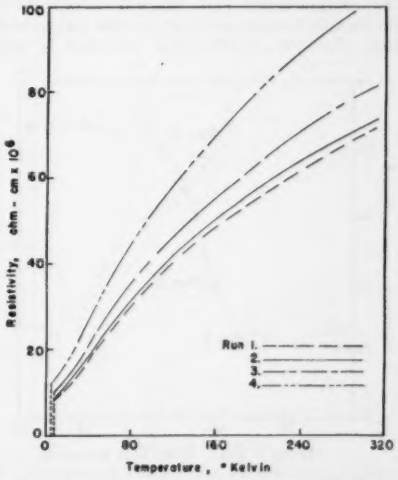

FIG. 1. Resistivity of lanthanum I as a function of temperature.

[1] Spedding, Wilhelm, Keller, Ahmann, Daane, Hach, and Erickson, Ind. Eng. Chem. 44, 553 (1952).

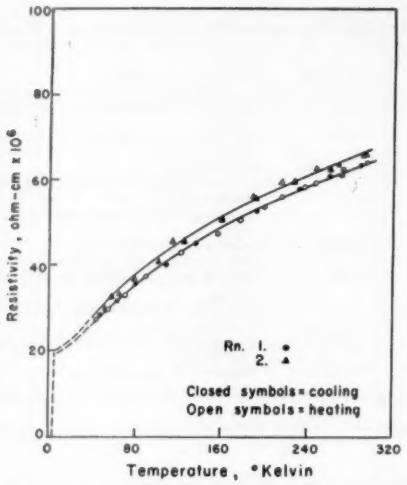

FIG. 2. Resistivity of lanthanum II as a function of temperature.

mately ½ ampere was sufficient to give a measurable potential drop across the samples at all temperatures. Potential drops were measured on a Rubicon Type B potentiometer.

The sample holder contained clamps for three rods and space for the two thermometers. Selector switches permitted any one sample to be connected into the circuit. The thermometers, placed as close together as possible, were approximately one cm from two of the samples and three cm from the third. Current connections to the samples were rigid brass wedges against which the rods were forced by small brass springs under tension. The ends of the springs were filed to wedge shapes and were used for potential connections. Before the rods were mounted in the holder, the oxide coating was removed with fine sandpaper and crocus cloth. The separation of the potential leads was marked by dividers and estimated to the nearest 0.1 mm. The mean of three readings, with a probable error never greater than 0.1 mm, was used in the calculations. In these preliminary measurements no correction was made for the change in length due to temperature variation.

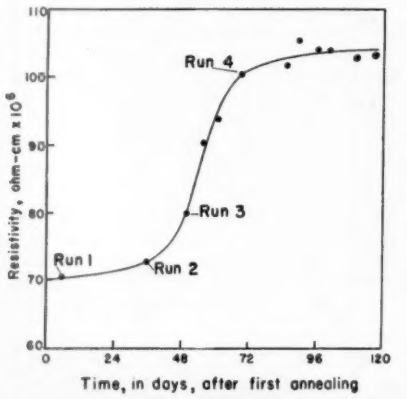

FIG. 3. Resistivity at room temperature of lanthanum I as a function of length of time after first annealing of the sample.

III. RESULTS AND CONCLUSIONS

A. Lanthanum

There is a marked difference in the behavior of the two specimens of lanthanum as can be seen in Figs. 1 and 2. After La sample I was first annealed, its resistivity at room temperature increased over a period of 90 days following which it remained essentially constant. This is shown in Fig. 3 where the room temperature resistivity is given as a function of time in days. Data on the resistivity as a function of temperature were taken during the time that the room temperature resistivity was changing slowly, and this accounts for the spread in the curves of Fig. 1. The points at which the temperature runs were made are indicated on Fig. 3. An x-ray analysis, obtained 123 days after the first annealing, showed the sample (La I) to be predominantly hexagonal close-packed (h.c.p.).

TABLE II. Calculated superconducting transition temperatures and ranges of lanthanum.

Sample	Run	T_s, °K	ΔT_s
La I	2	5.9	0.4
	3	6.0	0.3
	4	5.5	0.9
La II	1	5.8	0.3
	2	5.9	0.9

The resistivity of La sample II increased only slightly from run 1 to run 2 (see Fig. 2). The resistivity did not change appreciably thereafter with time. La II was found to contain approximately equal amounts of the hexagonal close-packed (h.c.p.) and the face-centered cubic (f.c.c.) modifications. The results suggest the possibility that the stable modification of lanthanum at room temperature is h.c.p. and that the cast sample, La I, underwent a spontaneous transformation from the f.c.c. to the h.c.p. structure with an accompanying increase in resistivity while, at the same time, this transformation was inhibited in the extruded specimen, probably by the work done during extrusion.

Previous measurements of the superconducting transition of lanthanum have led to considerable disagreement. Mendelssohn and Daunt[2] observed the transition by magnetic methods at 4.71°K; Shoenberg[3] using the

[2] K. Mendelssohn and J. G. Daunt, Nature **139**, 473 (1937).
[3] D. Shoenberg, Proc. Cambridge Phil. Soc. **33**, 577 (1937).

magnetic method observed it at 4.2°K; Ziegler[4] found by the magnetic method for two samples 4.85±0.15 and 4.45±0.10°K, with a transition range of less than 0.1 degree. Ziegler, Floyd, and Young[5] found by the magnetic method for various specimens transition temperatures which ranged from 3.9 to 5.0°K and which were increased by annealing the specimens. Parkinson, Simon, and Spedding[6] found by specific heat measurements the transition, not perfectly sharp, at 4.37°K. Earlier work by Allen, McLennan, and Wilhelm[7] on the electrical conductivity indicated no superconducting transition down to 1.5°K. There is no doubt that the transition temperature is affected by many factors and that the explanation of the observed differences is not a simple one.

In the present investigation, the transition temperature, T_s, was taken at the mid-point of then early vertical portion of the resistivity curve. The transition range, ΔT_s, was taken to be that over which the vertical portion would have extended had there been no rounding of the curve. The calculated temperatures and transition ranges are given in Table II. The transition temperatures for both samples are higher than previously reported values, and in only one other case has such a large transition range as that reported here been found.[5] This is perplexing in view of the fact that many of the specimens used by these workers were obtained from this laboratory.

Factors which appear significant as causes for the varied results are the method for detection and the grain size, purity, state of strain, and crystal structure of the samples. The samples described here were as pure as those used by others and in some cases considerably better so this does not seem to resolve the difficulty. In the present study La I, which was annealed, exhibited approximately the same transition temperature and range as did La II, which was given no heat treatment other than that required by the extrusion process. The transition range of La I was not measured before the specimen was first annealed; however, as can be seen in Table II, reannealing the rod after the second run did not change the range.

B. Cerium

A transition in cerium has been observed at approximately liquid nitrogen temperatures by Owen,[8] Trombe,[9] Trombe and Foex,[10,11] Schuch and Sturdivant,[12] and by Parkinson, Simon, and Spedding.[6] It has been shown[13] by the application of pressure that the normal f.c.c. modification of cerium (lattice constant $a=5.140$A) undergoes a transformation to a condensed f.c.c. form

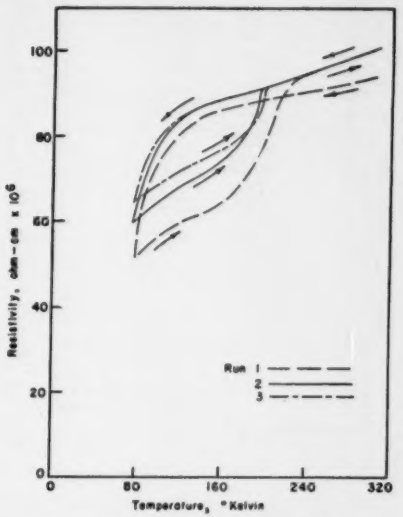

FIG. 4. Resistivity of cerium I as a function of temperature above 78°K.

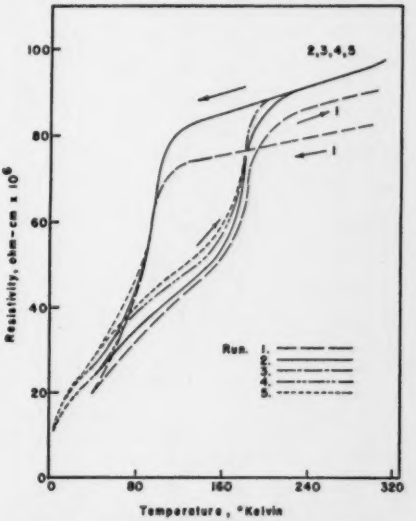

FIG. 5. Resistivity of cerium II as a function of temperature.

[4] W. T. Ziegler, J. Chem. Phys. **16**, 838 (1948).
[5] Ziegler, Floyd, and Young, O.N.R. Tech. Report No. 2. Georgia Inst. Tech. State Eng. Exp. Station (unpublished) (1950).
[6] Parkinson, Simon, and Spedding, Proc. Roy. Soc. (London) **A207**, 137 (1951).
[7] Allen, McLennan, and Wilhelm, Phil. Mag. **10**, 500 (1930).
[8] M. Owen, Ann. phys. **37**, 657 (1912).
[9] F. Trombe, Compt. rend. **198**, 1591 (1934).
[10] F. Trombe and M. Foex, Compt. rend. **217**, 501 (1943).
[11] F. Trombe and M. Foex, Ann. chim. **19**, 417 (1944).
[12] A. F. Schuch and J. H. Sturdivant, J. Chem. Phys. **18**, 145 (1950).
[13] A. W. Lawson and T. Tang, Phys. Rev. **76**, 301 (1949).

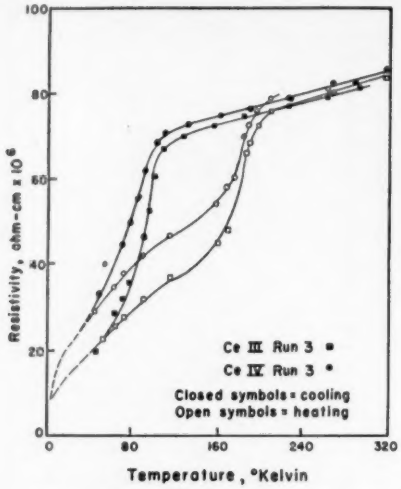

FIG. 6. Resistivity of cerium III and cerium IV as a function of temperature.

(lattice constant $a=4.84\pm0.03$A). The transition was attributed to a shift of a $4f$ electron to a $5d$ orbit. It has also been shown[6,12] that the same transition is temperature induced, and the latter reported smaller proportions of the condensed form appearing on successive coolings.

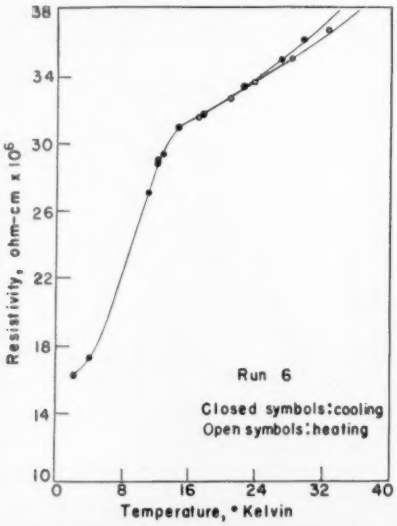

FIG. 7. Resistivity of cerium I as a function of temperature below 40°K.

Cerium has also been found to exhibit anomalous behavior at lower temperatures. Slight hysteresis in the magnetic susceptibility was observed by Starr and Kaufmann[14] at 13.9 and at 20.4°K. A peak in the atomic heat *versus* temperature curve,[6] centered about 11.5°K for one specimen, about 12.5°K for a second specimen, was attributed to a splitting of the lowest energy level of the ion by the field of its neighbors and a consequent redistribution of the electrons among the states.

In the present investigation, all specimens showed on cooling a sudden decrease in resistivity which began at a temperature between 100 and 120°K and which probably corresponded to the transition from the normal f.c.c. structure to the more compact f.c.c. form. The data are shown in Figs. 4, 5, and 6. The corresponding

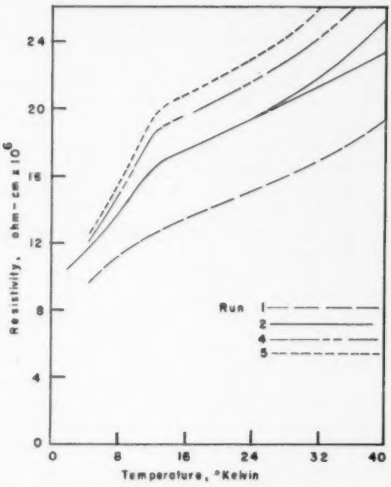

FIG. 8. Resistivity of cerium II as a function of temperature below 40°K.

increase in resistivity became apparent, during heating, at approximately 170°K and was complete at approximately 220°K giving the appearance of a hysteresis loop. It should be remarked that this data has not been corrected for changes in density caused by structure changes or by temperature changes.

Ce I, cooled only to liquid nitrogen temperatures during the first three sets of measurements, showed (Fig. 4) a smaller decrease in resistivity each of these times, an effect similar to that observed by Trombe and Foex.[11] The same observation was made on the other cerium specimens only at temperatures lower than that of liquid nitrogen. From the x-ray analyses, it is apparent that there occurred a gradual transition from the f.c.c. form to the h.c.p. An explanation of the smaller

[14] C. Starr and A. R. Kaufmann, Phys. Rev. **58**, 657 (1940).

decrease in resistivity at liquid nitrogen temperatures with successive thermal cycles is afforded by the slow transition to the h.c.p. structure and the probable inability of that form to undergo a transition to the condensed f.c.c. structure at these temperatures.

At the end of the first set of measurements on each sample, the value of the room-temperature resistivity was higher than it had been at the beginning of the run. With the exception of Ce II (Fig. 5), the resistivity at room temperature of all samples remained essentially constant after the first run. That of Ce II increased further while the sample was stored, but reached a constant value before the second series of measurements was made. The greater reproducibility of the curves after the first set of measurements may indicate that

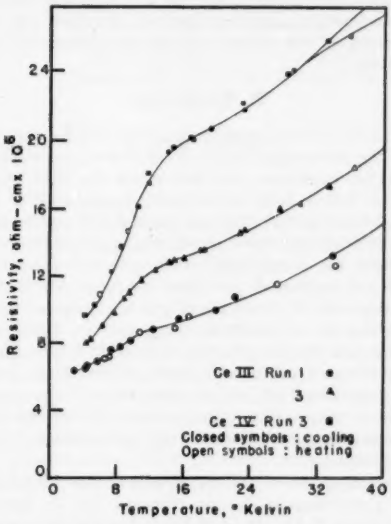

FIG. 9. Resistivity of cerium III and cerium IV as a function of temperature below 40°K.

those microcrystals most easily transformed to the hexagonal form are induced to do so by the first thermal cycle.

A second anomalous decrease in resistivity occurred at a temperature between 11 and 14°K. The data for T below 40°K are shown in Figs. 7, 8, and 9. The height of the knees in the curves increased with successive thermal cycles. The cooling rate was approximately the same for each series of measurements. That successive cycles effected more pronounced knees in the curves as well as greater amounts of the hexagonal form suggests the possibility that the h.c.p. crystals transform into the condensed f.c.c. structure (or into a condensed h.c.p. structure) at this lower temperature. The possibility

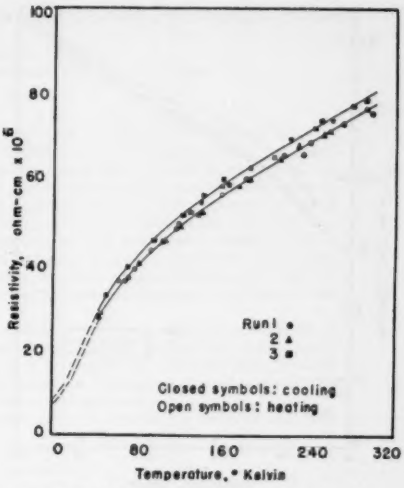

FIG. 10. Resistivity of praseodymium I as a function of temperature.

exists that the crystal splitting of the $^2F_{\frac{1}{2}}$ level, which would show a specific heat anomaly near this temperature, may trigger the transition of the $4f$ electron to the $5d$ shell (due to the temperature dependent population distribution of the crystalline electronic structure) and thereby make more probable a crystalline transformation from the room temperature hexagonal

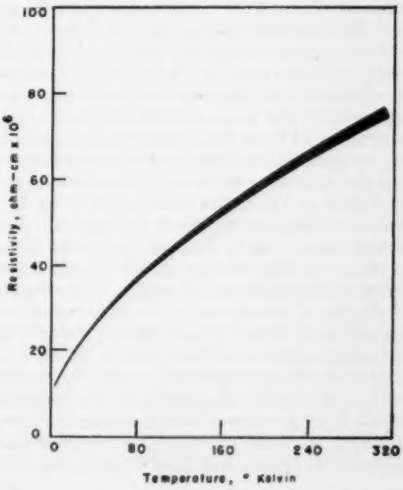

FIG. 11. Resistivity of neodymium I as a function of temperature.

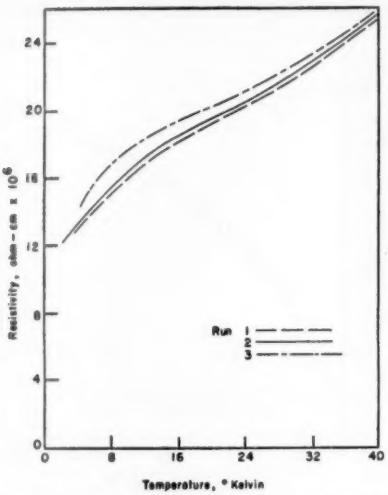

FIG. 12. Resistivity of neodymium I as a function of temperature below 40°K.

form to a condensed cubic or hexagonal form. The onset of ferromagnetism in the hexagonal crystals at this temperature has not been ruled out as an explanation of the anomaly.

The rate of cooling from an annealing temperature to ordinary temperatures has been thought by several investigators[10–12] to affect the behavior of cerium. The effect of the rate of cooling from the annealing temperature is evident from a comparison of Ce III with Ce IV. The specimens, having been cut from the same rod, were identical except for the length of the cooling period. Ce III was quenched in water at 25°C immediately after annealing; the x-ray analysis did not indicate the presence of any h.c.p. crystals. Ce IV was cooled in a period of 24 hours and contained a fair amount of the h.c.p. modification. After the third series of measurements the proportion of the h.c.p. form had increased only slightly in Ce III but considerably in Ce IV. A pronounced difference appears in the resistivity curves shown in Figs. 6 and 9. Data obtained from the first two series of measurements of Ce IV are omitted because of incompleteness. However, these data gave no indication of inconsistencies. The resistance of Ce IV decreased more slowly at liquid nitrogen temperatures and correspondingly, a greater knee in the curve appeared at the lower temperature. Again, the curves of Ce III in Fig. 9 show the increase in the low temperature anomaly which accompanies the increase in the amount of the h.c.p. structure. The results here obtained uphold the theory of Trombe and Foex[10,11] that slow cooling after annealing and repeated thermal cycles between room temperature and low temperatures invoke a gradual structural transition. However, in the present investigation, the quenched specimen did not exhibit perfectly reproducible behavior, but transformed also, although at a much slower rate.

C. Praseodymium

The data for praseodymium are shown in Fig. 10. It will be noted that on successive runs an increase in the resistivity occurs which is caused, we believe, by an increase in the amount of the h.c.p. modification. The figure also shows that in the temperature region below 50°K the slope of the curve is considerably greater than that of lanthanum or neodymium. While at present this remains unexplained it suggests the possibility that in this temperature region a gradual transition may be occurring of the cerium type. Investigations on this continue.

D. Neodymium

The behavior of neodymium above 24°K (Fig. 11) was the most reproducible of the rare earths studied. Data for three runs were well within the broad curve shown. Below 24°K an anomaly appeared (Fig. 12) which was centered at approximately 12°K and became more evident with successive thermal cycles. Anomalous peaks in the atomic heat curves appeared at 7 and at 19°K.[6] A splitting of the lowest energy level of the ion by the field of its neighbors and a consequent redistribution of the electrons, suggested by Parkinson, Simon, and Spedding,[6] might well result in a modification of the expected resistivity pattern. Since x-ray analysis showed no f.c.c. crystals present in the sample at room temperature, it is apparent that the low temperature anomaly is not associated with the usual f.c.c. modification.

A comparison of the resistivities of the three h.c.p. (or predominantly h.c.p.) elements (La I, Run 4, Fig. 1; Pr I, Fig. 10; and Nd I, Fig. 11) indicates a decrease in resistivity may occur with an increase in atomic number. The abnormal negative derivative of the slope of the low temperature end of the neodymium curves makes it highly desirable to pursue the investigation at temperatures lower than 2°K.

The authors acknowledge their indebtedness to the following members of Dr. Spedding's research group: Mr. J. Powell for the preparation of the pure rare earths; to Mr. J. P. Flynn and Dr. A. H. Daane for the preparation of the rods; to Mr. J. R. Banister and to Dr. V. Fassel's group for the x-ray and spectrographic analyses; and to Mr. R. Anderson and Mr. F. Barson for their assistance in building the apparatus and in taking the data.

High Energy Proton-Proton Scattering and Associated Polarization Effects*

L. J. B. GOLDFARB AND D. FELDMAN
Department of Physics, University of Rochester, Rochester, New York

(Received August 18, 1952)

Three phenomenological descriptions of p-p scattering have been proposed to date, two of which, the singular tensor-force model of Christian-Noyes and the $\mathbf{L}\cdot\mathbf{S}$ force model of Case-Pais, are characterized by a singular triplet potential. The Jastrow model introduces a hard core in the singlet interaction. The parameters of these various potentials were all determined, in part, by use of Born approximation estimates of triplet scattering cross sections at high energies. Inasmuch as the validity of such estimates is not clear in those cases where the interaction is singular, more exact calculations have been performed at 240 Mev with the singular potentials (and also, for comparative purposes, with the well-behaved triplet interaction of Jastrow) using Schwinger's variational method and/or numerical integration procedures. Such calculations have also been performed at 450 Mev for the singular tensor-force model. To insure the existence of solutions, a zero cutoff has been introduced in the singular potentials at distances of the order of the nucleon Compton wavelength.

It is found that, in all instances where the potential is singular, the Born approximation and the use of Born approximation trial functions in a variational treatment are completely unreliable. More exact calculations of the differential scattering cross sections than those in Born approximation introduce large anisotropies in the case of the singular interactions and, in particular, in the case of the $\mathbf{L}\cdot\mathbf{S}$ potential. The hard-core model, on the other hand, is in qualitative agreement with experiment.

Also discussed are the results of calculations of polarization effects in a double p-p scattering and their implications for the various potentials considered.

I. INTRODUCTION

WITH the advent of high energy accelerating machines, the range of energies available in p-p scattering experiments has progressed beyond the classical domain of less than 10 Mev[1] so as to include energies up to 450 Mev. Scattering in the classical domain is consistent with pure S-wave scattering in singlet states. It is nonetheless clear[2] that this can only provide knowledge of two parameters, the scattering length and the effective range, and leaves undetermined the shape of the potential. In addition, no knowledge can be obtained of scattering in triplet states. It was accordingly believed that experiments at higher energies which would include contributions from higher angular momentum states would provide a more unique phenomenological description of the proton-proton interaction.

As experiments were pushed to higher energies, it became increasingly evident that the predictions of conventional central-force potential models, adjusted so as to explain the low energy scattering data, would be in complete contradiction with experiment. These predictions are characterized by a preponderance of scattering in the forward direction and relatively negligible scattering at 90°; in contrast to this, experiments give a fairly isotropic distribution after one takes into account the Coulomb scattering at smaller angles. In Fig. 1, we have indicated the general behavior of the differential cross sections as obtained at 32 and 345 Mev at Berkeley[3] and as obtained at 240 Mev at Rochester.[4] The isotropy at the two higher energies persists down to angles[5] less than 15° below which occurs the expected rise due to Coulomb scattering. Other data not shown in the figure give the same characteristic flatness at 105 Mev[6] and at 146 Mev,[7] with the magnitude of the differential cross section ~5 mb corresponding to the cross section reported by the Rochester group. There is still a discrepancy of ~1 mb in magnitude between results quoted by the Berkeley group and those quoted by others; however, there is general agreement as to the angular dependence.

Although the parameters of the singlet potentials are predetermined by the low energy results, there is still freedom in the choice of the triplet potential. Since the anomalous high energy scattering cannot be accounted for in terms of central forces, one is led to consider the only other interactions which may occur in the p-p system subject to the restriction that the velocities appear in no higher power than the first, *viz.*, tensor (S_{12}) and $\mathbf{L}\cdot\mathbf{S}$ forces.[8] We shall refer to these, collectively, as spin-orbit forces. Various phenomenological models have been suggested using spin-orbit coupling; in particular, Christian and Noyes[9] have employed a tensor force, whereas Case and Pais[10] have proposed an

* This research was supported in part by the AEC.

[1] Energies quoted correspond to the kinetic energy of the incident proton as measured in the laboratory system.

[2] J. Schwinger, Harvard lecture notes (1946–47) (unpublished); H. A. Bethe, Phys. Rev. **76**, 38 (1949); G. Breit, Revs. Modern Phys. **23**, 238 (1951).

[3] Chamberlain, Segrè, and Wiegand, Phys. Rev. **83**, 923 (1951); W. K. H. Panofsky and F. Fillmore, Phys. Rev. **79**, 57 (1950); Cork, Johnston, and Richman, Phys. Rev. **79**, 71 (1950).

[4] C. L. Oxley and R. D. Schamberger, Phys. Rev. **85**, 416 (1952); O. A. Towler, Phys. Rev. **85**, 1024 (1952).

[5] Angles of scattering correspond to those measured in the center-of-mass system.

[6] Birge, Kruse, and Ramsey, Phys. Rev. **83**, 274 (1951).

[7] Cassels, Stafford, and Pickavance, Nature **168**, 468 (1951).

[8] L. Eisenbud and E. Wigner, Proc. Nat. Acad. Sci. **27**, 281 (1941).

[9] R. S. Christian and H. P. Noyes, Phys. Rev. **79**, 85 (1950).

[10] K. M. Case and A. Pais, Phys. Rev. **80**, 203 (1950).

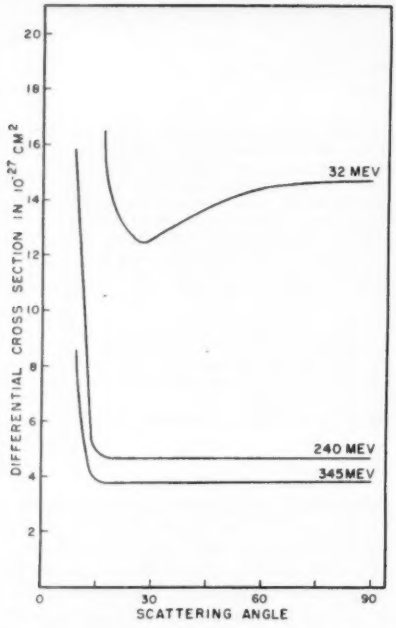

FIG. 1. Experimental differential cross sections for p-p scattering at 32, 240, and 345 Mev.

alternative description in terms of $\mathbf{L}\cdot\mathbf{S}$ forces. In both cases the interactions are singular, the former varying near the origin as $1/r^2$ and the latter as $1/r^3$. Jastrow,[11] on the other hand, has proposed a well-behaved triplet tensor potential in conjunction with a repulsive core in the singlet interaction. All of these models were adjusted so as to fit the low energy and 32-Mev data, and Born approximation estimates were made of the scattering at 350 Mev (except for the singlet scattering with the hard-core potential for which exact calculations were performed). The parameters of the different models are shown in Table I.

In view of the singular nature of both the $\mathbf{L}\cdot\mathbf{S}$ potential of Case and Pais and of the tensor potential of Christian and Noyes, the validity of the Born approximation, even at high energies, is uncertain, and, for this reason, more exact calculations are highly desirable. Accordingly, calculations with these models have been performed using variational and numerical methods in integrating the differential equations. In order to insure the existence of solutions to the scattering problem, a zero cutoff has been introduced in the singular potentials at distances of the order of the nucleon Compton wavelength. The calculations, which we describe here, are confined to 240 Mev in line with experiments currently in progress at the Rochester 130-inch cyclotron. Calculations have also been performed for the singular tensor force at 450 Mev (the Chicago energy) in order to obtain an estimate of the energy dependence for a singular potential. The results bear out that, at these energies, the Born approximation is, indeed, poor for these potentials. Comparable calculations performed with the Jastrow model which has a well-behaved triplet potential show that the Born approximation is much better, as expected. The resultant cross sections and their implications for the various potential models considered will be discussed in Sec. III following a brief resumé of the methods used in the computation which is given in Sec. II.

A particular consequence of spin-orbit forces is that they lead to a mixing of the triplet spin states so that, after a single p-p scattering, the outgoing particles are polarized.[12] A second scattering of these particles results in a distribution exhibiting an azimuthal asymmetry. Since polarization effects are confined to triplet states, and the relative importance of scattering in these states increases with energy, such effects might very well provide a means of distinguishing among various potential models which can be adjusted to fit the unpolarized cross sections.[13] Calculations of the polarization effects have accordingly been performed for each of the three potential models considered in this paper despite the fact that the agreement with the ordinary scattering cross-section data is, in some cases, poor. The results of these calculations are discussed in Sec. IV.

II. METHODS OF CALCULATION

The analysis which follows is based entirely on the nonrelativistic Schrödinger equation. Actually, relativistic corrections involving both dynamic and kinematic effects begin to assume importance at the energies which we are considering and, at 240 Mev, can amount to $\sim$15 percent.[14] Hence, one must allow for deviations of this order of magnitude in making any comparisons with experiment.

The differential cross section in the center-of-mass system for the scattering of a beam of unpolarized protons by protons for the general case of spin-orbit forces, taking into account the identity of the particles, can be written, in the notation of Ashkin and Wu,[15] as

$$\sigma = \tfrac{1}{4}\sigma_{\text{sing}} + \tfrac{3}{4}\sigma_{\text{trip}} = |S_0(\theta)|^2 + \sum_{m_s, m_s'} |S_{m_s' m_s}(\theta, \phi)|^2, \quad (1)$$

[11] R. Jastrow, Phys. Rev. **81**, 165 (1951).

[12] J. Schwinger, Phys. Rev. **69**, 681 (1946); L. Wolfenstein, Phys. Rev. **75**, 1664 (1949).

[13] We should like to thank R. E. Marshak for suggesting the use of polarization effects as a test of potential models which suggestion served as the initial motivation for the present investigation.

[14] H. Snyder and R. E. Marshak, Phys. Rev. **72**, 1253 (1947); see also reference 10.

[15] J. Ashkin and T. Y. Wu, Phys. Rev. **73**, 973 (1948).

where the singlet amplitude is given by

$$S_0(\theta)=(1/2ik)\sum_{\text{even } L'}[4\pi(2L'+1)]^{\frac{1}{2}}\times\{\exp(2i\delta_{L'})-1\}Y_{L'}{}^0(\theta), \quad (2)$$

and the triplet amplitude by

$$S_{m_s'm_s}(\theta,\phi)=(1/2ik)\sum_{\text{odd } L}\sum_{J=L-1}^{L+1}[4\pi(2L+1)]^{\frac{1}{2}}\times\{\exp(2i\delta_L{}^{Jm_s})-1\}(SLm_s-m_s'm_s'|SLJm_s)\times(SLJm_s|SL0m_s)Y_L{}^{m_s-m_s'}(\theta,\phi). \quad (3)$$

Here, $\delta_{L'}$ is the singlet phase shift corresponding to the partial wave of orbital angular momentum L', and $\delta_L{}^{Jm_s}$ is the triplet phase shift corresponding to the orbital angular momentum L and total angular momentum J with z-component m_s. The spherical harmonics $Y_L{}^{m_s}$ and the expansion coefficients $(SLm_s-m_s'm_s'|SLJm_s)$ are as defined in Condon and Shortley.[16] The magnitude of the momentum of each proton in the center-of-mass system is given by $\hbar k$.

It is clear from our introductory remarks that our essential problem is to obtain a more accurate estimate of the triplet scattering cross section than is given in Born approximation for the various potential models considered. In discussing methods of computation of triplet phase shifts, we shall for the sake of generality assume that the spin-orbit interaction includes a tensor force so that we have to deal with both coupled and uncoupled radial wave equations.

Three methods were adopted for the calculation of the triplet phase shifts. Generally speaking, phase shifts corresponding to small values of angular momentum were calculated by variational and/or exact procedures. The remaining phase shifts were always included in the scattering amplitude in Born approximation. The computation of phase shifts in Born approximation for spin-orbit forces is well known and will not be discussed here.[10,15]

The variational treatment of coupled and uncoupled states was carried out using the procedure of Schwinger.[17] It will be recalled that the scattering is considered in the parity representation which is designated by the quantum numbers $(-)^L$, S, J, m, where, for a given value of J, there are two modes or scattering eigenstates corresponding to the coupling of the $L=J-1$ and $L=J+1$ states, and one mode corresponding to $L=J$. In the p-p system, the situation is somewhat simplified in that, for even values of J, one can have only $L=J\pm1$, and for odd values of J, only $L=J$. The variational treatment of the uncoupled states is comparatively straightforward and will not be discussed further except to note that the trial functions used were $\bar{v}_L=krj_L(kr)$, where $j_L(kr)=(\pi/2kr)^{\frac{1}{2}}J_{L+\frac{1}{2}}(kr)$.

[16] E. U. Condon and G. H. Shortley, *Theory of Atomic Spectra* (The Macmillan Company, New York, 1935), p. 76.

[17] F. Rohrlich and J. Eisenstein, Phys. Rev. **75**, 705 (1949).

The coupled modes are characterized by the wave functions $(u_J{}^\alpha F_{J-1}{}^{Jm}+w_J{}^\alpha F_{J+1}{}^{Jm})/r$ and $(u_J{}^\gamma F_{J-1}{}^{Jm}+w_J{}^\gamma F_{J+1}{}^{Jm})/r$, where α and γ label the two modes and where the $F_L{}^{Jm}$ are the normalized spin spherical harmonics.[15] The essential property of the scattering eigenstates is that, asymptotically, for each mode, u_J and w_J involve the same real phase shift. A variational expression can be obtained for $k\cot\delta_J$ in terms of the functions u_J and w_J for which appropriate trial functions can then be chosen, say, $\bar{u}_J$ and $\xi_J\bar{w}_J$. Two values of ξ_J, *viz.*, $\xi_J{}^\alpha$ and $\xi_J{}^\gamma$, are then determined by requiring $k\cot\delta_J$ to be stationary with respect to variations in ξ_J, leading finally to the two phase shifts $\delta_J{}^\alpha$ and $\delta_J{}^\gamma$. In our calculations, $\bar{u}_J$ and $\bar{w}_J$ were chosen to correspond to Born approximation functions, i.e., $\bar{u}_J=krj_{J-1}(kr)$ and $\bar{w}_J=krj_{J+1}(kr)$.

The scattering, for each mode, is determined not only by the phase shift but also by the constant asymptotic ratio of $-w_J/u_J$ which we call the amount of admixture η_J. An integral expression for η_J can be obtained in terms of the functions u_J and w_J which one can again replace with the trial function $\bar{u}_J$ and $\xi_J\bar{w}_J$. The two amounts of admixture $\eta_J{}^\alpha$ and $\eta_J{}^\gamma$ are not independent but satisfy

$$1+\eta_J{}^\alpha\eta_J{}^\gamma=0. \quad (4)$$

It is to be noted that the scattering amplitude involves three independent parameters for a given even value of J, *viz.*, $\delta_J{}^\alpha$, $\delta_J{}^\gamma$ and $\eta_J{}^\alpha$. On the other hand, in the $LSJm$ representation, the phase shifts $\delta_{J\pm1}{}^{J0}$ and $\delta_{J\pm1}{}^{J1}$ are complex so that one apparently has eight parameters but only three are independent.[18] It is to be borne in mind that it is only the phase shifts $\delta_J{}^\alpha$ and $\delta_J{}^\gamma$ which are computed by a variational principle but not the amount of admixture $\eta_J{}^\alpha$.

The Born approximation in the parity representation is obtained from the variational formulation by assuming the potential to be a small perturbation, so that only leading terms in the potential are considered. We again use trial functions corresponding to plane wave solutions. It then follows that the amount of admixture is unaltered from its value assumed in the trial function, resulting in the equality $\eta_J=\xi_J$. This definition of the

TABLE I. Parameters for phenomenological p-p potential models.

	Potential model		
	Singular tensor force	Hard core	$\mathbf{L}\cdot\mathbf{S}$ force
Singlet potential	$-V_s$, $r<r_s$ 0, $r\geq r_s$	$-V_s e^{-(r-r_0)/r_s}$, $r\geq r_0$	$-V_s\frac{e^{-r/r_s}}{r/r_s}$
Triplet potential	$V_t S_{12}\frac{e^{-r/r_t}}{(r/r_t)^3}$	$V_t S_{12} e^{-r/r_t}$	$V_t\frac{\mathbf{L}\cdot\mathbf{S}}{(r/r_t)}\frac{d}{d(r/r_t)}\left(\frac{e^{-r/r_t}}{r/r_t}\right)$
	Parameters		
r_s in 10^{-13} cm	2.6	0.40	1.18
r_t in 10^{-13} cm	1.6	0.75	1.07
r_0 in 10^{-13} cm		0.60	
V_s in Mev	13.27	375	45.8
V_t in Mev	±18	−50.8	±29.8

[18] W. Rarita and J. Schwinger, Phys. Rev. **59**, 436 (1941).

TABLE II. Singlet phase shifts for the singular tensor-force model at 240 Mev.

L	δ_L (Born)	δ_L (exact)
0	0.232	0.261
2	0.232	0.237
4	0.032	0.035

TABLE III. Triplet phase shifts for the singular tensor-force model at 240 Mev.

		$r_c=0.84\hbar/Mc$ V_t in Mev				$r_c=1.40\hbar/Mc$ $V_t=18$ Mev		
Phase shifts	± 18 Born	-18 Variational	18 Variational	18 Exact	Born	Variational	Exact
δ_1^{10}	± 0.897	-0.521	1.119	2.570	0.884	1.067	1.8105
δ_1^{11}	∓ 0.449	0.559	-0.337	-0.3345	-0.442	-0.338	-0.3379
K_1^{10}	∓ 0.035	0.233	0.020	0.1268	-0.037	0.018	0.1108
ζ_1^{10}	0	-0.006	0.005	0.0223	0	0.005	0.0203
K_2^{10}	∓ 0.024	-0.033	-0.029	-0.0399	-0.024	-0.029	-0.0405
ζ_1^{10}	0	0.004	-0.004	-0.0139	0	-0.003	-0.0127
K_1^{21}	± 0.173	0.198	0.202	0.3386	0.172	0.200	0.3237
ζ_1^{21}	0	0.004	-0.004	-0.0139	0	-0.003	-0.0127
K_2^{21}	± 0.184	-0.068	0.153	0.1719	0.184	0.154	0.1725
ζ_1^{21}	0	-0.006	0.005	0.0223	0	0.005	0.0203
δ_1^{21}	∓ 0.074	0.077	-0.071		-0.074	-0.071	
η_1^{01}	-0.862	0.069	-0.627	-0.4093	-0.867	-0.634	-0.4324
δ_1^{01}	± 0.176	0.214	0.186	0.2994	0.177	0.185	0.2864
δ_1^{12}	∓ 0.029	-0.049	-0.013	-0.0007	-0.029	-0.013	-0.0032

Born approximation in the parity representation is equivalent to that in the $LSJm$ representation provided one consistently neglects terms in δ^2.

By an exact procedure, we mean a numerical integration of the differential equations. The solution of uncoupled equations was carried out using the particular method of Feinstein and Schwarzchild.[19] The extension to coupled equations was carried through as follows.

The differential equations take on the general form

$$\begin{aligned} u''(x)+f(x)u(x)+g(x)w(x)&=0,\\ w''(x)+h(x)w(x)+g(x)u(x)&=0, \end{aligned} \tag{5}$$

where $u(x)/x$ and $w(x)/x$ are the radial wave functions for $L=J-1$ and $L=J+1$, respectively. Now consider the Taylor series expansions about x of $u(x\pm\Delta)$. Then

$$u(x+\Delta)+u(x-\Delta)=2u(x)+\Delta^2u''(x)+(\Delta^4/12)u^{iv}(x)+\cdots. \tag{6}$$

Neglecting $(\Delta^4/12)u^{iv}(x)$ and denoting $x+n\Delta$ by x_n and $u(x_n)$ by u_n, we have

$$u_{n+1}=B_nu_n-u_{n-1}+C_nw_n, \tag{7}$$

where

$$B_n=2-\Delta^2f(x_n), \tag{8}$$

$$C_n=-\Delta^2g(x_n). \tag{9}$$

We find, similarly,

$$w_{n+1}=D_nw_n-w_{n-1}+C_nu_n, \tag{10}$$

where

$$D_n=2-\Delta^2h(x_n). \tag{11}$$

Clearly, if u_0, w_0 and u_1, w_1 are known, then u and w can be extended into the asymptotic region by simultaneous application of (7) and (10). The choice of Δ is governed by consideration of the error involved in neglecting the fourth and higher order derivatives. In practice, it is convenient to integrate the differential equations as far out from the origin as possible in terms of power series expansions and then to extend these by the numerical procedure.

We can generally find two independent sets of u and w which are regular at the origin.[20] If these solutions are u_a, w_a and u_b, w_b, a Wronskian condition holds,

$$u_au_b'-u_bu_a'+w_aw_b'-w_bw_a'=0, \tag{12}$$

which supplies a useful check on the numerical analysis. The phase shifts themselves are determined by forming the appropriate linear combinations which asymptotically represent the incident plus outgoing spherical waves.

III. UNPOLARIZED SCATTERING CROSS SECTIONS

(a) Singular Tensor-Force Model

Christian and Noyes[9] attempted a fit of both the 32-Mev and 345-Mev p-p data without seeking to maintain the charge-independence hypothesis. On the basis of the lower energy data, they chose for the singlet potential a square well since potentials of other conventional shapes yield too much small angle scattering. Since the singlet potential contributes only to forward scattering at the higher energy, most of the scattering must take place in triplet states. In consequence of the large momentum transfers which are required, i.e., large cross sections at large angles, they were ultimately led to choose a triplet potential which is singular at the origin and of the form $V_{\text{trip}}=V_tS_{12}e^{-x}/x^2$, where $x=r/r_t$ (see Table I for the values of the parameters). Good agreement is obtained with the 32-Mev data, and Born approximation estimates give a fairly flat cross section for angles greater than 30° at 345 Mev. It is to be noted that no choice of sign was made for V_t since the analysis at 32 Mev is still confined to exploring the tail of the potential. This holds even though one might have expected the Coulomb-nuclear interference to be sensitive to the choice of sign.

In actual fact, it is known that solutions to the scattering problem may not exist for potentials which have a $1/r^2$ singularity at the origin.[21] Considering, for the moment, the radial equations corresponding to the

[19] L. Feinstein and M. Schwarzchild, Rev. Sci. Instr. **12**, 405 (1941).

[20] If the potentials are so singular that no such solutions can be found, a cutoff can be applied at $x=x_c$ to the potentials, in which case the solutions for $x>x_c$ are obtained by equating values and derivatives at $x=x_c$ to those of the inside solutions.

[21] N. F. Mott and H. S. W. Massey, *The Theory of Atomic Collisions* (Oxford University Press, Oxford, 1949), second edition, p. 40.

uncoupled P_0 and P_1 states for either sign of V_t, we have

$$(u_1{}^{J\pm})''+(1-2/x^2-\lambda_J e^{-x/K}/x^2)u_1{}^{J\pm}=0, \quad J=0,1 \quad (13)$$

where $x=kr$, $K=kr_t$, $\lambda_0=\mp 4.444$, $\lambda_1=\pm 2.222$ for $V_t=\pm 18$ Mev. For small x, the solutions of this equation are given by $xj_\nu(x)$, where $\nu(\nu+1)=2+\lambda_J$. Since $xj_\nu(x)\sim x^{\nu+1}$ when $x\sim 0$, well-behaved solutions exist provided $\nu\geqslant 0$.[22] Thus, we must have

$$\nu=\tfrac{1}{2}[-1\pm(9+4\lambda_J)^{\frac{1}{2}}]\geqslant 0, \quad (14)$$

or $\lambda_J\geqslant -2$. Regardless of the sign of V_t, this relation cannot be satisfied for both $J=0$ and $J=1$. If $-2.5<\lambda_J<-2$, both radial wave functions $u(x)/x$ are unbounded at the origin; however, one is less singular than the other. If the potential is so attractive that $\lambda_J\leqslant -2.5$, the wave functions $u(x)/x$ behave as $x^{-\frac{1}{2}}\exp[\pm\frac{1}{2}i(|9+4\lambda_J|)^{\frac{1}{2}}\log x]$ near the origin, oscillate rapidly and their proper linear combination is unknown. Therefore, in order to insure the existence of well-behaved solutions for the $J=0$ and $J=1$ partial waves, we have introduced a zero cutoff in the triplet potential from the origin to distances $r_c\sim\hbar/Mc$. The introduction of such a cutoff would of course, at the same time, guarantee the existence of well-behaved solutions for coupled or uncoupled states corresponding to higher angular momenta; in actual fact, such solutions do exist in these states in the absence of a cutoff. It is clear that these considerations are independent of energy.

Table II lists the singlet phase shifts for the singular tensor-force model at 240 Mev. Since the shape of the singlet potential is that of a square well, exact analytical solutions are easily found, and comparison with Born approximation phase shifts illustrates the good agreement to be expected at high energies for well-behaved central potentials. The cross section due to singlet scattering alone is contained in Fig. 3 and is seen to be peaked in the forward direction and to fall off rapidly with increasing angle. The concentration in the forward direction is due to the constructive interference of the even Legendre polynomials at 0° and the destructive interference at 90° (the phase shifts are all of the same sign).

In virtue of the coupling of different angular momentum states, the triplet phase shifts for even J (with the exception of the degenerate case $J=0$) are all complex; in the parity representation, they are real. Phase shifts for odd J correspond to uncoupled states and are consequently always real. Table III incorporates the results of Born, variational and exact calculations of phase shifts for $J\leqslant 3$ at 240 Mev for two choices of cut-off radius, $r_c=0.84\hbar/Mc$ and $r_c=1.40\hbar/Mc$. In the case of the coupled phase shifts, we use the notation $\delta_L{}^{Jm_s}=K_L{}^{Jm_s}+i\zeta_L{}^{Jm_s}$. Also listed are the corresponding quantities $\delta_J{}^\alpha$, $\delta_J{}^\beta$ and $\eta_J{}^\alpha$ in the parity representation.[23]

[22] For a solution to be well-behaved, the radial wave function $u(x)/x$ must be finite when $x=0$.

[23] We adopt the convention that $\eta_J{}^\alpha$ is always less than one in absolute value.

The variational calculation for $r_c=0.84\hbar/Mc$ was performed for both signs of V_t. Comparison with the Born approximation shows that considerable changes occur for $V_t=-18$ Mev, and the resultant cross section as shown in Fig. 2 is very anisotropic.[24] A more reasonable cross section is obtained with $V_t=+18$ Mev, and this choice of sign was hence used in all further calculations and is implied throughout the following discussion.[25]

The uncoupled phase shift $\delta_1{}^{11}$ corresponds to a repulsive potential, and there is very good agreement between the variational and the exact values. On the other hand, $\delta_1{}^{00}$ corresponds to a strongly attractive

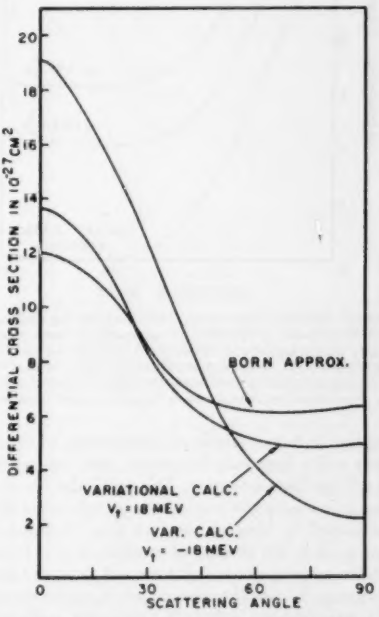

FIG. 2. Differential scattering cross sections for the singular tensor-force model at 240 Mev corresponding to Born approximation and variational treatments of the triplet scattering ($V_t=\pm 18$ Mev, $r_c=0.84\hbar/Mc$). In the latter case, phases with $J\leqslant 3$ were included in variational treatment, higher J phases in Born approximation. The singlet scattering cross section is exact.

[24] Throughout this paper, Born approximation cross sections always correspond to those obtained by replacing $\exp(2i\delta_B)-1$ in the scattering amplitude by $2i\delta_B$, where δ_B represents the Born approximation phase shift.

[25] The fact that there is moderate agreement between the Born approximation cross section and that obtained by the variational method for one sign of the potential, $V_t=+18$ Mev, but not for the other, is to be regarded as quite fortuitous in view of the large differences in the phase shifts as obtained by the two procedures. It is evident from Fig. 3 that more exact calculations for the case $V_t=+18$ Mev maintain the correspondence in cross section with that given in Born approximation, although the phase shifts differ considerably (see Table III). This conclusion has also been reached by Don R. Swanson [Phys. Rev. 87, 208 (1952)].

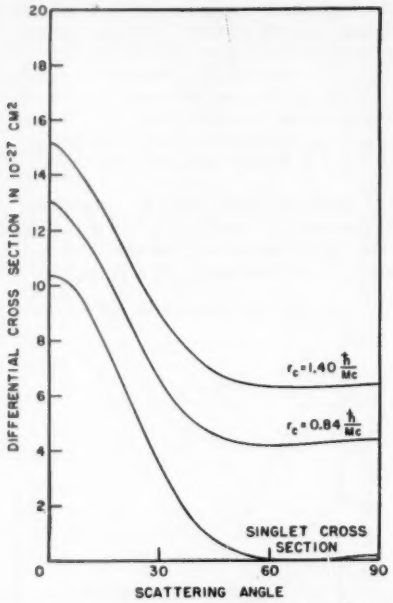

FIG. 3. Differential scattering cross sections for the singular tensor-force model at 240 Mev corresponding to exact treatment of triplet scattering for two values of cut-off radius ($V_t = 18$ Mev). Phases with $J \leqslant 2$ were calculated exactly, those with $J = 3$, 4, and 5 were included in variational treatment, higher J phases in Born approximation. Also shown is the exact singlet cross section.

potential, and the variational calculations, while giving results which approach the correct ones, are nevertheless still far from adequate. This particular phase shift depends in a sensitive way on the cut-off radius as is to be expected in view of the fact that no phase shift exists at all in the absence of a cutoff. It is to be noted that the coupled phase shifts are not very sensitive to the change in cut-off radius which is again reasonable since well-behaved solutions exist even without the cutoff.

For purposes of simplicity, it is best to compare the results for the coupled states in the parity representation (see Table III). Here, the inadequacy of the Born approximation trial functions is clearly indicated by the large changes in the amount of admixture $\eta_2{}^a$ as one proceeds from the Born approximation to the variational calculation, and then to the exact calculation. Note that a comparison of Born approximation with variational estimates for the phase shifts in the more complicated $LSJm$ representation can be misleading, although the agreement with the exact results is, in any case, inadequate.

The cross sections corresponding to the exact phase shifts for $J = 0$, 1, 2 and the two choices of cut-off radius, $0.84\hbar/Mc$ and $1.40\hbar/Mc$, are shown in Fig. 3. Phase shifts corresponding to $J = 3$, 4, 5 were computed by means of the variational method and found to be generally small ($\lesssim 0.05$). Higher angular momentum phase shifts were inserted into the scattering amplitude in Born approximation. The cross sections remain essentially flat at ~ 4.4 and 6.4 mb, respectively, between 45° and 90° and show a rapid rise at smaller angles. Thus, below 25°, the rise of singlet scattering to values greater than 5 mb renders impossible any satisfactory fit in this region. The experimental cross section at 90° corresponds to an intermediate value of r_c.

Calculations have also been made of the scattering cross sections at 450 Mev. Potential models become quite questionable at these energies; nonetheless, it is of interest to study the qualitative predictions of the present nonrelativistic theory in the absence of any better theory.

Table IV includes the 450-Mev phase shifts for $J \leqslant 3$ as obtained in Born approximation, by variational treatment and by exact calculation. At this energy, the Born approximation appears to be even more unreliable. The fact that the cut-off radius used for the Born and variational calculations was $1.02\hbar/Mc$ does not prevent a comparison of the results as obtained by the various methods except for the $\delta_1{}^{00}$ phase shift.

If we compare the results of the exact calculations as the energy is varied from 240 Mev to 450 Mev (see Tables III and IV), we see that $\delta_1{}^{00}$ is altered only slightly, while the other phase shifts show increases of roughly 40 percent. The cross sections as shown in Fig. 4 are similar in shape for both values of cut-off radius, the difference at 90° being 0.7 mb in contrast to 2 mb at 240 Mev. The rise at small angles is again a manifestation of the singlet scattering.

TABLE IV. Triplet phase shifts for the singular tensor-force model at 450 Mev ($V_t = 18$ Mev).

	r_c in $\hbar/Mc$			
Phase shifts	1.02 Born	1.02 Variational	0.84 Exact	1.40 Exact
$\delta_1{}^{00}$	1.093	1.160	2.4135	1.7085
$\delta_1{}^{11}$	−0.546	−0.409	−0.4406	−0.4373
$K_1{}^{20}$	−0.041	0.010	0.1992	0.1629
$\tilde{\epsilon}_1{}^{20}$	0	0.003	0.0364	0.0316
$K_2{}^{20}$	−0.009	−0.017	−0.0352	−0.0376
$\tilde{\epsilon}_2{}^{20}$	0	−0.002	−0.0216	−0.0190
$K_1{}^{21}$	0.210	0.201	0.4373	0.4065
$\tilde{\epsilon}_1{}^{21}$	0	−0.002	−0.0216	−0.0190
$K_2{}^{21}$	0.241	0.175	0.2030	0.2060
$\tilde{\epsilon}_2{}^{21}$	0	0.003	0.0364	0.0316
$\delta_2{}^{21}$	−0.113	−0.108		
$\eta_2{}^a$	−0.928	−0.711	−0.3599	−0.3987
$\delta_2{}^a$	0.223	0.191	0.3996	0.3615
$\delta_2{}^7$	−0.023	−0.007	0.0125	0.0074

(b) Hard-Core Model

An attempt to give a phenomenological description of p-p scattering within the framework of the charge-independence hypothesis has been made by Jastrow.[11] There is introduced in the singlet state an infinite potential barrier at small distances surrounded by an attractive exponential well. The presence of the repulsive core allows for agreement with the 32-Mev data even though an exponential well is used. At high energies, the main effect of the core is to change the sign of the S-phase shift with respect to the sign of the D, G, $\cdots$ phase shifts. The resultant S-D interference is such as to diminish the singlet scattering at small angles and to enhance it at 90° which is in sharp contrast to the singlet scattering observed for the singular tensor-force model. In triplet states, the hard-core model has an exponential-well tensor force (the parameters of the singlet and triplet potentials are included in Table I). In comparing the predictions of the hard-core model for scattering at high energies with experiment, the singlet cross section was evaluated exactly, while the triplet scattering was calculated in Born approximation only.[11] The latter is peaked at ~45° and combines with the singlet scattering to give reasonably flat cross sections.

In order to test the validity of the Born approximation for the case of a well-behaved spin-orbit potential, a calculation of the triplet scattering has been performed at 240 Mev using the variational procedure. The Born approximation phase shifts together with those obtained by use of the variational method are listed in Table V. It is evident that the plane-wave trial functions are in this case reliable, as is to be expected.

In Fig. 5, we compare the differential scattering cross section obtained in pure Born approximation with an improved cross section based on the variational estimates of the triplet phase shifts for $J \lesssim 3$ (higher angular momentum states, as always, being included in Born approximation). For the singlet scattering, we have used the exact cross section as abstracted from Jastrow's published curve at 250 Mev, the variation in cross section over the energy interval 240–250 Mev being considered inconsequential. Unlike the case of the singular tensor-force model, the corrections introduced by the variational treatment are quite small ($\lesssim$0.3 mb for $\theta > 30°$).[26] In view of the nonrelativistic nature of the calculations and of the present experimental discrepancy as to the magnitude of the cross section, the quantitative agreement is encouraging.

TABLE V. Triplet phase shifts for hard-core model at 240 Mev.

Phase shifts	Born	Variational
δ_1^{30}	−0.555	−0.546
δ_1^{11}	0.277	0.282
K_1^{30}	0.047	0.042
ζ_1^{30}	0	−0.005
K_2^{30}	0.004	−0.009
ζ_2^{30}	0	0.003
K_1^{31}	−0.124	−0.115
ζ_1^{31}	0	0.003
K_2^{31}	−0.166	−0.166
ζ_2^{31}	0	−0.005
δ_2^{31}	0.080	0.082
η_2^{α}	0.952	0.877
δ_2^{α}	0.024	0.016
δ_2^{γ}	−0.143	−0.137

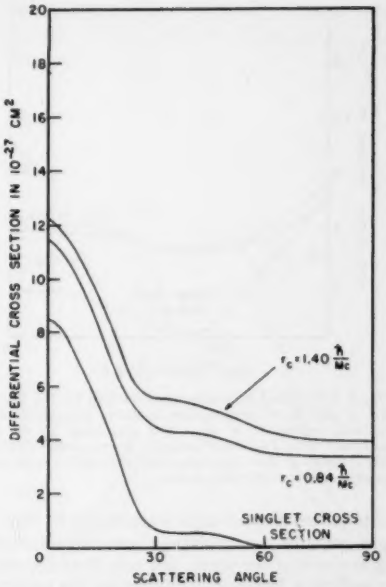

FIG. 4. Differential scattering cross sections for the singular tensor-force model at 450 Mev corresponding to exact treatment of triplet scattering for two values of cut-off radius ($V_t = 18$ Mev). Phases with $J \leq 2$ were calculated exactly, those with $J = 3$, 4, and 5 were included in variational treatment, higher J phases in Born approximation. Also shown is the exact singlet cross section.

(c) L·S Force Model

Case and Pais[10] incorporate in their model the other type of spin-orbit force which can act between two protons, *viz.*, the **L·S** force. They also try to retain the charge-independence hypothesis. The model, as proposed, can only be considered qualitatively since no attempt was made to fit the low energy data with any degree of precision. For example, the singlet potential was chosen to be of Yukawa shape; actually, this would

[26] In the text, we have confined ourselves to one sign of the odd-parity force, *viz.*, $V_t = -50.8$ Mev. For the other choice of sign, $V_t = 50.8$ Mev, the deviations of the results of the variational calculations from those of the Born approximation are somewhat larger ($\gtrsim$0.7 mb). The resultant differential cross section is smaller than that in Born approximation except at small angles.

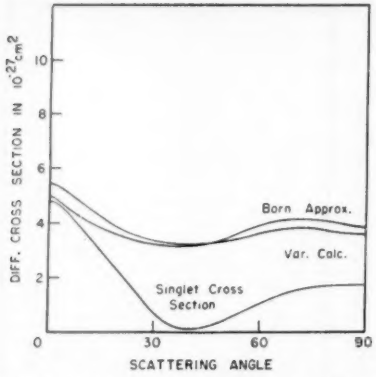

FIG. 5. Differential scattering cross sections for the hard-core model at 240 Mev corresponding to Born approximation and variational treatments of the triplet scattering. In the latter case, phases with $J \leqslant 3$ were included in variational treatment, higher J phases in Born approximation. Also shown is the singlet scattering cross section which is exact.

lead to too much small-angle scattering at 32 Mev. The triplet potential is very singular, varying as $1/r^3$ in the neighborhood of the origin, and only Born approximation estimates were used to determine the parameters of the model. The extreme singularity cannot, of course, be taken literally[27] and, in making more exact calculations, we have accordingly introduced a zero cutoff at $r_c = \hbar/Mc$.

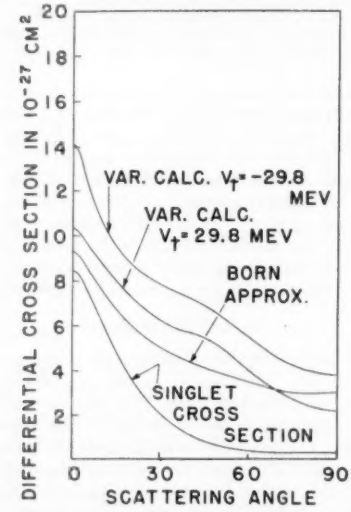

FIG. 6. Differential scattering cross sections for the L·S force model at 240 Mev corresponding to Born approximation and variational treatments of the triplet scattering ($V_t = \pm 29.8$ Mev, $r_c = \hbar/Mc$). In the latter case, phases with $L \leqslant 3$ were included in variational treatment, higher L phases in Born approximation. Also shown is the singlet scattering cross section calculated in Born approximation.

In the $LSJm$ representation, the operator $\mathbf{L}\cdot\mathbf{S}$ has definite eigenvalues, so that states corresponding to different values of L are unmixed in the presence of the interaction. Hence, the phase shifts are all real.

Table VI shows the results of variational calculations of the triplet phase shifts for both signs of V_t[28] (the actual parameters employed with the model are listed in Table I). We note that the P-phase shifts change rather considerably in going from the Born approximation to the variational estimates. In view of the singular nature of the potential, one can expect further large changes in performing an exact calculation. For example, for $V_t = 29.8$ Mev an exact calculation of the P_2-phase shift was performed giving $\delta_1^2 = 0.539$. Although the results of the variational calculation cannot be taken too seriously, the large deviations from the Born approximation are significant.

The corresponding cross sections which are plotted in Fig. 6 illustrate the complete inadequacy of the Born approximation for this type of potential. In fact, the qualitative fit with experiment obtained in Born approximation is almost wholly destroyed by the variational calculations. Inasmuch as the parameters of the present model were originally based on a Born approximation analysis, there appeared to be no point in carrying out more exact calculations.

TABLE VI. Triplet phase shifts for L·S force model at 240 Mev.

Phase shifts	V_t in Mev ±29.8 Born	29.8 Variational	−29.8 Variational
δ_1^0	∓0.524	−0.301	1.039
δ_1^1	∓0.262	−0.193	0.381
δ_1^2	±0.262	0.381	−0.193
δ_2^2	∓0.080	−0.074	0.088
δ_2^3	∓0.020	−0.020	0.020
δ_2^4	±0.060	0.064	−0.056

IV. POLARIZATION EFFECTS

Consider the scattering, in their center-of-mass system, of unpolarized protons by unpolarized protons. In the presence of spin-orbit forces, it can be shown that the outgoing particles will be polarized in a direction normal to the plane of scattering.[29] Thus, if we consider that the incoming particles move in the z-direction, then, particles scattered through an angle θ_1, ϕ_1 will generally have a nonzero expectation value

[27] This was clearly recognized by Case and Pais who note that their Born approximation results are only qualitative (see reference 10).

[28] If we put aside the question of charge independence and do not consider the n-p interaction, then the analysis of Case and Pais does not uniquely fix the sign of the triplet p-p force.

[29] L. Wolfenstein, Phys. Rev. **75**, 1664 (1949); **76**, 541 (1949); **82**, 308 (1951).

for the y-component of the spin which is given by

$$\delta_y(k_1, \theta_1, \phi_1) = \frac{1}{(2)^{\frac{1}{2}}} \frac{\mathrm{Im} \sum_{m_s} S_{0m_s}(S_{1m_s}^* - S_{-1m_s}^*)}{|S_0|^2 + \sum_{m_s, m_s'} |S_{m_s' m_s}|^2}, \quad (15)$$

where k_1, the momentum of either particle, and δ_y are in units of $\hbar$. For convenience, we consider particles scattered through θ_1, $\phi_1 = 0°$, since δ_y will then represent the only nonvanishing component of the polarization. If the polarized particles are now scattered again by an unpolarized proton target, then a consideration of the scattering in their center-of-mass system shows that the intensity of outgoing particles will have an azimuthal asymmetry given by

$$I = I_0(k_1, k_2, \theta_1, \theta_2)[1 + 2\delta_y(k_1, \theta_1, \phi_1 = 0°) \times P(k_2, \theta_2, \phi_2)], \quad (16)$$

where the y_2-axis is parallel to the y_1-axis of the first scattering and the z_2-axis is in the direction of incidence of the polarized beam. I_0 represents the unpolarized intensity. According to Wolfenstein and Ashkin[30] and Dalitz,[31]

$$P(k, \theta, \phi) = 2\delta_y(k, \theta, \phi), \quad (17)$$

so that

$$I = I_0(k_1, k_2, \theta_1, \theta_2)[1 + P(k_1, \theta_1, \phi_1 = 0°) \times P(k_2, \theta_2, \phi_2)]. \quad (18)$$

This last expression can be further simplified if one neglects the degradation of energy of the proton in the first scattering. This approximation is a reasonable one for the cases of interest to us since the largest polarization effects occur in the neighborhood of 45° in the center-of-mass system (on general grounds,[29] $P \sim \sin\theta \cos\theta \cos\phi \sum_n a_n \cos^{2n}\theta$), and, corresponding to this angle of scattering, a particle initially having a kinetic energy of 240 Mev in the laboratory system will come off with 205 Mev.

Hence, assuming $\theta_1 = \theta_2 = \theta$, and $k_1 = k_2 = k$, Eq. (18) becomes

$$I = I_0(k, \theta)[1 + \delta(k, \theta) \cos\phi], \quad (19)$$

where

$$\delta(k, \theta) = [P(k, \theta, \phi)]_{\phi = 0°}^2. \quad (20)$$

Perhaps the more interesting quantity from an experimental point of view is 2δ, which we shall refer to as the asymmetry in a double-scattering experiment:

$$2\delta = \frac{I(\phi = 0°) - I(\phi = 180°)}{I(\phi = 90°)}. \quad (21)$$

It is a straightforward matter to use the variational and/or exact triplet phase shifts computed in Sec. III in conjunction with the above formulas to evaluate the polarization effects in a double p-p scattering for each of the potential models which we have considered. The results are shown in Figs. 7–9. As expected, the maximum in 2δ tends to occur at $\theta \sim 45°$. In the case of the singular tensor-force model, $2\delta_{\max}$ is 0.18 and 0.28 for the energies 240 and 450 Mev, respectively, if we choose the cut-off radius $r_c = 0.84\hbar/Mc$; the polarization effects

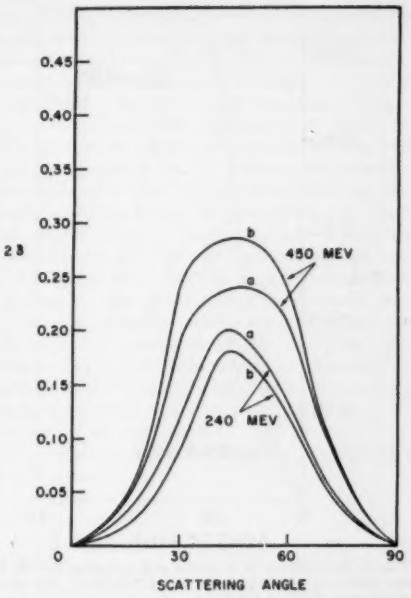

FIG. 7. Asymmetries in a double p-p scattering for singular tensor-force model at 240 and 450 Mev for (a) $r_c = 1.40\hbar/Mc$, (b) $r_c = 0.84\hbar/Mc$. The phases correspond to those used in Figs. 3 and 4.

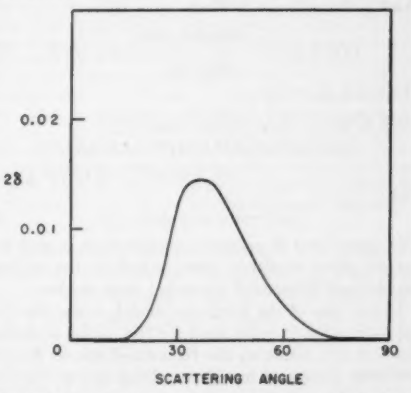

FIG. 8. Asymmetry in a double p-p scattering for the hard-core model at 240 Mev. The phases correspond to those used in Fig. 5.

[30] L. Wolfenstein and J. Ashkin, Phys. Rev. **85**, 947 (1952).
[31] R. H. Dalitz, Proc. Phys. Soc. (London) **A65**, 175 (1952).

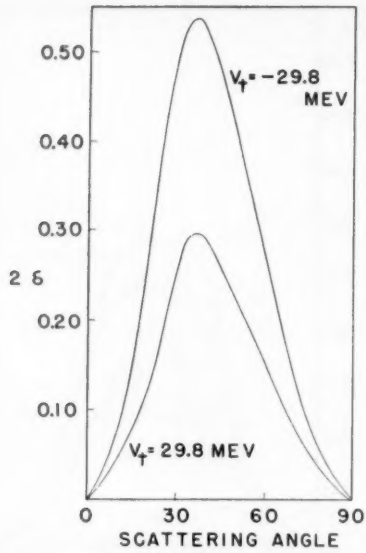

FIG. 9. Asymmetries in a double p-p scattering for the $\mathbf{L}\cdot\mathbf{S}$ force model at 240 Mev with $V_t=\pm 29.8$ Mev. The phases correspond to those used in Fig. 6.

are not very different for the larger cut-off radius $r_c=1.40\hbar/Mc$. The $\mathbf{L}\cdot\mathbf{S}$ force model also yields large asymmetries, *viz.*, $2\delta_{\max}\sim 0.3$ and 0.5 for $V_t=29.8$ Mev and -29.8 Mev, respectively. The hard-core model, on the other hand, predicts rather small asymmetries with $2\delta_{\max}\sim 0.015$.[32]

One can understand these results qualitatively by expressing $P(k,\theta,\phi)$ in terms of the phase shifts. For simplicity, let us consider only the real parts of the phase shifts with $J<3$. Then

$$P(k,\theta,\phi)=\frac{2\sin\theta\cos\theta\cos\phi}{k^3\sigma(k,\theta)}(\alpha+\beta\cos^2\theta), \quad (22)$$

where α is given by

$$\alpha=3[\delta_3{}^{21}\delta_1{}^{00}]-3[\delta_1{}^{21}\delta_1{}^{00}]+4.5[\delta_1{}^{11}\delta_1{}^{20}]+4.5[\delta_3{}^{20}\delta_1{}^{11}]+9[\delta_1{}^{21}\delta_3{}^{20}]-1.5[\delta_3{}^{21}\delta_3{}^{20}]-1.5[\delta_1{}^{21}\delta_1{}^{20}]-6[\delta_3{}^{21}\delta_1{}^{20}], \quad (23)$$

with

$$[xy]=\sin x\sin y\sin(x-y). \quad (24)$$

The quantity β is generally smaller than α and need not be given explicitly here; $\sigma(k,\theta)$ is the ordinary unpolarized differential scattering cross section.

In the case of the hard-core model, where the Born approximation is quite good for the triplet scattering, the first two terms on the right-hand side of Eq. (23) are large compared to the remaining terms. Since $\delta_1{}^{00}$ is a comparatively large phase shift, the quantity

$$3[\delta_3{}^{21}\delta_1{}^{00}]-3[\delta_1{}^{21}\delta_1{}^{00}]$$

depends in an important way on the difference between $\delta_1{}^{21}$ and $\delta_3{}^{21}$ which are of the same order of magnitude and of the same sign. Thus, the polarization effects tend to be small.[33] For this particular model, tensor scattering is predominant only in the neighborhood of 45°. The singlet scattering gives no polarization so that the asymmetry falls off very rapidly with angle on either side of the maximum.[34]

In the case of the singular tensor-force model, the Born approximation phase shifts are unreliable. If one uses the exact values for $\delta_1{}^{00}$ and $\delta_1{}^{11}$, and the $J=2$ phase shifts obtained by the variational treatment (which do not differ greatly from Born approximation phase shifts), the asymmetry is, indeed, small. Thus, at 240 Mev, $2\delta_{\max}$ is calculated to be ~ 0.02 for $r_c=0.84\hbar/Mc$. On performing an exact calculation, however, the coupled P-phase shifts are changed considerably. This enhances the difference between $\delta_1{}^{21}$ and $\delta_3{}^{21}$ and, in addition, increases the importance of terms in Eq. (23) involving $\delta_1{}^{20}$. The result is an increase in the asymmetry for a double p-p scattering by a factor of 10.[35]

The largest polarizations of all are predicted by the $\mathbf{L}\cdot\mathbf{S}$ force model. In this case, the main contribution to α comes from

$$3[\delta_3{}^2\delta_1{}^0]-3[\delta_1{}^2\delta_1{}^0]+4.5[\delta_1{}^1\delta_1{}^2].$$

We note first that $\delta_1{}^1$ and $\delta_3{}^2$ are now of opposite sign, since, for $J=2$, the eigenvalues of $\mathbf{L}\cdot\mathbf{S}$ are 1 and -4 for $L=1$ and 3, respectively. Furthermore, the P-phases are large in comparison with the higher angular momentum phase shifts. The net result is that one obtains very large asymmetries. However, it must be borne in mind that these calculations are not exact and that, in any case, the agreement with experiment of the unpolarized cross sections is poor, so that these results should not be taken too seriously.

V. CONCLUSIONS

It appears clear that the use of the Born approximation to provide estimates of scattering for singular potentials is unjustified, even at high energies. Thus we have found that the result of more exact calculations, when performed for the three potentials which

[32] We should like to remark that $P(k,\theta,\phi=0°)$ turns out to be always positive for all the potentials considered for $0<\theta<\pi/2$ except for the case of the $\mathbf{L}\cdot\mathbf{S}$ force model with $V_t=-29.8$ Mev.

[33] This is not unexpected since the Born approximation is reliable in this case for the triplet phase shifts and it is known that polarization effects vanish identically in Born approximation. (See reference 29.)

[34] For the other choice of sign of the odd-parity force, $V_t=50.8$ Mev (see reference 26), the asymmetry in a double scattering is of the order of several tenths of a percent. For this case, $P(k,\theta,\phi=0°)<0$ for $\theta\sim 45°$.

[35] We should like to emphasize that the results for the singular tensor-force model previously reported [L. J. B. Goldfarb and D. Feldman, Phys. Rev. **87**, 208 (1952)] were based on variational calculations of the $J=2$ phase shifts and accordingly the polarization effect was considerably underestimated. We are indebted to Don R. Swanson for pointing out to us that large polarization effects actually do obtain with this particular model.

have been proposed to describe the p-p interaction, has been to modify strongly the previous predictions for those potentials which are singular. Indeed, the use of Born approximation trial functions in the variational procedure is, in itself, inadequate for these cases.

The singular tensor-force model of Christian and Noyes, which was treated exactly, now presents only moderate agreement with experiment for the choice of sign $V_t = +18$ Mev, but only for angles greater than 45°. The predominance of singlet scattering at lower angles introduces too much anisotropy, so that deviations from experiment become considerable. The large corrections, introduced by the variational treatment of the $\mathbf{L}\cdot\mathbf{S}$ force model of Case and Pais, lead to an even less encouraging picture. While it is conceivable that more exact calculations would remove the large anisotropies, there is no *a priori* reason to expect this. On the other hand, the predictions of Jastrow's hard-core model are essentially unchanged on performing a variational calculation for the triplet scattering (which is reliable for this case). The cross section is reasonably flat, although its magnitude is somewhat low.

It must be emphasized that the preceding remarks in regard to the singular potentials are based on calculations performed with a zero cutoff at distances of the order of the nucleon Compton wavelength. It is always possible that a better fit with experiment might be obtained with a different choice of cutoff. In any case, the exact nature of the cutoff must be taken seriously.

The asymmetry in a double p-p scattering experiment was calculated in order to provide an additional means for distinguishing among the potential models. On this basis, the hard-core model which is found to yield small asymmetries is quite different from the singular tensor-force potential which predicts large asymmetries. The $\mathbf{L}\cdot\mathbf{S}$ potential also predicts large asymmetries, but it must be emphasized that this model, particularly, gives a poor fit with experiment. Finally, we should like to reiterate that the foregoing analysis is completely nonrelativistic, and it is quite possible that polarization effects, in particular, would be modified in a more consistent relativistic theory.

We should like to thank Professor R. E. Marshak for useful discussions.

PHYSICAL REVIEW VOLUME 88, NUMBER 5 DECEMBER 1, 1952

An Analysis of the Energy Levels of the Mirror Nuclei, C^{13} and N^{13}

R. G. THOMAS*
Kellogg Radiation Laboratory, California Institue of Technology, Pasadena, California

(Received February 19, 1951)
(Revised manuscript received August 15, 1952)

An analysis employing the recent nuclear reaction theories of Wigner and others is given of the experimental data on the low energy interactions of s, p, d orbital neutrons and protons with C^{12} and s neutrons and protons with O^{16}. Assuming the equality of nn and pp nuclear interactions, it is possible to account for the data on the s interactions if the level spacing is considered in addition to the customary two resonance parameters: reduced width and level position; in particular, the displacement of conjugate levels can be attributed to the difference of the external wave functions for the odd particle, although with an uncertainty of about 25 percent which is due primarily to the lack of precise knowledge of the internal Coulomb energy of the excited states. The large magnitudes of the reduced width and level spacing indicate that two-body potential interactions exist between the odd particle and the C^{13} and O^{16} cores, and the values of the respective logarithmic derivatives indicate that these interactions are of about equal strengths. The energy dependence of the radiative capture cross section of s neutrons and protons with C^{12} can be understood if an additional quantity, the final-state reduced width, is included in the theory to take into account the energy-dependent external contribution to the transition moment. The experimental data are only sufficient to treat the p and d interactions in the one-level approximation; a reasonable explanation can be given of the observed displacements of conjugate levels in terms of the differences of the electromagnetic properties of the odd particle such as: external wave functions, spin-orbit interactions, and variations of the internal Coulomb energy. There is some indication from the data on radiative transitions that the independent-particle model also prevails in the p states; on the other hand, the small reduced widths of these states suggest a many-body description. Derivations based on the recent theories are given of the one-channel formulas and of the general one-level formulas which include the negative-energy alternatives. The radial dependences of the resonance parameters are discussed.

I. INTRODUCTION

SINCE there is considerable experimental material on the low levels of the mirror nuclei, N^{13} and C^{13}, it seems worth while to attempt a detailed investigation of such matters as the extent of the validity of the independent-particle model, the assumption of equality of nn and pp nuclear forces, and the applicability of the recent theories of nuclear reactions. The analysis is carried out by means of the theories due to Wigner and others,[1-9] and we are therefore concerned with the de-

* Now at Los Alamos Scientific Laboratory, Los Alamos, New Mexico.

[1] E. P. Wigner, Phys. Rev. **70**, 15 (1946).
[2] E. P. Wigner, Proc. Am. Phil. Soc. **90**, 27 (1946).
[3] E. P. Wigner, Phys. Rev. **70**, 606 (1946).
[4] Feshbach, Peaslee, and Weisskopf, Phys. Rev. **71**, 145 (1947), referred to as FPW.
[5] E. P. Wigner and L. Eisenbud, Phys. Rev. **72**, 29 (1947), referred to as W-E.
[6] E. P. Wigner, Phys. Rev. **73**, 1002 (1948).

termination from the data of the characteristic quantities: partial reduced level widths, unshifted level positions, displacements of corresponding levels, and level spacings; we are also concerned with radiative transition moments. The displacement of corresponding s states[10] has already been investigated by Ehrman;[11] the present treatment offers several new aspects to this problem. Section II presents the terminology and derivations of the formulas used for the interpretations of the data given in Secs. III and IV. The derivations include the negative-energy alternatives which enter in the consideration of level displacements. A formula is given for the electric dipole radiative capture which includes an energy-dependent contribution from the external moment in addition to the resonance contribution from the internal moment, the former being important for the treatment of transitions between levels with large reduced widths. Some relations between the quantities of the nuclear reaction theory in the one-channel approximation and the effective range theory are discussed as the latter theory is appropriate for the analysis of the scattering of low energy neutrons by C^{12}.

The available experimental data are surveyed in the introduction to Sec. III, and the subsequent analysis is given in three parts covering the interaction of s, p, d neutrons and protons with C^{12}. The s interaction data are rather extensive and permit some consideration of the level spacing in addition to the two resonance parameters (of the one-level approximation): reduced width and level position; the treatment of the p and d interactions, however, is limited to the one-level approximation. A comparison of the low energy interactions of s neutrons and protons with C^{12} and O^{16} is made in Sec. IV.

II. THEORY

A. Terminology

The terminology of Wigner and Eisenbud[5,6] is used to describe the nuclear configuration space. The external region of this space is subdivided into channels which comprise alternative pairs c of two bodies with an energy of relative motion ϵ_c, which may be positive or negative, relative angular momentum $l\hbar$, and reduced mass M_c; the members of the pair are separated by distances r_c which are greater than or equal to the channel radii a_c. We attempt to choose the a_c greater than the range of nuclear forces between the bodies in order that the external wave functions reflect the solutions of the wave equation containing only the Coulomb interaction. It is desirable, on the other hand, to choose the a_c as small as possible, consistent with the above requirement, so that the characteristic quantities of the resonance theory which are determined from the data will contain primarily information concerning the nuclear interactions. A common prescription for the channel radii (which we shall follow) is $a_c=(e^2/2mc^2)\times(A_{1c}^{\frac{1}{3}}+A_{2c}^{\frac{1}{3}})$, A_{1c} and A_{2c} being the mass numbers of the bodies of the pair. The letter c is used to describe all of the features of the channel, unless it is necessary to distinguish the positive-energy ($\epsilon_{c+}>0$) from the negative-energy ($\epsilon_{c-}<0$) channels in which case the symbols $c+$ and $c-$ will be used, respectively.

The rest of the nuclear configuration space is the internal region τ which includes not only that part wherein all particles are close together but also that part representing pairs c with separation $r_c<a_c$ and the total subspace with three or more bodies in relative motion. The hypersurface which separates the internal from the external region is denoted by S. In order to keep the number of characteristic quantities of the theory to a minimum, one can usually ignore the $c-$ channels by allowing their radii to be infinite in which case they become a part of the internal region. However, in the treatment of level displacements and, as emphasized by Wigner,[6] in the consideration of the behavior of cross sections near threshold, it is necessary to include the near-threshold channels in the external region.

If the channel radii are large enough, the external wave function can be factored as

$$P_l(\Omega_c)\psi_c\mathfrak{F}_{cl}(r_c)r_c^{-1}, \tag{1}$$

where $\mathfrak{F}_{cl}(r_c)r_c^{-1}$ and $P_l(\Omega_c)$ describe the relative radial and angular distributions, and ψ_c is the product of the wave functions for the internal distributions of the pair. We will simplify the equations by absorbing the factors $P_l(\Omega_c)$ and r_c^{-1} into ψ_c; the subscript c will then also be used to characterize the l and will be omitted from all but one of the symbols in an equation, provided there is no ambiguity.[12] It is assumed that on S

$$\int_S \psi_c\psi_{c'}dS=\delta_{cc'}. \tag{2}$$

B. External Wave Functions

The radial factor in (1) satisfies the wave equation

$$\mathfrak{F}_c''+(2M_c/\hbar^2)(\epsilon_c-\mathcal{V}_c)\mathfrak{F}_c=0, \tag{3a}$$

(where a prime signifies differentiation with respect to r) with the interaction

$$\mathcal{V}_c=Z_{1c}Z_{2c}e^2r_c^{-1}+(\hbar^2/2M_c)l(l+1)r_c^{-2}. \tag{3b}$$

In the notation of Yost, Wheeler, and Breit,[13] the posi-

[7] T. Teichmann, dissertation, Princeton University (1949), (unpublished).
[8] T. Teichmann, Phys. Rev. **77**, 506 (1950).
[9] T. Teichmann and E. P. Wigner, Phys. Rev. **87**, 123 (1952).
[10] The letters s, p, d are used throughout to denote the relative orbital angular momentum of the channel (C^{12} or O^{16}+proton or neutron) which is a good quantum number since C^{12} has zero spin; the $\frac{1}{2}$-integer subscript denotes the total nuclear spin. It is not intended that this notation imply that configuration is a good quantum number in the internal region.
[11] J. B. Ehrman, Phys. Rev. **81**, 412 (1951).
[12] The letter s (c in this paper) is used by W-E to characterize the channel spin. For the present problem this is not necessary since the channel spin is always $\frac{1}{2}$.
[13] Yost, Wheeler, and Breit, Phys. Rev. **49**, 174 (1936).

tive-energy solution which is regular at the origin is designated by $F(kr)$ and has the asymptotic form for large r,

$$F_{c+}\sim\sin(x-\tfrac{1}{2}l\pi-\eta\log 2x+\sigma), \tag{4a}$$

and a solution which is linearly independent of F and irregular at the origin is conveniently taken with the asymptotic form for large r,

$$G_{c+}\sim\cos(x-\tfrac{1}{2}l\pi-\eta\log 2x+\sigma); \tag{4b}$$

the quantities entering (4) are

$$x_{c\pm}=kr;\quad k_{c\pm}=(2M|\epsilon|/\hbar^2)^{\frac{1}{2}};$$
$$\eta_{c\pm}=MZ_1Z_2e^2/\hbar^2k;\quad \sigma_{c+}=\arg\Gamma(1+l+i\eta).$$

The general solution $\mathfrak{F}(r)$ will be a linear combination of F and G. The Wronskian relation for these two particular solutions, which directly follows from (3) and (4), is

$$F'G-G'F=k_{c+}. \tag{5}$$

Extensive tables have been prepared by Breit and his collaborators[14] for obtaining F and G and their derivatives when $\eta>0$; they are used here. If there is no Coulomb interaction, F and G are related to the Bessel functions

$$F_{c+}=(\pi x/2)^{\frac{1}{2}}J_{l+\frac{1}{2}}(x),$$
$$G_{c+}=(-1)^l(\pi x/2)^{\frac{1}{2}}J_{-l-\frac{1}{2}}(x). \tag{6}$$

For the $c-$ channels only the solution to (3) vanishing at large distances from the origin can occur; it is the Whittaker function[15]

$$W_{-\eta,\,l+\frac{1}{2}}(2x_{c-})$$
$$=\frac{\exp(-x-\eta\log 2x)}{\Gamma(1+l+\eta)}\int_0^\infty t^{l+\eta}e^{-t}\left(1+\frac{t}{2x}\right)^{l-\eta}dt. \tag{7}$$

When $\eta>0$, this form is convenient for obtaining the radial dependence of W; for obtaining its logarithmic derivative to the required accuracy, it was expedient to use the power series expansion,[15] which is too lengthy to be given here. If there is no Coulomb interaction in a $c-$ channel, we have from (7) for s, p, d orbitals

$$W_{0,\frac{1}{2}}(2x)=\exp(-x), \tag{8s}$$
$$W_{0,\frac{3}{2}}(2x)=(1+x^{-1})\exp(-x), \tag{8p}$$
$$W_{0,\frac{5}{2}}(2x)=(1+3x^{-1}+3x^{-2})\exp(-x). \tag{8d}$$

Another convenient set of linearly independent solutions to (3) consists of a unit-flux emerging wave E_{c+} and a unit-flux incident wave $E_{c+}{}^*$; in terms of F and G, they are

$$E_{c+}=(M/k\hbar)^{\frac{1}{2}}(G+iF)\exp i(\tfrac{1}{2}l\pi-\sigma), \tag{9a}$$

and

$$E_{c+}{}^*=\text{complex conjugate } E_{c+}.$$

We also put

$$E_{c-}=(M/k\hbar)^{\frac{1}{2}}W_{-\eta,\,l+\frac{1}{2}}(2x). \tag{9b}$$

According to (5), (9) the flux equation is

$$(\hbar/2iM_{c+})(E^*E'-EE'^*)=1, \tag{10}$$

and it is, of course, zero for the $c-$ channels.

In discussing conditions at the nuclear surface, we shall need to evaluate the real and imaginary parts of the logarithmic derivatives, $g_c=E'/E$. From (5) and (9), these are

$$g_{c+}{}^{\mathrm{Re}}=(FF'+GG')(F^2+G^2)^{-1},$$
$$g_{c+}{}^{\mathrm{Im}}=k(F^2+G^2)^{-1}=M/\hbar|E|^2, \tag{11}$$
$$g_{c-}{}^{\mathrm{Re}}=W'W^{-1},\quad g_{c-}{}^{\mathrm{Im}}=0,$$

where

$$g_c=g^{\mathrm{Re}}+ig^{\mathrm{Im}},\quad r_c=a_c.$$

As there are no tables of $W_{-\eta,\,l+\frac{1}{2}}$ and as it is difficult to evaluate $g_{c-}{}^{\mathrm{Re}}$ from the power series expansion for W, the WKB approximation was investigated, *viz.*,

$$ag_{c-}=-\xi+\tfrac{1}{2}[\eta x+l(l+1)]\xi^{-2}, \tag{12}$$

where

$$\xi=[l(l+1)+2\eta x+x^2]^{\frac{1}{2}}.$$

In three different cases (12) was compared with exact evaluations and found to be quite satisfactory if $(l+\frac{1}{2})^2$ is substituted for $l(l+1)$ as observed by Yost, Wheeler, and Breit for the positive-energy solutions.[13,16] Expression (12) with this substitution is used hereafter for the evaluation of g_{c-} when $\eta\neq 0$.

The quantity $dg_{c+}{}^{\mathrm{Re}}/d\epsilon$ enters in the determination of the reduced width from the experimental width. In the barrier region where $G\gg F$, $G'\gg F'$, it can be obtained by approximating $g_{c+}{}^{\mathrm{Re}}=G'/G$ and taking the slope of a plot of G'/G as a function of ϵ. However, in the case of the s proton interaction with C^{12}, this slope could not be obtained with sufficient accuracy so that we used the expression[17]

$$d(aG'/G)/d\log\epsilon$$
$$=x_c\Theta_0^{-2}(x_c)\left[H(\eta)-\int_0^{x_c}\Theta_0^2(x)dx\right], \tag{13}$$

[14] Bloch, Hull, Broyles, Bouricius, and Breit, Phys. Rev. **80**, 553 (1950), and Revs. Modern Phys. **23**, 147 (1951).

[15] W. Magnus and F. Oberhettinger, *Formeln und Sätze für die Speziellen Funktionen der Mathematische Physik* (J. Springer, Berlin, 1948), second edition, Chap. VI, Sec. 2.

[16] As an illustration of the validity of this approximation, the table below lists the various evaluations for the first excited s states of O^{17} and F^{17}, which are treated in IV. The difference of the logarithmic derivatives of the mirror levels enters in the determination of the level displacement, and it is apparent from this example that it can be obtained accurately from the WKB—$(l+\frac{1}{2})^2$ approximation for F^{17} and the simpler, exact expression (8s) for O^{17}.

Values of $-ag_{c-}$; $a=4.60\times10^{-13}$ cm.

Channel	Exact	WKB—$(l+\frac{1}{2})^2$	WKB—$l(l+1)$
$O^{16}+n$, $x=1.770$, $\eta=0$	1.770	1.802	1.770
$O^{16}+p$, $x=0.275$, $\eta=4.36$	1.387	1.384	1.330

[17] This expression can be obtained from Eqs. (49) and (50) of reference 24 by setting $\delta_1=\delta_2=\frac{1}{2}\pi$ and then taking the limit as $E_\pi\to E_1$.

where

$$\Theta_0(x)=C_0G(x), \quad x_c=ka,$$

$$C_0=\left(\frac{2\pi\eta}{e^{2\pi\eta}-1}\right)^{\frac{1}{2}}, \quad H(\eta)=\eta-2\eta^3\sum_{\nu=1}^{\infty}\frac{\nu}{(\nu^2+\eta^2)^2},$$

the quantity $\Theta_0(x)$ being tabulated as an auxiliary function for G.[14]

C. One-Level, Many-Channel Formulas

The essential elements of the one-level nuclear reaction formula, which will be needed in the later discussion, can be obtained quite simply from a consideration of the boundary conditions which must be satisfied by the external wave functions at the surface S and by an application of Green's theorem. The present steady-state derivation draws mainly from the first of Wigner's recent papers[1] but includes the negative-energy alternatives as indicated in later papers;[6,9] as we require less general results than those obtained by him, a somewhat simpler treatment will suffice. A more general derivation employing the R matrix formalism of Wigner and Eisenbud[5] leads to essentially the same results. Some aspects of the present treatment were suggested by the work of Feshbach, Peaslee, and Weisskopf.[4]

On the surface S the value and normal gradient of any general solution to $H\Psi=E\Psi$ are represented as

$$\Psi=\sum_c\psi_cV_c, \tag{14a}$$

$$\mathrm{grad}_n\Psi=\sum_c\psi_c(D_c-a_c^{-1}V_c), \tag{14b}$$

and the logarithmic derivatives as

$$f_c=D_c/V_c; \tag{14c}$$

the quantities V_c and D_c denote the value and derivative of $\mathfrak{F}_c$ at $r_c=a_c$ (note that ψ_c contains the factor r_c^{-1}). We consider now the particular solution Ψ_e which has an incident wave, normalized to unit flux, only in the e (entrance) channel, and emerging waves in the positive-energy r (reaction) channels, and exponentially-decaying wave functions in the $c-$ channels ($c+$ will denote any or all positive-energy channels if it is unnecessary to distinguish the e from the r channels). In the external region this particular solution can be represented as

$$\Psi_e=\psi_e(E_e^*-U_{ee}E_e)-\sum_{c+}\psi_cU_{ec}E_c. \tag{15}$$

The submatrix $U_{c+,\,e+}$ is the unitary, symmetric collision matrix giving the coefficients of the unit-flux emerging waves in terms of the coefficients of the unit-flux incident waves; the submatrix $U_{e,\,c-}$ gives the coefficients of the E_{c-}. The important quantities are the logarithmic derivatives on S which, for the r and $c-$ channels, are the g_c of (11); the e channel, however, contains a scattered wave in addition to the incident wave so that

$$f_e=f_e^{\mathrm{Re}}+if_e^{\mathrm{Im}}=(E_e'^*-U_{ee}E_e')(E_e^*-U_{ee}E_e)^{-1}. \tag{16a}$$

Expressing U_{ee} in terms of f_e, we have

$$U_{ee}=(E_e^*/E_e)(f_e-g_e^*)(f_e-g_e)^{-1}, \tag{16b}$$

all external wave functions being evaluated at $r_e=a_e$. Comparing (14) with (15) and using (11) and (16b), we find

$$|V_e|^2=(4M_e/\hbar)g_e^{\mathrm{Im}}/|f_e-g_e|^2, \tag{17a}$$

$$|V_r|^2=(M_r/\hbar)|U_{er}|^2/g_r^{\mathrm{Im}}, \tag{17b}$$

$$|V_{c-}|^2=|U_{e,\,c-}|^2\cdot E_{c-}^2. \tag{17c}$$

The reduced widths are defined here by the relations

$$\gamma_c^2\equiv(\hbar^2/2M_a)|V_a|^2/\int_\tau|\Psi_a|^2d\tau \tag{18}$$

each of which is a measure of the probability that the pair of particles c appears at the nuclear surface; the reduced widths and the logarithmic derivatives contain all the information needed concerning conditions within the internal region. Introducing (18) into (17b), the reaction cross sections and the coefficients of the exponentially-decaying wave functions are expressed in terms of the reduced widths:

$$\begin{aligned}\sigma_{er}&=\pi k_e^{-2}(2l_e+1)|U_{er}|^2,\\ |U_{er}|^2&=4\gamma_r^2g_r^{\mathrm{Im}}g_e^{\mathrm{Im}}/\gamma_e^2|f_e-g_e|^2,\\ |U_{e,\,c-}|^2&=4\gamma_{c-}^2k_{c-}W_{c-}^{-2}g_e^{\mathrm{Im}}/\gamma_e^2|f_e-g_e|^2.\end{aligned} \tag{19}$$

By applying Green's theorem it may be shown that the width term in the denominator of the resonance formula arises from the imaginary part of (f_e-g_e) and that the energy term and the level shift arise from the real part.

For two general solutions $\Psi_1(E_1)$ and $\Psi_2(E_2)$ of the equation $H\Psi=E\Psi$ we have, using Green's theorem, (14), and (2):

$$\begin{aligned}(E_2-E_1)\int_\tau\Psi_1\Psi_2^*d\tau&=\int_\tau[\Psi_1(H\Psi_2)^*-\Psi_2^*H\Psi_1]d\tau\\ &=\int(\hbar^2/2M_c)(\Psi_2^*\,\mathrm{grad}_n\Psi_1-\Psi_1\,\mathrm{grad}_n\Psi_2^*)dS\\ &=\sum_c(\hbar^2/2M_c)V_{1c}V_{2c}^*(f_{1c}-f_{2c}^*).\end{aligned} \tag{20}$$

By defining quantities analogous to (18),

$$\gamma_{12,\,c}^2\equiv(\hbar^2/2M_c)V_{1c}V_{2c}^*\Big/\int_\tau\Psi_1\Psi_2^*d\tau \tag{21}$$

(20) may be simplified to

$$E_2-E_1=\sum_c\gamma_{12,\,c}^2(f_{1c}-f_{2c}^*). \tag{22}$$

If we set $E_1=E_2$, the imaginary part of (22) becomes

$$\gamma_e^2f_e^{\mathrm{Im}}+\sum_r\gamma_r^2g_r^{\mathrm{Im}}=0, \tag{23a}$$

which is equivalent to the expression for conservation of flux,

$$|U_{ss}|^2+\sum_r|U_{rs}|^2=1. \tag{23b}$$

The $c-$ channels do not appear in (23) since $g_{c-}{}^{\mathrm{Im}}=0$. Because $g_{c+}{}^{\mathrm{Im}}\geqslant 0$, (23a) requires that $f_c{}^{\mathrm{Im}}\leqslant 0$. Adding and subtracting a term $\gamma_c{}^2 g_c{}^{\mathrm{Im}}$ in (23a), we can write

$$g_c{}^{\mathrm{Im}}-f_c{}^{\mathrm{Im}}=\Gamma/2\gamma_c{}^2 \tag{23c}$$

where

$$\Gamma=\sum_{c+}\Gamma_c,\quad \Gamma_{c+}=2\gamma_c{}^2 g_c{}^{\mathrm{Im}};$$

Γ is the total width and the Γ_{c+} are the partial widths.

In order to treat the real part of (22), we introduce the one-level approximation which is to consider that $\gamma_{1\lambda\,c}{}^2=\gamma_c{}^2=$constant for a finite range of energies and of boundary conditions on S. This amounts to the assumption that over the resonance region, which must be narrow compared with the level spacing, the shape of the internal wave function does not change in first approximation [according to (20) its logarithmic derivatives on S will change in second approximation—see reference (1)], its amplitude, however, depends critically on the external conditions. Variations of the reduced widths are attributed to other levels and expected to be of order $(E-E_{res})/D$, where D is the level spacing. We let $E_1=E_{\text{resonance}}$ be the energy at which $f_c{}^{\mathrm{Re}}=g_c{}^{\mathrm{Re}}$ and let $E_2=E$ be the variable energy, then the real part of (22) becomes

$$(f_c{}^{\mathrm{Re}}-g_c{}^{\mathrm{Re}})=(E_{res}+\Delta-E)/\gamma_c{}^2 \tag{24a}$$

where

$$\Delta=\sum_{c\pm}\Delta_c=-\sum_{c\pm}\gamma_c{}^2[g_c{}^{\mathrm{Re}}(E)-g_c{}^{\mathrm{Re}}(E_{res})]. \tag{24b}$$

Inserting (24a) and (23c) into (19) we obtain the absolute square of the components of the collision matrix:

$$|U_{s\,c'\mu'}|^2=\Gamma_c\Gamma_{c'\mu'}[(E_{res}+\Delta-E)^2+\tfrac{1}{4}\Gamma^2]^{-1}, \tag{25}$$

this expression also being applicable to the $c-$ channels with $\Gamma_{c-}=2\gamma^2 kW^{-2}$. (The Γ_{c-} are not, however, real widths since they do not contribute to the total width Γ.) A relation typifying the resonance theory, which follows from (18) and (17a), is

$$\int_\tau|\Psi_c|^2 d\tau=\hbar\Gamma_c[(E_{res}+\Delta-E)^2+\tfrac{1}{4}\Gamma^2]^{-1}. \tag{26}$$

The quantity Δ, which as defined above is zero at $E=E_{res}$, is generally not constant, even in the one-level approximation, but a function of energy through the external wave function factors. In many cases, a linear expansion of Δ with respect to E about the resonance is adequate. With such an expansion the cross section given by (19) and (25) becomes[18]

$$\sigma_{sr}=\pi k_c{}^{-2}(2l_c+1)\Gamma_c{}^{\dagger}\Gamma_r{}^{\dagger}[(E-E_{res})^2+\tfrac{1}{4}\Gamma^{\dagger 2}]^{-1} \tag{27a}$$

with

$$\Gamma_{c+}{}^{\dagger}=\Gamma_{c+}[1+\Sigma_{c\pm}\gamma_c{}^2(dg_c{}^{\mathrm{Re}}/dE)]^{-1}{}_{E=E_{res}},\qquad \Gamma^{\dagger}=\Sigma_{c+}\Gamma_{c+}{}^{\dagger}. \tag{27b}$$

[18] R. G. Thomas, Phys. Rev. **81**, 148 (1951).

Equation (27a) is the type of expression with which experimental resonance data are usually compared so that the $\Gamma_{c+}{}^{\dagger}$ may be regarded as the observed widths. As a consequence of the distinction between Γ_{c+} and $\Gamma_{c+}{}^{\dagger}$, it is not strictly correct to obtain reduced widths by merely dividing the observed width by the barrier factor, $2g_c{}^{\mathrm{Im}}$, more detailed considerations being required. Generally $dg^{\mathrm{Re}}/dE\lesssim Mah^{-2}$ (it is, however, zero for s neutron positive-energy channels) so that those terms in the sum of (27b) should be considered for which $\gamma_c{}^2\gtrsim\hbar^2/10Ma$. It is apparent from (20) that the inclusion of the $c-$ channels in the sum in (27b) is simply a consequence of not including them in the volume integral τ appearing in (20) and (21). Provided E_{res} is not near a threshold for a $c-$ channel, these channels may be ignored by a redefinition of τ and then the only concern is the $c+$.

The above expression for Δ differs from that given by W-E,[19] but this distinction is purely formal, lying entirely in the choice of the reference energy. We can obtain their expression for Δ_λ by assuming the existence of a solution $X_\lambda(E_\lambda)$ satisfying the equation $HX_\lambda=E_\lambda X_\lambda$ and the boundary condition[9]

$$f_{\lambda c}=-b_c \tag{28}$$

for all c, the b_c being an arbitrary set of finite real numbers. Substituting $X_\lambda(E_\lambda)$ for $\Psi_2(E_2)$ and $\Psi(E)$ for $\Psi_1(E_1)$, and assuming that $\gamma_{1\lambda\,c}{}^2=\gamma_c{}^2=$constant, the real part of (22) reduces again to (24a) but with

$$\Delta_\lambda=\sum_{c\pm}\Delta_{\lambda c}=-\sum\gamma_c{}^2(g_c{}^{\mathrm{Re}}(E)+b_c) \tag{24c}$$

and with E_{res} replaced by E_λ, the reference energy; Δ_λ is interpreted as the total level shift and the $\Delta_{\lambda c}$ as the partial level shifts, referred to the boundary condition (28).[19]

If a level is bound, all channels are then $c-$ and the cross section formula is of no significance; nevertheless, Δ_λ signifies the shift of the level from its position with the reference boundary condition given by (28).

The same type of argument as that which led to Eqs. (24) can be used to compare corresponding levels of mirror nuclei. In Eq. (20) we replace $\Psi_1(E_1)$ by $\Psi_p(E_p)$, a solution to $H_p\Psi_p=E_p\Psi_p$, and $\Psi_2(E_2)$ by $\Psi_n(E_n)$, a solution to $H_n\Psi_n=E_n\Psi_n$, where the subscripts n and p denote the nucleus with the odd neutron or proton, respectively. If we assume equality of nn and pp nuclear interactions, then $H_p-H_n\equiv V$ is the difference of the Coulomb, electromagnetic spin-orbit, and mass energies. Furthermore, in the one-level approximation we assume that, irrespective of the boundary conditions, in the internal region Ψ_p and Ψ_n are the same to within a multiplicative constant. Then the real part of (22) reduces to

$$E_n-E_p=-\langle V\rangle_\tau+\Delta_{\lambda n}-\Delta_{\lambda p}, \tag{30a}$$

[19] In W-E the boundary condition on the X_λ is $b_c=l_c/a_c$, where l_c is the channel orbital angular momentum; in reference 6 the condition $b_c=-1/a_c$ is used. A detailed discussion on the choice of b_c is given in reference 9.

if we take $b_{nc}=b_{pc}$. The difference,

$$\Delta_{\lambda n}-\Delta_{\lambda p}=\sum_{c\pm}\gamma_c^2(g_{pc}^{\mathrm{Re}}-g_{nc}^{\mathrm{Re}}), \quad (30b)$$

is referred to as the boundary-condition level displacement[20] and $\langle V\rangle_\tau$ is the mean value of V in the internal region.

D. One-Channel Approximation

In the one-channel approximation, we disregard the terms in (22) with $c\neq e$ as regards their effect on f_e but otherwise consider the reactions if there are r channels. That is, the total level shift and width are attributed entirely to the e channel. This approximation is suited to the treatment of the levels of C^{13} and N^{13} below 6 Mev since the channel for emission of the odd neutron or proton can be taken as the e channel and, aside from radiation, all others are $c-$ channels of high binding energy; these $c-$ channels may be eliminated from (22) by allowing their radii to be infinite in which case the $\gamma_{c-}{}^2$ vanish. Expression (30b) for the displacement of corresponding levels will depend only on the boundary conditions on the e channels; (in III, however, we consider the possible effect of the $c-$ on this displacement). Although the formulas of the one-channel case may be well known from the treatments of the two-body interactions, they are repeated here in order to indicate the notation, only those formulas being given which are needed in the later discussion. Here we are not restricted to the one-level approximation.

In the one-channel case the imaginary part of (22) is assumed to be zero so that $f_e^{\mathrm{Im}}=0$, and in the limit as $E_\Sigma\to E_1$ the real part of (22) is

$$-\gamma_e^{-2}=df/dE, \quad (31a)$$

and (27b), which relates the reduced widths to the observed widths in the one-level approximation, becomes

$$\gamma_e^{-2}=(2g^{\mathrm{Im}}/\Gamma^\dagger)-(dg^{\mathrm{Re}}/dE), \quad E=E_{\mathrm{res}}. \quad (31b)$$

In connection with (24a), the resonance energy was defined as the energy at which

$$f=g_e^{\mathrm{Re}}; \quad (31c)$$

the maxima of the reaction cross sections may, however, be shifted slightly from the resonance energy on account of the energy dependences of the factors g_e^{Im}, g_r^{Im}, k_e^{-2} in (19). If the e channel has negative energy, the bound levels will appear where (31c) is satisfied.

According to (16b) the ee component of the collision matrix for positive energy e channels has modulus one and can be written

$$U_{ee}=(-1)^{l_e}\exp 2i(\sigma_e+\delta_e), \quad (32a)$$

the nuclear phase shift being

$$\delta_e=\tan^{-1}[g^{\mathrm{Im}}/(f-g^{\mathrm{Re}})]-\tan^{-1}(F/G). \quad (32b)$$

If the incident part of the wave function for the e channel arises from an incident plane wave beam of unit flux, the particular solution (15) is to be multiplied by $(-1)^{l_e}\pi^{\frac{1}{2}}k^{-1}(2l_e+1)^{\frac{1}{2}}$; in the external region, r times the radial part of its wave function is then given by

$$-i^{l_e+1}(4\pi M/\hbar k^2)^{\frac{1}{2}}(2l_e+1)^{\frac{1}{2}}\exp[i(\sigma_e+\delta_e)]\times(F\cos\delta+G\sin\delta). \quad (32c)$$

In the interaction of s nucleons with C^{12}, the one-level approximation is shown to be inadequate by the observed variation of γ_e^2 by about a factor of three in the energy range investigated; according to (31a) this variation will also be indicated by a deviation of the energy dependence of f_e from linearity. The effects of other levels can be included by means of the R-matrix formalism; in the one-channel case the R-matrix is simply the R function and equal to the reciprocal of f if we set $b_e=0$:[9]

$$f^{-1}=R=\sum_\lambda\gamma_\lambda^2(E_\lambda-E)^{-1}. \quad (33)$$

The γ_λ^2 are the energy-independent reduced level widths. They are to be distinguished from the energy-dependent quantity $\gamma^2(E)$ which we have designated as the reduced width; according to (33) and (31a)

$$\gamma^2(E)=R^2/\sum_\lambda\gamma_\lambda^2(E_\lambda-E)^{-2}, \quad (34)$$

and

$$\gamma^2(E=E_\lambda)=\gamma_\lambda^2.$$

It is γ^2 which can be determined from the width of a resonance level rather than γ_λ^2 unless E_{res} should happen to coincide with E_λ; thus, we are primarily concerned with the former quantity. However, in the one-level approximation γ^2 is considered to be constant, only one term in the R function being considered, and there is then no distinction. Expressions (33) and (34) involve too many parameters for applications. A satisfactory way of treating deviations from the one-level approximation with but one additional parameter is to approximate

$$R=R_\infty+\gamma_\lambda^2(E_\lambda-E)^{-1}, \quad (35)$$

R_∞ being a constant which is the order of magnitude of the average reduced width divided by the level spacing. Wigner[1] has shown that this form will give accurately the cross section for scattering over a wide range of energies provided there are no intervening resonances. Another way of introducing the effects of the other levels is, as suggested by FPW, to represent the energy dependence of f by

$$f(E)=-K\tan Z(E), \quad (36)$$

where K is a wave number for the incident particle

[20] We distinguish here between "shift" and "displacement." The former is used to denote the shift of a level for any particular reason and the latter denotes the difference of the corresponding shifts of conjugate levels. For example, the Δ_λ are the level shifts which contribute an amount $\Delta_{\lambda n}-\Delta_{\lambda p}$ to the displacement of conjugate levels. The net displacement is the difference of the displacements of a conjugate pair of excited states from that of the ground states; it is the displacement which is apparent when the energy level diagrams of the mirror nuclei are placed side by side with their ground states at the same level, as in Fig. 1.

within the nucleus, $\sim 1\times 10^{13}$ cm^{-1}, and $Z(E)$ is a monotonic increasing function which is anticipated to have a fairly smooth energy dependence. This representation is particularly convenient and will be used in III and IV. Wigner[21] has shown that every R function can be put in this form with a convergent series representation for $Z(E)$.

In comparing mirror interactions we assume that V is sufficiently uniform in the internal region so that

$$f_n(E_n)=f_p(E_p-\langle V\rangle_\tau). \tag{37}$$

The net displacements of mirror levels are obtained by matching the ground states, as in Fig. 1, thus correcting for the energy difference given by (30a) for the ground state. However, (37) and (30a) indicate that in order to have a common scale for the nuclear excitation energy of the excited states, the ground state of the odd-neutron nucleus should be displaced by an amount equal to the ground-state boundary-condition displacement, $\Delta_{\lambda n}-\Delta_{\lambda p}$, above the ground state of the odd-proton nucleus, assuming that the quantity $\langle V\rangle_\tau$ is the same in the excited state as in the ground state.

It has been shown by Teichmann[22] that nuclear resonance levels and their widths may be interpreted in terms of the quantities of the effective range theory, such as scattering length and effective range. This theory has been applied with considerable success to the analysis of the s np and pp interactions;[23,24] the s $(C^{12}+n)$ interaction will be shown to be similar in some respects to the $^3S_1$ np interaction so that it is appropriate to use the effective range theory in the former case in order to bring out the similarity. Moreover, we will be able to use the graphs given by Blatt and Jackson[24] for interpreting the interaction parameters in terms of the strengths and intrinsic ranges of various potentials. In dealing with broad levels, the nuclear resonance theory is considered objectionable on account of the sensitivity of its characteristic parameters to the channel radius; the effective range theory, on the other hand, does not contain a channel radius.[25]

If there is no Coulomb or centrifugal interaction, the comparison-function potential is conveniently taken to be zero everywhere, and the expansion of the effective range theory is

$$k\cot\delta_0=-\alpha+\tfrac{1}{2}r_0k^2-Pr_0^3k^4+\cdots \tag{38}$$

where r_0 is the effective range, α^{-1} the scattering length, and P the shape factor. Expression (38) holds for a bound state with the substitutions: $\cot\delta=-i$, $k=-i(2MB/\hbar^2)^{\frac{1}{2}}$; B is its binding energy. According to (32c) and (38) the relation between the logarithmic derivative and the scattering length at a nuclear energy E_0 corresponding to the neutron threshold is given by

$$f^{-1}(E_0)=a(1-\beta^{-1}),\quad \beta=\alpha a, \tag{39a}$$

where a is the channel radius, which is not to be mistaken here for the scattering length. The reduced widtl. at E_0 is given by

$$\gamma^2(E_0)=(\hbar^2/2Ma)(1-\beta)^2(1-\beta+\tfrac{1}{3}\beta^2-\tfrac{1}{2}r_0a^{-1})^{-1}, \tag{39b}$$

which follows from (31a), (32c), and (38).

E. Radiative Capture

Channels for radiation were not included in the considerations of II-C. It is evident that Eq. (23a), expressing conservation of flux, must include a term in $f_c^{\rm Im}$ to take account of the radiation and there will thus be terms in the total width for partial radiative widths, as already shown by FPW. No investigations have been reported concerning the effect of radiation on the real part of f_c, leading to terms in the total level shift from the partial radiative shifts; such terms are expected to be negligible owing to the smallness of radiative widths.

An expression is given here for the electric dipole s-wave capture cross section, obtained from the usual formula for the transition rate between states, which separates the contributions to the transition moment from the external and internal regions. The reduced width of the final state, to which the external contribution is proportional, enters as a parameter additional to those contained in the familiar resonance capture formulas. The contribution to the radiation from the internal region is assumed to be proportional to $\int_\tau^*|\Psi|^2d\tau$ as given by (26) in the one-level approximation; the contribution from the external region is calculable in terms of the known wave functions. It is known that the contribution to the dipole transition moment in the photodisintegration of the deuteron arises predominantly from beyond the range of nuclear forces so that it should not be surprising that in the treatment of radiative capture in light nuclei, some of which have rather large reduced widths, it is also necessary to include the external contribution.

Only the one-channel case is considered and in order to simplify the notation a two-body type of wave function is used to describe the internal as well as external regions. Neglecting exchange effects, the cross section for electric dipole emission is given by[26]

$$\sigma_\gamma(c\to f)=64\pi^4(h\nu)^3e^2A^2q_cq_f'\left|\int_0^\infty ru_cu_fdr\right|^2/3h^4c^3, \tag{40a}$$

[21] E. P. Wigner, Ann. Math. **53**, 36 (1951).
[22] T. Teichmann, Phys. Rev. **83**, 141 (1951); Th. Sexl, Naturwiss. **19**, 454 (1951).
[23] J. M. Blatt and J. D. Jackson, Phys. Rev. **76**, 118 (1949).
[24] H. A. Bethe, Phys. Rev. **76**, 38 (1950).
[25] However, an attempt to adapt this theory to the $(C^{13}+p)$ s interaction encounters the difficulty, due to the strong Coulomb barrier, that the comparison function, usually designated ψ, is in the internal region much larger than the actual wave function, and as a result the effective range has little significance and the expansion which is analogous to (38) has poor convergence. One may overcome this difficulty by suitably modifying the comparison-function potential, but then the computation becomes unnecessarily difficult and available graphs cannot be used for interpretation.
[26] G. Breit and D. M. Yost, Phys. Rev. **48**, 203 (1935).

where $h\nu$ is the transition energy, q_c is the statistical factor for the formation of the initial state $((l_c+\frac{1}{2}\pm\frac{1}{2})/(2l_c+1)$ for the state with spin $J=l\pm\frac{1}{2}$), $A=(Z_1A_2-A_1Z_2)/(A_1+A_2)$ is the reduced charge number, q' is the angle-spin integration factor ($s_1\rightarrow p_1$, $q'=\frac{2}{3}$; $s_1\rightarrow p_1$, $q'=\frac{1}{3}$) and u_c and u_f ($\int_0^\infty u_f^2dr=1$) are r times the radial parts (the angle-spin part being normalized to unity) of the initial- and final-state wave functions. As we are not concerned here with interference from the various partial waves, u_c can be taken real and is given by the modulus of (32c). Equation (40a) can be put in a convenient form by separating the radial integration into internal and external parts and by introducing the quantities

$$\theta_c^2=au_c^2(a)\Big/\int_0^a u_c^2dr,\quad \theta_f^2=au_f^2(a)\Big/\int_0^a u_f^2dr,$$

$$\mathfrak{M}=a^{-1}\int_0^a ru_cu_fdr\Big/\left[\int_0^a u_c^2dr\cdot\int_0^a u_f^2dr\right]^{\frac{1}{2}};\quad (40b)$$

$\mathfrak{M}$ is a dimensionless measure of the transition moment from the internal region (if the radiation is due to the nucleon from the entrance channel, $\mathfrak{M}\leq 1$); θ_c^2 and θ_f^2 are dimensionless measures of the reduced widths, $\gamma^2=(\hbar^2/2Ma)\theta^2$, for the two states. With the quantities (40b) and (17a) for evaluating $u_c^2(a)=\pi k_c^{-2}(2l_c+1)\times|V_c|^2$, we find

$$\left|\int_0^\infty ru_cu_fdr\right|^2=4\pi Mk_c^{-2}\hbar^{-1}(2l_c+1)a^3g_c^{\mathrm{Im}}\times(\mathfrak{M}+\theta_c\theta_fJ)^2|f_c-g_c^{\mathrm{Re}}|^{-2}N^{-1}\theta_c^{-2}\quad (40c)$$

where

$$J=a^{-2}\int_a^\infty rw_cw_fdr,\quad w(r)=u(r)/u(a),$$

$$N=1+\theta_f^2a^{-1}\int_a^\infty w_f^2dr.$$

In the case of proton capture, N and the energy-dependent quantity J are found by numerical integration, the quantity w_f being obtained from (7). In the radiative capture of thermal neutrons to a final p state with binding energy B, they are

$$N=1+\theta_f^2(x_f+2)/2(x_f+1)^2,\quad J=\beta Q(\beta-1)^{-1},$$
$$Q=[(x_f^2+3x_f+3)-x_f(x_f+2)\beta^{-1}]/x_f^2(1+x_f),\quad (40d)$$
$$x_f=(2MBa^2/\hbar^2)^{\frac{1}{2}}.$$

The dimensionless quantity J is a function of the energy both because w_c, which is a multiple of (32c), contains the energy-dependent phase shift δ_c and because the external wave functions F and G are functions of the energy. By means of (32b) the energy dependence contained in δ can be factored out in the form

$$J=k_c^{-1}(f-g^{\mathrm{Re}})FGJ'+J''$$

where

$$J'=a^{-2}\int_a^\infty[F(r)F(a)^{-1}-G(r)G(a)^{-1}]rw_fdr,$$

$$J''=a^{-2}(F^2+G^2)^{-1}_{r=a}\int_a^\infty[G(r)G(a)+F(r)F(a)]rw_fdr.\quad (40e)$$

Although the critical energy dependence of F and G in the barrier region, which is attributed to the factor C_0 of (13), does not appear in J', J'', and (FG), the latter quantities are nevertheless expected to be mildly energy dependent.

If the radiative capture formula is written in the usual one-level form

$$\sigma_{c\gamma}=\pi k_c^{-2}\omega\Gamma_c\Gamma_\gamma[(E_{res}+\Delta-E)^2+\tfrac{1}{4}\Gamma^2]^{-1},\quad (40f)$$

$\omega=(2l_c+1)q_c$ being the statistical factor, then by comparing (40a, c, e) with (40f) and introducing the one-level formula, Eq. (24a), we find that

$$\Gamma_\gamma=\frac{4}{3}\left(\alpha\frac{h\nu}{m_0c^2}\right)^3A^2q'\left(\frac{a}{r_0}\right)^2N^{-1}\times\left[\mathfrak{M}'+2\theta_c\theta_f\left(\frac{E_{res}+\Delta-E}{\Gamma_c^*}\right)J'\right]^2m_0c^2,$$

where

$$\mathfrak{M}'=\mathfrak{M}+\theta_c\theta_fJ'',\qquad \alpha=e^2/\hbar c,$$
$$\Gamma_c^*=2\gamma_c^2(FG)^{-1}_{r=a},\quad r_0=e^2/m_0c^2.$$

The energy dependence of the interference between the internal and external contributions is thus clearly evident. This dependence is also expected to occur with radiations of other multipolarities.

III. THE ENERGY LEVELS OF C^{13} AND N^{13}

Experimental Data

The experimental data on the energy levels of C^{13} and N^{13} published prior to July, 1950 have been surveyed in "Energy Levels III."[27] Considerable additional information has subsequently been gathered, so that it is necessary to give a brief summary.

Levels in N^{13} shown in Fig. 1 have been observed at 2.37 and 3.52 Mev from the $C^{12}(p,\gamma)N^{13}$ resonances. By reason of the large width-without-barrier of the 2.37 resonance, it is attributed to s capture.[28] The resonance at 3.52 Mev was first observed by Van Patter and its energy dependence found to be adequately described by a one-level Breit-Wigner formula.[29] These two levels were also observed by Grosskreutz[30] in the

[27] Hornyak, Lauritsen, Morrison, and Fowler, Revs. Modern Phys. **22**, 291 (1950).
[28] Fowler, Lauritsen, and Lauritsen, Revs. Modern Phys. **20**, 236 (1948).
[29] D. M. Van Patter, Phys. Rev. **76**, 1264 (1949).
[30] J. C. Grosskreutz, Phys. Rev. **76**, 482 (1949).

energy spectrum of neutrons from $C^{12}+d$ and by Goldhaber and Williamson[31] in the elastic scattering of protons by C^{12}. A partial wave analysis[32] of the elastic scattering at the 2.37 resonance shows it to be due to s-waves; however, the anomalous energy-dependence of the cross section in the vicinity of 3.5 Mev is interpreted as due to a doublet, rather than a single level, with one component at 3.50 which is $p_{\frac{1}{2}}$ and the other at 3.55 which is $d_{\frac{3}{2}}$. No evidence for any other levels below 6-Mev excitation was found in the elastic scattering experiment. The fact that only a single level was observed at 3.52 from $C^{12}(p, \gamma)$ presents no difficulty because the radiation from a $d_{\frac{3}{2}}$ level to the $p_{\frac{1}{2}}$ ground state would be magnetic quadrupole which is expected to be considerably weaker than magnetic dipole radiation from the $p_{\frac{3}{2}}$ component. The angular distribution of the radiation from the 2.37 level was found to be isotropic by Devons and Hine in agreement with an $s_{\frac{1}{2}}$ assignment.[33] The angular distribution of the radiation from the 3.52 level, as measured by Day and Perry, was found to be anisotropic with the coefficient of $\cos^2\theta$ at resonance agreeing with the calculated value for a level spin $\frac{3}{2}$; however, the energy dependence of this coefficient indicates that the level may be formed by d-waves with an s-wave background.[34] The angular distribution of neutrons from $C^{12}+d$ also indicates that the 2.37 level is formed by the capture of an s neutron in the stripping process;[35] the level at 3.5 Mev, though not resolved, indicates d, rather than p capture or a mixture, which may be due to the fact that the reduced width, which enters as a yield factor in this process, is 5-times greater for the $d_{\frac{3}{2}}$ component than it is for the $p_{\frac{3}{2}}$ component (see below).

The level of C^{13} at 3.10 Mev is well established from measurements of proton groups and gamma-radiation from $C^{12}+d$.[37] The measurement of Rotblat[36] and the analysis, by means of the stripping theory due to Butler,[37] of the angular distribution of protons from this reaction, associated with this level and the ground state, indicate that they are $s_{\frac{1}{2}}$ and $p_{\frac{1}{2}}$, respectively, and the fact that the resulting radiation is electric dipole, as determined from the measurement of the internal pair formation coefficient for the transition,[38] is consistent with these assignments. Rotblat[39] has also observed in photographic emulsions proton groups associated with levels at 3.7 and 3.9 Mev, and from their angular distribution he determined that the levels are formed by the capture of p and d neutrons, respectively. This finding is in accord with the mirror nuclei hypothesis and the observed doublet in N^{13}, comprising $p_{\frac{1}{2}}$ and $d_{\frac{3}{2}}$ components, provided that the additional splitting in C^{13} can be accounted for as a result of the differences of the electromagnetic properties of the odd nucleons. The 3.68-Mev level is most clearly evident in the $N^{15}(d, \alpha)C^{13}$ reaction which was investigated with magnetic analysis of the reaction products by Malm and Buechner[40] who, however, failed to observe the 3.9 level but noted that a weak group associated with such a level might be obscured by the presence of a broad group associated with the 9.6 level in C^{12} formed from the competing $N^{14}(d, \alpha)C^{12}$ reaction.

TABLE I. Q values of the $B(\alpha, p)$ reactions. From the compilation of reaction energies, (see reference 45) the ground-state Q-values are: $B^{10}(\alpha, p)C^{13}$, $Q=4.071\pm0.010$ Mev; $B^{11}(\alpha, p)C^{14}$, $Q=0.778\pm0.007$ Mev.

Reference (41)	(42)	(43)	(44)	Remarks
3.8	4.07	4.08 ± 0.12		$B^{10}(\alpha, p)C^{13}$ (ground state)
		3.35 ± 0.25		Weak
0.75 ± 0.01	0.85	0.65 ± 0.15	0.63	$B^{11}(\alpha, p)C^{14}$ (ground state)
0.24 ± 0.02	0.31			(2nd state in C^{13})
		0.15 ± 0.15	0.00	
-0.22	0.07			(3rd state in C^{13})
	-0.31	-0.57 ± 0.15	-0.55	$B^{10}(\alpha, d)C^{12}$?
	-1.57		-1.75	Weak

Additional results concerning the C^{13} levels have been obtained from the $B^{10}(\alpha, p)C^{13}$ reaction. Because they are not easily interpreted, we list the more recent Q values[41–45] in Table I. Reference 41 used magnetic analysis of the particle groups, the others range measurements. References 43 and 44 apparently do not resolve the second and third excited states. The first excited state of C^{13} is evidently not formed in this reaction. The group with $Q=3.35$ found by reference 43 may come from another reaction as Blundell and Rotblat[46] report that there is no level in C^{13} in the vicinity of 1 Mev. We assume that the weak groups with Q values of -1.57 and -1.75 Mev belong to another reaction since no levels appear in C^{13} from the scattering by C^{12} of neutrons with an energy less than 2 Mev,[47] except for the broad background which is attributed to the s interaction associated with the 3.10 bound level.[18] A complete survey of these and earlier $B(\alpha, p)$ investigations has been given by Slätis, Hjalmar, and Carlsson.[48] A 3.8-Mev gamma-ray has been observed with 1.4-Mev

[31] G. Goldhaber and R. M. Williamson, Phys. Rev. **82**, 495 (1951).
[32] H. L. Jackson and A. I. Galonsky, Phys. Rev. **84**, 401 (1951).
[33] S. Devons and M. G. N. Hine, Proc. Roy. Soc. (London) **A199**, 56 (1949).
[34] R. B. Day and J. E. Perry, Jr., Phys. Rev. **81**, 662 (1951) and R. B. Day, Ph.D. thesis, California Institute of Technology (1951), (unpublished).
[35] El-Bedewi, Middleton, and Tai, Proc. Phys. Soc. (London) **A64**, 1055 (1951).
[36] J. Rotblat, Nature **167**, 1027 (1951).
[37] S. T. Butler, Phys. Rev. **80**, 1095 (1950) and Proc. Roy. Soc. (London) **A208**, 559 (1951).
[38] R. G. Thomas, Phys. Rev. **80**, 138 (1950).
[39] J. Rotblat, Phys. Rev. **83**, 1271 (1951).
[40] R. Malm and W. W. Buechner, Phys. Rev. **81**, 519 (1951).
[41] G. M. Frye and M. L. Wiedenbeck, Phys. Rev. **82**, 960 (1951).
[42] R. J. Creagan, Phys. Rev. **76**, 1769 (1949).
[43] J. L. Perkin, Phys. Rev. **79**, 175 (1950).
[44] Slätis, Hjalmar, and Carlsson, Phys. Rev. **81**, 641 (1951).
[45] Li, Whaling, Fowler, and Lauritsen, Phys. Rev. **83**, 512 (1951).
[46] M. Blundell and J. Rotblat, Phys. Rev. **81**, 144 (1951).
[47] D. W. Miller, Phys. Rev. **78**, 806 (1950).
[48] Slätis, Hjalmar, and Carlsson, Arkiv. Fys. **17**, 315 (1951).

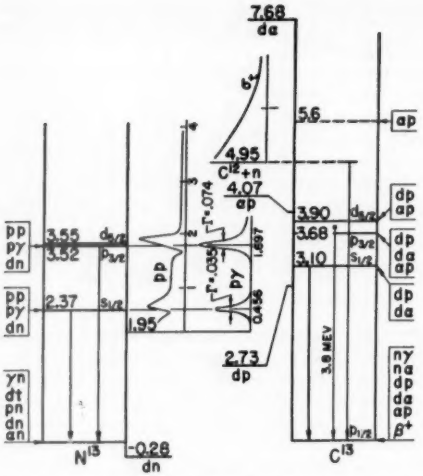

FIG. 1. The energy levels of C^{13} and N^{13} below 6 Mev.

alpha-particles;[49] this gamma-ray may be emitted from either or both the 3.7- and 3.9-Mev levels. In Fig. 1, which shows the levels of C^{13} and N^{13} below 6 Mev, we have adopted Rotblat's value of 3.9 for the position of the second excited level of C^{13}; the $B^{10}(\alpha, p)$ data, however, favor a somewhat higher energy.

Thus, there appear at low excitation energies levels in C^{13} and N^{13} which may be characterized as s, p, d neutrons and protons interacting with a C^{12} core. We turn to the study of the widths, displacements, spacings, and radiative properties of these levels.

s Interaction

According to (31c), the known positions of the $C^{12}+p$ resonance at 2.37 and the C^{13} bound level at 3.10 determine $f(E)$ and therefore $Z(E)$ from (36) at the respective excitation energies; these data are plotted in Fig. 2(a) for $Ka=2.5$ and 3.5 and with a channel radius $a=4.9$.[50] Tentatively we assume that the nuclear energy of N^{13} is the same as that of C^{13} when both energies are referred to their ground states. A third value of Z at $E=4.95$ is obtained from the epithermal neutron scattering length for carbon using (39a). This scattering length, as measured by Havens and Rainwater,[51] is $\alpha^{-1}=(\sigma/4\pi)^{\frac{1}{2}}=6.11\times10^{-13}$ cm; this datum is in agreement with that of Jones.[52] Since there is no measurable spin or isotopic effect in the coherent scattering of thermal neutrons,[52] the presence of a small amount of C^{13} can be disregarded. We obtain dZ/dE at 2.37 from the width, $\Gamma^{\uparrow}=35$ kev, of the $C^{12}+p$ resonance using (31a, b). This slope appears as a solid line in Fig. 2.

The sensitivity of the computation from (31b) of γ^2, and likewise of dZ/dE, to the choice of a for the resonance at 2.37 is illustrated in Fig. 3 by plotting $\theta^{-2}=\hbar^2/2Ma\gamma^2$ as a function of a, using (13) for obtaining dg^{Re}/dE. The radial dependence is due to the positive quantities g^{Im} and dg^{Re}/dE; g^{Im} decreases with decreasing a more than dg^{Re}/dE and to such an extent that for $a<2.7$ the positive-definite θ^2 becomes negative. This difficulty arises from the fact that we assume that only the Coulomb interaction exists in the external region ($r>a$) when, evidently, nuclear interactions are also present. The net effect of ignoring these (attractive) nuclear interactions is that a value of g^{Im} is used which is too small and a value of dg^{Re}/dE which is too large; consequently the value obtained for θ^{-2} is low and, for sufficiently small a, can even have the wrong sign. From the plot of Fig. 3 and the sum rule for reduced widths,[54] one can infer that the range of the nuclear interaction is $\gtrsim 3.6$. The determination of γ^2 at this resonance is also especially sensitive to the experimental value of $\Gamma^{\uparrow}$; this sensitivity is an indication that the strong Coulomb

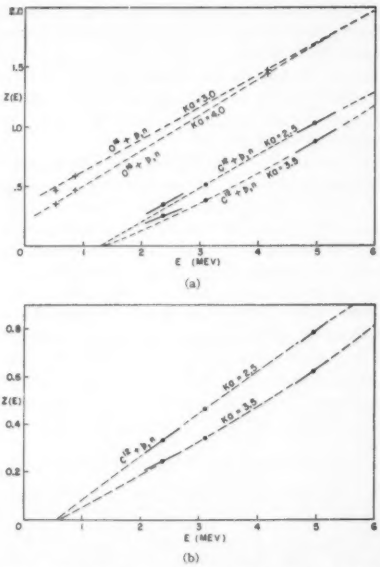

FIG. 2. A plot of $Z=\tan^{-1}(-f/K)$ as a function of E for the s interactions: (a) $a=4.9$ for $C^{13}+p, n$; $a=5.27$ for $O^{16}+p, n$; (b) $a=4.4$ for $C^{13}+p, n$.

[49] Bennett, Roys, and Toppel, Phys. Rev. **82**, 22 (1951).

[50] The energy of relative motion, ϵ, will be given in laboratory units unless stated otherwise. The nuclear excitation energy E is referred to the ground state and given in Mev in the center-of-mass system. Nuclear radii are given in units of 10^{-13} cm.

[51] W. W. Havens, Jr., and L. J. Rainwater, Phys. Rev. **75**, 1296 (1949).

[52] W. B. Jones, Phys. Rev. **74**, 364 (1948).

[52] E. O. Wollan and C. G. Shull, Phys. Rev. **73**, 830 (1948); Burgy, Ringo, and Hughes, Phys. Rev. **84**, 1164 (1951); W. C. Koehler and E. O. Wollan, Phys. **85**, 491 (1952).

[54] $\Sigma_{c\pm}\gamma_{\lambda c}^2\approx 3\hbar^2/2Ma$; E. P. Wigner, Am. J. Phys. **17**, 99 (1949).

barrier for the incident proton makes it difficult to obtain accurate information concerning the nuclear interaction. Published values of nuclear radii of carbon, which have been obtained in various ways, are indicated at the top of the graph.

The evaluation of reduced widths from (31b) is also particularly sensitive to the value of l which is assumed for the incident particle, and this fact can be used advantageously to set an upper limit on l. As shown by Ehrman,[11] assignments of $l>0$ to the 2.37 resonance level in N^{13} are excluded because γ^2 would be negative for any reasonable choice for a, thus conclusively establishing that this resonance is due to s protons.

A value for dZ/dE at 4.95 Mev can be obtained from the plot of $k\cot\delta_0$ for the low energy scattering of neutrons by carbon shown in Fig. 4. The data obtained by Miller, although of high relative accuracy (the $k\cot\delta_0$ plot considerably exaggerates the scatter of the points), is not claimed to be precise in absolute magnitude;[56] since it is in excellent agreement with the absolute measurements of Williams,[56] it is assumed to be absolute throughout.

In order to compute $k\cot\delta_0$, it is necessary to subtract the scattering contribution from the higher angular momenta,

$$4\pi k^{-2}\sum_{l\neq 0}(2l+1)\sin^2\delta_l, \qquad (41a)$$

δ_l being given in terms of f and the external functions by (32b). The subtraction was actually carried out for scattering from a hard sphere, $f_{l\neq 0}=\infty$, of radius 3.9. Subsequently, however, Wigner[57] has shown that as a consequence of the finite contribution to the R function

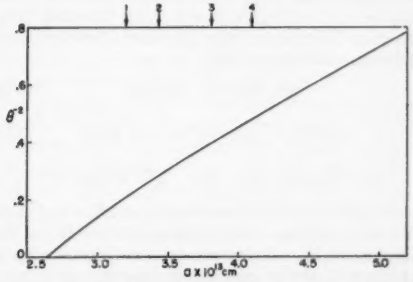

FIG. 3. Reciprocal of the reduced width, in dimensionless units, plotted as a function of the channel radius for the $C^{13}+p$ resonance at $\epsilon_p=0.456$ kev. Nuclear radii obtained in various ways are indicated at the top of the graph: (1) Neutron scattering at 95 Mev (theory: *transparent nucleus*)—J. De Jurenand N. Knable, Phys. Rev. **77**, 606 (1950); (2) From the ground-state Coulomb energy difference, $R_c=1.46A^{\frac{1}{3}}$; (3) Neutron scattering at 25 Mev (theory: *schematic*)—H. Feshbach and V. F. Weisskopf, Phys. Rev. **76**, 1550 (1949); (4) Total neutron cross section at 42 Mev (theory: *opaque nucleus*)—P. H. Hildebrand and C. E. Leith, Phys. Rev. **80**, 842 (1950).

[56] D. W. Miller (private communication).
[56] Lampi, Freier, and Williams, Phys. Rev. **80**, 853 (1950); Freier, Fulk, and Williams, Phys. Rev. **78**, 508 (1950).
[57] E. P. Wigner, Proc. Cambridge Phil. Soc. **47**, 790 (1951).

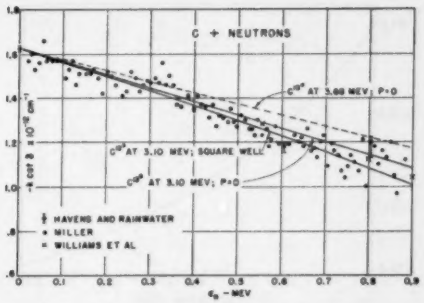

FIG. 4. Plot of $k\cot\delta_0$ for the scattering of low energy neutrons by carbon. The points at $\epsilon_n=0.4$, 0.6, 0.8 Mev have vertical lines through them to indicate the possible uncertainty of the correction for the scattering of the higher partial waves.

from distant high energy levels, the value

$$f^{-1}{}_{l\neq 0}=S_R(E)\log(X^{\frac{1}{2}}+T^{\frac{1}{2}})/(X^{\frac{1}{2}}-T^{\frac{1}{2}}) \qquad (41b)$$

is to be preferred. Here $E=\epsilon+B$, $X=E+T$, B being the binding energy of the incident neutron (or proton), T its kinetic energy in the nucleus, and $S_R(E)=\langle\gamma_\lambda^2\rangle_{Av}D^{-1}$ is the average reduced level width divided by the level spacing, evaluated at an excitation energy E. With this expression for f_l, (41a) yields a negligibly small contribution, but since (41b) is only an estimate, we have indicated the possible uncertainty of the $k\cot\delta$ plot by drawing vertical lines through the points at 0.4, 0.6, 0.8 Mev; the tops of these lines correspond to scattering from a hard sphere of radius 4.1 and the bottoms to no correction, as indicated by (41b). In any case, the correction is almost negligible below 0.8 Mev and resonances in the scattering do not occur below $\epsilon_n=2.1$ Mev[58] so that the plot should be of some significance.

From the plot, together with the datum from the bound s state at 3.10, we find that the interaction parameters lie between: $[r_0=2.9\times10^{-13}$ cm, $P=0.02]$ and $[r_0=3.6\times10^{-13}$ cm, $P=-0.08]$. From (39b) we then find $\theta^2(E=4.95)=0.55\pm0.25$ with $a=4.9$, and the value of $dZ/dE=2MaK/\hbar^2\theta^2(f^2+K^2)$ corresponding to it is represented on Fig. 2(a). This value of θ^2 is clearly smaller than the value $\theta^2(E=2.37)=1.4$ obtained from Fig. 3 for the same a. This variation of θ^2 indicates that the one-level approximation is inadequate for treating the s interaction over a $2\frac{1}{2}$-Mev range.

The curves given by Blatt and Jackson enable one to say something about the nature of the neutron interaction; according to Figs. 6 and 10 of their paper, the long-tailed interactions are excluded and a square well would have a radius of about 4.7 and a depth of about 11 Mev. In connection with the use of these curves, we note that according to almost any model, a node is

[58] Bockelman, Miller, Adair, and Barschall, Phys. Rev. **84**, 69 (1951).

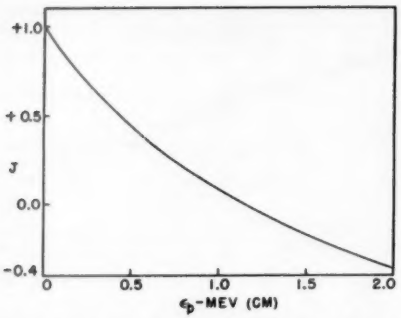

FIG. 5. The quantity J of Eq. (40c) as a function of the proton energy for an $s \rightarrow p$ transition in the capture of protons by C^{12} using a channel radius of 4.9×10^{-13} cm.

predicted for the internal wave function. Consequently, these may not apply exactly to our case although we would not expect very much change, other than in the determination of well depths, if the node were included. We have verified that a square well wave function with a node gives a $k\cot\delta$ plot that is nearly identical with that shown in Fig. 4 for the case without the node. However, the radius of the well is 4.0 and the depth is 35 Mev.

Also shown in Fig. 4 are the straight lines corresponding to $P=0$ with either the 3.68 or 3.10 levels as the bound s state. If the 3.68 level is taken as the bound s state, we find $P=-0.14$ with r_0 about 3.0; judging from Fig. 10 of reference 23, these values are unreasonable.

Returning to Fig. 2(a), it appears that in order to have the points and slopes determine a smooth curve, it is necessary to increase E for N^{13} with respect to C^{13} by about 150 kev. In the ensuing analysis of the p-interaction, it is shown that due to the level shift terms Δ_λ and the differences of the electromagnetic spin-orbit interactions of the odd particle, the ground-state excitation energy of N^{13} is shifted downwards with respect to C^{13} by about (39−27)-kev. Consequently, either the quantity $\langle V\rangle_r$ is (150+12)-kev less in the s state than in the ground state or else the $C^{12}+n$ and the $C^{12}+p$ nuclear interactions differ by this much. This diminution is only 5 percent of the total Coulomb energy due to the odd proton, and it is reasonable to expect this amount for a state having a large reduced width compared to that of the ground state (which will be shown to be about 15 times smaller). From a compilation of various theoretical calculations of Coulomb energies,[59] it appears that ±200 kev may be a reasonable estimate of possible variations of the internal Coulomb energy in different states of N^{13}.

The energy at which $Z(E)=0$ is the unshifted level position in the theory of W-E, corresponding to the boundary condition $b=0$ in (28); thus, $E_\lambda=1.3$ for C^{13} and 1.1 Mev for N^{13}. The reduced width at E_λ is $\theta_\lambda^2=1.5$. The energy required to increase Z by π is the level spacing, which is about 12 Mev. This large reduced width (the upper estimate given by the sum rule[64] is 3.0) and level spacing demonstrate that the interaction is essentially a two-body type with no amalgamation of the odd particle within the C^{12} core; (the number of nuclear traversals of the incident particle is θ^{-2} in the classical sense).

There is an additional datum on the s-wave interaction from the angular distribution of the scattering of 4.2-Mev protons by C^{12} ($E=5.9$ Mev.[60] From a phase shift analysis it was concluded that s-waves alone could account for this distribution with $\delta_0=127°$.[60] By means of (32b) we determine that $f=9.6$ and thus $Z=1.9$ for $Ka=3.0$, a value which is considerably displaced from the curves of Fig. 2a. This discrepancy may be due to the omission of the higher partial waves in the phase shift analysis or to the presence of narrow s resonances at higher energies causing Z to behave erratically (see IV on the $O^{16}+p, n$ s interactions where such erratic behavior is observed).

By introducing the neutron scattering data into the analysis and the use of (36), which effectively amounts to including the level spacing as a third parameter in the analysis, it has been possible partially to overcome the critical dependence on the channel radius in the level displacement computation, which was observed by Ehrman.[11] Figure 2(b) gives a plot of Z using $a=4.4$ wherein the N^{13} datum at 2.37 is displaced by less than 50 kev from the smooth curve determined by the $C^{12}+n$ data. Although a 150-kev discrepancy was observed with $a=4.9$, we would in fact expect $\langle V\rangle_r$ to decrease with increasing a. The resonance parameters as obtained from Fig. 2(b) are: $\theta_\lambda^2=2.0$, $E_\lambda=0.6$, $D=19$ Mev; these differ from those found with $a=4.9$. The quantities θ_λ^2 and E_λ are, however, by definition functions of a. This dependence has been investigated by Teichmann who shows that[7]

$$dE_\lambda/da=(\mathcal{U}-\epsilon_\lambda)\theta_\lambda^2/a \tag{42a}$$

and

$$d\gamma_\lambda^2/da=[2(\epsilon_\lambda-\mathcal{U})R_\infty-\gamma_\lambda^2]\theta_\lambda^2/a, \tag{42b}$$

where

$$R_\infty=\textstyle\sum_{\mu\neq\lambda}\gamma_\mu^2/(E_\mu-E_\lambda), \quad \theta_\lambda^2=2Ma\gamma_\lambda^2/\hbar^2;$$

$\mathcal{U}$ and ϵ are the quantities entering (3), and $R_\infty\approx\langle\gamma_\lambda^2\rangle_{\text{Av}}/D$. These two relations are a consequence of (3) and the definitions of E_λ, γ_λ^2. The observed radial dependences of θ_λ^2 and E_λ are in qualitative agreement with these derivatives. However, the variation of D with a is more than expected, which is probably, to a certain extent at least, because we are trying to obtain more information from the data than entitled to.

Having determined the s interaction parameters, we should be able to account for the energy dependence of the electric dipole radiative capture cross section for transitions to the ground state. The reduced charge number entering in (40a) is 6/13 for both neutron and proton capture so that, aside from a common E de-

[59] W. E. Stephens, Phys. Rev. **57**, 938 (1940).

[60] Heitler, May, and Powell, Proc. Roy. Soc. (London) **190**, 180 (1947).

pendence, the differences of the cross sections should be due to differences of the external wave functions. The $C^{12}(p, \gamma)$ resonance cross section, as measured by Fowler, Lauritsen, and Lauritsen[58] and also by Seagrave,[61] is $(1.25\pm0.15)\times10^{-4}$ barn. Hall and Fowler[62] as well as Bailey and Stratton[63] measured this cross section below resonance and found deviations from the usual Breit-Wigner formula, which increased with decreasing proton energy. In particular, the cross section at $\epsilon_p=120$ kev is $(6.1\pm0.9)\times10^{-10}$ barn, which is about two-times greater than the value predicted by the extension of the Breit-Wigner curve fitted to the resonance data (and taking into account the $(h\nu)^3$ dependence of the radiative width).

The thermal neutron capture cross section of graphite is listed as 4.5 mb and that of C^{13} as about 100 mb, so that the C^{12} isotopic cross section is about 3.5 mb[64] and perhaps less considering the possibility of contributions from impurities. This cross section is about five times smaller than that calculated by extending the $C^{12}(p, \gamma)$ resonance data, taking account of the differences of the external wave functions and the $(h\nu)^3$ factor but neglecting the external contribution to the transition moment.

Because of the large reduced width and level spacing of the initial s-state, these deviations are attributed to the omission in the usual resonance formula of the external contribution to the transition moment, rather than to large variations of the internal transition moment $\mathfrak{M}$ of (40b). Contributions to the capture from higher partial waves are estimated to be negligible.

When the values of f_c and θ_c obtained from Fig. 2(a) are substituted into (40c), the possible values of $\mathfrak{M}$ and θ_f which will satisfy the $C^{12}(p, \gamma)$ measurements at $\epsilon_p=456$ and 120 kev can be determined. Considering the experimental uncertainties, these values lie in the region of Fig. 6 common to the two sets of parallel lines for each measurement. The values of J required in (40c) are given in Fig. 5. The possible range of values for $\mathfrak{M}$ and θ_f can be considerably reduced by including the thermal neutron capture cross section to the ground state of C^{13} (for which $J=-0.70$ according to (40d)) which we assume to be between 1.8 and 3.5 mb considering the possibility that a part of the cross section may be due to transitions to excited states, as indicated below; (there are two sets of parallel lines because of the ambiguity in sign of $\mathfrak{M}+\theta_c\theta_f J$). With the assumption that $\mathfrak{M}$ can be treated as constant over a 2.9-Mev range of nuclear excitation energy (about one-fifth of the level spacing), the possible range of values is narrowed to the regions in Fig. 6 labeled I and II. Further comments on Fig. 6 follow the discussion of the p interaction.

Qualitatively, the anomalous behavior of the $C^{12}(p, \gamma)$ cross section is due to the fact that the external contribution to the moment is of the same sign as the internal contribution and increases with decreasing proton energy. Since the neutron scattering length of C^{12} is positive and only slightly larger than the channel radius, the external contribution to the $C^{12}(n, \gamma)$ process is opposite in sign to the internal contribution thus yielding a small cross section. In contrast, in the capture of thermal neutrons by Li^7 the negative scattering length provides a large external electric dipole transition moment, which is qualitatively capable of explaining the anomalously large cross section.[65]

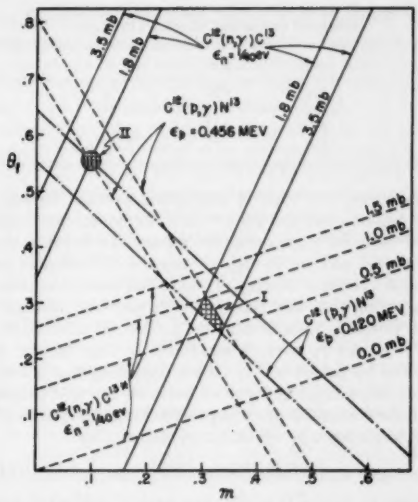

FIG. 6. Square root of the final-state reduced width plotted as a function of the internal transition moment $\mathfrak{M}$ for various transitions in the capture of s protons and neutrons by C^{12}.

In connection with the energy production in stars by means of the carbon cycle, it is required to know the C^{12} proton capture cross section at stellar temperatures. This cross section can be obtained with sufficient accuracy by writing (40f) as

$$\sigma_{c\gamma}=\pi\lambda_c^{-2}\omega(h\nu/h\nu_{res})^3\Gamma_{\gamma-res}{}^{\dagger}\Gamma_c{}^{\dagger} \times[1+C(E_{res}-E)]^2/[(E_{res}-E)^2+\tfrac{1}{4}\Gamma_c{}^{\dagger 2}], \quad (43)$$

the parameters $\Gamma_{\gamma-res}{}^{\dagger}$, $\Gamma_c{}^{\dagger}$ being found from the behavior of the cross section in the vicinity of the resonance and the constant C from the cross section at $\epsilon_c=120$ kev. At proton energies which are sufficiently below the resonance so that the width term in the denominator of (43) can be ignored, the expression obtained by this procedure is

$$\sigma_{c\gamma}=6.8\times10^{-6}(h\nu)^3\epsilon_c^{-1}[(0.42-\epsilon_c)^{-1}+2.7]^2\exp(-5.74\epsilon_c^{-\frac{1}{2}})$$

with $h\nu$ and ϵ_c in units of Mev, measured in the c.m. system. For example, at $\epsilon_c=28$ kev, $\sigma_{c\gamma}=6.1\times10^{-17}$ barn.

p Interaction

The magnetic moment of C^{13} falls very close to the Schmidt line for $J=l-\frac{1}{2}=\frac{1}{2}$ suggesting that an inde-

[61] J. Seagrave, Phys. Rev. **84**, 1219 (1951).
[62] R. N. Hall and W. A. Fowler, Phys. Rev. **77**, 197 (1950).
[63] C. L. Bailey and W. R. Stratton, Phys. Rev. **77**, 194 (1950).
[64] M. Ross and J. S. Story, Repts. Progr. Phys. **12**, 291 (1948).
[65] R. G. Thomas, Phys. Rev. **84**, 1061 (1951).

TABLE II. Level shifts in kev due to the electromagnetic spin-orbit interaction. $R_c=3.5\times10^{-13}$ cm.

Level	N^{13}	C^{13}
$d_{5/2}$	−21	18
$d_{3/2}$	32	−27
$p_{3/2}$	−11	9
$p_{1/2}$	21	−18

pendent-particle type of interaction prevails between the odd neutron and the C^{12} core. Moreover, the radiative width for a magnetic dipole transition between the $p_{\frac{1}{2}}$ excited and the $p_{\frac{1}{2}}$ ground states of N^{13} indicates an almost complete overlap of the radial wave functions, suggesting that this type of interaction may also prevail in the $p_{\frac{1}{2}}$ state with $J=l+\frac{1}{2}$. The radiative width, $\omega\Gamma_\gamma$[66] of the $p_{\frac{1}{2}}$ level, as measured by Van Patter[29] as well as by Seagrave,[61] is 1.3 ev. Assuming that a two-body interaction is involved between the odd proton and the core and neglecting possible interaction effects,[67] the width for a $p_{\frac{1}{2}}\rightarrow p_{\frac{1}{2}}$ transition is given by[68]

$$\omega\Gamma_\gamma=(2/9)(h\nu)^3(e^2/\hbar c)(Mc^2)^{-2}(g_s-g_l)^2x^2, \quad (44)$$

where g_s, g_l are the spin and orbital g factors, and $x(\leqslant 1)$ measures the extent of overlap of the radial wave functions. With $g_s=5.58$, $g_l=0.96$, $h\nu=3.52$, we find $x=0.90$. Such a slight difference of the wave functions is to be expected, even with similar interactions, because of the difference of the binding in the external region. Further evidence for the similarity of these two states is provided by the fact that the intensities of the $N^{15}+d$ alpha-particle groups associated with them are very nearly equal.[40]

From a consideration of the shell model with strong spin-orbit coupling and of level assignments in other nuclei, it has been proposed that the odd proton of the $p_{\frac{1}{2}}$ state of N^{13} is an excited $2p_{\frac{1}{2}}$ configurational state whereas in the ground state it is in a $1p_{\frac{1}{2}}$ configurational state.[69] If this hypothesis is correct, we would expect a much smaller value of the overlap, x. On the other hand, it would seem consistent with the evidence for the large overlap to consider the $p_{\frac{1}{2}}$ state as a $p_{\frac{1}{2}}$ hole in the $1p$ proton shell and the $p_{\frac{1}{2}}$ ground state as a $p_{\frac{1}{2}}$ hole in the $1p$ proton shell.

According to the analysis of Jackson and Galonsky,[32] the resonance parameters ascribed to the $p_{\frac{1}{2}}$ component of the doublet at $\epsilon_p=1.7$, as observed in the elastic scattering measurement, are: $E_{res}=3.501$, $E_\lambda=3.508$ (with the boundary condition $b=a^{-1}$), $\Gamma^\dagger$ (c.m.)$=0.042$ Mev, $\gamma_\lambda^2=0.377\times10^{-13}$ Mev·cm ($\theta^2=0.08$). The observed width is smaller than the value 74 ± 9 kev obtained by Van Patter or 70 ± 10 kev obtained by Seagrave from $C^{12}(p,\gamma)$. As mentioned above, the capture data fit a one-level formula and it is unlikely that the $d_{\frac{3}{2}}$ component of the doublet contributes significantly; therefore, we use the 70-kev value, which corresponds to $\theta^2=0.12$, for computing the boundary-condition displacement of the corresponding $p_{\frac{1}{2}}$ levels. In the one-channel, one-level approximation the contribution to this displacement from the $p_{\frac{1}{2}}$ levels is then

$$\Delta_{p_{\frac{1}{2}}}(C^{13})-\Delta_{p_{\frac{1}{2}}}(N^{13})=\gamma^2(g_p{}^{Re}-g_n{}^{Re})=90 \text{ kev},$$

from (30b) with $a=4.9$. In order to compute the effect on the net displacement from the ground-state boundary condition difference, it is necessary to know the ground-state reduced widths. Assuming them to be equal, this information is provided by Fig. 6, there being, however, the two possible values $\theta_l^2=0.07$ or 0.3, from regions I and II, respectively. With these values and $l=1$, the ground-state boundary-condition displacement is $\Delta_{p_{\frac{1}{2}}}(C^{13})-\Delta_{p_{\frac{1}{2}}}(N^{13})=27$ or 100 kev, respectively.

Inglis[70] and Mottelson[71] have considered the difference of the electromagnetic spin-orbit interactions in their treatments of the displacements of the first excited states of Be^7 and Li^7; a part of the displacements of the $N^{13}-C^{13}$ levels may be due to this effect. Assuming again a two-body interaction and a uniform distribution of charge throughout a radius R_c, the contribution to $\langle V\rangle_\tau$ from a particular level is[70,72]

$$Ze^2(T^--g_s)\mathbf{I}\cdot\mathbf{s}/2M^2c^2R_c^3, \quad (45)$$

where Z is the core charge, $T^-=1$, 0 for an odd proton or neutron respectively, and g is the spin g-factor. Table II lists the shifts for various states using the Coulomb radius, $R_c=1.46A^{\frac{1}{3}}$. If some of the orbital motion is shared by the core, the shifts are expected to be smaller in absolute value.

From Table II, the contribution to the differences of the E_λ are then

$$E_{p_{\frac{1}{2}}}(C^{13})-E_{p_{\frac{1}{2}}}(N^{13})=\quad 20 \text{ kev},$$
$$E_{p_{\frac{1}{2}}}(C^{13})-E_{p_{\frac{1}{2}}}(N^{13})=-39 \text{ kev}.$$

The net displacement of the excited $p_{\frac{1}{2}}$ states, as would appear in Fig. 1, is the difference of the total displacements of the excited and ground states: $90-(27 \text{ or } 100)+20+39=122$ or 49 kev, the observed value being 160 kev. Although neither of the calculated values can be considered as in good agreement with the observed value, the ground state reduced width $\theta^2=0.07$ from

[66] The difference between Γ_γ and $\Gamma_\gamma{}^\dagger$ at this resonance is only a few percent and may therefore be ignored. This difference is small because the proton reduced width is small.

[67] R. G. Sachs and M. Ross, Phys. Rev. **84**, 379 (1951).

[68] E. U. Condon and G. Shortley, *Theory of Atomic Spectra* (Cambridge University Press, Cambridge, 1935).

[69] Koester, Jackson, and Adair, Phys. Rev. **83**, 1250 (1951).

[70] D. R. Inglis, Phys. Rev. **82**, 181 (1951), Eq. (15). This equation should read $E_m=(2/A)(137/1837)^2Zgmc^2=0.0032Z(g/2)mc^2$. The magnetic contributions there attributed to the droplet model should thus be reduced by a factor of two, bringing them much more nearly in agreement with the results of the more refined oscillator treatment on which the main conclusions of the paper were based [D. R. Inglis (private communication)].

[71] Ben R. Mottelson, Phys. Rev. **82**, 287 (1951).

[72] L. Rosenfeld, *Nuclear Forces* (Interscience Publishers, New York, 1948), Sec. 15.22, Eq. (11).

region I of Fig. 6 is preferred; the 38-kev discrepancy may be due to the diminution of the internal Coulomb energy of the excited state from that of the ground state. Although it was noted that this energy may be uncertain by as much as 200 kev, the overlap of the $p_{\frac{1}{2}}$ and $p_{\frac{3}{2}}$ radial wave functions indicates that the diminution is probably small. By fitting square-well wave functions to the logarithmic derivatives of these states, a Coulomb energy of the excited state is obtained which is 50 kev less than that of the ground state. This observation, however, is only intended to be suggestive, because square well wave functions are not compatible with the observed reduced widths of these levels.

It is noteworthy that the ground-state reduced width $\theta^2=0.07$ is the same order magnitude, although somewhat smaller, as that of the $p_{\frac{3}{2}}$ excited state. If the $p_{\frac{1}{2}}$ and $p_{\frac{3}{2}}$ states are indeed similar, we would in fact expect the reduced width of the more tightly bound ground state to be smaller.

It is possible to give some justification to the use of the one-channel approximation in the boundary-condition level displacement calculations by giving an upper-limit estimate of the displacements from other possible (negative-energy) alternatives. Because the reduced widths of the p levels are considerable smaller than $3\hbar^2/2Ma$, the sum over reduced widths,[64] other alternatives may have large reduced widths and contribute significantly to the displacements. As an example, we consider as alternatives for the $p_{\frac{1}{2}}$ states,

$$C^{13*}: Be^9+\alpha, \quad \epsilon=-7.0 \text{ Mev},$$
$$N^{13*}: B^9+\alpha, \quad \epsilon=-6.0 \text{ Mev};$$

and for the $p_{\frac{3}{2}}$ states,

$$C^{13}: Be^{9*}+\alpha, \quad \epsilon=-13.1 \text{ Mev},$$
$$N^{13}: B^{9*}+\alpha, \quad \epsilon=-11.9 \text{ Mev},$$

the excited state of Be^9 being the one at 2.4 Mev which we assume to be $P_{\frac{3}{2}}$ and B^{9*} being its mirror; the alpha-particle is assigned zero orbital angular momentum. If the reduced widths for both pairs of alternatives are taken to be the upper estimate, $3\hbar^2/2Ma$, the displacements are found to be 120 kev in both states. The net displacement of the excited levels would be the difference and thus zero. (If the reduced widths for these alternatives were not assumed to be equal, any net displacement between ± 120 kev could be obtained.) Other possible alternatives for these levels would have larger binding energies (smaller $|g_s^{Be}-g_p^{Be}|$) and thus give rise to smaller shifts. As this is an extreme example, we have some assurance that these alternatives do not contribute significantly to the net level displacement.

We return to the discussion of the radiative capture of thermal neutrons by C^{13}. The cross section for transition to the 3.68 level is predicted in Fig. 6 as a function of $\mathfrak{M}$ and θ_f. Although the factor $q'(h\nu)^3$ of (40a) is 30 times smaller for a transition to this level than to the ground state, the external contribution to the moment may predominate because the binding energy of the final state is small ($B=1.27$ Mev so that $J=-4.6$). From the width of the mirror level of N^{13}, θ_f is expected to be about 0.35 and from the evidence for the similarity of the $p_{\frac{1}{2}}$ and $p_{\frac{3}{2}}$ radial wave functions it is plausible that $\mathfrak{M}\approx 0.3$. With these values we obtain from Fig. 6 a cross section of about 1.5 mb, which is not inconsistent with the measurements by Kinsey *et al.*[73] of the carbon neutron capture spectrum. Although these investigators do not report a gamma-ray of this energy, a rise in the counting rate with an end point corresponding to a 3.7-Mev transition is visible in Fig. 3 of their paper; considering the rapid diminution of the pair spectrometer sensitivity with decreasing gamma-ray energy, we estimate the upper limit for the intensity of this gamma-ray to be about 75 percent of that of the 4.95 ground-state transition, which puts an upper limit of 1.5 mb on the cross section. Additional evidence favoring such a transition is given by ionization-chamber measurements of photoprotons from the disintegration of deuterons by the capture gamma-rays;[74] a 3.65-Mev transition having an intensity comparable to that of the 4.95-Mev gamma-ray was observed. However, gamma-rays of 3.05, 3.40, and 4.1 Mev were also observed which we cannot account for in terms of the proposed level assignments; a cascade through the 3.10 level should not occur since a single nucleon $s_{\frac{1}{2}}\rightarrow s_{\frac{1}{2}}$ (forbidden) transition would be required. The possibility of impurity contributions in this measurement is indicated.

d Interaction

According to the analysis of Jackson and Galonsky, the resonance parameters ascribed to the $d_{\frac{3}{2}}$ level of N^{13} are: $E_{res}=3.549$ Mev, $E_\lambda(b=2/a)=3.593$, $\Gamma^\dagger$ (c.m.) $=0.040$ Mev, $\gamma_\lambda^2=2.36\times 10^{-13}$ Mev·cm ($\theta^2=0.50$). In the one-channel, one-level approximation the calculated displacement of the corresponding $d_{\frac{3}{2}}$ levels due to the boundary-condition difference is $\Delta_{d_{\frac{3}{2}}}(C^{13})-\Delta_{d_{\frac{3}{2}}}(N^{13})=190$ kev. To this amount, 78 kev is added for the differences of the electromagnetic spin-orbit interactions (from Table II) and 27 kev subtracted for the ground-state boundary-condition displacement, obtaining a net displacement of 240 kev, which is 100-kev smaller than observed. This discrepancy may be due to the diminution of the internal Coulomb energy of the excited state as a consequence of its higher angular momentum and rather large reduced width. For instance, a square well, d orbital wave function has 80 kev less internal Coulomb energy in a uniformly charged sphere than a corresponding p function; but again, this observation is intended only to be suggestive as a square well wave function with the proper f value has a reduced width four-times larger than observed.

As the reduced width for this interaction is large and as there are no data permitting consideration of the level spacing, the boundary-condition shift computation is rather sensitive to the assumed channel radius. For example, with $a=4.4$ the boundary-condition displacement is 240 kev rather than 190 kev; with $a=3.9$ it is 320 kev.

[73] Kinsey, Bartholomew, and Walker, Can. J. Phys. **29**, 1 (1951).
[74] Richard Wilson, Phys. Rev. **80**, 90 (1950).

No evidence has been found below 6 Mev for a $d_{\frac{1}{2}}$ interaction in either nucleus.

IV. COMPARISON OF THE $F^{17}-O^{17}$ WITH THE $N^{13}-C^{13}$ s LEVELS

The analysis of the angular distribution of protons and neutrons from the $O^{16}+d$ reaction indicates that the first excited states of O^{17} at 0.871 Mev and of F^{17} at 0.536 Mev are formed by the capture of an s neutron and proton, respectively, and that the ground states are formed by the capture of a d neutron and proton, respectively.[76-77] The spin of O^{17} in the ground state is 5/2 making the assignment $J=l+\frac{1}{2}$ in agreement with the observed magnitude of the magnetic moment on the independent-particle model.[78] The measured quadrupole moment is also consistent with this assignment if the O^{16} core is considered to be undistorted but its center displaced from the center of mass due to the presence of the odd neutron.[79] These assignments are consistent with the measured internal conversion coefficient of the O^{17*} radiation, which indicates that the transition is electric quadrupole or a mixture of this and magnetic dipole;[80] the $s_{\frac{1}{2}}$ assignment to O^{17*} is also compatible with the observed isotropy of the gamma-radiation accompanying the deuteron reaction.[81] Koester, Jackson, and Adair[69] have noted that these two levels of $F^{17}-O^{17}$ are the analogs of the first and third excited states of N^{13}, though in reverse order, and fit in a shell model scheme. Here we show that there is indeed a similarity in the energy dependence of the interactions of s nucleons with O^{16} and C^{12}.

Figure 2(a) also shows $Z(E)$ for the $O^{16}+p$, n interactions with $Ka=3.0$, 4.0 using a channel radius of 5.27. The points at $E=0.536$ and 0.871 are obtained from the values of f_s for the bound levels. The point at $E=4.145$ Mev is from the O^{16} epithermal neutron scattering cross section, 3.73 ± 0.04 barns, as measured by Melkonian.[82] The points determine a straight line which is parallel to the $C^{12}+p$, n line, indicating that the respective reduced widths and level spacings are about the same. Since the C^{13} neutron binding energy is 0.8-Mev greater than that of O^{17}, the 2½-Mev displacement of the lines indicates that the O^{16} interaction is about 1½-Mev stronger despite the use of a larger channel radius. The low energy neutron scattering cross section for O^{16} can be calculated from the extrapolation of $Z(E)$ beyond 4 Mev; the values obtained are consistent with the observed "nonresonant" scattering up to $\epsilon_n=2$ Mev. In this range Z is near $\pi/2$ so that f is large and the scattering essentially potential for the channel radius, 5.27, used in the calculation.

Heitler, May, and Powell[60] also measured the s-wave phase shift from the scattering of 4.2-Mev protons by O^{16} ($E=4.6$). From a phase shift analysis they conclude that $\delta_0=140°$; for this shift we find $Z=2.2$, a value lying considerably off the dashed lines of Fig. 2(a) through the low energy points. As with their $C^{12}+p$ measurement, the discrepancy may be due to the omission of the higher partial waves in the analysis or to an erratic behavior of Z. In connection with the latter possibility, Baldinger, Huber, and Proctor[83] find from a phase shift analysis of the scattering of neutrons by O^{16} an inverted s resonance at $\epsilon_n=2.4$ Mev ($E=6.4$) having a width of 180 kev; this level is also identified as s-wave by Bockelman *et al.*[58] The presence of such a narrow level implies that Z increases by π in a narrow energy interval. A similar phenomenon has been observed by Laubenstein from the scattering of protons by O^{16};[84] at $\epsilon_p=2.66$ ($E=3.1$) there is an inverted resonance which is only 20-kev wide and attributed to s protons, implying that Z also increases by π in a narrow region about $E=3.1$. According to the sum-over-levels,[7,9] the width of this resonance corresponds to a level spacing of about 150 kev and the neutron resonance at $E=6.3$ to a level spacing of about 1 Mev. Such level spacings are not compatible with the observed level density. However, it is not known to what extent the sum-over-levels is valid or, equivalently, to what extent a smooth energy dependence for Z is to be expected. At any rate, it appears that there are narrow s-levels in addition to the broad levels, the latter being depicted by Fig. 2(a).†

The energy difference of the ground states of F^{17} and O^{17}, as obtained from recent Q determinations,[48] is about 140 kev less than the value obtained from the assumption of a uniform distribution of charge throughout a volume with a radius equal to $1.46A^{\frac{1}{3}}$. This deviation may be partly due to the boundary-condition level displacement. If the reduced widths of the ground states of F^{17} and O^{17} are assumed to be the same as that of the $d_{\frac{1}{2}}$ state of N^{13}, we obtain a boundary-condition displacement of $\Delta d_{\frac{1}{2}}(O^{17})-\Delta d_{\frac{1}{2}}(F^{17})=190$ kev and an additional displacement of 40 kev due to the electromagnetic spin-orbit interaction (from Table II). Therefore, the nuclear excitation energy of F^{17}, referred to the ground state of O^{17}, may be about 200 kev less than its value referred to the ground state of F^{17}; if this is the case, the point in Fig. 2(a) at $E=0.536$ should actually be placed somewhere between $E=0.3$ and 0.4 when comparing with the O^{17} data. The possibility of this shift does not affect the above conclusions concerning the $O^{16}+p$, n s interaction.

V. CONCLUSIONS

An analysis using recent nuclear resonance theories has been made of the available data on the interaction

[76] Burrows, Gibson, and Rotblat, Phys. Rev. **80**, 1095 (1950).
[77] Fay Ajzenberg, Phys. Rev. **83**, 693 (1951).
[78] El-Bedewi, Middleton, and Tai, Proc. Phys. Soc. (London) **A64**, 756 (1951).
[79] F. Alder and F. C. Yu, Phys. Rev. **81**, 1067 (1951).
[80] Geschwind, Gunther-Mohr, and Silvey, Phys. Rev. **85**, 474 (1952).
[81] R. G. Thomas and T. Lauritsen (to be published).
[82] Jacques Thirion, Compt. rend. (1951).
[83] E. Melkonian, Phys. Rev. **76**, 1750 (1949).
[84] Baldinger, Huber, and Proctor, Phys. Rev. **84**, 1058 (1951).
[85] Laubenstein, Laubenstein, Koester, and Mobley, Phys. Rev. **84**, 12 (1951); R. A. Laubenstein and M. J. W. Laubenstein, Phys. Rev. **84**, 18 (1951).

† *Note added in proof:* According to a private communication from F. J. Eppling of the University of Wisconsin, angular distributions of protons scattered by O^{16} indicate that the $E=3.1$ Mev level is $p_{\frac{1}{2}}$ rather than $s_{\frac{1}{2}}$.

of s, p, d nucleons with C^{12}, and of s nucleons with O^{16}. The large reduced widths and level spacings characterizing the s interactions at low excitation energies are indications that two-body types of potentials predominate between the odd nucleon and the C^{12} and O^{16} cores; the near equality of the resonance parameters for the s-nucleon interaction with C^{12} and O^{16} is an indication that the respective potentials are similar. The displacement of the corresponding s states of N^{13} and C^{13} is accounted for within an uncertainty of about 25 percent which is due to the lack of precise knowledge concerning the internal Coulomb energy of the excited states. Within this uncertainty, there is no evidence for the inequality of nn and pp nuclear forces. In the $O^{16}+p$, n s interactions there appear to be narrow levels in addition to the broad level. By utilizing radiative capture data between various states, it is possible to compute the level displacement of the conjugate $p_{\frac{1}{2}}$ states, again with an uncertainty of about 25 percent, the agreement with observation being satisfactory. The reduced widths of the $p_{\frac{1}{2}}$ and $p_{\frac{3}{2}}$ states are about 15-times smaller than the value expected for a simple two-body potential, such as a square well, between the odd particle and core, and it is inferred from the sum rule for processes that other alternatives are involved. In contrast, the magnetic moment of the $p_{\frac{3}{2}}$ state of C^{13} and the large value of the internal transition moment $\mathfrak{M}$ connecting the $s_{\frac{1}{2}}$ and $p_{\frac{3}{2}}$ states suggests that the single alternative, odd nucleon plus C^{12} core, occurs a major fraction of the time in the p states. Thus, there is evidence for both the independent- and many-particle models; this paradox is not new, and we refer to interesting discussions by Weisskopf.[85]

The position of the $d_{\frac{3}{2}}$ state in C^{13} is somewhat uncertain and the computation of the displacement sensitive to the assumed channel radius. At any rate, the splitting in C^{13} of the $p_{\frac{1}{2}}$ and $d_{\frac{3}{2}}$ levels, which are almost unresolved in N^{13}, can be qualitatively understood as due to the differences of the electromagnetic properties of the odd nucleon.

[85] V. F. Weisskopf, Helv. Phys. Acta **23**, 187 (1950); Science **113**, 101 (1951).

Some concluding remarks concerning the channel radius may be appropriate. In the present investigation a rather large radius, $a=4.9\times10^{-13}$ cm in the case of the C^{12} interactions, was used to insure that the nuclear forces do not extend significantly into the external region. It was found that a 10 percent smaller radius gave a better account of the level displacements associated with the s and d interactions with C^{12}; however this observation is not particularly significant in view of the other uncertainties in the computation, such as in the internal Coulomb energy and in the representation used for the energy dependence of the logarithmic derivatives. It does not appear possible to solve for a from the given data,[86] although a lower limit of 3.6×10^{-13} cm could be set in the case of the $C^{12}+p$ s-wave interaction. The value $a=4.9$ is from 20- to 50-percent larger than the values obtained in various measurements (indicated on Fig. 3), but this is not unreasonable because these measurements do not necessarily indicate the limit of the nuclear interactions. The resonance parameters are found to be sensitively dependent upon a, which is to be expected in the barrier region where these parameters are, by definition, functions of a. On the other hand, in applications involving approximations the cross-section formulas are found to be rather insensitive to reasonable variations of a, provided that the same value is consistently used.

The author wishes to express his appreciation to Professors T. Lauritsen, R. F. Christy, W. A. Fowler, and Dr. Claude Bloch for their helpful discussions and suggestions. He is grateful to the AEC for a predoctoral fellowship which enabled him to carry out this investigation.

[86] In a recent paper by D. C. Peaslee, Phys. Rev. **85**, 555 (1952), a "phenomenological" radius for C^{13} is determined from the same data as treated here. The significance of this determination is questionable because the critical radial dependence of the N^{13} s proton reduced width was apparently neglected. Taking into account this radial dependence, the radius so determined would actually be that radius which would enable the one-level approximation to fit the interaction data from $E=2.37$ to 4.95 Mev; we could not determine such a radius.

Some Neutron Deficient Strontium Isotopes*

STANLEY V. CASTNER† AND D. H. TEMPLETON
Radiation Laboratory and Department of Chemistry, University of California, Berkeley, California
(Received August 25, 1952)

Bombardment of rubidium with protons produced Sr^{81}, half-life 29 minutes, Sr^{82}, half-life 25 days, and Sr^{83}, half-life 38 hours. Sr^{81} and Sr^{82} are assigned on the basis of their positron decay to known Rb^{81} and Rb^{82}, respectively. The half-life of Rb^{83} has been redetermined as 83 days, and it has been shown that it decays in part to the 1.8-hour Kr^{83m}. Sr^{82} probably decays by electron capture to a short-lived isomer of Rb^{82}, which in turn decays by emission of 3.15-Mev positrons. In this case, the mass assignment is based on the energy required to produce the activity in a bombardment, because the known Rb^{82} was not observed as a decay product.

BY bombarding rubidium chloride with protons at energies from 25 Mev to 100 Mev in the Berkeley 184-inch synchrocyclotron, we have prepared three new strontium isotopes and have studied their radioactivities. Sr^{81} and Sr^{83} have been identified by their decay to Rb^{81} and Rb^{83}, whose masses were assigned by Karraker and co-workers[1,2] with a mass spectrograph. The third activity is assigned to Sr^{82} on the basis of the energy required to produce it. There seems to be no previous report of any strontium isotopes of mass less than 84.

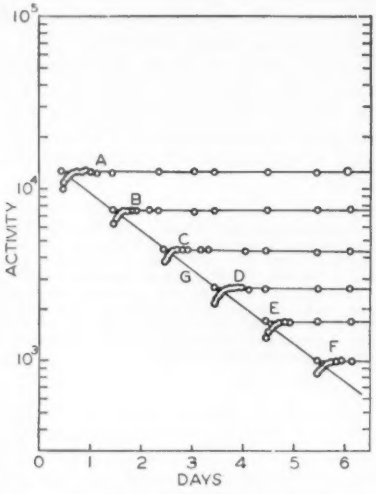

FIG. 1. Yield of Rb^{83} as a function of time of separation from Sr^{83}, curve *G*. Curves *A* to *F* show the growth of Kr^{83m} into the individual rubidium samples. Each curve is corrected for chemical yield of rubidium.

Sr^{83}

In a bombardment of a thick target of rubidium chloride for 1 hour with 25-Mev protons, the strontium fraction, isolated as described below, showed the following activities: Sr^{85m}, 70 minutes half-life; Sr^{85}, 65-days half-life, Sr^{87m}, 2.7-hours half-life; and an unknown activity of 38-hours half-life. Subsequent bombardments at higher energy also produced this new activity. From a single aliquot of strontium activity, rubidium was separated at 24-hour intervals for a week. The slope of the yield *vs* time curve (Fig. 1) corresponded to a 34-hour half-life. Each rubidium sample showed an initial growth at a rate consistent with the 1.8-hour half-life of Kr^{83m}. The assignment of Kr^{83m} has been checked by Bergström, Thulin, and Andersson[3] with an electromagnetic isotope separator. The subsequent decay, measured in four cases for more than 2 years, corresponded to a half-life of 83 days. Thus the 38-hour activity is Sr^{83}, decaying to Rb^{83} which in turn decays in part to Kr^{83m}. The discrepancy between the half-life of Sr^{83} determined by decay and that determined by the yield of rubidium is probably due to a small loss of strontium in each step, and the former value is considered more reliable. The value 83 days determined here for the half-life of Rb^{83} is much more reliable than the value 107 days reported previously[2] which was based on decay of a much weaker sample. The decay of Rb^{83} to Kr^{83m} was not observed previously.

Measurements on the $\pi\sqrt{2}$ beta-spectrometer described by Hyde and O'Kelley[4] have shown that Sr^{83} has positrons with 1.15 ± 0.05 Mev energy limit as determined by a Kurie plot of the spectrum (Fig. 2), and electron lines corresponding to *K* and *L* conversion of gamma-rays of energies 0.040, 0.074, 0.101, 0.151, and 0.165 Mev. Absorption measurements with beryllium, silver, and lead showed the presence of *K* x-rays and gamma-rays. The energies of the gamma-rays are not estimated because of interference from other activities.

Rb^{83}

Aluminum, beryllium, and lead absorption measurements show that Rb^{83} (half-life 83 days) emits elec-

* This research was performed under the auspices of the AEC.
† Now with E. I. du Pont Company, Oak Ridge, Tennessee.
[1] Reynolds, Karraker, and Templeton, Phys. Rev. **75**, 313 (1949).
[2] D. G. Karraker and D. H. Templeton, Phys. Rev. **80**, 646 (1950).
[3] Bergström, Thulin, and Andersson, Phys. Rev. **77**, 851 (1950).
[4] E. K. Hyde and G. D. O'Kelley, Phys. Rev. **82**, 944 (1951).

trons, K x-rays, and gamma-rays. The most energetic gamma-ray is estimated to be 0.8 Mev in energy. Measurements with a crude beta-spectrograph ("bender") indicate that the energies of the electrons correspond to gamma-rays of 0.15 and 0.45 Mev, but these values are only approximate.

Sr^{81}

With protons of 60-Mev energy and above, another activity, with half-life 29 minutes, was observed in the strontium fraction. Separation of rubidium at 20-minute intervals for 4 hours resulted in yields which fell off with time according to a half-life of 22 minutes. Again the discrepancy was assumed to be due to loss of strontium at each separation step. This rubidium decayed with a 4.7-hour half-life. Its identity as Rb^{81} was further confirmed by the detection with the "bender" of soft electrons (~0.2 Mev) whose intensity was decreased by flaming, but which rapidly grew in again. These electrons are due to Kr^{81m}, with 13-second half-life. The "bender" also showed positrons, whose energy by aluminum absorption was 1.1 Mev, compared with 0.990 Mev reported by Karraker and Templeton.[2] Thus the 29-minute activity is Sr^{81}.

To eliminate the possibility that growth of daughters distorted the original decay curve and thereby caused an incorrect half-life to be derived, the following experiment was carried out. Strontium was separated from several aliquots at regular intervals and immediately counted. A plot of these initial activities, which are substantially free of daughter activities, represents the decay of the strontium itself. Such a curve gave 31 minutes as the half-life of Sr^{81}.

Sr^{81} emits both positrons and conversion electrons, but time did not permit determination of their energies.

Sr^{83}

With protons of 40-Mev energy and above, a strontium activity of 25-day half-life was observed. A search for a rubidium daughter activity revealed none with half-life between a few minutes and 1 year. This activity is tentatively assigned to Sr^{83} on the basis that more energy is required to produce it than Sr^{82}, and less than Sr^{81}. Because of the failure to observe the 6.3-hour Rb^{82} as a daughter, additional chemical tests were made to verify that the activity was actually a strontium isotope. Passage through a cation exchange resin produced no change in the ratio between the 25-day and 38-hour activities. In addition, no activity of similar half-life and radiation characteristics has been reported for any other element. Thus we are forced to conclude that Rb^{82} exhibits isomerism, and that little or none of the Sr^{82} decays to the 6.3-hour state.

Measurements with the $\pi\sqrt{2}$ spectrometer have shown that Sr^{82} emits positrons with 3.15 ± 0.03 Mev energy limit (Fig. 3). Because of their high energy, these positrons probably come from a short-lived rubidium daughter rather than from Sr^{82} itself. Lead

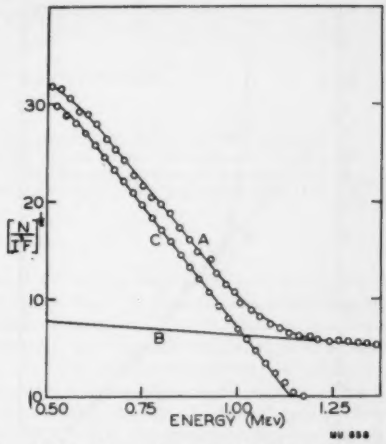

FIG. 2. Kurie plot of positron spectra of Sr^{82} and Sr^{83}. A, combined spectra; B, extrapolation of Sr^{83} spectrum; C, spectrum for Sr^{82}.

absorption measurements indicate gamma-rays of 0.95 and 0.15 Mev. The "bender" showed electrons corresponding to at least two gamma-rays in the range 0.15 to 0.40 Mev. Without more data it is impossible to say which of these radiations belong to Sr^{83} and which to Rb^{82m}.

TARGET PREPARATION

Spectrographic analysis of stock rubidium nitrate showed its cation to consist of 86 percent rubidium, 5 percent cesium, 8 percent potassium, and 1 percent sodium. About 1 gram of this salt was purified by elution from a Dowex-50 cation exchange column 11 mm in diameter and 81 cm in length, washing with 6 M HCl at a rate of 0.2 ml per minute. The sodium and cesium were eluted in peaks well separated from the rubidium, and most of the potassium was removed. About 0.6 g of rubidium chloride was obtained containing 0.4 percent potassium and spectroscopically free of sodium and cesium. Targets for bombardment in the 184-inch cyclotron were made by wrapping 25 to 50 mg of this purified rubidium chloride in aluminum foil 0.001 inch thick.

CHEMICAL SEPARATIONS

After bombardment with protons the rubidium chloride was dissolved in water. The solution was boiled to expel any inert gas isotopes. Strontium carrier was added and precipitated with excess fuming nitric acid. The resulting suspension was chilled in an ice bath for 5 minutes and then centrifuged. The supernatant solution containing the rubidium was removed, and the strontium nitrate was dissolved in a small amount of water. A few milligrams of the stock rubidium nitrate

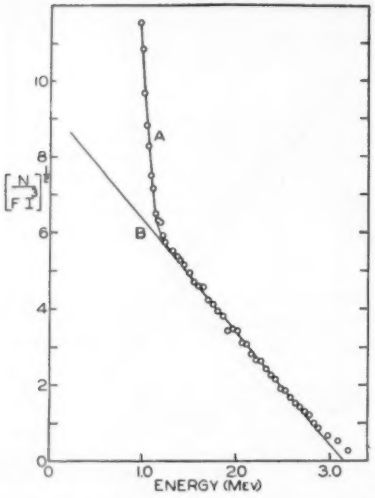

FIG. 3. Kurie plot of positron spectrum of Sr^{85}, curve *B*; these positrons probably belong to a short-lived Rb^{85m}. The initial part of the curve, marked *A*, contains activity due to Sr^{83}.

was added to the solution, and the strontium was reprecipitated with fuming nitric acid. After removal of the supernatant, the precipitate was redissolved and diluted to an arbitrary volume from which several accurately measured aliquots were taken. The strontium in an aliquot was again reprecipitated with fuming nitric acid. After removal of the supernatant, the precipitate was dissolved in water and the solution neutralized by bubbling ammonia through the solution. A few milliliters of a saturated solution of ammonium oxalate was added to precipitate the strontium as $SrC_2O_4 \cdot H_2O$. After removal of the supernatant, the precipitate was washed once with water, once with 95 percent ethanol and finally slurried up in 0.5 ml of 95 percent ethanol and placed on a previously weighed aluminum dish 0.002 inch thick and approximately 1.0 inch in diameter. The ethanol was evaporated to dryness with a heat lamp. The sample was allowed to cool and was then weighed to determine the chemical yield of the strontium. The dish was mounted for counting. In the initial bombardments, the purification procedures were extended to include a silve chloride precipitate scavenge, and a portion of the strontium fraction was passed throguh a Dowex-50 cation resin column. As no differences were noted between the decay curves of the strontium which had undergone these additional steps of purification, and the decay curves of the strontium which had not undergone such measures, these steps were omitted in subsequent bombardments as consuming too much time.

To isolate the radioactive rubidium in an aliquot which resulted from the strontium decay, the following procedures were used: a solution containing a known amount of stable rubidium was added to the aliquot. The strontium was precipitated with excess fuming nitric acid. The resulting suspension was chilled in an ice bath for 5 minutes and then centrifuged. The supernatant was removed to a clean centrifuge cone and evaporated to approximately 0.5 ml. A few milligrams of strontium was added and precipitated with more fuming nitric acid. Again the supernatant was removed to a clean centrifuge cone and evaporated to about 0.5 ml. The solution was chilled and 0.5 ml of 70 percent $HClO_4$ was added to precipitate the rubidium as $RbClO_4$. This precipitate was washed once with 50 percent ethanol, once with 95 percent ethanol and finally slurried up with 0.5 ml of 95 percent ethanol onto a previously weighed aluminum dish. The ethanol was evaporated with a heat lamp. The sample was allowed to cool and was then weighed to determine the chemical yield of rubidium. The sample was mounted for counting.

Radioactive krypton was expelled from rubidium samples by heating the rubidium sample with a bunsen burner to dull redness. For the purposes of this separation, the rubidium was mounted on 0.020-inch Monel metal disks.

Decay and absorption measurements were made with Amperex, chlorine-quenched, argon-filled, end-window Geiger-Müller counters. The window thickness was approximately 4 mg/cm² of mica.

Samples for the $\pi\sqrt{2}$ beta-spectrometer were mounted on Tygon films of 20 to 30 μg/cm² with about 10 to 50 μg of material in the sample.

Radiations of Ce^{143}†

W. H. Burgus
Los Alamos Scientific Laboratory, Los Alamos, New Mexico
(Received July 31 1952)

A spectrometric investigation of the radiations of Ce^{143} has revealed that there are beta-ray groups of 1.090±0.005, 1.390±0.005, and 0.710±0.010 Mev maximum energy. In addition, there was evidence for a fourth lower energy group which could not be resolved. Electromagnetic radiations of energies 0.0349 ±0.001, 0.126±0.005, ~0.160±0.010, 0.289±0.005, 0.356±0.005, 0.660±0.010, and 0.720±0.010 Mev were found. A decay scheme for Ce^{143} is proposed.

I. INTRODUCTION

EARLY studies of the radiations of Ce^{143} using absorption methods showed the presence of a beta-ray of maximum energy ~1.36 Mev[1–3] and gamma-rays of energy about 0.5 Mev[1] or 0.6 Mev.[2] Later absorption and coincidence studies[4] indicated additional gamma-rays of 0.040, 0.20, and 0.89 Mev. More recent spectrometric studies[5] have shown gamma-rays of 0.0575, 0.2906, and 0.3484 Mev, obtained through observation of internal conversion lines. A recent spectrometric investigation[6] of the beta-spectrum has revealed that there are at least two beta-groups of 1.09 and 1.37 Mev with indications of a third of lower energy, about 0.37 Mev. Also found[6] were gamma-rays of energy 0.705, 0.649, 0.283, 0.057, and 0.0354 Mev.

In the present investigation the radiations of Ce^{143} have been examined in a magnetic lens spectrometer and in a sodium iodide scintillation spectrometer, with a few gamma-gamma coincidence experiments employing two sodium iodide scintillators. The Ce^{143} sources employed were prepared both by pile irradiation of cerium oxide enriched in Ce^{142} and by isolation from fission product mixtures. The enriched Ce^{142} was obtained through the Isotopes Division of the U. S. Atomic Energy Commission and showed the following mass analysis: Ce^{136}—0.016 atom percent; Ce^{138}—0.055 atom percent; Ce^{140}—16.51 atom percent; Ce^{142}—83.42 atom percent. The principal impurity listed for the samples was 0.15 percent gadolinium. To remove radioactive gadolinium formed during neutron-irradiation of the cerium, three cerium-gadolinium chemical separations were made, employing lanthanum as a stand-in carrier for gadolinium. The chemical procedure used was based on the cerium-rare earth separation commonly employed,[7] i.e., precipitation of ceric iodate from a strongly acidic solution leaving rare earths in the supernatant liquid. This procedure also served to remove all Pr^{143} grown from Ce^{143} during irradiation and during the time between the end of the irradiation and the beginning of chemical separations. The principal radioactive contaminant in Ce^{142} samples freshly prepared in this way was the Ce^{141}, which amounted to ~1 percent of the radioactive disintegrations in the sample. In the beta-spectrum, this impurity contributed only at energies below 0.581 Mev, the maximum beta-ray energy[8] of Ce^{141}. For the preparation of Ce^{143} sources from fission products, samples of uranium enriched in U^{235} were irradiated with thermal neutrons in a pile. To minimize the amount of Ce^{141} isolated along with Ce^{143}, advantage was taken of the difference in the half-lives of the La^{141} (3.7 hr)[9] and La^{143} (19 min)[10] parents, and the fact that Ce^{141} has a very low independent fission yield[11] while Ce^{143} has an independent fission yield of about 1.6 percent. (The total yields of Ce^{141} and Ce^{143} are 5.7 and 5.4 percent, respectively.[12]) With an irradiation of about one-half hour duration, followed by isolation of Ce within the next hour, Ce^{143} could be separated before much Ce^{141} had grown from La^{141}. Sources freshly prepared in this way contained small amounts of Ce^{141} activity but could be obtained in higher specific yield than when the Ce^{143} was made by neutron-irradiation of enriched Ce^{142}. A disadvantage of fission product sources was that in addition to Ce^{141} a small amount of Ce^{144} was also isolated along with the Ce^{143} (~0.5 percent of the total activity).

II. BETA-SPECTRA

The beta-ray spectrometer used in this study was a single coil magnetic lens type described in a previous paper from this laboratory.[13] In running the beta-spectra a resolution of about 2.5 percent was used, and a G-M counter with a 3.5-mg/cm² mica end window served as the detector.

Beta-spectra were taken with two kinds of sources. The $Ce^{142}(n,\gamma)Ce^{143}$ sources consisted of approximately 6 mg of cerium oxide spread over an area of ~0.3 cm² and mounted on a 0.3-mil Dural backing. The source was cemented to the backing with a drop of ~20-to-1

† This work was supported by the AEC.
[1] N. Ballou and W. Burgus, *Radiochemical Studies: The Fission Products* (McGraw-Hill Book Company, Inc., New York, 1951), Paper No. 177, National Nuclear Energy Series, Plutonium Project Record, Vol. 9, Div. IV.
[2] W. Bothe, Z. Naturforsch. **1**, 179 (1946).
[3] M. Pool and L. Krisberg, Phys. Rev. **73**, 1035 (1948).
[4] E. Shapiro and C. Mandeville, Phys. Rev. **78**, 319 (1950).
[5] H. Keller and J. Cork, Phys. Rev. **84**, 1082 (1951).
[6] E. Kondaiah, Phys. Rev. **83**, 471 (1951).
[7] W. Boldridge and D. Hume, reference 1, Paper 294.
[8] M. Freedman and D. Engelekemeir, Phys. Rev. **79**, 897 (1950).
[9] S. Katcoff, reference 1, Paper 172.
[10] H. Gest and R. Edwards, reference 1, Paper 171.
[11] Goldstein, Schuman and Rubinson, reference 1, Paper 181.
[12] E. Steinberg and M. Freedman, reference 1, Paper 219.
[13] L. Langer, Phys. Rev. **77**, 50 (1950).

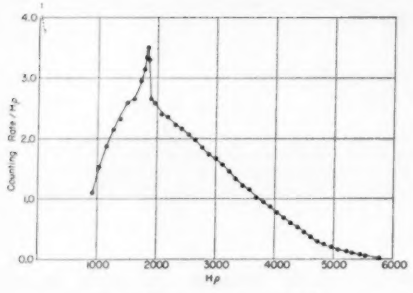

FIG. 1. Electron spectrum of Ce^{143}.

acetone dilution of Duco cement added to the powdered CeO_2 and allowed to dry under a heat lamp. The fission product Ce^{143} sources consisted of ~1 mg of CeO_2 mounted in a similar manner over about the same area. The spectrometer was calibrated with a source of $Cs^{137}-Ba^{137m}$ using the conversion line of the 663-kev gamma-ray for calibration.

The momentum distribution of the electrons from a fission product source is shown in Fig. 1. Measurements were begun one hour after final separation of Pr^{143} from the Ce^{143} source and required about three hours. In addition to the Ce^{141} and Ce^{144} initially present, the source contained Pr^{143} which grew in over this four hour period. This nuclide did not contribute electrons with energies above 0.92 Mev, its maximum energy.[14] An internal conversion line corresponding to K conversion of a gamma-ray of energy 0.289±0.005 Mev is seen superimposed on the beta-spectrum. Figure 2 shows the Fermi plot of the Ce^{143} analyzed into three components. The maximum energies are 1.390±0.005, 1.090±0.005, and 0.710±0.010 Mev. Assuming straight line Fermi plots, the intensities of the 1.39-, the 1.09-, and the 0.71-Mev beta-groups are in the ratio 1.0:1.33:1.0. The values of F, the Fermi function, were taken from the graphs of Moszkowski.[15] In addition to the three beta-groups found, there was evidence of a fourth group of somewhat lower energy. This could not be resolved due to the presence of Ce^{141} and Pr^{143}, which had grown in, and to conversion lines. Its intensity appeared to be less than the intensities of the 0.71- or 1.39-Mev beta-groups. With the assumption that the three beta-ray groups found represent nearly all of the beta-transitions, the log ft values for the 1.39-, and 1.09-, and the 0.71-Mev betas are 7.75, 7.2, and 6.7, respectively. If the fourth group could have been resolved, and its intensity computed, it is not expected that the above values of log ft for the three higher energy beta-rays would be changed by very much. The 1.39-Mev beta and probably the 1.09-Mev beta have linear Fermi plots. Because of the pile-up of errors after two subtractions, plus the presence of Ce^{141} and the conversion contributions, it is not possible to make a statement regarding the shape of the 0.71-Mev component.

III. GAMMA-SPECTRA

Gamma-ray measurements were made from both $Ce^{142}(n,\gamma)$ sources and from fission product sources. Figure 3 shows the electron spectrum from a 1-mil uranium radiator with a fission product Ce^{143} source and with the spectrometer set to ~2.8 percent resolution. The Ce^{143} beta-rays were absorbed out with a copper absorber placed between the source and uranium radiator. As in all measurements of photoelectrons ejected from uranium radiators, the source was left in the spectrometer for three days to check on the decay of the photopeaks. In Fig. 3 the photopeaks correspond to gamma-rays of 0.289±0.005, 0.356±0.005, 0.660 ±0.010, and 0.720±0.010 Mev. The spectrometer was calibrated with the 0.663-Mev gamma of $Cs^{137}-Ba^{137m}$.[16]

In addition to the gamma-ray measurements made with the lens spectrometer, some measurements were also carried out with a scintillation spectrometer. The instrument consisted of a sodium iodide crystal, an RCA 7140A photomultiplier tube used in conjunction with a ten-channel pulse analyzer. With this instrument it was possible to measure x-rays and gamma-rays of energies below those measurable with the beta-ray spectrometer, but with much poorer resolution (~20 percent). The scintillation spectrometer was calibrated in appropriate energy regions with the 0.057-Mev[17] x-rays of Ta^{181}, the 0.320-Mev[18] gamma-ray of Cr^{51}, the 0.4112-Mev[19] gamma-ray of Au^{198}, and the 0.663-Mev gamma-ray of $Cs^{137}-Ba^{137m}$. Measurements were made on Ce^{143} from both fission product and (n,γ) sources

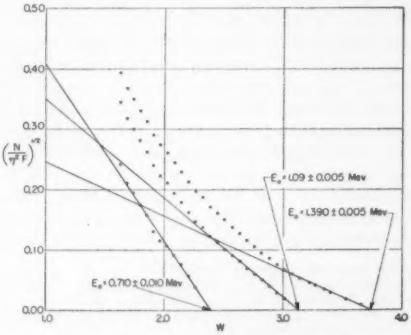

FIG. 2. Fermi plot of electron spectrum of Ce^{143}.

[14] Ter-Pogossian, Cook, Goddard, and Robinson, Phys. Rev. **76**, 909 (1949).
[15] S. Moszkowski, University of Chicago, Institute for Nuclear Studies, Progress Report, August, 1948–September, 1949, Part IV (unpublished).
[16] J. Osaba, Phys. Rev. **76**, 345 (1949).
[17] G. Wilkinson, Nature **160**, 864 (1947).
[18] F. Kurie and M. Ter-Pogossian, Phys. Rev. **74**, 677 (1948).
[19] DuMond, Lind, and Watson, Phys. Rev. **73**, 1392 (1948).

and gamma-rays were observed at 0.0349±0.001, 0.126 ±0.005, 0.290±0.005, and 0.660±0.010 Mev. A typical gamma-ray spectrum as measured on the scintillation spectrometer is shown in Fig. 4. The 0.057-Mev gamma-ray reported by Kondaiah[6] and by Keller and Cork[5] and observed through its conversion electrons was not observed in the scintillation spectrum, and is apparently highly converted. Within experimental error, the 0.0349-Mev line corresponds to Pr K x-rays arising from internal conversion. With the poorer resolution of the scintillation spectrometer, the 0.356-Mev gamma-ray could not be resolved. It is estimated that it is approximately a factor of 5 less intense than the 0.290-Mev gamma-ray. Likewise the 0.720-Mev gamma-ray could not be seen. It appears from the lens spectrometer data to be of lower intensity than the 0.660-Mev line, although it is difficult to estimate their ratio. The intensity ratio of the 0.290-Mev gamma to the 0.660-Mev gamma is very roughly 4, in agreement with the estimate of Kondaiah.[6] The intensity ratio of the 0.290-Mev gamma to the 0.126-Mev gamma is very approximately 5.

Supplementing the gamma-ray measurements made with a single sodium iodide crystal, a few coincidence experiments were run utilizing two sodium iodide scintillators. In this way it was hoped to find lower intensity gamma-rays in coincidence with previously found gammas, but which had not been resolved above the high Compton backgrounds in the single crystal experiments. The coincidence circuit had a resolving time of 0.95×10^{-6} second. The circuit was gated by pulses from one crystal corresponding to a chosen energy interval, and coincidences registered between the first and second crystals were measured as a function of the energy of the coincident gammas counting in the second crystal. In these experiments the Ce^{143} samples were placed between the two sodium iodide crystals separated only by the thickness of the sample plus Lucite absorbers to remove betas (a few centimeters). When the coincidence circuit was gated with pulses from the first crystal corresponding to the energy interval 0.095 to 0.145 Mev, a coincident gamma-ray of ~0.160 Mev was found. The energies of the 0.160-Mev and the 0.126-Mev gamma-rays add to (within experimental error) the energy of the 0.290-Mev transition and apparently offer an alternative mode of decay from the 0.290-Mev level. In another similar experiment the 0.035-Mev line was found in coincidence with the 0.356-Mev gamma ray, and probably with the 0.290-Mev gamma-ray. As both gamma-rays are partially internally converted this result might be expected, assuming the decay scheme proposed below.

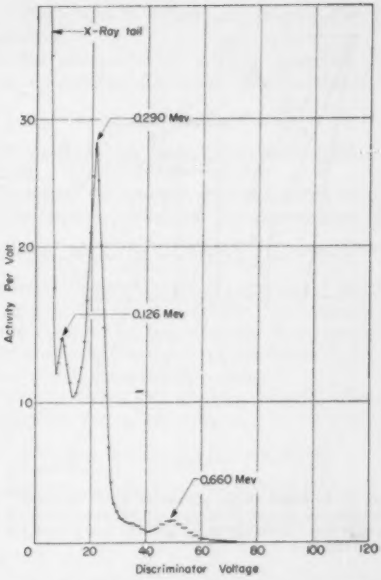

FIG. 4. Scintillation spectrum of gamma-rays of Ce^{143}.

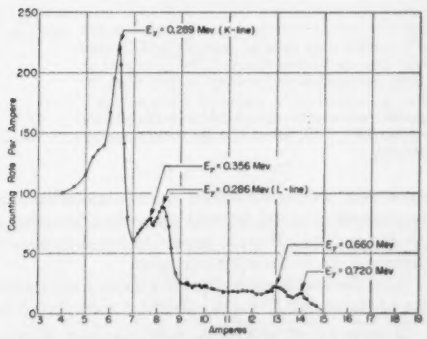

FIG. 3. Photoelectrons ejected from a 1-mil U radiator by gamma-rays of Ce^{143}.

IV. PROPOSED DECAY SCHEME FOR Ce^{143}

Figure 5 gives a proposed decay scheme for Ce^{143}. The log ft values for the 1.39- and 1.09-Mev beta-groups are 7.75 and 7.2, respectively, placing these beta-transitions in the first-forbidden group.[30] The log ft value of 6.7 for the 0.71-Mev beta-group seems too high for an allowed transition but is consistent for a transition where $\Delta I=1$, No, $\Delta l=2(l\text{-forbidden})$ thus the choice $f_{7/2}\rightarrow h_{9/2}$. This leaves the question of the place of a fourth beta-group in the decay scheme. Were the fourth beta-group to feed directly the level lying only 0.057 Mev above what is proposed as the $h_{9/2}$ level of Pr^{143}, it is possible that the two beta-groups were not resolved. If the higher of the two Pr^{143} levels were

[30] Mayer, Moszkowski, and Nordheim, Argonne National Laboratory Report No. 4626, May, 1951.

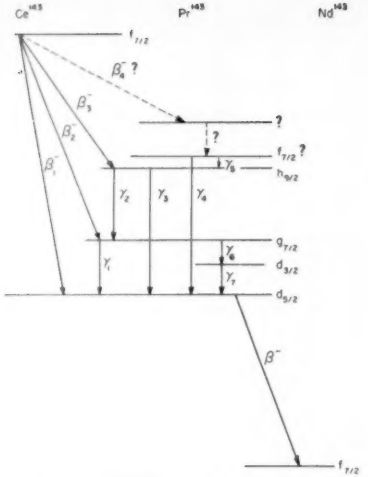

FIG. 5. Proposed decay scheme of Ce^{143}: $\beta_1^-=1.39^{\S}$ Mev; $\beta_2^-=1.09^{\S}$ Mev; $\beta_3^-=0.71$ Mev; $\gamma_1=0.290$ Mev; $\gamma_2=0.360$ Mev; $\gamma_3=0.660$ Mev; $\gamma_4=0.720$ Mev; $\gamma_6=0.057$ Mev; $\gamma_8=0.126$ Mev; $\gamma_7=\sim 0.160$ Mev.

assigned to $f_{7/2}$, then the beta-ray feeding that level should be an allowed transition on the basis of the assignment of $f_{7/2}$ for the Ce^{143}. Such a transition should produce a beta-group of greater intensity than any of the others. Because the 0.71-Mev group is less intense than the 1.09-Mev group, it seems likely that it is not an unresolved combination of the allowed and forbidden transitions. The assignment $f_{7/2}$ as shown in Fig. 5 is therefore questionable. It also seems unlikely that this level is $f_{7/2}$ because the K/L conversion ratio of the 0.057-Mev gamma as measured by Keller and Cork is less than unity, suggesting an $E2$ (or higher) transition.[21] If the 0.057-Mev transition were an $f_{7/2}\rightarrow h_{9/2}$ ($M1$) the K/L conversion ratio should be much greater than unity.[21] Perhaps the 0.057-Mev gamma-ray is in cascade with an undiscovered gamma which in turn is fed by the fourth lower energy beta-ray group. A more careful examination of the low energy end of the beta-spectrum of Ce^{143} is required to determine the place of a lower energy beta-group in the decay scheme and a more clear picture of the upper-lying levels of Pr^{143}. This must involve obtaining samples of Ce^{143} without serious contamination by Ce^{141}. A further possibility, of course, is that the assignment $h_{9/2}$ is also incorrect and β_3^- may be simply a first-forbidden transition.

The K/L conversion ratio of the 0.290-Mev gamma is approximately[5] 10, and the assignment $g_{7/2}\rightarrow d_{5/2}$ is consistent with this measurement. From our coincidence experiments we cannot, of course, say whether the 0.126-Mev gamma lies above or below the 0.160-Mev gamma in the decay scheme.

The assistance of L. M. Langer and M. Bunker with the β-spectrometer measurements and of J. W. Starner with the scintillation experiments is gratefully acknowledged.

[21] M. Goldhaber and A. W. Sunyar, Phys. Rev. **83**, 906 (1951).

PHYSICAL REVIEW VOLUME 88, NUMBER 5 DECEMBER 1, 1952

The Parallel Susceptibility of an Antiferromagnet at Low Temperatures*

JACK R. TESSMAN†
Department of Physics, University of California, Berkeley, California
(Received July 10, 1952)

The spin wave method of Heller and Kramers is applied to a cubic antiferromagnetic crystal, oriented so that the direction of alignment of the sublattice spins is parallel to an external magnetic field. Taking into account exchange interactions and an anisotropy term, then the parallel susceptibility $\chi_{\parallel}$ is zero at $T=0°$K, in agreement with the result of the molecular field treatment of the problem by Van Vleck. If nearest neighbor magnetic dipole interactions are included, $\chi_{\parallel}$ is nonzero but negligibly small: $\chi_{\parallel}\sim 10^{-11}$ at $T=0°$K. For $T>0$ but much less than the antiferromagnetic Curie temperature, if the dipole interactions are neglected and the anisotropy is small, such that $\zeta=S(24JK)^{\frac{1}{2}}/kT\ll 1$, where K is an anisotropy constant, then $\chi_{\parallel}\propto T^3$. If $\zeta\gg 1$, then $\chi_{\parallel}\propto T^{\frac{1}{2}}\exp[-S(24JK)^{\frac{1}{2}}/kT]$.

1. INTRODUCTION

AN antiferromagnetic crystal does not exhibit any net spontaneous magnetization in the absence of an external magnetic field, because the magnetizations of the ordered sublattices, below the antiferromagnetic Curie temperature, are equal and opposite. In an external field, the magnetization of a two-sublattice antiferromagnetic crystal depends upon the orientation of the external field $\mathbf{H}$ with respect to the directions of alignment $\pm\mathbf{e}$ of the sublattice spins.

Using the modification of the Bloch spin wave method due to Heller and Kramers,[1] Hulthén[2] investigated the

* This work was assisted in part by the ONR.
† Now at Department of Physics, Pennsylvania State College, State College, Pennsylvania.

[1] G. Heller and H. A. Kramers, Proc. Roy. Acad. Sci. (Amsterdam) **37**, 378 (1934).
[2] L. Hulthén, Proc. Roy. Acad. Sci. (Amsterdam) **39**, 190 (1936).

susceptibility of a two-sublattice antiferromagnet at low temperatures, when $\mathbf{H}\perp\mathbf{e}$. He found, after quantization, that the perpendicular susceptibility $\chi_\perp \propto (1-bT^2)$, where b is a constant. Hulthén recognized that, for small external fields, it is energetically favorable for the sublattice spins to set themselves approximately perpendicular to the external field if only exchange interactions are considered. Hence, he did not investigate the case when $\mathbf{H}\|\mathbf{e}$. However, if some anisotropy is present and $\mathbf{H}$ is applied parallel to $\mathbf{e}$, the sublattice spins may remain parallel and antiparallel to the field rather than turn perpendicular to it.

Generalizing work by Néel[3] and by Bitter,[4] Van Vleck[5] investigated both the perpendicular and parallel susceptibility using a molecular field model. He found that $\chi_\perp$ should be constant between 0°K and the antiferromagnetic Curie temperature, and that $\chi_\|$ should be zero at $T=0$.

In this paper we apply the spin wave method used by Hulthén,[2] and the recent clarifications of the method,[6,7] to the case when $\mathbf{H}\|\mathbf{e}$. We investigate the ground state of the system taking into account exchange interactions, an external field, anisotropy, and nearest neighbor magnetic dipole interactions. This will yield $\chi_\|$ at $T=0$. Then, omitting the dipole interaction term, we shall obtain expressions for $\chi_\|$ at $T>0$ for the cases of small and large anisotropy.

2. $\chi_\|$ AT $T=0$°K

A. Neglecting Magnetic Dipole Interactions

Let the lattice structure of our crystal be simple cubic with N atoms and lattice constant a, subdivided into two face-centered cubic sublattices, $\mathbf{m}$ and $\mathbf{n}$, such that the six nearest neighbors of any one atom, of either sublattice, are all members of the other sublattice. We shall assume that, for each of the atoms, $S_{\mathbf{m}}{}^z \simeq S$ or $S_{\mathbf{n}}{}^z \simeq -S$, where S is the spin quantum number of the atom. Then, writing $\check{S}^2=S(S+1)$, since

$$(S_{\mathbf{m}}{}^x)^2=\check{S}^2-[(S_{\mathbf{m}}{}^x)^2+(S_{\mathbf{m}}{}^y)^2] \quad \text{and} \quad (S_{\mathbf{n}}{}^x)^2=\check{S}^2-[(S_{\mathbf{n}}{}^x)^2+(S_{\mathbf{n}}{}^y)^2],$$

therefore

$$\begin{aligned} S_{\mathbf{m}}{}^z &\simeq \check{S}-[(S_{\mathbf{m}}{}^x)^2+(S_{\mathbf{m}}{}^y)^2]/2\check{S}, \\ S_{\mathbf{n}}{}^z &\simeq -\check{S}+[(S_{\mathbf{n}}{}^x)^2+(S_{\mathbf{n}}{}^y)^2]/2\check{S}. \end{aligned} \tag{1}$$

The antiferromagnetic exchange interaction energy of the crystal is

$$\mathcal{H}_1=J\sum_{\langle \mathbf{m},\mathbf{n}\rangle}\mathbf{S}_{\mathbf{m}}\cdot\mathbf{S}_{\mathbf{n}},$$

where J is positive and the summation is over all pairs of nearest neighbors. We note that the sign convention for J is opposite to that usually employed in ferromagnetism.

In the presence of an external magnetic field $\mathbf{H}$ in the $+z$ direction, there is an additional energy,

$$\mathcal{H}_2=-g\mu_B H(\textstyle\sum_{\mathbf{m}} S_{\mathbf{m}}{}^z+\sum_{\mathbf{n}} S_{\mathbf{n}}{}^z),$$

where $g\mu_B\mathbf{S}_{\mathbf{m}}$ is the magnetic moment operator for atom $\mathbf{m}$.

We assume the presence of an anisotropy energy of uniaxial symmetry which may be approximated by

$$\mathcal{H}_3=K\{\textstyle\sum_{\mathbf{m}}[(S_{\mathbf{m}}{}^x)^2+(S_{\mathbf{m}}{}^y)^2]+\sum_{\mathbf{n}}[(S_{\mathbf{n}}{}^x)^2+(S_{\mathbf{n}}{}^y)^2]\}.$$

This term will maintain the $\pm z$ axes as the directions of magnetization of the sublattices. In a magnetic field $\mathbf{H}$, the directions of magnetization of the sublattices would become approximately perpendicular to the field were it not for the anisotropy energy.

Collecting terms, and applying Eqs. (1), the total Hamiltonian, $\mathcal{H}=\mathcal{H}_1+\mathcal{H}_2+\mathcal{H}_3$, is

$$\begin{aligned} \mathcal{H}=&-3JNS(S+1)+3J\{\textstyle\sum_{\mathbf{m}}[(S_{\mathbf{m}}{}^x)^2+(S_{\mathbf{m}}{}^y)^2] \\ &\times(1+K'-\alpha)+\textstyle\sum_{\mathbf{n}}[(S_{\mathbf{n}}{}^x)^2+(S_{\mathbf{n}}{}^y)^2](1+K'+\alpha)\} \\ &+J\sum_{\langle \mathbf{m},\mathbf{n}\rangle}(S_{\mathbf{m}}{}^zS_{\mathbf{n}}{}^z+S_{\mathbf{m}}{}^yS_{\mathbf{n}}{}^y). \end{aligned} \tag{2}$$

Here,

$$K'=K/3J \quad \text{and} \quad \alpha=Hg\mu_B/6J\check{S}. \tag{3}$$

Consistent with the approximation of (1), we have dropped terms of higher order than the small quantities $(S_{\mathbf{m}}{}^x)^2/\check{S}^2$ and $(S_{\mathbf{m}}{}^y)^2/\check{S}^2$.

We introduce, following Anderson,[7] two sets of spin waves through the transformation,

$$\begin{aligned} S_{\mathbf{m}}{}^z &= (2S/N)^{\frac{1}{2}}\textstyle\sum_{\mathbf{k}} Q_{1\mathbf{k}}\exp(i\mathbf{k}\cdot\mathbf{m}), \\ S_{\mathbf{m}}{}^y &= (2S/N)^{\frac{1}{2}}\textstyle\sum_{\mathbf{k}} P_{1\mathbf{k}}\exp(-i\mathbf{k}\cdot\mathbf{m}), \\ S_{\mathbf{n}}{}^z &= (2S/N)^{\frac{1}{2}}\textstyle\sum_{\mathbf{k}} Q_{2\mathbf{k}}\exp(i\mathbf{k}\cdot\mathbf{n}), \\ S_{\mathbf{n}}{}^y &= -(2S/N)^{\frac{1}{2}}\textstyle\sum_{\mathbf{k}} P_{2\mathbf{k}}\exp(-i\mathbf{k}\cdot\mathbf{n}), \end{aligned} \tag{4}$$

where $\mathbf{k}$, the spin wave vector, takes on $N/2$ discrete values with $k_{x,y,z}$ going from $-\pi/a$ to $+\pi/a$.

The new operators approximately satisfy the commutation relations

$$[Q_{1\mathbf{k}}, P_{1\mathbf{k}'}]=i\delta_{\mathbf{k}\mathbf{k}'}, \quad [Q_{2\mathbf{k}}, P_{2\mathbf{k}}]=i\delta_{\mathbf{k}\mathbf{k}'}.$$

All other commutators are zero. Also,

$$\textstyle\sum_{\mathbf{m}}[(S_{\mathbf{m}}{}^x)^2+(S_{\mathbf{m}}{}^y)^2]=S\sum_{\mathbf{k}}(Q_{1\mathbf{k}}Q_{1\mathbf{k}}{}^*+P_{1\mathbf{k}}P_{1\mathbf{k}}{}^*),$$

$$\textstyle\sum_{\mathbf{n}}[(S_{\mathbf{n}}{}^x)^2+(S_{\mathbf{n}}{}^y)^2]=S\sum_{\mathbf{k}}(Q_{2\mathbf{k}}Q_{2\mathbf{k}}{}^*+P_{2\mathbf{k}}P_{2\mathbf{k}}{}^*),$$

$$\begin{aligned} \sum_{\langle \mathbf{m},\mathbf{n}\rangle}(S_{\mathbf{m}}{}^xS_{\mathbf{n}}{}^x+S_{\mathbf{m}}{}^yS_{\mathbf{n}}{}^y)=&S\textstyle\sum_{\mathbf{k}}(Q_{1\mathbf{k}}Q_{2\mathbf{k}}{}^*+Q_{1\mathbf{k}}{}^*Q_{2\mathbf{k}} \\ &-P_{1\mathbf{k}}P_{2\mathbf{k}}{}^*-P_{1\mathbf{k}}{}^*P_{2\mathbf{k}})(\cos k_xa+\cos k_ya+\cos k_za). \end{aligned}$$

$Q_{1\mathbf{k}}{}^*$ is the Hermitian conjugate of $Q_{1\mathbf{k}}$. Henceforth, as a convenient abbreviation, we shall drop the conjugate sign and write Q^2 for QQ^*, etc. None of the succeeding arguments is affected thereby.

[3] L. Néel, Ann. phys. **5**, 256 (1936).
[4] F. Bitter, Phys. Rev. **54**, 79 (1937).
[5] J. H. Van Vleck, J. Chem. Phys. **9**, 85 (1941).
[6] M. J. Klein and R. S. Smith, Phys. Rev. **80**, 1111 (1950).
[7] P. W. Anderson, Phys. Rev. **86**, 694 (1952). I should like to express my gratitude to Dr. Anderson for having had the opportunity to study his paper prior to publication.

The Hamiltonian (2) now takes the form

$$\mathcal{H}=-3JNS(S+1)+3JS\sum_k[\mathfrak{A}(Q_{1k}^2+P_{1k}^2)+\mathfrak{B}(Q_{2k}^2+P_{2k}^2)+2\mathfrak{C}_k(Q_{1k}Q_{2k}-P_{1k}P_{2k})], \quad (5)$$

where

$$\mathfrak{A}=1+K'-\alpha,\qquad \mathfrak{B}=1+K'+\alpha,\qquad \mathfrak{C}_k=\tfrac{1}{3}(\cos k_x a+\cos k_y a+\cos k_z a). \quad (6)$$

The bracketed expression in (5) has the form

$$\Phi=\mathfrak{A}(Q_1^2+P_1^2)+\mathfrak{B}(Q_2^2+P_2^2)+2\mathfrak{C}(Q_1Q_2-P_1P_2).$$

Let us transform to new variables q, p by the canonical transformation[8]

$$Q_1=(1+w)^{-1}(wq_1+q_2),\quad P_1=(1-w)^{-1}(-wp_1+p_2),$$
$$Q_2=(1+w)^{-1}(q_1+wq_2),\quad P_2=(1-w)^{-1}(p_1-wp_2).$$

The mixed terms in Φ will be eliminated if w satisfies the equation

$$\mathfrak{C}w^2+(\mathfrak{A}+\mathfrak{B})w+\mathfrak{C}=0. \quad (7)$$

The resulting expression for Φ is

$$\Phi=(\mathfrak{A}w^2+\mathfrak{B}+2\mathfrak{C}w)[(1+w)^{-2}q_1^2+(1-w)^{-2}p_1^2]+(\mathfrak{A}+\mathfrak{B}w^2+2\mathfrak{C}w)[(1+w)^{-2}q_2^2+(1-w)^{-2}p_2^2].$$

Since $[q_1, p_1]=[q_2, p_2]=i$ and all other commutators vanish, therefore the eigenvalues of Φ are

$$\Phi=(2\mu+1)(\mathfrak{A}w^2+\mathfrak{B}+2\mathfrak{C}w)/(1-w^2)+(2\nu+1)(\mathfrak{A}+\mathfrak{B}w^2+2\mathfrak{C}w)/(1-w^2),\quad \mu,\nu=0,1,2,\cdots.$$

Substituting the values of w and $1/w$ from the solution of Eq. (7), we obtain

$$\Phi=(\mu+\tfrac{1}{2})\{\mathfrak{B}-\mathfrak{A}+[(\mathfrak{A}+\mathfrak{B})^2-4\mathfrak{C}^2]^{\frac{1}{2}}\}+(\nu+\tfrac{1}{2})\{\mathfrak{A}-\mathfrak{B}+[(\mathfrak{A}+\mathfrak{B})^2-4\mathfrak{C}^2]^{\frac{1}{2}}\},\ \mu,\nu=0,1,2,\cdots.$$

In terms of K' and α, we have

$$\Phi=(2\mu+1)\{\alpha+[(1+K')^2-\mathfrak{C}^2]^{\frac{1}{2}}\}+(2\nu+1)\{-\alpha+[(1+K')^2-\mathfrak{C}^2]^{\frac{1}{2}}\}.$$

Only α contains the external field H.

The eigenvalues of the Hamiltonian (5) are, therefore,

$$\mathcal{H}=-3JNS(S+1)+3JS\sum_k(2\mu_k+1)\{\alpha+[(1+K')^2-\mathfrak{C}_k^2]^{\frac{1}{2}}\}+3JS\sum_k(2\nu_k+1)\{-\alpha+[(1+K')^2-\mathfrak{C}_k^2]^{\frac{1}{2}}\}. \quad (8)$$

In the ground state, $\mu_k=\nu_k=0$, and we have

$$\mathcal{H}_0=-3JNS(S+1)+6JS\sum_k[(1+K')^2-\mathfrak{C}_k^2]^{\frac{1}{2}}. \quad (9)$$

The ground state is independent of H. Therefore, at $T=0$, when the antiferromagnet is in its ground state, the magnetization $M_0=-(1/V)(\partial\mathcal{H}_0/\partial H)$ is zero. V is the volume of the crystal. Likewise, the parallel susceptibility $\chi_{\parallel}(T=0)=M_0/H=0$. This agrees with the result obtained by Van Vleck[5] from a Weiss molecular field approach to the problem.

The above analysis is not valid for a sufficiently strong external field, for then the antiferromagnetic direction becomes perpendicular to the applied field, despite the anisotropy term, and the nonzero perpendicular susceptibility allows the energy of the system to decrease. Mathematically, it can be seen that if $\alpha>[(1+K')^2-\mathfrak{C}_k^2]^{\frac{1}{2}}$, then, from Eq. (8), the ground state is given by $\nu_k=\infty$. That is, spin waves of infinitely large amplitude are energetically favored. It is no longer true that $S_m^z\simeq S$, and the above analysis is invalid.

B. Including Nearest Neighbor Magnetic Dipole Interactions

Thus far we have considered only the exchange interaction energy. We shall now investigate the effect, on $\chi_{\parallel}$ at $T=0°$K, of including the nearest neighbor magnetic dipole interaction energy. The effect of the dipole interactions on the magnetization of a ferromagnet has been previously investigated by Holstein and Primakoff.[9]

The nearest neighbor magnetic dipole interaction energy adds to the Hamiltonian a term

$$\mathcal{H}_4=G\sum_{\langle m,n\rangle}\mathbf{S}_m\cdot\mathbf{S}_n-\frac{3G}{a^3}\sum_{\langle m,n\rangle}(\mathbf{S}_m\cdot\mathbf{r}_{mn})(\mathbf{S}_n\cdot\mathbf{r}_{mn}),$$

where $G=g^2\mu_B^2/a^3$. The coordinates of the nearest neighbors to a lattice point at the origin are

$$\mathbf{A}=\pm(a,0,0),\quad \mathbf{B}=\pm(0,a,0),\quad \mathbf{C}=\pm(0,0,a).$$

Thus,

$$\mathcal{H}_4=G\sum_{\langle A\rangle}(-2S_m^xS_n^x+S_m^yS_n^y+S_m^zS_n^z)+G\sum_{\langle B\rangle}(S_m^xS_n^x-2S_m^yS_n^y+S_m^zS_n^z)+G\sum_{\langle C\rangle}(S_m^xS_n^x+S_m^yS_n^y-2S_m^zS_n^z),$$

where the summation over $\langle\mathbf{A}\rangle$ means summation over all pairs of nearest neighbors, $\mathbf{m}$ and $\mathbf{n}$, such that point $\mathbf{n}$ has the coordinates $\mathbf{A}$ relative to point $\mathbf{m}$.

The approximation (1) reduces $\mathcal{H}_4$ to the terms

$$\mathcal{H}_4=G\sum_{\langle A\rangle}(-2S_m^xS_n^x+S_m^yS_n^y)+G\sum_{\langle B\rangle}(S_m^xS_n^x-2S_m^yS_n^y)+G\sum_{\langle C\rangle}(S_m^xS_n^x+S_m^yS_n^y).$$

After the transformation (4), we have

$$\mathcal{H}_4=2GS\sum_k[(-2\cos k_xa+\cos k_ya+\cos k_za)Q_{1k}Q_{2k}-(\cos k_xa-2\cos k_ya+\cos k_za)P_{1k}P_{2k}].$$

[8] F. Keffer, thesis, University of California, Berkeley, 1952 (unpublished).

[9] T. Holstein and H. Primakoff, Phys. Rev. **58**, 1098 (1940).

The total Hamiltonian, $\mathcal{H}=\mathcal{H}_1+\mathcal{H}_2+\mathcal{H}_3+\mathcal{H}_4$, including exchange interaction, external field, anisotropy term, and nearest neighbor dipole interaction, is now

$$\mathcal{H}=-3JNS(S+1)+3JS\sum_k[\mathfrak{A}(Q_{1k}^2+P_{1k}^2)+\mathfrak{B}(Q_{2k}^2+P_{2k}^2)+2\mathfrak{D}_kQ_{1k}Q_{2k}-2\mathfrak{F}_kP_{1k}P_{2k}], \quad (10)$$

where $\mathfrak{A}$ and $\mathfrak{B}$ are defined in (6) and

$$\mathfrak{D}_k=\tfrac{1}{3}(\cos k_xa+\cos k_ya+\cos k_za)+(G/3J)(-2\cos k_xa+\cos k_ya+\cos k_za),$$
$$\mathfrak{F}_k=\tfrac{1}{3}(\cos k_xa+\cos k_ya+\cos k_za)+(G/3J)(\cos k_xa-2\cos k_ya+\cos k_za). \quad (11)$$

The bracketed expression in (10) has the form

$$\Phi'=\mathfrak{A}(Q_1^2+P_1^2)+\mathfrak{B}(Q_2^2+P_2^2)+2\mathfrak{D}Q_1Q_2-2\mathfrak{F}P_1P_2.$$

Transform to new variables q, p by the canonical transformation

$$Q_1=[1+(vw)^{\frac{1}{2}}]^{-1}(vq_1+q_2),$$
$$P_1=[1-(vw)^{\frac{1}{2}}]^{-1}(-wp_1+p_2),$$
$$Q_2=[1+(vw)^{\frac{1}{2}}]^{-1}(q_1+wq_2), \quad (12)$$
$$P_2=[1-(vw)^{\frac{1}{2}}]^{-1}(p_1-vp_2).$$

If v and w satisfy the simultaneous equations

$$\mathfrak{A}v+\mathfrak{D}w+\mathfrak{C}(1+vw)=0,$$
$$\mathfrak{D}v+\mathfrak{A}w+\mathfrak{C}(1+vw)=0, \quad (13)$$

then there will be no mixed terms in Φ'. We get

$$\Phi'=\frac{\mathfrak{A}v^2+\mathfrak{B}+2\mathfrak{D}v}{[1+(vw)^{\frac{1}{2}}]^2}q_1^2+\frac{\mathfrak{A}w^2+\mathfrak{B}+2\mathfrak{F}w}{[1-(vw)^{\frac{1}{2}}]^2}p_1^2+\frac{\mathfrak{A}+\mathfrak{B}w^2+2\mathfrak{D}w}{[1+(vw)^{\frac{1}{2}}]^2}q_2^2+\frac{\mathfrak{A}+\mathfrak{B}v^2+2\mathfrak{F}v}{[1-(vw)^{\frac{1}{2}}]^2}p_2^2.$$

The commutators $[q_1, p_1]=[q_2, p_2]=i$, and all other commutators vanish. Thus the eigenvalues of Φ' are

$$\Phi'=(2\mu+1)(1-vw)^{-1}(\mathfrak{A}v^2+\mathfrak{B}+2\mathfrak{D}v)^{\frac{1}{2}}(\mathfrak{A}w^2+\mathfrak{B}+2\mathfrak{F}w)^{\frac{1}{2}}+(2\nu+1)(1-vw)^{-1}(\mathfrak{A}+\mathfrak{B}w^2+2\mathfrak{D}w)^{\frac{1}{2}}(\mathfrak{A}+\mathfrak{B}v^2+2\mathfrak{F}v)^{\frac{1}{2}},$$
$$\mu, \nu=0, 1, 2, \cdots.$$

In the ground state of the Hamiltonian (10), we have $\mu=\nu=0$, yielding

$$\mathcal{H}_0=-3JNS(S+1)+3JS\sum_k(1-vw)^{-1}\times[(\mathfrak{A}v^2+\mathfrak{B}+2\mathfrak{D}_kv)^{\frac{1}{2}}(\mathfrak{A}w^2+\mathfrak{B}+2\mathfrak{F}_kw)^{\frac{1}{2}}+(\mathfrak{A}+\mathfrak{B}w^2+2\mathfrak{D}_kw)^{\frac{1}{2}}(\mathfrak{A}+\mathfrak{B}v^2+2\mathfrak{F}_kv)^{\frac{1}{2}}]. \quad (14)$$

Now, at $T=0$, the magnetization $M_0=-(1/V)(\partial\mathcal{H}_0/\partial H)=-(g\mu_B/6J\check{S}V)(\partial\mathcal{H}_0/\partial\alpha)$. Thus, M_0 can be obtained by differentiating (14) and inserting the values of v and w from (13). A persistent application of the rules and procedures of algebra and differential calculus leads to

$$M_0=\frac{g^2\mu_B^2H}{6J(S+1)V}\sum_k\frac{2\mathfrak{A}_0}{(\mathfrak{D}_k-\mathfrak{F}_k)^2}\times\left\{\left[1-\frac{\mathfrak{D}_k+\mathfrak{F}_k}{2\mathfrak{A}_0}\right]^2\left[\frac{1+\mathfrak{F}_k/\mathfrak{A}_0}{1-\mathfrak{D}_k/\mathfrak{A}_0}\right]^{\frac{1}{2}}+\left[1+\frac{\mathfrak{D}_k+\mathfrak{F}_k}{2\mathfrak{A}_0}\right]^2\left[\frac{1-\mathfrak{D}_k/\mathfrak{A}_0}{1+\mathfrak{F}_k/\mathfrak{A}_0}\right]^{\frac{1}{2}}-2[(1-\mathfrak{D}_k/\mathfrak{A}_0)(1+\mathfrak{F}_k/\mathfrak{A}_0)]^{\frac{1}{2}}\right\}. \quad (15)$$

Here $\mathfrak{A}_0=1+K'(=\mathfrak{A}+\alpha=\mathfrak{B}-\alpha)$. Second-order terms and higher in the small quantity, $\alpha=g\mu_BH/6J\check{S}$, have been dropped. In addition, it has been possible to eliminate a number of terms by noticing the symmetry relationships between $\mathfrak{D}_k$ and $\mathfrak{F}_k$ over the range of $\mathbf{k}$ values.

If we expand the expression in curly brackets, in (15), in powers of $\mathfrak{D}_k/\mathfrak{A}_0$ and $\mathfrak{F}_k/\mathfrak{A}_0$, the lowest nonvanishing even power term has the value

$$(1/32\mathfrak{A}_0^5)(\mathfrak{D}_k-\mathfrak{F}_k)^4(\mathfrak{D}_k+\mathfrak{F}_k)^2.$$

Odd power terms need not be considered since they vanish when $\sum_k$ is performed. ($\mathfrak{D}_k^\beta\mathfrak{F}_k^\gamma$ is an even or odd power term according as $\beta+\gamma$ is even or odd.) Thus,

$$M_0=\frac{g^2\mu_B^2H}{96J(S+1)\mathfrak{A}_0^5}\frac{N}{2V}\langle(\mathfrak{D}_k-\mathfrak{F}_k)^2(\mathfrak{D}_k+\mathfrak{F}_k)^2\rangle_{\mathbf{k}}.$$

Substituting the values of $\mathfrak{D}_k$ and $\mathfrak{F}_k$ from (11) and noting that

$$\langle\cos k_{x,y,z}a\rangle_{\mathbf{k}}=\langle\cos^3k_{x,y,z}a\rangle_{\mathbf{k}}=0,$$
$$\langle\cos^2k_{x,y,z}a\rangle_{\mathbf{k}}=\tfrac{1}{2}, \quad \langle\cos^4k_{x,y,z}a\rangle_{\mathbf{k}}=\tfrac{3}{8},$$

we get

$$\langle(\mathfrak{D}_k-\mathfrak{F}_k)^2(\mathfrak{D}_k+\mathfrak{F}_k)^2\rangle_{\mathbf{k}}=G^2/3J^2+O(G^3/J^3).$$

Therefore,

$$M_0\simeq\frac{H}{576(S+1)}\frac{g^2\mu_B^2}{a^3}\frac{G^2}{J^3}=\frac{H}{576(S+1)}\frac{G^2}{J^3}, \quad (16)$$

and

$$\chi_{11}(T=0)=M_0/H\sim10^{-3}G^2/J^3\sim10^{-11}. \quad (17)$$

Thus, we see that the dipolar interactions mix into the ground state a negligible amount of states having total $S^z\neq0$.

3. χ_{11} FOR $T>0°$

Let us now determine the behavior of χ_{11} at temperatures above $T=0°$K but at temperatures low compared to the antiferromagnetic Curie temperature, so that we may continue our assumption that $S_m{}^z\simeq S$ and $S_n{}^z\simeq-S$.

The magnetization is given by $M=-(1/V)(\partial F/\partial H)$, where $F=-kT\ln Z$ is the Helmholtz free energy func-

tion and $Z=\sum \exp(-H/kT)$ is the partition function, the summation being over all eigenvalues.

We shall take (5) as the Hamiltonian, that is, we shall include exchange interactions, anisotropy, and an external field, but not dipole interactions. The eigenvalues of this Hamiltonian are given in Eq. (8), which we shall write as

$$\mathcal{H}=-3JNS(S+1)+\sum_{\mathbf{k}}(\mu_{\mathbf{k}}+\tfrac{1}{2})\hbar\omega_{\mathbf{k}}^{+}+\sum_{\mathbf{k}}(\nu_{\mathbf{k}}+\tfrac{1}{2})\hbar\omega_{\mathbf{k}}^{-},$$

where $\hbar\omega_{\mathbf{k}}^{\pm}=6JS\{\pm\alpha+[(1+K')^2-\mathcal{C}_{\mathbf{k}}^2]^{\frac{1}{2}}\}$.

The partition function is, therefore,

$$\begin{aligned}Z&=e^{-3JNS(S+1)/kT}\sum_{\mu_{\mathbf{k}},\nu_{\mathbf{k}}=0}^{\infty}\exp\{-\sum_{\mathbf{k}}[(\mu_{\mathbf{k}}+\tfrac{1}{2})\hbar\omega^{+}{}_{\mathbf{k}}\\&\qquad+(\nu_{\mathbf{k}}+\tfrac{1}{2})\hbar\omega_{\mathbf{k}}^{-}]/kT\}\\&=e^{-3JNS(S+1)/kT}\prod_{\mathbf{k}}\sum_{\mu_{\mathbf{k}},\nu_{\mathbf{k}}=0}^{\infty}\exp\{-[(\mu_{\mathbf{k}}+\tfrac{1}{2})\hbar\omega_{\mathbf{k}}^{+}\\&\qquad+(\nu_{\mathbf{k}}+\tfrac{1}{2})\hbar\omega_{\mathbf{k}}^{-}]/kT\}\\&=e^{-3JNS(S+1)/kT}\prod_{\mathbf{k}}\exp[-\hbar(\omega_{\mathbf{k}}^{+}+\omega_{\mathbf{k}}^{-})/2kT]\\&\quad\times[1-\exp(-\hbar\omega_{\mathbf{k}}^{+}/kT)]^{-1}[1-\exp(-\hbar\omega_{\mathbf{k}}^{-}/kT)]^{-1},\end{aligned}$$

where $\sum_{\mathbf{k}}$ and $\prod_{\mathbf{k}}$ are over the $N/2$ values of $\mathbf{k}$. Thus,

$$\begin{aligned}F&=-kT\ln Z=3JNS(S+1)+\tfrac{1}{2}\sum_{\mathbf{k}}(\hbar\omega_{\mathbf{k}}^{+}+\hbar\omega_{\mathbf{k}}^{-})\\&\quad+kT\sum_{\mathbf{k}}\ln[1-\exp(-\hbar\omega_{\mathbf{k}}^{+}/kT)]\\&\quad+kT\sum_{\mathbf{k}}\ln[1-\exp(-\hbar\omega_{\mathbf{k}}^{-}/kT)].\end{aligned}$$

Only the last two terms involve the external magnetic field, and therefore, only they need be considered in obtaining the magnetization $\mathbf{M}=-(1/V)(\partial F/\partial H)$.

Expanding the logarithm in an infinite series, we have

$$\begin{aligned}&\ln[1-\exp(-\hbar\omega_{\mathbf{k}}^{+}/kT)]+\ln[1-\exp(-\hbar\omega_{\mathbf{k}}^{-}/kT)]\\&\quad=-\sum_{\rho=1}^{\infty}\rho^{-1}[\exp(-\rho\hbar\omega_{\mathbf{k}}^{+}/kT)+\exp(-\rho\hbar\omega_{\mathbf{k}}^{-}/kT)]\\&\quad=-2\sum_{\rho=1}^{\infty}\rho^{-1}\cosh(6\rho JS\alpha/kT)\\&\qquad\times\exp\{-6\rho JS[(1+K')^2-\mathcal{C}_{\mathbf{k}}^2]^{\frac{1}{2}}/kT\}.\end{aligned}$$

Substituting $\alpha=Hg\mu_B/6JS$, we obtain

$$\begin{aligned}M&=(2/V)(g\mu_BS/\check{S})\sum_{\mathbf{k}}\sum_{\rho=1}^{\infty}\sinh(\rho SHg\mu_B/\check{S}kT)\\&\qquad\times\exp\{-6\rho JS[(1+K')^2-\mathcal{C}_{\mathbf{k}}^2]^{\frac{1}{2}}/kT\}.\end{aligned}$$

For large values of ρ, the exponential becomes negligibly small; thus we can write, for $Hg\mu_B\ll kT$,

$$\sinh(\rho SHg\mu_B/\check{S}kT)=\rho SHg\mu_B/\check{S}kT.$$

Then,

$$M=\frac{2}{V}\frac{S}{S+1}\frac{Hg^2\mu_B^2}{kT}\sum_{\rho=1}^{\infty}\sum_{\mathbf{k}}\rho\exp\{-6\rho JS[(1+K')^2-\mathcal{C}_{\mathbf{k}}^2]^{\frac{1}{2}}/kT\}. \quad (18)$$

The $\sum_{\mathbf{k}}$ can be evaluated as follows:

$$\begin{aligned}\sum_{\mathbf{k}}&=(N/2)\langle\rho\exp\{\ \}\rangle_{\mathrm{Av}}\\&\simeq\frac{N}{2}\left(\frac{a}{2\pi}\right)^3\int_{k_x,k_y,k_z=-\pi/a}^{\pi/a}\rho\exp\{\ \}d\mathbf{k}.\end{aligned} \quad (19)$$

For $K'\ll1$, we have $(1+K')^2\simeq1+2K'$. The principal contribution to the integral will come from values of $\mathcal{C}_{\mathbf{k}}$ in the neighborhood of 1. From (6), we see that this means $k_{x,y,z}\simeq0$. In this region, $\mathcal{C}_{\mathbf{k}}^2\simeq1-\frac{1}{3}k^2a^2$ and the integral in (19) can be written

$$\begin{aligned}I&=\int_{-\infty}^{\infty}\rho\exp\left\{-\rho\frac{6JS}{kT}(2K'+\tfrac{1}{3}k^2a^2)^{\frac{1}{2}}d\mathbf{k}\right.\\&=\frac{4\pi\rho}{a^3}\left(\frac{kT}{2(3)^{\frac{1}{2}}JS}\right)^3\int_0^{\infty}u^2\exp[-\rho(\zeta^2+u^2)^{\frac{1}{2}}]du,\end{aligned}$$

where $\zeta^2=(72J^2S^2/k^2T^2)K'=24S^2JK/k^2T^2$, and we have let $k=(kT/2(3)^{\frac{1}{2}}JSa)u$. ($k$, the magnitude of the wave vector, on the left side, is not to be confused with the Boltzmann k on the right side.)

In the limit of vanishingly small anisotropy constant K, and thus ζ, the integral can be performed readily, and we get

$$I=(\pi/3(3)^{\frac{1}{2}}a^3)(kT/JS)^3\rho^{-2}. \quad (20)$$

Combining (18), (19), and (20), and noting that

$$\sum_{\rho=1}^{\infty}\rho^{-2}=\pi^2/6,$$

we obtain[10]

$$\chi_{\mathrm{II}}=\frac{M}{H}=\frac{1}{144(3)^{\frac{1}{2}}S^3(S+1)}\frac{g^2\mu_B^2}{a^3}\frac{(kT)^2}{J^3}, \quad (21)$$

for $\zeta=S(24JK)^{\frac{1}{2}}/kT\ll1$, and $T\ll T_c$.

At low temperatures and for large values of K, we have $\zeta\gg1$, and the integral I can be evaluated by the method of steepest descents. We need only consider $\rho=1$. We get

$$I=\frac{\pi^{\frac{1}{2}}}{3(3)^{\frac{1}{2}}a^3S^3}\left(\frac{kT}{J}\right)^3\zeta^{\frac{1}{2}}e^{-\zeta}. \quad (22)$$

Combining (18), (19), and (22) gives

$$\begin{aligned}\chi_{\mathrm{II}}=\frac{M}{H}&=\frac{1}{24(3)^{\frac{1}{2}}\pi^{\frac{1}{2}}S^{\frac{1}{2}}(S+1)}\frac{g^2\mu_B^2}{a^3}\frac{(24JK)^{\frac{1}{2}}(kT)^{\frac{1}{2}}}{J^3}\\&\qquad\times\exp[-S(24JK)^{\frac{1}{2}}/kT].\end{aligned} \quad (23)$$

[10] After obtaining this relationship, there came to the attention of the author a recent manuscript by T. Nakamura in which this same result is obtained. Nakamura only considers the case of vanishingly small anisotropy. I should like to thank Dr. Nakamura for having had the opportunity to see his manuscript prior to publication.

Note added in proof: Two additional articles have appeared recently in which the method of spin waves is applied to antiferromagnetism: J. M. Ziman, Proc. Phys. Soc. (London) **65A**, 540 (1952) and R. Kubo, Phys. Rev. **87**, 568 (1952).

The temperature dependence is

$$\chi_{\parallel} \propto T^{\frac{1}{2}} \exp[-S(24JK)^{\frac{1}{2}}/kT], \quad (24)$$

for $\zeta = S(24JK)^{\frac{1}{2}}/kT \gg 1$.

4. CONCLUSION

There is, as yet, very little information concerning the separate values of $\chi_{\parallel}$ and $\chi_{\perp}$ for an antiferromagnet. Griffel and Stout[11] have obtained values of $\chi_{\parallel} - \chi_{\perp}$ for MnF_2 at various temperatures, which, together with previous work by de Haas, Schultz, and Koolhaus[12] on the powder susceptibility of MnF_2, enable them to plot the values of $\chi_{\parallel}$ and $\chi_{\perp}$. It is quite clear from their work that $\chi_{\perp}$ is not constant below the Curie point but increases as T decreases toward zero. This is the type of behavior predicted by Hulthén, and differs from the prediction of the molecular field theory. $\chi_{\parallel}$ decreases as the temperature is lowered and seems to approach zero at $T=0$. The data are not sufficient to allow the temperature dependence of either $\chi_{\parallel}$ or $\chi_{\perp}$ to be determined very much more specifically.

It is a pleasure to thank Professor C. Kittel for the suggestion of the problem and for many discussions concerning it.

[11] M. Griffel and J. W. Stout, J. Chem. Phys. **18**, 1455 (1950).
[12] de Haas, Schultz, and Koolhaus, Physica **7**, 57 (1940).

PHYSICAL REVIEW VOLUME 88, NUMBER 5 DECEMBER 1, 1952

Ionization Loss and Straggling of Fast Electrons*

E. L. Goldwasser, F. E. Mills,† and A. O. Hanson
Department of Physics, University of Illinois, Urbana, Illinois
(Received June 16, 1952)

The most probable energy loss of 9.6- and 15.7-Mev electrons in samples of about one gram per cm² of beryllium, polystyrene, aluminum, copper, and gold has been measured. The losses measured were of the order of one Mev, and the resolution of the apparatus made possible an accuracy of 20 kev. The observed distributions of energy losses are found to be in good agreement with the Landau straggling calculations for the light elements. For the heavier elements there is a spreading of the distribution introduced by radiation and K electron effects. Calculations made by Yang and Kennedy for gold, including these effects, check well with the experimental data.

Applying Fermi's correction for the polarization effect at extreme relativistic velocities to Landau's result for the most probable energy loss, one obtains for the predicted loss in Mev $\Delta_{pc} = 0.1537 D(\Sigma Z/\Sigma A) \times [19.43 + \ln(D/\rho)]$, where D is the absorber thickness in g/cm² and ρ is the absorber density in g/cm³. Experimental results for the light elements are in excellent agreement with this theory. The heavier elements show losses somewhat smaller than those calculated.

INTRODUCTION

THERE have been a number of measurements of the ionization loss and energy straggling suffered by electrons in passing through matter, and the general processes appear to be well understood. A recent study of the energy loss distributions for electrons having initial energies up to 1 Mev has been reported by Chen and Warshaw.[1] They find that the observed most probable energy loss as well as the energy loss distributions are in good agreement with the calculation of Landau.[2] Further work with electrons having energies up to 5 Mev has been carried out by Paul and Reich[3] and is discussed by Schultz.[4] They find that the energy loss at these energies is less than that given by the theory and attribute the decrease to the effect of polarization in the material.

The present work represents an attempt to measure the energy losses and energy distributions at higher energies using highly monoenergetic electrons from the 22-Mev betatron.

EXPERIMENTAL ARRANGEMENT AND PROCEDURE

The experimental arrangement for the removal of the electrons from the betatron and the focusing of the beam into the chamber has been described in previous work.[5,6] The modifications of the scattering chamber and the detector arrangements for the present experiments are shown in Fig. 1. The electron beam is brought to a focus upon the absorber samples, which were mounted on the remotely controlled sample holder at the center of the chamber. A horizontal slit one inch long and 0.020 inch high was mounted in the center of the chamber directly behind the absorbers. This slit was formed by two pieces of gold $\frac{1}{16}$ inch thick. The adjustable aperture and adjustable collimating slit in front of the ionization chamber were edged with pieces of gold $\frac{1}{8}$ inch thick, as described in the previous work.[6] Gold was chosen as the slit edging with the idea that electrons impinging on the slit edge would be scattered completely out of the beam or be so degraded in energy

* Work supported in part by the joint program of the ONR and AEC.
† AEC Predoctoral Fellow.
[1] J. J. L. Chen and S. D. Warshaw, Phys. Rev. **84**, 355 (1951).
[2] L. Landau, J. Phys. (U.S.S.R.) **8**, 201 (1944).
[3] W. Paul and H. Reich, Z. Physik **127**, 429 (1950).
[4] Walter Schultz, Z. Physik **129**, 530 (1951).
[5] Lyman, Hanson, and Scott, Phys. Rev. **84**, 626 (1951).
[6] Scott, Hanson, and Lyman, Phys. Rev. **84**, 638 (1951).

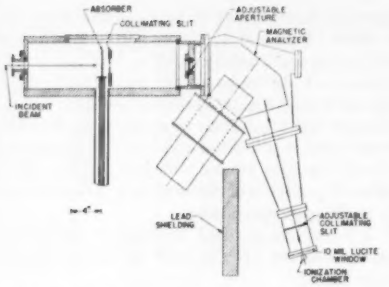

FIG. 1. Side view of experimental arrangement of absorber and analyzer.

that they would be removed from the energy range under consideration. The collimation defined by the aperture at the entrance to the analyzer was such as to limit the electrons entering the analyzer to those which were within two degrees of the direction of the incident beam.

The magnetic analyzer was the same as that used for the earlier experiments. The magnetic field in this instrument was measured and automatically regulated by comparing the emf generated in a rotating coil placed in the magnet gap with an accurately known fraction of the emf generated in a similar coil on the same shaft in the field of a permanent magnet. Special tests indicated that the regulator maintained the field at the position of the rotating coil constant to about 0.03 percent. Since the measuring coil could not be placed in the path traversed by the electrons passing through the analyzer, it was found that precautions had to be taken to insure that the magnet was on an established hysteresis cycle. This effect was not large, but if not kept in control it would easily introduce an error of about 0.2 percent.

The resolution of the analyzer as well as the absolute calibration of the instrument was checked by passing lithium ions of accurately known energies through the system. The lithium ions were evaporated from a platinum filament coated with a thin film of spodumene and accelerated through potentials of from 2 to 25 kilovolts. The momenta of these lithium ions lay in the same range as the momenta of the electrons used in this experiment and could be measured and controlled to about 0.01 percent.

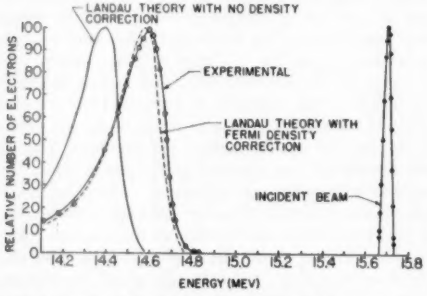

FIG. 2. Energy distribution of unobstructed electron beam and calculated and experimental distributions of electrons after passing through 0.86 g/cm² of aluminum.

The experimental procedure was simply to make alternate runs with and without the absorbers in the beam. In each run the analyzer field was varied through the range for which there was appreciable intensity detected by the ionization chamber, and the currents corresponding to the analyzer settings were recorded.

In the case of gold the intensity of the beam reaching the analyzer was greatly attenuated because of multiple scattering, and in this case a background of about 20 percent of the maximum intensity at the detector had to be subtracted. This background was apparently caused by x-rays produced in the vicinity of the absorber and entrance slit and was nearly independent of the analyzer setting.

Typical plots of the results are shown in Figs. 2 and 3, which show the energy loss spectrum of the electrons in passing through aluminum and gold.

It may be of interest to note that the observed width of the unobstructed beam could be accounted for by the widths of the entrance and exit slits. The energy of the electrons emerging from the betatron, therefore, must have an inherent energy spread that is less than the resolution of the equipment or about 0.1 percent. It was noticed, however, that the energy of the emerging electrons at a particular integrator setting varied by about 0.3 percent during a warming-up period of the order of an hour.

In order to be more certain of the observed energy losses a practice was made of checking the analyzer settings corresponding to the half-maximum intensity point on the steepest side of the observed straggling distribution and both the half-intensity points for the unobstructed beam. Since the half-intensity point of the straggling distribution can be located with greater precision than the maximum, it was often convenient to use this point in the calculation of the most probable energy loss. For light elements the relation between this point and the most probable energy loss is given accurately by the Landau theory, namely,

$$\Delta_p = \Delta_{\frac{1}{2}} + 1.58 S_0,$$

where S_0 has values as defined in the next section.

Since the energy band passed by the analyzer was less than the energy width of the steepest slope in the observed distributions, the distortion of the actual straggling distributions because of the resolution of the analyzer is very small and it is not necessary to make any correction to the observed widths at half height. There is, however, considerable error in the measurements of these widths since these are only about 0.25 Mev. An error of 0.1 percent (of the incident energy of

16 Mev) in the location of the two half-intensity points would therefore account for an uncertainty of about 20 kev or 8 percent of the width itself. The error in the most probable energy loss is considerably less than this, about 2 percent, since the observed losses are of the order of 1 Mev.

THEORY

The straggling in energy of electrons in passing through material has been calculated by Williams[7] and by Landau[2] on the assumption that the straggling is due only to collisions with essentially free electrons and that energy losses associated with the excitation of energy levels in the bound states are sufficiently small so as to effect only the total energy loss. Although the mathematical methods used are different, the resulting straggling distributions are almost identical. In treating the problem, Williams has pointed out that it is useful to classify the collisions suffered by the electrons into two groups. The first group includes all those collisions that occur with a frequency sufficiently great that the probability distribution of the losses due only to these collisions can be treated as a statistical problem of large numbers and therefore is a Gaussian distribution. The second group of collisions consists of the relatively large energy losses that are responsible for the long tail of the straggling distribution. The boundary between these two groups is chosen so that the integrated probability for an electron to make a collision in the second group is exactly unity. The value of this boundary energy S_0 is shown to be

$$S_0=2\pi e^4 nt/mv^2, \tag{1}$$

where e and m are the charge and rest mass of an electron, v is the velocity of the incident particle, n is the number of electrons per unit volume in the absorber, and t is the thickness of the absorber.

Williams finds a straggling distribution which has a full width at half-height $\Gamma=3.86S_0$. The effect of the collisions in the second group is to displace the maximum of the Gaussian due to the energy losses less than S_0 by an amount $0.3S_0$. The most probable loss, which corresponds to the maximum of the straggling distribution, is given by the relation.

$$\Delta_p=\Delta_0+0.3S_0,$$

where Δ_0 represents the mean energy loss associated with individual energy losses of less than S_0.

Landau's calculations are based on the use of the transport equation and are carried out in a continuous manner rather than in Williams' stepwise fashion. The width of his distribution at half-height is $3.98S_0$, and the most probable energy loss is given as

$$\Delta_p=\Delta_0+0.37S_0. \tag{2}$$

The difference between the Williams and the Landau relations for the most probable energy loss amounts to only $0.07S_0$, which for our work (where S_0 is of the order of 60 kev) amounts to only 4 kev for losses of the order of 1 Mev.

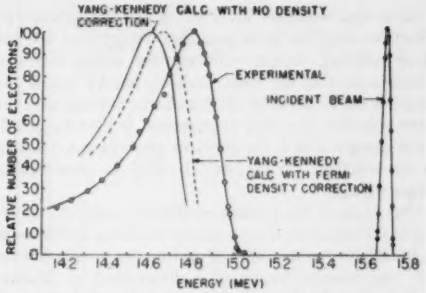

FIG. 3. Energy distribution of unobstructed electron beam and calculated and experimental distributions of electrons after passing through 0.97 g/cm² of gold.

The energy loss Δ_ξ, associated with individual losses less than ξ, is the same for all particles of unit charge moving with the velocity v and is given by the relation[8]

$$\Delta_\xi=S_0\left[\ln\frac{2mv^2\xi}{(1-\beta^2)I^2}-\beta^2\right]. \tag{3}$$

Thus, the loss due to interactions in which S_0 is the maximum energy transfer can be written

$$\Delta_0=S_0\left[\ln\frac{2mv^2S_0}{(1-\beta^2)I^2}-\beta^2\right]. \tag{4}$$

TABLE I. Observed and calculated most probable energy losses. The values given for S_0, Δ, and Γ are all in Mev.

	Be	Poly	Al	Cu	Au
D (g/cm²)	0.7483	0.8090	0.8586	0.8400	0.9658
ρ (g/cm³)	1.839	1.055	2.694	8.808	19.51
			15.7-Mev data		
S_0	0.05094	0.06590	0.06353	0.05885	0.05945
Δ_p (Landau)	1.170	1.482	1.325	1.130	1.020
Δ_{pc} (Fermi)	0.950	1.270	1.135	1.005	0.965
Δ_p (exptl.)	0.945	1.235	1.110	0.980	0.902
Δ_{pc} (Yang-Kennedy)	—	—	—	—	1.045
Γ/S_0 (Landau)	3.98	3.98	3.98	3.98	3.98
Γ/S_0 (exptl.)	3.97	3.98	4.18	4.69	6.99
Γ/S_0 (Yang-Kennedy)	—	—	—	—	6.98
			9.6-Mev data		
S_0	0.05103	0.06602	0.06364	—	—
Δ_p (Landau)	1.125	1.422	1.264	—	—
Δ_{pc} (Fermi)	0.952	1.272	1.137	—	—
Δ_p (exptl.)	0.931	1.227	1.145		

[7] E. J. Williams, Proc. Roy. Soc. (London) **A125**, 445 (1929).

[8] A detailed discussion of the processes of ionization loss, Čerenkov radiation, and polarization effects has been given by M. Schönberg, Nuovo cimento **8**, 169 (1951); **9**, 372 (1952). Application of the theory to the problem at hand was made by P. Janssens and M. Huybrechts, Bull. Cent. Phys. Nucl. Brussels no. 29 (1951).

Since the electrons involved in the straggling distribution near the most probable energy loss are not those suffering violent collisions, the energy-loss distribution around the most probable energy loss is the same for heavy particles of unit charge moving with the same velocity. The only requirement is that the maximum energy which the incident particle can transfer to an electron $[W_m=2mv^2/(1-\beta^2)]$ is considerably larger than S_0.

The value of the average excitation energy I appearing in the equation is very nearly the same in this work as for the energy loss for fast protons, and one could use the experimental values of I determined by Mather and Segrè.[9] If, however, we consider the effect of polarization of the medium on the energy loss, we find by Fermi's treatment that the reduction in energy loss for particles having velocities less than $c/\sqrt{\epsilon}$ is $S_0 \ln\epsilon$, where ϵ is the effective dielectric constant.[10]

A formally more correct interpretation of the experimental values of I obtained from the proton range data is that these are equal to $\epsilon^{\frac{1}{2}}I'$, where I' is the value of the mean excitation potential without the polarization effect. The effective value of ϵ, however, is expected to be close to unity except for the lightest elements. Since we hope to investigate the polarization correction more specifically in future experiments, we have not examined the effect in detail. We have, in this work, used the simple expression $I=13.5Z$ in computing the energy losses from the Landau formula.

The most probable loss, corrected for the polarization effect for extreme relativistic electrons can be treated more simply, since it will not depend on the excitation energies of the material. This can be seen by considering the reduction in energy loss due to polarization, Δ_ϵ, which is applicable to this case.[10,11]

$$\Delta_\epsilon=S_0\left[\ln\left(\frac{\epsilon-1}{1-\beta^2}\right)-\frac{1-\epsilon\beta^2}{1-\epsilon}\right] \text{ for } v>c/\sqrt{\epsilon}, \quad (5)$$

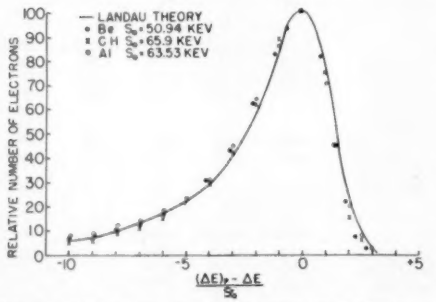

FIG. 4. Calculated and experimental straggling distributions of 15.7-Mev electrons after passing through absorbers of about 1 g/cm² of beryllium, polystyrene, and aluminum plotted *versus* energy in units of $S_0=2\pi e^4 nl/mv^2$.

[9] R. Mather and E. Segrè, Phys. Rev. **84**, 191 (1951).
[10] E. Fermi, Phys. Rev. **57**, 459 (1940).
[11] O. Halpern and H. Hall, Phys. Rev. **73**, 477 (1948).

where $\epsilon=1+(4\pi ne^2\hbar^2/mI^2)$;

$$\Delta_\epsilon\simeq S_0\left[\ln\left(\frac{4\pi e^2 n\hbar^2}{(1-\beta^2)mI^2}\right)-1\right] \text{ for } v\to c. \quad (6)$$

This reduction in energy loss involves only remote collisions which give rise to small energy transfers of the order of the excitation potentials. These collisions are therefore not expected to change the observed straggling distributions in the cases where the simple straggling theory is applicable. Substituting Eq. (4) in Eq. (2) and subtracting Eq. (6), we find that the corrected most probable energy loss in condensed materials for extreme relativistic particles is given by

$$\begin{aligned}\Delta_{pc}&=\Delta_p-\Delta_\epsilon=S_0[\ln(c^2mt/\hbar^2)+0.37],\\&=S_0[\ln(t/a_0)+0.37],\end{aligned} \quad (7)$$

where a_0 is the Bohr radius of the hydrogen atom. This formula may be written in another way, which states explicitly the dependence on the volume density ρ and the surface density D of the sample. Putting in the constants with ρ and D in units of grams per cm³ and grams per cm², respectively, one obtains

$$\Delta_{pc}=0.1537(\Sigma Z/\Sigma A)D[19.43+\ln(D/\rho)] \text{ Mev}. \quad (8)$$

The simple formulas and straggling distributions do not hold very accurately for elements of higher atomic number for several reasons. One important complication is the fact that when the K or L excitation energies are of the same order as S_0 these energy losses must be treated separately in evaluating the straggling. Such a treatment of the straggling for lower energy electrons has been made by Blunck and Leisegang,[12] who found that they could account for the now classic straggling distributions of White and Millington.

The effect of bremsstrahlung on the most probable energy loss is very small, even in the case of gold where the mean radiation loss is about twice the mean ionization loss. The reason for this is that the radiation loss represents the effect of a small number of large energy transfers. An order of magnitude estimate of the fraction of the radiative losses which may contribute to the shift and broadening of the distribution curve can be made by considering the total radiation loss associated with energy losses less than $2S_0$. This fraction of the radiative loss is about 30 kev for the present gold sample for which the mean loss is about 2 Mev and only about 5 kev for the aluminum sample. From such an estimate it is seen that the radiation losses must be included in the case of gold, if one is to obtain results having a precision equal to that of the experimental measurements, but that such considerations are unnecessary for aluminum and elements of lower Z.

Multiple scattering can have only a small effect in most of the samples used in this work. Yang has shown that, in the case of electrons which enter and leave the

[12] O. Blunck and S. Leisegang, Z. Physik **128**, 500 (1950).

absorber normal to the surface, the effective thickness of the sample is increased by the factor $(1+t_r/6.9)$, where the thickness t_r is in radiation lengths.[13] This results in less than a 3 percent increase in the path length in the gold absorber and about ½ percent in the aluminum absorber. The effect of multiple scattering is therefore completely accounted for by simply increasing the thickness of the absorber by the above factor.

The three above complications have been taken into account for our particular gold sample by Yang and Kennedy who have made numerical calculations for the expected straggling distributions suffered by 15.7-Mev electrons neglecting the effect of polarization.[14] This curve is shown with the experimental data for gold in Fig. 3.

DISCUSSION OF RESULTS

The results for the observed most probable energy losses in the various samples are given in Table I. The samples of lower atomic number were used with both 9.6- and 15.7-Mev electrons, while the gold and copper samples were used only at 15.7 Mev. The losses and the widths of the straggling distributions as calculated by the Landau equation are included in each case. For gold we have also included the values calculated by Yang and Kennedy.

The nature of the agreement between experiment and the calculations for the light elements is apparent in Figs. 2 and 4. The observed most probable energy loss is about 20 percent less than that calculated by the Landau equation without the density correction, but it is in good agreement with the simple asymptotic equation which includes the effect of polarization. The agreement between the observed and calculated distributions shown in Fig. 4 is well within the probable error of the experiments.

The corresponding results for gold are shown in Figs. 3 and 5. It can be seen that the shape of the straggling distribution is in very good agreement with the Yang-Kennedy calculation. The observed energy loss is less than that calculated without the polarization effect by about 0.20 Mev. The expected reduction due to the polarization effect as calculated by the asymptotic equation is 0.06 Mev. The reduction (as obtained from the more detailed calculations of Halpern and Hall for lead), increased by the density term

$$\{S_0 \ln[(\rho/ZA)_{Au}(AZ/\rho)_{Pb}]\},$$

is 0.10 Mev.

The distribution for copper is also given in Fig. 5,

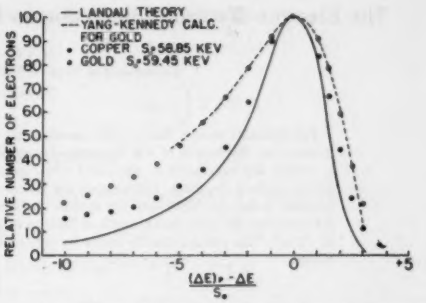

FIG. 5. Calculated and experimental straggling distributions of 15.7-Mev electrons after passing through absorbers of about 1 g/cm² of copper and gold plotted *versus* energy in units of $S_0=2\pi e^4 nl/mv^2$.

and it is apparent that the straggling distribution is somewhat wider than the Landau curve. The observed energy loss is somewhat less than that given by the asymptotic formula. No more exact calculations are available for copper.

The most probable energy loss has been measured for cosmic-ray mesons by Bowen and Roser.[15] They find that the most probable energy loss of fast mesons in a 3-cm crystal of anthracene ($C_{14}H_{10}$, density=1.25) is 6.15 Mev. This is in good agreement with the value of 6.25 Mev calculated by the asymptotic formula [Eq. (8)].

SUMMARY

The agreement between experiment and theory is very good for the light elements both with respect to the magnitude of the energy loss and to the energy distribution.

The broadening of the energy-straggling distribution in gold is completely accounted for in a numerical calculation which includes the effect of the high K and L excitation energies and the additional straggling introduced by the radiation losses.

The only difficulty is the failure to account for an apparent polarization effect in gold, which is somewhat larger than the theoretical estimates of this effect.

It is a pleasure to express our thanks to T. J. Keegan for his cooperation in operating and maintaining the betatron and to J. C. Buchta, J. H. Malmberg, and G. E. Modesitt for their contributions in the development of the equipment and for their assistance in obtaining the data and organizing the results. We are very much indebted to Dr. C. N. Yang for valuable discussions and his stimulating interest in this work.

[13] C. N. Yang, Phys. Rev. **84**, 599 (1951).

[14] C. N. Yang and J. M. Kennedy, private communication. (Schultz in reference 4 carried out similar calculations for the data of Paul and Reich.)

[15] T. Bowen and F. X. Roser, Phys. Rev. **85**, 992 (1952).

The Electron-Neutron Interaction as Deduced from Pseudoscalar Meson Theory

BURTON DAVID FRIED*
Department of Physics, University of Chicago, Chicago, Illinois
(Received June 13, 1952)

Pseudoscalar meson theory with pseudoscalar coupling is used to find a value for the electron-neutron interaction. By means of the Feynman-Dyson-Wick techniques, the one-neutron matrix elements of the S matrix are calculated in the usual weak coupling perturbation theory, carried to second order in the meson-nucleon coupling. Expressions for the magnetic moment and the electron-neutron interaction are deduced from this. By using the former to fix the coupling constant, it is found that the potential well representing the latter has a depth of 5380 ev if, as is conventional, this is taken to be square, with a radius of e^2/mc^2. The various results found by previous authors and their relation to the present work are discussed.

I. INTRODUCTION

SEVERAL years after Dee's[1] attempt to detect an interaction between neutrons and electrons, Condon[2] pointed out that the rather large upper limit given by Dee could be reduced by a factor of about one thousand from a consideration of the effect which such an interaction would have on the scattering of slow neutrons. Experiments were carried out in 1947, almost simultaneously, by Havens, Rabi, and Rainwater[3] at Columbia University and by Fermi and Marshall[4] at the University of Chicago, in which the interference between the electronic and nuclear scattering of slow neutrons was studied. Both groups gave values of less than 10 kev for the depth of the interaction potential well, assuming, conventionally, that this is square with a radius equal to e^2/mc^2. Since that time, more precise measurements have been made, typical results being (5300 ± 1000) ev,[5] (4100 ± 1000) ev,[6] and (4200 ± 600) ev.[7]

The calculation of the electron-neutron interaction from meson theory has been carried out by several authors.[8–11] Of the several varieties of meson theory, the pseudoscalar is currently in vogue since the pseudoscalar nature of the pi-meson has been generally accepted. However, even with the same theory—pseudoscalar mesons, pseudoscalar coupling, with the usual weak coupling perturbation theory carried to the second order in the meson nucleon coupling—different methods of calculation led to well depths ranging from 1300 ev[8,11] to 5220 ev.[10] Since it has not been certain whether these discrepancies were due to errors, to different methods of evaluating divergent integrals, or to the use of different formal procedures in carrying out the perturbation theory, a clarification of the theoretical situation seems very desirable.

Moreover, still another result is obtained from Foldy's treatment[12] which makes no use of meson theory. A Pauli term is simply added to the Dirac equation to represent the empirical neutron magnetic moment. As a consequence of the relativistic covariance of the Dirac equation, it then follows that the neutron will also interact with an external electric field. If this interaction is expressed in terms of an electron-neutron well depth, a result of 4080 ev is obtained, which agrees with none of the values which have been calculated from meson theory.

Of course, meson theory weak coupling calculations of such effects cannot be taken too seriously—for instance, they do not even give the correct neutron to proton magnetic moment ratio—but it certainly should be possible to state definitely just what value pseudoscalar meson theory does predict for this effect. In this paper, the electromagnetic properties of neutrons are investigated with the aid of the Feynman-Dyson-Wick techniques. Special attention is given to the interpretation of the terms obtained from field theory so that the relationship of the various results obtained by previous authors can be made quite clear. Naturally, the result of this calculation should not be expected to agree very closely with the experiments, even if field theory is correct, since terms of higher order in the meson nucleon coupling g have not been taken into account and g is by no means small. In fact, the mesonic analog of the fine structure constant must have a value of about 7 in order to fit the neutron magnetic moment [see Eq. (56) below]. The chief purpose of this investigation is to clear away the confusion arising from the number of theoretical values which have been reported. The results obtained are in agreement with those found by Slotnick and Heitler[8] and by Dancoff and Drell.[10]

A similar calculation has been made for the case of pseudovector coupling but no new results were obtained. It is found that the magnetic moment is un-

* Now at Radiation Laboratory, University of California, Berkeley, California.
[1] P. E. Dee, Proc. Roy. Soc. (London) **A136**, 727 (1932).
[2] E. U. Condon, Phys. Rev. **49**, 459 (1936).
[3] Havens, Rabi, and Rainwater, Phys. Rev. **72**, 634 (1947).
[4] E. Fermi and L. Marshall, Phys. Rev. **72**, 1139 (1947).
[5] Havens, Rainwater, and Rabi, Phys. Rev. **82**, 345 (1951).
[6] Hammermesh, Ringo, and Wattenberg, Phys. Rev. **85**, 483 (1952).
[7] Harvey, Hughes, and Goldberg, Phys. Rev. **87**, 220 (1952).
[8] M. Slothick and W. Heitler, Phys. Rev. **75**, 1645 (1949).
[9] K. M. Case, Phys. Rev. **76**, 1 (1949).
[10] S. M. Dancoff and S. D. Drell, Phys. Rev. **76**, 205 (1949).
[11] S. Borowitz and W. Kohn, Phys. Rev. **76**, 818 (1949).
[12] L. L. Foldy, Phys. Rev. **83**, 628 (1951).

changed (provided that, as usual, the coupling constant is multiplied by twice the nucleon to meson mass ratio) as might be expected from the theorems on the "equivalence" of the two couplings.[13] However, the electron-neutron interaction is found to be logarithmically divergent in agreement with Feynman's conclusions.[14]

The field theory calculation of the S matrix is outlined in Sec. II, most of the algebraic details being left for Sec. III. These results are discussed and interpreted in Sec. IV and the status of previous calculations is explained.

II. CALCULATION OF THE S MATRIX

The system to be studied consists of quantized nucleon and pseudoscalar meson fields in presence of an external, c-number electromagnetic field. The charge symmetric formalism will be used according to which the mesons are described by three Hermitian fields, ϕ_1, ϕ_2, ϕ_3, or, alternatively, by the field ϕ_3 and the complex fields

$$\phi=(\phi_1+i\phi_2)/\sqrt{2}, \quad \phi^*=(\phi_1-i\phi_2)/\sqrt{2}. \tag{1}$$

The potentials of the external electromagnetic field will be denoted by A_ν, ($\nu=1, 2, 3, 4$). It will be convenient to use the isotopic spin formalism and combine the proton and neutron spinor fields, ψ_P, ψ_N, into a single, eight component spinor,

$$\psi=\begin{pmatrix}\psi_N\\ \psi_P\end{pmatrix}.$$

The Lagrangian density is

$$\mathfrak{L}=\mathfrak{L}_0+\mathfrak{L}_g+\mathfrak{L}_e$$

with

$$\mathfrak{L}_0=-\frac{1}{2}\left(\frac{\partial\phi_a}{\partial x_\nu}\frac{\partial\phi_a}{\partial x_\nu}+\mu^2\phi_a\phi_a\right)+i\psi^\dagger\left(\gamma^\nu\frac{\partial}{\partial x_\nu}+M\right)\psi,$$

$$\mathfrak{L}_g=-g\psi^\dagger\gamma^5\tau^a\phi_a\psi,$$

$$\mathfrak{L}_e=-eA_\nu\left\{\frac{\partial\phi_1}{\partial x_\nu}\phi_2-\frac{\partial\phi_2}{\partial x_\nu}\phi_1-\psi_P^\dagger\gamma^\nu\psi_P\right\}-e^2A_\nu A_\nu\frac{\phi_1^2+\phi_2^2}{2},$$

where τ^1, τ^2, τ^3 are the Pauli isotopic spin matrices which operate on the charge index of ψ; $\psi^\dagger$ and γ^ν are as defined in reference 15; and natural units, $\hbar=c=1$, are used. The usual canonical formalism[15] leads to a Hamiltonian density

$$\mathfrak{IC}=\mathfrak{IC}_0+\mathfrak{IC}_I,$$

where $\mathfrak{IC}_0$ is the part which remains when e and g are set equal to zero. Going over to the interaction representation, the development in time of the Schrödinger state functional, $F(t)$, is given by

$$F(t)=e^{-iH_0t}G(t),$$

where

$$H_0=\int d^3x\mathfrak{IC}_0(x)$$

and $G(t)$ satisfies

$$i\partial G(t)/\partial t=H_1(t)G(t)=\left[\int d^3x\mathfrak{IC}_1(x)\right]G(t).$$

Here

$$\begin{aligned}\mathfrak{IC}_1(x)&\equiv e^{iH_0t}\mathfrak{IC}_Ie^{-iH_0t}=g\psi^\dagger\gamma^5\tau^a\phi_a\psi\\&+eA_\nu\left\{\frac{\partial\phi_1}{\partial x_\nu}\phi_2-\frac{\partial\phi_2}{\partial x_\nu}\phi_1-\psi_P^\dagger\gamma^\nu\psi_P\right\}\\&+e^2(A_\nu A_\nu-A_4^2)\frac{\phi_1^2+\phi_2^2}{2}\\&=g\sqrt{2}(\psi_P^\dagger\gamma^5\psi_N\phi+\psi_N^\dagger\gamma^5\psi_P\phi^*)\\&+g\psi^\dagger\gamma^5\tau^3\psi\phi_3-eA_\nu\psi_P^\dagger\gamma^\nu\psi_P\\&+ieA_\nu\left(\frac{\partial\phi}{\partial x_\nu}\phi^*-\frac{\partial\phi^*}{\partial x_\nu}\phi\right)+e^2(A_\nu A_\nu-A_4^2)\phi^*\phi.\end{aligned} \tag{2}$$

The commutation relations for the field operators in this interaction representation are:

$$[\phi(x), \phi^*(y)]=[\phi_3(x), \phi_3(y)]=-i\Delta(x-y),$$
$$\{\psi(x), \psi^\dagger(y)\}=\Gamma(x-y),$$

with

$$\Delta(x)=\Delta(\mathbf{x}, t)\equiv\frac{1}{(2\pi)^3}\int d^3k e^{i\mathbf{k}\cdot\mathbf{x}}\frac{\sin[(\mathbf{k}^2+\mu^2)^{\frac{1}{2}}t]}{(\mathbf{k}^2+\mu^2)^{\frac{1}{2}}},$$

and

$$\Gamma(x)\equiv\left(M-\gamma^\nu\frac{\partial}{\partial x_\nu}\right)\Delta(x).$$

The actual calculation consists of finding the matrix elements, between two one-neutron states, of the operator S which carries the initial state function into the final one:

$$G(\infty)=SG(-\infty), \quad S=1+\sum_{n=1}^{\infty}S_n,$$

$$S_n=\frac{(-i)^n}{n!}\int d^4x_1\cdots\int d^4x_nT[\mathfrak{IC}_1(x_1)\cdots\mathfrak{IC}_1(x_n)],$$

where T denotes the temporal ordering of operators.[16] Applying Wick's formalism to the T-product leads to the Feynman rules, which will be used in what follows.

The one-neutron, time-independent state functionals will be called F_1, F_2, while F_0 will be used to denote the vacuum state (no neutrons or mesons present). It is assumed that F_1 describes a state with one free neutron

[13] K. M. Case, Phys. Rev. **76**, 14 (1949).
[14] R. P. Feynman, Phys. Rev. **76**, 769 (1949).
[15] G. Wentzel, *Quantum Theory of Fields* (Interscience Publishers, Inc., New York, 1949).
[16] G. C. Wick, Phys. Rev. **80**, 268 (1950).

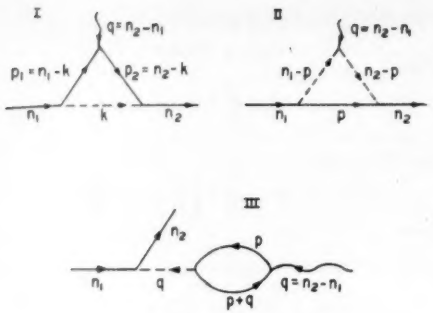

FIG. 1. Feynman diagrams.

of momentum n_1, spinor u_1, i.e., that

$$(F_0, \psi(x)F_1) = u_1 e^{in_1\cdot x},$$

where $u_1 e^{in_1\cdot x}$ is a solution of the unperturbed Dirac equation,

$$\left(\gamma^\nu \frac{\partial}{\partial x_\nu} + M\right) u_1 e^{in_1\cdot x} = 0.$$

This gives

$$(M + i\boldsymbol{n}_1)u_1 = 0, \tag{3}$$

with

$$\boldsymbol{n}_1 \equiv (n_1)_\nu \gamma^\nu.$$

(If f_ν is any four-vector, the symbol $\boldsymbol{f}$ will denote the matrix $\sum_{\nu=1}^{4} f_\nu \gamma^\nu$. Also, $f\cdot g$ will mean the scalar product $\sum_{\nu=1}^{4} f_\nu g_\nu$, and $\mathbf{f}$ will be used for the three-vector with components f_1, f_2, f_3.) Taking the Hermitian conjugate of (3) and multiplying on the right by γ^4 yields

$$u_1^\dagger(M + i\boldsymbol{n}_1) = 0.$$

Similarly, the state F_2 has one free neutron with momentum n_2, spinor u_2, and

$$(M + i\boldsymbol{n}_2)u_2 = 0, \quad u_2^\dagger(M + i\boldsymbol{n}_2) = 0.$$

If F_1 and F_2 are different states,

$$(F_2, F_1) = (F_2, S_1 F_1) = (F_2, S_2 F_1) = 0,$$

so the lowest order contribution will come from S_3. It will be proportional to eg^2 if terms of higher order in e or eA are neglected. (In this approximation, the e^3 term of $3\mathcal{C}_1$, Eq. [2], may be dropped.) Thus, to order eg^2,

$$(F_2, SF_1) = (F_2, S_3 F_1) = M_\mathrm{I} + M_\mathrm{II} + M_\mathrm{III},$$

where $M_\mathrm{I}, M_\mathrm{II}, M_\mathrm{III}$ are the matrix elements associated with the Feynman diagrams of Fig. 1. In these diagrams solid lines denote nucleons, dotted lines stand for mesons, and the wavy line indicates the external electromagnetic field. Neutron momenta are labeled n, proton momenta, p. The mesons in I and II are charged, while that of III is neutral.

Specifically,

$$M_\mathrm{I} = \frac{-eg^2}{8\pi^4} \int d^4k u_2^\dagger \gamma^5 \frac{1}{M + i(\boldsymbol{n}_2 - \boldsymbol{k})} \times \boldsymbol{a}(q) \frac{1}{M + i(\boldsymbol{n}_1 - \boldsymbol{k})} \gamma^5 u_1 \frac{1}{\mu^2 + k^2},$$

$$M_\mathrm{II} = \frac{-ieg^2}{8\pi^4} \int d^4p u_2^\dagger \gamma^5 \frac{1}{M + i\boldsymbol{p}} \times \gamma^5 u_1 \frac{(n_1 + n_2 - 2p)\cdot a(q)}{[\mu^2 + (n_1 - p)^2][\mu^2 + (n_2 - p)^2]},$$

$$M_\mathrm{III} = \frac{-eg^2}{16\pi^4} \int d^4p u_2^\dagger \gamma^5 u_1 \times \mathrm{Sp}\left\{ \gamma^5 \frac{1}{M + i\boldsymbol{p}} \boldsymbol{a}(q) \frac{1}{M + i(\boldsymbol{p} + \boldsymbol{q})} \right\} \frac{1}{\mu^2 + q^2},$$

where $a_\nu(k)$ is the Fourier transform of the electromagnetic potential

$$A_\nu(x) = \frac{1}{(2\pi)^4} \int d^4k e^{ik\cdot x} a_\nu(k), \tag{4}$$

$$a_\nu(k) = \int d^4x e^{-ik\cdot x} A_\nu(x), \tag{5}$$

and

$$q \equiv n_2 - n_1.$$

Hereafter, $a_\nu(q)$ will be written simply as a_ν, so that $\boldsymbol{a}$ stands for the matrix $a_\nu(q)\gamma^\nu$. As usual, the nucleon and meson masses, M and μ, are to be understood to have negative imaginary parts which are set equal to zero after all integrations have been performed.

We consider first the integral M_III. It is formally quadratically divergent, but the spur of the Dirac matrix in the curly braces vanishes since γ^5, $\gamma^5\gamma^\mu$, $\gamma^5\gamma^\mu\gamma^\nu$, $\gamma^5\gamma^\mu\gamma^\nu\gamma^\lambda$ all have zero spur. Thus, any cut-off or regularization procedure which makes the integral finite will give M_III the value zero, so in this sense we may simply set

$$M_\mathrm{III} = 0.$$

The other terms, M_I and M_II, are also divergent, although only logarithmically. The subsequent algebraic manipulations in which the "convergent" parts are separated from the "divergent" parts are therefore meaningful only if we imagine these integrals regularized or cut off in some manner. The terms which appear "convergent" are those which would remain finite if, say, the cut-off momentum were allowed to become infinite, while the "divergent" terms are those which would not approach any finite limit. The interpretation of the latter is discussed in more detail below.

The expressions for $M_{\rm I}$ and $M_{\rm II}$ can be simplified by rationalizing the denominators and bringing the γ^5 factors together. Using also the Dirac equations for u_1 and u_2,

$$(M+in_1)u_1=0, \quad u_2^\dagger(M+in_2)=0 \tag{6}$$

we find

$$M_{\rm I}=\frac{-eg^2}{8\pi^4}\int d^4k \times\frac{u_2^\dagger \boldsymbol{k}a\boldsymbol{k}u_1}{[M^2+(n_2-k)^2][M^2+(n_1-k)^2][\mu^2+k^2]}. \tag{7}$$

In terms of the average neutron momentum,

$$n\equiv(n_1+n_2)/2,$$

$M_{\rm II}$ may be written

$$M_{\rm II}=\frac{-eg^2}{8\pi^4}2\bar{N}\int d^4p \times\frac{u_2^\dagger(M+i\boldsymbol{p})u_1(n-p)\cdot a}{[M^2+p^2][\mu^2+(n_1-p)^2][\mu^2+(n_2-p)^2]}. \tag{8}$$

Thus, evaluation of $M_{\rm I}$ and $M_{\rm II}$ depends upon a knowledge of integrals of the form

$$\int d^4k\frac{(1,\ k_\mu,\ k_\mu k_\nu)}{(k^2-2n_1\cdot k+\Delta_1)(k^2-2n_2\cdot k+\Delta_2)(k^2+\Delta_3)}. \tag{9}$$

These will now be computed and the result, Eq. (13), will be substituted into Eqs. (7) and (8) for $M_{\rm I}$ and $M_{\rm II}$. It will be shown that both of these are of the form

$$u_2^\dagger[H(q^2)\boldsymbol{a}+K(q^2)(\boldsymbol{aq}-\boldsymbol{qa})+L(q^2)q^2\boldsymbol{a}]u_1,$$

where H, K, and L are definite integrals containing q^2 as a parameter. If the external fields are slowly varying so that only small values of q^2 are relevant, it will be in order to make an expansion in powers of q. Retaining only terms of order q^2, we have

$$M_{\rm I}+M_{\rm II}=u_2^\dagger(E\boldsymbol{a}-\tfrac{1}{2}F[\boldsymbol{a},\boldsymbol{q}]-Gq^2\boldsymbol{a})u_1, \tag{10}$$

where E, F, and G are calculable constants, or, expressed in terms of the actual electromagnetic potentials and fields,

$$M_{\rm I}+M_{\rm II}=\int d^4x u_2^\dagger e^{-in_2\cdot x}(E\boldsymbol{A}+\tfrac{1}{2}F\mathfrak{F}_{\mu\nu}\sigma_{\mu\nu} +G\Box^2\boldsymbol{A})u_1e^{in_1\cdot x}, \tag{11}$$

with

$$\mathfrak{F}_{\mu\nu}=\partial A_\nu/\partial x_\mu-\partial A_\mu/\partial x_\nu, \quad \sigma_{\mu\nu}=[\gamma^\mu,\gamma^\nu]/2i. \tag{12}$$

The statements made in this paragraph will be substantiated in Sec. III and the values of E, F, and G will be calculated explicitly. The interpretation of the result (11) will then be discussed in Sec. IV.

III. ALGEBRAIC DETAILS

The integrals (9) can be evaluated by standard methods.[17] We have

$$\int d^4k\frac{(1,\ k_\mu,\ k_\mu k_\nu)}{(k^2-2n_1\cdot k+\Delta_1)(k^2-2n_2\cdot k+\Delta_1)(k^2+\Delta_2)} =\int_0^1 dx\int_0^1 dy\int d^4k\frac{2x[1,\ (xn_y)_\mu,\ k^2\delta_{\mu\nu}/4+(xn_y)_\mu(xn_y)_\nu]}{(k^2+\Delta)^3}$$

$$=\frac{\pi^2 i}{2}[A(\Delta),\ 2B(\Delta)n_\mu,\ C(\Delta)\delta_{\mu\nu} +D(\Delta)(n_{1\mu}n_{2\nu}+n_{1\nu}n_{2\mu})+E(\Delta)(n_{1\mu}n_{1\nu}+n_{2\nu}n_{2\mu})], \tag{13}$$

where

$$\Delta=x\Delta_1+(1-x)\Delta_2+M^2x^2+q^2x^2y(1-y), \tag{14}$$

$$n_y=n_1y+n_2(1-y), \tag{15}$$

and

$$\left.\begin{aligned} A(\Delta)&=2\int_0^1 dx\int_0^1 dy\frac{x}{\Delta}, \quad B(\Delta)=2\int_0^1 dx\int_0^1 dy\frac{x^2y}{\Delta},\\ C(\Delta)&=\frac{1}{\pi^2 i}\int_0^1 dx\int_0^1 dy\int d^4k\frac{k^2x}{(k^2+\Delta)^3}\\ &=\frac{1}{\pi^2 i}\int_0^1 dx\int_0^1 dy\int d^4k\frac{x}{(k^2+\Delta^2)}-\frac{1}{4},\\ D(\Delta)&=2\int_0^1 dx\int_0^1 dy\frac{x^2y(1-y)}{\Delta},\\ E(\Delta)&=2\int_0^1 dx\int_0^1 dy\frac{x^2y^2}{\Delta}. \end{aligned}\right\} \tag{16}$$

All of these integrals are "convergent" in the sense explained above except for C, which is logarithmically "divergent." However, it will be seen that in the sum $M_{\rm I}+M_{\rm II}$ the difference of two such terms appears and that this is "convergent."

The result (13) may now be substituted into (7) and (8) to find $M_{\rm I}$ and $M_{\rm II}$. In the case of $M_{\rm I}$, $\Delta_1=0$, since $n_1^2=n_2^2=-M^2$, and $\Delta_2=\mu^2$, so

$$\Delta_{\rm I}=M^2X_{\rm I}+x^2y(1-y)q^2, \tag{17}$$

where

$$X_{\rm I}\equiv x^2-\eta x+\eta, \tag{18}$$

$$\eta\equiv\mu^2/M^2. \tag{19}$$

For $M_{\rm II}$, $\Delta_1=\mu^2-M^2$ and $\Delta_2=M^2$, so

$$\Delta_{\rm II}=M^2X_{\rm II}+x^2y(1-y)q^2, \tag{20}$$

$$X_{\rm II}=x^2+(\eta-2)x+1. \tag{21}$$

[17] See, for instance, the appendix of Feynman's article, reference 14.

Writing A_1 for $A(\Delta_1)$, A_{11} for $A(\Delta_{11})$, etc., Eqs. (6), (7), and (13) give

$$M_1=-(ieg^2/16\pi^2)u_2^\dagger\{iM(D_1+E_1)[\boldsymbol{a},\boldsymbol{q}] +D_1q^2\boldsymbol{a}-2(M^2E_1+M^2D_1+C_1)\boldsymbol{a}\}u_1. \quad (22)$$

Similarly, from (6), (8), and (13) we find

$$M_{11}=(eg^2/8\pi^2)u_2^\dagger\{[2iM^2(D_{11}+E_{11}-2B_{11}) +iM^2A_{11}-iC_{11}]\boldsymbol{a} +\tfrac{1}{2}M(D_{11}+E_{11}-2B_{11}+A_{11}/2)[\boldsymbol{a},\boldsymbol{q}]\}u_1. \quad (23)$$

Adding the two results,

$$M_1+M_{11}=(eg^2/16\pi^2)u_2^\dagger\{[4iM^2(D_{11}+E_{11}-2B_{11}) +2iM^2(A_{11}+E_1+D_1)+2i(C_1-C_{11})]\boldsymbol{a} -iD_1q^2\boldsymbol{a}+M(D_{11}+E_{11}-2B_{11}+A_{11}/2 +D_1+E_1)[\boldsymbol{a},\boldsymbol{q}]\}u_1. \quad (24)$$

Note that the two divergent integrals appear only in the combination

$$C_1-C_{11}=\frac{1}{\pi^2 i}\int_0^1 dx\int_0^1 dy\int d^4k\cdot k^2x \times\left(\frac{1}{(k^2+\Delta_1)^3}-\frac{1}{(k^2+\Delta_{11})^3}\right), \quad (25)$$

which is "convergent" since

$$1/(k^2+\Delta_1)^3-1/(k^2+\Delta_{11})^3 \quad (26)$$

behaves as $1/(k^2)^4$ for large values of k^2.

As remarked above, an expansion in powers of q^2 is indicated, e.g.,

$$A(q^2)=A(0)+A'(0)q^2+\cdots \quad (27)$$

so that to order q^2, (24) gives

$$M_1+M_{11}=\frac{eg^2}{16\pi^2}u_2^\dagger(P\boldsymbol{a}+Q[\boldsymbol{a},\boldsymbol{q}]+Rq^2\boldsymbol{a})u_1, \quad (28)$$

where P, Q, and R are the constants

$$\left.\begin{aligned} P&=4iM^2[D_{11}(0)+E_{11}(0)-2B_{11}(0)]+2iM^2A_{11}(0) \\ &\quad +iM^2E_{11}(0)+2i[C_1(0)-C_{11}(0)], \\ Q&=M[D_{11}(0)+E_{11}(0)-2B_{11}(0)+[A_{11}(0)/2] \\ &\quad +D_1(0)+E_1(0)], \\ R&=-iD_1(0)+4iM^2[D_{11}'(0)+E_{11}'(0)-2B_{11}'(0)] \\ &\quad +2iM^2A_{11}'(0)+2iM^2[E_1'(0)+D_1'(0)] \\ &\quad +2i[C_1'(0)-C_{11}'(0)]. \end{aligned}\right\} \quad (29)$$

The evaluation of Q and R is quite straightforward and involves only elementary quadratures. For instance, by using (16) through (21) we have

$$Q=2M\int_0^1 dx\int_0^1 dy\left\{\frac{x^2y(1-y)+x^2y^2-2x^2y+x/2}{M^2X_{II}} +\frac{x^2y(1-y)+x^2y^2}{M^2X_I}\right\}=\frac{1}{M}\int_0^1 dx\frac{x^2}{X_I},$$

since $X_{II}\to X_I$ if $x\to 1-x$. Thus

$$Q=\frac{1}{M}\int_0^1 dx\frac{x^2}{x^2-\eta x+\eta}=\frac{1}{M}f_0(\eta), \quad (30)$$

$$f_0(\eta)=1-\frac{\eta}{2}\log\eta+\frac{\eta^2-2\eta}{(4\eta-\eta^2)^{\frac{1}{2}}}\cos^{-1}\frac{\eta^{\frac{1}{2}}}{2}. \quad (31)$$

Similarly,

$$R=-(2i/M^2)f_1(\eta), \quad (32)$$

$$f_1(\eta)=\frac{13-4\eta}{3(4-\eta)}+\left(\frac{1}{4}-\frac{2\eta}{3}\right)\log\eta +\frac{\eta^{\frac{1}{2}}[-(4/3)\eta^2+(17/2)\eta-(35/3)]}{(4-\eta)^{\frac{1}{2}}}\cos^{-1}\frac{\eta^{\frac{1}{2}}}{2}. \quad (33)$$

However, some care must be excerised in the case of P, for it contains the difference of two divergent integrals. The C terms which appear in R, i.e., $C_1'(0)$ and $C_{11}'(0)$, are individually "convergent" since in the expansion of C_1 or C_{11} in powers of q^2 the coefficient of q^2 is a "convergent" integral. On the other hand, the terms in these expansions which are independent of q, i.e., the $C_1(0)$ and $C_{11}(0)$ which appear in P, are each divergent and only their difference is finite. Therefore, unless the evaluation of P is done rather carefully, almost any result may be found. The procedure adopted here is simply to compute M_1+M_{11} directly from (7) and (8) for the case $n_1=n_2$, $u_1=u_2$, using a Lorentz frame in which

$$\mathbf{n}_1=\mathbf{n}_2=0.$$

Then $q=0$ and we can find P from the equation

$$M_1+M_{11}=\frac{eg^2}{16\pi^4}u_1^\dagger P\boldsymbol{a}u_1=\frac{ieg^2}{16\pi^4}Pa_4,$$

where only the a_4 term remains because

$$u_1^\dagger\gamma u_1=0, \quad u_1^\dagger\gamma^4u_1=i.$$

A straightforward computation leads to the result

$$M_1+M_{11}=\int d^3k f(\mathbf{k}),$$

where $f(\mathbf{k})$ is a sum of terms which, taken separately, would lead to divergent integrals. However,

$$f(\mathbf{k})\equiv 0,$$

so we may conclude that, in this case,

$$M_{\mathrm{I}}+M_{\mathrm{II}}=0, \tag{34}$$

and consequently

$$P=0.$$

It has now been shown that (10) is correct:

$$M_{\mathrm{I}}+M_{\mathrm{II}}=u_2^\dagger(E\boldsymbol{a}-\tfrac{1}{2}F[\boldsymbol{a},\boldsymbol{q}]-G\boldsymbol{q}^2\boldsymbol{a})u_1, \tag{10}$$

with

$$E=0,\quad F=\frac{-eg^2}{8\pi^2M}f_0(\eta),\quad G=\frac{eg^2i}{8\pi^2M^2}f_1(\eta). \tag{35}$$

Remembering Eqs. (4) and (5), we have:

$$M_{\mathrm{I}}+M_{\mathrm{II}}=\int d^4x u_2^\dagger e^{-i\mathbf{q}\cdot\mathbf{x}}(\tfrac{1}{2}F\sigma_{\mu\nu}\mathfrak{F}_{\mu\nu}+G\Box^2\boldsymbol{A})u_1e^{i\mathbf{q}_1\cdot\mathbf{x}}. \tag{36}$$

IV. INTERPRETATION

We shall now discuss the interpretation of the result (36) of the field theory calculation for the one-neutron matrix elements of S. Of course, quantities such as the scattering cross section for neutrons in an external electromagnetic field can be obtained directly from (36) in the usual way, but in order to find the neutron magnetic moment and the electron-neutron interaction it is convenient to deduce from (36) an effective Hamiltonian for neutrons moving in an electromagnetic field. Indeed, if the ordinary Dirac equation for the neutron wave function ψ (nonquantized) were

$$(H^0+V)\psi=(m\beta+\boldsymbol{\alpha}\cdot\mathbf{p}+V)\psi=i\dot{\psi},\quad(\mathbf{p}=-i\nabla) \tag{37}$$

with

$$V=-\beta(\tfrac{1}{2}F\sigma_{\mu\nu}\mathfrak{F}_{\mu\nu}+G\Box^2\boldsymbol{A}), \tag{38}$$

then the properties of neutrons deduced from Eq. (37) using the first Born approximation would be the same as those obtained from (36). A plane wave expansion of ψ proves this immediately.

Since the electron-neutron interaction experiments use slow neutrons, it will be in order to consider the two-components Pauli-Schrödinger equation to which (37) reduces in the nonrelativistic limit. This reduction may, for instance, be accomplished by means of a unitary transformation,

$$\psi=e^T\chi,$$

with

$$T=(\boldsymbol{\alpha}\cdot\mathbf{p}/2M)\beta=-T^*.$$

Then the Dirac equation,

$$H\psi=(H^0+V)\psi=i\dot{\psi},$$

becomes

$$e^{-T}He^T\chi=i\dot{\chi}.$$

For the transformed Hamiltonian we have

$$\begin{aligned}H'&=e^{-T}He^T\\&=(1-T+\tfrac{1}{2}T^2+\cdots)(H^0+V)(1+T+\tfrac{1}{2}T^2+\cdots)\\&=M\beta+(\mathbf{p}^2/2M)\beta+V+[V,T]+\cdots.\end{aligned} \tag{39}$$

Thus, in the absence of the perturbation V, states χ which have only the first and second components different from zero will be steady states of positive energy, while those with vanishing 1, 2 components will be negative energy states. Treating V as a small perturbation, we may expect that for states of positive energy, χ_3, χ_4 will be negligibly small compared to χ_1, χ_2, so that in a nonrelativistic approximation, odd[18] matrices, i.e., those which connect the upper two components with the lower two, may be dropped. Since

$$V=-\beta F(\mathbf{H}\cdot\boldsymbol{\sigma}-i\mathbf{E}\cdot\boldsymbol{\alpha})+4\pi\beta GJ,$$

where

$$J_\mu=-(1/4\pi)\Box^2A_\mu,$$

and E, H are the external electromagnetic fields, we find

$$\begin{aligned}V+[V,T]+\cdots=&-\beta F\mathbf{H}\cdot\boldsymbol{\sigma}+4\pi GJ_4\\&+iF[\beta\mathbf{E}\cdot\boldsymbol{\alpha},T]+\cdots.\end{aligned}$$

Here, odd matrices have been omitted as well as terms which are of higher order in the neutron momentum, $\mathbf{p}$, or which involve second or higher derivatives of the external fields, since we assume the latter to be slowly varying. Evaluating the commutator, we have

$$\frac{iF}{2M}[\beta\mathbf{E}\cdot\boldsymbol{\alpha},\boldsymbol{\alpha}\cdot\mathbf{p}\beta]=-\frac{F}{2M}\operatorname{div}\mathbf{E}-\frac{F}{2M}\boldsymbol{\sigma}\cdot(\mathbf{E}\times\mathbf{p}-\mathbf{p}\times\mathbf{E}), \tag{40}$$

so

$$\begin{aligned}V+[V,T]=&-\beta F\mathbf{H}\cdot\boldsymbol{\sigma}-\frac{F}{2M}\operatorname{div}\mathbf{E}\\&+4\pi GJ_4-\frac{F}{2M}\boldsymbol{\sigma}\cdot(\mathbf{E}\times\mathbf{p}-\mathbf{p}\times\mathbf{E}).\end{aligned} \tag{41}$$

If χ' denotes the two component spinor composed of the 1,2 components of χ, then in a nonrelativistic approximation, χ' satisfies the Pauli-Schrödinger equation

$$\left(M+\frac{\mathbf{p}^2}{2M}+V'\right)\chi'=i\dot{\chi}'; \tag{42}$$

$$\begin{aligned}V'=&-F\mathbf{H}\cdot\boldsymbol{\sigma}-\frac{F}{2M}\operatorname{div}\mathbf{E}+4\pi GJ_4-\frac{F}{2M}\\&\cdot(\mathbf{E}\times\mathbf{p}-\mathbf{p}\times\mathbf{E}).\end{aligned} \tag{43}$$

If $\mathbf{E}=0$, then $\mathbf{H}$ is static and we may set $J_4=0$, giving

$$V'=-F\mathbf{H}\cdot\boldsymbol{\sigma}.$$

This shows that F is the magnetic moment of the neutron. Since

$$F=-(g^2/4\pi^2)f_0(\eta)(e/2M), \tag{44}$$

the value of this moment in nuclear magnetons is seen

[18] L. L. Foldy and S. A. Wouthuysen, Phys. Rev. 78, 29 (1950).

to be

$$\mu_N = -(g^2/4\pi^2) f_0(\eta), \tag{45}$$

in agreement with previous calculations.[8,9,11,19]

Consider next the case where $\mathbf{H}=0$ and $\mathbf{E}$ has as source a static charge distribution

$$\operatorname{div}\mathbf{E} = 4\pi\rho.$$

Then

$$J_4 = -\frac{1}{4\pi}\nabla^2 A_4 = \frac{i\operatorname{div}\mathbf{E}}{4\pi} = i\rho,$$

and

$$V' = 4\pi\left(iG - \frac{F}{2M}\right)\rho - \frac{F}{2M}(\mathbf{E}\times\mathbf{p} - \mathbf{p}\times\mathbf{E})$$

$$= \frac{eg^2}{2\pi M^2}\left(\frac{f_0(\eta)}{2} - f_1(\eta)\right)\rho - \frac{F}{2M}\boldsymbol{\sigma}\cdot(\mathbf{E}\times\mathbf{p} - \mathbf{p}\times\mathbf{E}). \tag{46}$$

As pointed out by Fermi,[4] the $\boldsymbol{\sigma}\cdot(\mathbf{E}\times\mathbf{p}-\mathbf{p}\times\mathbf{E})$ term has no effect on the usual experiments on the electron-neutron interaction and we shall drop it for the remainder of this discussion. (Since the experiments use unpolarized neutrons, this term, which involves spin flip of the neutron but not of the nucleus, cannot interfere coherently with the nuclear scattering, in which the neutron and nucleus both change their spin states or both remain unchanged.)

The case where the charge cloud represents an electron with fixed location has often been used for stating the results. In this case,

$$\rho = -e\rho_0, \quad \int d^3x\rho_0 = 1;$$

so

$$V' = \frac{-e^2g^2}{2\pi M^2}\left(\frac{f_0(\eta)}{2} - f_1(\eta)\right)\rho_0. \tag{47}$$

The neutron sees, then, a potential given by (47). Since

$$W \equiv \int d^3x V' = \frac{-e^2g^2}{2\pi M^2}\left(\frac{f_0(\eta)}{2} - f_1(\eta)\right), \tag{48}$$

a square well of radius e^2/mc^2 with the same volume integral would have a depth

$$V_0 = W\Big/\left[\frac{4\pi}{3}\left(\frac{e^2}{m}\right)^3\right]$$

$$= \frac{3}{2\pi}\frac{g^2}{4\pi}\left(\frac{m}{M}\right)^2\frac{m}{e^2}\left[\frac{f_0(\eta)}{2} - f_1(\eta)\right]. \tag{49}$$

It is now possible to point out the relation between these results and those found by previous authors. Foldy's phenomenological calculation, based on the anomalous magnetic moment, gives the same result as dropping the $f_1(\eta)$ term in (49). His success in thus finding correctly the part of V_0 which involves $f_0(\eta)$ stems from the fact that both it and the magnetic moment originate in the $\mathfrak{F}_{\mu\nu}\sigma_{\mu\nu}$ term of V, (38). Consequently, both are proportional to $g^2 f_0(\eta)$ and since their ratio is determined merely by relativistic invariance, not by meson theory, fixing one empirically—thus determining $g^2 f_0(\eta)$—makes it possible to find the other without the use of field theory. However, an approach of this sort could not predict the part of V_0 which involves $f_1(\eta)$, since even if a term $\Box^2 A$ were added[20] to the Dirac equation Hamiltonian along with $\mathfrak{F}_{\mu\nu}\sigma_{\mu\nu}$, phenomenological considerations would not indicate the ratio of the coefficients of the two terms.

The value of V_0 found by Case[9] and by Borowitz and Kohn[11] corresponds to dropping the $f_0(\eta)$ term in (49), retaining only the part involving $f_1(\eta)$. Since $f_1(\eta)$ has a magnitude about $\frac{1}{3}$ that of $f_0(\eta)/2$, this leads to a low value for V_0.[21]

For comparison with the result of Slotnick and Heitler and Dancoff and Drell, it is convenient to convert (45) and (49) to practical units,

$$V_0 = \frac{3}{2\pi}\frac{g^2}{4\pi\hbar c}\left(\frac{m}{M}\right)^2\left(\frac{\hbar c}{e^2}\right)^2 mc^2\left(\frac{f_0(\eta)}{2} - f_1(\eta)\right)$$

$$= 1.36\frac{g^2}{4\pi\hbar c}\left(\frac{f_0(\eta)}{2} - f_1(\eta)\right)\text{ kev}, \tag{50}$$

$$\mu_N = \frac{-g^2}{4\pi\hbar c}\frac{f_0(\eta)}{\pi}. \tag{51}$$

Using for η the value found by Barkas, Smith, and Gardner,[22]

$$\sqrt{\eta} = \mu/M = 0.151, \tag{52}$$

we find from (31) and (33)

$$f_0(\eta) = 0.820, \quad f_1(\eta) = -0.131; \tag{53}$$

so

$$V_0 = 0.736 g^2/4\pi\hbar c\text{ kev}, \tag{54}$$

$$\mu_N = -(0.820/\pi)g^2/4\pi\hbar c. \tag{55}$$

If (55) is used to fix g^2, with[23]

$$\mu_N = -1.913,$$

then

$$g^2/4\pi\hbar c = 7.33, \tag{56}$$

and

$$V_0 = 9.97[\tfrac{1}{2}f_0(\eta) - f_1(\eta)]\text{ kev} = 5380\text{ ev}. \tag{57}$$

The f_0 and f_1 parts ("magnetic" and "electrostatic"

[19] J. M. Luttinger, Helv. Phys. Acta **21**, 483 (1948).

[20] L. L. Foldy, Phys. Rev. **87**, 688, 693 (1952).

[21] Both of these authors have slight errors in their expressions for $f_1(\eta)$. In Case's Equation (103), the term $(13-4\eta)/3(4-\eta)$ is given as $[(13/3)-4\eta](4-\eta)^{-1}$. In Borowitz and Kohn's Eq. (6.11), the coefficient of the $\cos^{-1}$ contains $17\eta/3$ instead of $17\eta/2$. However, neither of these errors has an appreciable effect on the numerical value of $f_1(\eta)$.

[22] Barkas, Smith, and Gardner, Phys. Rev. **82**, 102 (1951).

[23] Bloch, Nicodemus, and Staub, Phys. Rev. **74**, 1025 (1948).

parts) are 4080 and 1300 ev, respectively. The total value agrees fairly well with Slotnick and Heitler's figure of 5000 ev and with the 5220 ev[24] obtained by Dancoff and Drell. [These values have been re-computed using the choice (56) for the coupling constant.]

[24] This figure was incorrectly stated as 6100 ev in the author's letter, Phys. Rev. **86**, 434 (1952). The error was pointed out by Dr. Drell in a private communication.

The discrepancies between their results and the 5380 ev can probably be attributed to their having used, in their numerical integrations, slightly different values for the meson-nucleon mass ratio.

This problem was suggested by Professor G. Wentzel, whose advice and encouragement are very gratefully acknowledged. Thanks are also due Dr. M. Goldberger and Dr. M. Gell-Mann for many helpful discussions.

PHYSICAL REVIEW VOLUME 88, NUMBER 5 DECEMBER 1, 1952

Cross Section and Angular Distribution of the D(d, p)T Reaction*

W. A. WENZEL AND WARD WHALING
Kellogg Radiation Laboratory, California Institute of Technology, Pasadena, California

(Received August 11, 1952)

The D(d, p)T reaction cross section has been measured by two methods using D_2O ice targets. For E_d from 206 to 516 kev, a double-focusing magnetic spectrometer was used to obtain the momentum spectrum of the protons and tritons, from which the reaction cross section can be determined. For E_d from 35 to 550 kev, the proton yield from a thick target was differentiated to obtain the cross section. Both thin and thick target methods were used to measure the angular distribution over the energy range E_d from 35 to 550 kev. The angular distribution is expressed in terms of a Legendre polynomial expansion. Various sources of experimental error are considered and the probable error of the total cross section is found to be ±5 percent.

I. INTRODUCTION

SINCE the discovery by Lawrence, Lewis, and Livingston[1] in 1933 that two deuterons can react with the emission of long-range protons, the reaction $H^2+H^2 \rightarrow H^1+H^3+4.032$ Mev has been studied extensively. Although early investigators determined that the yield was large and anisotropic, accurate measurements of the cross section have been possible only in the past few years.[2-6] In attempts to extend the measurements to very low energies, some experimental problems which are minor at higher energies become increasingly troublesome. The use of thin gas targets with differential pumping is subject to uncertainties due to beam neutralization and energy loss. The use of foils introduces straggling in the beam energy and requires an accurate knowledge of the window thickness at each energy at which the reaction is to be studied. The accuracy of the thick solid target measurements has been limited by uncertainties in the stopping cross section, which is needed to obtain the reaction cross section from the thick target yield. Recent measurements in this laboratory[7] of the stopping cross section of D_2O ice for protons of 18–550 kev enable us to measure the D(d, p)T cross section by the thick target method with higher accuracy than has been attained previously.

At higher energies, E_d from 206 to 516 kev, the cross section was obtained by another method. A double-focusing magnetic spectrometer was used to measure the yield of protons and tritons from a thick target as a function of their momenta. This spectrum of the emitted particles can be used to determine the "thin target" cross section, and the observation of both protons and tritons provides a check on the internal consistency of the experimental method.

The angular distribution of the reaction was measured by making observations at 10° intervals over the range θ_{lab} from 80° to 150°. Above 200 kev a thin ice target was used, and the yield at each angle relative to a monitor counter at $\theta_{lab}=70°$ gives the angular distribution. For deuteron energies below 200 kev it was necessary to measure the thick target yield at each angle. The differentiated thick target yield gives $d\sigma/d\Omega$ at each angle.

II. CROSS SECTION MEASURED WITH THE MAGNETIC SPECTROMETER

A double focusing magnetic spectrometer was used to observe particles emitted at an angle of 90.3° with respect to the incident deuteron beam. The D_2O ice target was deposited on a copper surface cooled with liquid nitrogen in a target chamber that has been described previously.[7] The aperture of the spectrometer was adjusted to subtend a small solid angle, 0.00127 steradian, at the target, in order to obtain high effective resolution. A scintillation counter was used to detect

* Assisted by the joint program of the ONR and AEC.
[1] Lawrence, Livingston, and Lewis, Phys. Rev. **44**, 56L (1933).
[2] Bretscher, French, and Seidl, Phys. Rev. **73**, 815 (1948).
[3] Blair, Freier, Lampi, Sleator, and Williams, Phys. Rev. **74**, 1599 (1948).
[4] Moffatt, Sanders, and Roaf, Proc. Roy. Soc. (London) **212**, 225 (1952).
[5] Sawyer, Arnold, Phillips, Stovall, and Tuck, Phys. Rev. **86**, 583 (1952).
[6] K. G. McNeill and G. M. Keyser, Phys. Rev. **81**, 602 (1951).
[7] W. A. Wenzel and W. Whaling, Phys. Rev. **87**, 499 (1952).

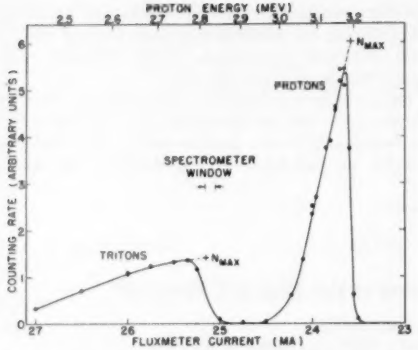

FIG. 1. Proton and triton spectrum obtained at $E_d = 413$ kev. Spectrometer resolution $R_c = P/\Delta P = 235$. The fluxmeter current is inversely proportional to the magnetic field. The proton energy scale refers to laboratory coordinates.

the protons and tritons after they had been deflected through 180° in the magnetic spectrometer.

Figure 1 shows a typical momentum spectrum of protons and tritons from the $d-d$ reaction for a bombarding energy of 413 kev. Momentum separation of the protons and tritons occurs because of the motion of the center of mass relative to the laboratory. We obtain the differential cross section $(d\sigma/d\Omega)$ at $\theta_{lab} = 90.3°$ from the formula of Snyder *et al.*[8]

$$4\pi d\sigma/d\Omega = N_{max}\epsilon_{eff}R_c/\Omega E_2 q,$$

where N_{max} is obtained by extrapolating the trailing edge of the momentum spectrum to the midpoint of the leading edge, R_c and Ω are the spectrometer resolution and solid angle, respectively, q is the integrated target current in microcoulombs, E_2 is the energy in electron volts of the particles analyzed by the spectrometer, and $(d\sigma/d\Omega)$ is the differential cross section in millibarns per steradian. The effective stopping cross section, ϵ_{eff}, is related to the stopping cross sections ϵ_1 and ϵ_2 of the incident and emitted particle by the formula:

$$\epsilon_{eff} = \epsilon_1 dE_2/dE_1 + \epsilon_2 \cos\theta_1/\cos\theta_2.$$

Cross-section measurements with the spectrometer were not extended to energies below 200 kev because the large energy dependence of the cross section makes extrapolation of the trailing edge uncertain.

III. CROSS SECTION FROM THICK TARGET YIELD

The yield of protons from a thick D_2O ice target was measured at $\theta_{lab} = 150°$ for deuteron bombarding energies between 20.6 and 578 kev. Proportional counters were used to detect the protons. Three different counters were used in different geometrical arrangements to check the consistency of the results. The thick target yield as a function of deuteron energy is shown in Fig. 2, the points plotted as circles and crosses show the excellent agreement between results taken with different counters with targets prepared from two different samples of D_2O. The differential cross section is given by $(d\sigma/d\Omega) = \epsilon dY(150°)/dE_d$, where $Y(150°)$ is the number of protons emitted into unit solid angle at $\theta_{lab} = 150$ degrees for each deuteron incident on the thick target, and ϵ is the stopping cross section per deuterium atom in the target for deuterons of energy E_d. Methods of differentiation are discussed in Sec. VI, 10.

IV. ANGULAR DISTRIBUTION

For the angular distribution measurements a 7-inch diameter target chamber was constructed with windows 0.125 inch in diameter every 10° for θ_{lab} from 0° to 180°. The beam entered the window at 180°, and a quartz cover over the window at 0° served for alignment. The remaining windows were covered with 0.001-inch aluminum foil. The target holder was located accurately in the center of the chamber. A proportional counter fixed in position facing the 70° window was used as a monitor. A second counter, mounted on an arm which could be rotated about the center of the chamber, could be moved in front of any of the windows between 80° and 170°. A 4-inch diffusion pump under the chamber and a liquid nitrogen trap between the

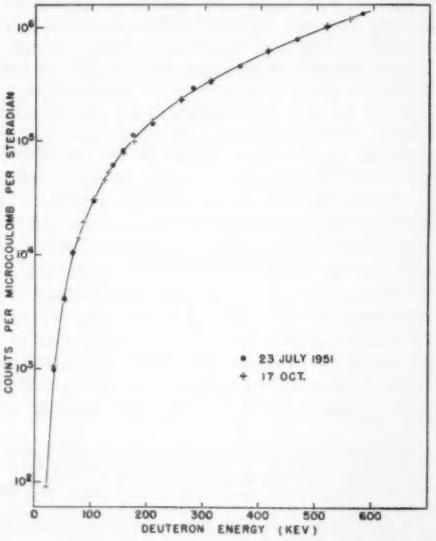

FIG. 2. Thick target yield of protons at $\theta_{lab} = 150°$. The solid circles were taken with the spectrometer target chamber and the crosses with the angular distribution target chamber. The energy scale refers to laboratory coordinates.

[8] Snyder, Rubin, Fowler, and Lauritsen, Rev. Sci. Instr. **21**, 852 (1950).

chamber and the pump maintained an operating pressure of 10^{-6} mm Hg in the chamber.

For deuteron energies above 200 kev the angular distribution was obtained with thin targets. A thin layer of ice was deposited on the cold target set at an angle of 45° to the incident beam. The ratio of the counting rate at an angle θ_{lab} to the rate at 70° measured with the monitor counter was obtained for θ_{lab} from 80° to 170° in 10° intervals. From the measured ratios and the kinetics of the reaction the angular distribution in the center-of-mass system was calculated. The effective energy at which the thin target yields were obtained was calculated in each case from the absolute thin target yield at 150° and the slope of the thick target yield at 150° as a function of energy

$$E_{eff} \approx E - \frac{1}{2} \frac{n(E_{eff}, 150°)}{[dN(E, 150°)/dE]_{E_{eff}}},$$

where $N(E, 150°)$ is the thick target yield at 150° and bombarding energy, E, and $n(E_{eff}, 150°)$ is the thin target yield at 150°. E_{eff} is the effective energy at which the angular distribution has been determined. The thickness of the targets used varied from 20 to 50 kev, and it was found that a given target varied less than 10 percent in thickness while measurements were being taken at all angles. The thin target angular yield as a function of energy and center-of-mass angle, normalized to a target of constant thickness, is plotted in Fig. 3.

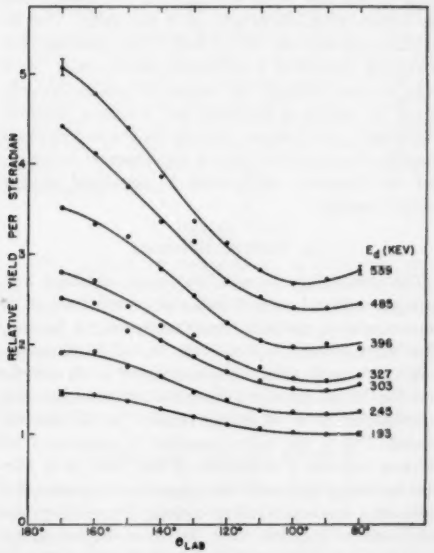

FIG. 3. The yield as a function of angle using thin ice targets at several bombarding energies. The yields are normalized to a fixed target thickness.

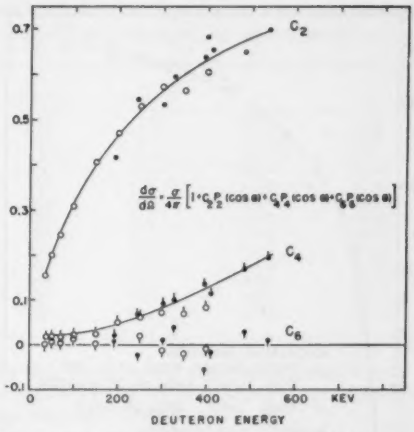

FIG. 4. D(d, p)T angular distribution. The solid circles were obtained from thin target yields and the open circles from thick target yields. Points with upward pointing tails refer to C_4. Downward pointing tails refer to C_6. The energy scale refers to laboratory coordinates.

The distribution for $\theta_{c.m.}$ between 90° and 180° is sufficient to determine the total angular distribution because of the symmetry of the reaction in the center-of-mass coordinates.

The rapid variation with energy of the cross section below 200 kev makes the thin target yield very sensitive to fluctuations in the target thickness. Therefore the angular distribution at low energies was obtained by differentiating with respect to energy the thick target yield curve at each angle to obtain the equivalent thin target yield. The thick target yield as a function of energy was expressed as the product of a barrier factor and a slowly varying function of energy and angle, $F(E_d, \theta_{lab})$. For each angle from 80° to 170°, the function $F(E_d, \theta_{lab})$ was determined from the ratio of the observed yield to the barrier factor. $F(E_d, \theta_{lab})$ was then plotted and differentiated graphically.

The angular distribution has been expanded in terms of Legendre polynomials. The variation of the coefficients in the expansion with energy is shown in Fig. 4. The solid points were obtained from thin target measurements, the open points from thick targets.

V. THE TOTAL CROSS SECTION

Knowing the cross section at one angle and the angular distribution, we have calculated the total cross section of the reaction. Figure 5 shows the results obtained in several ways. The points plotted as circles in Fig. 5 were obtained from the spectrometer measurements of $(d\sigma/d\Omega)$ at $\theta_{lab} = 90.3°$ and the angular distribution obtained by thin target methods. The points plotted as X's are based on the thick target yield at $\theta_{lab} = 150°$ and the thin target angular distribution. The

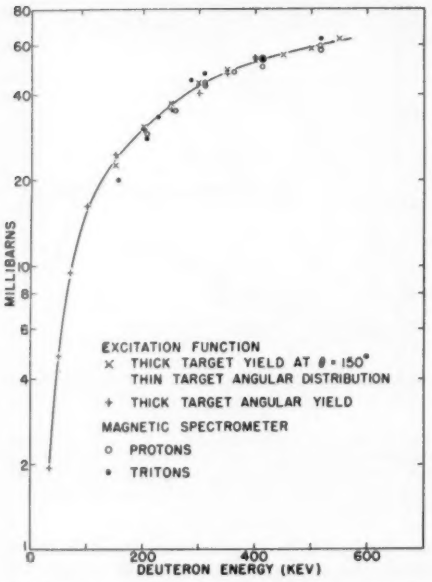

FIG. 5. Total cross section for the D(d, p)T reaction. The energy scale refers to laboratory coordinates.

points plotted as plus signs show the integral over all angles of the differential cross section obtained by differentiating the thick target yield at each angle.

At high bombarding energies the cross section obtained from the thick target yield has been corrected for a small contribution from the $O^{16}(d, p)O^{17}$ reaction, since both of the proton groups from this reaction were counted along with the protons from the $d-d$ reaction. The cross sections have been measured for both $O^{16}(d, p)O^{17}$ proton groups with the magnetic spectrometer and are represented approximately by:

$$\text{Long-range group } -4\pi(d\sigma/d\Omega)_{90^\circ} = (0.5\times 10^{10}/E_d) \times \exp(-355E_d^{-\frac{1}{2}}) \text{ millibarns,}$$

$$\text{Short-range group } -4\pi(d\sigma/d\Omega)_{90^\circ} = (1.2\times 10^{10}/E_d) \times \exp(-355E_d^{-\frac{1}{2}}) \text{ millibarns,}$$

where E_d is the deuteron energy in the laboratory measured in kev. These values have been subtracted from the cross sections obtained from the thick target yield. We have assumed that the angular distribution for the $O^{16}(d, p)O^{17}$ reaction is spherically symmetric over the angular range investigated.

VI. DISCUSSION OF ACCURACY

1. Solid Angles

The solid angles for the various proportional counters were determined by direct measurement of the diameter of the milled counter windows, 0.250 inch in diameter, and of the distance from the target to the counter window, which varied from 3.5 to 6.5 inches for the different counter arrangements. The solid angles determined by these measurements should be accurate to ± 2 percent.

The 0.125-inch diameter windows in the angular distribution chamber were smaller than the window in the counter outside the chamber so that the windows in the chamber determined the solid angle. The relative window size at each of the ten angles of observation from 80° to 170° was checked with a ThC′ source at the target position. The average solid angle is known to within 1 percent, and the relative solid angles in the angular distribution chamber are known with somewhat higher accuracy.

The solid angle of the spectrometer was determined geometrically by the use of a known aperture at a measured distance from the target. The procedure is described in detail in reference 7. As an additional check, the proton spectrum obtained with the spectrometer was integrated to give the total yield of protons at 90.3°. This result was in excellent agreement with the total yield measured with the proportional counter set at $\theta_{lab}=90^\circ$.

2. Current Integration

The current integrator was of conventional design using a condenser which was charged to a known voltage before being discharged by a fast relay. The integrator constant was determined under operating conditions by the use of a calibrated galvanometer. By a more accurate method, the integrator constant was obtained by means of batteries and precision resistors. The integrator constants obtained by the two methods of calibration agree within the experimental accuracy, and the integrator calibration is considered reliable within 2 percent.

3. Counter Efficiency

The pulse-height integral bias curve obtained with each proportional counter indicated an efficiency of 99 percent with a statistical uncertainty of ± 1 percent. The scintillation counter with the ZnS phosphor, which was used with the spectrometer to detect the reaction tritons and also for some of the proton spectra, was assumed to be 94 percent efficient, at the bias employed. This is the value measured in reference 7 for 500-kev protons. Comparison of the yield of 3 Mev protons taken first with the proportional counter and then with the scintillation counter attached to the spectrometer indicates that for these higher energy particles the efficiency of the scintillation counter may be nearer 92 percent. A 2-percent uncertainty is assigned to the value of the scintillation counter efficiency.

4. Target Contamination

The deuterium content of our heavy water was 99.8 percent according to the assay by the Stuart Oxygen Company. The liquid and its vapor were handled in an all-metal system. Reaction yields were reproducible over a period of three months and after refilling the liquid reservoir. Target contamination by the incident deuteron beam would tend to increase the relative concentration of deuterium in the target. If we assume that the incident particles are deposited over a volume equal in cross section to the size of the beam spot and in depth to the range of the bombarding particles, we find that for 50-kev deuterons a contamination of the order of +1 percent would exist after 1000 microcoulombs of bombardment. If the deuterons tend to collect on the surface of the target, a more serious error in measured yield would be expected. By replenishing the target surface frequently, we have sought to avoid such surface contamination. No time dependent increase in yield which might be attributed to this effect was ever observed.

5. Beam Contamination

A comparison of the reaction yields from the monatomic, diatomic, and triatomic ions indicated that the beam contamination was low. The DD^+ and the DDD^+ yields were regularly somewhat higher than the D^+ yield, but this effect never exceeded 3 percent and seemed to be independent of energy. Contamination of the D^+ beam by the HH^+ ion would not be expected to produce even this effect if it resulted from the $\frac{1}{2}$ percent impurity in the supply to the ion source. Presumably the somewhat larger contamination comes from the production of H_2 gas from oil vapor and the gaskets. In another check on beam contamination the magnitude of the H^+ beam was found to be of the order of 1 percent of the D^+ beam under the same generator operating conditions.

6. Energy Scale

Correct calibration and linearity of the energy scale are very important because of the critical energy dependence of the cross section at low energy. Calibration and linearity measurements of the generator voltage are described in reference 7. The good agreement between the D^+, DD^+, DDD^+ yields at corresponding individual deuteron energies is taken as further evidence for the linearity of the generator voltage scale.

7. Secondary Electron Emission

The target was maintained at a potential of 300 volts positive with respect to the surrounding chamber to suppress the emission of secondary electrons from the target. Between the last beam defining slit and the target was placed a ring-shaped electrode through which the beam passed. This ring was held at 180 volts negative with respect to the surrounding chamber walls to prevent secondary electrons knocked out of the slits from reaching the target.

TABLE I. $D(d, p)H^3$ total cross section and angular distribution. $\frac{d\sigma}{d\Omega}=\frac{\sigma_T}{4\pi}[1+C_2P_2(\cos\theta)+C_4P_4(\cos\theta)+C_6P_6(\cos\theta)+\cdots]$.

E (kev)	σ_T millibarns	C_2	C_4
35	1.94	0.155	0.02
50	4.81	0.195	0.02
70	9.49	0.247	0.02
100	15.8	0.310	0.023
150	23.8	0.400	0.031
200	30.6	0.470	0.045
250	37.0	0.523	0.052
300	43.1	0.566	0.080
350	48.1	0.601	0.103
400	52.3	0.632	0.126
450	55.8	0.660	0.150
500	59.0	0.684	0.175
550	62.0	0.704	0.203

8. Beam Neutralization

The effect of beam neutralization was measured by deflecting the beam magnetically in the 60-cm tube between the electrostatic analyzer and the target chamber. The magnet was located 5 cm from the target chamber. With the beam coming through the analyzer, the ratio of the $D(d, p)T$ yields with the beam on the target and deflected away from the target gives a direct measurement of the percentage of neutralization. With the normal operating pressure of 1.0×10^{-6} mm of Hg in the target chamber and 4×10^{-6} mm of Hg in the tube between the analyzer and the target chamber, the neutralization measured was 0.7 percent. When air was admitted to the analyzer, raising the ion gauge pressures to 5.0×10^{-6} in the target chamber and 2.5×10^{-5} mm of Hg in the connecting tube, the measured neutralization was 3 percent. These measurements were made at 51.5 kev; measurements of the neutralization at lower energies was not feasible because of the low yields. However, Bartels[9] and Keene[10] have found that the electron capture cross section of protons in hydrogen increases by less than a factor of two when the bombarding energy decreases from 25 to 17.5 kev. These energies correspond to 50 and 35 kev, respectively for bombarding deuterons. Kanner[11] finds that the capture cross section in air is of the same order of magnitude as in hydrogen. On the basis of these results we have made no correction for beam neutralization.

9. Beam Intensity

Evaporation of the ice target occurred if the beam power became too large. To determine whether this effect was important, the DD^+ current on a $\frac{1}{4}$-inch diameter target spot was varied from 0.3 μa to 1.8 μa

[9] H. Bartels, Ann. Physik **13**, 373 (1932).
[10] J. P. Keene, Phil. Mag. **40**, 369 (1949).
[11] H. Kanner, Phys. Rev. **84**, 1211 (1951).

at a bombarding energy of 103 kev. There was no observable difference in yield.

10. Statistical Uncertainty and Differentiation

The statistical uncertainty in the individual experimental points varies from 1 to 3 percent for the thick target measurements, and from 1 to 4 percent for the thin target results. The error introduced in the differentiation has been minimized by the method of differentiation. At low energies we expect the cross section to have the approximate form: $\sigma(E) \propto E^{-1} \exp(-44.4\, E^{-\frac{1}{2}})$, and the stopping cross section: $n^{-1}(dE/dX) \propto E^{\frac{1}{2}}$, where E is in kev. Hence the thick target yield is given approximately by $N(E_0) \propto \int_0^{E_0} dE\ E^{-\frac{1}{2}} \exp(-44.4\ E^{-\frac{1}{2}}) \propto \exp(-44.4\ E^{-\frac{1}{2}})$. For each angle we have plotted $F(E, \theta) = N(E, \theta) \exp(44.4\ E^{-\frac{1}{2}})$ and differentiated $F(E, \theta)$ with respect to the energy. The quantity dN/dE is then found from $dN(E, \theta)/dE = \exp(-44.4\ E^{-\frac{1}{2}})[dF(E, \theta)/dE + 22.2\ F(E, \theta) E^{-\frac{1}{2}}]$. $F(E, \theta)$ is a smoothly varying function of energy and the differentiation can be carried out accurately. Moreover, in the differentiation of $N(E, \theta)$, the term containing F is much larger than the one containing dF/dE. Hence, at low energies, it is felt that the errors introduced by differentiation are not significant.

In the energy range 100–500 kev it was found that the total yield varied approximately as E^2. A plot of $N(E, \theta)$ *vs* E^2 yielded more consistent values for $dN(E, \theta)/dE$ than either of two semilog plots tried. At energies above 150 kev the differentiation introduces some uncertainty into the measured cross section and angular distribution. An estimate of the amount of this uncertainty may be obtained from the difference in angular distribution and cross section obtained by the use of thin target and thick target techniques. From Fig. 5, for example, the difference in cross section is seen to be of the order of a few percent in the energy range $E_d = 150$ to 400 kev.

11. Stopping Cross Section

Since the experiment measures the ratio of the reaction cross section to the stopping cross section, ϵ, the uncertainties in the measurement of ϵ, described in reference 7, appear in our value for the reaction cross section. It is significant that certain possible systematic errors cancel out when the stopping cross section and reaction cross-section experiments are considered together. For example, an error in the integrator constant would produce a corresponding error in the calculated values of ϵ, but not in the D(d, p)T cross section. An error in the spectrometer constant R_s/Ω, would directly affect ϵ, but not the reaction cross section obtained with the spectrometer. In fact, the spectrometer has effectively measured the ratio of the D(d, p)T reaction cross section to the $O^{16}(p, p)O^{16}$ scattering cross section. Here we have assumed that the ratio $\epsilon(D_2O)/\epsilon(\text{air})$ is the same for protons of 500 kev and 3 Mev. However, since $d\epsilon_{\text{eff}}/d\epsilon(\text{air}) \approx \frac{1}{3}$, small variations in the assumed stopping power of D_2O are not significant. Values for ϵ(air) were obtained from the literature.[12] The stopping cross section for reaction tritons is obtained from reference 7.

12. Probable Error

The largest contribution to the probable error is the 4 percent uncertainty in the value of $\epsilon(D_2O)$. If the D(d, p)T cross section were based on the thick target yield alone, additional errors due to solid angle, counter efficiency, target and beam contamination, energy calibration, neutralization, and statistics would raise the probable error to slightly over 5 percent. However, the partial cancellation of systematic errors from the spectrometer measurements tends to reduce the error. The good agreement of the spectrometer results, using both protons and tritons, with the results from the thick target excitation function is significant. Thus we have assigned a probable error of 5 percent to the values of the total cross section listed in Table I. These values were taken from the solid curve drawn through the experimental points in Fig. 5.

VII. COMPARISON WITH OTHER MEASUREMENTS

The thick target yield is about 25 percent lower than that obtained by Bretscher *et al.*[2] using the same technique. No explanation for this discrepancy can be offered. Agreement with Moffatt *et al.*[4] and with Arnold *et al.*[5] in the low energy region is within 5 percent, and the agreement with McNeill and Keyser[6] in the middle energy range is good. Regarding the angular distribution, the agreement with the results of Bretscher *et al.*, and of Moffatt *et al.*, is good, although the finite amount of $P_4(\cos\theta)$ which we find makes exact comparison difficult.

One of the authors (WAW) would like to express his appreciation to the Eastman Kodak Company for a fellowship given to him during the course of the work described in this paper.

[12] H. A. Bethe, Revs. Modern Phys. **22**, 213 (1950).

The Beta-Spectra of Pu^{239}, Pu^{240}, and Pu^{241}

MELVIN S. FREEDMAN, F. WAGNER, JR., AND D. W. ENGELKEMEIR
Argonne National Laboratory, Chicago, Illinois
(Received April 24, 1952)

The beta-spectrum of Pu^{241} measured in a double lens spectrometer on samples containing Pu^{239}, Pu^{240}, and Pu^{241}, exhibits an allowed shape from $E_0 = 20.5$ kev to 14 kev, where instrumental effects distort it. Conversion lines found beyond the end point combined with gamma-scintillation counter measurements lead to the assignment of gammas of 39, 53, 100, 124, and 384 kev associated with the alpha-decay of Pu^{239}, and a gamma of 49.6 kev accompanying the alpha-decay of Pu^{240}; and the existence of 26.4- and 59-kev gammas in Am^{241} alpha-decay is confirmed. A conversion line corresponding to a highly converted 41-kev gamma in Am^{241} was found. Gammas of 100 and 145 kev probably associated with the alpha-branch in Pu^{241} were also found.

The influence of the orbital electronic rearrangement energy on the beta-decay is discussed.

EXPERIMENT

THE beta-spectrum of 10-yr Pu^{241} was examined on samples of radiochemically pure plutonium containing the isotopes Pu^{239}, Pu^{240}, and Pu^{241}, isotopically enriched in Pu^{241} by pile neutron irradiation. Isotopic compositions were determined mass spectrographically.

The plutonium was deposited on a *ca* 10-$\mu g/cm^2$ film of LC 600 by the evaporation of a solution of plutonium nitrate. Prepared samples had an average thickness of *ca* 10-$\mu g/cm^2$, but inspection with a microscope showed some local clumping.

The beta-spectrum was taken on a double lens spectrometer having a transmission of *ca* 2 percent and a resolution of *ca* 2 percent. An atmospheric pressure methane-flow proportional counter was used as detector. The counter window was built up of layers of thin Duco and Formvar films to a thickness of *ca* 60-$\mu g/cm^2$. A 50 percent transmission grid was used to support the window.

Window transmission characteristics of the counter were determined with the use of a sample of Pm^{147}. This sample was vacuum volatilized onto a 10-$\mu g/cm^2$ LC 600 film as a chelation compound of prometheum with trifluoroacetyl-acetone $[Pm(F_3C_5H_4O_2)_3]$, to produce a very uniform sample of an average thickness *ca* 10-$\mu g/cm^2$. Since it has been shown by Langer, Motz, and Price[1] that the Kurie plot of thin samples of Pm^{147} is straight to less than 8 kev, the Kurie plot was extrapolated for Pm^{147} back from 20 kev where it began to fall below the straight line, and the ratio of the observed to extrapolated data was used below 20 kev as a window transmission correction factor.

RESULTS

By using the correction factors so obtained, the Kurie plot (Fig. 1) (uncorrected for orbital electron screening) of the Pu^{241} sample exhibited an allowed shape ($\log ft = 5.7$) from $E_0 = 20.5(+1.2, -0.3)$ kev to 14 kev, where source thickness effects and large window corrections tend to make the data unreliable. The *ft* value and shape are consistent with the spin-orbit coupling shell model predictions for the state assignments, $g_{9/2}$ and $f_{7/2}$ for Pu^{241} and Am^{241}, respectively, giving $\Delta J = -1$, yes, corresponding to a first forbidden beta-transition. The log*ft* value falls somewhat below the boundary value of 6.0[2] found for first forbidden beta-decays in lighter isotopes. Since $Z_0 \approx 1.6 W_0 \approx 1.6 \ll Z$,[3] the shape of a first forbidden transition with $\Delta J = 1$ should almost exactly conform to the allowed shape.[3] Considering the experimental limitations on the quality of the data and the omission of shielding corrections to the Fermi function, any conclusions on the significance of the allowed shape must be drawn with reservations. This applies particularly in view of the possible effects of orbital rearrangement energy on the spectrum shape (see discussion below).

CONVERSION LINE AND GAMMA-SPECTRA

Seven very low intensity conversion lines were observed beyond the end point of the beta-spectrum. The maximum energy surveyed was 60 kev. In order to determine the assignment of these lines among the three plutonium isotopes or the Am^{241} [4] present, the

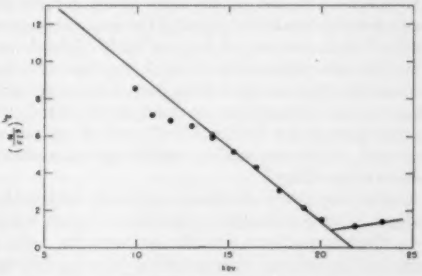

FIG. 1. Kurie plot for Pu^{241}.

[1] Langer, Motz, and Price, Phys. Rev. 77, 798 (1950).

[2] Mayer, Moszkowski, and Nordheim, Revs. Modern Phys. 23, 315 (1951).

[3] E. J. Konopinski, Revs. Modern Phys. 15, 209 (1943).

[4] We are indebted to G. T. Seaborg and Frank Asaro for pointing out this latter possibility to us.

TABLE I. Gamma-ray energies and relative intensities for Pu^{239} and Pu^{240} from conversion electrons, scintillation counter spectrometer, and proportional counter spectrometer.

Isotope to which gamma is assigned	Conversion electron energy (kev)	Conversion shell	Binding energy of (kev)	Gamma-energy conv. elec. (kev)	Gamma-energy NaI(Tl) (kev)	Gamma-energy prop. spect., (kev)	Gamma-energy best value (kev)	Relative intensity of gammas
Pu^{239}					17.5-$L_{\alpha,\beta,\gamma}$			100
					21.6-L_γ	20.9-L_γ		
						39	39	0.4
	31.4	*LI*	21.9	53.3	54.0	53.2		
	35.3	*LIII*	17.2	52.5				
	47.1	*MI*	5.56	52.7			53.1	1.4
	50.2	*MIV*	3.72	53.9				
					100		100	1.1
					124		124	0.5
					384		384	0.3
Pu^{240}						13.7-L_α		
					17.1-$L_{\alpha,\beta,\gamma}$	17.2-L_β		100
						21.2-L_α		
	32.9	*LIII*	17.2	50.1	47	48	49.6	3
	44.4	*MII*	5.20	49.6				
	27.6	*LI*	21.8	49.4				
Pu^{241}					100			100
					145			20
Am^{241}					18-$L_{\alpha,\beta,\gamma}$			25
					28	26.4	26.4	25
	23.8	*LIII*	17.6	41.4			41.4[a]	
	37.9	*LII*	21.7	59.6	61.1	60.2	59.0	100
	41.0	*LIII*	17.6	58.6				
	52.9	*MI*	5.75	58.7				

[a] C. A. Prohaska, University of California Radiation Laboratory Report 1395 (unpublished) (August, 1951) refers to observation of highly converted 41-kev gamma-ray in Am^{241} decay. Wagner, Freedman, Engelkemeir, and Huizenga (to be published) observed conversion lines of a 42-kev gamma in the beta-decay of U^{237}.

spectrum of a sample of almost isotopically pure Pu^{239} was examined, and four conversion lines were found, none identical with and all of still lower intensity than the first seven. A third sample containing a different relative isotopic abundance of Pu^{240}: Pu^{241} was run, and the intensities of the first seven conversion lines were observed to vary approximately with the amount of Pu^{240} present. However, it was noted that the Am^{241} which had grown in from the beta-decay of Pu^{241} was, in these samples, almost in constant ratio to the amount of Pu^{240}, and that some of the lines corresponded to previously observed lines[5] following alpha-decay of Am^{241}. From this and on the basis of the gamma-ray measurements (see below), three of the lines are assigned to Pu^{240} alpha-decay and four to Am^{241} alpha-decay. The data are tabulated in Table I, together with the gamma-ray assignments of these lines. Binding energies characteristic of uranium are used in calculating the gamma-energies for Pu^{239} and Pu^{240}, and of neptunium for Am^{241}, on the assumption that the gamma-emission follows alpha-decay.

Gamma-rays were also observed directly with both a sodium iodide scintillation spectrometer and an argon-CO_2 filled proportional counter spectrometer, using a pure Pu^{239} sample and three samples containing different ratios of Pu^{240} and Pu^{241}, from which the Am^{241} had been freshly separated. We are indebted to Professor G. T. Seaborg for pointing out to us the necessity for separating Am^{241} from samples containing Pu^{241} immediately before attempting to observe the plutonium gamma-spectra, since the intense 26.5- and 60-kev gammas of Am^{241} soon mask the weak gammas of the plutonium isotopes. In the first experiments in which americium was not separated, the most prominent gammas observed in a sample containing Pu^{240} and Pu^{241} were the 26.5- and 60-kev gammas of Am^{241}. In a later group of experiments, americium was separated and the measurements completed within 6 hours, during which time no perceptible growth of Am^{241} occurred.

L x-rays of uranium and gammas with energies of 39, 53, 100, 124, and 384 kev were observed in the pure Pu^{239} sample. In the three samples containing Pu^{240} and Pu^{241}, additional gammas with energies of 47, 100, and 145 kev were observed. The Pu^{238} and Pu^{239} contributions to the total gamma-spectrum were small in these samples and were subtracted off. Comparison of the intensity of the *L* x-ray and the 47-, 100-, and 145-kev gammas with the amount of each plutonium isotope present in the three samples indicated that the 47-kev gamma and most of the *L* x-rays are due to Pu^{240}. The 100- and 145-kev gammas are definitely not assignable to Pu^{240} but may be assigned fairly definitely to Pu^{241} on the basis of line intensities relative to isotopic abundances. The 100-kev line has a full width at half-height of 25 percent, whereas a width of 19 percent is expected (the 89-kev Ag^{109} gamma-line has a width of 20 percent). This line broadening is quite reproducible and must be due to the presence of two or more unre-

[5] G. D. O'Kelley and C. A. Prohaska (private communication from F. Asaro); Charles I. Browne, Jr., University of California Radiation Laboratory Report 1764 (unpublished) (June, 1952); Beling, Newton, and Rose, Phys. Rev. 86, 797 (1952).

solved lines. The observed line width is very nearly equal to the width expected for uranium K x-rays which could arise from the internal conversion of the 145-kev gamma. Thus, the line may be entirely K x-rays.

Since approximately ten 100-kev gammas and two 145-kev gammas are emitted per 10^6 Pu^{241} betas, it is evident that the gammas cannot follow the Pu^{241} beta-disintegration. It is possible that these gammas are emitted in the alpha-branching of Pu^{241}; the gamma to total alpha-ratios are 0.35 for the 100-kev and 0.07 for the 145-kev gammas.

The gammas found and their assignments are given in Table I.

DISCUSSION

It has been pointed out by Schwartz[6] and by Edwards[7] that in beta-decay in a heavy element, where the beta-energy is low, the difference between the total orbital electron binding energies of parent and daughter atoms will be comparable to the maximum beta-energy. This energy difference, which is negative for a beta-minus-decay, must appear associated with the beta-transition, either partly or wholly as kinetic energy of the beta or neutrino or as quantum radiation (possibly converted).

It is predicted theoretically,[6,8] that this energy will, except for an experimentally indeterminable amount of the order of one hundred electron volts,[6] be emitted in the decay as kinetic energy of the beta-particle and neutrino. The manner by which this extra energy affects the energy distribution is taken into account by the use of the Fermi function $F(Z,W)$, *with shielding corrections*, using for the total energy of the transition the sum of the specifically nuclear contribution plus the electron binding energy difference, namely, the observed maximum energy.

A distribution of low energy excited states of the daughter atom will, in general, be formed, of average excitation energy about 100 volts for high Z. To each such state a beta-spectrum will be associated. Thus, the observed spectrum will be a composite of many distributions, differing only in their maximum energies by a small amount, and thus with present techniques, indistinguishable experimentally from a single normal spectrum. This is shown in curve c, Fig. 2, which exhibits, very closely, the characteristic allowed shape for an allowed beta-transition.

An alternative theoretical approach[9] assigns all the orbital binding energy difference to the beta-spectrum, on the basis that the coupling of the neutrino to the electrostatic field is negligible. In consequence, the beta-spectrum distribution (a, Fig. 2), characteristic of the decay of a bare nucleus, is shifted into curve b by

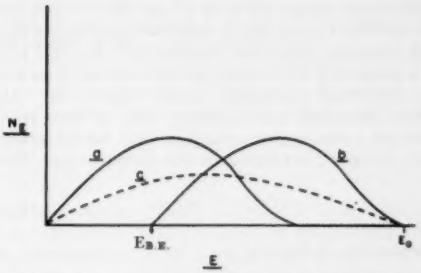

FIG. 2. Orbital rearrangement effect on beta-spectrum. (a) Beta-spectrum of bare nucleus. (b) Beta-spectrum of whole atom if only electron partakes of orbital electron binding energy ($E_{B.E.}$) difference. (c) Beta-spectrum of whole atom if orbital electron binding energy difference is shared between electron and neutrino.

this difference, resulting in a low energy cutoff. Further possibilities involve high energy excitation of the daughter atom, with subsequent radiation or extensive ionization.

The total orbital electron binding energy for high Z atoms is given by Foldy[10] as

$$-32.64Z^{7/6} \text{ ev.}$$

For the beta-transition $Pu^{241} \rightarrow Am^{241}$, the difference in binding energies is 19.0 kev. Other evaluations of this quantity give values between 14 and 22 kev. It can be seen from the Kurie plot that no low energy cutoff of the spectrum lies in this range, so the theory of Hebb[9] is not substantiated. Our past experience with other low energy spectra in lighter isotopes has shown that the cutoff observed below 10 kev is ascribable to sample and detector window absorption.

The approximate allowed shape of the upper half of the spectrum is in agreement with the predictions of references 6 and 8, and indicates that the neutrino does share in the orbital energy difference. However, detailed verification of the theoretical predictions as to the spectral shape cannot be made, as screening corrections were not included. Such corrections are not available to the desired precision for such low energies and high Z, except by uncertain extrapolation from the calculations of Reitz.[11] Although the screening correction accounts for the influence of the orbital electron binding energy difference on the shape of the spectrum,[8] since the *observed* maximum energy already includes the contribution of the orbital binding energy difference to the decay energy, application of the screening correction should not grossly affect the shape, i.e., it cannot alter the maximum energy or the low energy intercept. It would be desirable to have Reitz's calculations extended to cover this problem.

With Foldy's value, the specific nuclear contribution

[6] H. M. Schwartz, Phys. Rev. **85**, 733 (1952); Phys. Rev. **86**, 195 (1952).
[7] R. R. Edwards, Sixth Southwest Regional Meeting, American Chemical Society (1950).
[8] R. Serber and H. S. Snyder, Phys. Rev. **87**, 152 (1952); M. Hamermesh, private communication.
[9] M. H. Hebb, Physica **5**, 701 (1938).
[10] L. L. Foldy, Phys. Rev. **83**, 397 (1951).
[11] J. R. Reitz, Phys. Rev. **77**, 10 (1950).

to the decay energy is only *ca* 1.5 kev (20.5−19.0), but the spectrum shape and *ft* value are appropriate to a first forbidden, unfavored transition with $E_0 = 20.5$ kev. It is interesting to note that the experimental errors and the theoretical uncertainty in the value of the total orbital electronic binding energy may be such as to allow for a zero or even a negative value for the specifically nuclear contribution to the decay energy. Thus a stripped Pu^{241} nucleus is probably only slightly (1.5 kev) unstable with respect to beta-minus-decay, or a stripped Am^{241} nucleus may even be energetically unstable with respect to a stripped Pu^{241} nucleus, although neither positron emission nor electron capture processes could occur.

We wish to thank Mr. Maurice Rusnak for aid in the calculations.

PHYSICAL REVIEW VOLUME 88, NUMBER 5 DECEMBER 1, 1952

The Nuclear Moments of Ta^{181}

B. M. BROWN* AND D. H. TOMBOULIAN
Department of Physics, Cornell University, Ithaca, New York

(Received August 18, 1952)

An analysis of the hfs pattern of several Ta II lines has made it possible to determine the separations of the three levels of the hfs multiplet associated with the $5d^36s\ ^5F_1$ state of Ta II. For this multiplet, the constants A and B appearing in the energy expression $W = W_J + \frac{1}{2}AK + BK(K+1)$ have the numerical values $A = (-0.079 \pm 0.001)$ cm^{-1} and $B = (-0.77 \pm 0.4) \times 10^{-3}$ cm^{-1}. Calculations are carried out in order to evaluate the magnetic and quadrupole moments of the Ta^{181} nucleus. On the basis of the above measurements the magnetic moment as calculated by the Goudsmit-Fermi-Segrè formula has the value of 1.9 nuclear magnetons. Taking into account effects due to the spatial extension of the nucleus, this result is raised to 2.1 nuclear magnetons when the correction factor of 12 percent as listed by Klinkenberg is applied. The result for the quadrupole moment as calculated by the Casimir formula is $+5.9 \times 10^{-24}$ cm^2. According to Sternhermer this moment should be increased by a factor of 10 percent in order to include the effect of an induced quadrupole moment in the closed shell electrons. With this correction the quadrupole moment has the value of $+6.5 \times 10^{-24}$ cm^2.

INTRODUCTION

IT was deemed desirable to undertake an investigation of the hyperfine structure in the spectrum of Ta II taking advantage of recent identification of levels[1] arising from the $5d^36s$ configuration. These levels should exhibit a large hyperfine splitting due to the presence of a single s electron. For a term with a small J-value optimum conditions are provided for the measurement of deviations due to the presence of an electric nuclear quadrupole moment both from the point of view of pattern size and the number of hfs components. These considerations led to the study of the structure of the $^5F_1$ level—the lowest state arising from the $5d^36s$ configuration. Previous researches[2–4] indicate that the Ta nucleus has a spin of 7/2 and a magnetic moment of 2.1 nuclear magnetons. In addition, Schmidt[5] has assigned a value of $\sim 6 \times 10^{-24}$ cm^2 to the nuclear quadrupole moment on the basis of hfs measurements in connection with the lowest states ($^4F_{3/2}$ and $^4F_{5/2}$) of the Ta I spectrum. Values of the quadrupole moment obtained by him from the study of two other levels were found to disagree with the above value. The purpose of the present measurements was to attempt an independent determination of the nuclear magnetic and quadrupole moments.

TABLE I. Wavelengths and transitions of Ta II lines whose hyperfine patterns were investigated. In each case the final state arises from the $5d^36s$ configuration. The term values of the $^3P_0$ and $^5F_1$ states are equal to 4124.77 and 0.00, respectively.

Wavelength in air in angstroms	Transition
3379.49	$(33706.50)_1 \rightarrow {}^3P_0$
3042.06	$(36987.73)_1 \rightarrow {}^3P_0$
2965.92	$(33706.50)_1 \rightarrow {}^5F_1$
2965.13	$(33715.15)_2 \rightarrow {}^5F_1$
2763.37	$(36177.12)_2 \rightarrow {}^5F_1$
2702.80	$(36987.73)_1 \rightarrow {}^5F_1$
2595.59	$(38515.55)_2 \rightarrow {}^5F_1$

EXPERIMENTAL

The Ta II spectrum was excited in a hollow cathode discharge tube containing argon. The hfs patterns were obtained by the use of a Fabry-Perot interferometer crossed with a 21-ft concave grating in a modified Wadsworth mounting. The interferometer plates were coated with aluminum and three separators having thicknesses of 3, 3.7, and 4 mm were utilized. Measurements were carried out on the seven lines whose wave-

* Now at the General Electric Research Laboratory, Schenectady, New York.

[1] Kiess, Harrison, and Hitchcock, J. Research Natl. Bur. Standards 44, 245 (1950).

[2] J. H. Gisolf and P. O. Zeeman, Nature 132, 566 (1933).

[3] N. S. Grace and E. McMillan, Phys. Rev. 44, 949 (1933).

[4] J. H. Gisolf, dissertation, Amsterdam (1935) (unpublished).

[5] T. Schmidt, Z. Physik 121, 63 (1943).

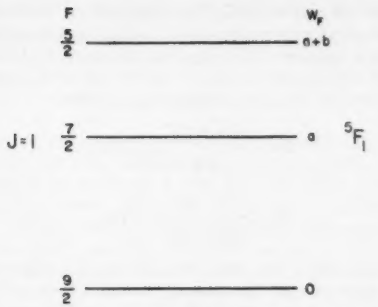

FIG. 1. Hyperfine multiplet belonging to the $5d^36s\ ^5F_1$ ground state of Ta II.

lengths in air and atomic transitions are listed in Table I. An additional line at 2249.8A was also investigated but the fringes were not sufficiently well resolved. It is fortunate that Ta has but one isotope; otherwise, the study of patterns in a spectrum which is already so rich would have been prohibitively difficult.

LINE STRUCTURES AND THE DETERMINATION OF THE CONSTANTS *A* AND *B*

In a hfs multiplet, the energy of a level with total quantum number F is given by[6]

$$W_F = W_J + \tfrac{1}{2}AK + BK(K+1), \qquad (1)$$

where W_J is the center of gravity of the multiplet, A is the splitting factor due to the interaction of the nuclear magnetic moment with atomic electrons, and B is a factor determined by the interaction of the nuclear quadrupole moment and the electrons. The quantity K is defined by $K=F(F+1)-I(I+1)-J(J+1)$, where J and F are the electronic and atomic quantum numbers and I is the nuclear spin.

The study of the various line structures was directed towards the determination of the hfs separations of the $^5F_1$ state. The intervals of interest are designated by a and b on the level diagram shown in Fig. 1. The constants A and B were evaluated from the relations:

$$A=-(70a+54b)/504; \quad B=-a/144+b/112, \qquad (2)$$

by substituting in Eq. (1) the best experimental values of the intervals a and b. The nuclear moments were then calculated by the use of appropriate theoretical expressions involving A and B.

We now turn to a discussion of the procedure followed in obtaining the numerical values of the intervals a and b from observations of hfs patterns. As indicated in the level diagram shown in Fig. 2, the lines 2702A and 3042A are due to transitions which have the same upper level with $J=1$. The hfs intervals of this common upper level were measured directly from the triplet

[6] H. Kopfermann, *Kernmomente* (Edwards Brothers, Ann Arbor, 1945)

TABLE II. The hfs intervals of the $^5F_1$ state and the associated splitting factors derived from the structures of lines listed in the first column. All quantities are expressed in cm^{-1}.

(*A*)	*a*	*b*	(*a*+*b*/2)	*A*	*B*
2702 3042	0.395	0.220	0.505	−0.078	-0.77×10^{-3}
2966 3379	...	...	0.500	...	...

structure associated with the pattern of line 3042A. The magnitudes of these intervals as designated in Fig. 2 were found to be $a_u=0.327$ cm^{-1} and $b_u=0.262$ cm^{-1}. In the case of line 2702A, the component pairs labeled as 2, 3 and 5, 6 were not resolved. These components have equal intensities and the center of gravity of each pair is located midway between the two components. Component 7 was so weak that its position could not be determined accurately. Hence, from the line 2702A, it was possible to measure only the two intervals of magnitude equal to 0.361 cm^{-1} and 0.602 cm^{-1} as designated in Fig. 2. From these considerations, the desired intervals of the $^5F_1$ are found to be: $a=0.395$ cm^{-1} and $b=0.220$ cm^{-1}.

A partial confirmation of the above values for a and b may be obtained by investigating the patterns of two other lines, namely, $\lambda=2965.9$A $(J=1\rightarrow J=0)$ and $\lambda=3379$A $(J=1\rightarrow J=1)$. Here, the situation is similar

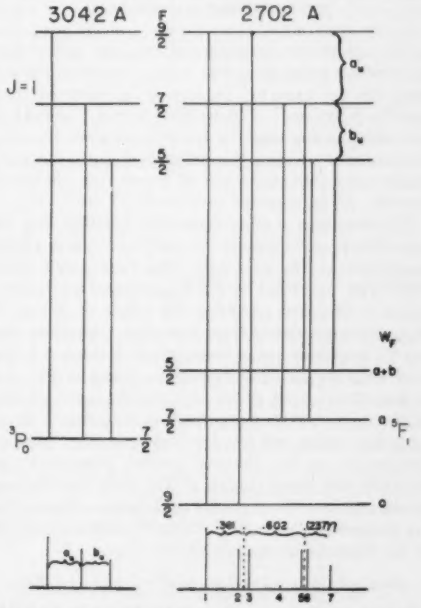

FIG. 2. Level diagram and line structure for λ2702 and λ3042. Intervals are expressed in cm^{-1}. The spin of Ta^{181} is 7/2.

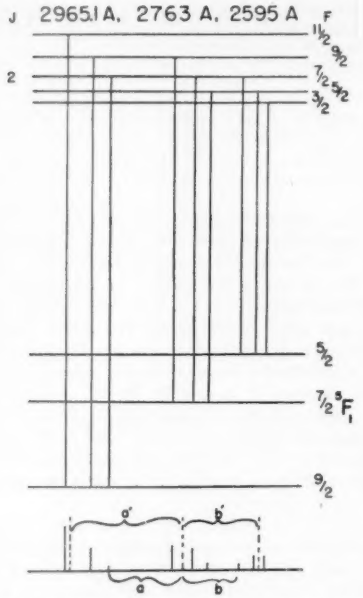

FIG. 3. Line structure arising from transitions into the lowest $^5F_1$ level from a higher level with $J=1$.

to the case of the preceding pair of lines, except that the common upper level with $J=1$ is inverted. From a study of the expected pattern it is observed that $a+b/2=0.500$ cm^{-1}. This result is within 1 percent of the corresponding value for $(a+b/2)$ obtained from the previous pair of lines. A summary of these measurements along with the values of A and B as computed from Eq. (2) is presented in Table II.

The structures of other lines which combine with the ground level are in general too complex to yield reliable measurements. However three other lines (λ2595, 2763, 2965) were examined to see if additional information might be obtained regarding the values of A and B. The above-mentioned lines represent transitions into the $^5F_1$ level from upper states whose J value is 2. The level diagram and the hfs pattern shown in Fig. 3 is typical of this group of lines. Due to the small splitting of the upper levels, the individual components of the multiplet could not be resolved and the intensity distribution of the observed pattern resembled that shown in the lower portion of Fig. 3. If the intervals between the centers of gravity of the observed groupings are designated as a' and b', then, the desired intervals of the $^5F_1$ level are related by

$$a=a'-6.75A_u-114B_u; \quad b=b'-5.25A_u+148B_u,$$

where A_u and B_u are the constants which determine the splitting of the upper level involved. The expressions above are arrived at by applying Eq. (1) to the hfs levels of the upper state and by taking into account the relative intensities of components as given by tables.[7] Upon substitution in Eq. (2) of the values of a and b specified by the above relations one obtains,

$$A=-\frac{70a'+54b'}{504}+1.50A_u, \qquad B=-\frac{a'}{144}+\frac{b'}{112}+2.11B_u. \tag{3}$$

For each line of this group a' and b' were measured from the patterns and the value of A_u was estimated from the width of the unresolved components. This method of arriving at the value of A_u is sufficiently accurate since a 10 percent error in the measurement of the width introduces only a 2 percent error in the calculated value of A. Corresponding estimates of the value of B_u cannot be obtained. For a level with $J=2$, the constant B is expected to be only $\frac{1}{6}$ as large as the one deduced from a level with $J=1$. The information gleaned from a study of these transitions $(J=2\rightarrow J=1)$ is presented in Table III. Since the magnitude of the correction B_u is not known this quantity is included in the results for B.

The agreement between the values of A appearing in Table II and Table III is satisfactory. In obtaining the average value of A, the mean of the three values shown in Table III was weighted equally with the determination listed in Table II. Two of the values listed for B in Table III are in fair agreement with the result given in Table II. The reason for the discrepancy in the case of λ2965 is not known. Kiess[8] has indicated that this wavelength may satisfy two atomic transitions. The discrepancy may also be ascribed to the presence of a large quadrupole effect associated with the structure of the upper level involved in this particular transition. The individual values of B listed in Table III cannot be regarded as reliable as the value of B obtained from measurements on the 2702A line. Consequently, these determinations were disregarded in the calculation of the quadrupole moment. The various considerations presented in the preceding discussion lead to the following values of the constants:

$$A=(-0.079\pm0.001)\text{ cm}^{-1}; \qquad B=(-0.77\pm0.04)\times10^{-3}\text{ cm}^{-1}. \tag{4}$$

TABLE III. Values of the splitting factors deduced from the partially resolved structures of the lines listed in the first column. These represent transitions from upper levels with $J=2$ into the $^5F_1$ state. All quantities are expressed in cm^{-1}.

λ(A)	a'	b'	A_u	A	B
2595	0.521	0.347	0.018	−0.083	$(-0.52+2.1B_{u1})\times10^{-3}$
2763	0.510	0.306	0.017	−0.079	$(-0.81+2.1B_{u2})\times10^{-3}$
2965	0.500	0.426	0.024	−0.079	$(+0.33+2.1B_{u3})\times10^{-3}$

[7] H. E. White and A. Y. Eliason, Phys. Rev. **44**, 753 (1933).
[8] C. C. Kiess (private communication).

THE CALCULATION OF THE MAGNETIC MOMENT

According to the calculations of Breit and Wills,[9] the magnetic splitting factor A of the $^5F_1$ state may be written as

$$A=(5/4)a_F-\tfrac{1}{4}a_s,$$

where a_s and a_F are the coupling coefficients for the s electron and the d electron complex, respectively. It is necessary to evaluate a_s for the calculation of the magnetic moment. The value of A is already available, but a_F must still be determined. The expressions for the magnetic coupling coefficient for the d electron complex as given by Fermi and Segrè,[10] yield the ratio

$$\frac{a_F}{a'_F}=\frac{\langle 1/r^3\rangle_{\text{Ta II}}}{\langle 1/r^3\rangle_{\text{Ta I}}}.$$

In the above ratio a'_F is the magnetic coupling coefficient of the d complex in Ta I and is known to have the value of 0.0167 cm^{-1} according to measurements carried out by Schmidt[5] on the structure of the $^4F_{3/2}$ state of Ta I. The averages indicated in the ratio on the right-hand side are for a d electron. The numerical value of the ratio may be obtained from a study of a series of spectra where a similar situation exists; that is, where the ionization involves the removal of one of a pair of s electrons and where the remainder of the configuration has the form d^ns. Such a procedure sets the average value of the ratio at 1.05. It should be mentioned that the ratio has the value of 1.00 when calculated from the fine structure intervals of the spectra of Ta I and Ta II. However, the low-lying ^4F multiplet in Ta I shows a large deviation from the interval rule, so that the value of 1.05 as deduced from the spectra of neighboring elements was considered as more reliable. On the basis of this information, the factor a_F comes out to be 0.0175 cm^{-1}, and consequently $a_s=0.405\pm0.005$ cm^{-1}.

The connection between the magnetic moment μ (in nuclear magnetons) and the coupling factor a_s (in cm^{-1}) is given by [10,11]

$$a_s=\frac{8R\alpha^2}{3I}\frac{Z(1+z)^2}{n^{*3}}\left(1-\frac{d\sigma}{dn}\right)1836\mathfrak{C}(Z,j)\mu. \qquad (5)$$

The various quantities in Eq. (5) have the meaning and numerical values listed below:

R=Rydberg constant, $\alpha=1/137$; Z=the interior charge number here equal to 73 for an s electron; z=the stage of ionization, hence for Ta II, $(1+z)^2=4$; $I=7/2$, n^*=the effective quantum number$=(n-\sigma)$ where σ is the quantum defect; $\mathfrak{C}$=relativity correction factor. The value of n^{*3} was determined by plotting n^{*3} against Z for a large number of singly ionized atoms throughout the periodic table. The effective quantum number n^* is the one associated with the lowest term in a series originating from the excitation of an s which is shielded by p, d, and f electrons. For Ta II, the value of n^{*3} as read from the resulting smooth curves is 6.6. The quantity $[1-(d\sigma/dn)]$ was found to have the average value of 1.05 as determined from a study of similar spectra. Here $d\sigma/dn$ represents the change in the quantum defect observed in the lowest pair of s series terms in the fine structure levels. As tabulated by Kopfermann,[6] the relativity correction factor $\mathfrak{C}$ is 1.92. Upon substitution in Eq. (5) the nuclear moment of Ta^{181} is found to be

$$\boxed{\mu_{181}=4.6a_s=1.9 \text{ nuclear magnetons.}}$$

CALCULATION OF THE QUADRUPOLE MOMENT

The evaluation of the quadrupole moment was carried out by the use of the Casimir[12] formula:

$$q=-\frac{8}{3}\frac{I(2I-1)J(2J-1)}{e^2\left[\sum_i\left\langle\frac{3\cos^2\theta_i-1}{r_i^3}\right\rangle_{\text{Av}}\right]_{M_J=J}}B. \qquad (6)$$

The indicated summation is carried out over the electron coordinates i for those electrons which contribute to the quadrupole interaction with the nucleus for the state $M_J=J$. In order to include the effects of relativity corrections dependent on the j-values of individual electrons, the wave function of the $^5F_1$ state was written as the zero-order Russell-Saunders sum of products of one electron functions in the $m_l{}^{m_s}$ representation. Following the scheme used by Schmidt,[5] the $m_l{}^{m_s}$ matrix elements were then expressed in terms of the $d_j{}^{m_j}$ elements.[13] The result obtained for the quantity in brackets found in Eq. (6) is

$$\left[\sum_i\left\langle\frac{3\cos^2\theta_i-1}{r_i^3}\right\rangle_{\text{Av}}\right]=\frac{8}{875}(13R_2'+14R_2''-12S_2)\langle 1/r_d^3\rangle_{\text{Av}},$$

where R_2', R_2'', and S_2 are the relativity corrections for d electrons. From the fine-structure splitting of the two lowest ^5F intervals of Ta II, the average inverse cube of the radius of $5d$ electron in Ta II was estimated to be 0.37×10^{25} cm^{-3} by the method of Fermi and Segrè.[10] (See also Condon and Shortley.[14]) From tables prepared

[9] G. Breit and L. A. Wills, Phys. Rev. **44**, 475 (1933).
[10] E. Fermi and E. Segrè, Z. Physik **82**, 729 (1933).
[11] S. A. Goudsmit, Phys. Rev. **43**, 636 (1933).

[12] H. Casimir, *On the Interaction between Atomic Nuclei and Electrons* (Teylers Tweede Genootschap, XI, Haarlem, 1936).

[13] Two typographical errors exist in the 5th and 7th elements as listed by Schmidt. These should read:

$$(0^{\pm}|3\cos^2\theta-1|0^{\pm})=\frac{4}{175}(12R_2'+7R_2''+6S_2);$$

$$(0^{\pm}|3\cos^2\theta-1|\pm1^{\mp})=\frac{2\sqrt{6}}{175}(8R_2'-7R_2''-S_2).$$

[14] E. U. Condon and G. H. Shortley, *Theory of Atomic Spectra* (Cambridge University Press, Cambridge, 1951), p. 196.

by Kopfermann,[6] one finds $R_2'=S_2=1.07$ and $R_2''=1.24$. Hence for the bracketted expression above one obtains the numerical value of 6.3×10^{24} cm^{-3}. Combining this factor with the experimental value for B already determined, the nuclear quadrupole moment of Ta^{181} is evaluated with the aid of Eq. (6). The result is

$$q=+5.9\times10^{-24}\text{ cm}^2.$$

DISCUSSION OF RESULTS

A source of error in the determination of the magnetic moment may lie in the procedure followed in obtaining the coupling coefficient of the s-electron. This step involves the removal of the contribution of the d-electrons to the coupling coefficient of the $^5F_1$ state. Since the term due to the d-electrons represents 20 percent of the $^5F_1$ coupling coefficient, the error introduced in a_s cannot be in excess of this amount and probably is not as high. It is believed that this is the best approach to the evaluation of the magnetic moment, since, results derived from s-electron coupling coefficients are in general expected to be most reliable in spectroscopic determinations.

A second error may arise from the method adopted in the calculation of a_F, the coupling coefficient associated with the d-electron complex. This involves the transfer of measurements of the hfs of the $^4F_{3/2}$ state of Ta I to the Ta II structure by means of the ratio of $\langle r_d^{-3}\rangle_{Av}$ terms. The error here cannot be greater than that involved in the evaluation of $\langle r_d^{-3}\rangle_{Av}$ by the use of fine structure splitting factors and is estimated to be of the order of a few percent. It is gratifying to note that magnetic moment of 1.9 nuclear magnetons as obtained from the present measurements is in agreement with the value of 2.1 nuclear magnetons arrived at by Gisolf.[4]

In a review article[15] Klinkenberg points out that the value of μ derived from optical hfs on the basis of the original Goudsmit-Fermi-Segrè formula should be increased by 12 percent in the case of Ta. The correction is introduced to take into account two effects due to the spatial extension of the nucleus. The greater of the two is the influence upon the electronic wave functions exerted by the uniform electric charge distribution. The second effect is the result of the presumed uniform distribution of the magnetic dipole moment over the nuclear volume. With this correction, the value of the magnetic moment is increased to 2.1 nuclear magnetons.

On the basis of observations carried out on the $^5F_1$ level of Ta II, the present investigation yields a value of $+5.9\times10^{-24}$ cm^2 for the quadrupole moment of Ta^{181}. Previous measurements on the $^4F_{3/2}$ level of Ta I reported by Schmidt lead to the result of $+6\times10^{-24}$ cm^{-2} for the same quantity. It must be borne in mind that the determination of the quadrupole moment does depend on the detailed form of the coupling between the three d-electrons. Although the Landé interval rule is obeyed more closely by the fine structure levels of Ta II than those of Ta I, significant deviations from the rule still exist in the spectrum of the ion. Hence, the present calculation of q based on R-S coupling cannot be justified completely. The agreement which appears in the values of q as obtained from two different stages of excitation is not necessarily a reliable index as to the correctness of the type of coupling assumed. In the electron configurations $5d^36s^3$ and $5d^36s$ which give rise to the $^4F_{3/2}$ and $^5F_1$ levels of Ta I and Ta II, respectively, the s electron gives no quadrupole interaction with the nucleus. Hence, the errors due to a departure from R-S coupling in the case of Ta I may be similar to those encountered in the present determination dealing with Ta II. It is difficult to assign values to the expected errors, since the main source lies in the assumptions which must be made in order to approximate the electronic averages.

Recent calculations by Sternheimer[16] indicate that the value of the nuclear quadrupole moment as deduced above should be increased by 10 percent due to an induced quadrupole moment in the electrons belonging to closed shells. The value of the quadrupole moment then becomes

$$+6.5\times10^{-24}\text{ cm}^2.$$

The authors gratefully acknowledge the generous assistance of Mr. C. C. Kiess of the National Bureau of Standards in matters relating to the spectrum of Ta II. They also wish to thank Dr. N. Schwartz and Mr. G. Sprague for aid rendered in the course of these calculations.

[15] P. F. A. Klinkenberg, Revs. Modern Phys. 24, 63 (1952).

[16] R. Sternheimer, Phys. Rev. 86, 316 (1952).

The Effect of Final State Interactions on Reaction Cross Sections

KENNETH M. WATSON
Physics Department, Indiana University, Bloomington, Indiana
(Received August 18, 1952)

Particles produced in a reaction often interact strongly with each other before getting outside the range of their mutual forces. Formal effects of such interactions are discussed, and in particular it is shown that the effect for very strong attractive interactions can be calculated explicitly without having detailed knowledge of the properties of the reaction. Application is made to some meson phenomena.

I. INTRODUCTION

IT frequently happens that, when particles are produced in a nuclear or elementary particle reaction, some of these interact among themselves so strongly that they influence appreciably the properties of the reaction cross section. These interactions we shall call "final state interactions." Their influence is well known in nuclear physics where the Coulomb attraction plays an important role in such phenomena as β-decay.

Recently, strong short-range nuclear interactions have been found to play a striking part in certain reactions involving mesons. It is with such interactions as these that we shall be primarily concerned. The importance of recognizing and analyzing the role played by these interactions lies partly in the observation that they may greatly modify the angular distributions and energy spectra of the produced particles and yet play no important part in the primary mechanism by which the reaction takes place. That is, it is as if the reaction first takes place as if there were no final state interaction and then is distorted by the short-range nuclear interactions before the particles can get out of the range of their mutual forces. It is to be expected that an analysis of the reaction will be considerably simplified by separating the effect of these two mechanisms, which we shall frequently refer to as the "primary mechanism" of the reaction and the "final state interaction," respectively. We shall find that under certain conditions these terms can be made meaningful by explicitly exhibiting their individual contributions to the reaction cross section. Conversely, this separation, when possible, will provide an indirect means of measuring the scattering interaction between two particles produced in a reaction.

Perhaps the most striking example of final state interactions in meson phenomena is that occurring in meson production by nucleon-nucleon collisions,[1,2] where the final state nuclear force influences considerably the spectrum of the produced mesons.[3,4] The capture of π^- mesons by deuterons leads, in a certain fraction of the events, to a single high energy γ-ray and to two neutrons.[5] The nuclear force between the two neutrons modifies the γ-ray spectrum and leads to a means of measuring the neutron-neutron (n-n) force.[6] Present experimental results[7,8] are in agreement with other known characteristics of the n-n force. Finally, there is a slight suggestion from the work of Danysz, Lock, and Yekuteli[9] that a meson-meson interaction may modify multiple meson production cross sections.[10]

We shall be most interested in those reaction processes for which three general conditions are met. These conditions will imply that the final state interaction seriously modifies the reaction cross section and also that the effect of this is calculable. The first of these is that the mechanism of the reaction cross section be a short-range interaction, i.e., that the primary reaction (irrespective of the final state interactions) be confined to a certain volume V of order a^3, where a is the range of the interaction. It is not unlikely that this condition will be met by most of the nonelectromagnetic elementary particle reactions. Second, the effect of the final state interaction is to be considered only for low relative energies of the particles whose interaction is being considered. For high relative energies, this interaction will be expected to be of relatively little importance. Finally, the final state interaction must be strong and attractive, a restriction which will be made more precise in the following paragraphs.

To see this, let us suppose the reaction to be proceeding backwards. That is, we send the produced particles back into the region of their mutual interaction in such a manner that the initial state will result. We suppose that the two particles whose interaction we are studying have a small relative energy and that the scattering cross section of these two particles is large compared to the effective cross-sectional area of the volume of primary interaction. In this case the probability of the two particles "finding" each other in the vicinity in which the reaction is to proceed is proportional to their scattering cross section. That is, the two particles start to scatter and, if the interaction between them is attractive, they will tend to stick together

[1] Cartwright, Richman, Whitehead, and Wilcox, Phys. Rev. **78**, 823 (1950).
[2] Peterson, Iloff, and Sherman, Phys. Rev. **81**, 674 (1951).
[3] K. A. Brueckner, Phys. Rev. **82**, 598 (1951).
[4] K. Watson and K. Brueckner, Phys. Rev. **83**, 1 (1951).
[5] Panofsky, Aamodt, and Hadley, Phys. Rev. **81**, 565 (1950).
[6] K. M. Watson and R. N. Stuart, Phys. Rev. **82**, 738 (1951).
[7] Aamodt, Panofsky, and Phillips, Phys. Rev. **83**, 1057 (1951).
[8] R. Phillips, University of California Radiation Laboratory Report UCRL 1845 (to be published).
[9] Danysz, Lock, and Yekuteli, Nature **169**, 364 (1952).
[10] K. Brueckner and K. Watson, Phys. Rev. **87**, 621 (1952).

momentarily. This helps to bring them together into the region of space from which the primary inverse reaction can proceed—and thus the transition rate for the inverse reaction is expected to be proportional to the scattering cross section of the two particles. On the other hand, if this scattering cross section were less than the cross-sectional area of the primary reaction volume, the final state interactions would be of little help in "drawing the particles into this latter volume."

By detailed balancing we can then obtain the cross section for the reaction itself to be

$$d\sigma \simeq d^3q\sigma_q^0 \text{ times other factors,} \tag{1}$$

where q is the small relative momentum of the two particles and σ_q^0 is their scattering cross section for relative momentum q. The d^3q is, of course, just a factor in the volume of phase space into which the reaction proceeds. We suppose q to be small enough that σ_q^0 arises only from S-wave scattering. As long as $q \simeq 0$, one can neglect the q-dependence of the other factors in Eq. (1), keeping only that of

$$d^3q\sigma_q^0 \simeq dq \sin^2\delta_q, \tag{2}$$

where δ_q is the S-wave phase shift for the scattering at relative momentum q.

When $\sin^2\delta_q$ becomes of the order of unity for values of q such that $\hbar/q$ is still large compared to a, the range of the primary interaction, a strong correlation in the emission of the interacting particles will result which will be described by Eq. (2). This equation then gives a means of measuring δ_q from an observation of the reaction cross section.

II. BOUNDARY CONDITIONS

In the present section we shall express the transition rate for a reaction process in terms of the wave function which describes the final state interaction. We characterize the initial state of the reaction, containing the colliding particles, by the state function χ_a. χ_a describes the plane wave motion of the center of mass of each of the two incoming particles plus any internal coordinates and satisfies the Schrödinger equation

$$H_0\chi_a = E_a\chi_a, \tag{3}$$

where H_0 is the appropriate Hamiltonian and E_a is the energy of the system.

Among the possible alternate "channels" by which the reaction can proceed, we shall be interested in that one to be designated by the set of states "B." The set "B" refers to a unique set of particle occupation numbers, while a single member of the set "B" specifies also spins, momenta, etc., of each of the particles. We suppose H_0 to be so defined that the state functions χ_B also satisfy

$$H_0\chi_B = E_B\chi_B = E_a\chi_B. \tag{4}$$

The Hamiltonian H of the system will be given by adding to H_0 the interaction $\mathfrak{V}$, which is responsible for the transition $a \to B$:

$$H = H_0 + \mathfrak{V}. \tag{5}$$

The final state interaction v is introduced by decomposing $\mathfrak{V}$:

$$\mathfrak{V} = V + v, \tag{6}$$

where V is defined as $\mathfrak{V} - v$. v is that specific interaction between pairs of particles in the final state which leads to the correct scattering cross section for any pair of these particles (i.e., we neglect a possible modification of v due to many body forces—this assumption is discussed further in the final section). For simplicity in the following analysis, we can define v to vanish except when operating on that particular set of particle occupation numbers which we have designated by the set "B" above—i.e., we suppose the actual interaction to be multiplied by a projection operator which picks out the set "B." This is permissible since we define V as $\mathfrak{V} - v$.

Following the notation of Lippmann and Schwinger,[11] we can write the integral equation for the state function of the system as

$$\psi_a^{(\pm)} = \chi_a + \frac{1}{E_a \pm i\epsilon - H_0}(v+V)\psi_a^{(\pm)}. \tag{7}$$

Here ϵ is a positive real parameter which goes to zero after the implied integrations are done. We have similarly the wave function describing the scattering of the final state particles among themselves:

$$\phi_B^{(\pm)} = \chi_B + \frac{1}{E_a \pm i\epsilon - H_0} v\phi_B^{(\pm)}, \tag{8}$$

since $E_a = E_B$.

The probability amplitude for the transition $a \to b$ is[11]

$$T_{Ba} = (\chi_B, (v+V)\psi_a^{(+)}). \tag{9}$$

Following the notation of Chew and Goldberger,[12] we express $\psi_a^{(+)}$ in terms of the matrix operator $\Omega^{(+)}$:

$$\psi_a^{(+)} = \Omega^{(+)}\chi_a, \tag{10}$$

where

$$\Omega^{(+)} = 1 + \frac{1}{E_a + i\epsilon - H_0 - V - v}(V+v). \tag{11}$$

From Eqs. (9) and (10), we write the transition operator T as[12]

$$T = (v+V)\Omega^{(+)}, \tag{12}$$

with

$$T_{Ba} = (\chi_B, T\chi_a). \tag{13}$$

---

[11] B. Lippmann and J. Schwinger, Phys. Rev. **79**, 469 (1950).

[12] Relations (10) and (12) have been given by C. Moller, Kgl. Danske Videnskab. Selskab, Mat.-fys. Medd. **22**, No. 19 (1946). G. F. Chew and M. L. Goldberger [Phys. Rev. **87**, 778 (1952)] have introduced the expression (11). I am indebted to Dr. Chew and Dr. Goldberger for being informed of this and related algebraic relations in advance of publication.

Remembering that from its definition v vanishes when operating on the state χ_a and using Eqs. (11) and (12) and the operator relation,[13]

$$\frac{1}{A}-\frac{1}{B}=\frac{1}{A}(B-A)\frac{1}{B}, \tag{14}$$

we easily obtain

$$T=\omega^{(-)\dagger}V\Omega^{(+)}. \tag{15}$$

Here

$$\omega^{(-)\dagger}=1+v\frac{1}{E_a+i\epsilon-H_0-v} \tag{16}$$

and $\phi_B^{(-)}=\omega^{(-)}\chi_B$ [see Eq. (8)]. Inserting Eq. (15) into Eq. (13), we obtain

$$T_{Ba}=(\phi_B^{(-)}, V\psi_a^{(+)}). \tag{17}$$

The boundary condition $\phi_B^{(-)}$ in Eq. (17) has been derived previously for several special cases.[14–16] The physical basis rests on the requirement that the final state contain outgoing waves only and is formally expressed by the use of "$+i\epsilon$" in Eq. (16).

Equations (15) and (16) do not actually lead as directly to Eq. (17) as we have indicated. The point is that the parameter ϵ in $\omega^{(-)\dagger}$ [Eq. (16)] is the same as the "ϵ" in $\Omega^{(+)}$. This would mean taking the limit $\epsilon\to 0$ for $\phi_B^{(-)}$ and $\psi_a^{(+)}$ simultaneously for use in Eq. (17). Doing this is clearly not so convenient as being able to take independent limits for $\phi_B^{(-)}$ and $\psi_a^{(+)}$; i.e., using different ϵ's in $\omega^{(-)\dagger}$ and in $\Omega^{(+)}$. In Appendix (A) it is shown that this can indeed be done, it being only necessary to keep both ϵ's positive as the limit $\epsilon\to 0$ is being approached.

It is interesting that the boundary condition (17) follows also from the requirements of time reversal invariance. It is shown in Appendix (B) that Eq. (16) follows from the general detailed reversibility requirement

$$U\tilde{T}U^{-1}=T, \tag{18}$$

where $\tilde{T}$ is the transpose of the operator T and U is the unitary matrix introduced by Wigner[17] in connection with time reversal. It is not surprising that time reversal invariance should determine the boundary condition on ϕ_B in Eq. (17). We could not expect the reversed system to return to the (time reversed) initial state unless we start it in the correct (time reversed) final state.[18]

In Eq. (17) the final state interaction contributes most explicitly to $\phi_B^{(-)}$, but is also contained in $\psi_a^{(+)}$. We shall see in the next section that Eq. (17) is already in a useful form for the applications of that section. It is possible, however, to exhibit more explicitly the occurrence of v in Eq. (17). For this purpose we define $\Omega_0^{(+)}$ to be $\Omega^{(+)}$ [Eq. (11)] with $v=0$,

$$\Omega_0^{(+)}=1+\frac{1}{E_a+i\epsilon-H_0-V}V, \tag{19}$$

and

$$\psi_a^{0(+)}=\Omega_0^{(+)}\chi_a. \tag{20}$$

Using Eq. (14), we have

$$\Omega^{(+)}=\Omega_0^{(+)}+\frac{1}{E_a+i\epsilon-H_0-V-v}v\Omega_0^{(+)}. \tag{21}$$

From this and Eqs. (17), (19), and (20), we obtain

$$T_{Ba}=(\phi_B^{(-)}, V\psi_a^{0(+)})+(\psi_B^{(-)}-\phi_B^{(-)}, v\psi_a^{0(+)}), \tag{22}$$

where $\psi_B^{(-)}$ satisfies Eq. (7) with χ_a replaced by χ_B. The first term in Eq. (22) is similar to Eq. (17), except now v occurs only in $\phi_B^{(-)}$. Following the methods of Chew and Goldberger,[12] the second term can readily be developed in the form

$$(\phi_B^{(-)}, Q\psi_a^{0(+)}),$$

where Q is a power series in v.

The second term in Eq. (22) can be expected to be small compared to the first in two limiting cases. Remembering that v was defined in such a manner that it vanished except when operating on the set "B" of particle occupation numbers, we see that $v\psi_a^{0(+)}$ describes the production of a final state "B" followed by a scattering of the particles in this state. Since $\psi_B^{(-)}-\phi_B^{(-)}$ vanishes when $V\to 0$, this term describes the repeated interaction of the particles through the primary interaction V to produce again a state of the type "B." It is thus clear that when V can be treated as a small perturbation the second term in Eq. (22) is of higher order in V than is the first and can be neglected. On the other hand, if V is a strong interaction leading to many virtual states (many sets of particle occupation numbers) we note that the second term in Eq. (22) picks one very restricted set of intermediate states (i.e., of type "B") and may consequently be small to the extent that these intermediate states contribute relatively little to the reaction.

III. THE DEPENDENCE OF THE REACTION CROSS SECTION ON THE FINAL STATE INTERACTION

We return to the expression (17) for the transition amplitude T_{Ba}. We suppose that n particles are pro-

[13] G. F. Chew and G. C. Wick, Phys. Rev. **85**, 636 (1952).
[14] N. F. Mott and H. S. W. Massey, *The Theory of Atomic Collisions* (Oxford University Press, London, 1933).
[15] W. Rarita and J. Schwinger, Phys. Rev. **59**, 556 (1941).
[16] Rose, Biedenharn, and Arfken, Phys. Rev. **85**, 5 (1952).
[17] E. P. Wigner, Gottingen Nachr. **31**, 546 (1932).
[18] It seems likely that the boundary condition on ϕ_B expressed by Eq. (17) should probably also follow from "causality" requirements, as discussed by W. Schützer and J. Tiomno [Phys. Rev. **83**, 249 (1951)]. The work of these authors suggests that the matrix T has no singularities (except on the imaginary axis) in the positive-imaginary half-plane, when presented in diagonal form. $\Omega^{(+)}$ and $\omega^{(+)}$ contain the scattering matrix, and a related property is expected for these. On the other hand, $\omega^{(-)}$ is simply related to the complex conjugate of $\omega^{(+)}$, so $\omega^{(-)\dagger}$ should also have this causal property and thus the T of Eq. (15). This would not seem to be the case, however, had we used, for example, $\omega^{(+)\dagger}$ in Eq. (15).

duced in the state B with rest masses M_i, momenta k_i, and energies W_i. The differential cross section for the reaction in the center-of-mass system is then (we set $\hbar=c=1$)

$$d\sigma=\frac{(2\pi)^4}{\mu_r}\int\delta(\sum_{i=1}^{n}W_i-E_a)\delta(\sum_{i=1}^{n}\mathbf{k}i)\times\prod_{i=1}^{n}d^3k_i\sum_{\text{spins}}|T_{Ba}|^2. \quad (23)$$

Here μ_r is the relative velocity of the colliding particles. The integration is to be carried out over four of the $3n$ momentum variables in such a way as to satisfy the conditions imposed by the δ-functions. The expression $\sum_{\text{spins}}$ is an appropriate average and sum over initial and final spin substates, respectively.

Let us suppose that there are at least three particles in the final state and that the two whose interaction we are studying have momentum vectors $\mathbf{k}_1$ and $\mathbf{k}_2$. Let us introduce their relative momentum, $\mathbf{q}=\frac{1}{2}(\mathbf{k}_1-\mathbf{k}_2)$, and their total momentum $\mathbf{p}=\mathbf{k}_1+\mathbf{k}_2$. $d\sigma$ will now contain a factor $d^3q=q^2dqd\Omega_q$, where $d\Omega_q$ is an element of solid angle in the direction of $\mathbf{q}$. The values of $\mathbf{q}$, a relative momentum, will not be affected by the δ-function describing momentum conservation. When q is sufficiently small compared to E_a, we can neglect the effect of energy conservation on the values of q. We then have the q-dependence of the phase space factor in Eq. (23) as just

$$q^2dqd\Omega_q. \quad (24)$$

In any actual problem it is, of course, straightforward to calculate exactly the phase space factor, but for purposes of a general discussion it is convenient to use the simple form (24).

It now remains to find the dependence of T_{Ba} on q, subject to the restrictions mentioned in the introduction. Returning to the expression (17) for T_{Ba} we define

$$(\xi|R|a)=V\psi_a^{(+)}, \quad (25)$$

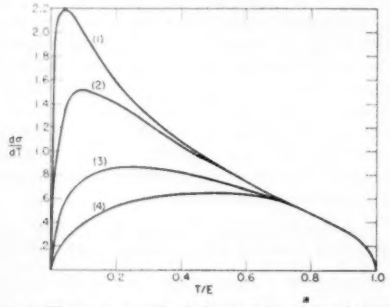

FIG. 1. The spectrum of relative energies of two interacting particles emitted in a reaction. The total energy of the two particles is considered to be constant. Curves (1) to (4) are calculated for the following respective values of $2a^2/ME$ [see Eq. (35)]: 0.1, 0.25, 1.0, ∞. A much sharper peak could, of course, have been obtained by taking even smaller values of this parameter.

where ξ is an appropriate set of coordinates. R is just the transition operator in a mixed representation and has been used previously[4] in the study of meson production in nucleon-nucleon collisions. Let $\mathbf{r}$ be that member of the coordinate set ξ which describes the relative position of particles "1" and "2." In accordance with the assumption that the reaction takes place within a certain volume, we suppose R to vanish as r becomes appreciably larger than a, the radius of this volume. Neglecting the interaction of particles "1" and "2" with others of the final state particles (phase space arguments lead one to expect a small probability that more than two particles will have small relative momenta) we can factor out of $\phi_B^{(-)}$ that part, $g_q^{(-)}(\mathbf{r})$, which describes the relative motion of particles "1" and "2." Writing $\phi_B^{(-)}=h_{B'}{}^{(-)}(\xi')g_q^{(-)}(\mathbf{r})$, where B' and ξ' do not contain q or r as variables, we next define

$$(r|\bar{R}|a)\equiv(h_{B'}{}^{(-)},R), \quad (26)$$

and have

$$T_{Ba}=(g_q^{(-)},\bar{R}). \quad (27)$$

Now it is important to note that $\bar{R}$ does not depend explicitly upon the variable q, so that the only dependence of T_{Ba} on q comes from $g_q^{(-)}$. Energy conservation will, of course, impose a q-dependence on $\bar{R}$, but we have seen above that this is a small effect when q is small.

Since q is considered to be very small, we shall for the moment suppose that only the S-wave part of $g_q^{(-)}$ is important. That is, we write

$$g_q^{(-)}=(e^{-i\delta}/qr)\sin(qr+\delta), \quad (28)$$

where δ is the S-wave phase shift for the scattering of particles "1" and "2." Equation (28) is valid outside the range of the interaction of these two particles. We next express δ in terms of the low energy scattering parameters:

$$q\cot\delta=\alpha+\tfrac{1}{2}r_0q^2. \quad (29)$$

We are interested in $r\simeq a$ or less, so when q is small enough that qr is small, we have

$$\sin(qr+\delta)\simeq\sin\delta[1+\alpha r+\tfrac{1}{2}q^2r(r_0-r)]. \quad (30)$$

Neglecting the q^2 term above, we have for the pertinent values of r,

$$g_q^{(-)}(r)\simeq e^{-i\delta}(\sin\delta/q)f(r), \quad (31)$$

where $f(r)$ is independent of q. Equation (31) is also valid inside the region of interaction of particles "1" and "2" since then $f(r)$ is the integral of the Schrödinger equation, which is to a good approximation independent of q for small q-values. (For more detail see the paper by Bethe[19] from which the present argument is taken.) Inserting Eq. (31) into Eq. (27), we have

$$T_{Ba}=e^{i\delta}(\sin\delta/q)(f(r),\bar{R}). \quad (32)$$

[19] H. A. Bethe, Phys. Rev. **76**, 38 (1949).

The factor $(f, \bar{R})$ is now essentially independent of q for small q-values (the only dependence coming from energy conservation, as remarked previously).

Inserting this expression into Eq. (23) and using (24) for the phase space factor, the cross section can be written as

$$d\sigma = \sin^2\delta \; dq \text{ times a factor independent of } q. \quad (33)$$

If we keep only the α-term in Eq. (29), this becomes

$$d\sigma \simeq q^2 dq/(\alpha^2+q^2). \quad (34)$$

In Eq. (30) we have neglected the term of order $\frac{1}{2}q^2a(r_0-a)$ compared to unity. Thus (34) is expected to be valid for q-values satisfying this condition or for a wavelength $\hbar/q$ large compared to the radius of the region of primary interaction. If α is larger than the maximum q-values for which Eq. (33) remains valid, Eq. (34) gives just the usual phase space dependence for the cross section which is expected to hold near threshold.[20] In this case we would not find so pronounced an effect from the final state interaction—and indeed might expect to be able to neglect it entirely.

We note that Eq. (33) agrees exactly with the estimate made in the introduction [Eq. (27)]. The criterion here found, that $|\alpha a|$ be appreciably less than unity, is just the condition described in the introduction, i.e., that the low energy scattering cross section of particles "1" and "2" be large compared to the cross section of the volume of primary interaction.

To illustrate Eq. (34), we suppose that particles "1" and "2" have a fixed total energy (we introduce the phase space factor for the center-of-mass motion of these two particles). The resulting energy spectrum of relative motion is plotted in Fig. 1. In Fig. 2 we plot the relative angle of emission of the two particles in the coordinate system in which the entire scattering system is at rest. For angles less than 15° to 20° there is a sharp peak, which for larger angles merges roughly with that dependence to be expected from phase space arguments. The shape of this correlation curve is approximately

$$\frac{d\sigma}{d\Omega_{12}} \simeq \left[\frac{(2\alpha)^2}{ME}+\theta^2\right]^{-1}, \quad (35)$$

where M is the mass of the particles, E is their total energy, and θ is the angle between them.

We have assumed that we need consider only S-state relative motion of particles "1" and "2," which is probably the case of most practical importance. On the other hand, gradient couplings do seem to occur in nature. If to a gradient coupling there should also correspond a strong P-state scattering at low energies of two emitted particles, again correlation can occur. Suppose that in a partial wave analysis of $\bar{R}$ it is found that only an orbital angular momentum L is important.

[20] E. P. Wigner, Phys. Rev. **73**, 1002 (1948).

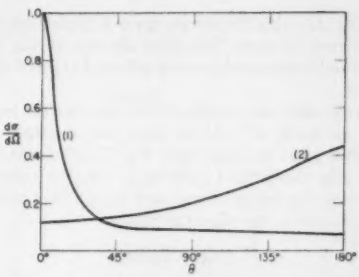

FIG. 2. The differential cross section for the production of a pair of interacting particles with an angular separation θ. Curve (1) is for an attractive interaction for which $\alpha^2/ME=0.01$ [see Eq. (35)]. Curve (2) is the correlation to be expected to a repulsive interaction of about ten times the strength of that for curve (1).

If the low energy scattering is this orbital state in large, an analysis such as that made for S-states leads to

$$T_{Ba} = e^{i\delta_L}\frac{\sin\delta_L}{q^{L+1}} \text{ times a quantity independent of } q. \quad (36)$$

Here δ_L is the phase shift for the Lth partial wave in the scattering of particles "1" and "2." Equation (33) now becomes

$$d\sigma \simeq \frac{\sin^2\delta_L}{q^{2L}}dq. \quad (37)$$

If the formula

$$q^{2L+1}\cot\delta_L = \alpha^{2L+1} \quad (38)$$

holds for a sufficient range of q-values, then

$$d\sigma \simeq q^{2L+2}dq/(\alpha^{4L+2}+q^{4L+2}), \quad (39)$$

and a considerable correlation could result. This would place quite stringent restrictions, however, on the interaction leading to δ_L.

IV. APPLICATION TO MESON PRODUCTION IN NUCLEON-NUCLEON COLLISIONS

There are at present two types of known mesonic phenomena in which the present theory is applicable[1,2,5] and possibly a third (the hypothetical meson-meson interaction[9,10]). These phenomena have been discussed previously,[4,6] so need not be considered in detail here. However, the observation of a bound final state of the neutron and proton in the reaction $p+p \rightarrow \pi^+ + n + p$ (or d) necessitates a slight extension of the theory of the last section. In reference 4 the meson energy spectrum was calculated by solving the Schrödinger equation explicitly for $g_a^{(-)}(r)$, the neutron-proton wave function, rather than by using the low energy scattering parameters. As argued in reference 4, the assumption that $|\alpha a|$ is small seems to be particularly good for this reaction, since the range a is expected to be (near the energetic threshold) considerably smaller than the range of the nuclear forces. Thus we can immediately

use Eq. (32) with the low energy n-p triplet[4] scattering parameters for $\sin\delta$. This gives the part of the meson spectrum corresponding to an unbound state of the n-p system.

To calculate the fraction of the time that the reaction goes as $p+p\rightarrow\pi^++d$, we need the deuteron wave function $g_D(r)$ to insert into Eq. (27).[21] Actually, we need only the ratio of $g_D(r)$ to $g_q^{(-)}(r)$, for values of r less than the range of the n-p force. To a sufficient approximation, we can write this as

$$g_D(r)=N_D f(r), \tag{40}$$

where $f(r)$ is the same as in Eq. (31) since the binding and kinetic energies are small compared to the well depth [see reference (19)]. N_D is a constant normalization factor.

An approximate evaluation of N_D can be obtained from Heisenberg's theory of the S-matrix.[22] We write $g_D(r)$ outside of the range of the n-p triplet force as

$$g_D(r)=Ce^{-\gamma r}/r, \tag{41}$$

where C is a normalization factor and γ^2 is the product of the nucleon mass by the deuteron binding energy. Let $S(q)$ be the S-matrix for n-p triplet S-wave scattering. Then Heisenberg's relation is

$$\oint dq S(q)=2(2\pi)^2|C|^2, \tag{42}$$

where the integral is a closed contour about the pole of the S-matrix in the positive imaginary half-plane at the point $q=i\gamma$. Expressing

$$S(q)=(\cot\delta+i)/(\cot\delta-i),$$

and using Eq. (29) (with α replaced by $-|\alpha|$) we readily evaluate the integral to find that

$$\gamma=|\alpha|(1+\tfrac{1}{2}r_0|\alpha|)$$

and

$$C=\left[\frac{\gamma}{2\pi(1-r_0\gamma)}\right]^{\frac{1}{2}}. \tag{43}$$

Using expression (30) and comparing the expression for $g_q^{(-)}(r)$ for the internal and external region near the edge of the interaction we have

$$\frac{\sin\delta}{q}\frac{[1-|\alpha|r]}{r}=\frac{\sin\delta}{q}f(r), \tag{44}$$

or $f(r)\simeq(1-|\alpha|r)/r$ near the boundary of the potential well. Using this expression and equating Eqs. (40) and (41), we have

$$N_D=Ce^{-\gamma r}/(1-|\alpha|r)\simeq C, \tag{45}$$

since $\gamma\simeq\alpha$ and both are sufficiently small that $e^{-\gamma r}/(1-|\alpha|r)\simeq 1$ at the well boundary. Then from Eq. (27), we have

$$T_{Ba}(\text{deuteron})=C(f(r),\bar{R}), \tag{46}$$

which is to be compared with Eq. (32).

From Eqs. (32) and (46) it is easy to calculate the corresponding cross sections in the center-of-mass system. Let T be the meson kinetic energy, μ its rest mass, M the nucleon mass, and T_0 the maximum kinetic energy of the meson. Then the differential cross section in the forward direction for an unbound n-p state is to within a numerical factor, G,

$$\frac{d\sigma}{d\Omega dT}=\frac{\sqrt{2}}{\pi}\left(\frac{M}{\mu}\right)^{\frac{1}{2}}T^{\frac{1}{2}}(T_0-T)^{\frac{1}{2}}\frac{\sin^2\delta}{q^2}G, \tag{47}$$

where q is the relative momentum of the nucleons and $\mu/2M$ has been neglected compared to unity. The corresponding cross section with the formation of a deuteron is

$$\frac{d\sigma_D}{d\Omega}=\frac{\gamma(p/\mu)^2}{1-r_0\gamma}G, \tag{48}$$

to within the same numerical factor G as that for Eq. (47). Here p is the meson momentum. In these equations, it was assumed[4] that $(f(r),\bar{R})$ contained a factor of p.

The foregoing cross sections have been transformed to the laboratory coordinate system and are compared with the experimental data of Cartwright, Richman, and Whitehead[23] in Fig. 3. Here G was taken to be $3.4(10)^{-30}$ cm^2 (steradian mev)$^{-1}$. For comparison, the monochromatic spectrum from $d\sigma_D/d\Omega$ was "smeared out" over the experimental energy resolution. The agreement with the experimental data seems to be satisfactory, except possibly at the lower meson energies. The agreement with the earlier[4] calculations, which involved integrating the Schrödinger equation for an exponential well, is quite good.

V. FURTHER APPLICATIONS

The applicability of Eqs. (32) and (36) is somewhat greater than was indicated in Sec. III. Let us suppose that the state B contains two particles whose scattering is described by a one-level Breit-Wigner resonance formula at energies for which Eqs. (32) and (36) are still valid. It is also supposed that the primary interaction is sufficiently weak that only the first term in

[21] When some of the produced particles can be in a bound state, Eq. (9) is not so useful [see, for example, H. S. Snyder, Phys. Rev. **83**, 1154 (1951)]. In this case it seems preferable to start with Eq. (17) as the defining equation for T_{Ba}. Then the boundary condition on $\phi_B^{(-)}$ is determined by the time reversal arguments of Appendix (B). When none of the particles are actually in a bound state, the arguments of Appendix (A) still imply the equality of expressions (9) and (17). For the part of $\phi_B^{(-)}$ referring to the bound state, the use of "$+ie$" is irrelevant.

[22] W. Heisenberg, Z. Naturforsch. **11/12**, 607 (1946).

[23] Cartwright, Richman, and Whitehead (to be published) and W. F. Cartwright, Ph.D. thesis, University of California, Berkeley, California (unpublished).

Eq. (22) need be kept. We write [see Eq. (36)]

$$\tan\delta_L=\tfrac{1}{2}\Gamma_L/(E_L-E).$$

The modification of the phase space factor for only two particles in the state "B" is such as to replace dq by q^{-1} in Eq. (37), neglecting numerical factors. This equation then becomes

$$\sigma\simeq\frac{1}{q^{2L+1}}\frac{\Gamma_L^2}{(E-E_L)^2+\frac{1}{4}\Gamma_L^2} \tag{37'}$$

except for the factors not explicitly written in Eq. (37).

Near threshold $q^{-(2L+1)}\Gamma_L^2=\Gamma_L$, except for a numerical factor. Writing all the neglected factors in the form $(2L+1)\Gamma_a K^{-2}$, we have the cross section for a one-level resonance reaction involving spinless particles:

$$\sigma=\frac{\pi(2L+1)}{K^2}\frac{\Gamma_L\Gamma_a}{(E-E_L)^2+\frac{1}{4}\Gamma_L^2}. \tag{49}$$

Here K is the relative momentum of the two incoming particles and $\Gamma_a\ll\Gamma_L$ by the assumption that V is a sufficiently weak interaction. The extension to particles with spin is straightforward.

The usefulness of Eq. (49) lies not in its generality (rather restrictive conditions were imposed on the model, such as $\Gamma_a\ll\Gamma_L$) but in its relation of the reaction cross section to the interaction of the two particles in the final state. Indeed, expressions (32) and (36) do not depend upon any specific dependence of δ_L on the energy, but upon being able to write the final state wave function in the general form (31) for small distances (when several partial waves are involved, Eq. (31) is to be replaced by a sum of such terms, one for each partial wave). This suggests a means of establishing phenomenological relationships between various processes—such as between meson-nucleon scattering and photomeson production.

VI. REPULSIVE INTERACTIONS

When the final state interaction between two particles is repulsive, one again expects a correlation in the relative angles and energies of these particles when produced in a given reaction. Since the particles repel each other, one expects a smaller probability that relative angles and energies will be small than if there were no interaction. There does not seem to be a general, simple theory to describe this, however, as there was for the case of the attractive interactions. Also, the correlations seem to be less pronounced for repulsive interactions, leading in general to smooth angular variations which would be difficult to separate from the relatively weak correlation which might be expected to occur in the primary interaction itself.

For these estimates a primary interaction in the form of a very short-range square well was taken. [R in Eq. (26).] The repulsive final state interaction was also taken to be a square well and the outgoing particles were considered to be mesons. Taking the repulsive potential to be the negative of a well 100 Mev deep and having a range of $3\hbar/\mu c$, the angular correlation given in Fig. 2 was obtained. The repulsive potential in this case was approximately ten times as strong as was the attractive potential whose correlation is also plotted in Fig. 2.

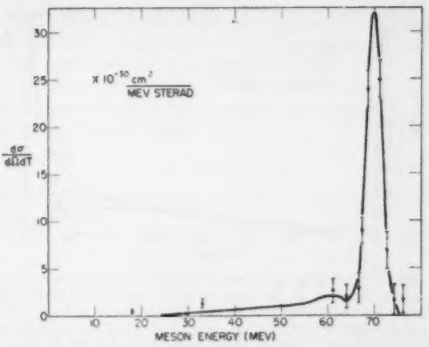

FIG. 3. The energy spectrum of Π^+ mesons produced in the forward direction in p–p collisions as calculated from Eqs. (47) and (48) is compared to the experimental data of Cartwright, Richman, and Whitehead (reference 22). Only the low energy triplet n–p scattering parameters enter into the shape of the curve, which is uniquely determined by the theory.

VII. CONCLUSIONS

To study the effect of final state interactions on a reaction cross section, we have been led to the expression (17) for the transition amplitude. In Eq. (22) the appearance of the final state interaction has been somewhat more explicitly exhibited. In a great many applications the first term only of Eq. (22) need be kept, the condition usually being that the "primary interaction" V can be considered to be a small perturbation (e.g., as in β-decay).

It has been possible to carry the analysis further for the consideration of strong final state interactions and low relative energies, the dependence of the transition amplitude in this case upon the relative momentum of two interacting particles being of the form given in Eq. (32).

In the development of Eq. (32), we have not considered the possibility that the final state interaction of two created particles might be modified in the presence of the primary interaction. This is not expected to change our conclusions in general, however. First, if the primary interaction V is weak or impulsive so that the first term only of Eq. (22) can be used, we need not expect a modification of v, since V is then essentially "turned off" once the particles are created. This condition should cover the photomesonic processes, for instance. Second, for processes such as meson production in nucleon-nucleon collisions, for which the range of V

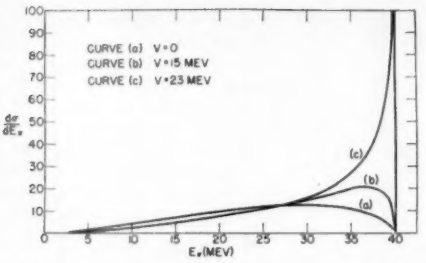

FIG. 4. The energy spectrum of Π-mesons produced in nucleon-nucleon collisions in the center-of-mass coordinate system. The final state nucleon-nucleon interaction was taken to be a square well of range 1.4 $\hbar/\mu c$ with the corresponding well depths indicated in the drawing. Curve (c) corresponds approximately to the n-p singlet force.

is considerably less than the range of v, there should be no serious modification of v since the effect of the final state interaction comes from regions of space for which $V=0$. Finally, the usefulness of Eq. (32) implies quite a predominantly strong final state interaction, which is not expected to be greatly modified if it is stronger than the other interactions involved. Here the argument is perhaps most clearly expressed by the discussion given in the introduction, which refers to final state interactions whose "effective area of interaction" is greater than the "effective area of the interaction V."

Much less correlation is to be expected when the reaction becomes weak. To see this we give in Fig. 4 the expected energy spectrum of mesons in the center-of-mass system when the final state nucleon-nucleon interaction has a range $1.4\hbar/\mu c$ and (a) a depth of zero Mev, (b) a depth of 15 Mev, (c) a depth of 23 Mev. Case (c) corresponds roughly to the n-p single potential. We have taken the range of the primary interaction $\bar{R}$ to be zero for this example, which is most favorable for obtaining large correlations.

APPENDIX A. THE FINAL STATE BOUNDARY CONDITION

We consider Eq. (15) for T, replacing ϵ by ϵ_0 in Eq. (16) for $\omega^{(-)\dagger}$. We wish to show that this equation is equivalent to Eq. (12) for calculating T_{Ba} as long as ϵ, $\epsilon_0>0$ and approach zero independently after the integrals are evaluated. From Eq. (11) with the use of Eq. (14) we readily find

$$\omega^{(-)\dagger}V\Omega^{(+)} = V+(V+v)\frac{1}{E_a+i\epsilon-H_0-V-v}(V+v)+\Delta, \quad \text{(A-1)}$$

where we have used the assumed property of v—that it (or any function of it) has no matrix elements connecting states χ_a and χ_B. The quantity Δ is

$$\Delta = i(\epsilon-\epsilon_0)v\frac{1}{(E_a+i\epsilon_0-H_0-v)} \times\frac{1}{(E_a+i\epsilon-H_0-v-V)}(V+v). \quad \text{(A-2)}$$

Except for Δ, Eq. (A-1) agrees with Eq. (12), the defining equation for T. It is now to be shown in the limit ϵ, $\epsilon_0\to 0$ that Δ gives no contribution to T_{Ba} when, and in general only when, ϵ, $\epsilon_0\to 0$ from positive values. We define

$$t=v\frac{1}{E_a+i\epsilon_0-H_0-v}v+v, \quad \text{(A-3)}$$

a scattering amplitude for particles in states "B." Then we easily obtain with the use of Eq. (14)

$$\Delta = i(\epsilon-\epsilon_0)t\frac{1}{(E_a+i\epsilon_0-H_0)}\frac{1}{(E_a+i\epsilon-H_0)}T, \quad \text{(A-4)}$$

where T is now given by its defining Eq. (12). If we choose a representation in which H_0 is diagonal with eigenvalue E_k, we see that Eq. (A-4) will contain an integral of the form

$$\int\cdots\frac{dE_k}{(E_k-E_a-i\epsilon_0)(E_k-E_a-i\epsilon)}\cdots. \quad \text{(A-5)}$$

In the limit when ϵ, $\epsilon_0\to 0$ the only contribution of the integral (A-5) to Δ will come from the vicinity of $E_k=E_a$. Thus we can factor t and T out of the integral, setting $k=a$ in them. This can be done as the scattering amplitudes are supposed to be well defined on the energy shell (that is, when k is set equal to a). We may also take infinite limits ($-\infty$ to $+\infty$) for the integral (A-5). If ϵ_0 is positive (ϵ is known to be positive), the integral vanishes. If ϵ_0 is negative, the integral is $2\pi/(\epsilon-\epsilon_0)$. Thus

$$\Delta=0, \text{ if } \epsilon,\ \epsilon_0\to 0(+);$$
$$\Delta=2\pi i[t\delta(H_0-E_a)T] \text{ if } \epsilon\to 0(+),\ \epsilon_0\to 0(-). \quad \text{(A-6)}$$

Had we used a "principal value" definition for $\omega^{(-)\dagger}$, Δ would again have been nonvanishing.

We recall that the role of ϵ and ϵ_0 was just to help keep track of the path of integration and that these could have been set equal to zero at the outset (by properly specifying the contour of integration). In particular, we can go to the limit ϵ, $\epsilon_0=0$ in $\phi_B^{(-)}$ and $\psi_a^{(+)}$ before evaluating Eq. (17).

APPENDIX B. THE REVERSAL REQUIREMENTS

We wish now to show that the use of $\phi_B^{(-)}$ in Eq. (17) is required by the time reversal invariance of the system. The time reversal operator has been given by

Wigner[17] and is

$$K = UK_0, \tag{B-1}$$

where K_0 is the operation of taking the complex conjugate and U is a unitary matrix. The "time reversed" of a given operator P is

$$P_t \equiv KPK^{-1} = UP^*U^{-1}. \tag{B-2}$$

For instance, time reversal leaves the Hamiltonian invariant but changes the sign of momenta, angular momenta, spins, etc.

In Eqs. (3) and (4) we have introduced the eigenfunctions χ_a of H_0. Let "A" represent a complete set of commuting operators for the χ_a, and let the set "a" represent the corresponding eigenvalues:

$$A\chi_a = a\chi_a. \tag{B-3}$$

Physically, the set "a" represents the momenta, angular momenta, spins, and any internal coordinates of the noninteracting particles of the state "a" (we are not distinguishing between states "a" and "B" here). Now under time reversal the momenta, angular momenta, and spin components change sign, but the internal coordinates are unchanged. Let us denote the eigenvalues for a system in this time reversed state by "$-a$" and the eigenfunctions by χ_{-a}. On the other hand, we denote the wave function which results from applying K to χ_a by χ_a'. Since χ_a' and χ_{-a} describe the same physical situation, they can differ only by a phase factor, say μ_{-a}. That is,

$$\chi_a' \equiv K\chi_a = U\chi_a^* = \mu_{-a}\chi_{-a}. \tag{B-4}$$

There is also the set

$$\chi_a'' \equiv K\chi_{-a} = U\chi_{-a}^* = \mu_a\chi_a. \tag{B-5}$$

We observe in passing that the relation between the $\psi^{(+)}$ and $\psi^{(-)}$ and the $\phi^{(+)}$ and $\phi^{(-)}$ of Eqs. (7) and (8) is

$$\psi_a^{(-)} = (1/\mu_a)K\psi_{-a}^{(+)}, \quad \phi_B^{(-)} = (1/\mu_B)K\phi_{-B}^{(+)}. \tag{B-6}$$

This relation gives a simple prescription for obtaining the $\phi_B^{(-)}$ to be used in Eq. (17) when the usual scattering wave function is known.

The detailed reversibility requirement, which is a direct consequence of time reversal, has been given by Schwinger[24] and Coester.[25] It is

$$T_{-B,-a} = \mu_a^*\mu_B T_{aB}, \tag{B-7}$$

where the phases μ_a and μ_B are those of Eqs. (B-4) and (B-5). We have

$$\begin{aligned} T_{-B,-a} &= (\chi_{-B}, T\chi_{-a}) = (T^*\chi_{-a}^*, \chi_{-B}^*) \\ &= (UT^*U^{-1}U\chi_{-a}^*, U\chi_{-B}^*) \\ &= \mu_a^*\mu_B(\chi_a, [UT^*U^{-1}]^\dagger\chi_B). \end{aligned} \tag{B-8}$$

We have used Eq. (B-5) in the last step. Comparing with Eq. (B-7) we see that

$$UT^*U^{-1} = T^\dagger \tag{B-9}$$

must hold on the energy shell.

Now writing T in the form of Eq. (A-1), we wish to show from Eq. (B-9) that the boundary condition on $\omega^{(-)\dagger}$ is the correct one. That is, we wish to show that

$$(B|\,T - (UT^*U^{-1})^\dagger\,|a) = 0, \tag{B-10}$$

only for the "$+i\epsilon$" boundary condition on $\omega^{(-)\dagger}$. Since the first term of Eq. (A-1) obviously satisfies Eq. (B-10), this equation reduces to

$$(B|\,\Delta - (U\Delta^*U^{-1})^\dagger\,|a) = 0. \tag{B-11}$$

Now Δ and $(U\Delta^*U^{-1})^\dagger$ have essentially the same structure, so the arguments given in Appendix A for the vanishing of Δ are here valid. (It may be noted that $(U\Delta^*U^{-1})^\dagger$ has the operator v standing on its right, so automatically vanishes if we wish to apply our condition that v vanishes when operating on χ_a.)

Thus, just as in Appendix A, we see that the boundary condition of Eq. (17) is here required.

[24] J. Schwinger, hectographed notes on nuclear physics (unpublished). Relations of the form (B-4) and (B-5) were introduced and used here in the proof of Eq. (B-7).

[25] F. Coester, Phys. Rev. **84**, 1259 (1951).

Some Properties of Superconductors below 1°K. III. Zr, Hf, Cd, and Ti†

T. S. SMITH AND J. G. DAUNT
Department of Physics and Astronomy, Ohio State University, Columbus, Ohio

(Received August 8, 1952)

Using techniques for the measurement of the magnetic threshold curves of superconductors below 1°K previously employed, investigations have been made on cadmium, zirconium, hafnium, and titanium, both before and after heat treatment. It was found that, in zirconium and hafnium, the magnetic superconducting properties were profoundly affected by heat treatment and that only after suitable annealing did these properties approach those of an ideal superconductor. The results for the annealed metals were as follows: the transition temperature, T_s, in zero magnetic field was 0.602°K for cadmium, 0.546°K for zirconium, 0.374°K for hafnium, 0.558°K for titanium and the slope of the magnetic threshold curves at $T=T_s$ in gauss/degree was 112 for cadmium, 170 for zirconium, 230 for hafnium, and 450 for titanium. The magnetic threshold curves for cadmium and zirconium were parabolic with $H_0=33.8$ gauss for cadmium and 46.4 gauss for zirconium. The thermodynamically computed specific heat of the normal electrons was $1.54\times10^{-4}T$ cal/mole-deg for cadmium and $3.92\times10^{-4}T$ mole-deg for zirconium. No thermodynamic computations were made for hafnium and titanium owing to the irreversibility of their superconducting transitions.

1. INTRODUCTION

IN continuation of measurements reported previously by Daunt and Heer[1,2] on the magnetic properties of superconductors below 1°K, we have extended the observations to other materials which only recently have been available to us in high purity. These measurements, carried out in the region obtainable by magnetic cooling methods, have enabled the specific heat of the electron assemblies in the normal state to be computed as has previously been done for superconductors in the helium region by Daunt and Mendelssohn.[3] They have led also to interesting results on the influence of physical strain on the magnetic properties of superconductors. The three metals, zirconium, hafnium, and titanium, are not only difficult to obtain in a strain-free state, because of their hardness, but also they all show a crystallographic modification from hcp to bcc at high temperatures, which makes heat treatment more complex than in many other superconductive metals. In our measurements, therefore, the influence of metallurgical properties of heat treatment has been considered, as is reported below. In the case of zirconium, it appears that after careful heat treatment, we have obtained a material which approaches the behavior of an "ideal" superconductor.

TABLE I. Physical properties of metals used.

Metal	Melting temp., °C	Recrystallization temp., °C	Transformation temp., °C (hcp to bcc)	Minimum hardness known (Rockwell scale)
Cd	321	about room temperature		*H*47
Zr	1865	~500	862	*E*58[a]
Hf[a]	2130	~800	1310	*B*88
Ti[b]	1800	~600	882	*B*22[d]

[a] See reference 6.
[b] See, for example, *Handbook on Ti-metal* (Titanium Metals Corporation, 1950).
[c] Our measurements on the zirconium listed in Sec. 5(b) of this paper.
[d] Our measurements on high purity titanium type No. 203–8 supplied by Foote Mineral Company.

2. THE EXPERIMENTAL ARRANGEMENTS

Temperatures below 1°K were produced by the magnetic cooling method. The paramagnetic salt used as the cooling substance in all experiments was chromium potassium alum. The superconducting metal to be investigated was pressed inside a "pill" composed of the metal and the powdered salt, and, as previously reported,[2,4] good thermal contact with the working substance was thereby obtained. Full details of our experimental arrangements and methods have been given previously by Daunt and Heer.[2] The temperature for transition from the superconducting to the normal state of the metal was observed, either in zero magnetic field or in an applied exterior magnetic field. The observation was made by measuring the magnetic susceptibility changes occurring in the "pill" as the temperature increased with time from a low temperature up to 1°K. The magnetic changes that occur in the metal at the transition are described fully in a previous paper.[2] By measuring the transition temperature as a function of the exterior field, the magnetic threshold curve is obtained for each metal, this magnetic threshold curve being in the nature of a phase diagram for the superconductor.

3. THE PROPERTIES OF THE SPECIMENS

In Table I, the relevant physical properties of the metals used in these investigations are set out. From this table, the appropriate annealing temperatures may be obtained, being between the recrystallization temperatures and the transformation temperatures.

† Assisted by a contract between the AEC and The Ohio State University Research Foundation.

[1] J. G. Daunt and C. V. Heer, Phys. Rev. **76**, 715 (1949).
[2] J. G. Daunt and C. V. Heer, Phys. Rev. **76**, 1324 (1949).
[3] J. G. Daunt and K. Mendelssohn, Proc. Roy. Soc. (London) **A160**, 127 (1937). See also Daunt, Horseman, and Mendelssohn, Phil. Mag. **27**, 754 (1939).
[4] N. Kurti and F. Simon, Proc. Roy. Soc. (London) **A151**, 610 (1935).

In preparing the specimens, the metal was placed inside a pill of powdered chromium potassium alum which was pressed to 5000 lb/in.² and then formed to an ellipsoidal shape. The dimensions of the metal specimens and of the final pills are given in Table II.

In computing the temperature, T_s^*, on the Curie scale for a spherically-shaped specimen, it is necessary to correct the observed T^* for the shape and filling factor of the salt. Details of the method of making these corrections are given elsewhere,[2,5] which involve the parameters f and Δ, where the salt filling factor f is defined by the ratio of the distributed density of the powdered salt to the crystalline density, and where Δ is defined by

$$\Delta = cf(4\pi/3 - N),$$

where c is the Curie constant per cc of the salt and N the demagnetization factor of the specimen. The values of f and Δ for each specimen are given in Table II.

TABLE II. Heat treatment, physical properties, and dimensions of specimens.

Specimen[a]	Heat treatment	Hardness, Rockwell scale	Dimensions of metal (mm)	Axes of ellipsoidal salt pill (mm)	f	Δ
Cd	Annealed at 150°C for 1.5 hours.		Ellipsoid with axes 19×6	36×13	0.81	0.022
Zr(U)	Unannealed	*E*61	11×5.5×3.3	39×12.7	0.90	0.017
Zr(A)	Annealed at 800°C for 2.5 hours.	*E*58	11×5.5×3.3	35×12.7	0.94	0.026
Hf(U)	Unannealed	*C*47	Cylindrical 50.5 long ×3.4 diam	29×12.7	0.98	0.015
Hf(A)	Annealed at 900°C for 3 hours.	*B*100	Cylindrical 50.5 long ×3.4 diam	19×13	0.92	0.007
Ti[b](U)	Unannealed	*B*32	Irregular pieces 2–3 mm	27×13	0.79	0.011
Ti(A)	Annealed at 800°C for 2.5 hours	*B*28	Irregular pieces 2–3 mm	22×12.7	0.94	0.011

[a] The suffixes (U) and (A) indicate the unannealed and the annealed specimens, respectively.
[b] See reference 1.

The sources and purities of the metals used were as follows: (a) cadmium: obtained from Johnson Matthey and Company, Lab. No. 2572, purity 99.99 percent: (b) zirconium: kindly loaned by Oak Ridge National Laboratory. The metal used was cut from a crystal bar formed by deposition from the iodide and was of purity 99.9 percent. The greatest single impurity was 0.04 percent by weight hafnium; (c) hafnium: kindly loaned by the U.S.A.F. Institute of Technology, Dayton, Ohio, and originally prepared by the Foote Mineral Co. It was Hf "783" (see paper by Litton[6]) of purity 98.92 percent, having approximately 0.9 percent zirconium impurity and was prepared by deposition from the iodide. It was in the form of a swaged rod; (d) titanium: This was the same as that previously used by Daunt and Heer[1] in their magnetic measurements. This specimen was kindly loaned by the Battelle Memorial Institute, Columbus, Ohio, and was prepared by deposition from the iodide.[7] Its purity was 99.95 percent.

TABLE III. Magnetic threshold values for the superconducting transition. Temperature is expressed on Curie scale, T_s^*, which approximates within experimental error the absolute temperature T°K. The suffixes (A) and (U) refer to the metals in the annealed and unannealed states, respectively.

Cd		Zr(A)		Hf(A)		Ti(A)	
T_s^*	H(gauss)	T_s^*	H(gauss)	T_s^*	H(gauss)	T_s^*	H(gauss)
0.602	0.0	0.546	0.0	0.383	0.0	0.558	0.0
0.560	6.03	0.516	5.93	0.372	0.0	0.527	10.4
0.502	9.95	0.516	6.93	0.367	0.0	0.491	20.8
0.490	11.0	0.464	11.0	0.327	6.6	0.444	36.4
0.428	16.5	0.436	16.5	0.340	11.0	0.436	51.0
0.408	18.7	0.382	22.0	0.312	16.5	0.408	62.3
0.359	22.0	0.314	23.0			0.408	78.0
0.326	23.1					0.395	88.5
0.264	27.5					0.334	104.0
		Zr(U)		Hf(U)		Ti(U)	
		0.565	0.0	No observable		0.523	0.0
		0.375	63.0	evidence of		0.528	0.0
		0.325	83.5	superconductivity.		0.517	8.0
						0.512	11.0
						0.487	16.3
						0.483	21.6
						0.447	27.2
						0.437	30.7
						0.410	36.0
						0.384	44.3
						0.360	50.3
						0.335	54.7
						0.325	57.4

The superconducting properties of zirconium, haf-

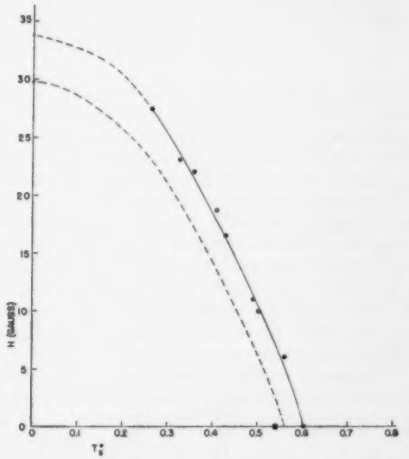

FIG. 1. Magnetic threshold curve for cadmium. ●—our results; – – – curve obtained by Goodman and Mendoza;[11] ■—result of Kurti and Simon. (See reference 4.)

[5] N. Kurti and F. Simon, Phil. Mag. **26**, 849 (1938).
[6] F. B. Litton, J. Electrochem. Soc. **98**, 488 (1951).
[7] Campbell, Jaffee, Blocher, Gurland, and Gonser, J. Electrochem. Soc. **93**, 271 (1948).

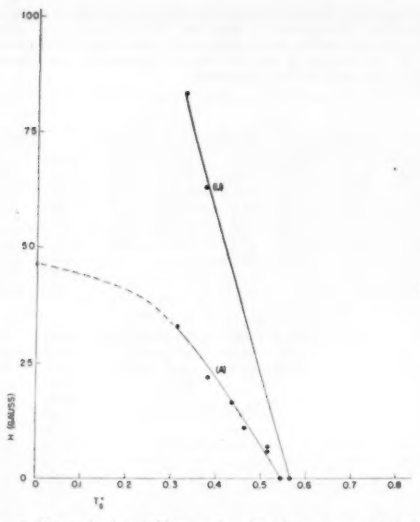

FIG. 2. Magnetic threshold curve for zirconium. Curve (U) is for unannealed zirconium; curve (A) for the annealed zirconium.

nium, and titanium were investigated both before and after vacuum annealing. For the cadmium, measurements were made only after annealing. The temperatures and duration of the annealing processes for each specimen are recorded in Table II. In each case the temperature was reduced slowly after the completion of the anneal. The hardness of the metals both before and after annealing was measured using a Tukon hardness testing machine for the hafnium and a Rockwell hardness machine for the titanium and zirconium, and is also recorded in Table II.

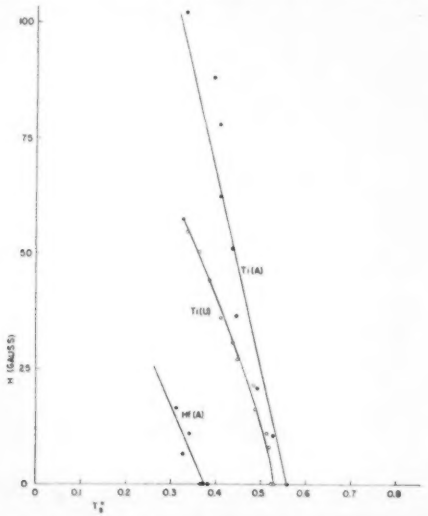

FIG. 3. Magnetic threshold curves for partially annealed titanium—Ti(A); unannealed titanium—Ti(U); and partially annealed hafnium—Hf(A).

4. THE RESULTS

The observed temperatures of the superconducting transition in zero field and in applied magnetic fields are tabulated in Table III and are shown in Figs. 1–3. The temperatures are expressed on the Curie scale, T_e^*, corrected to a spherically-shaped salt specimen. In the region of measurement the difference between T_e^* and the bsolute temperature T°K is estimated[8] to be within the experimental error.

For cadmium it was found that the results for the magnetic threshold curve could be expressed adequately by the parabolic formula:

$$H=H_0[1-(T/T_c)^2], \tag{1}$$

with H_0, the threshold field at $T=0$, equal to 33.8 gauss and T_c, the transition temperature in zero field, equal to 0.602°.

For zirconium it was found that the annealing made profound changes. Unannealed zirconium, Zr(U), gave $T_c=0.565°$ and the slope of the threshold field at T_c, namely $(\partial H/\partial T)_{T=T_c}$ equal to 335 gauss/degree. After annealing the zirconium, Zr(A), was found to show a parabolic threshold curve having $H_0=46.6$ gauss and $T_c=0.546°$. The reduction in the threshold field after the anneal was noteworthy,[9] as is shown in Fig. 2.

The unannealed hafnium, Hf(U), showed no magnetically observable sign of superconductivity down to 0.15°K. The annealed hafnium, Hf(A), was, however, found superconductive with $T_c=0.374\pm0.01$ and $(\partial H/\partial T)_{T=T_c}$ approximately equal to 230 gauss/degree.

The measurements on titanium showed little difference between the results for the annealed, Ti(A), and the unannealed, Ti(U), samples.

The relevant data are collected together in Table IV, along with the normal electronic specific heats which can be calculated thermodynamically from them.

5. DISCUSSION OF THE RESULTS AND THE THERMODYNAMIC DATA DEDUCIBLE THEREFROM

(a) Cadmium

Since a few measurements have been made previously of the threshold curve of cadmium,[4,10,11] our measurements were carried out largely in order to check the reproducibility of our technique. The previous results are indicated in Fig. 1 along with our present results.

[8] M. H. Hebb and E. M. Purcell, J. Chem. Phys. **5**, 388 (1937).
[9] A brief abstract of these results is given by T. S. Smith and J. G. Daunt, Phys. Rev. **86**, 818 (1952).
[10] J. G. Daunt, unpublished.
[11] B. B. Goodman and E. Mendoza, Phil. Mag. **42**, 594 (1951).

It will be seen that our value for the transition, T_c, in zero field is 0.602°K as compared with 0.560°K of Goodman and Mendoza[11] and 0.54°K of previous work.[4,10] Moreover, the threshold curve we observed is about 5 gauss higher than that given by Goodman and Mendoza.[11] This may be due to the difference in the materials used, the latter authors employing cadmium from the New Jersey Zinc Company of estimated purity 99.996 percent. Some confirmation of this conclusion comes from recent measurements by Steele[12] also on Johnson Matthey cadmium, who found $T_c = 0.650$ and a threshold curve in fair agreement with that reported here.

For a superconductor having a parabolic magnetic threshold curve, which marks the *reversible* boundary between the superconductive and the normal states, the specific heat of the normal electrons, $C_{el,n} = \gamma T$, can be calculated thermodynamically, as has been done previously,[3,13,14] and is given by

$$C_{el,n}/T = \gamma = (V/8\pi)(\partial H/\partial T)^2_{T=T_c}, \qquad (2)$$

where V is the atomic volume of the metal. Our results for cadmium lead to $\gamma = 1.54 \times 10^{-4}$ cal/mole-degree,[2] as compared with 1.28×10^{-4} cal/mole-degree[2] which was computed from the results of Goodman and Mendoza.[11]

(b) Zirconium

Our results for annealed zirconium, Zr(A), give threshold field values and transition temperatures lower than both the values of the unannealed, Zr(U), and the values obtained previously.[4,10] Indeed, it is noteworthy that our results for the unannealed Zr(U) of $T_c = 0.565$°K and $(\partial H/\partial T)_{T=T_c}$ equals 335 gauss/degree approximate closely those previously measured by Kurti and Simon,[4] of $T_c = 0.68$°K and $(\partial H/\partial T)_{T=T_c}$ equal 400 gauss/degree, and by Daunt,[10] of $T_c = 0.60$°K and $(\partial H/\partial T)_{T=T_c}$ equal 375 gauss/degree. It is concluded that the previous workers did not undertake heat treatment of their samples. The relatively low value of $(\partial H/\partial T)_{T=T_c}$ observed by us for the annealed Zr(A) indicates that annealing of the specimen produces a superconductor for which the magnetic transition approximates a reversible process and for which the magnetic threshold curve becomes parabolic. A similar approach of the behavior of superconductors to that of the "ideal" superconductor showing a reversible Meissner[15] effect on careful heat treatment has been observed previously for thorium by Shoenberg[16] and for vanadium by Wexler and Corak.[17] In the case of metals such as zirconium, hafnium, and titanium, however, all of which show an α- to β-phase transformation at elevated temperatures, it is not clear whether the approach to ideality in the superconductive behavior on heat treatment is due to the annealing out of strains in the lattice or is due, at least partly, to the removal by heat treatment of inclusions of metastable β-phase. It is well known from the work of Lazarew and Galkin[18] and of Khotkevich and Golik,[19] as well as that of Wexler and Corak,[17] that physical strain produces marked irreversibilities in the superconductive transition, as well as changes in the transition temperature T_c, and it would be possible to explain the effects of heat treatment on the basis of strain annealing. On the other hand, the following facts in the case of our measurements on zirconium are of interest. (a) There was little change in measured hardness by the anneal; the hardness, in fact, changing from Rockwell *E*61 to *E*58 (see Table II). This indicates that there was no great strain condition before the heat treatment. (b) If it is assumed that our results for the magnetic threshold curve represent a reversible transition curve, then using formula (2) we deduce that the normal electronic specific heat parameter $\gamma = 3.92 \times 10^{-4}$ cal/mole-degree.[2] This is to be compared with the result obtained calorimetrically by Friedberg, Estermann and Goldman[20] of $\gamma = 6.92 \times 10^{-4}$ cal/mole-degree[2] on a non-heat-treated sample. This discrepancy cannot be explained by a complete inapplicability of the assumption made above of reversibility of the magnetic transition, since irreversibilities tend to increase the thermodynamically computed γ-values. The discrepancy, therefore, is probably real. This discrepancy, together with the marked changes we observed in the superconducting behavior through heat-treatment, may be due to inclusions of metastable β-phase zirconium in samples that have not been heat treated. Calorimetric measurements also on carefully annealed zirconium, therefore, would be of interest.

TABLE IV. The observed properties of cadmium, zirconium, hafnium, and titanium.

Metal	T_c °K	H_0 gauss	$(\partial H/\partial T)_{T=T_c}$ gauss/deg	γ^a cal/mole-deg^2	γ/V^b cal/cc-deg^2
Cd	0.602	33.8	112	1.54×10^{-4}	1.18×10^{-5}
Zr(U)	0.565	···	335	···	···
Zr(A)	0.546	46.6	170	3.92×10^{-4}	2.76×10^{-5}
Hf(U)	No magnetically observable evidence of superconductivity.				
Hf(A)	0.374	···	230	···	···
Ti(U)[c]	0.53	···	470	···	···
Ti(A)	0.558	···	450	···	···

[a] The normal electronic specific heat $C_{el,n} = \gamma T$.
[b] V is the atomic volume. This column is included for reference to the correlation among superconductors proposed by one of us [see J. G. Daunt, Phys. Rev. **80**, 911 (1950); and J. G. Daunt and T. S. Smith, Phys. Rev. **88**, 309 (1952)].
[c] Data from Daunt and Heer (reference 1).

[12] M. C. Steele and R. A. Hein, Phys. Rev. **87**, 908 (1952).
[13] J. A. Kok, Physica **1**, 1103 (1934).
[14] J. G. Daunt, Phys. Rev. **80**, 911 (1950).
[15] W. Meissner and R. Ochsenfeld, Nature **21**, 787 (1933).
[16] D. Shoenberg, Proc. Cambridge Phil. Soc. **36**, 84 (1940).
[17] A. Wexler and W. S. Corak, Phys. Rev. **85**, 85 (1951).
[18] B. G. Lazarew and A. Galkin, J. Phys. (U.S.S.R.) **8**, 371 (1944).
[19] V. Khotkevich and V. R. Golik, J. Theor. Exp. Phys. (U.S.S.R.) **20**, 427 (1950).
[20] Friedberg, Estermann, and Goldman, Phys. Rev. **85**, 375 (1952).

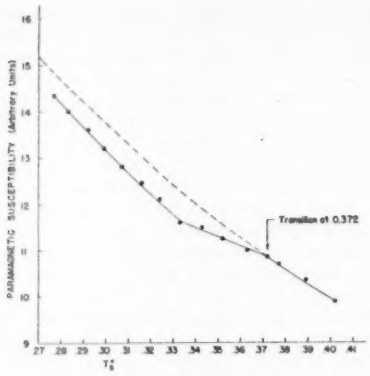

FIG. 4. Warm-up curve, in zero magnetic field, of chromium potassium alum and hafnium (A).

(c) Hafnium

The results given in Sec. 4 above for hafnium were found to be very strongly dependent on the method of preparation of the specimen. Before the annealing process above, the specimen was very hard (about Rockwell C47) and at low temperatures down to 0.15°K showed no sign of superconductivity. After the anneal, although evidence of superconductivity was observed, the transition did not correspond to zero magnetic induction over the entire volume of the specimen, as is shown by the curve of Fig. 4 which gives the susceptibility of the sample of metal and salt in zero magnetic field *versus* temperature; whereas for zirconium, titanium, and cadmium the measured magnetic induction corresponded to 100 percent of the volume of the metal becoming superconductive at the transition. Evidently, in hafnium the lack of 100 percent superconductivity and the irreversibility of the Meissner effect are due to extreme hardness of the samples. It is to be noted that even after our heat treatment the hafnium sample had a measured hardness of Rockwell *B*100, which, as is shown in Table II, is very considerably harder than the zirconium and titanium we employed. In consequence, no computations are made from our results of the γ-value for hafnium, since it is unlikely that the observed threshold curve represents a reversible transition. Moreover, since the hardness of our specimen, even after the anneal, was still somewhat greater than that quoted by Litton,[6] it is possible that a softer specimen would show 100 percent superconductivity by volume. Our value of $T_c=0.37$°K is to be compared with $T_c=0.35$°K given by Kurti and Simon.[4] It is possible that a softer specimen of hafnium may show a transition temperature, T_c, considerably smaller than that quoted here.[21] Our observations on the hafnium transition in a magnetic field did not have the same accuracy as those obtained for zirconium and titanium, as can be deduced from the scatter of the points. This was due to the fact that apparently only part of the volume underwent transition.

For a metal having such a low value of T_c, the slope of the magnetic threshold curve of $(\partial H/\partial T)_{T=T_c}$ equals 230 gauss/degree is very high (see reference 14), a result which is in line with the observed non-ideal behavior of the transition.

(d) Titanium

The observations on the titanium specimen were carried out in order to see whether the heat treatment altered the evaluations of T_c and $(\partial H/\partial T)_{T=T_c}$ previously observed by Daunt and Heer[1] on the same (untreated) specimen. The measured hardness before the heat treatment was Rockwell *B*32, whereas after the anneal at 800°C it was *B*28. The difference, therefore, was not great, and, as was expected, the observed values of $T_c=0.558$°K and $(\partial H/\partial T)_{T=T_c}$ equals 450 gauss/degree were practically identical with those previously observed, namely $T_c=0.53$°K and $(\partial H/\partial T)_{T=T_c}$ equals 470 gauss/degree. Evidently, the titanium, even after this heat treatment, still showed a highly irreversible superconductive transition, and for this reason no thermodynamic computations have been made from our results.

We wish to thank the Research Corporation for a grant which has greatly aided this research.

[21] *Note added in proof:* For example, a value of $T_c=0.30$°K for an annealed Hf sample (containing 10 percent Zr) has been reported by L. D. Roberts (1952 New York Meeting of the American Physical Society).

The Effect of Charge Symmetry on Nuclear Reactions*

NORMAN M. KROLL, *Columbia University, New York, New York*

AND

LESLIE L. FOLDY, *Case Institute of Technology, Cleveland, Ohio*

(Received August 26, 1952)

For a charge symmetric nuclear Hamiltonian, the operator which changes neutrons into protons and protons into neutrons (charge parity operator) commutes with the Hamiltonian and is therefore a constant of the motion. Since the charge parity operator anticommutes with the "3" component of the total isotopic spin, for nuclei with $T_3=0$ (self-conjugate nuclei) the charge parity is a good quantum number and in the absence of degeneracy the eigenstates of such nuclei have either odd or even charge parity. This leads to strong selection rules in nuclear reactions involving self-conjugate nuclei in the initial and final states which may reasonably be invoked to explain recent experimental results on such reactions. Since states of even total isotopic spin have even charge parity and states of odd total isotopic spin have odd parity, the selection rules arising from charge symmetry often coincide with those of charge independence and in such cases a definitive test of the charge independence hypothesis by the use of these selection rules is impeded. Some other applications of the charge symmetry principle are discussed.

THAT the neutron-neutron and proton-proton forces are equivalent apart from electromagnetic interactions is strongly indicated by the energy differences in the ground states and the general similarity of energy levels in the various mirror nuclei. It is the purpose of this note to point out that the assumption of such a charge symmetry of nuclear forces implies certain strong selection rules[1] which apply in a small but experimentally interesting group of nuclear reactions.

These selection rules arise in self-conjugate systems, that is, systems having equal numbers of neutrons and protons. For such systems under the assumption of charge symmetry the Hamiltonian is invariant under interchange of the neutron and proton space and spin coordinates. It is therefore possible to define an operator P which performs this interchange and can appropriately be called the charge parity operator.[2] It is clear that P is a constant of the motion with eigenvalues 1 and -1. The wave functions of the system can always be selected so as to be simultaneous eigenfunctions of the Hamiltonian and charge parity and therefore may be characterized as charge even or charge odd. Of course in the degenerate case where two states of opposite charge parity have the same energy a state of the system of this energy may be a superposition of charge even and charge odd states.

A formal exposition of the above described concept can be conveniently obtained in terms of the isotopic spin formalism. The operator P can be represented as a rotation in isotopic spin space of 180° about the 1 axis. That is, for a system of A particles the total isotopic spin $\mathbf{T}$ is given by

$$\mathbf{T}=\sum_{j=1}^{A}\boldsymbol{\tau}^{(j)}.$$

A rotation of 180° about the 1 axis is then given by

$$P=\exp\{i\pi T_1/2\}=\prod_{j=1}^{A}\exp\{i\pi\tau_1{}^{(j)}/2\}=i^A\prod_{j=1}^{A}\tau_1{}^{(j)},$$

since $\exp\{i\pi\tau_1{}^{(j)}/2\}=i\pi\tau_1{}^{(j)}$.

The charge symmetry of the Hamiltonian implies that it is a symmetric function of the A particles whose dependence upon the isotopic spin[3] can be expressed in terms of $\boldsymbol{\tau}^{(i)}\cdot\boldsymbol{\tau}^{(j)}$ and $\tau_3{}^{(i)}\tau_3{}^{(j)}$. Since $[\boldsymbol{\tau}^{(i)}\cdot\boldsymbol{\tau}^{(j)}, P]=[\tau_3{}^{(i)}\tau_3{}^{(j)}, P]=0$, it is clear that P commutes with the Hamiltonian and is a constant of the motion. This property is not, in fact, restricted to self-conjugate systems. On the other hand, nontrivial applications of the concept are in fact so restricted. This arises from the fact that $[P, T_3]=2PT_3$ that is, P and T_3 anticommute. Thus a system can be in a simultaneous eigenstate of P and T_3 only for states of $T_3=0$, which corresponds to the case of equal numbers of neutrons and protons. The physical meaning of the above is quite

* This research was supported by the AEC and carried out while the authors were Visiting Scientists at Brookhaven National Laboratory during the summer of 1952.

[1] The selection rules referred to would be rigorous were it not for the neutron-proton mass difference and the fact that the electromagnetic interactions between nucleons are not charge symmetric. This limitation on the universality of the charge symmetry hypothesis sets practical limits on all derived consequences of the hypothesis. The fact that these nonsymmetric interactions are generally weak compared to specifically nuclear interactions for the cases of interest implies, however, that the selection rules obtained have considerable potency.

[2] The earliest reference to the existence of a good quantum number for self-conjugate nuclei associated with the charge parity operator appears to be in a paper of E. Feenberg and E. P. Wigner, Phys. Rev. **51**, 95 (1937). Recently the concept of charge parity was discussed by L. Trainor, Phys. Rev. **85**, 962 (1952), in connection with its application to the problem of electric dipole radiation from self-conjugate nuclei. It has the consequence here of forbidding electric dipole radiation in a transition between two states of the same charge parity.

[3] This form of the Hamiltonian includes (in addition to the equality of nn and pp forces) the assertion that the interaction energy between neutrons and protons involves the neutron and proton space and spin coordinates symmetrically. It is clear that usually asserted consequences of charge symmetry with respect to the mirror nuclei are valid only when this additional assumption is included.

obvious. P simply transforms protons into neutrons and neutrons into protons. Since T_3 is simply $\frac{1}{2}(N-Z)$, the application of P to an eigenstate of T_3 with eigenvalue t_3 simply changes it to an eigenstate of T_3 with an eigenvalue $-t_3$.

We note that $P^2=(-1)^A$ so that for even A, P has eigenvalues $+1$ and -1. A further property of P which is of interest for the discussion to follow is the fact that $[T^2, P]=0$, so that T^2 and P have simultaneous eigenstates. Furthermore, a $T_3=0$ eigenstate of T^2 with eigenvalue $t(t+1)$ must, in fact, be an eigenstate of charge parity and odd or even as t is odd or even. This latter result follows from the fact that under a rotation in isotopic spin space, the eigenfunctions of T^2 corresponding to a given t must transform like the spherical harmonic of order t under the homologous rotation in coordinate space.

The principal application of the concept of charge parity arises in the case of reactions between nuclei for which the incident and product nuclei are individually self-conjugate. In just these cases, the initial and final states of the system will be eigenstates of charge parity. From the fact that P is a constant of the motion, the initial and final states must both be charge even or charge odd. As a specific example one might consider the $O^{16}(d,\alpha)N^{14}$ reactions recently investigated by various research groups.[4] In this case one finds prominent α-particle groups corresponding to the ground state and various excited states of N^{14} but none corresponding to the 2.3-Mev excited state. A reasonable interpretation of this result is simply that this particular state has charge parity opposite to that of the states observed.† It is almost certain that the ground state of N^{14} is charge even, while if the nuclear forces are only approximately charge independent one would expect a low-lying charge odd state.

In order to make clear the relevancy of having both the incident and product nuclei in charge conjugate states one might note that a reaction like $O^{16}(d,p)O^{17*}$ will never be forbidden by charge parity conservation in spite of the fact that the initial state is charge even. The requirement that the final state be charge even as well simply implies that the reactions $O^{16}(d,p)O^{17*}$ and $O^{16}(d,n)F^{17*}$ occur with equal probability, where the final states of O^{17*} and F^{17*} are mirror states.

On the other hand, the observation of nuclear resonances associated with compound nucleus formation can be affected by charge parity considerations when only the product nuclei or only the incident nuclei are self conjugate. For example, the observation of a resonance in the reaction $C^{12}(d,p)C^{13}$ due to the formation of an excited state of N^{14} implies that the state of N^{14} is charge even, although in this case the product nuclei are not self conjugate.

The existence of charge parity has certain interesting connections with the problem of charge independence of nuclear forces. As has been pointed out by Adair,[5] the assumption of charge independence also implies selection rules in nuclear reactions, which, while including those implied by charge symmetry, are considerably more far reaching. This is a consequence of the fact that total isotopic spin as well as charge parity must be conserved. It is unfortunate, however, that the role of isotopic spin is obscured in many reactions by the coincidence of its predictions with those of charge parity. It has, for example, been proposed that the 2.3-Mev N^{14} state is a member of an isotopic spin multiplet with $T=1$, while the ground state is $T=0$. It is important to realize that it is then not possible for these states to have the same charge parity. It follows that it is difficult to find suitable reactions involving these states ($T=0$ and $T=1$) which are allowed by charge parity conservation and prohibited by isotopic spin conservation. Thus the observed prohibition of the previously mentioned reaction, $O^{16}(d,\alpha)N^{14*}$, yields no direct information on the strength of np forces as compared with nn and pp forces.[6]

Another application of the charge parity operator is in determining the terms which may be admixed in a particular state of a nucleus. Thus consider the case of a neutron and a proton both in the same p orbital in a nucleus such as in the case of Li^6. The terms which may be constructed from this configuration with total angular momentum unity are $^3S_1$, $^3D_1$, $^1P_1$, and $^3P_1$. These terms will not all be admixed (except again in the case of a degeneracy), since the first three of these have even charge parity and the last has odd charge parity.

Our final application of charge parity will be to the problem of the β-decay[7] of O^{14} to the 2.3-Mev excited state of N^{14}. Definite identification of the excited state as belonging to the same isotopic spin triplet to which the ground state of O^{14} belongs (under the assumption of charge independence) would confirm the angular momentum assignment of this state as $I=0$ and thus allow an estimation of the β-decay coupling constant associated with Fermi selection rules. Blatt[8] has recently pointed out that Adair's interpretation of the aforementioned $O^{16}(d,\alpha)N^{14*}$ result would indeed confirm

[4] Ashmore and Raffle, Proc. Phys. Soc. (London) **A64**, 754 (1950); Burrows, Powell, and Rotblat, Proc. Roy. Soc. (London) **A209**, 478 (1951); Van de Graaff, Sperderto, Beuchner, and Enge, Phys. Rev. **86**, 966 (1952).

† *Note added in proof:* E. Feenberg (private communication) has pointed out that the negative results obtained by the Van de Graaff, etc. group using 2.1-Mev deuterons might possibly be attributed entirely to the effect of the Coulomb barrier on the outgoing α-particles combined with the effects of angular momentum and space parity conservation associated with the probable assignment of spin zero and positive space parity to the N^{14} state. These effects appear, however, to be unimportant in the other experiments, which made use of higher energy deuterons.

[5] R. K. Adair, Phys. Rev. **87**, 1044 (1952). The authors wish to acknowledge the fact that their thoughts on the substance of this article were initiated by Adair's work, and to thank V. F. Weisskopf for calling it to their attention.

[6] On the other hand, if one assumes the nuclear forces to be approximately charge independent then this result does contribute to the identification of the symmetry character of the state. The energy of the state is then entirely consistent with charge independence.

[7] Sherr, Muether, and White, Phys. Rev. **75**, 282 (1949).

[8] J. Blatt (to be published).

this identification. Furthermore, the fact that the transition is super-allowed implies that the matrix element has its maximum value (two).[9] The relevance of charge parity arises from the fact that it weakens the dependence of these conclusions on the assumption of charge independence and, therefore, strengthens the conclusions drawn. Thus if one considers the deviation from charge independence as a perturbation, one notes that there are no nearby states of N^{14} with which the $T=1$ state can mix. To elaborate, the energy level diagram of O^{14} indicates a separation of about 6 Mev between the ground state and first excited state. The several states in the vicinity of the $T=1$ state of N^{14} must, therefore, all be $T=0$ states. If one now considers the effect of a deviation from charge independence on the $T=1$ state of N^{14} it is clear that the charge even character of $T=0$ states prohibits the mixing (which might otherwise be large) of these states with the $T=1$ state. Thus the expectation that the matrix element of the $O^{14}\rightarrow N^{14*}$ transition is two is only weakly affected.

It is a pleasure to thank Professor V. F. Weisskopf for stimulating and contributory discussion.

[9] G. L. Trigg, Phys. Rev. **86**, 506 (1952).

PHYSICAL REVIEW VOLUME 88, NUMBER 5 DECEMBER 1, 1952

Elementary Particles at Rest

ENRIQUE BUSTAMANTE
Polytechnic Institute of México, México, D. F., México

(Received October 19, 1951)
(Revised version received June 19, 1952)

The object of this paper is to present a theory of the structure of elementary particles at rest. Some applications are included; in particular a solution to an unsolved problem in astronomy is presented.

I. THE UNCHARGED PARTICLE

IN order to study this particle, let us imagine something with spherical symmetry, associated with which there is a gravitational field $\mathbf{F}$. About this field we make some assumptions. In the first place, we assume that at each point there is a density of energy given by the scalar product $\mathbf{F}\cdot\mathbf{F}/8\pi\gamma$, where γ is the gravitational constant.[1] Next we assume, in accord with the principle of the inertia of energy,[2] that this density of energy is equivalent to a density of mass ρ given by the divergence $-\nabla\cdot\mathbf{F}/4\pi\gamma$.

We therefore have the following equation, where c is the speed of light in free space:

$$4\pi\gamma\rho=-\nabla\cdot\mathbf{F}=\mathbf{F}\cdot\mathbf{F}/2c^2. \tag{1}$$

If we imagine the particle at the origin of a system of spherical coordinates (r, ϑ, φ) then, on account of the spherical symmetry assumed, we can take the components of $\mathbf{F}$ in this system to be $(-F, 0, 0)$. Equation (1) then becomes one in F with the solution

$$F=r^{-2}\Big/\left(A+\frac{1}{2c^2r}\right), \tag{2}$$

where A is an integration constant. This is a rather decent function. It has a pole of order one at the origin (instead of a pole of order two, as in Newton's law) and is integrable square over all space. At the origin $F\sim 2c^2/r$, independent of the mass of the particle.

In general, if $\mathbf{F}$ is assumed to be the gradient of a scalar function ϕ, Eq. (1) will become one in ϕ with solution $2c^2$ times the natural logarithm of a harmonic function.[3]

In order to find the value of A in Eq. (2), we compute ρ by Eq. (1), integrate over all space, and equate the result to the mass m of the particle. In this way we find $A=1/\gamma m$, and Eq. (2) becomes

$$F=\frac{\gamma m}{r^2}\Big/\left(1+\frac{\gamma m}{2c^2r}\right)\sim\frac{\gamma m}{r^2}\quad\text{(for large } r\text{)}. \tag{3}$$

The density of mass results:

$$\rho=\frac{\gamma m}{8\pi c^2r^4}\Big/\left(1+\frac{\gamma m}{2c^2r}\right)^2. \tag{4}$$

The particle is thus seen to invade all space.[4] Therefore, interaction between two particles can be conceived as taking place by "intimate" contact, since each must be immersed in the other.

A potential ϕ defined by $\mathbf{F}=\nabla\phi$ is found to be $2c^2\ln(1+\gamma m/2c^2r)$. The potential energy of a "concentrated" mass m' in such a potential field would clearly not be symmetric in the masses m and m'. What then of the principle of equality of action and reaction? Of course what happens is that in this theory there are no such concentrated masses, and therefore this con-

[1] W. D. MacMillan, *Theory of the Potential* (McGraw-Hill Book Company, Inc., New York, 1930).
[2] G. Joos, *Theoretical Physics* (Blackie and Son, London, 1951), second edition.

[3] This observation is due to Professor John A. Wheeler, for the resultant field in the case of many particles.
[4] Things like this already appear in literature. See, e.g., the section on H. Weyl's Action Principle in *Mathematical Theory of Relativity*, A. S. Eddington (Cambridge University Press, Cambridge, 1930), second edition.

stitutes no violation of the principle. As a matter of fact it can be shown to hold. For the negative potential energy between two particles with fields $\mathbf{F}_1$ and $\mathbf{F}_2$ can be shown to be

$$U=\frac{1}{4\pi\gamma}\int \mathbf{F}_1\cdot\mathbf{F}_2 dV, \tag{5}$$

taken over all space. This is clearly symmetric in the two particles, and therefore the principle is guaranteed.

A slightly more general aspect is obtained if we require the field to remain finite throughout all space; but instead of infinities another kind of singularities appear, namely, discontinuities in the field.

The only analytic solution of Eq. (1) in a neighborhood $r<a$ of the origin is $\mathbf{F}=0$. Outside of some neighborhood we must have Eq. (2). Therefore the required result can be obtained by assuming F to be zero for $r<a$ and to be given by Eq. (2) for $r>a$. There will thus be a discontinuity of F at $r=a$, of saltus $F(a)$, which will require a surface distribution of matter on the sphere $r=a$ of density $\sigma=F(a)/4\pi\gamma$.

The mass m of the particle will then be

$$4\pi a^2\sigma+\int_a^\infty 4\pi r^2\rho dr.$$

It is easy to show that this expression equals $1/\gamma A$ independent of the radius a. Therefore we again have Eqs. (3) and (4) for $r>a$, but the radius a cannot be determined from a knowledge of the mass alone.

Again it is easy to show, for particles with this aspect, that the energy of interaction is given by the *same* Eq. (5), so that for these, the principle of equality of action and reaction is also guaranteed to hold.

II. THE CHARGE PARTICLE

Again let us imagine something with spherical symmetry, when at rest. This thing (the particle) shall have an associated electric field $\mathbf{E}$, and a gravitational field $\mathbf{F}$ only on account of the energy in the electric field. We now assume[6] that at each point of space there is a density of energy given by $\kappa\mathbf{E}\cdot\mathbf{E}/8\pi+\mathbf{F}\cdot\mathbf{F}/8\pi\gamma$, where κ is the permittivity of free space. We also assume that this is equivalent to a density of mass ρ given by the divergence $-\nabla\cdot\mathbf{F}/4\pi\gamma$. We therefore have

$$8\pi\gamma c^2\rho=-2c^2\nabla\cdot\mathbf{F}=\kappa\gamma\mathbf{E}\cdot\mathbf{E}+\mathbf{F}\cdot\mathbf{F}. \tag{6}$$

We also assume that at each point of space there is a density of charge ρ_Q given by the divergence $\kappa\nabla\cdot\mathbf{E}/4\pi$ (which could of course result zero). Finally we assume that the charge is held in place by the gravitational field $\rho\mathbf{F}+\rho_Q\mathbf{E}=0$. That is,

$$\kappa\gamma(\nabla\cdot\mathbf{E})\mathbf{E}=(\nabla\cdot\mathbf{F})\mathbf{F}. \tag{7}$$

If we imagine the particle at the origin of a system of spherical coordinates, the solution of Eqs. (6) and (7) for the radial components E and $-F$ of $\mathbf{E}$ and $\mathbf{F}$, respectively, is

$$F=B^{\frac{1}{2}}r^{-2}\tan c^{-2}B^{\frac{1}{2}}\left(C-\frac{1}{r}\right) \tag{8}$$

$$E=r^{-2}\left\{\frac{B}{\kappa\gamma}\left[1+\sec^2 c^{-2}B^{\frac{1}{2}}\left(C-\frac{1}{r}\right)\right]\right\}^{\frac{1}{2}}; \tag{9}$$

where B and C are integration constants. If we accept these equations to be valid all the way down to $r=0$, the structure of the particles would indeed be very complicated, owing to the essential singularities of $F(r)$ and $E(r)$ at $r=0$. Moreover, F would not be square integrable; and we know that it should because, except for an irrelevant factor, this should be equal to the mass of the particle. Still more, $F(r)$ would become negative as soon as r became smaller than $1/C$.

All this can be avoided by supposing Eqs. (8) and (9) to hold only for $r>1/C$, which we take as the "radius" a' of the particle. And at the same time we also avoid having trouble with any discontinuities in F, which would require surface distributions of matter (in which case the particle would not be of the pure charge type).

For $r<a'$ both F and E are zero, and $E(r)$ will have a discontinuity, $E(a')=(B/\kappa\gamma)^{\frac{1}{2}}/a'^2$, at $r=a'$. This will require a surface distribution of charge of density $\sigma_Q=\kappa E(a')/4\pi$.

The values of the constants B and C can be found from $\int\rho dV=m$ (the mass of the particle) and $4\pi a'^2\sigma_Q+\int\rho_Q dV=q$ (the charge of the particle), the integrals being taken over all space outside the sphere of radius $1/C$. In this way we find

$$2B=\gamma q^2/\kappa-\gamma^2m^2\approx\gamma q^2/\kappa$$

and

$$C=c^2B^{-\frac{1}{2}}\tan^{-1}\gamma mB^{-\frac{1}{2}}\approx 2\kappa c^2m/q^2.$$

Also, for large r, it follows that $F\sim\gamma m/r^2$ and $E\sim q/\kappa r^2$.

The negative potential energy between two of these particles (with fields indexed 1 and 2) can be shown to be

$$U=\frac{1}{4\pi\gamma}\int\mathbf{F}_1\cdot\mathbf{F}_2 dV-\frac{\kappa}{4\pi}\int\mathbf{E}_1\cdot\mathbf{E}_2 dV, \tag{10}$$

the integrals being taken over all space outside the two surfaces of discontinuity of the electric fields $\mathbf{E}_1$ and $\mathbf{E}_2$ of the two particles. Since this is clearly symmetric in the two particles, the principle of equality of action and reaction is also guaranteed to hold here.

III. THE CHARGED (MIXED) PARTICLE

In this case we imagine something (the particle) with spherical symmetry (when at rest) with a gravitational field quite of its own. The analysis of the preceding section leads us to expect this particle to have a surface (the sphere $r=a'$) of discontinuity of the electric field inside of which $\mathbf{E}=0$. For the outside of this surface we make the same assumptions as for the particle in Sec. II, so that we again get (for $r>a'$) Eqs. (8) and

[6] M. Planck, *Theoretical Physics* (Macmillan and Company, London, 1941), Vol. 4.

(9) for the radial components of the gravitational and electric fields, respectively; only now $F\neq 0$ for points inside the sphere $r=a'$ and outside the surface of discontinuity (the sphere $r=a$) of the gravitational field (with $a=0$ not excluded). Also, in this case, the "radius" a' of the particle is not equal to $1/C$.

Inside $r=a'$, where $\mathbf{E}=0$, we make the same assumptions as for the particle in Sec. I, so that we again get Eq. (2) for $a<r\leqq a'$; only now A is found by continuity of F at $r=a'$ in terms of the constants B and C. These latter are found from the equations

$$4\pi a^2\sigma+\int_a^\infty 4\pi r^2\rho dr=m \quad \text{(the mass)}$$

and

$$4\pi a'^2\sigma_Q+\int_{a'}^\infty 4\pi r^2\rho_Q dr=q \quad \text{(the charge)},$$

and even though these are slightly different to the corresponding equations in Sec. II, the same values for B and C are found. It is then easy to show that

$$A=B^{-\frac{1}{2}}\cot c^{-2}B^{\frac{1}{2}}\left(C-\frac{1}{a'}\right)-1/2c^3a'\approx 1/\gamma\dot{m},$$

where we have put: $\dot{m}=m-q^2/2\kappa c^3a'$. For heavy particles (where $m\gg q^2/2\kappa c^3a'$) we practically get for A the same value as for the uncharged particle and therefore practically the same field given by Eq. (3) (at small distances).

The energy of interaction between two mixed particles (with fields indexed 1 and 2) can also be shown to be given by Eq. (10), only that now the first integral is to be taken over all space outside the surfaces of discontinuity of the gravitational fields. Owing to the symmetry, the principle of action equals reaction is again guaranteed.

IV. APPLICATIONS

The stability[6] of atomic nuclei can easily be explained by conceiving nuclei to be mixed particles formed by the nucleons (conceived as uncharged and mixed particles), the charged nucleons having penetrated into each others surfaces of discontinuity of their electric fields.

The sizes[6] of atomic nuclei (conceived as mixed particles) can also be found, if we take the radii a' of the surfaces of discontinuity of the electric fields as their sizes. Denoting the nucleus of charge number Z and mass number $(N+Z)$ by (Z, N), its mass by $M(Z, N)$, and the mass of the (complete) atom with nucleus (Z, N) by $M_a(Z, N)$, we find its radius to be (neglecting the difference between M and $\dot{M}$)

$$a'(Z,N)=(Z-1)\epsilon^2/\kappa c^2[M(0,1)-M_a(1,0)+M_a(Z,N-1)-M_a(Z-1,N)],$$

where ϵ denotes the charge of a proton.

[6] C. F. v. Weizsäcker, *Die Atomkerne* (Akad. Ver., Leipzig, 1937).

The particular case of this equation, when $Z=N$, can be recognized as essentially the same familiar formula used to determine nuclear sizes by the method of electrostatic interaction of protons in nuclei,[7] where use is made of the "mirror" nuclei $(Z-1, Z)$ and $(Z, Z-1)$. This equation therefore gives the accepted sizes of atomic nuclei.

Saturation of nuclear forces,[8] in this theory, becomes particularly simple. For the increment in the binding energy of a nucleus when one neutron is brought in can be shown to be approximately equal to $\gamma M(0,1)M(Z,N-1)/a$ (which is known to be practically constant for not too light nuclei), where $a=a(Z,N)$ is the radius of the surface of discontinuity of the gravitational field of (Z, N). This means that $a(Z,N)$ is practically a linear function of the mass number.

The values of $a(Z,N)$ were computed from observed data for practically all nuclei from H^2 to Gd^{157}, where the errors of observation were sufficiently small to guarantee a significant result. Except for the nuclei Be^9, O^{17}, and Ni^{61}, the results checked nicely.

V. THE DISCREPANCY IN THE ADVANCE OF PERIHELION OF MERCURY

The observed advance of perihelion[9] in the case of mercury is known to be 574″ per century. Newtonian perturbation theory takes account of almost 534″ per century, while Einstein's theory of relativity[10] accounts for almost 43″ per century more.

There is thus a discrepancy of almost 3″ per century between theory and observation that remain unexplained (theoretical value in excess), outside of the known observational error.

In this theory, the gravitational field of the sun would be given by Eq. (3). The second term in the development in series of this function, namely, $-\gamma^2m^2/2c^2r^3$ is exactly of the same form as the term $6\gamma^2m^2/c^2r^3$, which gives the correction in Einstein's theory of relativity. The only difference is the sign of the term and the factor $\frac{1}{2}$ instead of 6.

Now the correction in the advance of perihelion is proportional to the coefficient of the term in r^{-3} (both in magnitude and sign).[11] Consequently Eq. (3) gives a correction of 1/12 that of the relativistic correction (i.e., a little more than 3.5″ per century) but of opposite sign. This brings back the theoretical value nearer to the observed value but now well within observational error.

[7] H. A. Bethe, *Elementary Nuclear Theory* (John Wiley and Sons, Inc., New York, 1947).

[8] W. Heisenberg, *Kosmische Strahlung* (Chap. 10 by v. Weizsäcker) (Springer, Berlin, 1943). Also H. A. Bethe, (reference 7).

[9] S. Newcomb, *Astronomical Constants* and W. De Sitter, Monthly Notices Roy. Astron. Soc. **76** (1916).

[10] A. Einstein, *The Meaning of Relativity* (Princeton University Press, Princeton, 1950), third edition.

[11] T. Levi-Civita, *Absolute Differential Calculus* (Blackie and Son, London, 1927).

The Specific Heat of Lead in the Temperature Range 1°K to 75°K*

M. HOROWITZ, A. A. SILVIDI, S. F. MALAKER, AND J. G. DAUNT
Department of Physics and Astronomy, The Ohio State University, Columbus, Ohio
(Received August 8, 1952)

The specific heat of pure Pb in the temperature range 1°K to 75°K has been measured calorimetrically, both in the normal and superconductive states. The measurements were made using a useful semiautomatic recording system. It was found that at the lowest temperatures (1°K to 4°K) the lattice specific heat of Pb in the normal state was a T^3 function, with a Debye $\theta=96.3$°K. It was found that the variation of θ with temperature over the whole range of temperature employed confirmed the theoretical computations made by Leighton for f.c.c. lattices. The normal electronic specific heat was found to be $7.48\times10^{-4}\ T$ cal/mole-deg, in good agreement with results from magnetic measurements on superconducting Pb. The measured value of the electronic specific heat of the superconducting state was $C_{el.s}=5\times10^{-4}\ T^3$ cal/mole-deg, in the temperature range 1°K to 4°K; this result was also in agreement with the magnetic measurements.

I. INTRODUCTION

NO previous measurements in the liquid helium temperature range have been made on lead in the normal state. Moreover, the only measurements of the specific heat of lead in the superconducting state below 4°K, namely, those of Keesom and van den Ende,[1] indicated the possibility of an anomaly at the lowest temperature. In view of the significance of an accurate determination of the temperature dependence of the specific heat with respect to theories both of lattice vibrations and of superconductivity and in view of the above-mentioned paucity of data for lead, it was considered of interest to carry out the experimental observations that are reported in this paper.

The experimental observations were made using, in the main, well-established techniques of adiabatic calorimetry, as two of us have previously reported.[2] However, by employing a variety of materials for resistance thermometers, by paying special attention to high vacuum isolation, and by using a chart-recording system for semiautomatic temperature observation, we have been able to extend these existing techniques both in range of temperature of observation and in accuracy, and at the same time to increase the speed of experimentation. Some detail is given below of the experimental procedures.

II. EXPERIMENTAL PROCEDURES

Lead of purity 99.99 percent supplied by Mallinckrodt Chemical Works was cast in the form of a cylinder 6.34 cm high and 4.54 cm in diameter, the total content being 5.11 moles. Radial slots parallel to the axis were cut in order to minimize eddy current effects when an axial magnetic field was switched on or off to change the specimen from the superconducting to the normal state, or vice versa. The lead specimen had wound on it a manganin heater wire of mass 0.069 gram and resistance 170 ohms at 0°C. As resistance thermometers we used (a) lead wire of diameter 0.00508 cm and resistance 331 ohms at 0°C, (b) leaded phosphor-bronze wire of diameter 0.00508 cm and resistance 36.2 ohms at 0°C and (c), "1-watt 10-ohm" carbon radio resistors supplied by the Allen-Bradley Company. These thermometric resistors made thermal contact with the specimen through a pure copper mounting. The lead wire was found convenient as a resistance thermometer at temperatures above 10°K, since it had a remarkably high temperature coefficient of resistance.[3] The phosphor-bronze wire, as originally pointed out by Keesom and van den Ende,[4] is satisfactory below about 5°K. The carbon resistor, as shown by Clement and Quinnell[5] and by Brown, Zemansky, and Boorse,[6] was found satisfactory not only at the lowest temperatures but also at temperatures as high as 80°K. In the computations of the data corrections were made, of course, for the heat capacity of the thermometers and their mountings. The specimen was mounted in a vacuum adiabatic calorimeter similar to that described previously by two of us.[2] In the calorimeter used for these measurements, however, a large diameter, high speed, high vacuum pumping line was used, terminating at the top of the cryostat in a DPI, VMF, 20-W, two-stage, fractionating oil diffusion pump. It was found that considerable care had to be taken to maintain vacuum of the order of 10^{-6} mm Hg, owing to the fact that (a) at the higher temperatures, namely, in the liquid nitrogen temperature region, it was found that by the generation of heat in the heater on the specimen gas would be desorbed, presumably from the varnish employed; and (b) at the lowest temperatures, namely, below the lambda-temperature of liquid helium, similar generation of heat would desorb the anomalous helium film. Only by fast and lengthy pumping could the

* Assisted by a contract between the AEC and the Ohio State University Research Foundation.

[1] W. H. Keesom and J. N. van den Ende, Leiden Comm. 203d (1930) and 213c (1931).

[2] A. A. Silvidi and J. G. Daunt, Phys. Rev. **77**, 125 (1950).

[3] de Haas, de Boer, and van den Berg, Physica **1**, 1115 (1934); G. J. van den Berg, Physica **14**, 111 (1948).

[4] W. H. Keesom and J. N. van den Ende, Leiden Comm. 203c (1929); see also W. H. Keesom and P. H. van Laer, Physica **5**, 541 (1938).

[5] J. R. Clement and E. H. Quinnell, Phys. Rev. **85**, 502 (1952); see also Proceedings of the International Conference on Low Temperature Physics, Oxford, p. 51 (1951) (unpublished).

[6] Brown, Zemansky, and Boorse, Phys. Rev. **84**, 1050 (1951).

spurious effects due to such gas desorption be avoided. It is of interest to note that we found it experimentally more difficult to avoid these effects at the higher temperatures. Indeed, it was all too easy at the higher temperatures to observe spuriously high specific heats because of this desorption and to notice apparent hysteresis in the observations.

In measuring temperature with the resistance thermometers, which were calibrated against the vapor pressures of liquid nitrogen, hydrogen, and helium, the potential difference generated across them by a constant current was balanced against a known emf provided by a White single potentiometer (catalog number 7620) before a heating cycle was started. The change in resistance following a heating cycle was observed by measuring the off-balance potential difference with a Liston-Folb dc amplifier (model number 14) and a recording microammeter. In this way temperature changes occurring in the heating cycles were automatically recorded. A typical chart of such an observation is given in Fig. 1, which is a photograph of a record

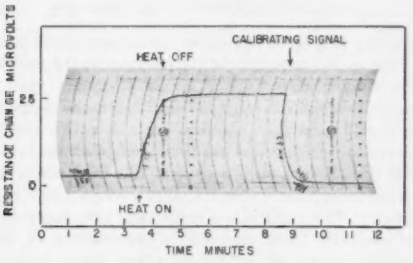

FIG. 1. A semi-automatically recorded heating cycle.

taken at 3.535°K. From the figure it will be seen that at minute 3.7 the heat was switched on and at minute 4.7 the heat was switched off. In this particular cycle the total heat energy provided was 16.56 millicalories. It will be seen further that after the heat was switched off, the temperature of the specimen, as indicated by the potential measurement on the chart, quickly settled down to a constant value. At minute 9, a dc calibrating signal of 25 microvolts was injected in order to correlate the chart difference change with the potential difference change and thus with the change in temperature of the specimen. It is of interest to note that this heating cycle, which is typical of all our observations, shows practically no drift in temperature, either before or after the period of heating. Such lack of drift enables the temperature difference to be estimated with high accuracy, without the need for doubtful extrapolation. This is to be compared favorably with previous techniques, as exemplified, for example, with the heating cycle given by Keesom and Kok.[7]

[7] W. H. Keesom and J. A. Kok, Proc. Amsterdam Acad. Sci. **35**, 294 (1932).

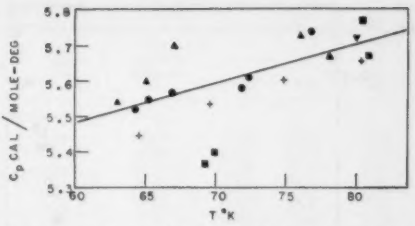

FIG. 2. The specific heat of lead at liquid nitrogen temperatures: ● Our observations; + Meads, Forsythe, and Giauque, J. Am. Chem. Soc. **63**, 1902 (1941); ▼ Griffiths and Griffiths, Proc. Roy. Soc. (London) **A90**, 557 (1914); ▲ W. Nernst, Ann. Physik **36**, 395 (1911); ■ Keesom and Onnes, Leiden Comm. 143.

III. RESULTS

The vapor pressures used in calibrating the thermometers were correlated with temperature using the data provided (a) for liquid helium by van Dijk and Shoenberg[8] [the so-called 1949 scale], (b) for liquid hydrogen by the National Bureau of Standards,[9] and (c) for liquid nitrogen by Henning and Otto.[10]

Our results are collected in Table I which shows all experimental data, such as heat input, temperature differences, etc., as well as the computed specific heats at constant pressure.

It was thought appropriate to make measurements in the liquid hydrogen and liquid nitrogen temperature regions, although many measurements have been made previously at these temperatures, in order to provide a check on the consistency and reliability of our equipment. The results at these temperatures are plotted graphically in Figs. 2 and 3, together with those

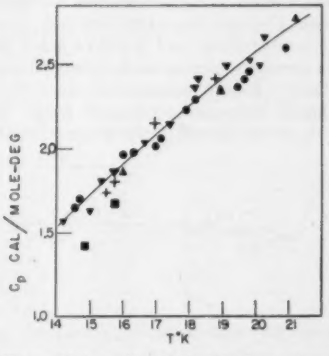

FIG. 3. The specific heat of lead at liquid hydrogen temperatures: ● Our observations; + Meads, Forsythe, and Giauque, J. Am. Chem. Soc. **63**, 1902 (1941); ▲ Eucken and Schwers, Verhandl. Deut. physik Ges. **15**, 578 (1913); ▼ Keesom and Onnes, Leiden Comm. 143; ■ Keesom and van den Ende (reference 1).

[8] H. van Dijk and D. Shoenberg, Nature **164**, 151 (1949).
[9] Wooley, Scott, and Brickwedde, J. Research Natl. Bur. Standards **41**, 379 (1948) RP 1932.
[10] F. Henning and J. Otto, Physik. Z. **37**, 633 (1936).

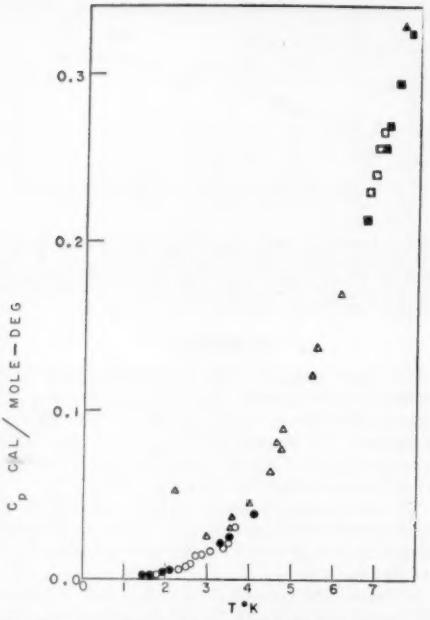

FIG. 4. The specific heat of lead at liquid helium temperatures: ● Our observations in normal state; ○ Our observations in superconducting state; ■ Clement and Quinnell, normal state (reference 5); □ Clement and Quinnell, superconducting state (reference 5); ▲ Keesom and van den Ende, normal state (reference 1); △ Keesom and van den Ende, superconducting state (reference 1).

of previous workers. It will be seen from the figures that the agreement between our results and those previously obtained is satisfactory, and it will be noted that the scatter in previous observations is considerably greater in the liquid nitrogen temperature range than that in the liquid hydrogen temperature range. We feel that this is due to the difficulties enumerated above in Sec. II, associated with gas desorption, which we have noted to be especially troublesome in this temperature region. Our results at liquid helium temperatures for the specific heat of lead both in the superconducting state and in the normal state, which latter was obtained by applying an external axial magnetic field greater than the threshold field, are given in Fig. 4. The figure also includes results obtained previously for lead in the superconducting state by Keesom and van den Ende[1] and the more recent results above 6°K of Clement and Quinnell.[5]

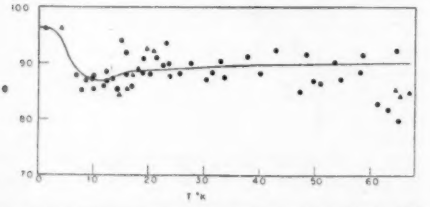

FIG. 5. Debye temperatures for normally conducting lead: ▲ Our observations; ● Previous observations by: Clement and Quinnell (reference 5); Keesom and van den Ende (reference 1); Simon, Z. Phys. Chem. **110**, 572 (1924); Eucken and Schwers, Verhandl. Deut. physik Ges. **15**, 578 (1913); Griffiths and Griffiths, Proc. Roy. Soc. (London) **A90**, 557 (1914); Keesom and Onnes, Leiden Comm. 143; W. Nernst, Ann. Physik **36**, 395 (1911); Meads, Forsythe, and Giauque, J. Am. Chem. Soc. **63**, 1902 (1941); ——— Theory (Leighton, reference 15).

IV. INTERPRETATION OF RESULTS

Our results (see Fig. 4) for C_p *versus* T for the specific heat of lead in the superconducting state show no sign of any anomaly at the lowest temperatures. It is therefore concluded that the anomalously high value of C_p, in amount 0.0523 cal/mole-deg at 2.20°K reported by Keesom and van den Ende,[1] is probably erroneous.

If it is supposed that at sufficiently low temperatures the specific heat in the normal state can be written as

$$C_p = C_V = 464.4(T/\theta)^3 + \gamma T \text{ cal/mole-deg}, \quad (1)$$

where the first term represents the lattice specific heat and the second term that of the electrons in the normal state, then a plot of C_V/T *versus* T^2 should yield a straight line the intercept of which with the ordinate axis should yield the numerical value of γ. Our results indicate that such a plot made for temperatures below 4.2°K does in fact yield a straight line from which we have deduced that $\theta = 96.3$°K and $\gamma = 7.48 \times 10^{-4}$ cal/mole-deg^2. This value of γ is in excellent agreement with that deduced from magnetic measurements of the threshold curve of superconducting lead, namely, 7.1×10^{-4} cal/mole-deg^2.[11,12] The observed C_V for Pb in the normal state, however, does not follow a Debye function. This can be shown by calculating a Debye θ-value corresponding to each measured value of C_V, The results of this computation[13] are shown in Fig. 5. in which it is seen that the θ-values are not independent of temperature, as they should be if a single Debye function described the whole specific heat curve. It is to be noticed that there is a distinct minimum in the θ *versus* T curve at 12°K and that at the lowest temperature θ flattens out to a value of 96.3°K. This behavior of the specific heat follows the general predictions of Blackman,[14] who showed that at sufficiently low tem-

[11] J. G. Daunt and K. Mendelssohn, Proc. Roy. Soc. (London) **A160**, 127 (1937).

[12] Daunt, Horseman, and Mendelssohn, Phil. Mag. **27**, 754 (1939).

[13] In computing the θ-values for $T > 7$°K the observed specific heat in the normal state (adjusted to constant volume) was equated to $D(T/\theta)$ neglecting any contribution due to the electronic term. Since the γ quoted above is relatively small, this neglect of the electronic term introduces an error which at most [i.e., at 7°K] is 3 percent and which for temperatures above 10°K is considerably less than the experimental error. The θ-value for $T \lesssim 4.2$°K has been found from the C_V/T *versus* T^2 plot mentioned above to be 96.3°K.

[14] M. Blackman, Repts. Prog. Phys. **8**, 11 (1941).

TABLE I. Data on specific heat of lead.

Date	External magnetic field gauss	Type of thermometer	Thermometer dissipation μwatts	Heater current ma	Heater resistance ohms	Heating time sec	Total heat input cal	Heat input to specimen cal	ΔT °K	T °K	C_p cal/mole-deg
At liquid nitrogen temperatures											
8-10-51	0	Pb	0.63	60.93	160	128.3	18.29	15.43	0.539	72.28	5.61
8-10-51	0	Pb	0.63	60.88	160	119.6	17.02	14.38	0.502	71.79	5.58
8-13-51	0	Pb	0.57	60.96	160	119.5	16.91	14.50	0.508	66.82	5.57
8-14-51	0	Pb	0.56	60.86	159	120.0	16.97	14.62	0.516	65.18	5.55
8-14-51	0	Pb	0.55	61.07	159	120.2	17.08	14.76	0.523	64.21	5.52
4-12-52	0	C	5.22	37.32	161	149.1	7.97	7.95	0.273	76.80	5.73
At liquid hydrogen temperatures											
5-9-51	0	Pb	0.96	28.33	154	59.4	1.754	1.722	0.130	20.92	2.59
5-9-51	0	Pb	0.94	28.33	154	59.4	1.754	1.722	0.129	20.79	2.61
5-10-51	0	Pb	0.85	28.33	154	59.8	1.766	1.737	0.138	19.80	2.45
5-10-51	0	Pb	0.19	28.32	154	89.8	2.651	2.607	0.212	19.65	2.41
5-10-51	0	Pb	0.82	28.36	154	60.0	1.776	1.746	0.144	19.45	2.36
5-10-51	0	Pb	0.69	28.29	154	60.1	1.769	1.745	0.149	18.15	2.29
5-10-51	0	Pb	0.16	28.32	154	69.8	2.060	2.033	0.175	18.02	2.26
5-10-51	0	Pb	0.66	28.34	154	45.0	1.330	1.312	0.115	17.86	2.23
5-10-51	0	Pb	0.60	28.32	154	59.8	1.764	1.742	0.166	17.15	2.06
5-10-51	0	Pb	0.58	14.62	154	239.7	1.885	1.861	0.181	16.98	2.01
5-10-51	0	Pb	0.57	28.33	154	45.4	1.341	1.325	0.127	16.83	2.04
5-10-51	0	Pb	0.52	32.28	153	44.8	1.707	1.688	0.166	16.33	1.98
5-10-51	0	Pb	0.51	14.34	153	239.6	1.801	1.781	0.175	16.16	1.99
5-10-51	0	Pb	0.50	28.31	153	60.0	1.758	1.739	0.173	15.99	1.96
8-1-51	0	Pb	0.39	24.22	153	59.8	1.282	1.269	0.146	14.66	1.70
5-10-51	0	Pb	0.37	28.31	153	60.0	1.758	1.741	0.202	14.58	1.69
8-1-51	0	Pb	0.36	24.22	153	60.0	1.287	1.274	0.151	14.51	1.65
8-1-51	0	Pb	0.36	24.22	153	59.6	1.278	1.266	0.149	14.37	1.66
At liquid helium temperatures in superconducting state											
2-16-52	0	Pb–Br	0.19	4.721	152	11.6	0.00942	0.00918	0.171	2.671	0.01046
2-16-52	0	Pb–Br	0.05	2.823	152	43.8	0.01272	0.01246	0.171	2.814	0.01409
2-22-52	0	Pb–Br	0.16	0.901	152	38.1	0.001125	0.001063	0.079	1.781	0.00263
2-22-52	0	Pb–Br	0.16	0.902	152	51.0	0.001506	0.001431	0.093	1.837	0.00301
2-22-52	0	Pb–Br	0.16	0.902	152	52.0	0.001538	0.001464	0.090	1.847	0.00318
2-22-52	0	Pb–Br	0.17	0.902	152	51.6	0.001528	0.001452	0.088	1.903	0.00322
2-22-52	0	Pb–Br	0.17	0.902	152	59.2	0.001750	0.001667	0.096	1.926	0.00339
2-22-52	0	Pb–Br	0.17	0.897	152	102.4	0.003000	0.002883	0.130	1.974	0.00433
2-22-52	0	Pb–Br	0.18	0.902	152	107.8	0.003181	0.003066	0.103	2.312	0.00582
2-22-52	0	Pb–Br	0.18	1.963	152	41.2	0.00578	0.00560	0.147	2.449	0.00743
2-22-52	0	Pb–Br	0.18	1.963	152	47.6	0.00668	0.00650	0.138	2.580	0.00917
2-22-52	0	Pb–Br	0.19	1.963	152	65.7	0.00922	0.00902	0.138	2.704	0.01275
2-22-52	0	Pb–Br	0.19	1.963	152	79.5	0.01115	0.01092	0.150	2.842	0.01423
2-22-52	0	Pb–Br	0.19	1.963	152	73.8	0.01035	0.01013	0.130	2.957	0.01522
2-22-52	0	Pb–Br	0.20	2.231	152	84.5	0.01530	0.01499	0.179	3.078	0.01633
2-22-52	0	Pb–Br	0.20	2.404	152	77.2	0.01632	0.01601	0.163	3.219	0.01917
2-22-52	0	Pb–Br	0.20	2.651	152	90.8	0.02320	0.02270	0.235	3.389	0.01884
2-22-52	0	Pb–Br	0.20	2.652	152	87.2	0.0223	0.02185	0.198	3.509	0.02155
2-22-52	0	Pb–Br	0.20	2.652	152	71.5	0.01830	0.01795	0.148	3.586	0.0237
2-22-52	0	Pb–Br	0.20	2.630	152	67.8	0.01705	0.01679	0.105	3.671	0.0312
At liquid helium temperatures in normal state											
6-6-52	940	C	0.0043	0.787	155	140.1	0.00321	0.00318	0.136	1.892	0.00458
6-6-52	940	C	0.011	1.144	155	23.2	0.001132	0.00112	0.086	1.403	0.00255
6-6-52	940	C	0.0062	1.145	155	36.6	0.001778	0.00175	0.126	1.619	0.00272
6-6-52	940	C	0.0046	1.145	155	63.4	0.00309	0.00306	0.102	1.855	0.00588
6-6-52	940	C	0.0035	1.137	155	107.8	0.00516	0.00512	0.170	2.087	0.00590
6-6-52	940	C	0.00087	4.567	155	30.3	0.0235	0.0234	0.116	4.118	0.0396
3-28-52	830	C	0.0013	1.864	152	64.7	0.00816	0.00813	0.074	3.295	0.0215
3-28-52	830	C	0.0012	2.788	152	49.8	0.01405	0.01400	0.119	3.407	0.0230
3-28-52	830	C	0.0011	2.789	152	58.6	0.01656	0.01650	0.130	3.535	0.0248

peratures a T^3 region would be evident and that as the temperature was raised the θ-value would pass through a minimum. Detailed computations of the specific heat of face-centered cubic lattices have been made by Leighton[15] based on consideration of the normal modes of vibration of the lattice. The results of these computations are shown in Fig. 5 by the full curve for θ *versus* temperature. This curve represents Leighton's computations for an f.c.c. lattice with $\gamma/\alpha=-0.1$, where α and γ are the force constants for central Hooke's law forces which are assumed to act between an atom and its nearest and next nearest neighbors, respectively. Furthermore, in fitting Leighton's com-

[15] R. B. Leighton, Revs. Modern Phys. **20**, 165 (1948).

putations to our results for Pb a θ-value of 96.3°K at 0°K has been taken.[16] It will be seen from the curve that a minimum in the θ-value occurs theoretically at about 10°K, in close agreement with the experimentally observed result and that over a wide range of temperature from liquid helium temperatures up to 70°K there is a close and satisfactory correlation between the theoretical and experimental results for this f.c.c. metal.

Our measurements of C_V in the superconducting state yield approximately a T^3 function. If the lattice specific heat, corresponding to $\theta=96.3$°K, is subtracted from our total observed value, we obtain an electronic specific heat in the superconducting state $C_{el,s}$, given approximately by

$$C_{el,s}=5\times10^{-5}\,T^3 \text{ cal/mole-deg.}$$

It is considered that the temperature range of measurement is too small to allow a conclusive deduction of the full variation of $C_{el,s}$ with temperature. However, in the limited temperature range of $1°K<T<4.2°K$, the computed value of $C_{el,s}=5\times10^{-5}\,T^3$ cal/mole-deg is exactly the same as can be computed from the magnetic measurements on Pb in the superconductive state.[11,12]

This work was supported in part from funds granted to The Ohio State University by the Research Foundation for aid in fundamental research.

[16] *Note added in proof:* The authors' attention has recently been drawn to the elastic data for Pb given by K. Lonsdale [Acta Cryst. **1**, 142 (1948)] from which, using Leighton's formulas, it can be computed that $\gamma/\alpha=-0.12$ and $\theta\approx98$ at 0°K. This further emphasizes the good agreement between Leighton's theory and our results.

PHYSICAL REVIEW VOLUME 88, NUMBER 5 DECEMBER 1, 1952

A Scintillation Spectrometer Study of the Decay of Tl^{204}†

E. DER MATEOSIAN AND A. SMITH
Brookhaven National Laboratory, Upton, New York

(Received August 26, 1952)

By means of a special technique of scintillation spectroscopy, whereby radioactivity is introduced into a NaI(Tl) crystal, the β-spectrum of Tl^{204} is investigated and the assignment of the transition as "first forbidden" is confirmed. A reported weak intensity photon radiation of 70-kev energy is uniquely identified as being due to K-electron capture, and the branching ratio of the K capture process to the beta-emission is determined to be ~0.015. Utilizing the formulas for forbidden β-transitions developed by Marshak, the transition energy for the orbital capture is calculated to be ~400 kev. The inner bremsstrahlung associated with the K-capture is detected by coincidence measurements, and its end-point value is found to be in agreement with the transition energy calculated from the branching ratios. An upper limit of 0.2 percent is set for any possible K capture in Au^{198}.

I. INTRODUCTION

THE β-spectrum of Tl^{204} was studied by Saxon and Richards,[1] who obtained a value of 0.783 Mev for its end-point energy and who found that the spectrum shape could best be classified as "first forbidden" ($\Delta I=2$, "yes"). These authors observed that their Kurie plot for the Tl^{204} β-rays, corrected for forbiddenness, diverged from a straight line for energies below ~350 kev to an extent which could not be explained by source thickness. A weak intensity 0.070-Mev photon was observed associated with Tl^{204} by Madansky and Rassetti[2] who suggested the presence of a K capture branch. A recent paper by Lidofsky, Macklin, and Wu[3] confirms the above results and reports a beta end-point value of 0.765 Mev and a Kurie plot which is straight to 150 kev.

A method of studying the decay of radioactive nuclei has been developed at our laboratory which is particularly applicable to the study of beta-spectra and to the detection of weak orbital electron capture branches accompanying β-decay. The technique consists of growing a thallium-activated sodium iodide crystal with a trace of a radioactive element of interest added,[4] so that one obtains a scintillating crystal that has a source of radioactivity distributed evenly throughout it.

A crystal containing a dispersed source of radiations has the following desirable properties: a 4π solid angle geometry; a source thickness which is, for practical purposes, equivalent to zero; the ability to add up simultaneous energy pulses into a single pulse equal in energy to the sum total of the energy of the component pulses. If the activity introduced into a crystal consists of a beta-decay followed by the emission of a prompt gamma-ray, the crystal detects the beta-particles and the conversion electrons arising from the gamma-radiation with ~100 percent efficiency. Each conversion electron is accompanied by a beta-particle which immediately preceded the emission of the gamma-ray;

† Work done under the auspices of the AEC.
[1] D. Saxon and J. Richards, Phys. Rev. **76**, 982 (1949).
[2] L. Madansky and F. Rassetti (private communication).
[3] Lidofsky, Macklin, and Wu, Phys. Rev. **87**, 391 (1952).
[4] Scharff-Goldhaber, der Mateosian, Goldhaber, Johnson, and McKeown, Phys. Rev. **83**, 480 (1951).

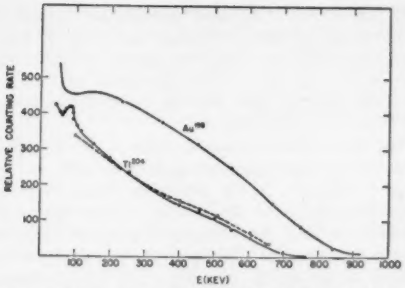

FIG. 1. The beta-spectra of Au^{198} and Tl^{204}. The solid dots and solid lines are uncorrected experimental points and curves. The open circles and dashed curves represent data corrected for the escape of electrons from the crystal.

so that if one studies the distribution of pulses in the crystal with some sort of pulse-height analyzer, one sees not a conversion line and a beta-spectrum but rather two beta-spectra, one starting at zero electron energy and the other starting at the energy equal to that of the conversion electron.

On the other hand, if the photon is in a K branch, the conversion electron is independent of the beta-particles; and one sees the conversion line due to the electrons as well as the beta-distribution. Thus, one has a sensitive means of isolating the radiation occurring in orbital electron capture from those following beta-decay.

II. EXPERIMENTAL RESULTS

A. Beta-Spectra

We introduced Tl^{204} into a crystal which we placed onto a 5819 RCA photomultiplier tube connected through a Chase and Higinbotham non-overloading amplifier[5] to an Atomic Instrument Company single-channel pulse analyzer. The beta-spectrum of Tl^{204} is shown in Fig. 1, as well as that of Au^{198}, which was introduced into a crystal in an identical fashion as was Tl^{204}. Au^{198} was chosen to check our technique and corrections since it is close to Tl^{204} in atomic number and beta end-point energy, and its beta-spectrum has been measured and found to have an allowed shape.

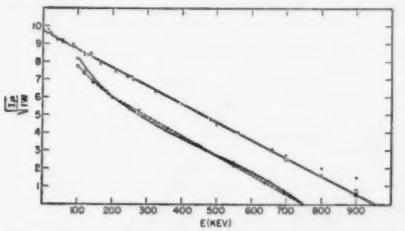

FIG. 2. Kurie plots for Au^{198} and Tl^{204}. The crosses in the Au plot and the open circles in the Tl^{204} plot are experimental points corrected only for the escape of electrons from the crystal. In the Au plot the open squares are points that have also been corrected for the addition of the conversion electrons of the 411-kev gamma-ray to the beta-spectrum, while the solid square has, in addition, the resolution correction. The solid dots in the curve for Tl^{204} are plots of $(I\mu/fWC_{1T})^{\frac{1}{2}}$, where $C_{1T}\sim(W_0-W)^2+A(W^2-1)$, ($A$ is calculated from Feister's f tables). C_{1T} is the correction factor for a $\Delta I=\pm 2$, "yes," first-forbidden transition.

[5] R. L. Chase and W. A. Higinbotham, Rev. Sci. Instr. 23, 24 (1952).

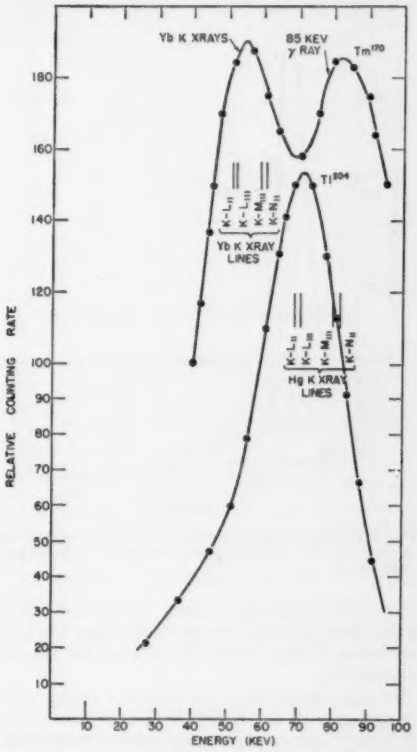

FIG. 3. Soft photon radiation associated with Tl^{204}. The upper curve shows the 85-kev gamma-ray of Tm^{170} and the K x-rays of Yb for calibration purposes.

The spectra in Fig. 1 were corrected for the resolution of the instrument[6] and the escape of electrons and x-rays from the crystals. Several runs were made in which crystals of different sizes were used in order to test the accuracy of our methods of correcting for the escape of radiations from the crystals, for the magnitude of this correction is a function of crystal size. Energy calibrations were effected by impressing the radiations of external standard sources, such as the 661-kev gamma-rays of Cs^{137} and the 85-kev gamma-

[6] An approximation method making use of the inverse function of the resolution effect was suggested by M. Fuchs of this laboratory.

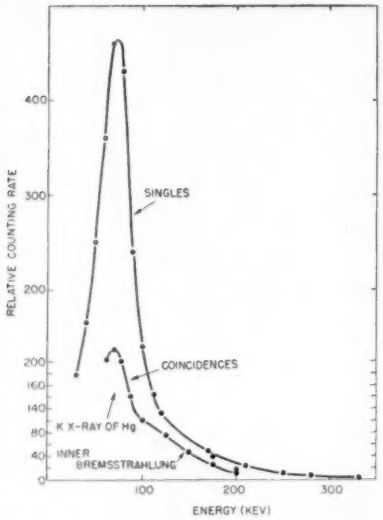

FIG. 4. Bremsstrahlung associated with Tl^{204}. $\gamma-\gamma$ coincidences show the 70-kev K x-ray of Hg plus a continuum whose end point is ~250 kev.

rays of Tm^{170}, upon the "active" crystals and measuring the positions of the photoelectron peaks. The Kurie plots shown in Fig. 2 were then constructed from the corrected data.

The value obtained for the end-point energy of the beta-spectrum of Tl^{204} is 760 ± 10 kev. This value is in satisfactory agreement with that reported by Lidofsky, Macklin, and Wu,[3] who obtained a value of 765 ± 10 kev with a lens spectrometer. The Kurie plot for the Tl^{204} exhibits an "s" shape characteristic of first-forbidden transitions of the $\Delta I=2$, "yes" type and can be straightened by applying the proper forbidden shape factor,[7] $(W_0-W)^2+A(W^2-1)$, to the data. A slight deviation from a straight line persists for electron energies below ~150 kev, which may be a real effect in view of the straight Kurie plot obtained with Au^{198} down to energies of ~50 kev. A search has been made for a weak beta-branch going to the first excited state in Pb^{204} and an upper limit of 10^{-4} γ's per β^- has been placed on such a transition.[8]

B. K Orbital Electron Capture

An inspection of Fig. 1 shows a small peak on the beta-spectrum of Tl^{204} at ~85 kev. A strong source of Tl^{204} placed on a standard scintillation gamma-ray spectrometer revealed a photon line (Fig. 3) whose energy was ~70 kev. Since the energy of Hg K x-rays is ~69 kev and the K work function is 83.3 kev, we conclude that the peak seen on the beta-spectrum of Tl^{204} is a K capture peak.

The ratio of the corrected areas of the K capture peak and the beta-spectrum is 0.015 ± 0.005, and this gives a measure of the branching ratio. From the branching ratio one can calculate the energy of the transition in the K capture process by means of lifetime-energy relationships developed by Marshak for forbidden transitions in beta-decay and orbital electron capture.[9] The value obtained for Tl^{204} is about 400 kev.

There is a possibility[10] that orbital electron capture occurs in Au^{198} since this would lead to stable Pt^{198}. Repeated measurements of the Au beta-spectrum failed to reveal a superimposed K peak. A comparison with the Tl^{204} spectrum, which illustrates the sensitivity with which a 1.5 percent branch is detectable, enables us to put an upper limit of ~0.2 percent on a possible K capture branch in Au^{198}.

One can also arrive at a value for the energy of the transition in orbital electron capture if one can detect and measure the inner bremsstrahlung spectrum associated with the capture process. One can isolate the inner bremsstrahlung spectrum in electron capture from other radiations by measuring coincidences between the K x-ray and gamma-rays as a function of the gamma-ray energy. Figure 4 illustrates the results of such an experiment. The plot shows the K capture peak of Tl^{204} superposed upon the inner bremsstrahlung spectrum; the K peak is seen with equal intensity as the inner bremsstrahlung because of the symmetry of the coincidence detectors.

If one plots $(I/E)^{\frac{1}{2}}$ one should obtain, in the first

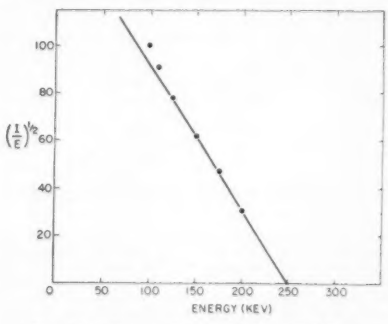

FIG. 5. Kurie type plot of inner-Bremstrahlung accompanying K capture in Tl^{204}.

[7] An approximation calculation of A was published by J. Davidson, Phys. Rev. **82**, 48 (1951), which straightened the Kurie plot down to ~350 kev. A method suggested by Macklin, Lidofsky, and Wu, Phys. Rev. **87**, 391 (1952), which extracts A from Feister's tables of the Fermi function, straightened the Kurie plot down to ~150 kev.

[8] der Mateosian, Friedlander, Goldhaber, and Sunyar (unpublished).

[9] R. E. Marshak, Phys. Rev. **61**, 431 (1942). Also see Appendix II.

[10] L. Simons, Phys. Rev. **86**, 570 (1952).

approximation, a straight line[11] similar to a Kurie plot. This is illustrated for Tl^{204} in Fig. 5. The end-point energy is about 250 kev. If the K work function (83.3 kev) is added to this, one obtains a value for the transition energy of about 335 kev. This is to be compared with the value obtained from the K capture branching ratio (400 kev).

III. CONCLUSION

The decay scheme[12] of Tl^{204} is shown in Fig. 6. The branching ratios and the transition energies for the beta and K capture branches are those reported in this paper. The lifetime of Tl^{204} was recently reported[13] to be 3.9 yr, which is longer than the previous value[1] by more than a year. The shape of the beta-spectrum and the log f_1t value[14] (8.84) supports the original proposal by Saxon and Richards that the beta-decay be classed as a $\Delta I=2$, yes (first forbidden) type transition.

The authors acknowledge with pleasure the valuable guidance of Dr. M. Goldhaber in all phases of this work and the aid generously contributed by Dr. M. Fuchs with theory and calculations. Miss J. Snover kindly helped with the computations and A. Layzer contributed to the coincidence studies on the inner bremsstrahlung. We wish to thank Dr. L. Mandansky for giving us a sample of Tl^{204} and Dr. C. S. Wu for allowing us to see preprints of her data on Tl^{204}.

APPENDIX I

The Correction for the Escape of Electrons from the Surface of a Crystal

It is assumed that the crystal is large compared with the range of the electrons so that a surface of the crystal can be considered to be an infinitely large interface. We make the simplifying assumption that the path of an individual electron is a straight line in the crystal, equal in length to its range, and that the density of light along the path of an electron in a scintillation is constant.

If an electron of energy E' escapes from a crystal

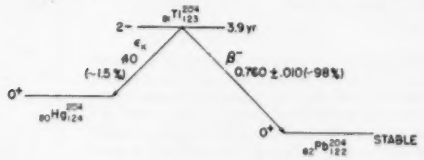

FIG. 6. Decay scheme of Tl^{204}.

[11] P. Morrison and L. I. Schiff, Phys. Rev. **58**, 24 (1940). J. M. Jauch, Oak Ridge National Laboratory Report 1102 (unpublished); P. R. Bell, Oak Ridge National Laboratory Report 1164 (unpublished).

[12] The notation is that introduced in a review article by M. Goldhaber and R. D. Hill (to be published).

[13] G. Harbottle, Brookhaven National Laboratory Report 132 (S-11), p. 100 (unpublished).

[14] E. Feenberg and G. L. Trigg, Revs. Modern Phys. **22**, 399 (1950); J. Davidson, Phys. Rev. **82**, 48 (1951).

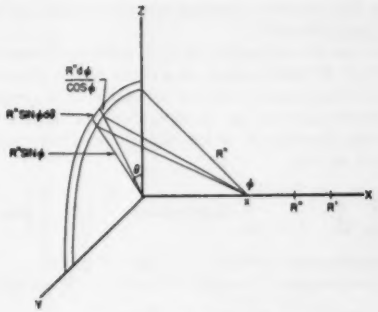

FIG. 7. Diagram for the electron escape calculation.

before it gives up all its energy, a pulse which should have an energy E' will appear to have the energy E'' where $E'>E''$. Let the range of electrons whose energy is E' be R' and E'' be R''. Let $N_{R'}d\tau$ be the number of electrons of energy E' produced in a volume $d\tau$ per second. Then if the YZ plane is taken to be the crystal surface, electrons of energy E' originating from a volume $d\tau$ at a depth $x<R''$ which escape from the surface in a ring of radius $R''\sin\phi$ will produce a scintillation of apparent energy E'' (Fig. 7).

The solid angle presented by this ring to the element of volume $d\tau$ is

$$\int_0^{2\pi}\frac{(R'')^2}{(R'')^2}\sin\phi d\phi d\theta=2\pi\sin\phi d\phi,$$

and

$$((N_{R'})d\tau/4\pi)2\pi\sin\phi d\phi=\tfrac{1}{2}N_{R'}\sin\phi d\phi d\tau$$

is the number of pulses per second of energy E'' due to electrons of energy E' emerging from the volume element $d\tau$.

If we consider a volume whose base is a square centimeter at the surface of the crystal, the integration over $d\tau$ can be replaced by one over dx, between the limits $x=0$ and $x=R''$. (Electrons of energy E' originating at depths greater than R'' will produce pulses of energy greater than E'' regardless of the angle at which they emerge from the crystal.) The total number of pulses of energy E'' due to electrons of energy E' in the volume of integration is

$$N_{E''}=\int_0^{R''}(N_{R'}/2)\sin\phi d\phi dx.$$

But $x/R''=-\cos\phi$ and, differentiating with respect to R'' and ϕ,

$$[-x/(R'')^2]dR=\sin\phi d\phi,$$

$$N_{E''}=-\int_0^{R''}\frac{N_{R'}}{2}\frac{x}{(R'')^2}dR''dx$$

$$=\frac{-N_{R'}}{2(R'')^2}dR''\int_0^{R''}xdx=-\frac{N_R}{4}dR'',$$

where $N_{E''}$ is now a counting rate per constant energy (or range) difference.

One can also calculate the total number of electrons of energy E' which escape as a check of the above result. If this is again done for a volume with a square centimeter base at the surface, the total number of electrons of energy E' which escape from a volume element $d\tau$ at x is

$$\int_0^{2\pi}\int_0^{\cos^{-1}x/R'}\frac{N_{R'}}{4\pi}\sin\phi d\phi d\theta dx=\frac{N_{R'}}{2}\left[1-\frac{x}{R'}\right]dx.$$

Integration over x from 0 to R' gives $N_{R'}/4R'$.

If we integrate $N_{E''}$ over R'' from 0 to R' we get

$$\int_0^{R'}\frac{N_{R'}}{4}dR''=\frac{N_{R'}}{4}R',$$

as we should, since the total count due to degraded pulses should equal the total number of electrons escaping.

The above result states that electrons of energy E' which escape from the crystal are degraded with equal probability into all energies below E', since the above results are independent of E' or E''. The fraction of electrons of energy E' which escape from the crystal is equal to $\frac{1}{4}$ the fraction of the volume of the crystal which lies in a surface layer of depth R'. These two facts can be used in a graphical method to correct distorted beta-spectra for the effect due to the escape of electrons.

A similar analysis can be made for the escape of photons from a crystal, substituting an exponential absorption for the range. The solution in this case involves the Γ-function, which is somewhat awkward, but one can consult tables of this function to obtain numerical answers.

APPENDIX II

Outline of the Calculation of the Transition Energy in K Orbital Electron Capture from a Knowledge of the Branching Ratio[15]

Marshak's lifetime formulas for first-forbidden β^--decay and orbital electron capture are, respectively,

$$\frac{1}{\tau_T}=\frac{1}{\tau_0}\frac{|M|^2}{[1.3]^2}R^2B_1(z,W_0)$$

and

$$\frac{1}{\tau_e}=\frac{1}{\tau_0}\frac{|M|^2}{|1.3|^2}R^2B_e'(z,W_0),$$

where τ_0 is a decay constant, R is the nuclear radius, M is a nuclear matrix element, and the B's are quantities which depend on the order of the transition, on the nuclear charge, and on the energy difference between the parent and product nuclei.

Dividing one equation by the other one gets

$$\frac{\tau_e}{\tau_T}=\frac{B_1(z,W_0)}{B_e^{(1)}(z,W_0)}=\frac{\%\ \beta\text{ emission}}{\%\ K\text{ capture}}.$$

Except for a numerical factor, B_1 is the same function as Davidson's[7] f_1 (in the low Z limit) and can be calculated with the help of Feenberg and Trigg's[14] curves of f_0.

$B_e^{(1)}$ is given by Marshak, and for K orbital electron capture alone it has the form

$$B_e^{(1)}=\tfrac{1}{2}\pi(W_0+W_K)^4n_Kg_K^2,$$

where n_K is the number of electrons in the K shell and g_K is the "large" radial Dirac wave function, for which an expression is given by Marshak. Using these relationships one can solve for W_0.

[15] This method for calculating the transition energies was very kindly shown to us by M. Fuchs of this laboratory.

PHYSICAL REVIEW VOLUME 88, NUMBER 5 DECEMBER 1, 1952

The Strong-Focusing Synchroton—A New High Energy Accelerator*

ERNEST D. COURANT, M. STANLEY LIVINGSTON,† AND HARTLAND S. SNYDER
Brookhaven National Laboratory, Upton, New York

(Received August 21, 1952)

Strong focusing forces result from the alternation of large positive and negative n-values in successive sectors of the magnetic guide field in a synchrotron. This sequence of alternately converging and diverging magnetic lenses of equal strength is itself converging, and leads to significant reductions in oscillation amplitude, both for radial and axial displacements. The mechanism of phase-stable synchronous acceleration still applies, with a large reduction in the amplitude of the associated radial synchronous oscillations. To illustrate, a design is proposed for a 30-Bev proton accelerator with an orbit radius of 300 ft, and with a small magnet having an aperture of 1×2 inches. Tolerances on nearly all design parameters are less critical than for the equivalent uniform-n machine. A generalization of this focusing principle leads to small, efficient focusing magnets for ion and electron beams. Relations for the focal length of a double-focusing magnet are presented, from which the design parameters for such linear systems can be determined.

BETATRON OSCILLATIONS

RESTORING forces due to radially-decreasing magnetic fields lead to stable "betatron" and "synchrotron" oscillations in synchrotrons. The amplitudes of these oscillations are due to deviations from the equilibrium orbit caused by angular and energy spread in the injected beam, scattering by the residual gas, magnetic inhomogeneities, and frequency errors. The strength of the restoring forces is limited by the

* Work done under the auspices of the AEC.

† Massachusetts Institute of Technology, Cambridge, Massachusetts.

stability condition:[1] $0<n<1$, where $n=-(r/B)(dB/dr)$. Frequencies of vertical and radial oscillations are given in terms of the frequency of revolution f_0 by

$$f_z=n^{\frac{1}{2}}f_0; \quad f_r=(1-n)^{\frac{1}{2}}f_0. \tag{1}$$

The corresponding amplitudes are inversely proportional to these oscillation frequencies, for a given angular deviation. Therefore, the aperture required to accommodate either mode can only be reduced at the expense of the other mode, and the minimum aperture for both occurs with $n=0.5$.

The focusing forces can be greatly strengthened by letting n vary in azimuth. Suppose the circular orbit to consist of N sectors of equal length with n_1 and n_2 in alternate sectors. The equations of vertical and radial oscillations are then

$$d^2z/d\theta^2+n_1z=0; \quad d^2r/d\theta^2+(1-n_1)r=0; \quad \text{(odd sectors).} \tag{2a}$$

$$d^2z/d\theta^2+n_2z=0; \quad d^2r/d\theta^2+(1-n_2)r=0; \quad \text{(even sectors).} \tag{2b}$$

Solutions can be obtained by the use of recursion formulas, and are of the form

$$Z_s=Ae^{i2\pi\mu_z s} \quad \text{and} \quad R_s=Be^{i2\pi\mu_r s}, \tag{3}$$

where the coefficient μ_z is given by

$$\cos 2\pi\mu_z=\cos\frac{2\pi n_1^{\frac{1}{2}}}{N}\cos\frac{2\pi n_2^{\frac{1}{2}}}{N}-\frac{n_1+n_2}{2(n_1n_2)^{\frac{1}{2}}}\sin\frac{2\pi n_1^{\frac{1}{2}}}{N}\sin\frac{2\pi n_2^{\frac{1}{2}}}{N}. \tag{4}$$

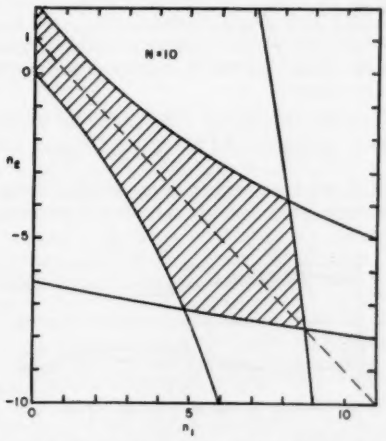

FIG. 1. Region of stability for both radial and vertical oscillations for $N=10$ sectors with n values alternating between n_1 and n_2.

[1] D. W. Kerst and R. Serber, Phys. Rev. 60, 53 (1941).

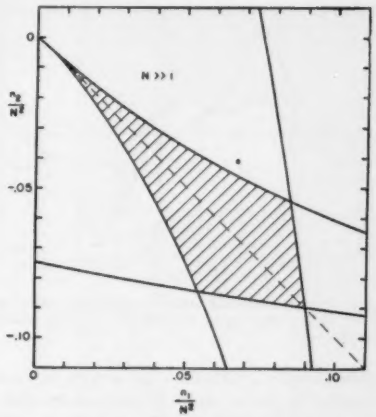

FIG. 2. Region of stability for radial and vertical oscillations for a large number of sectors N, in terms of the parameters n_1/N^2 and n_2/N^2.

The coefficient μ_r is given by the same expression, with n_1 and n_2 replaced by $(1-n_1)$ and $(1-n_2)$, respectively. If the motion is to be stable for both radial and vertical oscillations, the limits are established by the conditions

$$-1<\cos 2\pi\mu_z<1, \quad -1<\cos 2\pi\mu_r<1. \tag{5}$$

These limits have been plotted in Fig. 1 for the specific value $N=10$, and the region of stability is indicated. It is observed that the region of stability is widest for $n_2\simeq -n_1$. Figure 2 shows the stable region for very large N, and the coordinates are given in terms of n_1/N^2 and n_2/N^2. The range of stable values of n is widest when N is large and when $n_2=-n_1$, and the center of the region of stability ($\cos 2\pi\mu=0$) occurs for

$$|n|=N^2/16. \tag{6}$$

The effective frequency of the "betatron" oscillations is given by:

$$f_z=f_r=(\mu N/2)f_0 \quad \text{(for large } N\text{)}, \tag{7}$$

which can be compared with the frequencies given in Eq. (1) for constant n. Therefore, the amplitudes of oscillation and the aperture requirements can be made much smaller by the use of a large number of sectors N and correspondingly large positive and negative values of n in successive sectors. As a numerical example, consider a synchrotron of 240 alternating sectors, with $n_1=3600$ and $n_2=-3600$. The radial aperture requirement is about 1/24 that for the corresponding synchrotron with a constant n of 0.6, and 1/20 for the vertical aperture. Ion trajectories are not sinusoidal as in the standard synchrotron, but are composed of sections of alternately harmonic and hyperbolic functions. Figure 3 is a schematic illustration of two typical oscillating orbits computed for the case discussed in the

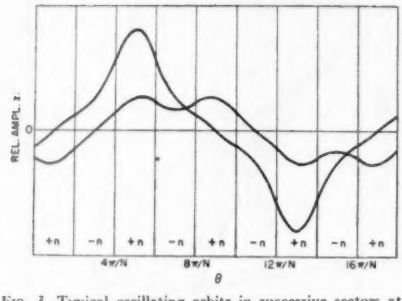

FIG. 3. Typical oscillating orbits in successive sectors at the center of the stability region ($|n|=N^2/16$), showing periodicity in 8 sectors.

foregoing showing a periodicity in 8 sectors, so there are 30 complete "betatron" oscillations around the orbit. The maximum amplitude of this nonharmonic function is found to be about twice that for a sine wave of the same frequency and starting with an equal angle at the axis. This factor has been included in estimating the aperture requirements above.

Deviations from a constant value of field gradient in the aperture have been considered. These would lead to nonlinear terms in Eq. (2). It is found that, provided the magnet sectors are symmetrical about their centerlines, such nonlinear terms do not give rise to any secular variations in the amplitudes of the oscillations. This same analysis shows that the fringing fields at the ends of the sectors, associated with the sharp change from large positive to large negative gradients, do not result in amplitudes which increase with time.

A practical requirement in the construction of such a field is that the sectors be separated by short gaps, to accommodate magnet windings, vacuum pump outlets, and other equipment. The effect of adding such short field-free sections is to change the relation given in Eq. (4) between μ and the parameters N and n, equivalent to adding terms on the right-hand side of the relation. The behavior of the betatron oscillations will be similar, and the results will not be significantly different if the length of the straight sections is less than 25 percent of that of the sectors.

SYNCHRONOUS STABILITY

The problems of "synchrotron" oscillations are the same as for the conventional proton synchrotron as discussed, for example, by Blachman and Courant,[2] except that the relation between particle energy and the circumference of the equilibrium orbit is changed. If the momentum of the particle differs from its value at the central circular orbit, the new equilibrium orbit is no longer a circle, but is a periodic alternation of harmonic and hyperbolic functions superimposed on a circle of a different equilibrium radius. The orbits for higher energy and lower energy particles than those at the central orbit are illustrated in Fig. 4, in which the curvature of the central orbit is neglected, so that it appears as a straight line. The dotted lines through the displaced orbits represent their mean radial positions. If the gradients in the two sectors are equal and opposite, the average field along these dotted lines is the same as that of the central orbit. However, the average field along the actual displaced orbit for the upper curve (energy excess) is higher than that of the dotted line in both sectors, and smaller in both sectors for the lower orbit. This illustrates the spread in mean orbit radius associated with a spread in momentum. If the momentum deviation is Δp, the fractional change in the circumference ΔL is given by

$$\Delta L/L=\alpha\Delta p/p,$$

where

$$\alpha=\frac{2-n_1-n_2}{2(1-n_1)(1-n_2)}-\frac{N}{2\pi}\frac{(n_1-n_2)^2}{[(1-n_1)(1-n_2)]^{\frac{1}{2}}}\times\frac{\sin\phi_1\sin\phi_2}{(1-n_1)^{\frac{1}{2}}\sin\phi_1\cos\phi_2+(1-n_2)^{\frac{1}{2}}\sin\phi_2\cos\phi_1},\quad(8)$$

$$\phi_1=(1-n_1)^{\frac{1}{2}}\pi/N,\quad\text{and}\quad\phi_2=(1-n_2)^{\frac{1}{2}}\pi/N.$$

For our particular case, with $n_1=-n_2=N^2/16\gg1$, this reduces to

$$\alpha=4.85/|n|,\quad(9)$$

while for a conventional synchrotron $\alpha=(1-n)^{-1}$.

Synchrotron stability is governed by the change of the period of revolution with momentum. In the standard synchrotron a particle with excess momentum traverses a path of larger radius and requires a longer time, since the relative increase in radius is greater than the relative increase in velocity. This is evident from the relation

$$\frac{\Delta t}{t}=\frac{\Delta L}{L}-\frac{\Delta v}{v}=\left(\alpha-\frac{E_0^2}{E^2}\right)\frac{\Delta p}{p}=\gamma\frac{\Delta p}{p},\quad(10)$$

where E_0 and E are the rest energy and total energy of the particle, respectively. In our case α is very small if

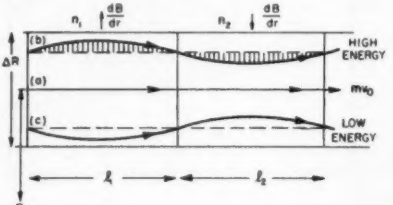

FIG. 4. Stable synchronous orbits in the radial aperture of the strong-focusing synchrotron. Higher energy particles traverse an average magnetic field larger than that at the central orbit, and vice versa, which leads to the strong radial compaction of orbits.

[2] N. M. Blachman and E. D. Courant, Rev. Sci. Instr. **20**, 596 (1949).

$|n|$ is large, so γ is negative for low particle energies, and changes sign at an energy $E_1=E_0/\alpha^{\frac{1}{2}}$, while for the ordinary synchrotron γ is always positive.[3] This means that acceleration occurs on the rising side of the voltage wave for low energies. For example, if the peak voltage is twice the mean energy increment per turn, the equilibrium phase angle is 30° as against 150° for the conventional synchrotron. This leads to electrical defocusing, as in the linear accelerator, but is more than compensated by the strong magnetic focusing described earlier.

As the energy passes through the value E_1, the equilibrium phase angle shifts from the rising to the falling slope of the voltage curve. At this point the frequency is independent of radius and of energy, as in the modification of the fixed-frequency cyclotron proposed by Thomas.[4] This transition occurs at a rather large energy. For example, in the design study for a 30-Bev accelerator described below, it occurs at about 25 Bev. The introduction of straight sections between sectors will modify this transition point, and may increase it above the top energy limit. Otherwise, it is reasonably certain that the radiofrequency phase can be shifted at this point to avoid a loss in intensity.

Another consequence of Eq. (8) is that the momentum spread Δp associated with a given radial aperture ΔR can be very large if the n-values are large. If we use the example of $|n|=3600$, the field will vary from zero to twice its average value in a radial distance of 2 inches, with the consequence that within this aperture $\Delta p/p$ can be as large as ± 10 percent! This extremely large momentum acceptance means that at injection the errors in injection energy and in the frequency of the accelerating voltage can be of this same order of magnitude. Furthermore, it shows that the radial amplitude of the synchronous oscillations is reduced by nearly the same factor α, as compared to the ordinary synchrotron.

DESIGN CONCEPTS FOR A 30-BEV ACCELERATOR

The potentialities of this strong-focusing principle can be illustrated by describing its application to the design of a high energy accelerator. We have chosen to design for 30-Bev protons, which is 10 times the maximum energy of the Brookhaven cosmotron, and which requires an orbit radius of about 300 ft with a guide field of about 11 kilogauss. The aperture within the vacuum chamber can be as small as 1×2 inches, and still provides a safety factor of 2 over the computed maximum oscillation amplitudes. With this radial aperture the n value is determined by the radius and by the field gradient of 1.1×10^4 gauss/inch:

$$|n|=-\frac{R}{B}\frac{dB}{dr}=\frac{300\times12\times1.1\times10^4}{1.1\times10^4}=3600. \qquad (11)$$

[3] In reference 2 it is pointed out that γ can also be negative in a conventional synchrotron with straight sections.

[4] L. H. Thomas, Phys. Rev. **54**, 580, 588 (1938).

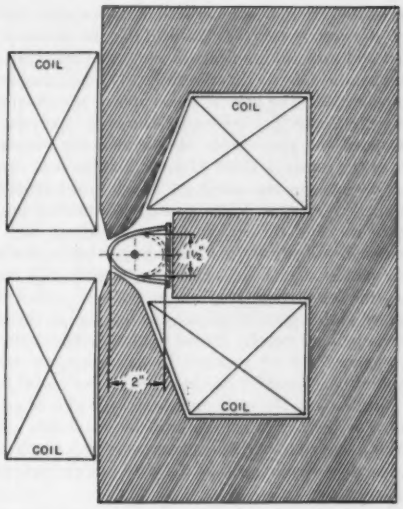

FIG. 5. Cross section of E-magnet with poles shaped to give $n=3600$ at an orbit radius of 300 ft. The vacuum chamber illustrated has an internal aperture of about 1×2 inches.

With this value of n the optimum number of magnet sectors $N=240$, and the length of each sector is 7.85 ft. We assume that short straight sections will be needed between sectors, and choose a length of 2.0 ft. The chosen injection energy of 4 Mev and the angle of divergence at injection of 10^{-3} radian, are those available from the Van de Graaff injector for the cosmotron. Detailed calculations of "betatron" oscillation amplitudes for this angle at injection, and those due to gas scattering at a residual pressure in the chamber of 1×10^{-6} mm of Hg, show that the maximum amplitudes (at injection) will be included within a square area of 0.5×0.5 inch. The radial amplitude of synchronous oscillations at injection depends on the frequency harmonic used for acceleration; a sufficiently high harmonic should be used to include the entire allowed phase oscillation range within the energy and radial limits defined by the chamber. This energy range accepted by the 2-inch radial aperture is found to be ± 10 percent, which is larger than the practical energy spread of the injector by a large factor. The conclusion from such studies is that the 1×2 inch aperture is entirely adequate for the chamber.

The basic magnet structure chosen to provide the large magnetic field gradients is a "3-pole" magnet with a single return circuit which can be called an "E-magnet," illustrated in Fig. 5. Two poles are shaped as rectangular hyperbolas, and the third "pole" is a vertical surface of iron along the vertical axis of the hyperbolas to maintain zero field at the center of the

coordinate system (the inner wall of the vacuum chamber). Between these poles the field has the property of equal and uniform gradients in the radial and vertical directions, as long as the iron surfaces remain magnetic equipotentials. The field at the center of the chamber, along the 2-inch gap chosen for the basic aperture, is considered the guide field. At injection the magnetic field at the center is about 30 gauss, and the field varies from 60 gauss to zero along the 2-inch radial extent of the aperture. As the field approaches saturation in the iron at the tips, the area of uniform-gradient, high n-value field will shrink to a smaller aperture, estimated to be no less than 1 inch. However, at such high energies, the oscillation amplitudes will be sufficiently damped so that aperture requirements are much smaller, and no loss in intensity should result. Model studies of the magnet will be required to determine the exact shape of pole faces for maximum extent of useful field at injection and the maximum practical value of guide field. For the design calculations this maximum guide field is assumed to be 11 kilogauss across the 2-inch gap, leading to a requirement of 4.5×10^4 ampere turns for excitation.

The alternation of field gradients in successive sectors can be accomplished by assembling the magnets alternately with outside and inside return legs, using the E-shape described above. Figure 6 is an illustration, not to scale, of this alternate assembly of outside-E and inside-E magnets. The center line along the axis of the chamber is on the circle of 300-ft radius, and is the axis of reversal of alternate sectors. This assembly retains many of the advantageous features of the C-magnet design. The magnet gap is available along its entire length for measurements, and the open side provides access for vacuum testing and for inspection. Injection is possible at small angles of inflection, even though the connecting straight sections are short. Ejection of a tangential emergent beam is simplified, and radiations, such as charged mesons from targets within the aperture, can be emitted through the thin chamber walls for experimental studies. On the other hand, the magnetic disadvantages of the C-magnet, which apply to the uniform-n accelerator, are largely averaged out by the use of alternating E's. The decrease in aperture due to fringing fields as the iron approaches saturation is now largely cancelled, and the primary effect is a reduction of n-values and a slight

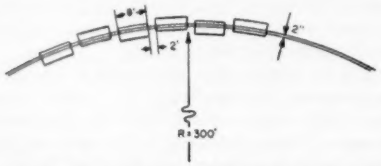

FIG. 6. Method of assembly of alternately inside-E and outside-E magnets around an orbit, with straight sections between sectors.

decrease in the focusing forces as particles approach maximum energy. Variations in the n-value due to remanent fields and eddy currents are unimportant. Thick iron laminations can be used, of 1- or 2-inch plate, determined by the economics of magnet construction.

The cross-sectional area assigned to the magnet windings is set by the power rating of the coil. Several factors enter in choosing the magnitude of the power. The primary consideration is the cost of the power, which is a significant item in operating costs. Another is the advantage to be gained by reducing the coil heating per unit length sufficiently to make water- or air-cooling of the coil windings unnecessary. Both these factors indicate a large coil cross section which means a large initial cost for the conductors and a proportionate increase in the dimensions and costs of the iron return circuit. It can also be argued that the power consumption per cycle should not exceed the circulating power required to provide the stored energy in the magnetic field. These features require detailed analysis and balancing. For the purposes of this study, we have chosen to use about half the power rating and the same duty cycle as for the present cosmotron, or 300 kilowatts averaged over a duty cycle of 1 sec up, 1 sec down, repeated at 5-sec intervals. With these assumptions the required cross section of copper windings is about 24 in.[2] Following the design shapes illustrated in Fig. 5 we find that the E-magnet iron has external dimensions of about 12 inches wide by 20 inches high, approximately the size illustrated in the figure. Since the cross section of iron is about $\frac{1}{10}$ that of the cosmotron, the total weight of iron is about the same; the weight of copper in the windings is increased by about a factor of 5.

The acceleration voltage required to attain 30-Bev energy in 1 second is about 100 kilovolts per turn, or 100 times larger than that for the cosmotron. It is clear that many accelerating units must be used, distributed around the orbit and properly phased, primarily to reduce the radiofrequency power. It is also likely that a high harmonic of the orbital frequency would be advantageous. The radial amplitude of synchronous oscillations will be reduced by the factor $h^{-\frac{1}{2}}$, where h is the order of the harmonic. The harmonic order should be a submultiple of the number of accelerating units around the orbit, in order to simplify the problems of phasing. Several methods of applying the accelerating field to the particles are available. That used in the cosmotron involves a ferrite-loaded cavity; in this case, with sectors of 8-ft length, one might use the metal-pipe vacuum chamber as a "drift tube." The driving frequency increases with time as in the cosmotron, and must be modulated over a frequency ratio of 1 to 12. The broad-band power amplifiers used to drive the accelerating units will be one of the most difficult and costly components.

The frequency tolerance is given by

$$\frac{\Delta f}{f}=\frac{|\alpha-E_0^2/E^2|}{\alpha}\frac{\Delta L}{L}=\left|\frac{E^2-E_1^2}{E^2}\right|\frac{\Delta L}{L}. \quad (12)$$

At injection and at energies small compared with the phase-reversal energy E_1, the allowable frequency error is large, and the frequency cycle can be "pre-cut." However, as the energy approaches E_1 the allowed error becomes very small, and precision methods of frequency control will be required. Electrical pick-up pulses from the beam of particles can be used for this frequency control, as can be demonstrated with the cosmotron.

The vacuum chamber can be constructed of thin-walled, nonmagnetic tubing, such as stainless steel. The effect of eddy currents will be negligible. Such a chamber can serve many purposes. As indicated, it can serve as a "drift tube" for radiofrequency acceleration. Units can also be utilized as sensing electrodes to observe the beam pulses. Such a thin metal-walled tube can be heated and out-gassed under vacuum to reduce the residual pressure in the chamber. Small vacuum pumps can be located at the straight sections between sectors at 10-foot intervals.

The injector assumed in this study is the equivalent of the present cosmotron 4-Mev Van de Graaff generator, although it is possible that higher energies would be helpful, as from a linear accelerator. Injection could be accomplished by electrical deflection at a small angle at one of the straight sections. The time interval for acceptance, about $\frac{1}{3}$ of a turn, is about 10 microseconds. Pulse injection at 1 milliampere would result in about 5×10^{10} particles being accepted, equivalent to the intensity per pulse of the present cosmotron. The radial contraction per turn at injection would be about 1 mm at 4 Mev, which seems large enough to result in a reasonable capture efficiency. The strong focusing and damping during further acceleration will retain the beam within the aperture, even through the synchrotron phase-reversal point. It seems probable that final intensities will be equivalent to those obtained with the cosmotron.

ION FOCUSING IN LINEAR SYSTEMS

An extension of the theory of magnetic focusing by successive reversals of field gradients leads to concepts which are applicable to ion optics and to linear accelerators. The principle involves a similar sequence of alternately converging and diverging magnetic lenses, and can be visualized most readily by considering the analogy to lens optics. A single region of inhomogeneous magnetic field which produces convergence of an ion beam in one plane will produce divergence in the plane at right angles. Consider a beam of ions having a momentum $p=BR$ (where R is the radius of curvature in a field B), moving in the x direction in a field with components: $B_x=0$, $B_y=kz$, and $B_z=ky$. The equations of motion, which are equivalent to Eqs. (2) for the circular orbit, become

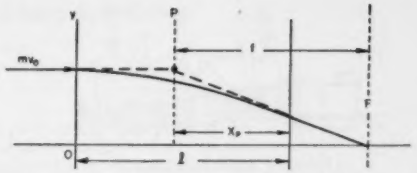

FIG. 7. Definition of focal length f and principal plane distance x_P for a convergent magnetic lens of length l.

$$\frac{d^2y}{dx^2}+\frac{1}{BR}\frac{dB_z}{dy}y=0, \quad \text{or} \quad \frac{d^2y}{dx^2}+Ky=0; \quad (13a)$$

$$\frac{d^2z}{dx^2}-\frac{1}{BR}\frac{dB_y}{dz}z=0, \quad \text{or} \quad \frac{d^2z}{dx^2}-Kz=0. \quad (13b)$$

The lens property of such a field is illustrated in Fig. 7, which shows the path of a particle entering the field parallel to the axis, in the convergent xy plane. If the length of the region of inhomogeneous field is l, the particle crosses the axis at F (the focal point), converging from a point P which defines the principal plane. The distance to the principal plane x_p and the focal length f measured from this plane are given by

$$x_P=\frac{1-\cos K^{\frac{1}{2}}l}{K^{\frac{1}{2}}\sin K^{\frac{1}{2}}l}, \quad (14)$$

$$f=\frac{1}{K^{\frac{1}{2}}\sin K^{\frac{1}{2}}l}, \quad (15)$$

where K defines the unit of length and is given by

$$K=\frac{1}{BR}\frac{dB_y}{dz}=\frac{1}{BR}\frac{dB_z}{dy}. \quad (16)$$

A sequence of two lenses of this class, separated by a distance q between principal planes, having coefficients K_1 and K_2 and lengths l_1 and l_2, will have a focal length given by the familiar lens equation

$$1/F=1/f_1+1/f_2-q/f_1f_2. \quad (17)$$

It can be noted at this point that F is positive, and so the combination of lenses is converging, if $f_2=-f_1$. This means that two equally strong converging and diverging lenses will be convergent. Applying this to the magnetic lens case by inserting the relations for principal plane distances and focal lengths for the two lenses, the combined focal length becomes

$$1/F=K_1^{\frac{1}{2}}\sin K_1^{\frac{1}{2}}l_1\cos K_2^{\frac{1}{2}}l_2+K_2^{\frac{1}{2}}\sin K_2^{\frac{1}{2}}l_2\cos K_1^{\frac{1}{2}}l_1 -dK_1^{\frac{1}{2}}K_2^{\frac{1}{2}}\sin K_1^{\frac{1}{2}}l_1\sin K_2^{\frac{1}{2}}l_2. \quad (18)$$

In this expression the distance d is the distance of sepa-

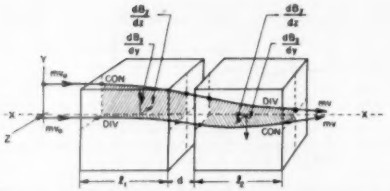

FIG. 8. Illustration of double-focusing in two magnetic lenses with field gradients in opposite directions, showing the alternately convergent and divergent forces and the net convergence of the system.

ration between the faces of the two magnetic lenses. If, for a simple example, we choose $-K_2=K_1=K$ and $l_2=l_1=l$, the equation for focal length reduces to

$$1/F=K^{\frac{1}{2}}\{\sinh K^{\frac{1}{2}}l\cosh K^{\frac{1}{2}}l-\sinh K^{\frac{1}{2}}l\cos K^{\frac{1}{2}}l+dK^{\frac{1}{2}}\sin K^{\frac{1}{2}}l\sinh K^{\frac{1}{2}}l\}. \quad (19)$$

The condition that the lens system be convergent is that the argument $K^{\frac{1}{2}}l$ be positive and not greater than some value approaching π, depending on the magnitude of the separation distance d. Thus, the lens can be designed for any desired focal length by suitable choice of $K^{\frac{1}{2}}l$ and d. In this simple case where the K's and l's are equal, the focal lengths are equal for displacements in both the xy and xz planes, as becomes evident when $-K$ is substituted for K in Eq. (19). However, the locations of the principal planes will differ, depending on whether the initial action is converging or diverging. This leads to an astigmatic image in the simple case assumed. This astigmatism can be corrected by modifying the lens system. The double focusing of the compensating lenses is illustrated in Fig. 8, showing alternately divergent and convergent forces in the two sections.

A doubly-divergent magnetic field having uniform and equal values of dB_x/dy and dB_y/dz exists between the poles of a 4-pole magnet with pole faces shaped as rectangular hyperbolas; the field is zero along the x axis. Figure 9 shows a cross section of such a magnet. The complete lens would consist of two such magnet units of length l, with the second unit rotated by 90° relative to the first. The effective aperture of such a lens would be a circle of diameter $D=(2)^{\frac{1}{2}}a$, where a is the spacing between the centers of the hyperbolic poles. Consider a numerical example in which the aperture, a, is 2 inches and the maximum field across this 2-inch gap is 10 kilogauss. The field gradient $dB/dy=dB/dz=10^4$ gauss/inch. Let us design a magnet to focus protons of 4-Mev energy, which have a momentum BR of about 10^5 gauss-inches, so $K=0.1$. If we choose $K^{\frac{1}{2}}l=\pi/4$, and the spacing d is 2 inches, the length of each magnet unit l is 2.5 inches, the total length is 7.0 inches, and the focal length computed from Eq. (19) is 4.4 inches. Choice of a smaller value of $K^{\frac{1}{2}}l$ will lead to shorter magnets and longer focal lengths. A simpler relation for computing focal lengths can be

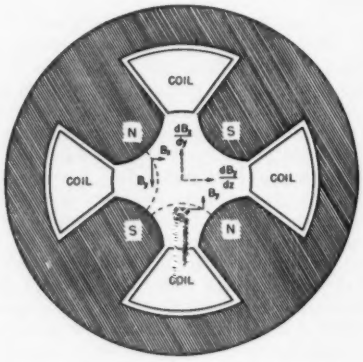

FIG. 9. Cross section of a 4-pole magnet with hyperbolic pole faces to produce uniform and equal field gradients dB_x/dy and dB_y/dz.

obtained from Eq. (19) by expanding in terms of the arguments and using only the first significant terms:

$$1/F=K^2l^2\{\tfrac{2}{3}l+d\}. \quad (20)$$

A continuous sequence of such convergent systems is itself convergent if the separation distance D between successive image and object focal points is less than $\pm 2F$. This relationship is equivalent to that given in Eq. (4) for the circular orbit. Thus, magnetic lenses of the type described can be used in succession to maintain a focused beam over long distances, as in the linear accelerator.

Radial Focusing in the Linear Accelerator*

J. P. BLEWETT
Brookhaven National Laboratory, Upton, New York
(Received August 26, 1952)

The focusing mechanism described in the previous paper is applied to the linear accelerator. The defocusing forces in the linear accelerator are derived, and the particular example of a 4-million-volt accelerator 10 meters long is discussed. It is shown that the defocusing forces can be compensated by magnetic or electric lenses of the alternating gradient type using easily attainable field gradients. For example, a defocusing field gradient of 1000 volts per centimeter on a 100-kv proton beam can be compensated by a lens 20 cm long with field gradients of the order of 1000 gauss per centimeter.

I. INTRODUCTION

THE method of focusing proposed by Courant, Livingston, and Snyder[1] for use in high energy synchronous accelerators seems to be applicable also to the linear accelerator. The usefulness of the linear accelerator to date has been limited by the defocusing which is associated with the mechanism of acceleration. In this paper a brief discussion of the focusing forces in the linear accelerator is followed by a presentation of the method of application of magnetic or electric focusing to compensate for these forces.

Although the linear accelerator is of considerable interest in its own right, it is particularly interesting to our laboratory as a possible injector for high energy positive ion accelerators. If the radial defocusing can be controlled, a linear accelerator injector would present important advantages associated with its geometry and the accessibility of its components. We shall, accordingly, confine this discussion to accelerators in the energy range low enough that relativistic effects can be neglected. Since, in general, the defocusing fields become weaker as the velocity approaches the velocity of light, and since the magnetic focusing procedures to be discussed are still valid at relativistic velocities, the limitation of the discussion to the nonrelativistic range is legitimate.

II. THEORY OF THE LINEAR ACCELERATOR

The z axis of a cylindrical coordinate system will be taken to be coincident with the axis of the accelerator. MKS units will be used.

Axial Electric Field Pattern

The separation between accelerating gaps, L, will be the distance traveled by a particle during one-half cycle of the accelerating signal

$$L=\pi v/\omega, \tag{1}$$

where v is particle velocity and $\omega/2\pi$ is the frequency of the accelerating signal. Now if w is the energy (measured in volts) gained per gap by a particle at the equilibrium phase of the accelerating signal, the rate of change of energy W of the equilibrium particle with distance will be

$$dW/dz=\omega w/\pi v. \tag{2}$$

This relation can be integrated if we assume a specific form for $w(z)$.

For our present purpose, we shall retain sufficient generality if we set

$$w=w_f(z/z_f)^n, \tag{3}$$

where w_f is the energy gain at the final gap and z_f is the length of the accelerator. It should be noted here that distances and times are to be measured on scales representing an accelerator whose injection is at zero volts.

We now substitute $\frac{1}{2}mv^2$ for W in Eq. (2) and integrate to obtain

$$v=v_f(z/z_f)^{(1+n)/2}, \tag{4}$$

$$(z/z_f)^{(2-n)/2}=(2-n)v_f t/3z_f, \tag{5}$$

and

$$W=W_f(z/z_f)^{(3+2n)/3}. \tag{6}$$

The accelerating field will be a complicated function of position along the tube. It can, however, be analyzed into component traveling waves, and it is evident that the only traveling wave component whose effects will average to a value different from zero is the component which travels with the particles at their average velocity. This component will have the form

$$E_z=E_0 f(z)\sin\omega\left[t-\int(dz/v)\right]. \tag{7}$$

If the equilibrium particle maintains a constant phase on this wave, $f(z)$ will depend on z in the same fashion as does dW/dz, which we can derive from (6). To retain E_0 as a quantity having the dimensions of an electric field, we write

$$f(z)=\frac{dW}{dz}\Big/\left(\frac{dW}{dz}\right)_f.$$

In terms of the assumption of Eq. (3) we can rewrite

* Research carried out under contract with the AEC.
[1] Courant, Livingston, and Snyder, preceding article [Phys. Rev. 88, 1190 (1952)].

(7) in the form

$$E_s = E_0(z/z_f)^{(2n-1)/3}\sin\omega\left[t-\frac{3(z/z_f)^{(2-n)/3}z_f}{(2-n)v_f}\right]. \quad (8)$$

The form of E_0 is discussed below and appears in Eq. (13).

Particle Phase Oscillations

In order to evaluate E_0 and to determine the possible limits of n, it is necessary to investigate the phase oscillations of the accelerated particles. Thus far, we have discussed only particles which travel at the equilibrium phase ϕ_0 and at the velocity v of the electric field wave. For a general particle, we now define a quantity δ in terms of which we shall discuss the particle velocity $\dot{z}$. δ will be defined by

$$\int dz/v = t-\phi_0/\omega-\delta/\omega, \quad (9)$$

whence we derive the relations

$$\dot{z} = v(1-\dot{\delta}/\omega), \quad (10)$$

$$\ddot{z} = -v\ddot{\delta}/\omega+v(dv/dz)(1-\dot{\delta}/\omega)^2. \quad (11)$$

We now substitute from (7), (9), and (11) in the relation $m\ddot{z}=eE_s$ to obtain

$$-mv\ddot{\delta}/\omega+mv(dv/dz)(1-\dot{\delta}/\omega)^2 = eE_0 f(z)\sin(\phi_0+\delta). \quad (12)$$

If δ is assumed to be small, (12) becomes approximately

$$\ddot{\delta}/\omega-(dv/dz)(1-2\dot{\delta}/\omega) + (eE_0/mv)f(z)(\sin\phi_0+\delta\cos\phi_0)=0. \quad (12a)$$

For δ and its derivatives equal to zero, (12a) defines E_0. Making the appropriate substitutions from (4), (5), (6), and (8) we find

$$E_0\sin\phi_0 = 2(1+n)W_f/3z_f, \quad (13)$$

and, from (4), (5), (12a), and (13) the equation describing the phase oscillation is

$$\frac{\ddot{\delta}}{\omega}+\frac{(1+n)}{(2-n)}\frac{2}{t}\frac{\dot{\delta}}{\omega}+\frac{(1+n)\omega\cot\phi_0}{(2-n)t}\frac{\delta}{\omega}=0. \quad (14)$$

The asymptotic solution of (14) for t large is

$$\frac{\delta}{\omega} = At^{-(3+4n)/(3-4n)}\sin\left(\frac{4(1+n)\omega t\cot\phi_0}{2-n}\right)^{\frac{1}{2}}, \quad (15)$$

where A is a constant. This represents a damped oscillation provided n lies between -0.4 and 2 and $\cot\phi_0$ is positive. Physically, n cannot be greater than 2; for n greater than 2, it is evident from (1) and (4) that L must increase at a rate faster than z, a situation which is not realizable in practice.

Radial Electric Field and Azimuthal Magnetic Field

The radial motion of the particles in a linear accelerator will be influenced by two field components, E_r and B_θ. To a first approximation, these components are given by

$$E_r = -\tfrac{1}{2}r\partial E_z/\partial z, \quad (16)$$

$$B_\theta = -\tfrac{1}{2}(r/c^2)\partial E_z/\partial t. \quad (17)$$

The form of these components can be derived from (8) and (13). (We neglect the small term which includes the derivative of $f(z)$ and those time varying fields which follow from other field components than (7).)

$$E_r = \frac{r(1+n)\omega W_f}{3\sin\phi_0 v_f z_f}(z/z_f)^{(n-2)/3}\cos(\phi_0+\delta), \quad (18)$$

$$B_\theta = \frac{r(1+n)W_f\omega}{3c^2\sin\phi_0 z_f}(z/z_f)^{(2n-1)/3}\cos(\phi_0+\delta). \quad (19)$$

Radial Forces on the Accelerated Particles

The radial force equation $m\ddot{r}=eE_r-evB_\theta$ becomes, upon substitution from (18), (19), and (4),

$$m\ddot{r} = \frac{r(1+n)\omega W_f}{3\sin\phi_0 z_f v_f}(z/z_f)^{(n-2)/3}(1-v^2/c^2)\cos(\phi_0+\delta). \quad (20)$$

Since we are neglecting relativistic effects, the second term in the bracket, which arose from the effect of B_θ, is negligible. Also, the average radial force on a particle will not differ materially from the radial force on the equilibrium particle. Thus, the radial deflections are those which result from the radial electric field

$$E_r = \frac{r\omega(1+n)W_f}{3z_f v_f}(z/z_f)^{(n-2)/3}\cot\phi_0. \quad (21)$$

Evidently, the closer n approaches its limiting value of 2, the more nearly constant becomes the defocusing field as a function of distance along the accelerator.

Numerical Example

As a numerical example, we consider a 4-million-volt linear accelerator 10 meters long. Protons will be injected into this accelerator at 100 kv and will be accelerated by a 30-megacycle signal. We assume, further, that the equilibrium phase is 45°. Evaluation of other parameters depends on the choice of n. We shall consider three cases: $n=0$ (voltage equal on all gaps), $n=\frac{1}{2}$ (constant amplitude axial electric field), and $n=1$ (gap voltage increasing linearly with distance along the accelerator).

From Eq. (21) we can now derive the radial field gradient,

$$G = E_r/r = 9.1\times10^5(1+n)(0.1z)^{(n-2)/3}(\text{volts/m})/\text{m}. \quad (22)$$

The value of z corresponding to injection follows from (6). The values of G for the three n's are as follows:

	$n=0$	$n=\frac{1}{2}$	$n=1$
G at injection (volts/cm)/cm	3640	870	455
G final (volts/cm)/cm	91	136	182

The $n=1$ case is obviously preferable from the standpoint of radial defocusing during the early stages of acceleration. The practical application of this case presents some difficulty, but the same desirable results can be achieved by accelerating in several stages, the accelerating voltage increasing stage by stage as the particle is accelerated.

III. THE FOCUSING MECHANISM

The technique of magnetic focusing proposed by Courant, Livingston, and Snyder[1] involves the passage of a beam of particles through successive magnetic fields of alternating transverse gradients. As in the preceding section, we choose the axis of the beam as the z axis. We suppose that the beam travels with velocity v, and that from $z=0$ to $z=l$ we apply a magnetic field having $B_x=B'y$ and $B_y=B'x$ where B' is a constant. From $z=l$ to $z=2l$, we apply a reversed field $B_x=-B'y$ and $B_y=-B'x$. Courant, Livingston, and Snyder demonstrate that this system acts like a converging lens whose focal length is given by their Eq. (19).

It is worthy of note that exactly the same technique will work with electric fields of the form $E_x=E'x$, $E_y=E'y$, etc. In this case the properties of the lens will be given by substituting E'/v for B' in the magnetic lens formulas.

IV. APPLICATION OF FOCUSING TO THE LINEAR ACCELERATOR

If the defocusing forces in the linear accelerator are to be compensated by magnetic lenses of the type discussed in the preceding section, we must take into account the fact that the effective electric gradient G given by Eq. (22) is acting throughout, in addition to the forces due to B'. The lens will now be one in which one section has an effective restoring field of $B'-G/v$ and the other has an effective field of $-B'-G/v$. The range of stability is given by Courant, Livingston, and Snyder's Eq. (5) and their Fig. 2 if only we substitute $\mathcal{F}e(B'\pm G/v)/4\pi^2mv$ for their n_1/N^2 and $-n_2/N^2$.

We now make an arbitrary choice of design parameters satisfying the stability conditions. We shall determine values for B' and l which correspond to the stable combination $n_1/N^2=0.07$, $n_2/N^2=0.05$. This choice yields the following relations:

$$B'=6G/v \text{ (or } E'=6G) \quad \text{and} \quad \mathcal{F}=0.79W/G, \quad (23)$$

where W is the particle energy.

TABLE I.

	Lens length ($2l$) cm	B' (gauss per cm)	E' (volts per cm per cm)
$n=0$	9.4	5050	21,800
$n=\frac{1}{2}$	19	1200	5200
$n=1$	26	620	2700

From (22) and (23) we can determine the lens parameters for our 4-Mev accelerator. The result of these operations for the injection end of the accelerator is summarized in Table I

As we progress along the accelerator, the permissible lens length increases and the magnetic or electric field gradients decrease. From (4), (22), and (23) we see that the lens length can increase as $z^{(n+4)/6}$. In this case B' will decrease with distance like $1/z$ or, if electric lenses are used, E' will decrease like $z^{(2-n)/3}$. The final lens length will be of the order of meters, and it will probably be desirable to make a new choice of stable parameters which results in shorter lenses near the exit end of the accelerator.

The applications of these principles to practical accelerators will place some limitations on the radio-frequency technique. If magnetic lenses are used, the accelerator tube diameter should be small, and it will be necessary to use lumped constant circuits rather than wave guides. Electric lenses could be combined with the drift tubes so that the same unit is both a lens component and a drift tube.

Lenses of this sort appear to be equally practicable for higher energy accelerators. We have computed possible lens parameters for an accelerator in which (as in the Berkeley linear accelerator) injection is at 4 million volts, energy gain is of the order of a million volts per foot, n is $\frac{1}{2}$, and the accelerating frequency is 200 megacycles. In this case, as usual, the worst defocusing is at the injection end of the accelerator where effective radial gradients exist of about 5000 volts per cm per cm. These could be compensated by lenses of our type 50 cm long having magnetic field gradients of 1100 gauss per cm or electric field gradients of 30,000 volts per cm per cm.

Letters to the Editor

PUBLICATION of brief reports of important discoveries in physics may be secured by addressing them to this department. The closing date for this department is five weeks prior to the date of issue. No proof will be sent to the authors. The Board of Editors does not hold itself responsible for the opinions expressed by the correspondents. Communications should not exceed 600 words in length and should be submitted in duplicate.

Spin-Lattice Relaxation in Ferromagnets*

ELIHU ABRAHAMS AND C. KITTEL
Department of Physics, University of California, Berkeley, California
(Received September 19, 1952)

A CALCULATION has been made of the spin-lattice relaxation time for ferromagnets. We introduce a macroscopic spin-lattice interaction which is large enough to account for the observed magnetoelastic energy. This approach should correspond more closely to the actual situation than the previous work of Akhieser,[1] whose pure dipolar interaction cannot account for the magnitude of observed magnetostrictive effects. Furthermore, the present calculation refers directly to the conditions existing in microwave resonance absorption experiments, whereas Akhieser's results in the main do not.[2]

In keeping with the macroscopic approach, we introduce a spin-wave field by expanding the transverse components of the magnetization into normal modes and quantizing according to the commutation relations between the components of the atomic spin.[3] The representation thus defined is one in which the Hamiltonian of the spin system is diagonal. A macroscopic phonon field, quantized in the usual way,[4] is set up to describe the lattice vibrations in an elastically isotopic solid.

The spin-lattice interaction used is the macroscopic magnetoelastic coupling energy[5]

$$H_{\rm int}=\int d\tau[(B_1/M_s^2)(M_x^2e_{xx}+M_y^2e_{yy}+M_z^2e_{zz}) +(B_2/M_s^2)(M_xM_ye_{xy}+M_yM_ze_{yz}+M_xM_ze_{xz})],$$

where the B's are magnetoelastic coupling constants, $\mathbf{M}$ is the magnetization, M_s its saturation value, and the e_{ij} are the strains which are derived from the lattice displacement vector $\mathbf{u}$ by differentiation.[6] The field-theoretic expressions for $\mathbf{M}$ and $\mathbf{u}$ are introduced in order to express $H_{\rm int}$ in terms of creation and destruction operators for spin waves and phonons, a_κ^*, a_κ and b_K^*, b_K. It turns out that the important part of $H_{\rm int}$ is that which describes scattering of a spin wave accompanied by the emission ($H_{\rm int}^e$) or absorption ($H_{\rm int}^a$) of a phonon

$$H_{\rm int}^e=-\Sigma_{K\kappa}b_K^*a_\kappa a_{\kappa'}^*f(\mathbf{K}),$$
$$H_{\rm int}^a=i\Sigma_{K\kappa}b_Ka_\kappa a_{\kappa'}^*f(\mathbf{K}),\quad \kappa'=\kappa+\mathbf{K},$$

where $f(\mathbf{K})=\text{const}\times K^{\frac{1}{2}}(1-3\cos^2\theta_K-\frac{3}{2}\sin\theta_K)$; κ, $\mathbf{K}$ are the wave vectors for spin waves and phonons; and θ_K is the polar angle of $\mathbf{K}$.

Each collision involving a phonon of wave number K transfers the energy ϵ_K of that phonon between the spins and the lattice. Then the rate of energy transfer to the lattice is given in terms of the matrix elements of the creation and destruction operators by the kinetic equation

$$\dot{Q}=(2\pi/\hbar)\Sigma_{K\kappa}\epsilon_K|f(\mathbf{K})|^2[N_Kn_\kappa(n_{\kappa'}+1)-(N_K+1)(n_\kappa+1)n_{\kappa'}] \times\delta(\epsilon_K+\epsilon_\kappa-\epsilon_{\kappa'}),$$

where ϵ_κ is the energy of a spin wave and the n_κ, N_K are occupation numbers for spin-wave and phonon states.

In order to define the relaxation time, we assume that in a resonance experiment the rf field excites spin waves, primarily of low wave number, and that the spin-spin interactions are strong enough to bring the spin system into equilibrium with itself before the spin-lattice transitions have time to proceed appreciably.[6] That is, we consider the spin system to be excited by the rf field to a higher temperature than that of the lattice.

The spin-lattice relaxation time τ is then the time constant in the exponential decay of this temperature different ΔT. In terms of the heat capacities C_S, C_L of the spins and lattice vibrations, we have

$$\tau=C_SC_L\Delta T/(C_S+C_L)\dot{Q}.$$

Under these circumstances, we may introduce Bose-Einstein factors for the occupation numbers in $\dot{Q}$ by defining a spin temperature and a lattice temperature. The quantity $\dot{Q}$ may be evaluated by transforming the summation into a double integral, expanding the integrand in powers of $\Delta T/T\ll1$[1], and performing several integrations. The result is

$$\dot{Q}=(VkB_1^2/16\pi^3kT^2\rho\gamma)(\hbar c/2A)^{\frac{1}{2}}(M_s/g\mu)^6\Delta TI(\gamma,F),$$

where $\gamma=(\hbar c)^2M_s/2g\mu AkT$, $F=2(g\mu/\hbar c)^2(AH_0/M_s)$,

$$I(\gamma,F)=\int\frac{x^4dx}{\cosh\gamma x-1}\left\{\log\frac{\exp[\frac{1}{4}\gamma(x-1)^2+\gamma F]-\exp(-x)}{\exp[\frac{1}{4}\gamma(x-1)^2+\gamma F]-1}\right\},$$

which must be evaluated numerically; ρ=density, c=sound velocity, A=Bloch wall coefficient,[3] g=spectroscopic splitting factor, μ=Bohr magneton, V=sample volume, H_0=applied field. For the heat capacities we use the Bloch $T^{\frac{3}{2}}$ approximation for C_S and the Debye approximation for C_L. We can then evaluate τ.

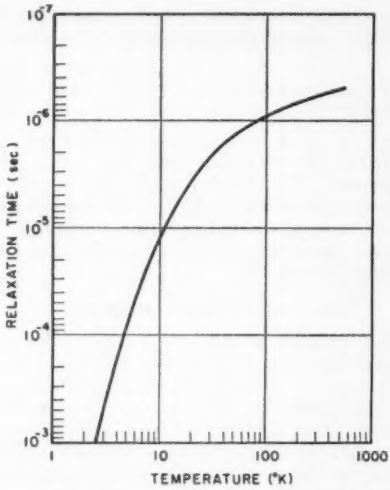

FIG. 1. Theoretical estimates of spin-lattice relaxation times in nickel. At 1°K, the theoretical relaxation time is 1 second.

The results for nickel are presented in Fig. 1 for $H_0=5300$ oersteds. It appears that no experiments have yet been performed which measure τ without including spin-spin relaxation effects as well.[6] It should be pointed out that τ depends sensitively upon parameters whose values are not well known.

We are indebted to Professor J. M. Luttinger for his very helpful interest during the early work on this problem.

* This research has been assisted in part by the ONR.

[1] A. Akhieser, J. Phys. (U.S.S.R.) **10**, 217 (1946)
[2] D. Polder, Phil. Mag. **40**, 99 (1949).
[3] C. Herring and C. Kittel, Phys. Rev. **81**, 869 (1951).
[4] A. Sommerfeld and H. A. Bethe, *Handbuch der Physik* (Verlag Julius Springer, Berlin, 1933), **24.2**, p. 500 ff.
[5] C. Kittel, Revs. Modern Phys. **21**, 541 (1949).
[6] Extensive arguments to support this view are given by C. Kittel and E. Abrahams, University of Maryland Magnetism Conference (1952), (to be published in the Reviews of Modern Physics).

Spontaneous Fission *versus* Alpha-Decay

ARNOLD KRAMISH
Rand Corporation, Santa Monica, California
(Received August 28, 1952)

FRENKEL[1] has suggested that alpha-decay could be considered as a distinct type of fission. He assumes that the alpha-particle is "constituted as a separate entity in the process of decay" rather than pre-existing in the original nucleus as in the Gamow theory. If this premise is correct, then alpha-decay and spontaneous fission should be regarded as closely related but competitive decay processes for heavy nuclei.

Recently, Seaborg[2] has found an empirical relationship between spontaneous fission rates and the fissionability parameter Z^2/A. Since there is as yet no adequate theoretical explanation of the observed spontaneous fission rates, it would appear desirable to correlate the alpha-decay competition with the same parameter. As a measure of the competition, we use the ratio of the spontaneous fission half-life,[3,4] to the alpha-disintegration half-life.[5] These are plotted in Fig. 1.

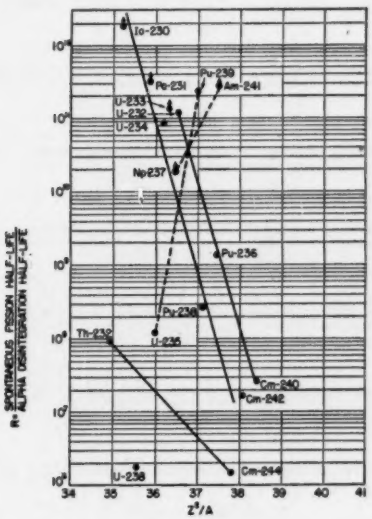

FIG. 1. Plot of the ratio of the spontaneous fission half-lives to the α-disintegration half-lives *vs* the fissionability parameter Z^2/A.

The nature of the competition may be seen by connecting consecutive alpha-decay products familywise or simply by constructing a median line. (Isotopes related by β-decay are not considered.) It is seen that for the even-even nuclei, the spontaneous fission mode of decay becomes the more predominant as Z^2/A increases. However, the opposite appears to be true for odd-neutron nuclides.

Thus, for odd-neutron nuclides, alpha-decay may be increasingly more competitive with spontaneous fission. This could explain the anomalously slow rates for odd-nucleons observed by Seaborg.[3] If the slower spontaneous fission rate for an odd-nucleon were to result from the expected larger radius, it would seem that this factor would also decrease the alpha-disintegration rates accordingly.

If we assume that the nucleus comes into optimum, nearly symmetric configuration for spontaneous fission, some 10^{21} times per second[6] the effect of the odd neutron may be such as to favor an anomalously higher frequency for the highly asymmetric configuration, i.e., a configuration leading to alpha-decay.

[1] J. Frenkel, J. Phys. (U.S.S.R.) **10**, 533 (1946)
[2] G. T. Seaborg, Phys. Rev. **85**, 157 (1951).
[3] E. Segrè, Phys. Rev. **86**, 21 (1952).
[4] Ghiorso, Higgins, Larsh, Seaborg, and Thompson, Phys. Rev. **87**, 163 (1952).
[5] G. T. Seaborg and I. Perlman, Revs. Modern Phys. **20**, 585 (1948).
[6] N. Bohr and J. A. Wheeler, Phys. Rev. **56**, 426 (1939).

Second-Order Effects in Nuclear Electric Quadrupole Interaction of Al^{27} in Spodumene*

H. E. PETCH,† G. M. VOLKOFF, AND N. G. CRANNA†
Department of Physics, University of British Columbia, Vancouver, Canada
(Received October 20, 1952)

IN an earlier paper[1] on the electric quadrupole splitting of nuclear magnetic resonance absorption lines in single crystals, our generalization of Pound's original work[2] to non-uniaxial crystals was carried through only to terms of the first order in the quadrupole coupling constant $C=eQ\varphi_{zz}/h$. We have now extended our generalization of Pound's theory to terms of order C^2, and have checked this extension on the experimental example of the Al^{27} resonance in $LiAl(SiO_3)_2$ (spodumene).

The general expression to terms of order C^2 for the dependence on crystal orientation of the frequency shift $\nu-\nu_0$ of the component of the resonance line corresponding to the transition between Zeeman levels m and $m-1$ for arbitrary crystal orientation, and for arbitrary values of I, m, and $\eta=(\varphi_{xx}-\varphi_{yy})/\varphi_{zz}$, will be given in the detailed paper to be submitted to the Canadian Journal of Physics. We quote here only the results for the central component $(\frac{1}{2}\leftrightarrow-\frac{1}{2})$ in the Al^{27} $(I=5/2)$ line in spodumene. It is known from crystal symmetry of spodumene that one of the principal axes (say x) of the crystalline electric field gradient tensor φ_{ij} at an Al site coincides with the b axis of the monoclinic crystal (which is also chosen as the X axis of crystal rotation, as explained in the earlier paper[1]). The y and z principal axes must then lie in the ac plane with the y axis making some angle δ with the crystal c axis (which is chosen as the Y axis of crystal rotation). The first-order shift of the central component is zero, and the second-order shift is given by

$$\nu-\nu_0=[C^2/800\nu_0]f(s). \tag{1}$$

Here $\nu_0=\mu H_0/hI$ is the unperturbed Larmor frequency (experimentally defined as the Al^{27} resonance in $AlCl_3$ solution into which the spodumene crystal was immersed), and $f(s)$ is given for the X rotation by

$$f_X(s)=4\eta^2-12(3+\eta)(2+\eta)s+9(3+\eta)^2s^2, \tag{2}$$

with $s=\cos^2(\theta_X+\delta)$, and for the Y rotation by

$$f_Y(s)=(3+\eta)^2-6[2\eta(1+3\eta)+5(3+\eta)(1-\eta)\cos^2\delta]s \\ +9[2\eta-(3+\eta)\cos^2\delta]^2s^2, \tag{3}$$

with $s=\cos^2\theta_Y$. These formulas reduce to Pound's results[2] for $\eta=0$, $C=40\Delta\nu/3$, and for $\delta=\pi/2$ for the X, or $\delta=0$ for the Y rotation.

We have used the above formulas to analyze our experimental results for the central component of the Al^{27} line in spodumene obtained with the apparatus and methods described earlier.[1] The inverse proportionality of $\nu-\nu_0$ to ν_0 for a fixed crystal position predicted by Eq. (1) was checked by using three different values of H_0 corresponding to $\nu_0=9.260$, 7.453, and 6.280 Mc/sec. For the crystal rotations described below, ν_0 was held fixed at $\nu_0=7.453$ Mc/sec. The points in Fig. 1 show experimental values of $\nu-\nu_0$ plotted *versus* $s=\cos^2(\theta_X+\delta)$ with $\delta=-55.5°$ for the X rotation (curve A), and *versus* $s=\cos^2\theta_Y$ for the Y rotation (curve B). Each point represents the average of four observations corresponding to $-\delta\pm(\theta_X+\delta)$, $\pi-\delta\pm(\theta_X+\delta)$ for curve A, and $\pm\theta_Y$, $\pi\pm\theta_Y$ for curve B. The solid curve A was graphically fitted to the experimental points by choosing $|C|=2956$ kc/sec in Eq. (1) and

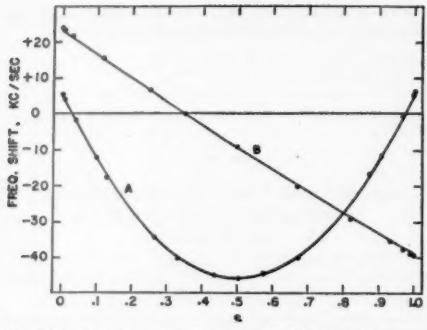

FIG. 1. The dependence of the frequency shift of the central component of the Al^{27} line in spodumene on crystal orientation. (A) X rotation about b axis of spodumene. (B) Y rotation about c axis of spodumene. $z=\cos^2(\theta_X-55.5°)$ for X rotation. $\theta_X=0$ when c axis of spodumene coincides with magnetic field H_0. $z=\cos^2\theta_Y$ for Y rotation. $\theta_Y=0$ when c axis of spodumene is at 90° to H_0. Each dot represents average of four observations. Solid curves are given by: (A) $(\nu-\nu_0)_X=1.46(3.610-139.8z+140.4z^2)$ kc/sec; (B) $(\nu-\nu_0)_Y=1.46(15.60-45.79z+3.606z^2)$ kc/sec. $\nu_0=7.453$ Mc/sec.

$\eta=0.95$ in Eq. (2). As a check on the experimental accuracy, the above values of $|C|$, η and δ, were inserted into Eqs. (1) and (3), and gave without any further adjustment the solid curve B for the Y rotation. The agreement obtained suggests the following results together with their estimated limits of error: $|C|=2960\pm10$ kv/sec, $\eta=0.95\pm0.01$, and $\delta=-55.5°\pm1°$ for Al^{27} in spodumene. The y principal axis of φ_{ij} [corresponding to the eigenvalue $-(1+\eta)\varphi_{zz}/2$] lies between the a and c axes of spodumene at an angle of 55.5°±1° with the c axis. The x axis [corresponding to $-(1-\eta)\varphi_{zz}/2$] lies along the b axis. The z axis (corresponding to φ_{zz}) is mutually orthogonal to these two.

In connection with theories of chemical binding, it seems suggestive that a principal axis of φ_{ij} at *both* the Li and the Al sites in spodumene appears to point directly at the projection of the nearest oxygen atom on the ac plane.

* Work supported by a grant from the National Research Council of Canada.

† Holders of Ontario Research Council Scholarships.

[1] Volkoff, Petch, and Smellie, Can. J. Phys. **30**, 270 (1952).

[2] R. V. Pound, Phys. Rev. **79**, 685 (1950).

τ-Meson Decay in Flight*

M. ANNIS AND N. F. HARMON
Washington University, St. Louis, Missouri

(Received October 7, 1952)

IN a series of cloud-chamber pictures taken at Berthoud Pass, Colorado[1] (680 g cm^{-2}), we have observed a probable example of the decay in flight of a τ-meson. These particles have been observed in nuclear emulsions,[2,3] and Leighton and Wanlass[4] recently observed two τ-meson decays in flight in the gas of a cloud chamber in a magnetic field, these latter examples being the only two decays in flight reported up to this time.

The cloud chamber (illuminated region approx 50 cm×50 cm ×12 cm) contains 11 silver-plated Pb plates 0.63 cm thick, separated by about 3.8 cm. The chamber is triggered by a penetrating shower detector placed above the chamber. Four photographs are taken of each event, the extreme cameras being mounted at 17° on either side of the center line.

The event is shown in Fig. 1. A particle enters the chamber at a, penetrates 7 Pb plates (about 8 radiation lengths) without appreciable deviation, and at b near the center of the illuminated region, splits into three charged particles. Each of the three secondary particles penetrates 4 Pb plates without interacting. They leave the chamber at c, d, and e. The low energy δ-ray

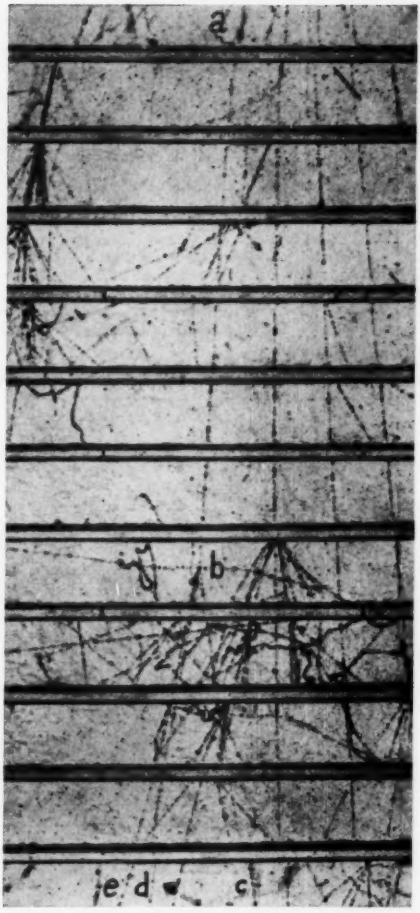

FIG. 1. A τ-meson decay in flight.

observed near b originates below the point where the splitting occurs. Likewise, the horizontal electron which seems to go through b is actually not space coincident. A small blob of ionization can be seen at b. This blob is no larger than other blobs observed along minimum ionization tracks in the picture, and it should also be pointed out that the τ-meson decay in flight differs from, say, the V decay in that the τ-meson decay involves 4 ionizing particles meeting at a point instead of 2 in the case of the V.

Of course, there is always the possibility that this event is a nuclear collision in the gas of the chamber. However, we feel that this is an unlikely possibility. First, no recoil nucleus of more than several hundred kev energy is observed. Hence, if this were a nuclear event, it would be one of those rare events classified as a peripheral collision, involving, as we shall see later, multiple meson production. Second, and most important, we show below that momentum is conserved by the visible ionizing prongs.

The primary particle ab and the three secondary particles lie roughly in a plane. Table I summarizes the relevant information

TABLE I. Summary of data on particles in Fig. 1.

Particle	Angle of deviation from primary in deg	Rms[a] angle of multiple scattering in deg	$pc\beta$ in Mev	pc in Mev[b]
ab	...	0.9 ±0.3	1000 ±270	1100 ±310
bc	13	1.9 ±0.7	480 ±170	490 ±170
bd	5	2.4 ±0.9	380 ±130	400 ±140
be	7	3.3 ±1.2	270 ±100	300 ±110

[a] The errors shown are the approximate standard deviations $1/(2n)^{\frac{1}{2}}$ (n = No. of plates). [See N. Arley and K. R. Buch, *Introduction to the Theory of Probability and Statistics* (John Wiley and Sons, Inc., New York, 1950), pp. 139 ff.]

[b] Assuming the primary to be a τ ($m_\tau = 970 m_e$), and the secondaries to be π-mesons.

about the event. Using the projected angles of multiple coulomb scattering,[5] one finds the values of $pc\beta$ given in the table (p = momentum, βc = velocity). The "noise level" scattering correction[6] is estimated to be small (less than 25 percent) in all cases, although we do not yet have enough data to evaluate this correction exactly.

Since each of the three secondaries penetrates 4 Pb plates without appreciable scattering or multiplication, these particles are all heavy compared to an electron. If these particles were protons, one can see from the values of $pc\beta$ given in Table I that their ionization would be between twice and three times the minimum. From Fig. 1, it is probably that these particles do not ionize this strongly.

Assuming the primary particle to be a τ-meson and the three secondaries to be π-mesons, we obtain the momenta given in the fifth column of Table I. It is evident that momentum is conserved in the direction of the primary particle; it is also conserved in the transverse direction, by the observed ionizing particles.

Following a suggestion of Wilson and Butler,[6] we quote the lifetime data as follows: In the rest frame of the τ-meson, the τ-meson lived $(3.31 \pm 0.56) \times 10^{-10}$ sec in the chamber. In the same frame, the τ-meson decay would have been observed if it had lived as long as $(5.02 \pm 0.85) \times 10^{-10}$ sec.

In the center-of-mass system, the π-meson were emitted at rather wide angles with respect to each other.

* Supported by the joint program of the ONR and AEC and by the Research Corporation.

[1] Brookhaven National Laboratory kindly loaned us their facilities at Berthoud Pass.

[2] Brown, Camerini, Fowler, Muirhead, Powell, and Ritson, Nature **82**, 163 (1949).

[3] P. E. Hodgson, Phil. Mag. **42**, 1060 (1952).

[4] R. B. Leighton and S. D. Wanlass, Phys. Rev. **86**, 426 (1952).

[5] S. Olbert, Phys. Rev. **87**, 319 (1952).

[6] J. G. Wilson and C. C. Butler, Phil. Mag. **43**, 993 (1952).

The Average Electric Charge of Daughter Atoms from β-Decay and Isomeric Transition*

SOL WEXLER AND T. H. DAVIES
Argonne National Laboratory and Institute for Nuclear Studies, University of Chicago, Chicago, Illinois

(Received October 14, 1952)

HIGH positive charges are predicted for the products of nuclear isomeric transition by internal conversion.[1,2] Positive bromine ions from the decay of 4.4-hr Br^{80m} in gaseous ethyl bromide have been observed.[3] Neither the average charge following transition by internal conversion nor the charge spectrum has been reported. However, the average charge of Cl^{37} from the similar process of electron capture by A^{37} has been recently determined.[4]

The charge carried by products of β-decay has been measured for the single case of Kr^{85} decay to Rb^{85}.[5] The extent to which change in nuclear charge should induce additional ionization in β-decay has been discussed by several authors.[6-8]

This communication will report the average charge found on the products of β-decay of H^3 present as molecular hydrogen, of C^{14} as CO_2, and of a mixture of Kr and Xe fission gases. Results with 18-min Br^{80} from the transition of 4.4-hr Br^{80m} present as C_2H_5Br will also be given.

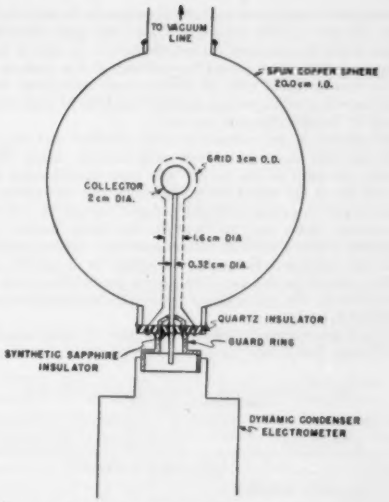

FIG. 1. Spherical ion collection chamber.

The experiments were performed in spherical and cylindrical ion chambers of copper (Figs. 1 and 2) in which a small central electrode was held at 1000 to 1500 volts negative to the outer shell. A grid was placed about the central collector and held at 100 to 200 volts negative potential relative to the ion collector, in order to return secondary electrons produced by impact of positive ions with the central electrode to that electrode. The vessels were filled with the radioactive gases to known pressures of from 5×10^{-6} to 1.5×10^{-2} mm. Ion currents across the chamber were then measured in an attached dynamic condenser electrometer and

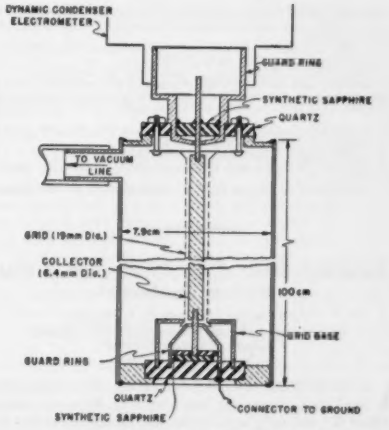

FIG. 2. Cylindrical ion collection chamber.

recorded as voltages across calibrated resistances. In some experiments the rate of drift method was used and gave concordant results. From the measured current the number of electron units of charge collected per second was calculated. The positive ion current was compared with the independently determined disintegration rate of an aliquot gas sample to give the average charge carried by the disintegration product.

Background current corrections were obtained with inactive gases and were the same as those with chamber empty. When feasible, the decay of the current with time was compared with the half-life of the radioactivity. Extensive tests at various gas pressures and at various collecting and grid voltages showed that the current values used to calculate the charge carried were saturation currents and that neither secondary electron emission from the collector nor ion-pair formation by β-particles and positive ions in the gas were contributing appreciably to the observed current. The spherical and cylindrical chambers gave indistinguishable results.

Table I summarizes the results of a number of repeat runs with each system. The Kr and Xe data are less reliable mainly because

TABLE I. Average charge of product atoms after β^- decay and isomeric transition.

Active species	Average electronic charge found
H^3 as H_2	0.87, 1.00, 0.91, 0.91, 0.89
C^{14} as CO_2	0.8, 1.2, 1.0
Fission gases (Kr^{85}, Kr^{87}, Kr^{88}, and Xe^{133})	1.7, 1.6, 0.8, 1.2, 1.6, 1.5, 1.2, 1.2, 1.1, 1.3
Br^{80m} as C_2H_5Br	9, 11, 9, 8, 10, 11, 8, 11, 9, 13, 10, 11, 13

of the complexity of the decay pattern of the several noble fission gases present. The experimental result here is not necessarily different from unity, which would be in accord with Jacobsen and Kofoed-Hansen[5] but at some variance with prediction.[6] The C^{14} and H^3 results show no loss or orbital electrons from the transformed species. The value of +10 for the charge of the fragments from isomeric transition is about twice that predicted.[1,2] More recently, however, Br^{80m} has been found to decay by two successive isomeric transitions and the high charge observed is probably connected with the presence of two steps in the decay.[9] Both transitions generally proceed via internal conversion, and to the heavy ionization of the first step should be added that accompanying an Auger process in the second.

A detailed account of the experiments will be submitted shortly.

* Presented before Division of Physical and Inorganic Chemistry, 122nd Meeting American Chemical Society, September 14–19, 1952, Atlantic City, New Jersey.

[1] D. C. DeVault and W. F. Libby, J. Am. Chem. Soc. **63**, 3216 (1941).
[2] E. P. Copper, Phys. Rev. **61**, 1 (1942).
[3] S. Wexler and T. H. Davies, J. Chem. Phys. **18**, 376 (1950).
[4] J. A. Miskel and M. L. Perlman, Phys. Rev. **87**, 543 (1952). This work, kindly shown us in manuscript, and the present studies stem from suggestions of Dr. A. O. Allen and others of the Brookhaven National Laboratory staff.
[5] J. C. Jacobsen and O. Kofoed-Hansen, Phys. Rev. **73**, 675 (1948).
[6] A. Migdal, J. Phys. (U.S.S.R.) **4**, 449 (1941).
[7] E. L. Feinberg, J. Phys. (U.S.S.R.) **4**, 423 (1941).
[8] A. Winther, Kgl. Danske Videnskab. Selskab, Mat.-fys. Medd. **27**, No. 2 (1952).
[9] E. Segrè and A. C. Helmholz, Revs. Modern Phys. **21**, 291 (1949).

A Statistical Study of the Distribution of Stars in Nuclear Emulsions*

F. B. BROWN, JR., AND A. V. MASKET
Department of Physics, University of North Carolina, Chapel Hill, North Carolina
(Received July 16, 1952)

A STATISTICAL study has been made of the distribution of 1723 stars (varying in size from 3 to 40 prongs) found on 11 Ilford G-5 nuclear plates. These were chosen at random from a group of 30 plates exposed at 84,000 ft for 6½ hours. Particular emphasis was placed on close groupings of stars, an anomaly previously reported by others.[1–3]

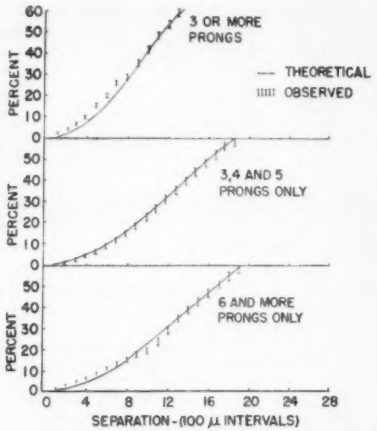

FIG. 1. Percentage of stars having nearest neighbor within distances shown.

Assuming random distribution of nuclear events, the probability of a star having a nearest neighbor lying within a distance r is given as a function of r by

$$P = 1 - \exp(-N\pi r^2/A),$$

where N is the total number of stars and A is the area scanned.

When actual measurements were made of the distribution of these minimum distances, measuring the distance from each star to its nearest neighbor, we obtained values which agreed within experimental accuracy except for small distances. In other words, the number of close pairs is much greater than anticipated, with a discrepancy of over 200 percent at very close distances. Figure 1 shows the percentage of stars that would be expected to have a nearest neighbor within a distance r together with the observed percentages, allowing for probable deviation from Poisson distribution. A cell size of 100μ was used in order to secure a sufficiently high frequency in each cell to be statistically significant.

A χ^2 test was applied to the distribution in the first five cells, which indicated a probability of less than 0.001 that random distribution would result in a greater discrepancy.

The next step was to determine the type of stars which was causing these nonrandom double star formations. Among other tests, the distribution of minimum distances was re-evaluated con-

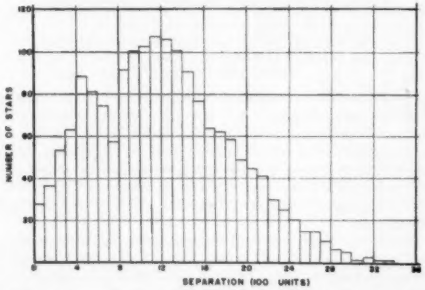

FIG. 2. Number of stars with nearest neighbor lying in annulus of radial width shown.

sidering only stars of 3, 4, and 5 prongs and disregarding the larger stars. The result was a curve for the 901 smaller stars which fits the theoretical distribution for this number of stars well within experimental accuracy at all points. Again the application of a χ^2 test proved instructive, giving a value of $P>0.94$ for the first five cells, and thus indicating a highly random distribution among the smaller stars. In a similar way, it was found that the distribution among large stars only was nonrandom.

Several mechanisms may be advanced as possible explanations for such nonrandom groupings of stars. One is the emission by large stars of a neutral particle with a very short lifetime. This seems unlikely, since the secondary thus created would tend to have always the same number of prongs, and this is not observed to be the case. Further, an analysis of the differential distribution in Fig. 2 indicates two peaks, one at 500μ and the other at about 1200μ; both of these lie above the level which we would predict on the basis of the stars being randomly distributed and, therefore, indicate a nonrandom clustering of stars having these separations. A decay scheme, unless we postulate two different types of particles, could not explain these two peaks. A possibility to be investigated is that of a collision with a nearby nucleus in the emulsion of a neutral particle emitted from a "parent" star, thus creating a neighbor. A third possibility is a narrow shower cascade of many particles, mostly neutral.

In an effort to ascertain the source of this phenomenon, an analysis is now being made of the spatial distribution of the light prongs on neighboring stars to determine the direction of the incident particles. Such a study is expected to reveal whether such pairs are created simultaneously by some outside mechanism such as a narrow shower, or whether one of the larger stars could, by neutral emission, create a nearby neighbor. A full report on this work will be submitted for publication in the near future.

* Supported by the AEC.

[1] L. Leprince-Ringuet and J. Heidman, Nature **161**, 844 (1948).
[2] T. T. Li and D. H. Perkins, Nature **161**, 844 (1948).
[3] T. T. Li, Phil. Mag. **41**, 1152 (1950).

Isothermal Ordering of Cu_3Au at 200°C

E. K. Halteman, G. F. Mechlin, and H. L. Glick
Westinghouse Electric Corporation, Pittsburgh, Pennsylvania
(Received October 3, 1952)

RECENT interest[1] in the effects of neutron irradiation on Cu_3Au alloy has prompted us to make measurements on the isothermal transformation of this material. A disordered sample (No. 1) was prepared by heating an ordered Cu_3Au wire for four hours at 400°C (14°C above the critical temperature) and quenching it to room temperature at a rate of 15°C/min. The wire was heated to a temperature of 208° in a period of 15 minutes. Resistance measurements were made at 208°C as a function of time by the current-potential method.

A second disordered sample (No. 2), provided with current and potential leads, was prepared from the same lot of wire by heating in an evacuated Vycor bulb for 16 hours at 800°C and quenching in iced brine at −10°C. The quench vessel was placed below the vertical tube heat-treating furnace, and the sample bulb was quickly thrust into the quench bath with a rod and was immediately broken by impact against a metal block in the quench bath. The sample was then placed in an oil thermostat (using Dow Corning No. 710 Fluid) operating at 197°C. The time to attain equilibrium in this bath was measured to be less than one second. Measurements of resistance were made using an expanded scale strip chart potentiometer, and later using a manually operated potentiometer. Approximately 45 seconds after placing the sample in the oil bath, the resistance had decayed to a value equal to the room temperature (23°C) resistance.

Figure 1 shows a comparison of our results without irradiation to those of Blewitt and Coltman at 200°C with pile irradiation. Our electrical resistance data for run No. 1 has been adjusted so that the initial resistance corresponds to the initial plateau shown

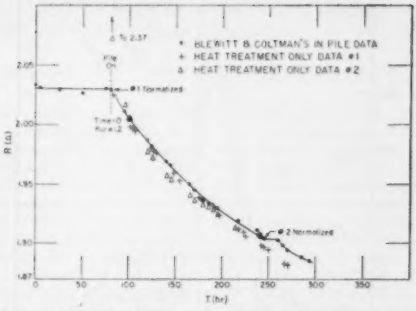

FIG. 1. Normalized resistance *vs* time dependence of Cu_3Au for several heat treatments compared to Blewitt and Coltman's in-pile data.

by Blewitt and Coltman. The time scale has been shifted for comparison purposes so that our zero time corresponds to the time of their initial drop. The resistance data for run No. 2 has been arbitrarily normalized to fit Blewitt and Coltman's data at $T=240$ hours (i.e., 160 hours after start-up). This procedure was necessary to avoid the transient region near start-up. It must be recognized that by such a procedure one must avoid all magnitude comparisons; it is still possible, however, to compare rates of change of resistance when these rates are computed as fractional changes per unit time.

The similarity in shape of the curves is noteworthy. It appears possible by heat treatment alone to closely duplicate the time dependence of resistance of Cu_3Au observed in the Oak Ridge Reactor by Blewitt and Coltman. Further investigations are in progress on the effect of heat treatment on the isothermal transformation rate of Cu_3Au.

[1] T. H. Blewit and R. R. Coltman, Phys. Rev. **85**, 384 (1952).

Polarization of the O^{16} Gamma-Rays*

L. W. Fagg and S. S. Hanna
Department of Physics, The Johns Hopkins University, Baltimore, Maryland
(Received September 24, 1952)

POLARIZATIONS of the 6.13-, 6.9-, and 7.1-Mev gamma-rays from $F^{19}(p,\alpha)O^{16*}(\gamma)O^{16}$, $E_p=0.874$ Mev, have been observed by using the $H^2(\gamma,p)n$ reaction as a polarization detector. If the alpha-particle is not observed in the fluorine reaction, the gamma-rays are polarized relative to the proton beam, and the maximum polarization is expected for radiation emitted at right angles to the beam.

Nuclear plates (400-micron Ilford C_2 emulsion), to which about 0.12 g/cm^3 of D_2O had been added,[1] were placed 4 cm from the thin fluorine target with the plane of the emulsion perpendicular to gamma-rays emitted at 90°. After exposure, the plates were scanned in a microscope, and the direction and projected range of each photoproton were measured. The following criteria were used: (1) the track must lie completely in the emulsion, (2) it must be straight enough to establish a direction to within 10°, and (3) it must be in sharp focus along its entire length.

The distribution of protons in the photoelectric process, $H^2(\gamma,p)n$, is given by: $Y(\theta,\phi)=\sin^2\theta\cos^2\phi$,[2,3] where θ and ϕ are polar coordinates taken with respect to the direction of propagation of the γ-ray. The polarization direction of the γ-ray is given by $\theta=90°$, $\phi=0°$. Experimentally, it is the distribution in ϕ and the projected range ρ, which is observed to be

$$Y(\rho,\phi)=\rho^2R^{-2}(R^2-\rho^2)^{-\frac{1}{2}}\cos^2\phi,$$

$$Y(\rho)=\int_0^{2\pi}Y(\rho,\phi)d\phi,\quad Y(\phi)=\int_{\rho_0}^{R}Y(\rho,\phi)d\rho,$$

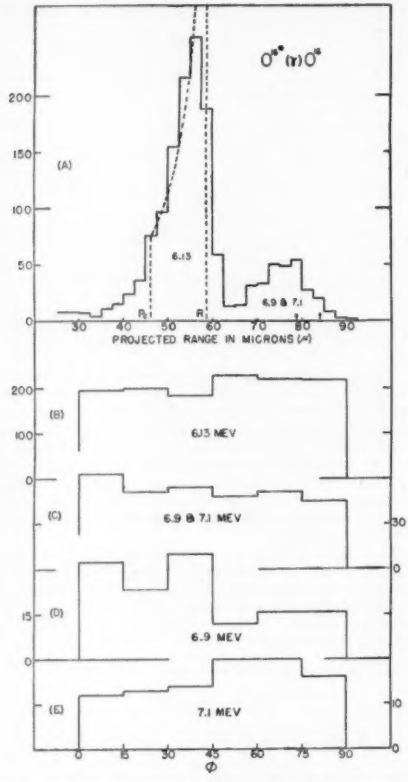

FIG. 1. Distributions in angle and projected range of the photoprotons produced by O^{16} γ-rays in the reaction $H^3(\gamma, p)_R$.

where R is the range of the photoproton. The lower limit p_t of the projected range is established by the requirement that the tracks be in sharp focus in the microscope. Its value depends, of course, on the depth of focus. The dotted curve in Fig. 1(A) shows the theoretical distribution $Y(p)$ for the 6.13-Mev γ-ray, together with the experimental distribution for all three γ-rays. The arrows at 78 and 83.5μ give the predicted ranges R for the two unresolved distributions of the 7-Mev group. The ratio of the 6.13 yield to the unresolved 6.9 and 7.1 yield is 2.9 ± 0.4, in good agreement with other investigations.

If the γ-ray under observation is only partially polarized, the ϕ-dependence is of the form, $Y(\phi)=1+B\cos^2\phi$. Figure 1(B) shows the experimental distribution $Y(\phi)$ for the tracks corresponding to the 6.13-Mev γ-ray (from 45 to 62.5μ); Fig. 1(C), the distribution for those in the unresolved 7-Mev group (67.5 to 92.5μ). Figures 1(D) and (E) represent an attempt to resolve the 6.9 and 7.1 distributions by plotting tracks between 67.5 and 75μ and between 82.5 and 92.5μ, respectively.

These observed polarizations may be used[4] in conjunction with the angular distribution coefficients of the γ-rays in the $F^{19}(p,\alpha)$-$O^{16*}(\gamma)O^{16}$ reaction to determine the parities of the states in O^{16}. A least square analysis of the distribution of the 7-Mev group gives a polarization ratio, $Y(0)/Y(90)=1+B=1.4\pm0.2$. Using this result and the value of 0.33 ± 0.06 given by Sanders[5] for the coefficient in the angular distribution $1+A\cos^2\theta_\gamma$, and assuming a ratio of two[6] for the intensity of 6.9- to 7.1-Mev radiation, the separate angular distribution coefficients for the 6.9- and 7.1-Mev radiation can be derived provided an assumption is made about the parities of the two states. Of the four possible combinations[2] only that of negative parity for the 7.1-Mev and positive parity for the 6.9-Mev state leads to results consistent with the trends in Figs. 1(D) and (E). This assignment of parities is in agreement with the work of Seed and French.[7] The angular distribution coefficients derived from the above information are 0.37 ± 0.16 and 0.25 ± 0.11 for the 6.9- and 7.1-Mev radiations, respectively.

The observed distribution in ϕ for the 6.13-Mev radiation is only in fair agreement with the flat distribution expected from the value of 0.01 ± 0.04 given by Sanders[5] for the angular distribution coefficient. Only one plate of three scanned showed the 90° rise in evidence in Fig. 1(B). Further work is in progress to investigate this effect.

We are indebted to Dr. N. P. Heydenberg for the use of the D.T.M. statitron for some of the exposures, and to Mr. F. Levin for some of the microscope reading.

* Assisted by a contract with the AEC.

[1] G. Goldhaber, Phys. Rev. **81**, 930 (1951).
[2] H. A. Bethe and R. F. Bacher, Revs. Modern Phys. **8**, 122 (1936).
[3] D. H. Wilkinson, Phil. Mag. **43**, 659 (1952).
[4] D. R. Hamilton, Phys. Rev. **74**, 782 (1948).
[5] J. E. Sanders, Phil. Mag. **43**, 630 (1952).
[6] Chao, Tollestrup, Fowler, and Lauritsen, Phys. Rev. **79**, 108 (1950).
[7] J. Seed and A. P. French, Phys. Rev. **88**, 1007 (1952).

Interference between Coulomb and Nuclear Scattering in p-p Collisions at 240 Mev*

H. P. NOYES AND H. G. CAMNITZ
University of Rochester, Rochester, New York
(Received August 19, 1952)

THE calculation by Goldfarb and Feldman[1] of the angular distributions predicted by the various potential models proposed to explain the high energy p-p scattering shows that the $\mathbf{L}\cdot\mathbf{S}$ potential of Case and Pais[2] is in qualitative disagreement with experiment, and that the singular tensor potential of Christian and Noyes[3] is ambiguous unless a cutoff is specified (though for a particular cutoff and sign of the potential, the large angle scattering is roughly correct), while the hard core Jastrow model[4] alone gives a fairly isotropic angular distribution. Since the data of Towler[5] are extremely isotropic down to 12° in the center-of-mass system, with one point that is presumably primarily Coulomb scattering at 8°, it seemed worthwhile to see if Coulomb-nuclear interference would improve the predictions of the Christian-Noyes potential and/or alter qualitatively the predictions of the Jastow model. The singlet phase shifts for these two cases are collected in Table I;

TABLE I. Phase shifts at 240 Mev.

Singlet phase shift	I. Christian-Noyes	II. Jastrow; $\mu=\frac{1}{2}M$	III. Jastrow; $\mu=(\gamma_d g_e/\beta_d)M$
S^a	15.28°	−16.89°	−8.738°
D^a	13.82°	11.75°	26.67°
G^b	1.98°	1.51°	1.78°

[a] Exact calculation.
[b] Born approximation.

Christian-Noyes potential:

Singlet: $V(r)=-13.273$ Mev, $r<2.615\times10^{-13}$ cm,
$=0$, $r>2.615\times10^{-13}$ cm,
Triplet: $V(r)=0$, $r<0.17664\times10^{-13}$ cm
$=18S_{12}\dfrac{e^{-r/R}}{(r/R)^2}$ Mev, $r>0.17664\times10^{-13}$ cm,
$R=1.6\times10^{-13}$ cm.

Jastrow potential:

Singlet: $V(r)=\infty$, $r<r_0$,
$=-375\ e^{-(r-r_0)/r_s}$ Mev, $r>r_0$,
Triplet: $V(r)=-50.784S_{12}\ e^{-r/r_t}$ Mev, $r>r_0$,

where $r_0=0.6\times10^{-13}$ cm, $r_s=0.4\times10^{-13}$ cm, $r_t=0.75\times10^{-13}$ cm.
$A_J{}^{J'}{}_{m_s}=\mathrm{Re}\,[\exp(2i\delta_J{}^{J'}{}_{m_s})-1]$; $B_J{}^{J'}{}_{m_s}=\mathrm{Im}\,[\exp(2i\delta_J{}^{J'}{}_{m_s})-1]$.

the tensor phase shifts are given in reference 1. The singlet phase shifts for the hard core potential are in close agreement with values supplied to us by Jastrow. The resulting angular distributions including Coulomb scattering and Coulomb-nuclear interference are plotted in Fig. 1 in comparison with Towler's data, and show that the Coulomb effects are insufficient to remove the forward peak predicted by the Christian-Noyes potential. This forward peak is characteristic of any smooth, nonsingular, monotonic singlet potential with the correct effective range and scattering length to fit the low energy data, and hence its absence in the observed scattering rules out any model such as that of Christian and Noyes which combines such a potential with a singular tensor force. The Jastrow model avoids this undesirable forward peak by means of a repulsive core in the singlet potential, and while not in quantitative agreement with Towler's data, could presumably be brought into agreement by a readjustment of the parameters (e.g., a stronger tensor force).

However, it became apparent in the course of the calculations that the Jastrow model could be extremely sensitive to kinematic relativistic effects that have been ignored on the grounds that they should be only of the order of $v_c^2/c^2=\beta_c^2=0.113$ in the zero-momentum system. In the above calculations the wave number k is taken to be half the relative momentum in the zero-momentum

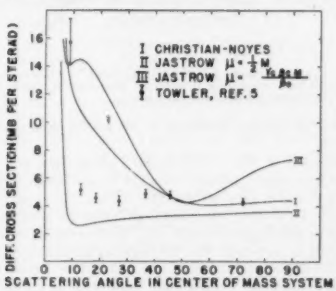
I CHRISTIAN-NOYES
II JASTROW
III JASTROW
TOWLER, REF. 5
DIFF. CROSS SECTION (MB PER STERAD)
SCATTERING ANGLE IN CENTER OF MASS SYSTEM
0 10 20 30 40 50 60 70 80 90
2 4 6 8 10 12 14 16

FIG. 1. Proton-proton scattering at 240 Mev including Coulomb effects predicted by the Christian-Noyes potential, and by the Jastrow potential with two interpretations of the reduced mass μ.

system, i.e., $k^2=\gamma_c^2\beta_c^2M^2c^2/\hbar^2=MT_0/2\hbar^2$, where $\gamma=1/(1-\beta^2)^{\frac{1}{2}}=(Mc^2+T_0)/Mc^2$ and $\gamma_c=[(\gamma_0+1)/2]^{\frac{1}{2}}$, which agrees with the nonrelativistic definition if one takes $T_0=240$ Mev rather than $T_0=Mv_0^2/2$; the reduced mass in the term $2\mu V(r)/\hbar^2$ is taken as $\mu=M/2$. But if the reduced mass is interpreted instead as one-half the relative momentum divided by the relative velocity, i.e., $\mu=\gamma_c\beta_c/\beta_0=1.18247M/2$, the resultant phase shifts and angular distributions are completely different from the nonrelativistic results (see column III of Table I and curve III of Fig. 1).[6] This is because the phase shift due to the repulsive core is unaltered while that due to the attractive well is changed (in the S wave case by about 20 percent) so that in this energy region where the two effects nearly cancel, the *net* change can be extremely large. While there is no particular theoretical justification for this choice of μ, it is clear that even replacing μ by the effective mass $\gamma_cM/2=1.06203M/2$ would give qualitatively different results. Consequently, it would seem pointless to make any refinements on the Jastow parameters without also attempting a correct relativistic treatment of the problem, including dynamic as well as kinematic effects. This is clearly true *a fortiori* at higher energies than 240 Mev.

* Work performed under the auspices of the AEC.

[1] L. Goldfarb and D. Feldman, Phys. Rev. **88**, 1099 (1952).
[2] K. M. Case and A. Pais, Phys. Rev. **80**, 203 (1950).
[3] R. S. Christian and H. P. Noyes, Phys. Rev. **79**, 85 (1950).
[4] P. Jastrow, Phys. Rev. **81**, 165 (1951).
[5] O. A. Towler, Jr., Phys. Rev. **84**, 1262 (1951).
[6] The triplet quantities $A\beta^{2n}$, $B\beta^{2n}$ used in the calculation of curve III were obtained by multiplying corresponding quantities for curve II by 1.18247.

Limit on Repulsive Core from 100-Mev Deuteron Photoeffect

N. AUSTERN*
Laboratory of Nuclear Studies, Cornell University, Ithaca, New York
(Received October 6, 1952)

IN view of the present interest in respulsive core nuclear potentials, it seems worthwhile to try to estimate the effects which would be produced in deuteron photodisintegration by a repulsive core potential for the ground state, merely computing for this the dominating electric dipole term. Comparison with older calculations of the same type,[1] which do not assume repulsive cores, show that the core tends to depress the cross section at very high energies, reducing it even further below the very high energy experimental data.[2] On the other hand, at energies of the order of 100 Mev the core causes an increase in the cross section, an increase which does not depend on the specific shape which may be assumed for the repulsion, and which might be used to set a rough upper bound on the permissible core radius in the ground state.

A simple form of "radial" wave function for the deuteron S wave, corresponding to infinite repulsion for radii less than R, is

$$\begin{aligned} u&=0, && r<R,\\ u&=Ne^{-\gamma r}\{1-e^{-\xi(r-R)}\}, && r>R. \end{aligned} \tag{1}$$

The requirement that this wave function yield a correct value for the effective range,

$$r_{01}=2\int_0^\infty \{e^{-2\gamma r}-N^{-2}u^2\}dr,$$

forces ξ to increase rapidly as R becomes at all large. As a consequence, the inclusion of a repulsive core actually makes the attractive part of the nuclear potential shorter tailed, and the wave function rises to its asymptotic form $e^{-\gamma r}$ at smaller r than when $R=0$. This behavior is characteristic of the introduction of a repulsive core,[3] and is independent of the exact type of core which may be used.

As the outer parts of the wave function are most effective in photodisintegration, an increase of ξ will lead to an increase of the photo cross section, the same effect which leads the square well curves of reference 1 to lie above their Hulthén curves. But this happens in a limited energy range. At very low energies the cross section is completely independent of the shape of the potential, and is given by Bethe and Longmire[4] as a simple renormalization

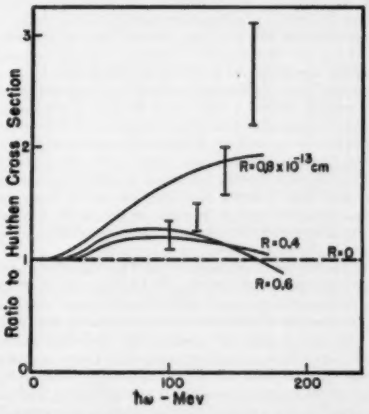

FIG. 1. Deuteron photodisintegration cross sections, expressed in terms of the cross sections of reference 1, computed in terms of a Hulthén type ground-state wave function.

of the Bethe-Peierls cross section. It is only toward sufficiently high energy that the final state wave function can "see" details of the ground-state function. But too high energies must also be avoided, for even if the model retained meaning, the effect which is of interest would be masked by more specific effects of the core and by the onset of meson exchange effects.

Figure 1 shows the ratios of the photoelectric cross sections, for cores of various radii, to the simple phenomenological cross section which is computed[1] for the Hulthén wave function, $u=Ne^{-\gamma r}\times(1-e^{-\xi r})$. The experimental points of Benedict and Woodward[5] are included on this graph, the only ones thus far obtained in the interesting energy region. The calculations were performed according to the same procedure as in reference 1, using free P waves in the final state (implying a "Serber potential") and with the ground-state wave function of Eq. (1). Calculations with another core shape are essentially in agreement with these.

It is clear that the 100-Mev effect remains slight until the core becomes of quite large radius. The experimental points indicate, as mentioned earlier, that the repulsive core is incapable of yielding the large experimental cross section at very high energy. A ground-state core of radius as large as 0.8×10^{-13} cm seems unlikely, although the present data do not permit setting any smaller upper limit on the core radius. It does not seem unreasonable to suggest that the specific effects which dominate the very high energy photodisintegration might become sufficiently weak towards low energy that experiments in the range 50–100 Mev might give interesting information about any ground-state core.

I am grateful to Dr. E. E. Salpeter and Dr. S. T. Butler for interesting conversations concerning this work.

[a] AEC Postdoctoral Fellow.
[1] L. I. Schiff, Phys. Rev. **78**, 733 (1950); J. F. Marshall and E. Guth, Phys. Rev. **78**, 738 (1950).
[2] S. Kikuchi, Phys. Rev. **85**, 1062 (1952); W. S. Gilbert and J. W. Rose, Phys. Rev. **85**, 766 (1952); R. Littauer and J. Keck, Phys. Rev. **85**, 1051 (1952).
[3] R. Jastrow, Phys. Rev. **81**, 165 (1951).
[4] H. A. Bethe and C. Longmire, Phys. Rev. **77**, 647 (1950).
[5] T. S. Benedict and W. M. Woodward, Phys. Rev. **85**, 924 (1952).

The S Wave in Pion-Nucleon Scattering

R. E. MARSHAK
University of Rochester, Rochester, New York
(Received October 14, 1952)

MEASUREMENTS of the angular distribution of positive and negative pions scattered by protons have been analyzed on the basis of the charge-independence hypothesis.[1] At 135 Mev, the S phase shift δ for the $\frac{3}{2}$ isotopic spin state[2] turns out to be $\pm25°$; at 110 Mev $\delta=\pm15°$. Recently,[2] the positive pion cross section has been measured at 78 Mev and is matched by $\delta=\pm5.8°$. Comparison of the S phase shifts with the P phase shifts[1,2] at these three energies exhibits a more rapid decrease of the former with decreasing energy than the latter, a feature which is contrary to expectation for a monotonic potential. Moreover, while the errors assigned to the phase shifts are large ($\pm5°$), there is a definite indication that the S phase will vanish somewhere in the region of 30–50 Mev. But δ cannot stay close to zero at lower energies, because the experiment of Panofsky *et al.*[4] on the absorption of slow negative pions by hydrogen requires a finite slope of the δ *vs* k curve (k is the wave number) at zero energy.[5]

It is the purpose of this note to point out that the observations can be explained by postulating that at least in the S state an effective attractive potential with a repulsive core exists between the two members of the pion-nucleon system. Qualitatively, it is clear that such a potential[a] possesses the desired properties; the attractive part leads to positive values of δ at low energies (and to a positive slope of the δ *vs* k curve at zero energy), and the repulsive core gives rise to negative values of δ at sufficiently high energies (and therefore to a crossover at some intermediate energy E_0 with respect to which the negative δ's will exhibit a rapid variation). A quantitative fit has been attempted with two shapes which allow analytic solutions,

$$\textit{Square well:}\quad V(r)=V_0,\quad r\geq r_0;\qquad =0,\quad r\geq r_0+r_0. \tag{1}$$

$$\textit{Exponential well:}\quad V(r)=V_0e^{-(r-r_0)/r_s},\quad r\geq r_0. \tag{2}$$

In both (1) and (2), r_0 is the width of the repulsive core which is treated as infinitely high. In each case, the three parameters r_0, V_0, and r_s were varied to fit (within the experimental errors) the slope at the origin and the δ's at 78, 110, and 135 Mev. The Klein-Gordan equation was employed for the pion and the finite mass of the nucleon was taken into account. Some characteristic results are shown in Fig. 1; the experimental data are plotted with their

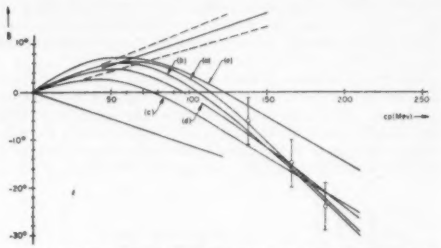

FIG. 1. S phase shifts as a function of $cp(p=\hbar k)$. The line represents the slope derived from reference 4 (the dotted lines show the limits of error). The points represent the δ's (with their errors).

errors and the curves correspond to the sets of parameters listed in Table I.

Examination of Fig. 1 and Table I shows how a fit can be obtained with widely different values of V_0 and rather comparable values of r_0 and r_s [see (a) and (b), (c) and (d)]; on the other hand, once V_0 is fixed, the computed curves are sensitive to the choice of r_0 and r_s [see (d) and (e)]. While a fit is possible for a square well, it is evident that the exponential well leads to more reasonable sets of parameters. Acceptable fits have been achieved with sets of parameters other than those listed in Table I, and it is certain that other potential shapes (e.g., the Yukawa well) will match the present experimental data within their rather large errors.

Despite the nonunique solution available at present, it is possible to draw several conclusions from our hypothesis of a Jastrow-type potential: (1) δ should change sign for $E_0\approx30$–50 Mev, (2) the maximum value of δ below E_0 should be $\sim5°$, (3) if an effective potential with a repulsive core (not necessarily the same as for the S state) operates for the P states of the pion-nucleus system, the crossover energies for the isotopic spin $\frac{3}{2}$ P phase shifts should be higher than for δ, (4) as a consequence of (3), there should be a forward maximum in the scattering cross section below E_0 and a backward maximum between E_0 and the P phase shift crossovers, and (5) the differential cross section should be symmetric about 90° in the barycentric system at E_0. The last two conclusions can be tested directly by experiment.[7]

Since the above calculations were performed, Drell and Henley[8] have shown that the $PS(PS)$ pion-nucleon interaction Hamiltonian can be rewritten in a form which contains a term corresponding to an S state repulsive core of short range plus terms which favor P emission of pions. The S term is quadratic in the pion wave function and is therefore representable by a potential,

TABLE I. Parameters for the curves of Fig. 1.

Curve	Well	V_0(Mev)	$r_0(10^{-13}$ cm)	$r_s(10^{-13}$ cm)
(a)	Square	100	0.95	1.50
(b)	Square	300	1.15	0.95
(c)	Exponential	187.5	0.6	0.6
(d)	Exponential	280	0.75	0.6
(e)	Exponential	280	0.6	0.6

whereas the chief P term is linear and therefore does not readily lend itself to a potential description. Our phenomenological calculations seem to lend some support to the Drell-Henley treatment of pion-nucleon scattering.

Thanks are due Richard Grover and Edith Halbert for assistance with the computations. This work was supported by the AEC.

[1] Anderson, Fermi, Nagle, and Yodh, Phys. Rev. **86**, 793 (1952).
[2] The sign of δ is left undetermined by the analysis of reference 1; moreover, the S phase shift associated with the $\frac{1}{2}$ isotopic spin state of the pion-nucleon system appears to be much smaller than δ and is therefore neglected for the purposes of our discussion.
[3] E. Fermi, private communication. In a very recent communication, Professor Fermi has listed the δ's as: $\pm 21°$ at 135 Mev, $\pm 13°$ at 113 Mev, $\pm 6°$ at 78 Mev. These new values do not alter the qualitative conclusion deduced on the basis of the old values.
[4] Panofsky, Aamodt, and Hadley, Phys. Rev. **81**, 565 (1951); the sign of the slope is left undetermined.
[5] See H. Anderson and E. Fermi, Phys. Rev. **86**, 794 (1952); also R. E. Marshak, Revs. Modern Phys. **23**, 137 (1952).
[6] Introduced by R. Jastrow [Phys. Rev. **81**, 165 (1951)] to explain high energy nucleon-nucleon scattering.
[7] In testing (4) and (3) it may be necessary to correct for Coulomb effects [see L. Van Hove, Phys. Rev. (to be published)].
[8] S. Drell and E. Henley, Phys. Rev. **88**, 1053 (1952). In this paper the repulsive core term actually does not contribute to charge exchange scattering. See also G. Wentzel, Phys. Rev. **86**, 802 (1952).

Magnetostriction of Single Crystals of Cobalt and Nickel Ferrites

R. M. Bozorth and J. G. Walker
Bell Telephone Laboratories, Murray Hill, New Jersey
(Received October 20, 1952)

An unusualy large magnetostrictive contraction $\Delta l/l = -540 \times 10^{-6}$ has been observed in the [100] direction in a crystal of cobalt ferrite having the approximate composition corresponding to $Co_{0.8}Fe_{2.2}O_4$. After cooling the crystal in a magnetic field, we observed $\Delta l/l = -720 \times 10^{-6}$.

The crystal was obtained from Dr. G. W. Clark of Linde Air Products Company. A disk was cut parallel to the (001) plane with dimensions 0.57×0.19 cm, and strain gauges[1] were set to measure the changes in length parallel to [100] and [110] directions. Fields up to 5000 oersteds were applied successively parallel and perpendicular to each gauge. The longitudinal and transverse changes so measured are shown in Fig. 1(a), where they are plotted against the applied field.

Similar data were taken for specimens cut from two crystals of nickel ferrite ($Ni_{0.7}Fe_{2.7}O_4$), one cut parallel to (001) as described above, and the other cut parallel to (011), the gauges in the latter case being set parallel to [100] and [111] directions. Results are shown in Fig. 1(b).

Definite saturation is obtained in all cases except in the [110] direction in the cobalt ferrite. The magnetostriction constants obtained for cobalt ferrite are $\lambda_{100} = -515 \times 10^{-6}$ and $\lambda_{111} = 45 \times 10^{-6}$, if we use the two-constant formula. The data for nickel ferrite are not entirely compatable with this formula, but we find approximately $\lambda_{100} = -36 \times 10^{-6}$, $\lambda_{111} = -4 \times 10^{-6}$; however, results for the two sets of data for the material are self-consistent if we use three constants:[9] $h_1 = -54 \times 10^{-6}$, $h_3 = -4 \times 10^{-6}$, $h_9 = -54 \times 10^{-6}$. The differences in the four curves for the [100] direction in Fig. 1(b) are attributed to differences in initial domain distributions in the two specimens. The broken lines show the values of magnetostriction at saturation calculated for specimens having domains distributed equally among the directions of easy magnetization in the demagnetized state.

The value of $\lambda_{100} = -515 \times 10^{-6}$ for cobalt ferrite is considerably higher than that reported for any other material, as far as the writers are aware. The previous high values of magnetostriction have been reported in a polycrystalline iron-cobalt-vanadium alloy,[2] and in polycrystalline cobalt ferrite.[4] In the single crystal the ratio $|\lambda_{100}/\lambda_{111}|$ is large, namely 11. This, combined with a slight misalignment of the gauges, may account for the peculiar shape and lack of saturation of the [110] curves.

After obtaining the data given above, the crystal was cooled from 400°C to room temperature in a magnetic field of 10,000 oersteds. The magnetostriction, measured in the [100] direction perpendicular to the field H_t present during the cooling, was -710×10^{-6}. That measured parallel to H_t was about $+70 \times 10^{-6}$. A preliminary measurement of the magnetic crystal anisotropy constant yielded $K = -1.7 \times 10^6$.

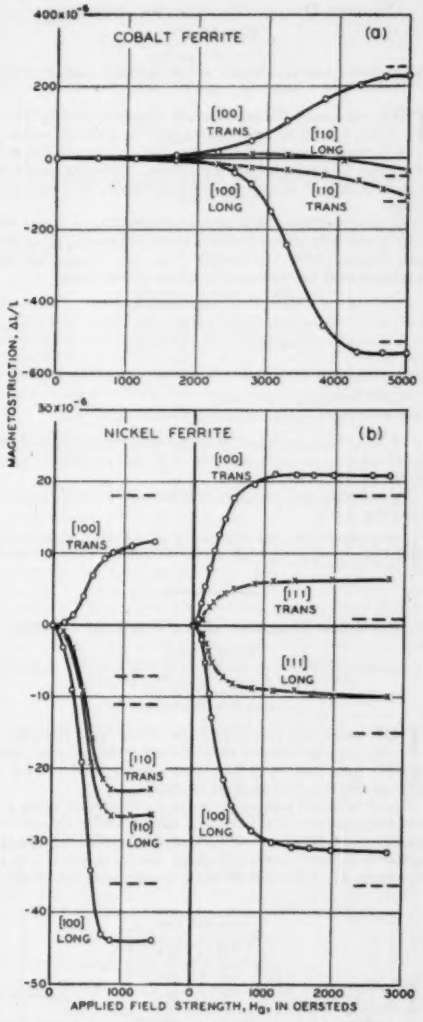

FIG. 1. Longitudinal and transverse magnetostrictive charges for Co and Ni ferrites, plotted against the applied field strength.

[1] J. E. Goldman and R. Smoluchowski, Phys. Rev. **75**, 140 (1949).
[2] R. M. Bozorth, *Ferromagnetism* (D. Van Nostrand and Company, New York, 1951), p. 650.
[3] E. A. Nesbitt [J. Appl. Phys. **21**, 879 (1950)] observed 130×10^{-6} in a cold-rolled tape.
[4] Guillaud, Vautier, and Medvedieff [Compt. rend. **230**, 60 (1950)] observed -200×10^{-6} in an "oriented" polycrystalline specimen (Vectolite), and this was confirmed by L. Weil [Compt. rend. **234**, 1351 (1952)].

Clausius-Mosotti Equation for Anisotropic Crystals*

HANS J. NEUGEBAUER
Eaton Electronics Research Laboratory, McGill University, Montreal, Canada
(Received August 21, 1952)

THE well-known Clausius-Mosotti equation, $3(\epsilon-1)/(\epsilon+2)=4\pi\alpha N$, exhibits a relation between the dielectric constant ϵ of an isotropic substance, the polarizability α of its particles, and the number N of particles per unit volume. The equation can be generalized in such a way as to be applicable to anisotropic crystals.

Such directions are chosen for the coordinates x, y, z that the tensor of dielectric constant reduces to the diagonal ϵ_x, ϵ_y, ϵ_z. The tensor of polarizability of a particle is α_{xx}, α_{xy}, $\cdots\alpha_{zz}$. Then the Clausius-Mosotti equation can be written in two ways:

$$3(\epsilon_x-1)/(\epsilon_x+2)=4\pi\beta_x N, \tag{1}$$

$$\frac{\epsilon_x+2}{\epsilon_x-1}+\frac{\epsilon_y+2}{\epsilon_y-1}+\frac{\epsilon_z+2}{\epsilon_z-1}=\frac{9}{4\pi NA}. \tag{2}$$

In (1) x can be replaced by y or z. The meaning of the symbols is

$$1/\beta_x=A_x+(\alpha_{yy}\alpha_{zz}-\alpha_{yz}^2)/|\alpha_{ik}|,$$
$$3/A=(\alpha_{xx}\alpha_{yy}+\alpha_{xx}\alpha_{zz}+\alpha_{yy}\alpha_{zz}-\alpha_{xy}^2-\alpha_{xz}^2-\alpha_{yz}^2)/|\alpha_{ik}|.$$

$A_x=\sum_k(r_k^{-2}-3x_k^2r_k^{-5})$ can be computed if the structure of the crystal is known. r_k is the distance of the kth particle from one selected particle, $x_k=r_k\cos(\mathbf{x},\mathbf{r}_k)$.

The necessary and sufficient condition for a dielectric to be isotropic is $A_x=0$.

* This research forms part of a project on microwave optics that is supported at McGill University by the United States Air Force through its Cambridge Research Center.

Electronic Structure of the Diamond Crystal

FRANK HERMAN
Department of Physics, Columbia University, New York, New York, and David Sarnoff Research Center, RCA Laboratories, Princeton, New Jersey
(Received October 6, 1952)

THE author has investigated the energy band structure of diamond by means of Herring's orthogonalized plane wave method.[1] Some features of the present solution, shown in Fig. 1, differ significantly from previous results.[2-5]

The three lowest conduction bands are degenerate (state Γ_{15}) at the central point of the Brillouin zone ($\mathbf{k}=000$). Calculations based on the cellular method[2,3] and on the tight-binding approximation[4,5] indicate a nondegenerate lowest conduction band (eigenstate Γ_2') at $\mathbf{k}=000$. Of the four valence bands, three are degenerate (state Γ_{25}') and have negative curvature at $\mathbf{k}=000$. This agrees with Morita's result;[4] other investigators[2,5] found two of these bands to have zero curvature. One of the three lowest conduction bands has negative curvature at $\mathbf{k}=000$ in certain crystallographic directions (e.g., 100) due to the perturbing effect of the Γ_1 conduction band. The uppermost valence bands have greater negative curvature in these directions. Thus, it appears likely that the minimum separation between valence and conduction bands occurs at $\mathbf{k}=000$.

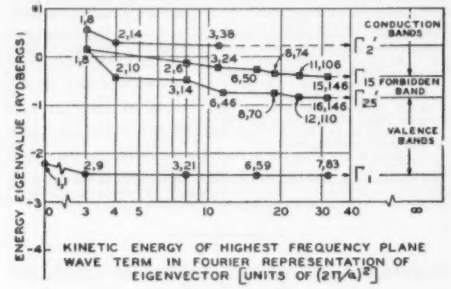
CONDUCTION BANDS
15 FORBIDDEN BAND
25
VALENCE BANDS
1
ENERGY EIGENVALUE (RYDBERGS)
KINETIC ENERGY OF HIGHEST FREQUENCY PLANE WAVE TERM IN FOURIER REPRESENTATION OF EIGENVECTOR [UNITS OF (2π/a)²]

FIG. 2. Convergence of energy eigenvalues for reduced wave vector $\mathbf{k}=000$. Symmetry types Γ_{25}' and Γ_{15} are orthogonal to the core states; the types Γ_1 and Γ_2' must be orthogonalized to the core states. The symbol m,n indicates that an mth order secular determinant yields the eigensolution, which contains n plane wave terms.

That the lowest conduction bands of diamond are degenerate and have nonspherical energy surfaces is particularly interesting in view of ingenious attempts[6,7] to account for the large anisotropic magneto resistance and the anomalous mobility effects observed in germanium. The first effect is interpreted in terms of nonspherical energy surfaces at the bottom of the lowest conduction band, and the second, by postulating that they are re-entrant. Degeneracy is sufficient to account for the former and is necessary for the latter. An investigation of the germanium crystal, just completed, indicates an energy band structure similar to that of diamond. The results will be submitted for publication shortly, as will a more detailed account of the diamond analysis.

The method of orthogonalized plane waves, successfully applied to metallic beryllium[8] and lithium,[8,10] appears to be suitable for diamond-type crystals as well. The precision of the method is dependent upon (1) the accuracy of the assumed potential, (2) the accuracy of the assumed core eigenstates, and (3) the number of terms admitted to the Fourier representations of the crystal wave functions. The Rayleigh-Ritz variational method is used to determine the crystal eigensolutions. Group theory is employed to simplify the computations.[11,12]

The present solution appears to be more reliable than previous investigations: cellular studies,[2,3,13] though useful qualitatively, are unsatisfactory quantitatively;[14] the approximation of tight binding[4,5] is inappropriate for valence and conduction states.

The Coulomb potential and the core eigenstates were obtained from a crystal model consisting of isolated carbon atoms in the $(1s)^2(2s)^1(2p)^3\,{}^5S_2$ state[15] arranged in the form of a diamond lattice. Slater's free-electron approximation[16] was used to represent the exchange potential. The orthogonalization procedure hastened convergence, as is shown in Fig. 2. The eigensolutions automatically orthogonal to the core states approached stable forms slowly as terms were added to the Fourier expansions; the others converged more rapidly, but not so rapidly as corresponding metallic solutions.[8-10] The high order secular equations were solved with the aid of IBM calculating machines at the Watson Scientific Computing Laboratory at Columbia University.

The energy gap remains close to 6 ev over a wide range of solutions. Fluctuations about this value are no longer than uncer-

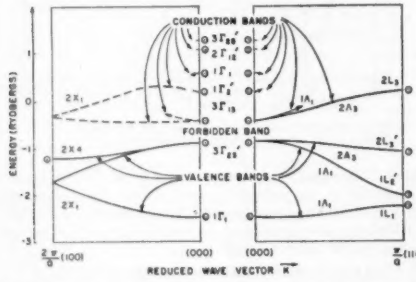

FIG. 1. Schematic of energy bands of diamond crystal in 100 and 111 directions. The notation follows references 11 and 12; for example, the symbol $3\Gamma_{25}$ indicates a threefold degenerate state of symmetry type Γ_{25}. The curves have horizontal slopes at points marked ⊙. Solutions at $2\pi(100)/a$ and at $\pi(111)/a$ are known with less precision than those at (000).

tainties in the assumed potential. Measurements[17,18] of the ultraviolet absorption of diamond indicate an energy gap of at least 5.5 ev. The calculated width of the valence band 22 ev is consistent with interpretations[19,20] of soft x-ray emission spectra from diamond.

The author wishes to express his appreciation to Professor H. M. Foley of Columbia University, Dr. C. Herring of Bell Telephone Laboratories, and Dr. D. O. North and Dr. A. R. Moore of the RCA Laboratories for stimulating discussions and valuable guidance. The author is grateful to Dr. I. Wolff and Mr. E. W. Herold of the RCA Laboratories for their continued interest and encouragement.

[1] C. Herring, Phys. Rev. **57**, 1169 (1940).
[2] G. E. Kimball, J. Chem. Phys. **3**, 560 (1935).
[3] J. F. Mullaney, Phys. Rev. **66**, 326 (1944).
[4] A. Morita, Science Repts. Tôhoku Imp. Univ. **33**, 92 (1949).
[5] G. G. Hall, Phil. Mag. **43**, 338 (1952).
[6] W. Shockley, Phys. Rev. **78**, 173 (1950).
[7] Pearson, Haynes, and Shockley, Phys. Rev. **78**, 295 (1950).
[8] C. Herring and A. G. Hill, Phys. Rev. **58**, 132 (1940).
[9] C. Herring, Phys. Rev. **55**, 598 (1939).
[10] R. H. Parmenter, Phys. Rev. **86**, 552 (1952).
[11] Bouckaert, Smoluchowski, and Wigner, Phys. Rev. **50**, 58 (1936).
[12] C. Herring, J. Franklin Inst. **233**, 525 (1942).
[13] D. H. Ewing, Masters' thesis, University of Rochester (1937), unpublished.
[14] W. Shockley, Phys. Rev. **52**, 866 (1937).
[15] A. Jucys, J. Phys. (U.S.S.R.) **11**, 49 (1947).
[16] J. C. Slater, Phys. Rev. **81**, 385 (1951).
[17] Robertson, Fox, and Martin, Trans. Roy. Soc. (London) **A232**, 463 (1934).
[18] S. Ramanathan, Proc. Indian Acad. Sci. **A24**, 137 (1946).
[19] H. W. B. Skinner, Rept. Progr. Phys. **5**, 257 (1939).
[20] H. Niehrs, Ergeb. exakt. Naturwiss. **23**, 359 (1950).

Bound States and the Interaction Representation

S. T. Ma
Division of Physics, National Research Council of Canada, Ottawa, Canada
(Received October 6, 1952)

In a recent article[1] the temporal development of the state vectors of the free and bound states has been derived from the time-independent formulation of quantum theory. According to this mathematical treatment the transformation operator $W_+(t)$ is non-unitary. On the other hand, it has been observed in Sec. IV of reference 1 that application of an iteration process leads to the conclusion that $W_+(t)$ is unitary. In the present note we shall clarify this apparent inconsistency.

From Eqs. (53) and (36) of reference 1 we see that the integral equations,

$$X(t)=1-i\int_{-\infty}^{t}[H_1(t'),X(t')]dt', \tag{1}$$

$$Y(t)=-i\int_{-\infty}^{t}[H_1(t'),Y(t')]dt', \tag{2}$$

are satisfied by

$$X(t)=W_+(t)W_+^{\dagger}(t)=\int\Psi_{+\lambda}(t)\Psi_{+\lambda}^{\dagger}(t)d\lambda, \tag{3}$$

$$Y(t)=\Sigma_s\Psi_s(t)\Psi_s^{\dagger}(t). \tag{4}$$

However, Eqs. (1) and (2) have also the solutions

$$X(t)=1, \tag{5}$$

$$Y(t)=0. \tag{6}$$

The iteration process described in Sec. IV of reference 1 leads to Eqs. (5) and (6), but not to Eqs. (3) and (4). One cannot, therefore, draw any conclusion about the product $W_+(t)W_+^{\dagger}(t)$ by means of the iteration process we have considered.

The fact that iteration of Eqs. (1) and (2) does not lead to the solutions given by Eqs. (3) and (4) indicates that these solutions cannot be expanded into power series that satisfy the convergence requirements for the validity of the iteration process. Consider, for example, the wave functions $\Psi_s(\mathbf{p})$ of the bound states of the hydrogen atom in the momentum representation. These wave functions contain the factors $[(na\rho/\hbar)^2+1]^{-1}$, where $n=1, 2, \cdots$, $a=\hbar^2/me^2$, and $\rho=|\mathbf{p}|$. Expansion of $\Psi_s(\mathbf{p})$ in powers of e involves the power-series expansion

$$[1+(\hbar/na\rho)^2]^{-1}=1-(\hbar/na\rho)^2+\cdots,$$

which diverges when $\rho<\hbar/na$. Similarly, the power-series expansion of the sum $\Sigma_s\Psi_s(\mathbf{p})\Psi_s^*(\mathbf{p}')$ diverges for small ρ and ρ'.

[1] S. T. Ma, Phys. Rev. **87**, 652 (1952).

Charge Independence and Multiple Pion Production*

L. Van Hove† and R. Marshak,
University of Rochester, Rochester, New York
and
A. Pais, *Institute for Advanced Study, Princeton, New Jersey*
(Received October 9, 1952)

Several authors have recently discussed the role of charge independence in processes involving pions and nucleons.[1] We have explored the consequences of charge independence for multiple pion products in nucleon-nucleon and in pion-nucleon collisions. Before presenting our results,[2] we wish to call attention to a point which has been overlooked in previous treatments of single pion production in nucleon-nucleon collisions and leads to an additional relation among the differential cross sections.

Let us denote by $\sigma(\nu_1\nu_2\to\nu_1'\nu_2'\pi^i)$ the differential cross section for the production of a pion $\pi^i(i=+,\ -,\ 0)$ in a collision of two nucleons ν_1 and ν_2 ($\nu=p$ or n), which are transformed into two nucleons ν_1' and ν_2'($\nu'=p$ or n), respectively. As the differential cross section refers the direction of motion of the outgoing pion to the direction of motion of the incident nucleons, and as all nucleon charges are specified, it follows that in general $\sigma(\nu_1\nu_2\to\nu_1'\nu_2'\pi^i)$ is distinct from $\sigma(\nu_2\nu_1\to\nu_1'\nu_2'\pi^i)$ [or from $\sigma(\nu_1\nu_2\to\nu_2'\nu_1'\pi^i)$] if the initial (or final) nucleons have different charges. If charge symmetry is taken into account, the number of distinct differential cross sections for single pion production reduces to seven which can be written in the form:

$$\begin{aligned}
&\sigma(np\to nn\pi^+)=|F_0/\sqrt{6}-F_1'/2|^2,\\
&\sigma(np\to np\pi^0)=|F_0/2\sqrt{3}+F_1/2|^2,\\
&\sigma(np\to pn\pi^0)=|F_0/2\sqrt{3}-F_1/2|^2,\\
&\sigma(pn\to nn\pi^+)=|F_0/\sqrt{6}+F_1'/2|^2,\\
&\sigma(pp\to np\pi^+)=|F_1/\sqrt{2}+F_1'/2|^2,\\
&\sigma(pp\to pn\pi^+)=|-F_1/\sqrt{2}+F_1'/2|^2,\\
&\sigma(pp\to pp\pi^0)=|F_1'/\sqrt{2}|^2,
\end{aligned}$$

where F_0 is the isotopic singlet amplitude and F_1, F_1' are the two isotopic triplet amplitudes. Thus, the seven cross sections depend on the three absolute values and the two relative phases of these amplitudes. Hence, there exist two relations among the σ's as a consequence of charge independence. One of these is linear:

$$\sigma_1^{+}+\sigma_3^{+}=2(\sigma_2^{+}+\sigma_4); \tag{1}$$

the other is essentially a phase relationship:

$$\begin{aligned}
&\cos^{-1}\{\sigma_2^{-}/2[(\sigma_3^{+}-\sigma_4)\sigma_4]^{\frac{1}{2}}\}+\cos^{-1}\{\sigma_1^{-}/2[(\sigma_1^{+}-\sigma_4)\sigma_4]^{\frac{1}{2}}\}\\
&\qquad=\cos^{-1}\{\sigma_2^{-}/[(\sigma_1^{+}-\sigma_4)(\sigma_2^{+}-\sigma_4)]^{\frac{1}{2}}\}.
\end{aligned} \tag{2}$$

Here we have set

$$\begin{aligned}
\sigma_1^{\pm}&=\sigma(np\to nn\pi^+)\pm\sigma(pn\to nn\pi^+),\\
\sigma_2^{\pm}&=\sigma(np\to np\pi^0)\pm\sigma(np\to pn\pi^0),\\
\sigma_3^{\pm}&=\sigma(pp\to pn\pi^+)\pm\sigma(pp\to np\pi^+),\\
\sigma_4&=\sigma(pp\to pp\pi^0).
\end{aligned}$$

Relation (2) can only be obtained by distinguishing between $\sigma(np\to nn\pi^+)$ and $\sigma(pn\to nn\pi^+)$, etc. Messiah[1] [see his Eq. (10)] and Luttinger[1] [see his Eq. (2)] do not make this distinction, so that their relation is only valid in so far as *total* cross sections are concerned.

The above considerations can be generalized to multiple pion production in nucleon-nucleon collisions; as the number k of pions increases, both the number S_k of distinct cross sections (in the

above sense) and the minimum number R_k of relations resulting from charge independence increase rapidly. It can be shown that

$$S_k=\tfrac{1}{2}I_k+I_{k+1}+\tfrac{1}{2}I_{k+2},$$
$$R_k=I_{k+3}-\tfrac{1}{2}I_{k+2}-4I_{k+1}-(5/2)I_k+1,$$
$$I_k=\pi^{-1}\int_0^\pi(1+2\cos\varphi)^k d\varphi.$$

For large k, $S_k\sim R_k\sim k^{-1}3^k$. Thus, for $k=2$, $R_2=7$; one relation is particularly interesting:

$$\begin{aligned}4[&\sigma(pp\to pp\pi^0\pi^0)+\sigma(np\to np\pi^0\pi^0)+\sigma(np\to pn\pi^0\pi^0)]\\&+[\sigma(pp\to np\pi^+\pi^0)+\sigma(pp\to np\pi^0\pi^+)+\sigma(pp\to pn\pi^+\pi^0)\\&+\sigma(pp\to pn\pi^0\pi^+)+\sigma(np\to pp\pi^-\pi^0)+\sigma(np\to pp\pi^0\pi^-)\\&+\sigma(np\to nn\pi^+\pi^0)+\sigma(np\to nn\pi^0\pi^+)]-2[\sigma(pp\to pp\pi^+\pi^-)\\&+\sigma(pp\to pp\pi^-\pi^+)+\sigma(pp\to nn\pi^+\pi^+)+\sigma(np\to np\pi^+\pi^-)\\&+\sigma(np\to np\pi^-\pi^+)+\sigma(np\to pn\pi^+\pi^-)+\sigma(np\to pn\pi^-\pi^+)]=0,\end{aligned}\quad(3)$$

where the notation is an obvious generalization of the single pion notation. If one now introduces the following numbers for the 2π production reactions:

$$N_{+,-,0}=\langle N_{+,-,0}\rangle_{pp}+\langle N_{+,-,0}\rangle_{np},$$

where, e.g., $\langle N_+\rangle_{pp}$ is the average number of positive pions produced in a pp collision in which two pions are emitted with given direction (the other quantities are likewise defined). One easily finds from (3)

$$N_++N_-=2N_0,\quad(4)$$

which is a special case of Watson's[1] general relation. One can start with Watson's relation which holds for an arbitrary number of pions and reverse the argument to obtain the generalization of Eq. (3) for an arbitrary pion multiplicity.[2]

The consequences of charge independence for multiple pion production in pion-nucleon collisions have also been examined;[3] unfortunately, some of the relations cannot be tested experimentally because they involve cross sections referring to an incident π^0. An illustration of the latter type of relationship which is independent of the pion multiplicity is

$$\sigma(\pi^+p)+\sigma(\pi^-p)=2\sigma(\pi^0p),\quad(5)$$

where $\sigma(\pi^+p)$ denotes the sum of all cross sections corresponding to a specified multiplicity produced by a pion π^+ incident on a proton. Secondly, considering $\pi-p$ collisions of given multiplicity, relation (4) again holds true provided one defines $N_+=\langle N_+\rangle_{p\pi^-}+\langle N_+\rangle_{p\pi^0}-\langle N_+\rangle_{p\pi^0}$, etc.

When there is only one final pion (i.e., pion scattering by a proton), (4) and (5) are the only relations which follow from charge independence and actually reduce to one, namely Heitler's[1] relation, because of charge symmetry and detailed balancing.

For k final pions, $R_k=I_{k+3}-\frac{1}{2}I_{k+2}-(5/2)I_{k+1}+1$, $R_k^{\rm ch}$ (referring to an incoming $\pi^\pm$ only)$=I_{k+3}-\frac{1}{2}I_{k+2}-3I_{k+1}-\frac{1}{2}I_k+1$. Thus, $R_1=6$, $R_2^{\rm ch}=1$, whereas asymptotically $R_k\sim R_k^{\rm ch}\sim k^{-1}3^k$.

Of course, if the further assumption is made that the pion-nucleon interaction is restricted to the state of total isotopic spin $\frac{3}{2}$,[4] the number of relations involving only incident charged pions is greatly increased; for example, Eq. (5) is replaced in this approximation by

$$\tfrac{1}{2}\sigma(\pi^+p)=\tfrac{1}{2}\sigma(\pi^0p)=\sigma(\pi^-p),\quad(6)$$

while additional relations hold for specific multiplicity, such as:

$$\begin{aligned}2[&\sigma(p\pi^-\to p\pi^-\pi^0)+\sigma(p\pi^-\to p\pi^0\pi^-)]\\&=\sigma(p\pi^-\to n\pi^+\pi^-)+\sigma(p\pi^-\to n\pi^-\pi^+)+4\sigma(p\pi^-\to n\pi^0\pi^0).\end{aligned}$$

* This work was supported by the AEC.

† On leave from the Institute for Advanced Study, Princeton, New Jersey during the summer of 1952.

[1] See K. M. Watson, Phys. Rev. **85**, 852 (1952); R. L. Garwin, Phys. Rev. **85**, 1045 (1952); A. M. L. Messiah, Phys. Rev. **86**, 430 (1952); J. M. Luttinger, Phys. Rev. **86**, 571 (1952), in addition to the original reference of W. Heitler, Proc. Roy. Irish Acad. **51**, 33 (1946). One of us (A.P.) is indebted to J. M. Luttinger for several discussions on these topics.

[2] Details of the method will be found in L. Van Hove, Rochester Report NYO-3074, unpublished.

[3] It may be pointed out that additional linear relations are obtained for pion production in nucleon-nucleon collisions when the nucleons emerge as a deuteron. See reference 2.

[4] See Proceedings of the Rochester Conference on Meson Physics, January, 1952, unpublished.

Lower Limits for Interaction Times in Photon Scattering Processes

E. GORA
Providence College, Providence, Rhode Island
(Received September 30, 1952)

IN a semi-classical treatment of the scattering of light by charged particles a switching-on function was used to avoid the appearance of "run-away" radiation reaction terms.[1] A consistent formulation appeared to be possible only if the duration of the interaction, the "interaction time," exceeded a lower limit. Recently, several authors[2] suggested that it might be necessary to use switching-on functions also in quantum theory. A tentative way of doing this, which leads to a confirmation of the semi-classical conclusions concerning interaction times, is to multiply the matrix elements H_{0l} for transitions from the initial state in the equations of the time dependent perturbation theory by a switching-on function f. In solving these equations, we retain the terms of lowest order containing time derivatives of f. Apart from this we follow the usual procedure and obtain for second-order processes[3]

$$\dot b_0=(i/4\pi)\int d\Omega(f\Delta+if\Gamma+i\dot f\Delta_1-\dot f\Gamma_1)\cdot b_0,\quad(1)$$

where

$$\Delta=\frac{1}{\hbar}\Sigma\frac{H_{01}H_{10}}{E_1-E_0},\quad \Delta_1=\Sigma\frac{H_{01}H_{10}}{(E_1-E_0)^2},$$
$$\Gamma=\frac{\pi}{\hbar}S_{FpF}\Big\{\Sigma\frac{H_{01}H_{1F}}{E_1-E_0}\Big\}^2,\quad(2)$$
$$\Gamma_1=\pi S_{FpF}\Big\{\Sigma\frac{H_{01}H_{1F}}{E_1-E_F}\Sigma\frac{H_{F11}H_{110}}{(E_{11}-E_0)^2}+\Sigma\frac{H_{01}H_{1F}}{(E_1-E_0)^2}\Sigma\frac{H_{F11}H_{110}}{E_{11}-E_0}\Big\}.$$

Σ denotes summation over the intermediate states I, II; and S_F summation and averaging over the directions of spin and polarization in the final state. Δ represents a frequency shift, and Γ a damping coefficient; Δ_1, Γ_1 are dimensionless.

The well-known formulas for scattering cross sections and self-energy effects follow from Eq. (1) if

$$(\tau_{1,2}\dot f)_{kt}\ll(f)_{kt}\cong 1,\quad(3)$$

where

$$\tau_1=\Delta_1/\Gamma,\quad(4a)$$
$$\tau_2=\Gamma_1/\Delta.\quad(4b)$$

Using $f=1-\exp(-\alpha t)$, we evaluate these averages for the time interval between $t=0$ and the interaction time t. It appears that condition (3) will be fulfilled if $1/\alpha\ll t$, and $\tau_{1,2}\ll t$. The times τ_1, τ_2 are thus seen to represent lower limits for the interaction time of processes for which the formulas of the quantum theory of radiation are known to be approximately valid.

For scattering of photons by electrons initially at rest, we evaluate Eqs. (2) in the usual way and obtain from Eqs. (4)

$$\tau_1=\left(\frac{\hbar c}{e^2}\right)^2\frac{r_0}{c}\frac{k_0^2}{k^2}\frac{\mu(k_0+k)}{(k_0+k)^2+k_0k(1+x^2)},\quad(5a)$$
$$\tau_2=\frac{r_0}{c}\frac{1+x}{2}\frac{k^2}{k_0^2}\frac{(k_0-k)^2+k_0k(1+x)}{\mu(k_0+k)},\quad(5b)$$

where $r_0=e^2/mc^2$, and x is the cosine of the scattering angle. Except for $k/\mu=\gamma>137$ and small scattering angles, $\tau_2\ll\tau_1$. We shall thus, at present, consider τ_1 only.

In the extreme relativistic case ($\gamma\gg1$) in which we are primarily interested, τ_1 is largest for $x\cong-1$: $\tau_{1\,\max}\cong4\gamma\tau_0$, $\tau_0=\hbar^3/me^4c$. The extreme relativistic average of τ_1 is $2\gamma\tau_0/\ln(2\gamma)$. These results confirm the conclusion arrived at in the semi-classical theory that a lower limit for interaction time of the order of magnitude $\gamma\tau_0$ should be taken into consideration.

The same method can be used to investigate the validity of quantum theoretical formulas for higher order processes. For extreme relativistic photon-photon scattering a rough estimate leads to the order of magnitude $\gamma\tau_0$ with $\tau_0=(\hbar c/e^2)^4(r_0/c)\cong3.3\times10^{-15}$ sec for the lower limit of the interaction time. The coin-

cidence of this order of magnitude with the observed lifetime of a neutral meson decaying into two photons could be accidental; still, it suggests the possibility of some connection between the apparent lifetime of unstable particles and a finite duration of the interaction between the particles which take part in the production and decay processes.

[1] E. Gora, Phys. Rev. **84**, 1119 (1951).
[2] B. Ferretti, Nuovo cimento **8**, 108 (1951); F. J. Dyson, Phys. Rev. **83**, 608 (1951); H. S. Snyder, Phys. Rev. **83**, 1154 (1951).
[3] For the notation used, see W. Heitler, *Quantum Theory of Radiation* (Clarendon Press, Oxford, 1944), second edition, Chap. III, p. 16.

Mass of K^{40}†

WALTER H. JOHNSON, JR.
Department of Physics, University of Minnesota, Minneapolis, Minnesota
(Received October 14, 1952)

THE determination of a decay scheme for K^{40} depends upon the magnitudes of the gamma- and beta-ray energies. In the past, a number of somewhat widely varying values have been reported. These varying values lead to an uncertainty in the decay scheme. Recent experiments suggest that a decay scheme having K^{40} decay to Ca^{40} by a beta-decay, and to A^{40} by a K capture followed by a gamma-ray emission is correct. In order to substantiate this conclusion, I have measured the masses of K^{40}, A^{40}, and Ca^{40} employing a double-focusing mass spectrometer.[1] The total energy differences between the three nuclides, found from the masses, can be compared with the beta- and gamma-ray energies.

A sample of potassium containing 7.74 percent of K^{40}, obtained from the Electromagnetic Separation Plant in Oak Ridge, Tennessee, on allocation from the Isotope Division, U. S. Atomic Energy Commission, was used as a source of potassium ions. In earlier determinations of the masses of A^{40} and Ca^{40}, the hydrocarbon fragment $(C^{12})_3(H^1)_4$ was used as a comparison peak. This it not a good fragment to use because of the large $(C^{12})_2C^{13}(H^1)_2$ unresolved satellite. While correction has been made for this, it is a possible source of error. In the present work, this difficulty has been eliminated by employing the fragment $(C^{12})_2O^{16}$ from acetic acid. Normal calcium metal was used as a source of Ca^{40} ions.

In this experiment, a run consisted of eight C_2O-A^{40} traces, ten C_2O-K^{40} traces, and then eight more C_2O-A^{40} traces. From each run, the C_2O-K^{40} result was compared with an average of the two C_2O-A^{40} results to obtain the mass difference of the $K^{40}-A^{40}$ doublet. In a similar manner, the doublet $Ca^{40}-A^{40}$ was determined. This method had to be employed because the K^{40}, A^{40}, and Ca^{40} ion peaks were not resolved in the mass spectrometer.

In the case of the potassium runs, a small correction had to be made because of the unresolved residual A^{40} peak, while in the calcium runs, because of the much larger beam current, no correction for residual A^{40} was necessary. A small calcium impurity found in the spectroscopic analysis of the K^{40} sample could cause a low $K^{40}-A^{40}$ result. Because of peak shape consistencies, this error was believed to be less than 10 percent of the $K^{40}-A^{40}$ difference.

The weighted averages of four calcium-argon runs for the doublets C_2O-A^{40}, C_2O-Ca^{40}, and $Ca^{40}-A^{40}$ yield 32.756 ± 0.010, 32.557 ± 0.009, and 0.201 ± 0.015 millimass units, respectively. The averages of five potassium-argon runs for the doublets C_2O-A^{40}, C_2O-K^{40}, and $K^{40}-A^{40}$ yield 32.735 ± 0.024, 31.140 ± 0.081, and 1.595 ± 0.071 mMU, respectively. The masses of the three nuclides may be calculated using C^{12} to be 12.003842 ± 4[1] and O^{16} to be exactly 16 atomic mass units. The masses of K^{40}, Ca^{40}, and A^{40} are then 39.97654 ± 8, 39.975127 ± 11, and 39.974940 ± 15 aMU, respectively. The argon mass is determined from a weighted average of all the argon data. The disagreement between the Ca^{40} and A^{40} masses reported here and those previously reported[2] may be attributed to several improvements in the instrument and to the elimination of the large C^{13} correction, necessary in the previous work.

From the masses, the total energies for the decay of K^{40} to Ca^{40} and A^{40} are 1.30 ± 0.07 and 1.49 ± 0.07 Mev, respectively. The energy released in the decay to Ca^{40} agrees well with the most recent beta end-point determinations which gave energies of 1.40 ± 0.03,[3] 1.36 ± 0.05,[4] 1.28 ± 0.03,[5] and 1.325 ± 0.015 [6] Mev. The result disagrees with earlier determinations which in several cases gave values higher than 1.45 Mev.[7,8] Two of the earlier determinations which gave lower values were 1.3 [9] and 1.35 [10] Mev. Several recent determinations of the gamma-ray energy for the K^{40} decay gave values of 1.47 ± 0.03,[11] 1.462 ± 0.01,[12] and 1.459 ± 0.007[13] Mev. Because the gamma-ray energy is greater than the total energy available in the decay to Ca^{40}, it must be associated with the decay to A^{40}, as is true in the presently accepted decay scheme.

I wish to thank Dr. A. O. Nier and Dr. T. L. Collins for their valuable assistance and advice.

† Research supported by joint programs of ONR and AEC.
[1] Collins, Nier, and Johnson, Phys. Rev. **84**, 717 (1951).
[2] A. O. Nier and T. R. Roberts, Phys. Rev. **81**, 507 (1951).
[3] D. E. Alburger, Phys. Rev. **75**, 1442 (1949).
[4] Bell, Weaver, and Cassidy, Phys. Rev. **77**, 399 (1950).
[5] M. L. Good, Phys. Rev. **83**, 1054 (1951).
[6] L. Feldman and C. S. Wu, Phys. Rev. **87**, 1091 (1952).
[7] S. Franchetti and M. Giovanozzi, Phys. Rev. **74**, 102 (1948).
[8] L. H. Borst and J. J. Floyd, Phys. Rev. **74**, 989 (1948); **75**, 1106 (1949).
[9] W. J. Henderson, Phys. Rev. **55**, 238 (1939); **71**, 323 (1947).
[10] Dzelepow, Kopjova, and Vorobjov, Phys. Rev. **69**, 538 (1946).
[11] Pringle, Standil, and Roulston, Phys. Rev. **77**, 841 (1950).
[12] P. R. Bell and J. M. Cassidy, Phys. Rev. **79**, 173 (1950).
[13] M. L. Good, Phys. Rev. **81**, 891 (1951).

Angular Distribution of Neutrons of the *d-d* Reaction

PAUL BAKER, JR., AND ARTHUR WALTNER*
North Carolina State College, Raleigh, North Carolina
(Received October 6, 1952)

WE have recently measured the angular distribution of neutrons from the $H^3(d,n)He^3$ reaction using 50-kev incident deuterons. The deuteron beam was furnished by a radio-frequency ion source of the type described by Moak *et al.*[1] and was focused on a deuterium target prepared by bombarding to saturation a thin copper plate. The diameter of the deuterium spot on the copper plate was approximately 3.5 mm.

Seven Ilford C-2 nuclear plates with emulsions 100 microns thick were positioned radially around the target at laboratory angles of 15°, 30°, 75°, 90°, 105°, 120°, and 135° with the deuteron beam. The plates were exposed to the neutron flux for forty hours. To discriminate against proton-recoil tracks caused by neutrons scattered on the plates by surrounding material, only those tracks whose visible horizontal projection was equal to or greater than 40 microns and whose angle with the neutron beam was equal to or less than $\sin^{-1}0.4$ were counted. The entire thickness of the emulsion was examined for each field of view. Five traverses, each 2 cm long, which were made across an unexposed background plate revealed only one acceptable track; consequently, background corrections were not considered necessary.

It is customary in angular distribution experiments to analyze the results so as to determine the values of asymmetry coefficients. At low deuteron bombarding energies, this amounts to selecting that value of A in the expression $N'(\theta')=N'(90°)(1+A\cos^2\theta')$, where primed quantities are in center-of-mass coordinates, which

TABLE I. The number of recoil protons $N(\theta)$ at different laboratory angles θ, with transformation to center-of-mass coordinates θ'. $g(\theta)$ is the transformation factor connecting $N(\theta)$ and $N'(\theta')$.

θ	θ'	$N(\theta)$	$g(\theta)$	$N'(\theta')$
15°	15.7°	423	0.918	388
30°	31.4°	398	0.925	368
75°	77.8°	343	0.977	335
90°	92.9°	256	1.000	256
105°	107.8°	340	1.024	348
120°	122.5°	350	1.047	366
135°	137.0°	366	1.068	391

yields the best fit for the experimental data. These data and the transformations from laboratory to center-of-mass coordinates are shown in Table I.

The value of the asymmetry coefficient A was determined by the method of least squares. The method yielded a value of 0.25 ± 0.05, which is in agreement with the value of 0.30 ± 0.03 for the protons of the reaction[2] and with the value of $0.15+0.0027E$ for the neutrons.[3] The photographic method appear to be in agreement with other methods for angular distribution measurements.

* Present address: A. B. Atomenergie, Stockholm, Sweden.
[1] Moak, Reese, and Good, *Nucleonics* **9**, 18 (1951).
[2] Bretscher, French, and Seidl, Phys. Rev. **73**, 815 (1948).
[3] I. Bartholdson, Arkiv. Fysik **2**, 271 (1950).

The Concept of Spin-Lattice Relaxation in Ferromagnetic Materials

P. W. Anderson
Bell Telephone Laboratories, Murray Hill, New Jersey
(Received October 9, 1952)

In the literature on the high frequency properties of ferromagnetic materials, it is often assumed that the distinction between spin-spin and spin-lattice relaxation will be as valid here as it is in paramagnetic relaxation and paramagnetic resonance. In fact, often the assumption is made that the two types of relaxation enter in exactly the same way as in the paramagnetic case, and thus that the Bloch equations of motion are valid. This letter contends that this cannot be the case.

The simplest physical explanation of the situation results from considering why, in the paramagnetic case, it is necessary to make the distinction between the two types of relaxation. In the paramagnetic case we apply an external field H_z which causes energy splittings large compared to the interaction energies between the spins. It is now true that these interactions can broaden the paramagnetic resonance line, and also they can cause the components S_x, S_y of the total spin perpendicular to the external field to relax toward the equilibrium value zero (these two effects being in fact equivalent). On the other hand, if energy is absorbed from some external magnetic field (usually rf or microwave) thus causing the component of total spin S_z to change, an entirely different relaxation mechanism is required to bring the sytsem back to thermal equilibrium. This is because the spins and their interactions are incapable of accepting this energy, which may be shown in two ways: in the first place, the energy is in the form of "Zeeman quanta" μH_z, which are large compared with the interaction quanta $\mu H_{\text{loc}}\sim\mu^2/r^3$; in the second place, the specific heat of the "spin system" is due almost entirely to the interaction with the external field H_z, so that there is simply no tendency to redistribute the energy which has been acquired among the spins alone; their interactions simply are not big enough to accept the energy. Thus interaction with the crystal lattice, "spin-lattice relaxation," is the only way in which thermal equilibrium can be re-established and S_z can relax to its original value. This interaction is often relatively slow, and spin-lattice relaxation can then be measured as a separate effect.

The situation in ferromagnetism is quite obviously entirely different. Here the exchange fields acting on the spins are large compared to the external field in all situations, and the specific heat of the spin system as a whole is large compared to that due to the interaction with the external field, being comparable with the lattice's specific heat. In such a situation we see that, if spin-spin interactions are capable of causing the major part of the line breadth, they will obviously be capable also of accepting the energy of the "Zeeman quanta" fed in by an external field, and, unless the total energy fed in is comparable with that necessary to heat the whole system to the Curie point, no effects due to saturation of the spin system as a whole can possibly occur.

Another way of phrasing this is to point out that changing the total spin S in any way other than the formation of domains of macroscopic size requires an energy of this same large order of magnitude (about $H_E M_S$, where H_E is the exchange field, $\sim10^6$ oersteds, and M_S is the saturation moment) and thus that in most experiments S_x and S_y cannot be independent of S_z; it is then hard to see how any relaxation formula containing two constants rather than one can be applicable. We see also that, if S cannot change, only interactions capable of changing S_z will be capable of relaxing S_x and S_y, and causing broadening.

Finally, we shall give an indication of the circumstances under which spin-lattice relaxation might actually be observed[1] in a typical relaxation experiment. In order to saturate the spin system, an energy $E_0=H_E M_S$ is required. Power can be fed into the system at ferromagnetic resonance at a rate

$$P_i=\chi''\omega_0 H_1^2\simeq(\gamma H_0)(H_1^2)(M_s)/(\Delta H),$$

where ΔH is the line width, H_1 the applied rf field. H_1 must be $\leq\Delta H$ or the system will be saturated spin-spinwise, so we set $H_1=\Delta H$ for a maximum possible energy input. Then the time T in which the energy input is large enough to saturate the whole spin system is

$$T=\frac{E_0}{P_i}\simeq\frac{H_E}{H_0}\left(\frac{1}{\gamma\Delta H}\right)=\frac{H_E}{H_0}\text{ (spin-spin relaxation time).}$$

Thus the time T is of order 10^3-10^4 times the spin-spin relaxation time, and unless the spin-lattice relaxation time is slower than this (of order $10^{-4}-10^{-5}$ sec, that is) no effect can be observed. In addition, the pulses of input power must also be of this length, which has not been the case in Damon's experiments on relaxation.[1]

I must acknowledge my gratitude for very helpful discussions with Dr. N. Bloembergen, Dr. J. K. Galt, Dr. W. A. Yager, and particularly Dr. C. Kittel.

[1] Unless direct spin-lattice relaxation due to interaction of the lattice with the zero wave-number spin wave into which the energy is fed is the primary broadening mechanism. This probably is not the case, according to calculations of D. Polder and J. K. Galt, unpublished; C. Kittel and J. M. Luttinger (reported in paper of C. Kittel, to be published in January, 1953, Revs. Modern Phys.); and R. W. Damon, thesis, Harvard University, 1951, unpublished.

Relativistic Corrections to Magnetic Moments of Nuclear Particles*

G. Breit and R. M. Thaler
Yale University, New Haven, Connecticut
(Received October 20, 1952)

Relativistic corrections to magnetic moments of nuclear particles have been of special interest in connection with the determination of the proportion of the ^3D state contained in the ground state of the deuteron and the additivity of magnetic moments of nucleons. The problem has been treated by various authors[1-6] with inconclusive results.

For the case referred to[5,6] as the scalar, the result of Sachs[4] for the deuteron, neglecting the ^3D state, is

$$(CF)_{2S}=1-\langle W/M\rangle+\langle T/3M\rangle, \quad (1)$$

where W and T are respectively the energy and kinetic energy of internal motion, and CF is the correction factor to the Dirac part of the proton's magnetic moment; $c=1$ in the units used. The corresponding calculation of Breit and Bloch[6] contained an error, the existence of which was inferred by Adams.[6] Although the Hamiltonian used by Sachs in this and the vector case is not covariant in the required order, the direct employment of the field to which a particle is exposed is justifiable, as may be inferred from the material below. For the two-body vector case the same manipulative slip (BB) entered,[5] and the employment of $\mathbf{p}$ in place of $\boldsymbol{\alpha}$ by Sachs is mainly responsible for a difference from the correct result, namely,

$$(CF)_{1V}=1, \quad (^3D\text{ neglected}). \quad (2)$$

While the Hamiltonians used by Breit and Bloch[5] lead to the above values and are covariant[7] to order v^2/c^2, the correction for retardation is not complete. The electromagnetic case suggests caution in its use for ψ. One can represent the results just mentioned as

$$(CF)_{2S}=\frac{M-\langle J_1\rangle}{M-\langle J_2\rangle}(CF)_{1S}, \tag{3}$$

and

$$(CF)_{2V}=1-\langle T/3M\rangle\langle 1-(\boldsymbol{\sigma}_1\boldsymbol{\sigma}_{II})\rangle,$$
$$[\text{elements diagonal in } (\boldsymbol{\sigma}_1+\boldsymbol{\sigma}_{II})]^2 \tag{4}$$

where[1,2]

$$(CF)_{1V}=1-\langle 2T_1/3M\rangle, \tag{5}$$

and[2]

$$(CF)_{1S}=1-\langle W_1/M\rangle-\langle T_1/3M\rangle=1-\langle 4T_1/3M\rangle+\langle J_1/M\rangle, \tag{6}$$

the nonrelativistic potential energy being denoted by $(-J)$, quantities referring to the one- and two-body problems being designated by subscripts 1,2, respectively, the proton being referred to by subscript I, and the neutron by II. The mean kinetic energy in the two-body problem is

$$\langle T_2\rangle=2\langle T_1\rangle, \tag{7}$$

where on the left $T_2=T_1+T_{II}$. The nonrelativistic energy is

$$W=\langle T-J\rangle \tag{7'}$$

in the one- and two-body cases. Euqation (3) shows that

$$[\text{Effective mass}]_S=M-\langle J\rangle. \tag{8}$$

This interpretation has been substantiated by decomposing the one-body effects into parts arising from unbound particle states. States of positive energy alone give

$$(CF)_{1(E>0)}\langle \mathbf{L}+\hbar\boldsymbol{\sigma}\rangle=\langle (M/E)(\mathbf{L}+\hbar\boldsymbol{\sigma})$$
$$+\hbar\{M/[2E^2(E+M)]\}[(\boldsymbol{\sigma}\mathbf{p})\mathbf{p}-p^2\boldsymbol{\sigma}]\rangle. \tag{9}$$

For s terms, to order v^2/c^2,

$$(CF)_{1(E>0)}=1-\langle 4T/3M\rangle. \tag{9'}$$

The remaining factors in Eqs. (5) and (6) are accounted for by cross terms for opposite signs of E. The role of J is to produce states with $E<0$ and the effectiveness of terms in J in the Dirac Hamiltonian depends on whether it is used as $E-J$ or $M-J$ as in the V and S cases. In the two-body problem $E<0$ states are caused by

$$J_2=J_2(|\mathbf{r}_I-\mathbf{r}_{II}|), \tag{10}$$

and it is clearly immaterial in first approximation whether $\mathbf{r}_{II}$ is fixed (one-body case) or moving (two-body case).

In the two-body vector case the term in the proton spin corresponds to Eq. (4), since $T_2=2T_1=T$. The term in $\boldsymbol{\sigma}_{II}$ can be traced to $-\boldsymbol{\alpha}_I\boldsymbol{\alpha}_{II}$ in the Hamiltonian. This effect has been verified to be a generalization of the magnetic induction produced in the spin current of one electron by the magnetic field caused by the spin current of a second electron. Usual "retardation" does not affect the "induced current" correction.

For a single particle with definite relativistic energy E in a pseudoscalar field, the Dirac current part of the magnetic moment is given by

$$\langle \mathbf{L}+\hbar\boldsymbol{\sigma}\rangle/E, \tag{11}$$

suggesting insignificant relativistic corrections in nuclei describable on the single-particle view. In the deuteron such a view does not hold. Analogy with the cases treated above suggests that the mesic field interaction contributes to the production of $E<0$ plane waves in the same way in the one- and two-body cases, while $\langle W_2\rangle$ contains $2T_1$ instead of T_1. This view suggests

$$CF=1+\langle T_2/2M\rangle-\langle W_2/M\rangle, \tag{12}$$

to which one may object because: (a) the PS field acting on the proton is not spherically symmetric complicating the isolation of spin-current effects; (b) within the repulsive core and on the inner edge of the attractive region the effective $|J|$ is large; (c) the large value of the usual interaction constant f suggests inclusion of mesic current effects; and (d) the presence of nucleon pairs may contribute additional magnetic moments.

* Assisted by the joint program of the ONR and AEC.
[5] G. Breit, Nature **122**, 649 (1928).
[2] H. Margenau, Phys. Rev. **57**, 383 (1940).
[3] G. Breit, Phys. Rev. **71**, 400 (1947).
[4] R. G. Sachs, Phys. Rev. **72**, 91 (1947).
[5] G. Breit and I. Bloch, Phys. Rev. **72**, 135 (1947).
[6] E. N. Adams II, Phys. Rev. **81**, 1 (1951); see footnote 20.
[7] G. Breit, Phys. Rev. **51**, 248 (1937).

PHYSICAL REVIEW VOLUME 88, NUMBER 5 DECEMBER 1, 1952

Proceedings of the American Physical Society

Minutes of the 1952 Autumn Meeting of the New York State Section at Cornell University

THE twenty-eighth meeting of the New York State Section was held at Cornell University, Ithaca, New York, on October 17 and 18, 1952, with a total registration of about 150.

The Friday morning session was devoted to two invited papers; the Friday afternoon session to a single invited paper and a group of five contributed papers. The Dinner on Friday evening was preceded by a Social Hour in the Club Rooms of the Statler Inn on the Cornell Campus, and followed by a delightful talk on "Acoustics and Bird Song Recording" by Professor P. P. Kellog of Cornell's Department of Ornithology.

The closing session, on Saturday morning, was given over to a Symposium on Lecture Demonstrations in Physics. The teaching and research laboratories in both Rockefeller Hall and the Nuclear Studies Laboratory were open to (and flooded by) visitors throughout the two-day period.

Titles of the invited papers and abstracts of the contributed papers, together with the Symposium program, are given below.

L. W. PHILLIPS, *Secretary*
New York State Section
The University of Buffalo
Buffalo 14, New York

Invited Papers

The Fundamental Particles of Physics. H. A. BETHE, *Cornell University.*

The Use of Large-Scale Computing in Physics. L. H. THOMAS, *Watson Scientific Laboratory.*

Recent Developments in p-n Junction Transistors. R. N. HALL, *General Electric Research Laboratory.*

Symposium on Demonstrations in Physics

(L. P. SMITH presiding)

Demonstrations of (a) Random Molecular Motion and (b) Motor and Generator. C. L. HENSHAW, *Colgate University.*

Pupil-Built Apparatus for Teaching Pascal's Principle. B. H. STASCH, *Corning Free Academy.*

Two New Peltier Demonstrations. C. L. ANDREWS, *New York State College for Teachers at Albany.*

Demonstrations of Two Simple Electrical Experiments: (a) The Power Transmission Line, and (b) Damped Oscillations in an RLC Circuit. H. F. NEWHALL, *Cornell University.*

A Luminous Lens-Graph. M. J. PRYOR, *New York State College for Teachers at Albany.*

Use of the Vidican Tube with Television to Illustrate Small-Scale Effects. G. E. GRANTHAM, *Cornell University.*

Contributed Papers

Frequency Response of PbS Cells. B. D. MCMICHAEL AND S. MROZOWSKI, *University of Buffalo.*—The frequency response of a lead sulfide photocell was investigated for various spectral excitations. Parts of the near infrared spectrum emitted by incandescent carbon were isolated by means of either filters or in infrared spectrometer. The light beam was chopped at frequencies of from 50 to 9000 cycles per second, and its intensity was adjusted for each excitation so as to have the same output at 150 cycles per second. The photocell studied was a commercial-type cell from the Continental Electric Company. All curves obtained for the voltage output of the cell as a function of chopping frequency overlap within the accuracy of the experiments; the frequency response of the cell is consequently shown to be independent of the wavelength of the exciting light in the range from the visible up to about 3.6 microns. For longer wavelengths complete curves could not be obtained because of insufficient sensitivity of the cell.

Electronegativity and Work Function. WILLIAM SQUIRE, *Cornell Aeronautical Laboratory.*—The concepts of electronegativity and work function are discussed. From the available data for 54 elements, an empirical relation $W.F. = 1.19 + 1.62\ E.N.$ is found.

Generalized Statistical Mechanics and the Onsager Relations. ALICE THOMPSON AND PETER G. BERGMANN, *Syracuse University.*—In the usual derivation of the so-called Onsager relations in irreversible processes, which state that the cross coefficients connecting noncorresponding forces and rates of change are equal in pairs, irreversible processes are assumed to obey the same laws as fluctuations, in spite of the fact that the structure of the underlying ensembles must be quite different. On the strength of the nonequilibrium ensembles we have called canonical (in a generalized sense), we have succeeded in showing that the Onsager relations hold in the limiting case of near-equilibrium, without reference to fluctuation theory. It turns out that the most general expressions for the cross coefficients which hold irrespective of near-equilibrium are the same as the cross correlations encountered in fluctuation theory.

Spin and Angular Momentum in the General Theory of Relativity.* ROBB THOMSON AND PETER G. BERGMANN, *Syracuse University.*—Ordinarily, the integral of angular momentum in Lorentz-covariant theories is associated with the invariance of the theory with respect to homogeneous Lorentz transformations, just as linear momentum belongs to rigid displacements. In the general theory of relativity, these transformations form subgroups of the group of general coordinate transformations but are without special significance. Nevertheless, it is possible to formulate a set of integrals of the motion which go over into the usual angular momentum when gravitation and space curvature may be disregarded. Spinors have been introduced into the general theory of relativity sometimes directly, sometimes with the help of local quadrupeds ("Beine"). In the latter case, there exists a group of transformations of these local frames of reference that in effect represents a different (homogeneous) Lorentz transformation at each point of space-time. Although this group is empty in the absence of spin fields, a theory that incorporates, e.g., a Dirac field, will yield an integral of the motion which, when properly extended, includes both orbital and spin angular momentum of the fields postulated. This result is of considerable value in our program to close the gap between general relativity and atomic (and nuclear) physical theory.

* Supported by ONR.

On the Lagrangian Formulation of Quantum Theories.* PETER G. BERGMANN, RALPH SCHILLER,† AND JAMES L. ANDERSON,‡ *Syracuse University.*—If the action integral of Feyman-Schwinger is considered an operator, then the requirement that it be stationary with respect to infinitesimal variations of the observables will lead to reasonable "wave equations" only if the class of variations is suitably restricted. We have conjectured that the most logical class of virtual variations is the group of invariant transformations. It can be shown that these requirements, weaker than those postulated by Schwinger, are sufficient to yield all the conservation laws of a given theory, and that the commutation laws follow from the requirement that each of the invariant transformations be generated by its appropriate constant (integral) of the motion. Our conjectured relationships work in both quantum mechanics and quantum field theories and lead to peculiar results in the case of covariant field theories.

* Supported by ONR.
† Now at University of Sao Paulo, Sao Paulo, Brazil.
‡ Now at Rutgers University, New Burnswick, New Jersey.

An Experimental Investigation of the Nucleon Cascade in Water. C. B. A. MCCASKER, H. MESSEL,* D. D. MILLAR,† AND N. A. PORTER, *Dublin Institute for Advanced Studies, Dublin, Ireland.*—The nucleon cascade in water produced by primaries of energy greater than 20×10^9 ev has been examined using an array of Geiger-Müller counters and a 31-channel hodoscope. Over 15,000 showers have been studied. Transition curves for various primary energies, barometric coefficients for various multiplicities and different depths, root mean square lateral spreads, and intensities at different depths are given. The experimental results are compared with the theory of the nucleon cascade developed by Messel and his co-workers. In particular, the variation of lateral spread with depth substantiates their conclusion that the differential cross section for nucleon-nucleon collision at high energies has an exponential form.

* Now at University of Sydney, Sydney, Australia.
† Now at University of Manchester, Manchester, England.

THE AMERICAN INSTITUTE OF PHYSICS

Incorporated

[illegible], N.Y.

[illegible]

[illegible]

[illegible]

THE PHYSICAL REVIEW

Magnetic Analysis of the $A^{37}(p,n)K^{37}$ Reaction
Magnetic Lens Spectrometer Measurements
Discharge Mechanism in Argon Counters
Range Distribution of Sea-Level Mesons
Remarks on Some Questions of Nuclear Structure
Angular Correlations in the Reaction
Interactions of High Energy Nucleons
Pressure, Densities, and Temperatures in
Scattering of Charge Symmetric Particles
Field Emission from Photoconductors
Nuclear Mass Determinations from
Color Centers in Alkali Halides at 2°K
Thermal Resistivity of Superconductors
Pendulum Masses with Applications to
Polarization Correlations of the Gamma-Rays
Spin Echo Measurements of Nuclear
Radiofrequency Spectra of $Li^{6,7}$ in
Resistivity of Lanthanum, Cadmium

High Energy Proton-Proton Scattering
Analysis of the Energy Levels of the
Some Neutron Deficient Rare-Earth
Radiations of Co^{58}
Parallel Spin Stability of an
Ionization Loss and Straggling of Fast
Electron-Neutron Interaction on Deuteron
Cross Section and Angular Distribution of the
Beta-Spectra of P_{32}, P_{33}, and P_{35}
Nuclear Moments of Ta^{181}
Effect of Final State Interactions on Reaction
Some Properties of Superconductors below 1°K
Effect of Charge Symmetry on Nuclear
Elementary Particles at Rest
Specific Heat of Lead in the Temperature
Substitution Spectrometer Study of the
Strong-Focusing Synchrotron with Many

Radial Focusing in Gas Mixer Accelerators

Letters to the Editor:

Spin-Lattice Relaxation in
Spectroscopic Mixing among
Second-Order Effects in

g-Means Theory in Field
Average Hyperfine Coupling of

Statistical Study of the Distribution of
Isothermal Ordering of Cubic
Polarization of the Co^{60} Gamma-Rays
Interference between Compton and

Limit on Secondary C^{14} from
S Wave in Pion-Proton
Magnetostriction of Single
Clausius-Mossotti Equation for
Electronic Structure of the
Bound States and the Interaction
Charge Independence and
Lower Limits for Ionization
Mass of K^0
Angular Distribution of Neutrons
Concept of Spin-Lattice
Relativistic Corrections to

Proceedings of the American Physical Society:

Minutes of the 1953 Summer